Energy Features of Underground Exploitation by Fluid Circulation

Murad S. Abuaisha

SORBONNE UNIVERSITÉ

HABILITATION À DIRIGER DES RECHERCHES

Sciences de la Terre et de l'Univers

Energy Features of Underground Exploitation by Fluid Circulation

---

Author:
Murad ABUAISHA

Defended publicly on July the 10th 2024 in front of the jury composed of:

Christophe Tournassat	Professor, ISTO/CNRS/Université d'Orléans	Reporter
Nicolas Espinoza	Professor, University of Texas at Austin	Reporter
Fabrice Golfier	HDR Lecturer, Université de Lorraine	Reporter
Laetitia Le Pourhiet	Professor, ISTeParis, Sorbonne Université	Examiner
Élie Hachem	Professor, MINES Paris - PSL	Examiner
Christophe Coquelet	Professor, IMT MINES Albi-Carmaux	Examiner
Ahmed Rouabhi	HDR Teacher-Reasercher, MINES Paris - PSL	Examiner

Centre de Géosciences
MINES Paris - PSL

إِلَيْكِ: إِلَيْكِ يَا أُمِّي ...
إِلَيْكِ يَا أُمِّي, يَا آيَتِي الَّتِي لَمْ يَجْعَلْهَا اللهُ لِلْعَالَمِين

"I have read, alas! through philosophy,
medicine and jurisprudence too,
and, to my grief, theology,
with ardent labour studied through.
And here I stand with all my lore,
poor fool no wiser than before."

Goethe/Faust

SORBONNE UNIVERSITÉ

Abstract

Centre de Géosciences
MINES Paris - PSL

Habilitation à Diriger des Recherches

Energy Features of Underground Exploitation by Fluid Circulation

by Murad ABUAISHA

This work presents the geomechanical and thermodynamic aspects related to the problem of exploiting underground energy resources by fluid circulation. The first chapter discusses the thermodynamics of continuous media. The two frameworks of thermodynamics of isotropic fluid mixtures and thermodynamics of multiphase compositional flows in porous media are briefly pointed out. The second chapter treats the problem of hydraulic stimulation of deep geothermal reservoirs. While considering a continuum approach, it investigates hydraulic fracturing effects on impedance and efficiency of thermal recovery from these reservoirs. The chapter continues to scrutinize the technique of hydraulic fracturing, particularly the fluid-injection related induced seismicity. In a continuum-discontinuum framework, it provides a strategy to relate induced seismicity to non-diffusive triggering fronts that encompass most of the seismic cloud.

Since renewable energy is limited to its intermittent nature, this research introduces gas storage in salt caverns as a large-scale storing technique. The increasing energy demands will, however, necessitate frequent utilization of these caverns. The fast cycling, and its subsequent severe mechanical and thermal charges, impose challenges regarding the thermodynamic state within the cavern, and the masses exchanged between the cavern phases. To have precise tracks of cycled gas quantities and to master losses, these challenges have to be considered. This work validates the mathematical models at the laboratory scale, and provides transferring techniques to real-scale applications. Each section provides a precise introduction concerning the discussed problem, and terminates by a conclusion. A general introduction and a review and perspectives are also furnished.

SORBONNE UNIVERSITÉ

Abstract

Centre de Géosciences
MINES Paris - PSL

Habilitation à Diriger des Recherches

Energy Features of Underground Exploitation by Fluid Circulation

by Murad ABUAISHA

Ce travail présente les aspects géomécaniques et thermodynamiques liés à la problématique de l'exploitation des ressources énergétiques souterraines par la circulation de fluides. Dans le premier chapitre, on traite de la thermodynamique des milieux continus. Les deux cadres de la thermodynamique des mélanges fluides isotropes et de la thermodynamique des écoulements multiphasiques et multiconstituants dans les milieux poreux sont brièvement soulignés. Dans le deuxième chapitre, on présente la problématique de la stimulation hydraulique des réservoirs géothermiques profonds. En considérant une approche continue, on étudie les effets de la fracturation hydraulique sur l'impédance et l'efficacité de la récupération de chaleur de ces réservoirs. On continue d'examiner la technique de la fracturation hydraulique, en particulier la sismicité induite liée à l'injection de fluide. Dans un cadre continu-discontinu, on propose une stratégie permettant de relier la sismicité induite aux fronts non-diffusifs englobant la majeure partie des événements sismiques.

Les énergies renouvelables étant intermittentes, cette recherche introduit le stockage des gaz dans les cavités salines comme une technique de stockage à grande échelle. Or, la demande croissante en énergie nécessitera des sollicitations fréquentes de ces cavités. Le cyclage rapide, et les charges mécaniques et thermiques sévères qui en résultent, imposent des défis concernant l'état thermodynamique de la cavité et les masses échangées entre les phases. Pour avoir une trace précise des quantités de gaz cyclées et maîtriser les pertes, ces défis doivent être relevés. Ces travaux valident les modèles mathématiques à l'échelle du laboratoire et permettent de les transférer vers des applications à l'échelle réelle. Chaque section fournit une introduction précise concernant le problème abordé et se termine par une conclusion. Une introduction générale ainsi qu'un bilan et des perspectives sont également fournis.

Acknowledgements

I cannot close these prefatory remarks without expressing a deep feeling of gratitude to Benjamin Loret. Benjamin was not only my PhD supervisor but also a friend who accompanied me during my scientific journey since 2010. I thankfully recognize the favors of all my colleagues at the Center of Geosciences, starting from fellows, to technicians, to postdocs and PhD students. I thank the members of the jury, both reporters and examiners, for having accepted to participate, your presence was much appreciated. I would like to thank our industrial partners who, with fervor, helped us put our theories into real-scale applications.

Contents

Introduction

For the last thirty years there has been a worldwide conscientiousness with regard to the consumption of available energy resources. Such concerns were also accompanied by awareness of the climate change crisis, the emergence of new economic world powers, and the geopolitical conflicts. All of these factors have caused energy prices to raise up bringing a considerable fraction of humanity to energy scarcity. Exploitation of abundant renewable energy resources is seen as the optimum solution to reply to these challenges. However, renewable energy resources are limited to their intermittent nature, and require the development and mastering of a new knowledge. This research is dedicated to studying the geomechanical and thermodynamic aspects pertaining to energy exploitation by underground fluid circulation.

Since I have started my PhD in 2011, I have chosen a research axis that focused on renewable energy exploitation. I began by using the hydraulic fracturing technique to explore its effect on thermal recovery from geothermal systems. I employed the same technique for applications related to shale gas extraction. For the last seven years, I have been working extensively on gas storage in salt caverns. The idea of this work emerged as I felt the need to put the information I collected and gained during developing this research axis in a general context. This work is divided into two main parts: the first part focuses on fluid (liquid) circulation in porous media; and the second part concerns fluid (gas) circulation (cycling) in salt caverns. Even-though the two applications may seem different, the physics behind them is similar.

Chapter one of this work presents the thermodynamic frameworks of fluid flow in continuous media. Both the thermodynamics of fluid mixtures and multi-phase compositional flows in porous media are briefly discussed. The second chapter concerns deep geothermy. Heat extraction from deep reservoirs is challenging in the sense that such reservoirs are impermeable. Hydraulic stimulation, through hydraulic fracturing or chemistry, enhances the reservoir fluid flow capacities leading to lucrative and productive utilization. This research provides a simple continuum modelling approach to perform hydraulic fracturing in a fully coupled therm-hydromechanical framework. A special emphasis is given to the nature of fracture evolution (mode I or mode II), to the used geothermal fluids, and to the impedance and efficiency of thermal recovery. However, public opinion may prevent future large-scale utilization of deep geothermal systems. This is attributed to uncontrolled induced seismicity which is perceived as an unsolicited side effect of geothermal energy exploitation. The development of geothermal systems therefore requires a better control on induced seismicity. For this reason, this work investigates induced seismicity related to fluid injection in a continuum-discontinuum (quasi-static) modelling tactic. Based on the injection information, a seismicity triggering front is predicted giving important information about the range of induced seismicity and hydraulic fracture size.

Clean energy resources are intermittent and production of geothermal energy requires storage, this necessitates the development of large-scale storage techniques. Gas storage in salt caverns is presenting a promising solution. Nevertheless, increasing energy demands entail frequent solicitations of such caverns. Fast charges, mechanical and thermal, impose several challenges that include:

– investigating the widely adopted hypothesis of a uniform thermodynamic state in the cavern, and consequently the precision of the used codes embracing this hypothesis;

– keeping good records of cycled gas quantities, which necessitates studying all possible mass exchanges between the cavern phases.

The third chapter of this work addresses the technology of gas storage in salt caverns while furnishing solutions to the two above mentioned challenges. The research approach/strategy presented in this work has many particularities, of which I may cite:

– the used/developed numerical models are validated by *in situ* or experimental data;

– the experimental setups are designed by common team reflection, and by the help of other research centers of MINES Paris, I may mention the Center of Thermodynamics of Processes (CTP);

– the transfer between laboratory and real applications is done by developing non-dimensional approaches or by adopting some physical simplifications;

– different gases are included in the performed analyses (hydrogen, helium, and carbon dioxide);

– research is conducted for different gas cycling scenarios in salt caverns (daily, weekly, and monthly). However, emphasis is given to fast cycling to reply to the increasing energy demands.

Each section of this work starts by a precise introduction that tackles the particular problem presented, and terminates by a conclusion. A general review and perspectives are offered at the end of this research.

Chapter 1

Thermodynamics of continuous media

The main objective of this chapter is to construct comprehensive thermodynamic frameworks for gas storage in salt caverns and multiphase compositional flows in porous media. Most of physical problems related to earth science and engineering require the employment of robust numerical techniques (Chen, Huan, and Ma, 2006; Kolditz et al., 2012). While improving the numerical methods is a vital topic, the mathematical and physical explanations behind the used models need to be based on thermodynamics. Unlike modelling strategies based on analogy, thermodynamics helps give theoretical and consistent foundations to the used macroscopic equations.

This work applies the principles of thermodynamics of irreversible processes to reply to problems related to the underground exploitation by fluid circulation. Macroscopic thermodynamic descriptions for such applications are explored since decades (Svendsen and Hutter, 1995; Rouabhi et al., 2017; Everett, 1975; Marle, 1982; Hassanizadeh and Gray, 1990). For its clarity, this chapter is based on the work of Rouabhi (2019). An important benefit of this approach is to avoid assuming specific processes at the microscale, only that the studied system is close to equilibrium. This framework is sufficient to introduce macroscopic constitutive laws that verify the second principle of thermodynamics. Physical assumptions can be also expanded to include additional processes.

1.1 Introduction

Let us consider a fluid mixture of q constituents. The total mass of this mixture $\mathcal{M}$ occupying a total volume $\mathcal{V}$ can be written as the sum of the constituent masses $\mathcal{M} = \sum \mathcal{M}_k$. Let $\mathcal{U}$ and $\mathcal{S}$ be the internal energy and entropy of the material in $\mathcal{V}$. If the studied system is closed, the first law of thermodynamics (Gibbs relation) takes the form $d\mathcal{U} = -pd\mathcal{V} + Td\mathcal{S}$. This relation is valid for any infinitesimal transformation of the system, in which the mixture thermodynamic pressure is $p = -\partial_{\mathcal{V}}\mathcal{U}$, and its absolute temperature is $T = \partial_{\mathcal{S}}\mathcal{U}$. If a thermodynamic system changes material with the surrounding, it becomes thermodynamically open which allows us to write the previous law as $d\mathcal{U} = -pd\mathcal{V} + Td\mathcal{S} + \sum \mu_k d\mathcal{M}_k$, where μ_k is the chemical potential of the k constituent in the mixture. All the quantities $\mathcal{U}$, $\mathcal{S}$, $\mathcal{V}$, $\mathcal{M}$ are extensive and do not depend on the size of the considered system. However, the partial derivatives of the internal energy with respect to its variables are intensive quantities that depend on the system size. By applying the Euler's homogeneous function theorem to the Gibbs relation, it is found that $\mathcal{U} = -p\mathcal{V} + T\mathcal{S} + \sum \mu_k \mathcal{M}_k$. By introducing the specific free enthalpy $\mathcal{G} = \mathcal{U} + p\mathcal{V} - T\mathcal{S}$, it is concluded that $\mathcal{G} = \sum \mu_k \mathcal{M}_k$ and $d\mathcal{G} = \mathcal{V}dp - \mathcal{S}dT + \sum \mu_k d\mathcal{M}_k$.

The homogeneous function theorem can be used as well to write the internal energy in terms of its specific quantities $u = -pv + Ts + \sum c_k \mu_k$, with $v = \mathcal{V}/\mathcal{M}$, $s = \mathcal{S}/\mathcal{M}$, and $c_k = \mathcal{M}_k/\mathcal{M}$ being the specific volume, the specific entropy, and the mass concentration of the constituent k. By definition $\sum c_k = 1$ and only $q-1$ concentrations are independent, therefore $\boldsymbol{c} = (c_1, c_2, ..., c_{q-1})$. Equivalently, the specific free enthalpy is $g = \sum \mu_k c_k$. With some manipulation, the Gibbs-Duhem relation is reached $vdp - sdT - \sum c_k d\mu_k = 0$. This relation shows that

when the extensive quantities $\mathcal{S}$, $\mathcal{V}$, $\mathcal{M}_k$ are fixed, the intensive quantities p, T, and μ_k become dependent. Establishing a relation between an extensive quantity and its density is interesting. For any extensive quantity, function of the thermodynamic state, $\Phi(p,T,\mathcal{M}_1,...,\mathcal{M}_q) = \mathcal{M}\varphi$ of the specific density $\varphi(p,T,\boldsymbol{c})$, it is written (Rouabhi, 2019),

$$\varphi(p,T,\boldsymbol{c}) = \sum c_k \bar{\varphi}_k(p,T,\boldsymbol{c}), \tag{1.1}$$

with $\bar{\varphi}_k(p,T,\boldsymbol{c}) = \partial_{\mathcal{M}_k}\Phi(p,T,\mathcal{M}_1,...,\mathcal{M}_q)$.

The first part of this section presents the thermodynamics framework of mixtures of isotropic fluids. The second part discusses the thermodynamics framework of fluid circulation in porous media.

1.2 Thermodynamics framework of mixtures of isotropic fluids

This work proposes a derivation of macroscopic equations for isotropic fluid flows in a continuous medium. It is assumed that local equilibrium applies at an elemental volume (Kondepudi and Prigogine, 2014). A mixture of isotropic fluid contains different phases. To construct thermodynamically compatible relations for any phase, the strategy adopted in this research introduces its thermodynamic potential. Consequently, all remaining state functions can be derived from this potential by using appropriate partial derivatives. For a thermodynamic state characterized by the independent variables $(p,T,\boldsymbol{c})$, the thermodynamic potential is the free enthalpy g, other state functions derive as (Rouabhi et al., 2017),

$$\begin{aligned} v = \partial_p g, \quad C_p = -T\partial_T^2 g, \quad s = -\partial_T g, \\ \mu_q = g - \sum_{j=1}^{q-1} c_j \partial_{c_j} g, \quad \mu_{k\neq q} = \mu_q + \partial_{c_k} g, \end{aligned} \tag{1.2}$$

with C_p being the mixture heat capacity.

The behavior of the mixture is described by its mass density $\rho = \sum c_k \rho_k$, its barycentric velocity $\boldsymbol{v} = \sum c_k \boldsymbol{v}_k$, its temperature T, and its constituent concentrations c_k. The conservation laws that govern the evolution of these fields are expressed macroscopically (Fer, 1971) by the following field equations:

$$\begin{array}{lllll} \text{total mass conservation:} & \dot{\rho} + \rho\,\boldsymbol{\nabla}\cdot\boldsymbol{v} & = & 0; & \text{completed by,} \\ k\text{-component mass conservation:} & \rho\dot{c}_k + \boldsymbol{\nabla}\cdot(\rho\boldsymbol{J}_k) & = & \pi_k; & \forall k = 1,\ldots,q-1, \\ \text{momentum conservation:} & \rho\,\dot{\boldsymbol{v}} - \boldsymbol{\nabla}\cdot\underline{\underline{\boldsymbol{\sigma}}} & = & \rho\,\boldsymbol{g}; & \\ \text{internal energy conservation:} & \rho\,\dot{u} + \boldsymbol{\nabla}\cdot\boldsymbol{\Psi}_u & = & \underline{\underline{\boldsymbol{\sigma}}} : \underline{\underline{\boldsymbol{\nabla}}}\boldsymbol{v} + Q_r; & \\ \text{entropy conservation:} & \rho\,\dot{s} + \boldsymbol{\nabla}\cdot(\boldsymbol{\Psi}_s/T) & = & (Q_r + \varpi)/T; & \end{array} \tag{1.3}$$

where $\boldsymbol{J}_k$ is the diffusive flux of constituent k, π_k is the mass production rate of component k per unit volume due to chemical reactions with the condition $\sum \pi_k = 0$, $\underline{\underline{\boldsymbol{\sigma}}}$ is the mixture stress tensor, $\boldsymbol{g}$ is the gravitational acceleration vector, $\boldsymbol{\Psi}_u$ is the internal energy flux vector, Q_r is the heating source per unit volume, $\boldsymbol{\Psi}_s$ is the entropy flux vector, and ϖ is the volumetric dissipation. For any physical quantity $\mathcal{F}(\boldsymbol{x},t)$, $\dot{\mathcal{F}} = d\mathcal{F}/dt = \partial_t\mathcal{F} + \boldsymbol{v}\cdot\boldsymbol{\nabla}\mathcal{F}$ is the material derivative of $\mathcal{F}$ following the motion of the mixture. The volumetric dissipation can be further expressed as,

$$\varpi = (\underline{\underline{\boldsymbol{\sigma}}} + p\underline{\underline{\boldsymbol{\delta}}}) : \underline{\underline{\boldsymbol{\nabla}}}\boldsymbol{v} - \boldsymbol{\Psi}_s\cdot\boldsymbol{\nabla}T/T - \sum \pi_k\,\bar{\mu}_k - \sum \rho\boldsymbol{J}_k\cdot\boldsymbol{\nabla}\bar{\mu}_k, \tag{1.4}$$

with $\bar{\mu}_k = \mu_k - \mu_q$ ($\bar{\mu}_q = 0$), and,

$$\boldsymbol{\Psi}_s = \boldsymbol{\Psi}_u - \sum \rho \bar{\mu}_k \boldsymbol{J}_k. \tag{1.5}$$

The mathematical relation between the two energy flux vectors $\boldsymbol{\Psi}_s$ and $\boldsymbol{\Psi}_u$ is very important to give a physical meaning to all the physical quantities presented in the fields of the system 1.3. For instance, in case of non-reacting components/no mass production and no diffusion ($\pi_k = 0$ and $\boldsymbol{J}_k = \boldsymbol{0}$), the system behaves as a closed system of a single phase component, and we can simply write $\boldsymbol{\Psi}_u = \boldsymbol{\Psi}_s = \boldsymbol{\psi}$, with $\boldsymbol{\psi} = -\Lambda \boldsymbol{\nabla} T$ being the heat flux vector and Λ is the mixture thermal conductivity (Fer, 1970). Furthermore, the volumetric dissipation becomes $\varpi = (\underline{\underline{\boldsymbol{\sigma}}} + p\underline{\underline{\boldsymbol{\delta}}}) : \underline{\underline{\boldsymbol{\nabla}}} \boldsymbol{v} - \boldsymbol{\psi} \cdot \boldsymbol{\nabla} T / T$ with irreversibilities related only to the presence of velocity and temperature gradients.

Even-though this approach sounds straight forward in the case of a closed system, ensuring a continuous production of entropy ($\varpi \geqslant 0$) becomes more complicated in the case of an open system. In this case, it is convenient to partition the volumetric dissipation into separate irreversibility sources (Rouabhi, 2019; Gelet, Loret, and Khalili, 2012a; Loret and Simões, 2017), where each inequality ($\varpi_n \geqslant 0$) is demanded. The first two dissipation partitions are simple and comparable to the case of a closed system. When the velocity field and the thermodynamic state are homogeneous ($\underline{\underline{\boldsymbol{\nabla}}} \boldsymbol{v} = \underline{\underline{\boldsymbol{0}}}$, $\boldsymbol{\nabla} T = \boldsymbol{0}$, and $\boldsymbol{\nabla} \bar{\mu}_k = \boldsymbol{0}$), the only irreversibility source is attributed to chemical interactions between the constituents $\varpi = \varpi_c = -\sum \pi_k \bar{\mu}_k$. When the thermodynamic state is only homogeneous ($\boldsymbol{\nabla} T = \boldsymbol{0}$ and $\boldsymbol{\nabla} \bar{\mu}_k = \boldsymbol{0}$) without any chemical interactions, the left irreversibility source is intrinsic and related to the viscous dissipation $\varpi = \varpi_i = (\underline{\underline{\boldsymbol{\sigma}}} + p\underline{\underline{\boldsymbol{\delta}}}) : \underline{\underline{\boldsymbol{\nabla}}} \boldsymbol{v}$. However, if the velocity filed is homogeneous without any chemical interactions between constituents ($\underline{\underline{\boldsymbol{\nabla}}} \boldsymbol{v} = \underline{\underline{\boldsymbol{0}}}$ and $\boldsymbol{\nabla} \bar{\mu}_k = \boldsymbol{0}$), the volumetric dissipation of Eq. 1.4 becomes $\varpi = -\boldsymbol{\Psi}_s \cdot \boldsymbol{\nabla} T / T - \sum \rho \boldsymbol{J}_k \cdot \boldsymbol{\nabla} \bar{\mu}_k$. If we consider that the temperature variations between constituents are attributed to pure heat conduction, then we may write,

$$\varpi = \underbrace{-\boldsymbol{\psi} \cdot \boldsymbol{\nabla} T / T}_{\varpi_\psi} \underbrace{- \sum \rho \boldsymbol{J}_k \cdot \boldsymbol{\nabla}_T \bar{\mu}_k}_{\varpi_J}, \tag{1.6}$$

where $\boldsymbol{\nabla}_T$ is the isothermal gradient operator. The introduction of this operator implies that the diffusion velocities contribute to the conjugate heat flux between constituents. Knowing that $\bar{\mu}_k = \partial_{c_k} g(p, T, \boldsymbol{c})$, it is concluded that:

$$\begin{aligned} \boldsymbol{\Psi}_s &= \boldsymbol{\psi} + \sum_{k=1}^{q-1} \rho T \partial_{c_k} s(p, T, \boldsymbol{c}) \boldsymbol{J}_k; \\ \boldsymbol{\Psi}_u &= \boldsymbol{\psi} + \sum_{k=1}^{q-1} \rho \partial_{c_k} h(p, T, \boldsymbol{c}) \boldsymbol{J}_k, \end{aligned} \tag{1.7}$$

with,

$$\varpi = \varpi_c + \varpi_i + \varpi_\psi + \varpi_J, \quad \text{restricted to,} \quad \varpi_c \geq 0,\ \varpi_i \geq 0,\ \varpi_\psi \geq 0,\ \varpi_J \geq 0, \tag{1.8}$$

with these definitions in mind, the internal energy and entropy conservation equations become equivalent. The mathematical problem is to be completed by initial and boundary conditions, and by constitutive laws that relate the secondary unknowns $\{\underline{\underline{\boldsymbol{\zeta}}},\ \pi_k,\ \boldsymbol{\psi},\ \boldsymbol{J}_k\}$ to the primary unknowns $\{\boldsymbol{v},\ \rho,\ T,\ \boldsymbol{c}\}$ while abiding to the second principle of thermodynamics.

The Fourier's heat conduction has been defined earlier, it relates the heat flux vector to the negative temperature gradient through the mixture thermal conductivity ($\boldsymbol{\psi} = -\Lambda \boldsymbol{\nabla} T$). The diffusive flux can be written in terms of the diffusion velocity of the constituent $\boldsymbol{J}_k = -D_k \boldsymbol{\nabla} c_k = c_k(\boldsymbol{v}_k - \boldsymbol{v})$, with D_k being the diffusion coefficient of the constituent k. The Stockes law is used to calculate the stress tensor in the moving mixture undergoing external effects,

$$\underline{\underline{\boldsymbol{\sigma}}} = \underline{\underline{\boldsymbol{\zeta}}} - p\,\underline{\underline{\boldsymbol{\delta}}}, \quad \text{with,} \quad \underline{\underline{\boldsymbol{\zeta}}} = 2\mu\,\underline{\underline{\boldsymbol{\mathcal{E}}}}^d, \tag{1.9}$$

where μ is the mixture dynamic viscosity, and $\underline{\underline{\boldsymbol{\mathcal{E}}}}^d$ is the deviatoric part of the rate of strain tensor $\underline{\underline{\boldsymbol{\mathcal{E}}}} = (1/2)\left(\underline{\underline{\boldsymbol{\nabla}}}\boldsymbol{v} + \underline{\underline{\boldsymbol{\nabla}}}\boldsymbol{v}^{\mathrm{T}}\right)$. The deviatoric part is calculated as $\underline{\underline{\boldsymbol{\mathcal{E}}}}^d = \underline{\underline{\boldsymbol{\mathcal{E}}}} - (1/3)\,\mathrm{tr}(\underline{\underline{\boldsymbol{\mathcal{E}}}})\,\underline{\underline{\boldsymbol{\delta}}}$. If the volumetric dissipation is caused only by a deviatoric mechanism, then $\underline{\underline{\boldsymbol{\mathcal{E}}}}^d = (1/2)\left(\underline{\underline{\boldsymbol{\nabla}}}\boldsymbol{v} + \underline{\underline{\boldsymbol{\nabla}}}\boldsymbol{v}^{\mathrm{T}}\right) - (1/3)(\boldsymbol{\nabla}\cdot\boldsymbol{v})\,\underline{\underline{\boldsymbol{\delta}}}$. Thus, the viscosity stress tensor is defined as,

$$\underline{\underline{\boldsymbol{\zeta}}} = \mu\left(\underline{\underline{\boldsymbol{\nabla}}}\boldsymbol{v} + \underline{\underline{\boldsymbol{\nabla}}}\boldsymbol{v}^{\mathrm{T}}\right) - (2/3)\mu(\boldsymbol{\nabla}\cdot\boldsymbol{v})\,\underline{\underline{\boldsymbol{\delta}}}. \tag{1.10}$$

1.3 Thermodynamics framework of multiphase compositional flows in porous media

There are several thermodynamic approaches that treat multiphase compositional flows in porous media. Generally, such approaches use the same strategy of developing a thermodynamic description at the pore level, and subsequently derive the macroscopic description from it. Linking properly the descriptions at the two levels is challenging. Though most studies use the notion of a length scale to relate the two levels, this length scale appears independently in porous media and continuum thermodynamics. In porous media, it is convenient to consider that the length scale corresponds to the Representative Elementary Volume (REV) (Bear, 1972). In the case of continuum thermodynamics, an elemental volume, that separates between uniform and non-uniform descriptions of the continuum, is used (Kondepudi and Prigogine, 2014). These two scales can be defined differently depending on the structure of the porous medium and the processes taking place inside it. Applying the thermodynamic principles to porous media involves using both length scales, and the way they relate has a considerable effect on the developed macroscopic description.

A porous medium is composed primarily of a deformable solid skeleton in which different fluid species circulate. Indeed, these fluids are composed of several immiscible phases. In this research, the concept of a REV is used. At this macroscale level, it is assumed that the thermodynamic quantities are uniform and that the porous medium is seen as a smooth continuum. At each point of this continuum, the different parts of the porous medium are independently at local equilibrium (or very close to it) and governed by their own equations of state (Gray and Miller, 2014). Let us consider a REV that occupies at time t the domain $\delta\Omega(t)$ with volume $\delta\mathcal{V}$ and mass $\delta\mathcal{M}$. It can be attributed to each phase α in this domain an apparent density ρ^α and a velocity $\boldsymbol{v}^\alpha$. The elementary mass of this phase in $\delta\mathcal{V}$ is $\delta\mathcal{M}_\alpha = \rho^\alpha\delta\mathcal{V} = \rho_\alpha n_\alpha \delta\mathcal{V}$ with $n_\alpha = \delta\mathcal{V}_\alpha/\delta\mathcal{V}$. Consequently, $\delta\mathcal{M} = \sum\delta\mathcal{M}_\alpha$ and $\rho = \sum\rho^\alpha$, with $\rho^\alpha = \rho_\alpha n_\alpha$. Knowing that each phase α is composed of q_α constituents, it can be assigned to each constituent k a density $\rho_{k\alpha}$ and a velocity $\boldsymbol{v}_{k\alpha}$. Thus, it is written that $\rho_\alpha = \sum\rho_{k\alpha}$ and $\boldsymbol{v}_\alpha = \sum\boldsymbol{v}_{k\alpha}$. If the mass of the k constituent in the phase α is $\delta\mathcal{M}_{k\alpha}$, then $\rho_{k\alpha} = \delta\mathcal{M}_{k\alpha}/\delta\mathcal{V}_\alpha$ and $c_{k\alpha} = \delta\mathcal{M}_{k\alpha}/\delta\mathcal{M}_\alpha = \rho_{k\alpha}/\rho_\alpha$ being the mass concentration of the constituent k in the phase α. With these definitions in mind, the conservation equations can be derived.

1.3.1 Conservation equations

The skeleton of the porous medium is considered deformable. For a solid particle initially at the position $\boldsymbol{x}_0$, deformation brings the particle to its a new position $\boldsymbol{x} = \boldsymbol{x}(\boldsymbol{x}_0, t)$ with velocity $\boldsymbol{v}_\sigma = \partial_t\boldsymbol{x}$. The evolution of the volume occupied by this particle through this position change is defined through the transformation Jacobian $\mathcal{J} = \delta\mathcal{V}/\delta\mathcal{V}_0$. All conservation equations are derived while taking the movement of the solid skeleton $\boldsymbol{v}_\sigma$ as a reference. For any physical quantity $\mathcal{F}(\boldsymbol{x}, t)$, $\dot{\mathcal{F}} = d\mathcal{F}/dt = \partial_t\mathcal{F} + \boldsymbol{v}_\sigma\cdot\boldsymbol{\nabla}\mathcal{F}$. For simplicity, in the coming descriptions the following notation is used $\boldsymbol{v}_\sigma = \boldsymbol{v}$. While the phase α is crossing through the elementary area

$\delta\mathcal{A}$ with normal vector $\boldsymbol{n}$, its mass flux is decomposed into two components,

$$\rho^\alpha \boldsymbol{v}_\alpha \cdot \boldsymbol{n}\delta\mathcal{A} = \underbrace{\rho^\alpha \boldsymbol{v}\cdot\boldsymbol{n}\,\delta\mathcal{A}}_{\text{due to solid movement}} + \underbrace{\rho^\alpha(\boldsymbol{v}_\alpha-\boldsymbol{v})\cdot\boldsymbol{n}\,\delta\mathcal{A}}_{\text{due to reltive movement}}, \tag{1.11}$$

which leads to the definition of filtration velocity $\boldsymbol{\omega}^\alpha = n_\alpha(\boldsymbol{v}_\alpha - \boldsymbol{v})$ of the phase α in the porous medium.

All the subsequent conservation laws are written in the Lagrangian form, i.e. with respect to the reference configuration of the solid phase. A local thermal equilibrium is assumed between all phases. The equation of mass conservation takes the form,

$$\bar{\mathcal{J}}\dot{m}^\alpha + \boldsymbol{\nabla}\cdot(\rho_\alpha\boldsymbol{\omega}^\alpha) = \bar{\pi}^\alpha, \quad \text{with,} \quad m^\alpha = \rho^\alpha\mathcal{J}, \tag{1.12}$$

while $\bar{\mathcal{J}} = 1/\mathcal{J}$, and $\bar{\pi}^\alpha$ being the total mass rate of all constituents exchanged through the interfaces of the phase α. If we consider only the solid skeleton of the porous media, Eq. 1.12 becomes $\bar{\mathcal{J}}\dot{m}^\sigma = \bar{\pi}^\sigma$. This indicates that the mass conservation of the solid phase is only verified when there are no chemical reactions contributing to the creation of a solid matter. Equation 1.12 has to be completed with the mass conservation equation of the constituent k,

$$\bar{\mathcal{J}}\dot{m}_k^\alpha + \boldsymbol{\nabla}\cdot(\rho_\alpha c_{k\alpha}\boldsymbol{\omega}^\alpha + \rho_\alpha \boldsymbol{J}_k^\alpha) = \pi_k^\alpha + \bar{\pi}_k^\alpha, \quad \text{with,} \quad m_k^\alpha = c_{k\alpha}m^\alpha, \tag{1.13}$$

and that $\sum_k \pi_k^\alpha = 0$ and $\bar{\pi}^\alpha = \sum_k \bar{\pi}_k^\alpha$.

The momentum conservation equation in the Lagrangian form is expressed as,

$$\sum(\rho^\alpha\dot{\boldsymbol{v}}_\alpha + \bar{\pi}^\alpha\boldsymbol{v}_\alpha) = \boldsymbol{\nabla}\cdot\underline{\underline{\boldsymbol{\sigma}}} + \rho\,\mathfrak{g}, \quad \text{with,} \quad \underline{\underline{\boldsymbol{\sigma}}} = \sum\underline{\underline{\boldsymbol{\sigma}}}^\alpha, \tag{1.14}$$

indicating that forces applied to the porous medium accelerate phase flow and mass convection that results from constituent exchanges on boundaries.

At interfaces, the surface tension between two phases α and β contributes to the conservation of momentum. According to Class, Helmig, and Bastian (2002), Forsyth and Simpson (2012), and Rouabhi (2019), the following macroscopic relation can be used,

$$\langle p_{|\alpha}\rangle_{\mathcal{S}_{\alpha\beta}} - \langle p_{|\beta}\rangle_{\mathcal{S}_{\alpha\beta}} = \langle \pm 2H_{\alpha\beta}\,\gamma_{\alpha\beta}\rangle_{\mathcal{S}_{\alpha\beta}}, \tag{1.15}$$

where $H_{\alpha\beta} = \pm(1/2)\boldsymbol{n}\cdot\boldsymbol{\nabla}_s\cdot(\underline{\underline{\boldsymbol{\delta}}} - \boldsymbol{n}\otimes\boldsymbol{n})$, the surface gradient operator $\boldsymbol{\nabla}_s$ is such that for any function ϕ we get $\boldsymbol{\nabla}_s\phi = (\underline{\underline{\boldsymbol{\delta}}} - \boldsymbol{n}\otimes\boldsymbol{n})\cdot\boldsymbol{\nabla}\phi$, and $\gamma_{\alpha\beta}$ is the surface tension between the two phases α and β. The numerical application of Eq. 1.15 is exhaustive. Usually the surface averaged quantities are replaced by their volume averaged equivalents ($\langle p\rangle_\alpha$ and $\langle p\rangle_\beta$) using a heuristic analogy completed by empirical relations that take temperature and volume fractions into consideration (Rouabhi, 2019).

The internal energy conservation equation is cast in the following form,

$$\bar{\mathcal{J}}\dot{\mathsf{U}} + \boldsymbol{\nabla}\cdot\left(\boldsymbol{\Psi}_u + \sum(\rho_\alpha u_\alpha\underline{\underline{\boldsymbol{\delta}}} - \underline{\underline{\boldsymbol{\sigma}}}_\alpha)\boldsymbol{\omega}^\alpha\right) = Q_r + \underline{\underline{\boldsymbol{\sigma}}} : \underline{\underline{\boldsymbol{\nabla}}}\boldsymbol{v} - \sum\rho_\alpha\boldsymbol{\omega}^\alpha\cdot(\dot{\boldsymbol{v}}_\alpha - \mathfrak{g}), \tag{1.16}$$

with $\underline{\underline{\boldsymbol{\sigma}}}_\alpha = \langle\underline{\underline{\boldsymbol{\sigma}}}\rangle_\alpha$, $\mathsf{U} = \sum\mathsf{U}^\alpha = \sum m^\alpha u_\alpha$, $\boldsymbol{\Psi}_u = \sum\boldsymbol{\Psi}_u^\alpha$, and $Q_r = \sum Q_r^\alpha$. The internal energy density U contained in the REV of the porous medium at time t can be expressed as $\mathcal{U} = \int_{\Omega(t)}\rho^\alpha u_\alpha\,d\mathcal{V} = \int_{\Omega(t=0)}\mathsf{U}\,d\mathcal{V}_0$.

While assuming local thermal equilibrium, the entropy conservation equation takes the form,

$$\bar{\mathcal{J}}\dot{\mathsf{S}} + \boldsymbol{\nabla}\cdot\left(\boldsymbol{\Psi}_s/T + \sum\rho_\alpha s_\alpha\boldsymbol{\omega}^\alpha\right) = (Q_r + \varpi)/T, \tag{1.17}$$

with $\mathsf{S} = \sum\mathsf{S}^\alpha = \sum m^\alpha s_\alpha$, $\boldsymbol{\Psi}_s = \sum\boldsymbol{\Psi}_s^\alpha$, $Q_r = \sum Q_r^\alpha$, and $\varpi = \sum\varpi^\alpha$. The entropy density S

contained in the REV of the porous medium at time t can be expressed as $\mathcal{S} = \int_{\Omega(t)} \rho^\alpha s_\alpha \, d\mathcal{V} = \int_{\Omega(t=0)} \mathsf{S} \, d\mathcal{V}_0$.

1.3.2 Constitutive laws

To verify the second principle of thermodynamics, a clear relation between the two fluxes ($\boldsymbol{\Psi}_u$ and $\boldsymbol{\Psi}_s$) needs to be established. The definition introduced in Sect. 1.2 can not be used directly here due to complexities related to the thermodynamic state of the solid phase. If it is assumed that the solid phase represents a closed system ($\boldsymbol{J}_k^\sigma = \boldsymbol{0}$ and $\bar{\pi}^\sigma = 0$), then the following expressions are reached,

$$\boldsymbol{\Psi}_s^\alpha = \boldsymbol{\Psi}_u^\alpha - \sum \rho_\alpha \bar{\mu}_{k\alpha} \boldsymbol{J}_k^\alpha \;\; (\alpha \neq \sigma), \quad \text{and,} \quad \boldsymbol{\Psi}_s^\sigma = \boldsymbol{\Psi}_u^\sigma. \tag{1.18}$$

If phases flow velocities are very small in the porous medium, viscous stresses can be neglected and the following expression is obtained for phase stresses $\underline{\underline{\boldsymbol{\sigma}}}_\alpha = -p_\alpha \underline{\underline{\boldsymbol{\delta}}} \;\; (\alpha \neq \sigma)$. The macroscopic state variables are used as defined previously (Sect. 1.2), therefore the partial derivatives of the free energy $f_\alpha(\nu_\alpha, T, \boldsymbol{c}_\alpha)$ give,

$$p_\alpha = -\partial_{\nu_\alpha} f_\alpha(\nu_\alpha, T, \boldsymbol{c}_\alpha), \quad s_\alpha = -\partial_T f_\alpha(\nu_\alpha, T, \boldsymbol{c}_\alpha), \quad \text{and,} \quad \bar{\mu}_{k\alpha} = \partial_{c_{k\alpha}} f_\alpha(\nu_\alpha, T, \boldsymbol{c}_\alpha), \tag{1.19}$$

with a rigorous assumption that mass is conserved for the α-phase. Even-though this assumption is correct in the case of an isotropic fluid flow, it is not necessarily the case in porous media (term $\bar{\pi}^\alpha$ of Eq. 1.12).

With these definitions in mind, the two energy equations can be combined to get the partitions of the volumetric dissipation,

$$\varpi = \varpi_c + \varpi_i + \varpi_\psi + \varpi_J + \varpi_\omega, \quad \text{restricted to,} \quad \varpi_c \geq 0, \; \varpi_i \geq 0, \; \varpi_\psi \geq 0, \; \varpi_J \geq 0, \; \varpi_\omega \geq 0. \tag{1.20}$$

This combination indicates that irreversibility sources are mostly due to chemical reactions, volumetric intrinsic dissipation, thermal conduction, constituents diffusion in phases, and phases transport with respect to the solid skeleton. These irreversibility sources can be expressed mathematically as,

$$\begin{aligned}
\varpi_c &= -\sum\!\!\!\!\!\!\diagup \sum \pi_k^\alpha \bar{\mu}_{k\alpha} - \sum\!\!\!\!\!\!\diagup \left(\bar{\pi}^\alpha \left(g_\alpha - \sum c_{k\alpha} \bar{\mu}_{k\alpha} \right) + \sum \bar{\pi}_k^\alpha \bar{\mu}_{k\alpha} \right); \\
\varpi_i &= \bar{\mathcal{J}} \left(T\dot{\mathsf{S}} - \dot{\mathsf{U}} + \mathcal{J} \underline{\underline{\boldsymbol{\sigma}}} : \underline{\underline{\boldsymbol{\nabla}}} \boldsymbol{v} + \sum\!\!\!\!\!\!\diagup g_\alpha \dot{m}^\alpha + \sum\!\!\!\!\!\!\diagup \sum m^\alpha \bar{\mu}_{k\alpha} \dot{c}_{k\alpha} \right); \\
\varpi_\psi &= -\boldsymbol{\psi} \cdot \boldsymbol{\nabla} T / T; \\
\varpi_J &= -\sum\!\!\!\!\!\!\diagup \sum \rho_\alpha \boldsymbol{J}_k^\alpha \cdot \boldsymbol{\nabla}_T \bar{\mu}_{k\alpha}, \quad \text{and;} \\
\varpi_\omega &= -\sum\!\!\!\!\!\!\diagup \rho_\alpha \boldsymbol{\omega}^\alpha \cdot \left(\boldsymbol{\nabla} g_\alpha + s_\alpha \boldsymbol{\nabla} T - \sum \bar{\mu}_{k\alpha} \boldsymbol{\nabla} c_{k\alpha} + \dot{\boldsymbol{v}}_\alpha - \boldsymbol{\mathfrak{g}} \right),
\end{aligned} \tag{1.21}$$

with $\boldsymbol{\psi} = \boldsymbol{\Psi}_s + \sum\!\!\!\!\!\!\diagup \sum \rho_\alpha T \partial_T \bar{\mu}_{k\alpha} \boldsymbol{J}_k^\alpha$ and $g_\alpha(p_\alpha, T, \boldsymbol{c}_\alpha)$ being the specific free enthalpy of the α-phase.

These volumetric dissipations can be used to derive the needed constitutive laws while ensuring a continuous production of entropy (Eq. 1.20). The Fourier's law of heat conduction is adopted to ensure the positivity of ϖ_ψ,

$$\boldsymbol{\psi} = -\underline{\underline{\boldsymbol{\Lambda}}} \cdot \boldsymbol{\nabla} T, \tag{1.22}$$

with $\underline{\underline{\boldsymbol{\Lambda}}}$ being the effective thermal conductivity tensor of the porous medium.

The positivity of ϖ_ω is ensured through the generalization of the Darcy's law for every phase α,

$$\boldsymbol{\omega}^\alpha = -\frac{\underline{\underline{\boldsymbol{k}}}_\alpha}{\mu_\alpha} \cdot \Big(\boldsymbol{\nabla} p_\alpha + \rho_\alpha (\dot{\boldsymbol{v}} - \mathfrak{g}) \Big), \tag{1.23}$$

with $\underline{\underline{\boldsymbol{k}}}_\alpha$ being the permeability tensor of the porous medium occupied by the α-phase, and μ_α is the dynamic viscosity of the α-phase.

For a binary mixture, the positivity of ϖ_J can be assured if the dissolved constituent has a poor concentration that it does not affect the specific volume of the α-phase ($\partial_c \nu_\alpha \approx 0$). Consequently, a relation similar to the Fickian diffusion in binary mixtures can be used where the reference velocity is the barycentric,

$$\boldsymbol{J} = -\underline{\underline{\boldsymbol{D}}}_\alpha \cdot \boldsymbol{\nabla} c, \tag{1.24}$$

with $\underline{\underline{\boldsymbol{D}}}_\alpha$ being the diffusion coefficient of the constituent k in the α-phase.

The positivity of ϖ_c is assured by considering the case of two phases α and β that exchange a single constituent k,

$$\varpi_c = \bar{\pi}_k^\alpha (\mu_{k\beta} - \mu_{k\alpha}), \tag{1.25}$$

indicating the difference between chemical potentials of this constituent in the two phases. By introducing a coefficient $\varrho_k^{\alpha\beta} \geq 0$ such that Eq. 1.25 is written as $\varrho_k^{\alpha\beta} \bar{\pi}_k^\alpha = \mu_{k\beta} - \mu_{k\alpha}$, the positivity of ϖ_c is ensured. When the two chemical potentials are equal $\varrho_k^{\alpha\beta} = 0$, a phase change without volumetric dissipation takes place.

The positivity of the volumetric intrinsic dissipation ϖ_i is ensured through the development of the solid skeleton state laws. If the solid skeleton deforms elastically, neglecting the volumetric intrinsic dissipation $\varpi_i = 0$ leads us to the following definition,

$$\dot{\mathsf{G}}^\sigma = \underline{\underline{\boldsymbol{\Pi}}} : \dot{\underline{\underline{\boldsymbol{\Delta}}}} - \mathsf{S}^\sigma \dot{T} - \sum n_\alpha \mathcal{J} \dot{p}_\alpha, \tag{1.26}$$

where the term $\underline{\underline{\boldsymbol{\Pi}}} : \dot{\underline{\underline{\boldsymbol{\Delta}}}}$ reflects the contribution of $\mathcal{J} \underline{\underline{\boldsymbol{\sigma}}} : \underline{\underline{\boldsymbol{\nabla}}} \boldsymbol{v}$ in Eq. 1.21_2. The symmetric Piola-Kirchoff tensor is $\underline{\underline{\boldsymbol{\Pi}}} = \mathcal{J} \underline{\underline{\boldsymbol{F}}}^{-1} \underline{\underline{\boldsymbol{\sigma}}} \underline{\underline{\boldsymbol{F}}}^{-T}$, the Cauchy Green tensor is $\underline{\underline{\boldsymbol{\Delta}}} = (\underline{\underline{\boldsymbol{F}}}^T \underline{\underline{\boldsymbol{F}}} - \underline{\underline{\boldsymbol{\delta}}})/2$, with $\underline{\underline{\boldsymbol{F}}}$ being the macroscopic transformation gradient of the solid skeleton. The free enthalpy of the solid skeleton is $\mathsf{G}^\sigma = \mathsf{F}^\sigma - \sum n_\alpha \mathcal{J} p_\alpha$, with $\mathsf{F}^\sigma = m^\sigma f_\sigma$ being the free energy density of the solid skeleton.

A thermodynamic potential $\mathsf{G}^\sigma(\underline{\underline{\boldsymbol{\Delta}}}, T, \boldsymbol{P})$ can be defined with the following set of independent state variables $(\underline{\underline{\boldsymbol{\Delta}}}, T, \boldsymbol{P})$, with $\boldsymbol{P} = (p_\alpha, p_\beta, ..., p_\omega)$ being the set of present fluid phase pressures. Therefore, Eq. 1.26 should be satisfied for every variation of the thermodynamic state,

$$\underline{\underline{\boldsymbol{\Pi}}} = \partial_{\underline{\underline{\boldsymbol{\Delta}}}} \mathsf{G}^\sigma(\underline{\underline{\boldsymbol{\Delta}}}, T, \boldsymbol{P}), \quad \mathsf{S}^\sigma = -\partial_T \mathsf{G}^\sigma(\underline{\underline{\boldsymbol{\Delta}}}, T, \boldsymbol{P}), \quad n_\alpha \mathcal{J} = -\partial_{p_\alpha} \mathsf{G}^\sigma(\underline{\underline{\boldsymbol{\Delta}}}, T, \boldsymbol{P}). \tag{1.27}$$

The macroscopic state laws of the solid skeleton are defined through the two Eqs 1.19 and 1.27, that relate the state variables $(\nu_\alpha, T, \boldsymbol{c}_\alpha)$ and $(\underline{\underline{\boldsymbol{\Delta}}}, T, \boldsymbol{P})$ to their associate equivalents $(p_\alpha, s_\alpha, \bar{\mu}_{k\alpha})$ and $(\underline{\underline{\boldsymbol{\Pi}}}, \mathsf{S}^\sigma, n_\alpha \mathcal{J})$.

The heat equation (Eq. 1.17) can be written in an explicit form ready to be used in the engineering applications. According to Rouabhi (2019), the heat equation of multiphase compositional flows in elastically deformable porous media is cast in the following form,

$$\begin{aligned} &\rho C_p \dot{T} + \sum \left[\left(\frac{\rho^\sigma}{\rho_0^\sigma} (\underline{\underline{\boldsymbol{\chi}}} : \underline{\underline{\boldsymbol{\kappa}}}_\alpha - \chi_{n\alpha}) - \frac{\rho^\alpha}{\rho_\alpha} \chi_{p\alpha} \right) T \dot{p}_\alpha + \boldsymbol{\omega}^\alpha \cdot \left(\rho_\alpha C_{p\alpha} \boldsymbol{\nabla} T - \chi_{p\alpha} T \boldsymbol{\nabla} p \right) \right] \\ &+ \frac{\rho^\sigma}{\rho_0^\sigma} T \underline{\underline{\boldsymbol{\chi}}} : \dot{\underline{\underline{\boldsymbol{\Pi}}}} = \varpi_\omega + Q_r + \boldsymbol{\nabla} \cdot (\underline{\underline{\boldsymbol{\Delta}}} \cdot \boldsymbol{\nabla} T) - \sum \sum \left(\bar{\pi}_k^\alpha \bar{h}_{k\alpha} + \pi_k^\alpha \partial_{c_{k\alpha}} h_\alpha + \rho_\alpha \boldsymbol{J}_k^\alpha \cdot \boldsymbol{\nabla} (\partial_{c_{k\alpha}} h_\alpha) \right), \end{aligned} \tag{1.28}$$

with:

- ρ_0^σ being the initial density of the solid skeleton;
- $\underline{\underline{\boldsymbol{\chi}}}$ being the second order tensor of volumetric thermal expansion. It relates linearly the increments of the strain tensor $\underline{\underline{\boldsymbol{\Delta}}}$ to any temperature increment at constant stresses and phase pressures;
- $\rho C_p = \rho^\sigma C_\sigma + \sum \rho^\alpha C_{p\alpha}$, where the heat capacity at constant stresses and fluid pressures is $C_\sigma = C_\Delta + (1/\rho_0^\sigma) T \underline{\underline{\boldsymbol{\chi}}} : \underset{\sim}{\boldsymbol{H}} : \underline{\underline{\boldsymbol{\chi}}}$. Noting that C_Δ is a scalar coefficient that corresponds to a mass heat capacity at constant strains and phase pressures, and $\underset{\sim}{\boldsymbol{H}}$ is the fourth order elasticity tensor of Hooke that relates linearly the increments of the stress tensor $\underline{\underline{\boldsymbol{\Pi}}}$ to any increment of the strain tensor $\underline{\underline{\boldsymbol{\Delta}}}$ at constant temperature and phase pressures (it is the drained isothermal elasticity modulus);
- $\underline{\underline{\boldsymbol{\kappa}}}_\alpha$ being the second order tensor of the hydro-mechanical coupling. It relates linearly the increments of the stress tensor $\underline{\underline{\boldsymbol{\Pi}}}$ to any α-phase pressure increment at constant temperature, strains, and phase pressure p_β ($\beta \neq \alpha$);
- $\chi_{n\alpha}$ being a scalar coefficient that relates linearly the increments of $n_\alpha \mathcal{J}$ to any increment of the temperature at constant strains and phase pressures;
- for any phase α, the specific entropy can be expressed in terms of the state variables $(p_\alpha, T, \boldsymbol{c}_\alpha)$,
$$\rho^\alpha T \dot{s}_\alpha = -\frac{\rho^\alpha}{\rho_\alpha} T \chi_{p\alpha} \dot{p}_\alpha + \rho^\alpha C_{p\alpha} \dot{T} + \sum \rho^\alpha T (\partial_{c_{k\alpha}} s_\alpha) \dot{\boldsymbol{c}}_{k\alpha}, \tag{1.29}$$
from which the heat capacity of the α-phase at constant pressure and composition is $C_{p\alpha} = T \partial_T s_\alpha(p_\alpha, T, \boldsymbol{c}_\alpha)$, and the volumetric thermal expansion at constant pressure and composition is $\chi_{p\alpha} = -\partial_T \rho_\alpha(p_\alpha, T, \boldsymbol{c}_\alpha)/\rho_\alpha$; and,
- $\bar{h}_{k\alpha}(p_\alpha, T, \boldsymbol{c}_\alpha) = h_\alpha + \partial_{c_{k\alpha}} h_\alpha - \sum c_{j\alpha} \partial_{c_{j\alpha}} h_\alpha$, with h_α being the specific enthalpy of the α-phase.

These coefficients, mostly of different tensorial nature, stem from the partial derivatives of G^σ. This heat equation is derived while considering the solid skeleton as a closed thermodynamic system ($\dot{m}^\sigma = \bar{\pi}^\sigma = 0$). The intrinsic volumetric dissipation is set equal to zero ($\varpi_i = 0$), and the Fourier's heat conduction law is adopted.

The final part of this chapter presents the Lagrangian derivatives of Eq. 1.27,

$$\begin{aligned} \dot{\underline{\underline{\boldsymbol{\Pi}}}} = \underset{\sim}{\boldsymbol{H}} : (\dot{\underline{\underline{\boldsymbol{\Delta}}}} - \underline{\underline{\boldsymbol{\chi}}} \dot{T}) + \sum \underline{\underline{\boldsymbol{\kappa}}}_\alpha \dot{p}_\alpha, \quad \dot{\mathsf{S}}^\sigma &= \underset{\sim}{\boldsymbol{H}} : \underline{\underline{\boldsymbol{\chi}}} : \dot{\underline{\underline{\boldsymbol{\Delta}}}} + \rho_0^\sigma C_\Delta \dot{T}/T - \sum \chi_{n\alpha} \dot{p}_\alpha, \\ \frac{d}{dt}(n_\alpha \mathcal{J}) &= \underline{\underline{\boldsymbol{\kappa}}}_\alpha : \dot{\underline{\underline{\boldsymbol{\Delta}}}} - \chi_{n\alpha} \dot{T} + \sum \bar{M}_{\alpha\beta} \dot{p}_\beta, \end{aligned} \tag{1.30}$$

with $\bar{M}_{\alpha\beta} = 1/M_{\alpha\beta}$ being a scalar coefficient that linearly relates an increment of $n_\alpha \mathcal{J}$ to an increment of the pressure p_β of the phase β in any evolution at constant temperature, deformation and fluid pressures p_γ ($\gamma \neq \beta$). The coefficients $M_{\alpha\beta}$ form the components of a symmetric matrix.

Chapter 2

Fluid circulation in porous media

The first part of this chapter addresses the technique of hydraulic fracturing for thermal recovery form geothermal systems. Aspects related to thermal efficiency, impedance, and effect of used geothermal fluids are briefly discussed. In the second part, hydraulic fracturing for applications related to oil an gas industry is presented, with a special emphasis on the non-diffusive induced seismicity triggering fronts.

2.1 A continuum approach to simulate fluid circulation in hydraulically stimulated geothermal reservoirs

In the context of energy transition, thermal recovery from Hot Dry Rock (HDR) reservoirs is becoming an alternative to grey energies (Turcotte and Schubert, 2002; Bruel, 1995a; Bruel, 1995b). Thermal extraction from geothermal systems is achieved by injecting cold fluids into deep reservoirs where the temperature gradient is favorable. The retrieved geothermal fluid is either used directly for heating purposes, or indirectly in generating electricity. The economic viability of the recovery process is controlled by crucial factors that include the evolution of the reservoir pressure, of the effective stresses, and of the fluid losses (Bruel, 1995a; Bruel, 1995b). Permeability changes and irreversible processes of thermo-mechanical nature may also play a significant role in the overall behavior of the HDR reservoirs (Papanastasiou, 1999).

Modern geothermal projects are nowadays focusing on enhancing the permeability of the reservoirs, the so-called Enhanced Geothermal Systems (EGS) (Jupe et al., 1995). Geothermal fluids are injected with high flow rates that the assumption of a time-independent permeability becomes improper. Extreme thermo-hydromechanical changes are expected to take place near the injection well. Indeed, such abrupt changes cause fractures to evolve and to connect and permeability to increase in a highly heterogeneous manner. The increase in HDR reservoir permeability due to hydraulic fracturing is bound to affect the thermal recovery process.

Hydraulic fracturing has been used for years to enhance oil and gas recovery (Fjaer et al., 2008). However, for heat recovery from geothermal reservoirs, a few key points should be emphasized:

- thermal effects on the fracturing process are quantitatively significant. They typically reduce the fracturing pressure by 50% or more;
- unlike simulations of drilling induced fractures, the length over which the permeability should be enhanced encompasses several hundred meters. The initial heterogeneities due to preexisting faults certainly attract and modify the enhancement that would develop in an otherwise homogeneous formation. Re-activation of these faults *alone* is to be avoided as the process would easily produce shortcuts and render the circulation paths inefficient. Therefore, even if large-scale spatial heterogeneities are unavoidable, a significant portion of the reservoir volume, where the fracture network can be considered homogeneous, should be sought;

– modeling of drilling induced fractures in petroleum engineering in a finite element context insists on creating a few fractures, typically extending over a borehole diameter, from existing singularities around the well based on numerically enhanced strain or pressure fields and cohesive fracture tricks. Such an approach is not viable in a geothermal context: indeed, as already indicated, a) the fracture network should be more homogeneously spread; b) the length scale is orders of magnitude larger; and c) critically, the width of the fractures is of capital importance for the permeability.

For these reasons, this study provides a continuum modelling approach for hydraulic fracturing in a thermo-hydromechanical framework. The Finite Element Method (FEM) is used, and fractures and their spatial evolutions are translated into spatial permeability evolutions.

2.1.1 Hydraulic fracturing in a thermo-hydromechanical framework

Hydraulic fracturing is addressed in a thermo-hydromechanical framework. As a key ingredient to this framework, a simple Hydraulic Fracturing Model (HFM) based on an opening mode of fracture evolution (Mode I), is used in a first step. The model is next modified to account for the influence of the deviatoric stress. At any time and any geometrical point, the state of fracture is embodied in a fabric that includes both the actual fracture length and actual fracture width in all directions of space. The local current anisotropic permeability tensor, which describes the evolving permeability of the fractured medium, is obtained by directional integration of the updated fracture fabric.

The fracture model is used to simulate circulation tests between an injection well and two production wells in a simplified geometrical setting. Field data from several references are collected to validate the numerical simulations. The effect of hydraulic fracturing on the designing characteristics of HDR reservoirs, primarily impedance and efficiency, is discussed based on the simulations (Grecksch et al., 2003; Jupe et al., 1995). The field record of the Soultz-sous-Forêts geothermal site presented in Bruel (1995b) indicates that hydraulic fracturing affects significantly the efficiency of the thermal extraction process. However, a minimal size of HDR reservoirs is required to ensure efficient thermal extraction and long-term low impedance (Jupe et al., 1995).

This section aims at studying the effect of hydraulic fracturing on the impedance and efficiency of HDR reservoirs using finite element simulations which are correlated to field data when available. It also discusses the effect of temperature change on the viscosity of geothermal fluids, and the subsequent implications on the hydraulic fracturing process and the resulting impedance and efficiency. The fracturing models, with and without a temperature-dependent viscosity, are implemented in a domestic Fortran 90 finite element code and the simulations, for the same reservoir, are systematically compared. Some designing considerations, in terms of injection pressure or flow rate, are included as well as issues pertaining to the stability of the wellbores.

2.1.1.1 Thermo-hydromechanical framework

The thermodynamics framework of this section features a single-phase single-constituent fluid seeping through an elastically deformed porous medium. Even-though the characteristic time of heat diffusion in the rock matrix is significantly larger than the characteristic time of heat propagation by convection in the fractures, the present study assumes Local Thermal Equilibrium (LTE). The mechanical response of a poroelastic medium undergoing thermal changes while in LTE is governed by two constitutive equations. The Biot's effective stress tensor of the mixture $\underline{\underline{\boldsymbol{\sigma}}} + \kappa \underline{\underline{\boldsymbol{\delta}}}$ expresses in terms of the strain tensor $\underline{\underline{\boldsymbol{\varepsilon}}}$ and the temperature departure

$\theta = T - T_0$ with respect to a reference T_0 as (McTigue, 1986),

$$\underline{\underline{\boldsymbol{\sigma}}} + \kappa p \underline{\underline{\boldsymbol{\delta}}} = 2G\underline{\underline{\boldsymbol{\varepsilon}}} + \frac{2G\nu}{1-2\nu}\mathrm{tr}(\underline{\underline{\boldsymbol{\varepsilon}}})\underline{\underline{\boldsymbol{\delta}}} - K\chi_{p\sigma}\theta\underline{\underline{\boldsymbol{\delta}}}, \tag{2.1}$$

where $\underline{\underline{\boldsymbol{\sigma}}}$ is the total stress tensor, p is the pore fluid pressure, $\mathrm{tr}(\underline{\underline{\boldsymbol{\varepsilon}}})\underline{\underline{\boldsymbol{\delta}}}$ is the volumetric strain, G is the shear modulus, ν is the drained Poisson's ratio, $\kappa = 1 - K/K_\sigma$ is the Biot's coefficient, K is the drained bulk modulus, K_σ is the bulk modulus of the solid constituent, and $\chi_{p\sigma}$ is the volumetric thermal expansion coefficient of the solid. Sign convention is that compressive stresses and strains are negative.

The change of the fluid mass content,

$$\tilde{m} = \kappa\mathrm{tr}(\underline{\underline{\boldsymbol{\varepsilon}}}) + \frac{p}{M} - \bar{\chi}_p\theta, \tag{2.2}$$

involves mechanical, fluid, and thermal contributions, with coefficients,

$$\frac{1}{M} = \frac{\kappa}{K_\sigma} + n_\lambda\left(\frac{1}{K_\lambda} - \frac{1}{K_\sigma}\right), \tag{2.3}$$

and $\bar{\chi}_p = \kappa\chi_{p\sigma} + n_\lambda(\chi_{p\lambda} - \chi_{p\sigma})$, that features the volumetric thermal expansion coefficient of the fluid $\chi_{p\lambda}$, the bulk modulus of the fluid K_λ, and the reference porosity of the porous medium n_λ (porous volume is full of the single phase fluid, hence $n_\sigma = 1 - n_\lambda$). The subscripts σ and λ refer to the solid and fluid phases respectively.

Two additional constitutive equations are needed to define the transport of fluid and transfer of heat. The first equation features the Darcy's law, that describes the seepage of the fluid through the porous medium. It relates the apparent fluid flux relative to the solid skeleton $\boldsymbol{\omega}$ to the effective pressure gradient $\boldsymbol{\nabla} p - \rho_\lambda \mathfrak{g}$,

$$\boldsymbol{\omega} = \boldsymbol{q} = n_\lambda(\boldsymbol{v}_\lambda - \boldsymbol{v}) = -\frac{\underline{\underline{\boldsymbol{k}}}}{\mu}\cdot(\boldsymbol{\nabla} p - \rho_\lambda \mathfrak{g}), \tag{2.4}$$

where $\underline{\underline{\boldsymbol{k}}}$ is the permeability tensor of the mixture, μ is the fluid dynamic viscosity, ρ_λ is the intrinsic fluid density, and $\mathfrak{g} = \mathfrak{g}\boldsymbol{e}$ with $\mathfrak{g}$ being the gravitational acceleration and $\boldsymbol{e}$ the unit vertical vector directed downwards. According to Fourier's law of heat conduction, the heat flux $\boldsymbol{\psi}$ is aligned with the negative of the temperature gradient $\boldsymbol{\nabla}\theta$,

$$\boldsymbol{\psi} = -\Lambda\boldsymbol{\nabla}\theta, \tag{2.5}$$

since the porous medium is in local thermal equilibrium, the effective thermal conductivity $\Lambda = n_\sigma\Lambda_\sigma + n_\lambda\Lambda_\lambda$ is obtained by volume averaging over the species. Though this analysis focuses on the evolving anisotropy of the permeability tensor, it is convenient to consider an isotropic thermal conductivity of the solid.

The displacement vector, pore pressure, and temperature satisfy three field equations:

$$\begin{aligned}
&\text{balance of momentum of the whole mixture :} && \boldsymbol{\nabla}\cdot\underline{\underline{\boldsymbol{\sigma}}} + \rho\mathfrak{g} = \boldsymbol{0};\\
&\text{balance of mass of the fluid :} && \boldsymbol{\nabla}\cdot\boldsymbol{q} + \frac{\partial\tilde{m}}{\partial t} = 0;\\
&\text{balance of energy of the whole mixture :} && \boldsymbol{\nabla}\cdot\boldsymbol{\psi} + \rho C_v\frac{\partial\theta}{\partial t} + \rho_\lambda C_{p\lambda}\boldsymbol{q}\cdot\boldsymbol{\nabla}\theta = 0.
\end{aligned} \tag{2.6}$$

Here $\rho = n_\sigma\rho_\sigma + n_\lambda\rho_\lambda$ is the mass density of the mixture. The heat storage contribution is expressed in terms of the volumetric isochoric heat capacity of the mixture, $\rho C_v = n_\sigma\rho_\sigma C_{v\sigma} +$

$n_\lambda \rho_\lambda C_{v\lambda}$, which is obtained by volume averaging over the species. The energy equation describes heat convection due to fluid seepage through the solid skeleton introduced by the isobaric heat capacity of the fluid $\rho_\lambda C_{p\lambda} = \rho_\lambda C_{v\lambda} + K_\lambda \chi_{p\lambda}^2 T$. The convective term can by no means be neglected in the context of geothermal reservoirs. Therefore, the equation of balance of energy can *not* be decoupled from the system of equations and solved independently. This thermo-hydromechanical framework is integrated into a Fortran 90 domestic finite element code. All details of matrices development, combination, and solving by several time integration schemes are documented in AbuAisha (2014) and AbuAisha, Loret, and Eaton (2016).

2.1.1.2 Mode I hydraulic fracturing model

This section provides the basic elements for a fracturing model (HFM) which is capable of ensuring a directionally stable mode I of fracture evolution in a fully coupled thermo-hydromechanical framework. Let us consider a group of penny-shaped fractures of average length ℓ and arbitrary normal direction $\boldsymbol{n}$ in the horizontal plane (x, y) around a borehole. If the borehole pressure is gradually increased to a point the normal effective stress $\sigma'_n = \boldsymbol{n} \cdot \underline{\underline{\boldsymbol{\sigma}}}' \cdot \boldsymbol{n}$ (at the fracture tip) becomes tensile and exceeds the limit of material tensile strength, the group of fractures starts propagating and consequently the average aperture increases. To track the evolution of the average length ℓ of a group of fractures in direction $\boldsymbol{n}$, a simple criterion is proposed,

$$F(\sigma'_n, \ell) = f(\ell)\, \sigma'_n \sqrt{\pi \ell} - K_{Ic} = 0, \tag{2.7}$$

where K_{Ic} is mode I fracture toughness of the rock, $f(\ell)$ is a positive scalar valued function which controls the stability of fracture propagation (Shao, Zhou, and Chau, 2005),

$$f(\ell) = \eta \begin{cases} \dfrac{\ell_f}{\ell}, & \ell < \ell_f; \\ 1, & \ell \geq \ell_f, \end{cases} \tag{2.8}$$

with ℓ_f denoting the critical fracture length for accelerated coalescence of fractures. In this study fracture healing or macroscopic damage are not considered and fracture length cannot grow beyond ℓ_f. The parameter η is the fracture growth stabilizing parameter. While $\ell < \ell_f$ fractures begin to propagate reflecting the relaxation of local tensile stresses as fractures grow away from zone of stress concentration. For $\ell \geq \ell_f$, the function $f(\ell)$ reaches an asymptotic value as fractures coalesce and damage localizes. Based on physical considerations, authors like Klimczak et al. (2010) and Shao, Zhou, and Chau (2005) and Papanastasiou and Thiercelin (1993) have related the fracture aperture to fracture face mismatch and local grain matrix interaction during fracture growth. Here, the fracture aperture w is taken as an increasing power function of the fracture length ℓ, i.e. $w(m) = 0.0002\, \ell^{0.25}$ (m) (AbuAisha, Loret, and Eaton, 2016).

The philosophy of integrating this fracture model into the developed thermo-hydromechanical framework starts by assuming that the reservoir has preexisting fractures distributed homogeneously over its volume. Once fluid injection starts, the state of effective stresses on each fracture group changes. Each Gauss point of the finite element mesh can be seen as a borehole[1] surrounded by fractures in all possible directions (Fig. 2.1). Solving for the thermo-hydromechanical framework gives the effective stresses at each Gauss point which can be substituted into the fracture criterion (Eq. 2.7) to get the updated length and aperture.

Knowing the fracture length $\ell(\boldsymbol{n})$ and aperture $w\big(\ell(\boldsymbol{n})\big)$ in the arbitrary direction $\boldsymbol{n}$, the local velocity field is calculated by implementing the Navier-Stokes equation for laminar flow between two parallel plates. The anisotropic permeability tensor, which is provided by the

[1] The radius of the borehole is assumed very small compared to the dimensions of the Boundary Value Problem (BVP).

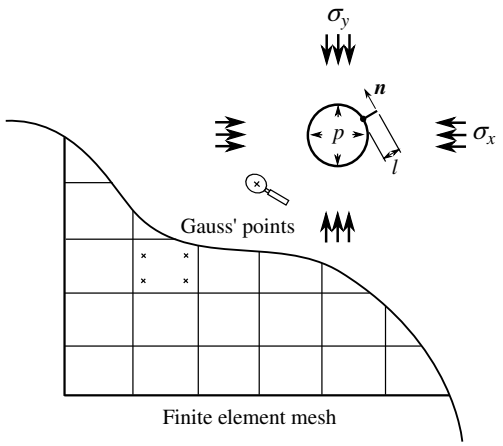

FIGURE 2.1: Integrating the fracturing model into the thermo-hydromechanical framework. Each Gauss point is seen as a borehole surrounded by preexisting fractures in all possible space directions.

fractures, is calculated by averaging the individual Poiseuille flows over all the directions of the space, i.e. by integrating over the unit sphere $\mathcal{S}$,

$$\underline{\underline{\boldsymbol{k}}}_c = \frac{1}{48}\frac{N}{\mathcal{V}}\int_{\mathcal{S}} C(\ell(\boldsymbol{n}))\, w\big(\ell(\boldsymbol{n})\big)^3\, \ell(\mathbf{n})^2\, (\underline{\underline{\boldsymbol{\delta}}} - \boldsymbol{n}\otimes\boldsymbol{n})\, d\mathcal{A}(\boldsymbol{n}), \tag{2.9}$$

where $N/\mathcal{V}$ is the fracture density (number of fractures N in the volume $\mathcal{V}$). The connectivity function $C(\boldsymbol{n})$,

$$C(\ell(\boldsymbol{n})) = c_c\,\frac{\ell(\boldsymbol{n}) - \ell_0}{\ell_f - \ell_0}, \tag{2.10}$$

indicates that connection between fractures increases as they grow in size from the initial length ℓ_0 to the final length ℓ_f, with c_c being a material constant. The overall permeability tensor of the fractured medium is composed of two parts: the initial permeability tensor denoted by $\underline{\underline{\boldsymbol{k}}}_0$ due to the initial porosity, and the fracture induced permeability tensor denoted by $\underline{\underline{\boldsymbol{k}}}_c$. The flows in the two cavities are assumed to take place in parallel and the total permeability tensor is obtained by summation $\underline{\underline{\boldsymbol{k}}} = \underline{\underline{\boldsymbol{k}}}_0 + \underline{\underline{\boldsymbol{k}}}_c$.

The method is numerically demanding that it requires an important spatial discretization to get a sufficient number of the vectors $\boldsymbol{n}$ to ensure a smooth evolution of the directional quantities. Figure 2.2 shows how the directional evolution of a fracture length is traced by spatial discretization.

Fractures are assumed to be penny-shaped and their lengths can grow in the three dimensions following the stress state evolution at each Gauss point.

2.1.1.3 Fracture initiation and wellbore stability

Once injection into the reservoir starts, the wellbore pressure increases and the rock formation cools down leading to more tensile effective stresses on the fractures. Knowing the initial geostatic conditions of the reservoir, the wellbore excess pressure needed to start hydraulic fracturing can be calculated. For a vertical borehole penetrating a rock formation with homogeneous and isotropic elastic and transport properties, the excess borehole pressure $p_b^{HF} - p_r$ to start fracturing parallel to the major principal stress depends on the presence of a mud cake and on the range of formation permeability (Fjaer et al., 2008). If a mud cake is present or if the formation is impermeable (permeability $< 10^{-18}$ m^2),

$$p_b^{HF} - p_r = -3\sigma_h + \sigma_H - p_r + \frac{E}{1-\nu}\,\frac{\chi_{p\sigma}}{3}\,\theta + \sigma_T, \tag{2.11}$$

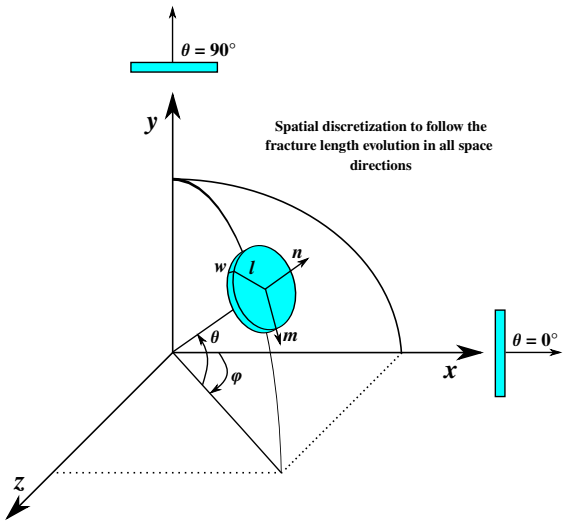

FIGURE 2.2: Directional evolution of a penny-shaped fracture length. The figure shows how space needs to be discretized to trace a smooth evolution of the directional quantities.

while if the rock formation is permeable/without a mud cake (permeability $> 10^{-18}$ m^2),

$$p_b^{HF} - p_r = (1-\nu)\Big[-3\sigma_h + \sigma_H - p_r + \frac{E}{1-\nu}\frac{\chi_{p\sigma}}{3}\theta + \sigma_T\Big] + \nu\, p_r, \tag{2.12}$$

where σ_H and σ_h are the maximum and minimum horizontal far-field stresses, p_r is the reservoir pressure just behind the wall of the borehole, $E > 0$ is the drained elastic modulus of the rock formation , $\sigma_T > 0$ its tensile strength, and θ its change of temperature after injecting the geothermal fluid. As expected, large longitudinal geological stress σ_H, formation pressure, and cooling ease fracturing. Meanwhile, large transversal confinement σ_h and high tensile strength hinder fracturing. The value of the excess pore pressure is used to parameterize the HFM, namely to calculate the stabilization parameter η (Eq. 2.8) so that hydraulic fracturing in the numerical model starts at this particular value of $p_b^{HF} - p_r$.

The other modelling aspect that needs to be considered concerns the stability of boreholes against shear failure. Shear failure of a borehole may be reached if the deviation of effective stresses around the borehole, due to the change in pore fluid pressure and temperature between the borehole and the formation, exceeds the failure criterion of the rock. To safeguard against this event, the borehole pressure p_b should not be lower than the minimum of these two values (Fjaer et al., 2008):

$$p_b^{\min} - p_r = -\frac{3\,\sigma_H - \sigma_h + 2\,p_r + \sigma_C}{1+\tan^2\beta} + \frac{1}{1+\tan^2\beta}\frac{E}{1-\nu}\frac{\chi_{p\sigma}}{3}\theta; \tag{2.13}$$

and,

$$p_b^{\min} - p_r = -\frac{\sigma_v + 2\,\nu(\sigma_H - \sigma_h) + p_r + \sigma_C}{\tan^2\beta} + \frac{1}{\tan^2\beta}\frac{E}{1-\nu}\frac{\chi_{p\sigma}}{3}\theta, \tag{2.14}$$

where σ_C is the compressive strength of the rock formation, σ_v is the vertical geostatic stress, ϑ is the angle of friction of the rock formation, and the angle $\beta = \pi/4 + \vartheta/2$ indicates the direction of the failure plane with respect to the maximum stress direction.

2.1.2 Stimulation tests: *In situ* results and simulations

This section presents numerical results for simulating heat extraction from the HDR reservoir of Soultz-sous-Forêts. It starts by validating the numerical approach by performing short time

simulations. Subsequently, simulations are conducted over the reservoir lifetime where the thermal recovery from the natural and the enhanced reservoir are compared systematically.

2.1.2.1 Stimulation tests of the Soultz-sous-Forêts HDR reservoir

A stimulation test of the well GPK1 (Fig. 2.4), between 2800 m and 3500 m, was conducted in 1993 at the Soultz-sous-Forêts HDR reservoir. Pressurized fluid led to fracture evolution which generated microseismic events. The works of Bruel (1995b) and Jupe et al. (1995) have fairly addressed this stimulation test and are used as a guiding reference for simulations.

This section is devoted to define the material data pertaining to the reservoir, the finite element mesh, and the initial and boundary conditions. In Sect. 2.1.2.2, the field flow history at the well GPK1 during a stimulation test for 17 days is simulated using the HFM implemented in the domestic finite element code, where injection is controlled by fluid volume (Fig. 2.3(a)). The time window of the simulations is next extended in Sect. 2.1.2.3 to study the permeability enhancement of the whole reservoir, where injection is controlled by fluid pressure (Fig. 2.3(b)). The effect of hydraulic fracturing on the reservoir impedance and efficiency is later highlighted.

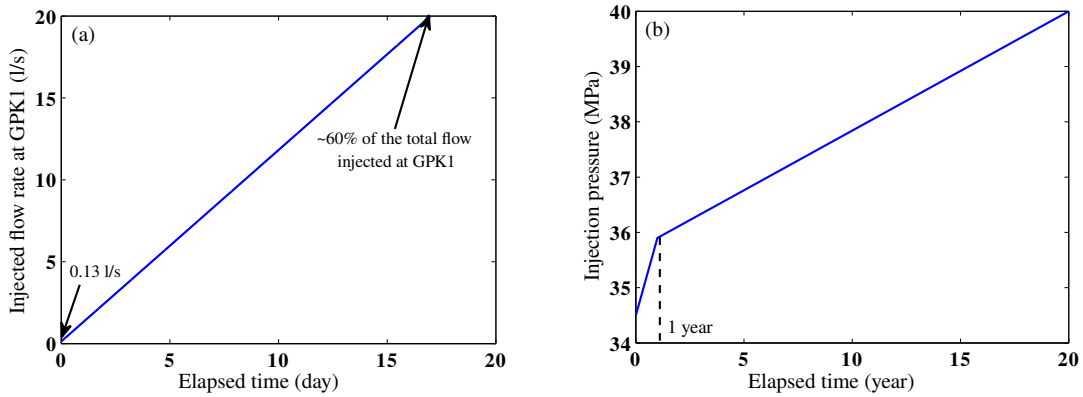

FIGURE 2.3: Two injection scenarios at the well GPK1: (a) the short period scenario is used here to validate the numerical model (Bruel, 1995b); (b) the injection scenario over the reservoir lifetime is purely numerical to serve the purpose of this research.

Based on the locations of the seismic events presented in Bruel (1995b) and on the geometrical information provided by Baumgärtner et al. (1996), the fractured zone to be stimulated (Fig. 2.4) lies at a depth that ranges between 2.8 to 2.9 km and has dimensions of 1 km and 400 m around the well GPK1 with N170 Azimuth and W70 Dip. The second well GPK2 is drilled 500 m away from GPK1 and in the direction of fracture evolution signaled by the seismic events. The initial pressure $p_0 = 28.5$ MPa, the initial temperature $T_0 = 155$ °C, and the geostatic stresses with the vertical stress being equal to the maximum horizontal stress, correspond to a typical depth of 2.85 km (Bruel, 1995b; Evans et al., 2009). The fluid is injected at $T = 50$ °C while the temperature at the outlet production well GPK2 is sought.

A mesh of 800 elements, 40 elements in x-direction and 20 elements in y-direction, is used to perform the simulations. The mesh is refined close to the inlet during the stimulation test of 17 days, otherwise, it is uniformly spread over the volume. Due to symmetry, only a quarter of the reservoir is modeled.

Table 2.1 summarizes the mechanical, the hydraulic, and thermal boundary conditions used in the stimulation process. The hydraulic boundary conditions are further discussed in Sect. 2.1.2.2. As for thermal insulation at the boundaries of the mesh, several studies (Jiang, Luo, and Chen, 2013; Gelet, Loret, and Khalili, 2013) have found that conductive heat contribution of the rock formation, external to a reservoir domain, is secondary for most of its lifetime.

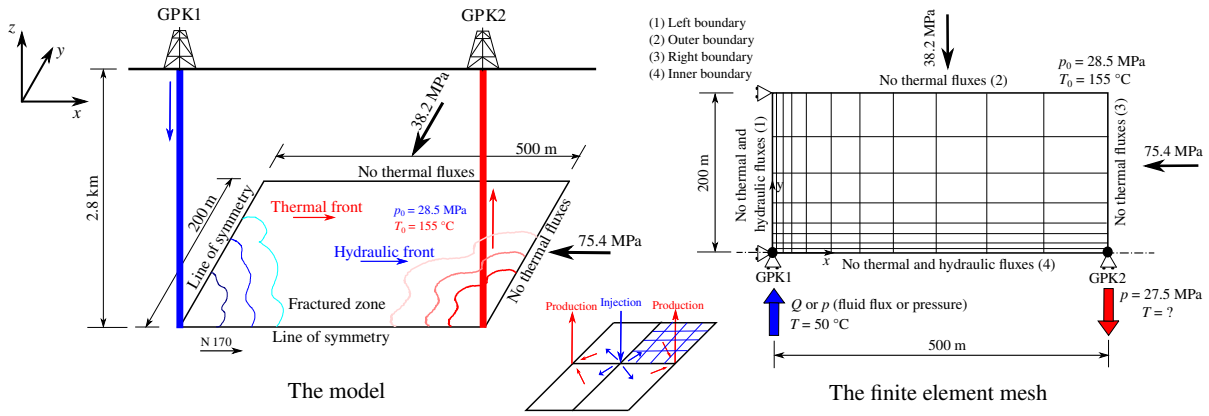

FIGURE 2.4: Schematic representation of the numerical model that is used to simulate the hydraulic fracturing tests at the HDR reservoir of Soultz-sous-Forêts. Boundary and initial conditions are displayed on the graph.

TABLE 2.1: Boundary conditions for the stimulation tests at Soultz-sous-Forêts: l=left, r=right, o=outer, and i=inner boundaries of Figure 2.4.

Type	Boundary	Condition
Displacements	l	No horizontal displacement
	i	No vertical displacement
	r and o	Calculated based on the stresses applied
Fluid flow	l, i	Impermeable
	r and o	Impermeable (scheme 1)/permeable (scheme 2)
	Injection well	Fluid flux or pressure (Fig. 2.3)
	Production well	Pore fluid pressure ($p = p_0 - 1$ MPa)
Heat flow	l, i, r and o	Thermally insulated
	Injection well	$T = 50$ °C
	Production well	Temperature is sought

The thermo-poroelastic properties of Soultz-sous-Forêts reservoir, shown in Table 2.2, are typical for the reservoir rock as reported by Evans et al. (2009).

TABLE 2.2: Material properties of Soultz-sous-Forêts HDR reservoir.

Property	Value	Unit
Drained Young's modulus E	54	GPa
Drained Poisson's ratio ν	0.25	-
Bulk modulus of solid grains K_σ	50	GPa
Bulk modulus of fluid K_λ	2.2	GPa
Dynamic viscosity of the fluid μ	3×10^{-4}	Pa×s
Initial porosity n_λ	0.1003	-
Initial permeability† k_0	2.85×10^{-14}	m^2
Solid thermal conductivity Λ_σ	2.49	W/m/K
Fluid thermal conductivity Λ_λ	0.6	W/m/K
Solid heat capacity at constant volume $C_{v\sigma}$	1000	J/kg/K
Fluid heat capacity at constant volume $C_{v\lambda}$	4200	J/kg/K
Density of solid ρ_σ	2910	kg/m^3
Volumetric thermal expansion of the solid $\chi_{p\sigma}$	7.5×10^{-6}	K^{-1}
Volumetric thermal expansion of the fluid $\chi_{p\lambda}$	1×10^{-3}	K^{-1}

The initial permeability† k_0 has been back-calculated from figure 5 of Bruel (1995b) by considering that the enhanced permeability of the reservoir has an order of magnitude of $\sim 10^{-11}$ m^2 (Evans et al., 2009). Material properties required by the HFM are listed in Table 2.3.

TABLE 2.3: Information required by the HFM to perform hydraulic stimulation

Type	Parameter	Value	Unit	Reference
Fracture	Initial length of fractures ℓ_0	0.25	m	Evans et al. (2009)
	Final length of fractures ℓ_f	0.80	m	estimated
	Toughness K_{Ic}	1.87	MPa$\sqrt{\text{m}}$	Atkinson (1991)
	Fracture stabilizing parameter η	0.2	-	calculated
	Fracture density	10^{-6}	$1/\text{m}^3$	Bruel (1995b)
Flow	Connectivity coefficient c_c	0.0001	-	calculated/parametrized

The excess borehole pressure $p_b^{HF} - p_r$ needed to start the fracturing process is provided by Eq. 2.12 since the initial permeability of the reservoir k_0 is larger than $10^{-18}\,\text{m}^2$. The rock tensile strength σ_T is taken equal to 10% of rock compressive strength $\sigma_C = 130\,\text{MPa}$ (Evans et al. (2009)). For a temperature change θ of -105 °C, the resulting casing shoe pressure at the injection well GPK1 should be around 39.15 MPa. This value is close to the actual pressure (around 40 MPa) implemented at Soultz-sous-Forêts to start hydraulic fracturing during the field tests at a depth of 2.85 km (Bruel, 1995b). Henceforth, the threshold of hydraulic fracturing is chosen to be as in the field, namely 40 MPa. It is of interest to observe that the thermal cooling eases considerably the hydraulic fracturing process. Indeed in the absence of thermal contribution, the borehole pressure required to start fracturing would be equal to 54.3 MPa.

The stabilizing parameter η is now determined by Eq. 2.7 knowing the effective normal stress σ_n' in the direction of the maximum far-field stress, the threshold of hydraulic fracturing, and the material properties of Table 2.3. The connectivity coefficient c_c is chosen so that it leads to an enhanced permeability of $\sim 10^{-11}\,\text{m}^2$ in agreement with Evans et al. (2009). In the absence of definite data, the length of fractures ℓ_f at which connectivity between fractures is complete is estimated to be a multiple of the initial fracture length ℓ_0.

Equations (2.13) and (2.14) provide the minimum borehole pressures that need to be applied to ensure the stability of the wellbore against shear failure. The friction angle ϑ of granite at 5 km depth is estimated to 42° (Cornet, Bérard, and Bourouis, 2007). For a failure angle $\beta = \pi/4 + \vartheta/2 \simeq 66°$, the minimum value of borehole pressure required to cause shear failure is 25.5 MPa by Eq. 2.13 and 12 MPa by Eq. 2.14. Since the borehole pressure is definitely larger than the initial reservoir pressure of 28.5 MPa during the fracturing process, the borehole GPK1 is not likely to fail in shear but rather in tension due to hydraulic fracturing.

2.1.2.2 Short period stimulation test: Numerical validation

The Boundary Value Problem (BVP) (Fig. 2.4) is stimulated by the HFM. The results of simulations are correlated to the flow logging injection tests performed at the well GPK1 of Soultz-sous-Forêts HDR reservoir. The most important level of the stimulation process is located at 2.85 km and absorbs about 60% of the injected fluid (Bruel, 1995b). The field test was performed by pumping geothermal fluid into the well GPK1 gradually until a total flow rate[2] of 40 l/s was reached at day 17. The *in situ* pressure curve at the injection well showed a non-linear behavior announcing the existence of turbulent flow (Grecksch et al., 2003).

Figure 2.3(a) shows the applied flow rate history at the well GPK1 as suggested by Bruel (1995b) and as applied in the simulations. The hydraulic boundaries are either impermeable (scheme 1) or permeable (scheme 2). Figure 2.5 displays the responses obtained by the numerical simulation and the *in situ* data for a period of 17 days.

When the reservoir is assumed impermeable at the outer and right boundaries (first scheme), the geothermal system reaches a pressure of 137 MPa at a flow rate 20 l/s with a plateau announcing the presence of extreme turbulent flow near the well GPK1 (Fig. 2.5(a)). This pressure value of 137 MPa is 3.5 times higher than the hydraulic fracturing pressure (40 MPa). However,

[2]The flow loss is approximately equal to 40%: the effective flow absorbed by the reservoir volume is about 60% of the total injected flow, i.e. 24 l/s. The value of 20 l/s used in the simulations is after Bruel (1995b).

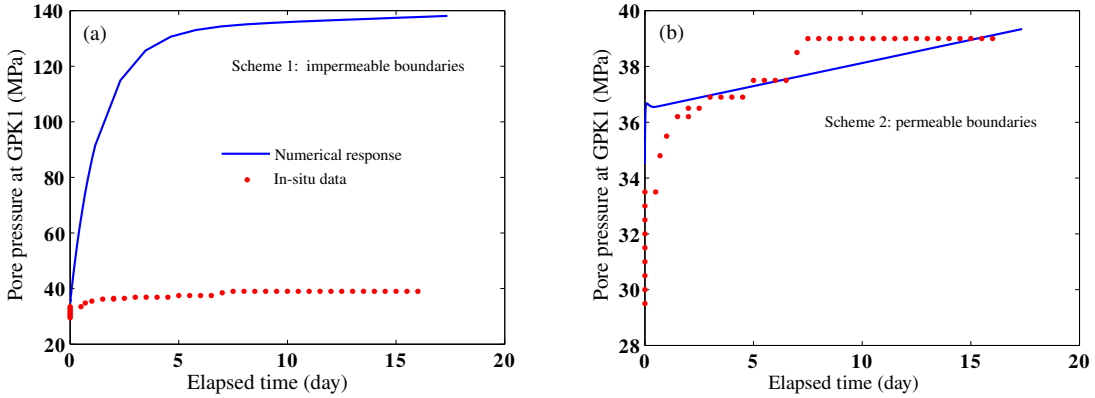

FIGURE 2.5: Injection pressure at the well GPK1 during the 1993 field injection test at Soultz-sous-Forêts. Comparison between the *in situ* data (Bruel, 1995b) and the response of the numerical model with (a) impermeable and (b) permeable boundaries.

when the outer and right boundaries of the reservoir are assumed permeable (second scheme), the geothermal system reaches the pressure of hydraulic fracturing at a flow rate of 20 l/s *almost* as applied in field. The numerical response in Fig. 2.5(b) is no longer showing an asymptotic plateau as the fluid turbulence is greatly eliminated when the outer and right boundaries are assumed permeable, i.e. smoother flow is achieved within the reservoir. As a conclusion to this section, the HFM is verified against field data and only permeable boundaries (scheme 2) are considered in next long term simulations as injection is controlled by fluid pressure (Fig. 2.3(b)).

2.1.2.3 Reservoir lifetime stimulation test: Impedance and efficiency of thermal recovery

While Sect. 2.1.2.2 presented the results of a short period stimulation test, the permeability enhancement over the whole reservoir is now addressed. The effects of the hydraulic fracturing process on the reservoir impedance and efficiency of thermal recovery are considered during the lifetime of the reservoir. In order to highlight the qualitative and quantitative effects of hydraulic fracturing, tests are run both with and without activating the HFM in the simulations.

Unlike the previous section, injection is now controlled by fluid pressure: pumping starts with 34.5 MPa and reaches 35.9 MPa at year 1. Thereafter, it continues to increase linearly but with a lower rate to reach a value of 40 MPa after 20 years of injection (Fig. 2.3(b)). Hydraulic fluxes are set to vanish on the model four boundaries. Convection of heat is treated *a priori* using the SUPG method. However, some stubborn numerical noises at the injection and production wells still require more attention (Sect. 2.1.5).

Simulations without hydraulic fracturing

The results of circulation tests in the natural/unenhanced reservoir are commented below for 5 and 10 years of simulations. Figure 2.6 shows that the pore pressure establishes in early times, in a matter of days. Therefore its contours are not showing any significant changes at subsequent times.

The fractured zone cools in x- and y-directions due to the strong fluid pressure gradients spreading all over the reservoir volume (Figs 2.7 and 2.8). These strong pressure gradients, particularly near the injection well, accompanied by thermal tensile stresses resulting from cooling help propagating and opening fractures.

Figures 2.9 and 2.10 show the contours of the effective horizontal stresses in x- and y-directions. The reservoir is relaxing faster in y-direction than in x-direction: the pace at which the stress σ'_{yy} returns to its geostatic value is faster than the stress σ'_{xx}. This effect is due to

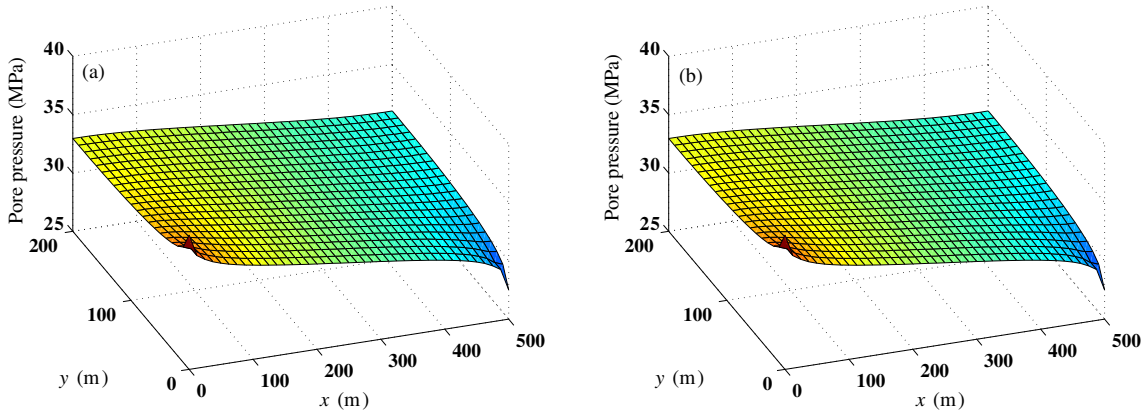

FIGURE 2.6: Contours of the unenhanced reservoir pore pressure at two times: (a) 5 years; and (b) 10 years. Contours are not showing any significant changes due to the fast hydraulic diffusion, in a matter of days.

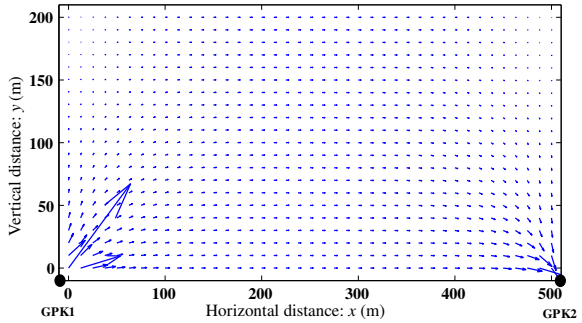

FIGURE 2.7: Scaled fluid velocity vectors spreading over the unenhanced reservoir volume.

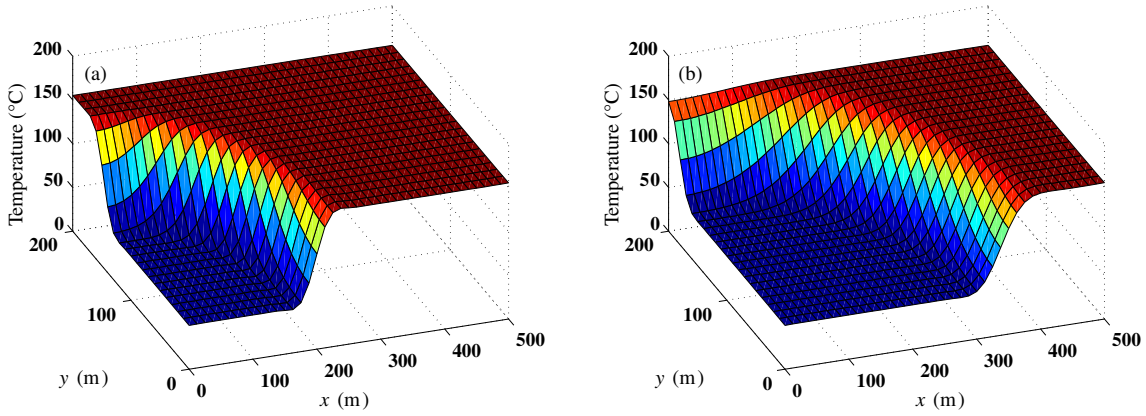

FIGURE 2.8: Contours of the unenhanced reservoir temperature at two times: (a) 5 years; and (b) 10 years.

the geologic far-field stress state which imposes smaller stresses on the outer boundary of the reservoir in the y-direction. Indeed, as expected, hydraulic fracturing is going to enhance the permeability of the HDR reservoir following the direction of the maximum far-field stress.

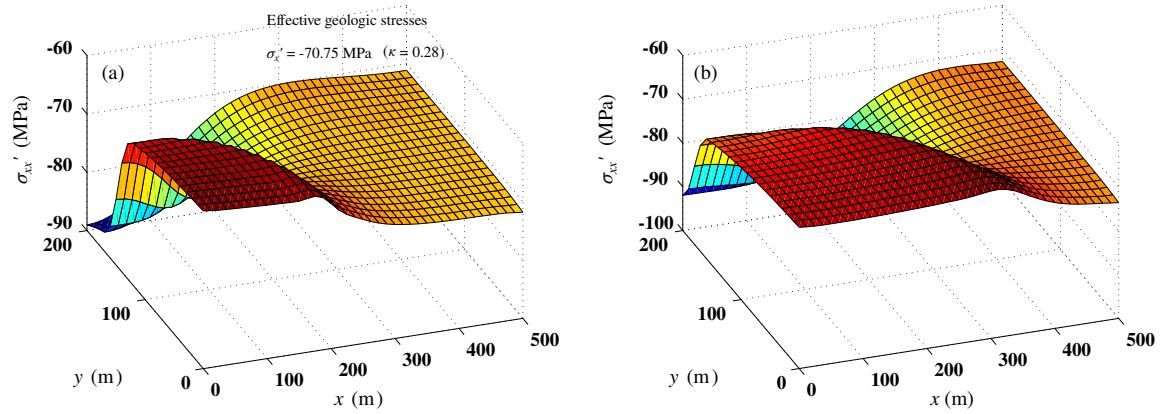

FIGURE 2.9: Contours of the unenhanced reservoir longitudinal effective stress σ'_{xx} at two times: (a) 5 years; and (b) 10 years. The Biot's coefficient $\kappa = 1 - K/K_\sigma$ is needed to calculate the effective stresses. According to Table 2.2, the drained bulk modulus K is equal to 36 GPa therefore $\kappa = 0.28$.

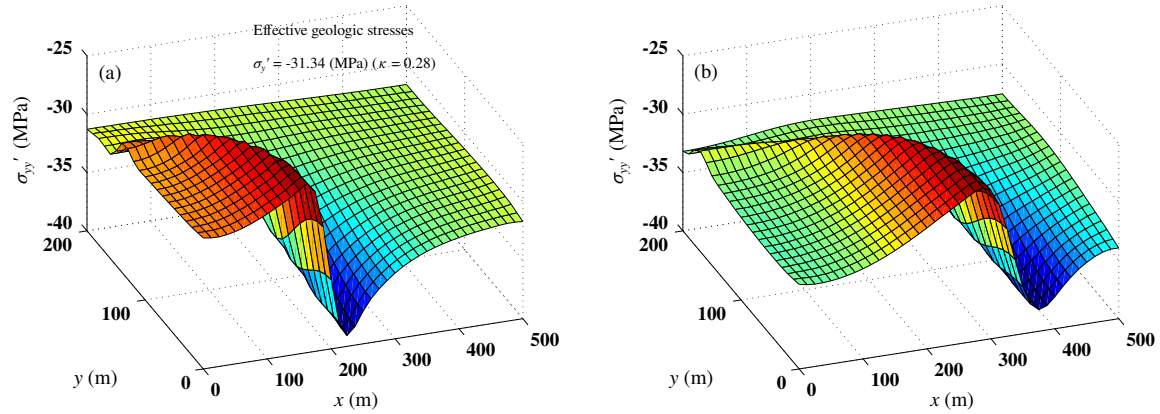

FIGURE 2.10: Contours of the unenhanced reservoir transversal effective stress σ'_{yy} at two times: (a) 5 years; and (b) 10 years.

The impedance $\mathcal{Z}$, defined as the ratio of the pressure differential between the injection and production wells required to ensure the produced flow rate Q,

$$\mathcal{Z} = \frac{p_{\text{inj}} - p_{\text{pro}}}{Q}, \tag{2.15}$$

is an important overall characteristic of a reservoir. The vertical section of the well GPK1, over which flow is taking place, is approximately 550 m extending to about 3.3 km and the radius of the well at such a depth is 15 cm (Baria et al., 2000; Bruel, 1995b). Therefore, the flow takes place over an area of $\sim$518 m^2. Assuming no leak off, the impedance of the unenhanced reservoir is obtained from the computed flux-pressure relation at the injection well GPK1 (Fig. 2.11(a)) . The time course of the injection pressure is displayed in Fig. 2.3(b) and the production pressure is maintained at $p = p_0 - 1 = 27.5$ MPa.

Impedance is seen to be virtually constant in time and greater than 1000 MPa/(m^3/s) (Fig. 2.11(b)). Such a large impedance indicates an inefficient operation where the power pumped through the reservoir exceeds a substantial fraction of the power produced by the reservoir (Murphy et al., 1999).

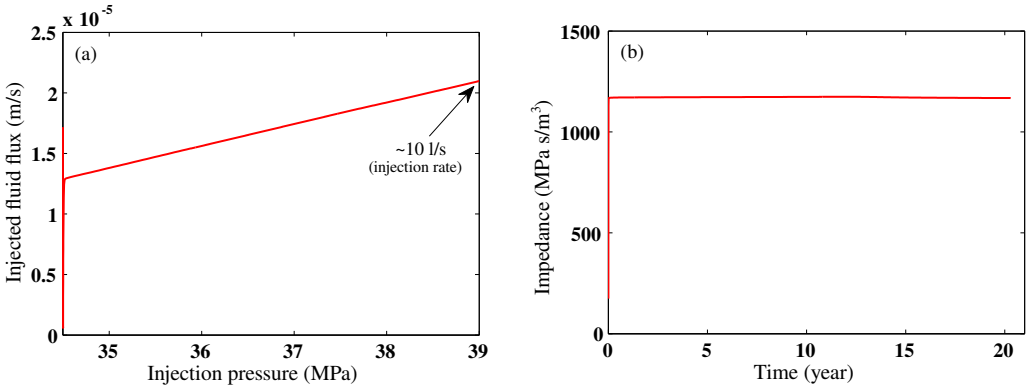

FIGURE 2.11: (a) The relation between the injected pore fluid pressure and the magnitude of created fluid flux at the injection well GPK1 of the unenhanced HDR reservoir of Soultz-sous-Forêts. Fluid flux increases linearly following the injection schedule of Fig. 2.3(b). (b) The impedance profile: impedance greater than 1000 MPa/(m^3/s) indicates inefficient operation (Murphy et al., 1999).

Simulations with hydraulic fracturing

If hydraulic fracturing is activated in the simulations, fractures are evolving in the direction of the maximum far-field stress (along the x-axis) causing the longitudinal permeability to reach its maximum value up to distances of $\simeq$80 m in y-direction and $\simeq$240 m in x-direction. The permeability contours for the enhanced HDR reservoir after 1 year of pumping at the GPK1 well are shown in Fig. 2.12. The results of these simulations are in a good agreement with the micro-seismic events diagram presented in Bruel (1995b) announcing the propagation of hydraulic front and fracture coalescence.

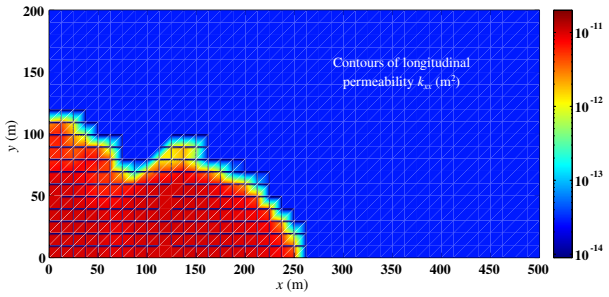

FIGURE 2.12: Contours of longitudinal permeability component k_{xx} after 1 year of pumping.

Figure 2.13 shows the projection of the contours of k_{xx}/k_{yy} in the x-y plane with some points (A, B, C, and D) where the evolution of fracture radii is studied. The degree of anisotropy between the longitudinal and the transversal permeability components remains in the range $k_{xx}/k_{yy} \in [2.5, 0.4]$ as documented by Schulze, Popp, and Kern (2001a).

Figure 2.14 shows the directional evolution of the fracture radius after 1 year of hydraulic fracturing at points A and D of Fig. 2.13. Point A represents a position very close to the injection well where the components of the permeability tensor increase rapidly and almost equally, nevertheless, with a little preference in the direction of the far-field longitudinal stress $\theta = 90°$ and $k_{xx}/k_{yy} = 1.05$. Point D is far away from the region of hydraulic enhancement and no change of the fracture radius is observed $\ell = \ell_0 = 25$ cm.

Figure 2.15 shows the directional evolution of fracture radii at points B and C. At point C, fractures evolve strongly in the longitudinal direction and slightly in the transversal direction $k_{xx}/k_{yy} = 1.7$. Meanwhile, a slighter evolution of fractures in the longitudinal direction is observed at point B which gives $k_{xx}/k_{yy} = 1.6$.

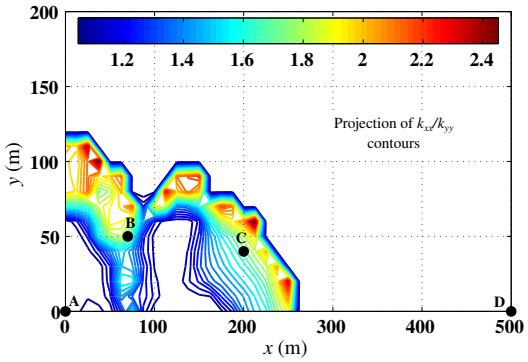

FIGURE 2.13: Projection of the contours of k_{xx}/k_{yy} in x-y plane with some points where the evolution of fracture radii is studied.

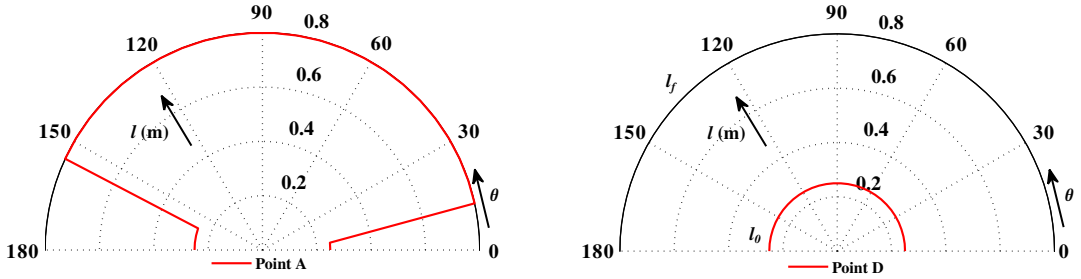

FIGURE 2.14: Directional evolution of fracture radii at points A and D after 1 year of hydraulic fracturing.

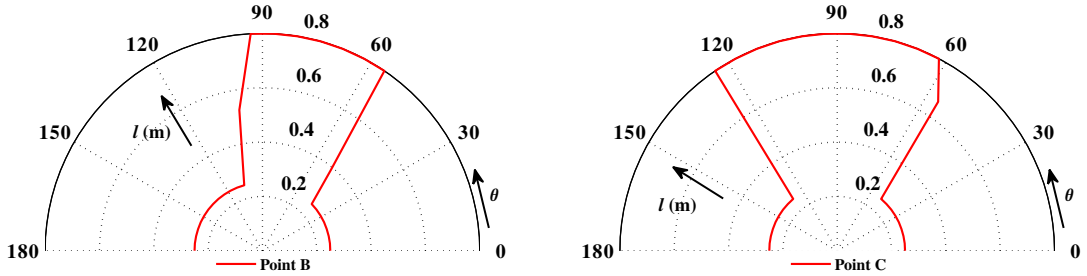

FIGURE 2.15: Directional evolution of fracture radii at points B and C after 1 year of hydraulic fracturing.

Figure 2.16 shows the evolution of the longitudinal permeability component k_{xx} at the injection well GPK1 during the hydraulic enhancement. The permeability evolution at the injection well happens very rapidly. This is due to modeling hydraulic fracturing while considering only mode I of fracture propagation.

The experimental work of Papanastasiou (1999) has proven that for every geothermal system there exists an optimum injection schedule (injection pressure and duration). Any further increase in stimulation effort, i.e. stimulation time for a given stimulation pressure, does not provide additional permeability enhancement. The injection pressure schedule (Fig. 2.3(b)) is sufficient to enhance the reservoir permeability (Fig. 2.12) up to one year. The subsequent increase in stimulation pressure over time did not enhance the reservoir permeability any more. The point N, indicated in Fig. 2.16, announces the end of hydraulic enhancement/fracturing,

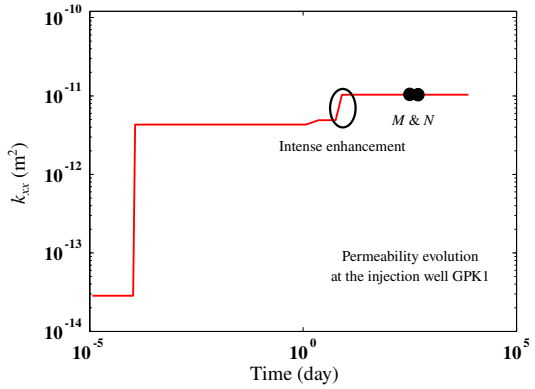

FIGURE 2.16: Longitudinal permeability k_{xx} history at the injection well GPK1.

i.e. $t = 1$ year.

Preferential cooling following the new paths of the enhanced permeability is thus expected: heat convection is dominant in the direction of the major far-field stress (direction of fracture evolution, Fig. 2.17). The numerical oscillations observed in temperature contours near the production well are related to stabilization of heat convection as fluid fluxes converge leading to high pore fluid velocity. The Subgrid Scale method (SGS) and the Discontinuity Capturing Method (DCM) have been seen to be more efficient in curing such numerical noises than the SUPG method (Sect. 2.1.5).

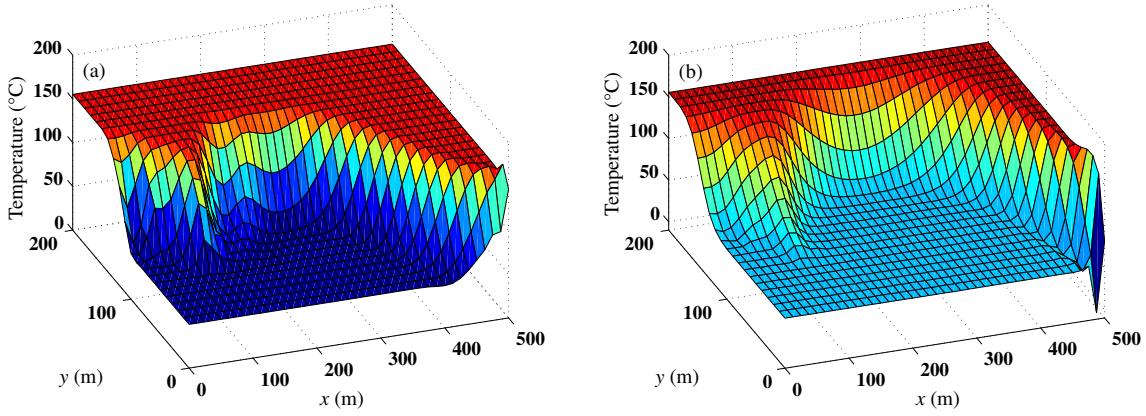

FIGURE 2.17: Contours of the enhanced reservoir temperature at two times: (a) 5 years; and (b) 10 years. Convection of heat is dominant in the direction of fracture evolution.

The velocity field at year 1 of hydraulic enhancement (Fig. 2.18) shows larger pore fluid velocity in the zone of active hydraulic enhancement, i.e. $\sim 2.75 \times 10^{-5}$ m/s against $\sim 0.62 \times 10^{-5}$ m/s in other regions.

The contours of pore fluid pressure at years 5 and 10 are shown in Fig. 2.19. The tremendous fast increase in the permeability in the zone of active enhancement makes the changes in pore fluid pressure quite small (kind of leveled up surfaces) in this zone as compared to the situation of unenhanced HDR reservoir (Fig. 2.6). This behavior of pressure distributions/contours was also observed by Lee and Ghassemi (2010) and Lee and Ghassemi (2011) for two-dimensional and three-dimensional BVPs.

The contours of the longitudinal and transversal effective stresses (Figs. 2.20 and 2.21) are following the preferential cooling derived by the hydraulic fracturing process. Compressive stresses are mitigated in the cooled regions as the reservoir is constrained to some degree on the

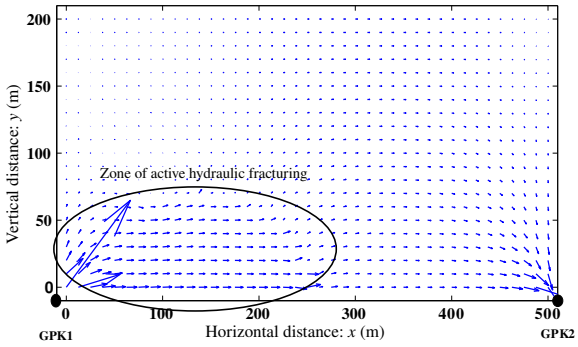

FIGURE 2.18: Scaled fluid velocity vectors spreading over the enhanced reservoir volume.

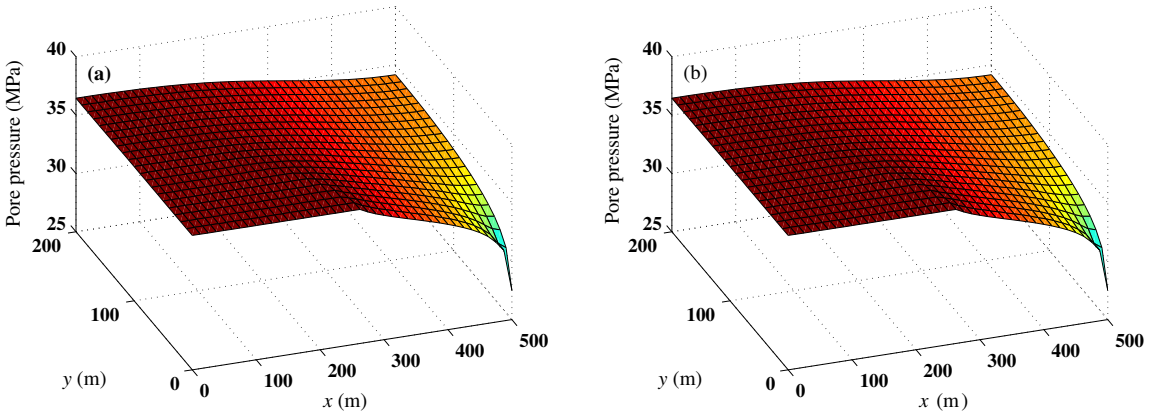

FIGURE 2.19: Contours of the enhanced reservoir pressure at two times: (a) 5 years; and (b) 10 years. The high permeability created by hydraulic fracturing levels up the contours in the regions of the enhancement.

boundaries of symmetry. The created new highly-permeable paths take most of the fluid flow in the direction of the maximum far-field stress causing increased compressive stresses near the outer boundary of the HDR reservoir. Thus, at the outer boundary, fractures are most likely closing and permeability is decreasing, unless shear dilatation copes for the reduction in the fracture aperture (Chen, Zhou, and Sheng, 2007).

The jump between the two points M and N in Fig. 2.22(a) is understood by studying the permeability history at the injection well GPK1 (Fig. 2.16). The period of intense permeability enhancement is taking place earlier at the injection well which is expected due to significant thermo-poroelastic changes at this location. However, if permeability histories are averaged over the whole reservoir, the period of intense permeability enhancement in the averaged curve corresponds to the jump M-N in Fig. 2.22(a). The process of HF, for only one year, has reduced the flow impedance of the HDR reservoir from $\sim$1170 MPa/(m^3/s) to $\sim$600 MPa/(m^3/s) (Fig. 2.22(b)). This reduction in the impedance lowers the power required to pump geothermal fluid through the reservoir and enhances its efficiency by about 49%.

Efficiency and thermal recovery

Figure 2.22(b) proves the effect of hydraulic enhancement on reducing the impedance of thermal recovery from HDR reservoirs. Besides, the profiles of the reservoir produced fluid temperatures with hydraulic fracturing (enhanced) (T_{hf}) and without hydraulic fracturing (natural) (T_{whf}) are displayed in Fig. 2.23(a). In most geothermal systems, the produced fluid is efficiently used as long as its temperature does not drop below 80 °C (Lund, 2009). The standard

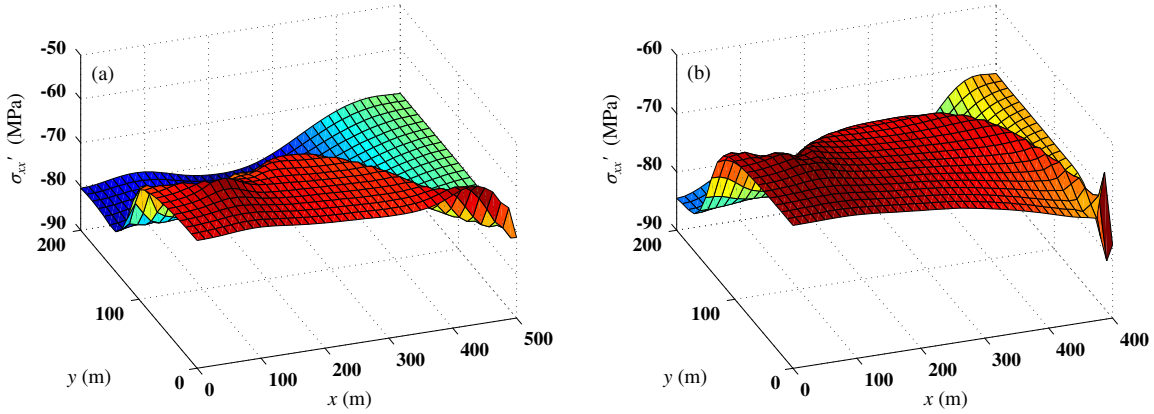

FIGURE 2.20: Contours of the enhanced reservoir longitudinal effective stress σ'_{xx} at two times: (a) 5 years; and (b) 10 years. Stresses are dawdled in compression in the cooled regions due to tensile stresses.

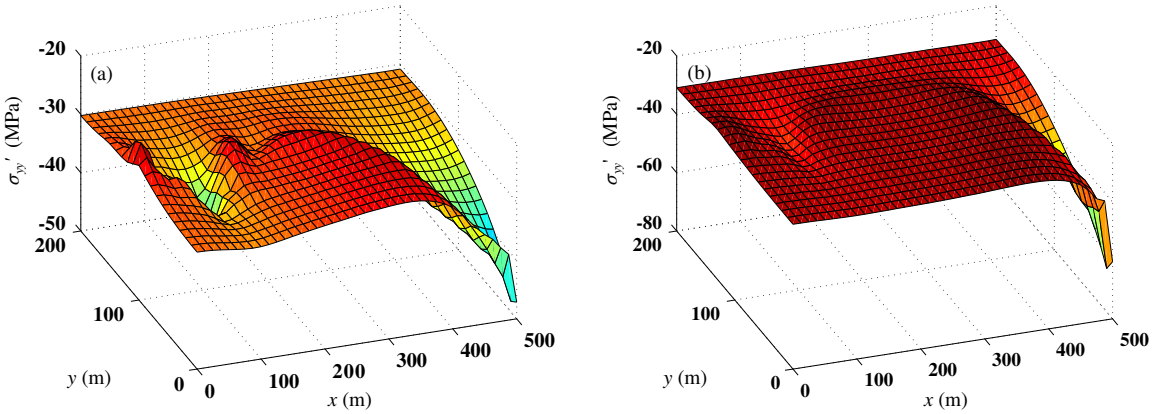

FIGURE 2.21: Contours of the enhanced reservoir transversal effective stress σ'_{yy} at two times: (a) 5 years; and (b) 10 years.

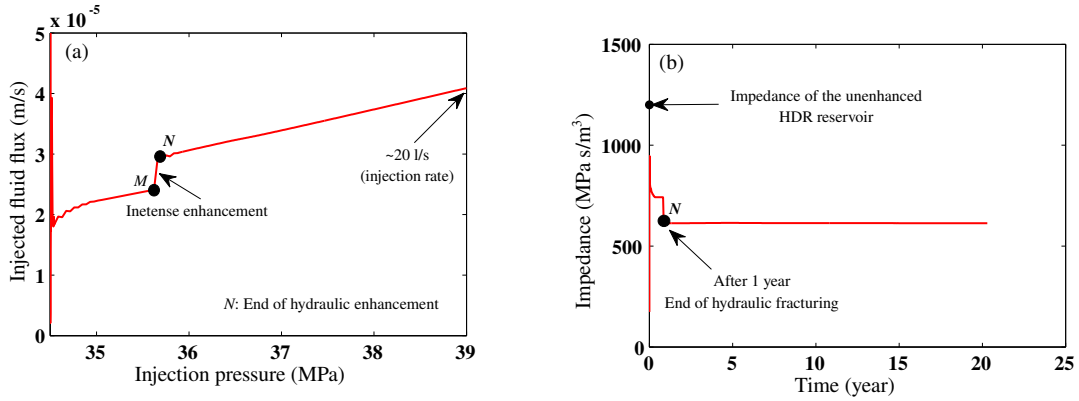

FIGURE 2.22: (a) The relation between the injected pore fluid pressure and the magnitude of created fluid flux at the injection well GPK1 of the enhanced HDR reservoir of Soultz-sous-Forêts. The non-linear behavior results from the the creation of improved connections (Bruel, 1995b). (b) the Impedance history.

mean production temperature curve (Fig. 2.23(a)) is based on the analytical solution provided by Kolditz (1995) for one-dimensional matrix heat diffusion and for 15 l/s injection flow rate.

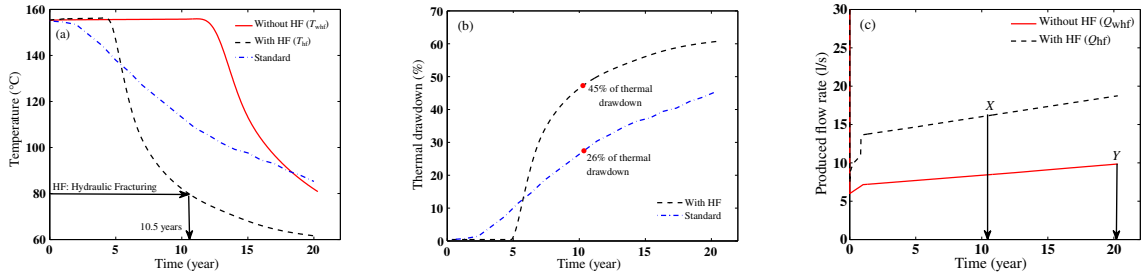

FIGURE 2.23: (a) Histories of produced fluid temperature from the enhanced reservoir (T_{hf}) compared to the natural reservoir (T_{whf}). (b) Thermal drawdown of the mean production temperature from the enhanced HDR reservoir against the standard production temperature as suggested by Kolditz (1995). (c) Profiles of produced flow rate from the enhanced reservoir (Q_{hf}) compared to the natural reservoir (Q_{whf}).

As another indicator of thermal recovery from geothermal reservoirs, Fig. 2.23(b) shows the thermal drawdown of the enhanced reservoir and the standard production curve as suggested by Kolditz (1995). Thermal drawdown $\mathcal{T}_{\mathcal{D}}$ is defined as the relative difference between initial temperature of the reservoir T_0 and production temperature T_{pro},

$$\mathcal{T}_{\mathcal{D}} = \frac{T_0 - T_{\mathrm{pro}}}{T_0}. \tag{2.16}$$

The standard solution shows a thermal drawdown of approximately 26% in 10 years, against 45% for the enhanced reservoir (Fig. 2.23(b)). In both cases, thermal drawdown exceeds the limits required by Jupe et al. (1995), namely 1% thermal drawdown per year. Still, this poor performance may be attributed in part for the fact that the present heat diffusion analysis is two- rather than three-dimensional (Kolditz, 1995).

If hydraulic fracturing is activated in the simulations, the HDR reservoir is exhausted in 10.5 years (Fig. 2.23(a)). However, without hydraulic enhancement, the HDR reservoir lasts for up to 20 years. Still, the benefit of using hydraulic fracturing is evident in terms of the energy used to pump fluid through the reservoir (Fig. 2.22(b)) and in terms of the produced flow rate (Fig. 2.23(c)).

After 1 year of hydraulic enhancement, the produced flow rate from the HDR reservoir is two-fold the produced flow rate from the natural reservoir. Considering that the stimulated reservoir operates efficiently for 10.5 years and that the unenhanced reservoir for 20 years, the volume of the produced fluid can be calculated by numerically integrating the curves of Fig. 2.23(c), to points X and Y: the volume of efficient fluid produced from the stimulated HDR reservoir over a period of 10.5 years is 4.922 Million m^3, compared to 5.364 Million m^3 from the natural reservoir over 20 years. These huge amounts of used fluids are not utterly lost; the geothermal fluids are recirculated in a closed loop. It becomes clear now that the hydraulic fracturing process has increased the efficiency of the HDR reservoir for up to 49%. Yet by the calculations of efficient fluid volume, only 7 to 8% of the total efficient fluid to be produced is lost over the entire effective life of the reservoir.

2.1.3 Influence of geothermal fluids on the thermal recovery

Fluids used usually in geothermal systems are brines with the dominance of chloride Cl^- and sodium Na^+ ions over a typical range of concentration. In most of the geothermal systems, as in Groß Schönebeck 50 km north of Berlin, the total of dissolved solids sums up to 265 g/l with a dominant mass fraction of 0.225 kg of NaCl per kg of solution corresponding to a molality of 4.968 mol of NaCl per kg of H_2O (Francke and Thorade, 2010; Battistelli, Calore, and Pruess, 1997).

This section aims at studying the effect of a temperature-dependent dynamic viscosity of geothermal fluids on the performance of natural and enhanced reservoirs.

2.1.3.1 Temperature and salinity dependence of viscosity

The dynamic viscosity of a fluid describes its resistance to gradual deformation, and hence flow. It can be thought of as a measure of fluid friction. Francke and Thorade (2010) collected experimental data from several studies to provide three models to estimate brine viscosity temperature dependence (Fig. 2.24(a)). The models, in their respective application range, resulted in very consistent values of brine viscosity with average deviation of 0.3% and maximum deviation of 0.9%. Figure 2.24(a) shows the viscosity of 0.225 kg of NaCl per kg of solution brine over a range of temperature of interest and at a constant pressure of 1.5 MPa. The brine viscosity $\mu_b = 1.57 \times 10^{-3} \times (T/293)^{-4.37}$ Pa s, with T the temperature in Kelvin, is found to represent the average of the three models of Francke and Thorade with a determination coefficient of $R^2 = 0.9957$.

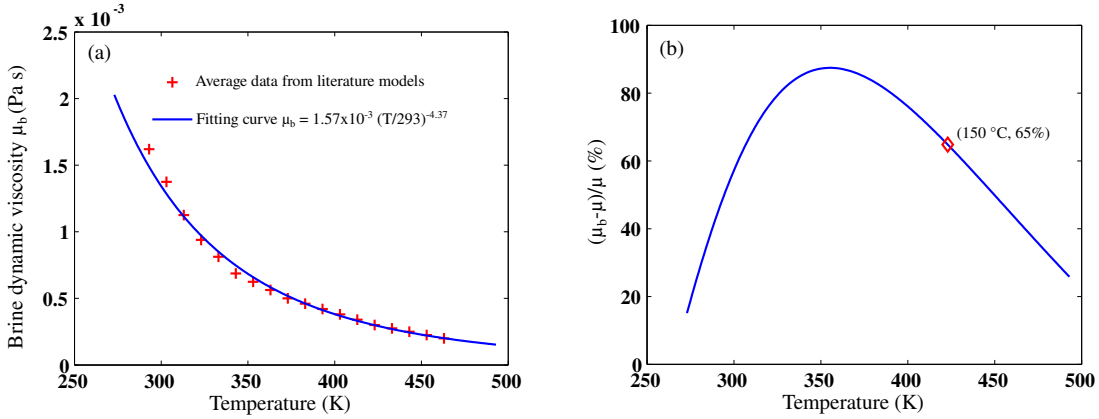

FIGURE 2.24: (a) Brine viscosity as a function of temperature while pressure and NaCl mass fraction are kept equal to 1.5 MPa and 0.225 kg of NaCl per kg of solution respectively. Solid line represents the fitting curve of the scattered data with a determination coefficient of $R^2 = 0.9957$. (b) Percentage of viscosity increase as result of using sodium chloride NaCl in a concentration of 0.225 kg of NaCl per kg of H_2O, fluid pressure is held at 1.5 MPa.

Francke and Thorade (2010) have also employed their models to study the effect of NaCl mass fraction on the viscosity of the brine. Brine viscosity has been proven to increase almost linearly by 76% for a mass fraction change from 0 to 0.25 kg of NaCl per kg of solution at a temperature of 150 °C and pressure of 1.5 MPa. On the other hand, in agreement with Likhachev (2003), the fluid pressure does not influence the brine viscosity at a temperature of 150 °C and a pressure in the range of 0.01 MPa to 50 MPa.

Figure 2.24(b) shows the percentage of increase of viscosity of the brine with respect to water as a function of temperature. The curve extends over a temperature range of 0 °C to 220 °C. This curve is built using the analytical expression of the water substance viscosity μ given by Burger, Sourieau, and Combarnous (1985) and AbuAisha (2014), yet the brine viscosity μ_b is obtained using the relation of Fig. 2.24(a).

2.1.3.2 Temperature-dependent viscosity: simulations without hydraulic fracturing

Increasing pore fluid viscosity decreases the velocity at which the hydraulic front is moving. It also increases the pressure differentials with respect to the wells and hence decreases the pore fluid pressure inside the reservoir. These phenomena are observed in Fig. 2.25 that shows pore fluid pressure profiles along the line joining the wells GPK1 and GPK2. The reduction in pore fluid pressure as result of increasing the brine viscosity hinders the process of hydraulic fracturing.

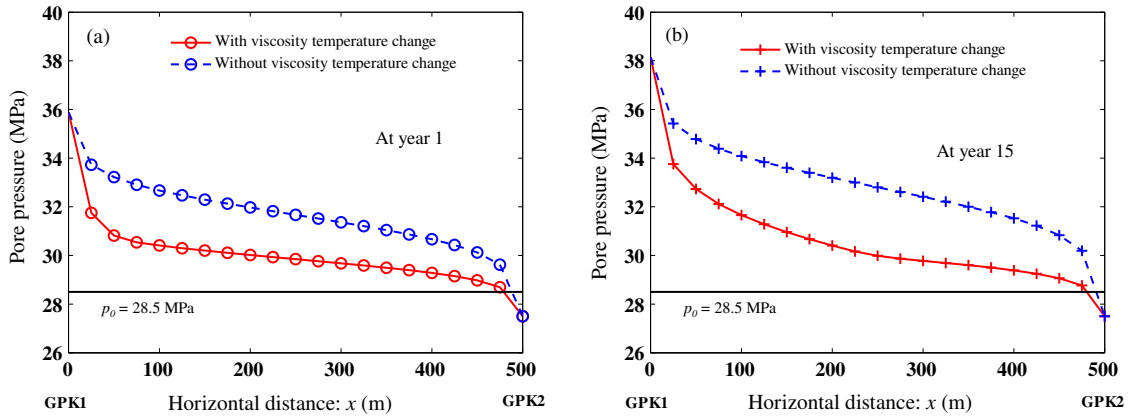

FIGURE 2.25: Pore pressure profiles along the line joining the injection and production wells, at (a) year 1 and (b) year 15. Solid lines: temperature-dependent viscosity; dashed lines: constant brine viscosity $\mu_b = 3 \times 10^{-4}$ Pa s.

Increasing brine viscosity also hinders the speed by which heat front is traveling through the reservoir: more viscous fluid moves at slower convective velocity, compare Figs 2.26 and 2.8.

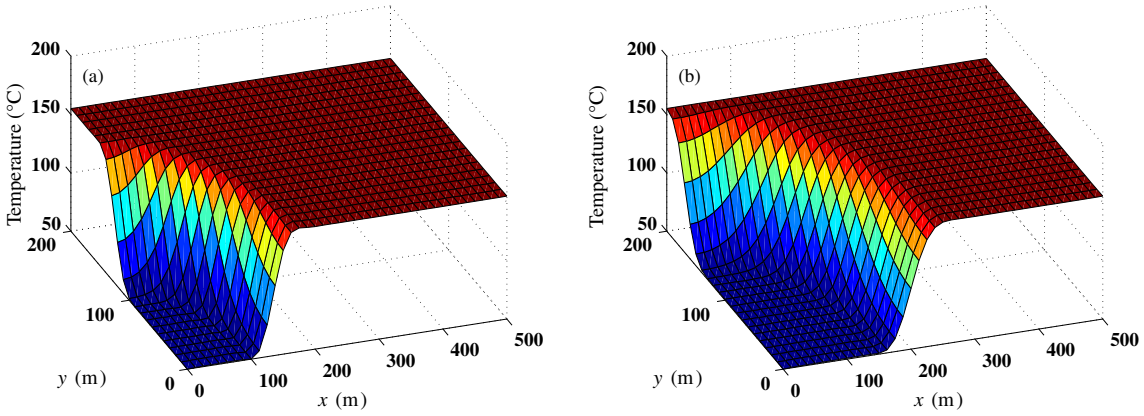

FIGURE 2.26: Contours of the natural reservoir temperature at two times: (a) 5 years; and (b) 10 years. Temperature-dependent viscosity is accounted for.

Figure 2.27(a) shows the relation between injection fluid pressure at the well GPK1 and the resulting flow rate. The relation is no longer linear (compare with Fig. 2.11(a)) even if no improved hydraulic connections are created by hydraulic fracturing. Besides, the flow rate is smaller than the value of the natural reservoir if temperature-dependent viscosity is not considered in the simulations (Fig. 2.11(a)). This non-linear relation announces a more turbulent flow near the injection well.

Figure 2.27(b) shows that increasing brine viscosity as a result of cooling increases the impedance $\mathcal{Z}$ of the unenhanced reservoir in the long range, announcing a less efficient thermal recovery from the reservoir (Murphy et al., 1999).

2.1.3.3 Temperature-dependent viscosity: simulations with hydraulic fracturing

Increasing pore fluid viscosity is expected to hinder the process of hydraulic fracturing as it reduces pore fluid pressure. Contours of the reservoir permeability at year 5 are shown in Fig 2.28. Unlike the case when constant brine viscosity is assumed, increasing viscosity by cooling

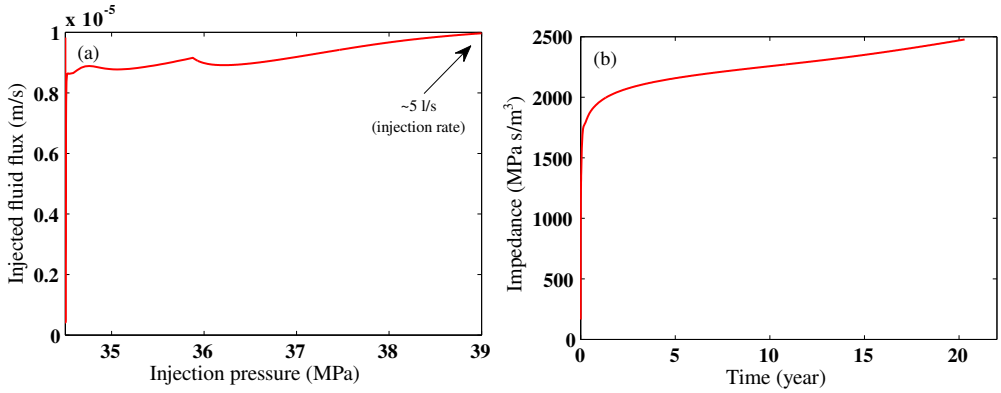

FIGURE 2.27: The relation between injection pressure and resulting flow rate at the injection well GPK1 of the natural reservoir and while accounting for a temperature-dependent viscosity. (b) The impedance profile.

tends to create high fluid pressure gradients near the injection well traveling strongly in both x- and y-directions and causing fractures to evolve and intersect. The lag in heat front, as result of increasing viscosity, renders the injection pressure schedule shown in Fig. 2.3(b) active[3] for 5 years.

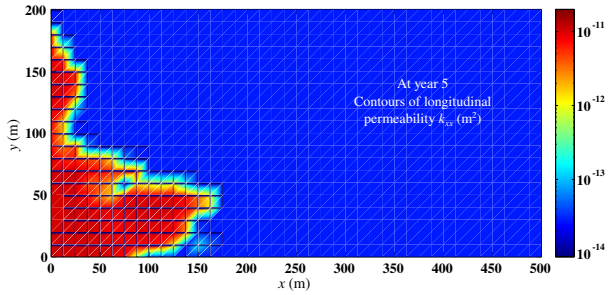

FIGURE 2.28: Contours of longitudinal permeability component k_{xx} at year 5 while accounting for a temperature-dependent viscosity. Injection pressure schedule (Fig. 2.3(b)) becomes active for 5 years.

Fractures continue to evolve following the direction of maximum far-field stress (x-direction) causing a permeability enhancement up to a distance of 170 m in x-direction in 5 years (Fig. 2.28). The reason why the injection pressure schedule (Fig. 2.3(b)) remains active for 5 years is explained by the following arguments: 1. increasing viscosity by cooling hinders the propagation of the heat front; 2. the slow propagation of the heat front gives rise to slower propagation of thermal tensile stresses; 3. which, along with the fluid pressure, keep on mitigating the geologic compressive stresses and hence helping fractures to evolve.

Figure 2.29 shows the contours of the reservoir temperature when hydraulic fracturing is activated and while accounting for viscosity increase due to brine cooling. Preferential cooling following the new paths of the enhanced permeability is obvious.

Figure 2.30(a) shows the relation between the injection pressure and the fluid flux at the injection well GPK1. During the first 5 years, while hydraulic enhancement is active, the produced fluid volume is obviously increasing even-though the viscosity of the brine fluid is increasing as result of cooling. Permeability enhancement due to hydraulic fracturing counteracts the hindrance related to viscosity increase: an approximate linear relation is observed during this period of active enhancement, compare with Fig. 2.22(a). After 5 years, hydraulic fracturing stops,

[3]Compare with Fig. 2.12 where optimum permeability enhancement is obtained after 1 year for the same injection pressure schedule.

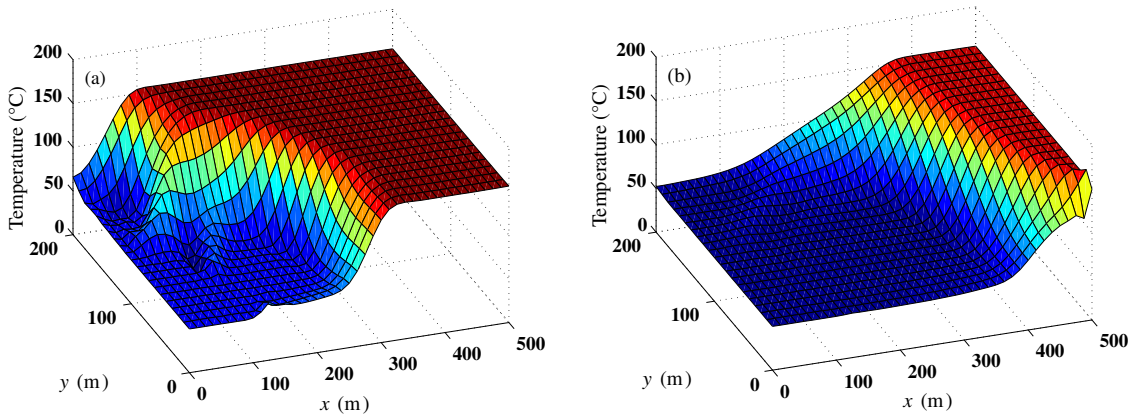

FIGURE 2.29: Contours of the enhanced reservoir temperature at two times: (a) 5 years; and (b) 10 years. Temperature-dependent viscosity is accounted for.

which eliminates the part counteracting the hindrance of viscosity increase. Subsequently, the produced fluid volume declines significantly.

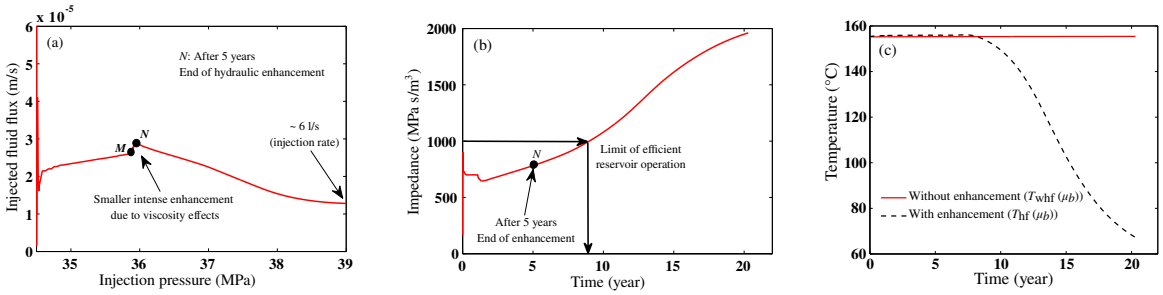

FIGURE 2.30: (a) The relation between injection pressure and resulting flow rate at the injection well GPK1 of the enhanced reservoir and while considering a temperature-dependent viscosity. An approximate linear relation is observed during the period of active hydraulic fracturing. (b) The impedance profile of the enhanced reservoir. (c) Profiles of produced fluid temperature with enhancement ($T_{\mathrm{hf}}(\mu_b)$) and without enhancement ($T_{\mathrm{whf}}(\mu_b)$).

Hydraulic fracturing reduces flow impedance of the HDR reservoir from ∼1700 MPa/(m^3/s) (Fig. 2.27(b)) when hydraulic fracturing is not activated, to ∼700 MPa/(m^3/s) (Fig. 2.30(b)). This impedance reduction should render the operation of the HDR reservoir efficient to a period of approximately 8.5 years. After 8.5 years, flow impedance becomes higher than 1000 MPa/(m^3/s) and the utilization of the reservoir becomes inefficient. This means that injection pressure must increase to a point hydraulic fracturing continues to work such that it counteracts the dragging effects of increased viscosity.

Figure 2.30(c) demonstrates that an HDR reservoir is going to last longer if the change of geothermal fluid viscosity with temperature is considered (compare with Fig. 2.23(a)). However this extended operational life is not of any importance as the impedance exceeds the limits of economic operation from the beginning if hydraulic fracturing is not activated and after ∼8.5 years when it is activated.

Before drawing a definitive conclusion, it is speculated that this disappointing performance is linked to the Newtonian constitutive behavior of the geothermal fluids. Authors like Santoyo et al. (2001) and Santoyo-Gutiérrez, Espinosa, and Amaro-Espejo (2005) have studied eleven Non-Newtonian geothermal fluids: they observed that the temperature changes associated with Non-Newtonian fluids are not as large as observed here. In other words, the Non-Newtonian character of the drilling fluids seems to counteract, at least partially, the thermal dependence of the dynamic viscosity. This statement clearly calls that future studies take into consideration

both thermal effects and Non-Newtonian nature of geothermal fluids. Possibly their effects may, in some circumstances, be cooperating rather than counteracting.

2.1.4 Combined mode I and mode II hydraulic fracturing model

The Hydraulic Fracturing Model (HFM), presented in Sect. 2.1.1.2, is developed to stand for fracture evolution which results from increasing fracture pressure to a point the minimum principal stress becomes tensile and exceeds the tensile strength of the material, and consequently normal separation of fracture surfaces (mode I) occurs. Since fractures in all spatial orientations are considered in the reservoir domain, shear displacement is expected during fracture opening by mode I (Fig. 2.31).

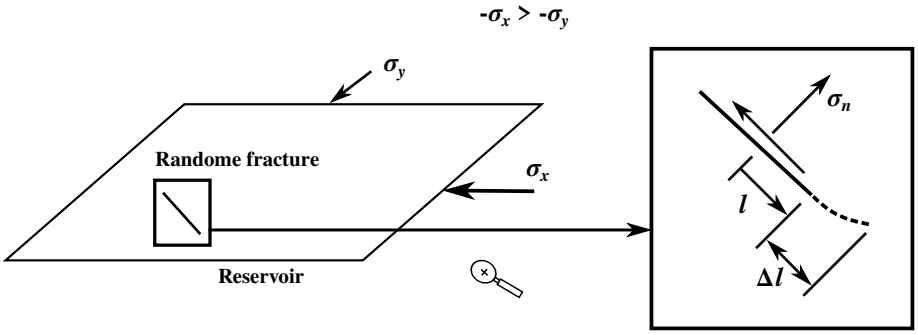

FIGURE 2.31: Fracture pinching due to deviatoric stresses (wing fracture evolution).

The modified fracturing model (HFM2) accounts for a pinching effect due to deviatoric stresses (AbuAisha, 2014; AbuAisha and Loret, 2016a),

$$F(\underline{\underline{\boldsymbol{\sigma}}}', \ell, \boldsymbol{n}) = \sqrt{\pi \ell}\left[\sigma_n' + 3f(\ell)\langle \sigma_n'^d \rangle^+\right] - C_{rc} = 0, \tag{2.17}$$

with,

$$\sigma_n' = \boldsymbol{n}\cdot\underline{\underline{\boldsymbol{\sigma}}}'\cdot\boldsymbol{n}, \quad \boldsymbol{\sigma}'^d = \underline{\underline{\boldsymbol{\sigma}}}' - \frac{\mathrm{tr}(\underline{\underline{\boldsymbol{\sigma}}}')}{3}\underline{\underline{\boldsymbol{\delta}}}, \quad \sigma_n'^d = \boldsymbol{n}\cdot\underline{\underline{\boldsymbol{\sigma}}}'^d\cdot\boldsymbol{n}, \tag{2.18}$$

and C_{rc} is the material toughness. The function $f(\ell)$ involves a fracture growth stabilizing parameter ξ in the same format as in Sect. 2.1.1.2:

$$f(\ell) = \xi \begin{cases} \dfrac{\ell_f}{\ell}, & \ell < \ell_f; \\ 1, & \ell \geq \ell_f. \end{cases} \tag{2.19}$$

The pinching effect is active only if normal deviatoric stress $\sigma_n'^d$ is positive. Consider axisymmetric loading about the axis 1, then $\sigma_n'^d = (\sigma_{11}' - \sigma_{22}')\,(n_1^2 - 1/3)$. For fractures normal to the symmetry axis ($n_1 = 1$), the term is effective if the radial stress is less tensile than the normal stress, e.g. $\sigma_{11}' = 0$ and $\sigma_{22}' < 0$. Conversely, for fractures parallel to the symmetry axis ($n_1 = 0$), the term is effective if the axial stress is less tensile than the radial stress, e.g. $\sigma_{11}' < 0$ and $\sigma_{22}' = 0$.

The same stimulation test (Sect. 2.1.2.3) is reconsidered in the following simulations. The stabilizing parameter ξ is determined such that the fracturing begins at a pressure p_b^{HF} corresponding to one of the cases demonstrated in Eqs 2.11 or 2.12 whichever applies. Material properties for hydraulic fracturing are indicated in Table 2.3, except for the stabilizing parameter $\xi = 0.0205$, which is calculated for a fracturing threshold of 40 MPa, and $C_{rc} = K_{Ic}$.

Figure 2.32 shows that the modified fracturing model requires less energy than the HFM. For the same pore fluid injection profile (Fig. 2.3(b)), hydraulic fracturing remains active for 2 years, meanwhile it is only active of a period of 1 year when the HFM is considered (Fig. 2.12).

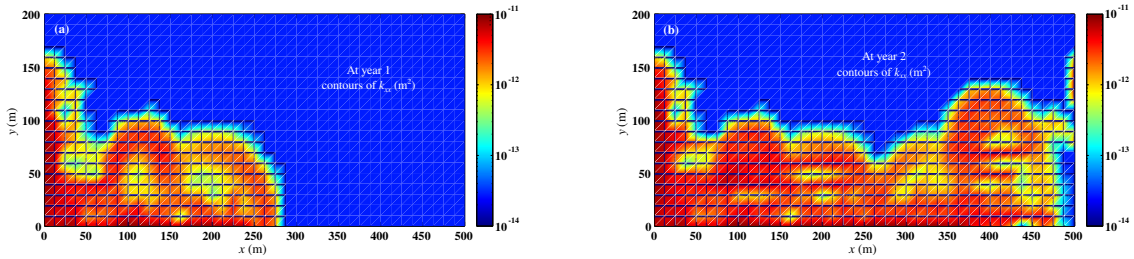

FIGURE 2.32: Contours of longitudinal permeability component k_{xx} at two times: (a) 1 year; and (b) 2 years. Fracture propagation is in the direction of maximum far-field stress. Injection pressure schedule (Fig. 2.3(b)) is sufficient to entirely enhance the reservoir in the longitudinal direction.

Clearly the HFM2 provides a more stable and a smoother evolution of porous block permeability which is translated into a slower propagation of the heat front and hence an improved hydraulic enhancement in terms of the stimulated volume.

The volume of the HDR reservoir enhanced by hydraulic fracturing, whether by applying the HFM or the HFM2, for a period of one year, shows that fractures are evolving in the direction of the maximum far-field stress (x-axis). This behavior causes an enhancement of the longitudinal permeability up to almost the same distances in x- and y-directions for both the HFM and the HFM2 (compare Figs 2.12 and 2.32(a)). These simulations are in good agreement with the microseismic events diagram presented in Bruel (1995b) after 1 year of hydraulic fracturing.

The preferential cooling following the new paths created by hydraulic fracturing is demonstrated in Fig. 2.33. The spurious oscillations on the temperature contours come from the shocks that disturb the heat front when the permeability is suddenly increased (Sect. 2.1.5).

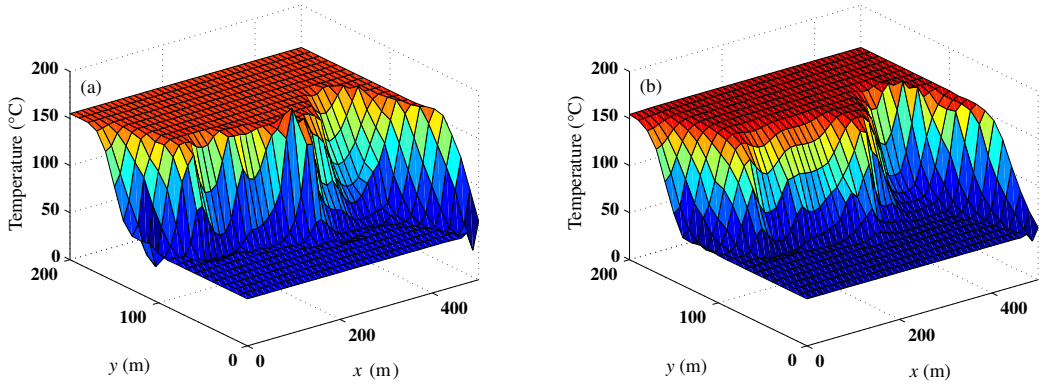

FIGURE 2.33: Contours of the enhanced reservoir temperature at two times: (a) 5 years; and (b) 10 years, and while using the HFM2.

The stabilizing effect of the modified fracturing model (HFM2) with respect to the HFM is also observed in Fig. 2.34, where the time course of the longitudinal permeability is smoother in the case of the HFM2.

The non-linear relation between the injection pressure and flow rate at the injection well GPK1 shows periods of intense enhancement during the first two years of the simulations (Fig. 2.35(a)).

Since the reservoir volume enhanced by the HFM2 is more important than in the case of the HFM for the same injection schedule, the reservoir is depleted faster (Fig. 2.36(a)).

The produced flow from the HDR reservoir when the HFM2 is used is, by average, 2.5 times higher (Fig. 2.36(b)). However, the reservoir works efficiently for 10.5 years in case of the HFM and only for 4 years when the HFM2 is employed (Fig. 2.36(a)). If flow profiles (Fig. 2.36(b)) are

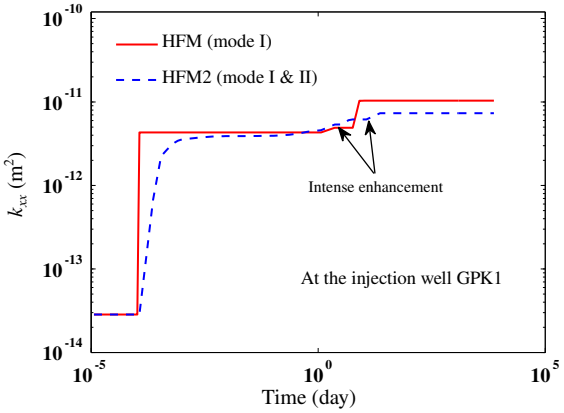

FIGURE 2.34: Longitudinal permeability k_{xx} history at the injection well GPK1 for the two models the HFM and the HFM2.

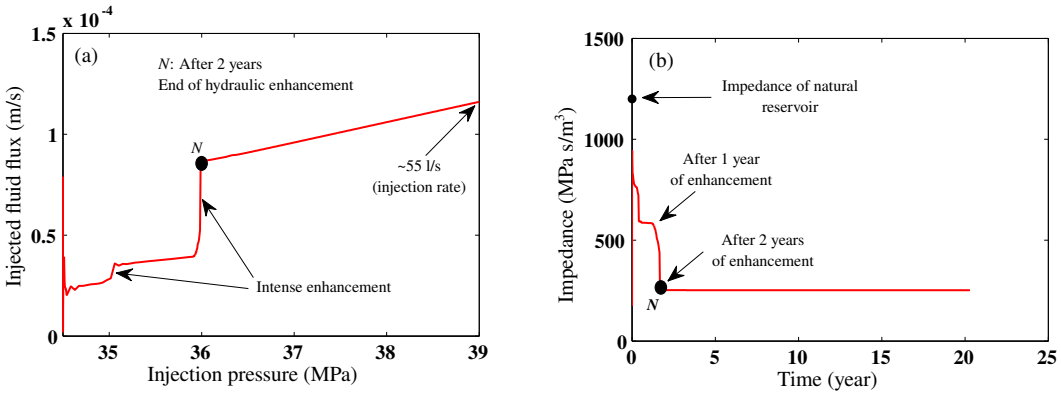

FIGURE 2.35: (a) The relation between injection pressure and resulting flow rate at the injection well GPK1 of the enhanced reservoir of Soultz-sous-Forêts and while considering the HFM2. (b) The impedance history.

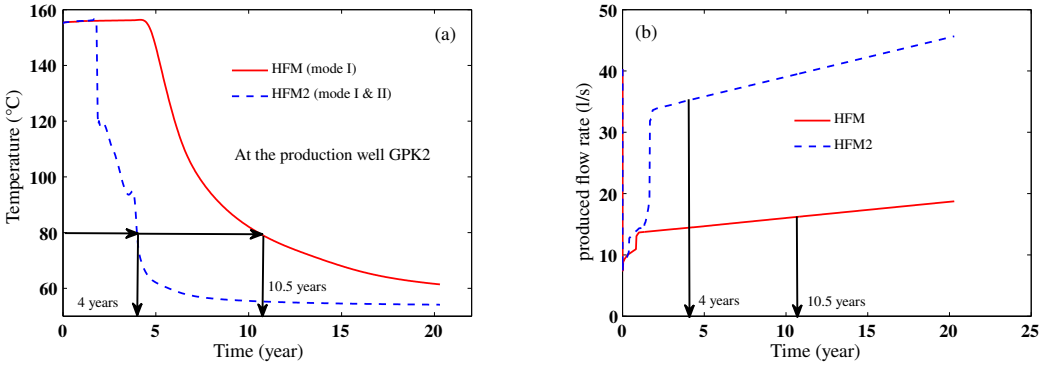

FIGURE 2.36: Time profiles of produced (a) temperatures (b) flow rates from the enhanced HDR reservoir, comparison between the HFM and the HFM2 simulation results.

numerically integrated over the efficient life of the HDR reservoir, the extracted fluid volumes are known: the volume of efficient fluid produced from the stimulated HDR reservoir by the HFM over a period of 10.5 years is 4.922 Million m^3 against 2.681 Million m^3 in the case of the HFM2.

Thus, about 45.5% of the efficient produced fluid is lost when the HFM2 is used in the simulations for the injection schedule (Fig. 2.3(b)). However, using the HFM2 has reduced the

power needed to operate the HDR reservoir by about 80% (Fig. 2.35(b)). The implementation of hydraulic fracturing is a matter of compromise: less consumption of energy requires stronger hydraulic fracturing which, regrettably, means a short effective life of the HDR reservoir and hence a reduction of the ultimate produced efficient fluid.

Murphy et al. (1999) have indicated that the ambitious goal is to enhance HDR reservoirs to a point their impedance becomes very small, i.e. $\mathcal{Z} < 100$ MPa/(m^3/s) on a consistent basis. This can be achieved numerically by applying the HFM2 and choosing such a strong injection schedule where more volume of the reservoir is enhanced. Yet, one should keep in mind that such a process strongly and regrettably reprimands the effective life of the reservoir and thus the amount of the efficient produced fluid.

2.1.5 Numerical stabilization of forced heat convection

The sudden increase of the permeability tensor at the geometrical points, where hydraulic fracturing is active, is accompanied by sudden increase in the velocity of the fluid front. Therefore, the convected heat front strongly strikes the stiff boundaries where the permeability is not yet enhanced. The reflection of the heat front is supposed to cause spurious numerical wiggles in the solution of the temperature field (Fig. 2.33). These oscillations in the temperature field result in spurious oscillations in the effective stress fields. Knowing that the effective stresses are the driving forces for fracture evolution, the numerical simulation of hydraulic fracturing cannot be trusted with such spurious oscillations.

The hydraulic fracturing stimulation tests are performed under extreme conditions where an enormous change of the reservoir pressure and temperature is expected at the injection well and at quite early stages. The commonly used stabilizing approaches for heat convection have proven to be inefficient for sudden large changes in the fluid velocity and at early stages with extreme injection conditions (AbuAisha, 2014; Yin, Dusseault, and Rothenburg, 2009). This section focuses on the computational difficulties associated with the phenomenon of forced heat convection. The disturbing spurious noises that can appear on the contours of temperature fields are healed and/or mitigated by applying multiple stabilization methods.

2.1.5.1 Limitations of the SUPG method

A method is needed to stabilize the spurious numerical oscillations in the hyperbolic solutions of the convection-dominated thermo-poroelastic BVPs. Among the several methods presented in literature to treat such oscillations, the Streamline-Upwind/Petrov-Galerkin (SUPG) method is used in the previous simulations. This method does not require to introduce additional testing functions, it nevertheless adds perturbations to the Galerkin test functions (Hughes, 2000). This advantage makes the SUPG method widely acceptable and easily implemented in the problems of heat convection.

The SUPG method originates from the upwind finite differences method which uses the artificial diffusion idea. The method taps on the work of Brooks and Hughes (1982) and the formalism of Fries and Matthies (2004). Based on the work of AbuAisha (2014), and the research of Gelet, Loret, and Khalili (2012b), Gelet, Loret, and Khalili (2013), and Gelet, Loret, and Khalili (2012a), the SUPG method is sufficient to give smooth numerical solutions except for the following cases:

- strong pumping near the injection well at early times;
- when hydraulic fracturing is activated with a strong increase in the permeability tensor components; and,
- at the production well at late times when the major part of the heat front reaches the stiff boundary.

The balance of energy of a thermo-poroelastic BVP (Eq. 2.6$_3$) with a source term f, can be written in the following format,

$$\mathcal{R}\theta - f = 0, \quad \text{with} \quad \mathcal{R}\theta = \rho C_v \frac{\partial \theta}{\partial t} + \boldsymbol{v}^{\text{conv}} \cdot \boldsymbol{\nabla}\theta - \boldsymbol{\nabla} \cdot (\Lambda \boldsymbol{\nabla}\theta)\,, \tag{2.20}$$

with $\boldsymbol{v}^{\text{conv}} = \rho_\lambda C_{p\lambda} \boldsymbol{q}$ being the convective velocity vector. The weak form associated with Eq. 2.20,

$$\int_{\mathcal{V}} \delta\theta (\mathcal{R}\theta - f)\, d\mathcal{V}, \tag{2.21}$$

uses different interpolation functions for the unknown temperature change θ and its variation $\delta\theta$:

$$\theta = \boldsymbol{N}_\theta \boldsymbol{\theta}^e; \quad \delta\theta = \boldsymbol{W}_{\boldsymbol{\theta}} \delta\boldsymbol{\theta}^e, \tag{2.22}$$

the weight function $\boldsymbol{W}_{\boldsymbol{\theta}}$ is taken as,

$$\boldsymbol{W}_{\boldsymbol{\theta}} = \boldsymbol{N}_\theta + \tau \boldsymbol{v}^{\text{conv}} \cdot \boldsymbol{\nabla} \boldsymbol{N}_\theta, \tag{2.23}$$

the stabilization parameter τ is expressed as,

$$\tau = \frac{h}{2|\boldsymbol{v}^{\text{conv}}|} \left(\coth(\text{Pe}) - \frac{1}{\text{Pe}} \right), \tag{2.24}$$

where h is the typical element length and $\text{Pe} = |\boldsymbol{v}^{\text{conv}}| h / \Lambda$ is the Péclet number.

By substituting the definition (2.23) into Eq. (2.21), the weak form of the problem is reached by discretizing the body into N_e non-overlapping generic elements of volume $\mathcal{V}^e$,

$$\sum_{e=1}^{N_e} [\delta\boldsymbol{\theta}^e]^T \int_{\mathcal{V}^e} (\boldsymbol{N}_\theta)^T \Big(\mathcal{R}\theta - f \Big)\, d\mathcal{V}^e + \underbrace{\sum_{e=1}^{N_e} [\delta\boldsymbol{\theta}^e]^T \int_{\mathcal{V}^e} \underbrace{\Big(\boldsymbol{\nabla}(\boldsymbol{N}_\theta)^T (\boldsymbol{v}^{\text{conv}})^T \Big) \tau}_{\text{Streamline perturbation}} \Big(\mathcal{R}\theta - f \Big)\, d\mathcal{V}^e}_{\text{Stabilizing part}} = 0. \tag{2.25}$$

As stated previously, the application of the SUPG method is not sufficient at small time steps. Actually, the characteristic time that weighs the stabilization of the SUPG method (Eq. 2.24) can be expressed as in Hughes, Franca, and Hulbert (1989) and Tezduyar and Park (1986),

$$\tau = \frac{1}{\sqrt{\left(\frac{2}{\Delta t}\right)^2 + \left(\frac{2|\boldsymbol{v}^{\text{conv}}|}{\rho C_v h}\right)^2 + 9\left(\frac{4\Lambda}{\rho C_v h^2}\right)^2}}, \tag{2.26}$$

for significantly small time steps ($\Delta t \to 0$), the stabilization coefficient τ becomes inefficient, i.e.,

$$\lim_{\Delta t \to 0} \tau = 0. \tag{2.27}$$

To overcome the deficiencies of the SUPG method for healing the oscillations in the numerical solutions of transient convection-diffusion problems at early times and when activating hydraulic fracturing, the Gradient Subgrid Scale GSGS method is presented in the next section. It is, henceforth, conceivable that the calculation of the stabilization parameter must take into account a time-dependent factor, where the transition between the convection-dominated and the diffusion-dominated situations in small time steps is indeed natural.

2.1.5.2 The Gradient Subgrid Scale GSGS method

The GSGS method includes two terms, an adjoint stabilization and a gradient adjoint stabilization (Harari, 2004). The two associated coefficients are tuned to attain nodal exactness for a specific one-dimensional problem. The method relies on a reactive term which may be either constitutive or resulting from a time semi-discretization scheme. For instance, it applies for the diffusion equations, the balance of mass for instance, which do not include convective terms nor constitutive reaction terms. A reaction term is exhibited by firstly discretizing in time and secondly in space. Unlike the SUPG method, the stabilizing terms vanish when the mesh gets significantly refined but not when time step is considerably reduced.

The field Eq. 2.20 is integrated at the time step $n+1$ by using a generalized trapezoidal scheme parameterized by the scalar $\beta \in]0,1]$,

$$\rho C_v \frac{\theta_{n+1}-\theta_n}{\Delta t} + \left(\boldsymbol{v}^{\text{conv}} \cdot \boldsymbol{\nabla}\theta - \boldsymbol{\nabla}\cdot(\Lambda\boldsymbol{\nabla}\theta) - f\right)_{n+\beta} = 0, \tag{2.28}$$

with the notation $a_{n+\beta} = (1-\beta)\, a_n + \beta\, a_{n+1}$. It is instrumental to define the operator $\mathcal{N}$ and its adjoint $\mathcal{N}_*$ such that,

$$\begin{aligned} \mathcal{N}\theta &= \boldsymbol{v}^{\text{conv}} \cdot \boldsymbol{\nabla}\theta - \boldsymbol{\nabla}\cdot(\Lambda\boldsymbol{\nabla}\theta) - s\theta, \\ -\mathcal{N}_*\theta &= \boldsymbol{v}^{\text{conv}} \cdot \boldsymbol{\nabla}\theta + \boldsymbol{\nabla}\cdot(\Lambda\boldsymbol{\nabla}\theta) + s\theta, \end{aligned} \tag{2.29}$$

which display the reaction coefficient $s < 0$,

$$s = -\frac{\rho C_v}{\beta \Delta t} < 0. \tag{2.30}$$

The steady convection-diffusion-reaction problem at step $n+1$ is, henceforth, cast in the following format,

$$\mathcal{N}\theta_{n+1} - F_{n+1} = 0, \tag{2.31}$$

where,

$$F_{n+1} = \frac{-(1-\beta)}{\beta}\left(\boldsymbol{v}^{\text{conv}} \cdot \boldsymbol{\nabla}\theta - \boldsymbol{\nabla}\cdot(\Lambda\boldsymbol{\nabla}\theta)\right)_n + \frac{f_{n+\beta}}{\beta} - s\theta_n. \tag{2.32}$$

For any variation w^h, the weak form of Eq. 2.31 takes the following form,

$$\begin{aligned} &\int_{\mathcal{V}} w^h \left(\mathcal{N}\theta^h_{n+1} - F_{n+1}\right) d\mathcal{V} \\ +\sum_{e=1}^{N_e} &\int_{\mathcal{V}^e} \left(-\mathcal{N}_* w^h_{n+1}\right) \tau^e_{00} \left(\mathcal{N}\theta^h_{n+1} - F_{n+1}\right) d\mathcal{V}^e \\ +\sum_{e=1}^{N_e} &\int_{\mathcal{V}^e} \boldsymbol{\nabla}\left(-\mathcal{N}_* w^h_{n+1}\right) \tau^e_{11} \boldsymbol{\nabla}\left(\mathcal{N}\theta^h_{n+1} - F_{n+1}\right) d\mathcal{V}^e = 0, \end{aligned} \tag{2.33}$$

includes the two stabilization parameters τ^e_{00} and τ^e_{11}. These parameters are defined in terms of two dimensionless coefficients t_{00} and t_{11} such that nodal exactness for a specific one-dimensional problem is assured (Hauke, Sangalli, and Doweidar, 2007),

$$\tau^e_{00} = \frac{h}{|\boldsymbol{v}^{\text{conv}}|} t_{00} \geq 0, \quad \tau^e_{11} = \frac{h^3}{|\boldsymbol{v}^{\text{conv}}|} t_{11} \leq 0, \tag{2.34}$$

with,

$$t_{00} = \left(-2\text{Da} + \frac{\text{Da}^2 \sinh(\text{Pe})}{-\cosh(\text{Pe}) + \cosh(\gamma) + \text{Da}\sinh(\text{Pe})}\right)^{-1}, \tag{2.35}$$

$$t_{11} = \frac{1}{6\mathrm{Da}^3}\left(-3-\mathrm{Da}^2+\frac{3\mathrm{Da}}{\mathrm{Pe}}+\frac{3\mathrm{Da}\cosh(\gamma)+(-3+\mathrm{Da}^2)\sinh(\mathrm{Pe})}{-2\cosh(\mathrm{Pe})+2\cosh(\gamma)+\mathrm{Da}\sinh(\mathrm{Pe})}\mathrm{Da}\right), \tag{2.36}$$

where, $\gamma = \sqrt{\mathrm{Pe}(-2\mathrm{Da}+\mathrm{Pe})}$, and Pe and Da are the Péclet and Damköhler numbers respectively,

$$\begin{aligned} \mathrm{Pe} &= \frac{|\boldsymbol{v}^{\mathrm{conv}}|h}{\Lambda} = \frac{\text{Advection}}{\text{Diffusion}} \quad \text{Péclet number;} \\ \mathrm{Da} &= \frac{s\,h}{|\boldsymbol{v}^{\mathrm{conv}}|} = \frac{\text{Reaction}}{\text{Advection}} \quad \text{Damköhler number.} \end{aligned} \tag{2.37}$$

Figure 2.37 shows the contours of the coefficients t_{00} and t_{11} as a function of Pe and Da. The first stabilizing coefficient t_{00} is always positive, whereas the coefficient t_{11} is always negative.

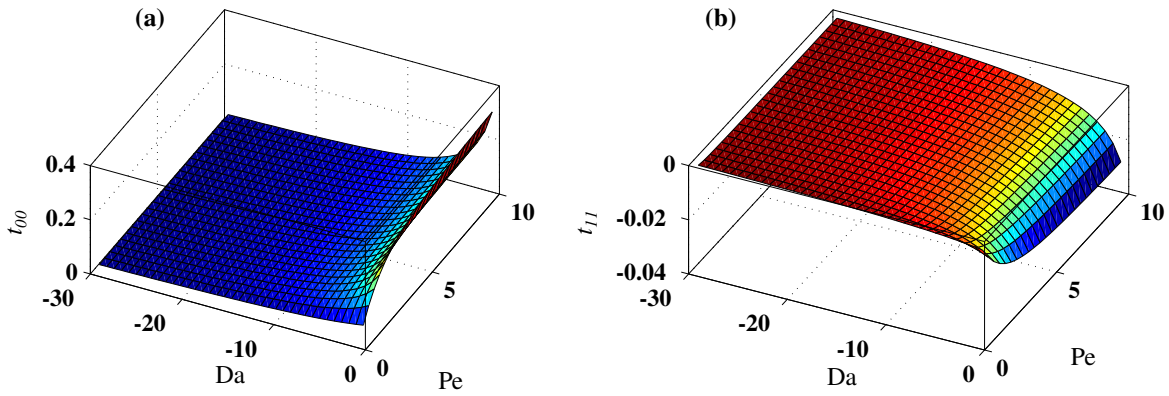

FIGURE 2.37: Dimensionless stabilizing parameters: (a) t_{00}; (b) t_{11} stemming from a one-dimensional nodal exactness of Hauke, Sangalli, and Doweidar (2007).

For linear elements in one-dimensional problems and under convective-diffusive dominant condition ($\mathrm{Da} \to 0$), the method (Eq. 2.33), produces the same modification as the SUPG method in absence of the reactive term[4],

$$\tau_{00}^e \xrightarrow{\mathrm{Da}\to 0} \frac{h}{2|\boldsymbol{v}^{\mathrm{conv}}|}\left(\coth(\mathrm{Pe})-\frac{1}{\mathrm{Pe}}\right). \tag{2.38}$$

Hauke, Sangalli, and Doweidar (2007) have provided several definitions for the stabilizing parameters τ_{00}^e and τ_{11}^e depending on the dominant limit: convective-diffusive with no reaction limit, without convection limit, reaction dominated limit, and high Péclet number limit. The only case where it is thought that the general expressions of Eqs. 2.35 and 2.36 are troublesome is when s is very small, generally less than $10^{-3} \times \rho\, C_v$. Then, the dimensionless stabilizing coefficients should be calculated as follows:

$$\begin{aligned} t_{00} &\to \frac{1}{2}\left(\coth(\mathrm{Pe})-\frac{1}{\mathrm{Pe}}\right) \xrightarrow{\mathrm{Pe}\to 0} \frac{\mathrm{Pe}}{6}; \quad \text{and,} \\ t_{11} &\to \frac{-1}{24}\left(\frac{3}{\mathrm{Pe}^3}(1-\mathrm{Pe}\coth(\mathrm{Pe}))+\coth(\mathrm{Pe})\right) \xrightarrow{\mathrm{Pe}\to 0} -\frac{\mathrm{Pe}}{60}. \end{aligned} \tag{2.39}$$

The details of the finite element formulations of both the SUPG and the GSGS methods, and the way they are integrated in the thermo-hydromechanical framework are provided in

[4]The third term of eq. (2.33) disappears as at least for linear elements in one-dimensional problems, the gradient stabilization term $\mathcal{N}_*$ disappears when $\mathrm{Da} \to 0$ since τ_{11}^e is uniformly bounded to a limit (Fig. 2.37(b)), whence $s^2\,\tau_{11}^e \to 0$. The previous remark becomes clear if the matrix form of Eq. 2.33 is derived for a one-dimensional problem with linear elements.

AbuAisha (2014) and AbuAisha and Loret (2016b). In the coming sections, the circulation tests in the Soultz-sous-Forêts HDR reservoir (Sect. 2.1.2.3) are re-performed while implementing the GSGS method in the FEM code.

2.1.5.3 The circulation test at the well GPK1 1993 without hydraulic fracturing

Simulations of the circulation test in the Soultz-sous-Forêts HDR reservoir (Sect. 2.1.2.3), and while implementing the GSGS method in the FEM code are presented. Hydraulic fracturing is not activated as this section aims at studying the stabilization of heat convection under normal circulation conditions.

Figure 2.38 compares the profiles of temperature and pressure, along the line of symmetry $y = 0$ m, for the GSGS and the SUPG methods at different times of 10 days, 6 months, and at years 1, 2, 5 and 10. The GSGS method heals quite satisfactorily the oscillations of the SUPG method even at small time interval of 10 days. The profiles of pore fluid pressure do not differ between the GSGS and the SUPG methods since hydraulic diffusion establishes quickly, i.e. in a few days. The jump in the pressure profiles at the injection well between the time intervals of 10 days and 6 months is due to the pumping schedule (Fig. 2.3(b)).

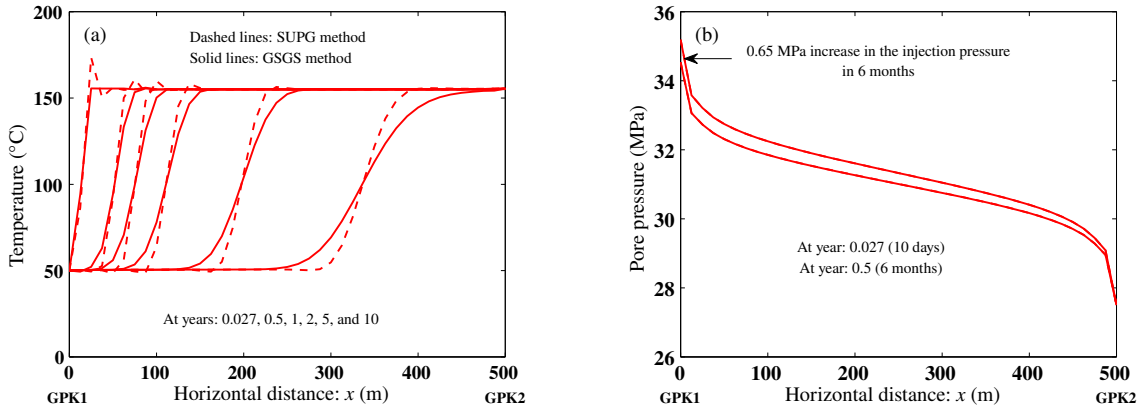

FIGURE 2.38: Temperature and pore pressure profiles along the line of symmetry $y = 0$ m: (a) heat convection oscillations near the injection well are stabilized when the GSGS method is applied; (b) pore fluid pressure profiles are not affected by the GSGS method since hydraulic diffusion establishes quickly.

Though the GSGS method is capable of circumventing the heat convection oscillations at very short and intermediate time intervals, its capacity deteriorates with time (Fig. 2.39).

At year 15 and despite mitigating the noises at the production well, the GSGS method still leaves serious temperature oscillations (Fig. 2.39). At large time intervals near the production well, the source term becomes negligible ($s \to 0$) meanwhile the convective velocity is considerably large. This causes the Damköhler number to disappear ($\mathrm{Da} \to 0$), therefore the capacity of the GSGS method is lost as a convection-dominated situation appears and the stabilizing method produces the same modification as the SUPG method.

2.1.5.4 The hydraulic fracturing test at the well GPK1 1993

The purpose of this section is to use the GSGS method to heal the numerical oscillations which appear on the contours of temperature field and hence affect the process of hydraulic fracturing. Fig. 2.40 shows the contours of the reservoir temperature during the process of stimulation at years 5 and 10, and while using the GSGS method.

The GSGS method cures almost all of heat convection oscillations, compare Figs. 2.33 and 2.40. Due to the diffusive nature of the GSGS method, the values of the contours of the enhanced

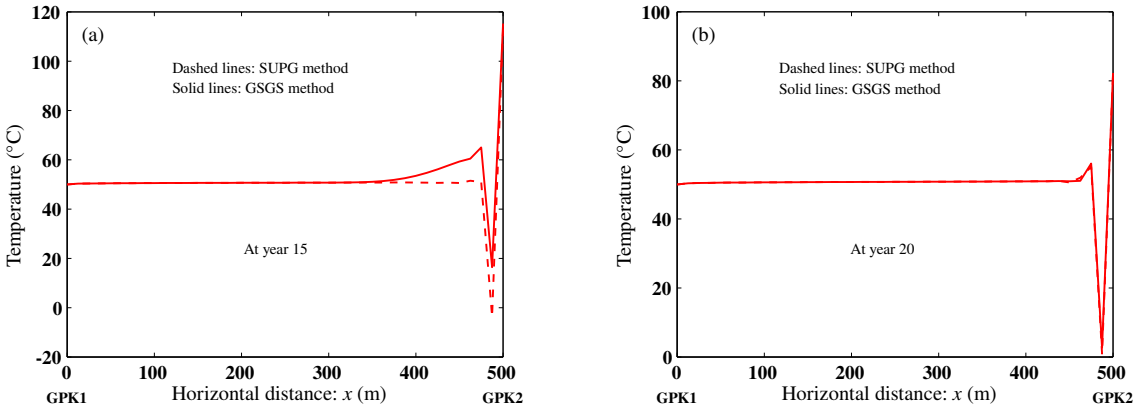

FIGURE 2.39: Temperature profiles along the line of symmetry $y = 0$ m: (a) heat convection oscillations are mitigated at the production well but still far from being healed; (b) at very large times, both the SUPG and GSGS methods are unable to stabilize oscillations near the production well.

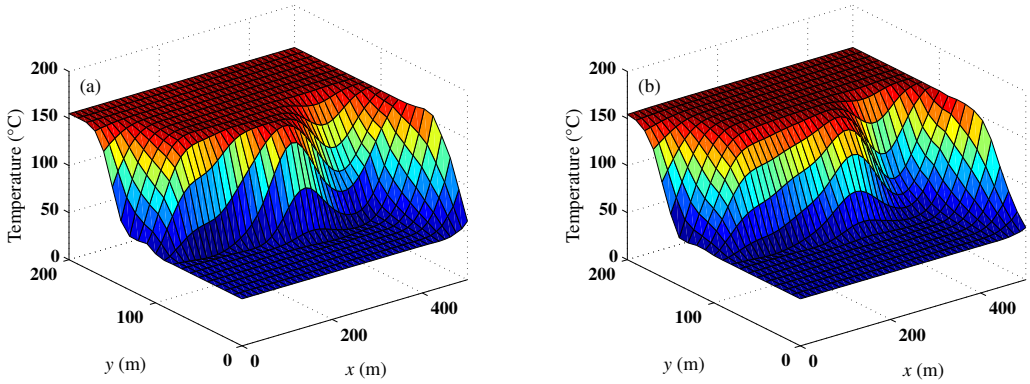

FIGURE 2.40: Contours of the enhanced reservoir temperature at two times: (a) 5 years; and (b) 10 years, heat convection is stabilized by the GSGS method

permeability of the HDR reservoir are about 0.96 less when the GSGS method is implemented. This becomes more evident when the history of the enhanced permeability is plotted at some point (Fig. 2.41). It is clear that the evolution of the longitudinal permeability is smoother in the case of the GSGS method as it provides more stabilization. Nonetheless, the same general evolution behavior is more or less obtained for both the GSGS and the SUPG methods.

The advantages and disadvantages of the GSGS method are listed as follows:

1. the GSGS method has been proven capable of efficiently healing the heat convection oscillations at very short and intermediate time intervals;

2. the GSGS method is also efficient in curing the stubborn heat convection oscillations even while tremendously enhancing the HDR reservoir permeability by hydraulic fracturing;

3. at quite large time intervals and if convection-dominated situations are present, the GSGS method loses its efficiency and the SUPG method is retrieved.

2.1.5.5 The Discontinuity Capturing Method (DCM)

Neither the GSGS method nor the SUPG method is capable of healing the numerical noises resulting from the heat front striking the stiff boundary at the production well. John and Knobloch

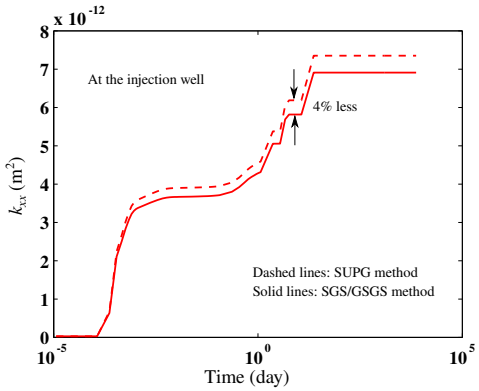

FIGURE 2.41: Longitudinal permeability k_{xx} history at the injection well: comparison between the simulations when implementing the GSGS method (solid lines) and the SUPG method (dashed lines).

(2007) have defined a modification to the SUPG method, referred to as the Discontinuity Capturing Method (DCM), such that it becomes capable of treating the spurious numerical noises at long periods.

The DCM suggests to modify the SUPG weighting function by an additional term parallel to the thermal gradient of the thermal analysis in the following format,

$$\boldsymbol{W_\theta} = \boldsymbol{N}_\theta + \tau_1 (\boldsymbol{v}^{\text{conv}})^T \cdot \boldsymbol{\nabla} N_\theta + \tau_2 (\boldsymbol{v}_{||})^T \cdot \boldsymbol{\nabla} N_\theta, \tag{2.40}$$

the projection $\boldsymbol{v}_{||}$ of $\boldsymbol{v}^{\text{conv}}$ on $\boldsymbol{\nabla}\theta$ being defined as[5],

$$\boldsymbol{v}_{||} = \begin{cases} \dfrac{(\boldsymbol{v}^{\text{conv}})^T \cdot \boldsymbol{\nabla}\theta}{|\boldsymbol{\nabla}\theta|^2} \boldsymbol{\nabla}\theta, & \boldsymbol{\nabla}\theta \neq \boldsymbol{0}, \\ \boldsymbol{0}, & \boldsymbol{\nabla}\theta = \boldsymbol{0}. \end{cases} \tag{2.41}$$

Since $(\boldsymbol{v}^{\text{conv}})^T \cdot \boldsymbol{\nabla\theta} = (\boldsymbol{v}_{||})^T \cdot \boldsymbol{\nabla\theta}$, it is concluded that,

$$\boldsymbol{W_\theta^T} (\boldsymbol{v}^{\text{conv}})^T \cdot \boldsymbol{\nabla\theta} = (\boldsymbol{N}_\theta)^T (\boldsymbol{v}^{\text{conv}})^T \cdot \boldsymbol{\nabla\theta} + \underbrace{(\boldsymbol{\nabla N}_\theta)^T \tau_1 \boldsymbol{v}^{\text{conv}} (\boldsymbol{v}^{\text{conv}})^T \cdot \boldsymbol{\nabla\theta}}_{\text{Streamline operator}} + \underbrace{(\boldsymbol{\nabla N}_\theta)^T \tau_2 \boldsymbol{v}_{||} (\boldsymbol{v}_{||})^T \cdot \boldsymbol{\nabla\theta}}_{\text{DCM operator}}. \tag{2.42}$$

While the SUPG matrix $\boldsymbol{v}^{\text{conv}} (\boldsymbol{v}^{\text{conv}})^T$ is a first-order positive semi-definite matrix acting only in the streamline direction, the discontinuity capturing matrix $\boldsymbol{v}_{||} (\boldsymbol{v}_{||})^T$ is also a first-order positive semi-definite matrix yet acting only in the direction of the discrete solution temperature gradient.

The stabilizing parameters τ_1 and τ_2 are defined such that,

$$\tau_1 = \tau, \quad (\text{of the SUPG method}) \quad \text{and,} \quad \tau_2 = \tau_{||}, \tag{2.43}$$

$\tau_{||}$ is deduced using the same strategy of calculating τ (Eq. 2.24), yet the parallel velocity $\boldsymbol{v}_{||}$ is introduced. In order to avoid the doubling of the stabilizing parameter τ when $\boldsymbol{v}^{\text{conv}} = \boldsymbol{v}_{||}$, the DCM parameter is re-defined,

$$\tau_1 = \tau, \quad \text{and,} \quad \tau_2 = \max[0, \tau_{||} - \tau]. \tag{2.44}$$

Fig. 2.42 shows that the DCM is capable of almost entirely healing the numerical oscillations at the production well, compare with Fig. 2.39.

[5]The DCM is a non-linear stabilizing method as $\boldsymbol{v}_{||} = \boldsymbol{v}_{||}(\boldsymbol{\theta}^e)$.

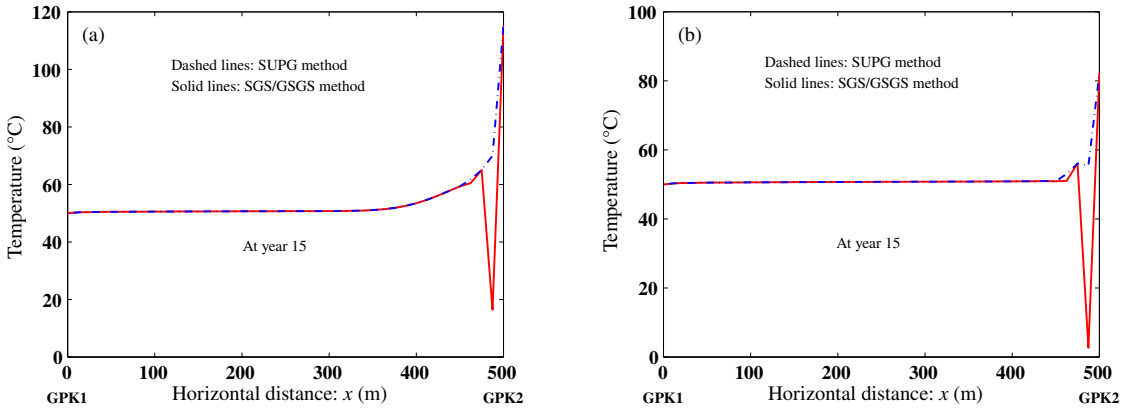

FIGURE 2.42: Temperature profiles along the line of symmetry $y = 0$ m. DCM is capable of treating the stubborn numerical oscillations at the production well where both the GSGS and SUPG methods are proven inefficient.

2.1.6 Conclusion and perspectives

The hydraulic fracturing technique is addressed in a thermo-poroelastic framework with emphasis on the impedance and efficiency of thermal recovery from HDR reservoirs. According to simulations, hydraulic fracturing is effective in a large zone adjacent to the injection well and the permeability in the direction of the production well is considerably enhanced. As a consequence, the impedance of the reservoir is improved.

A modification to the fracture model to account for both opening and pinching of fractures results in more long term positive effects on the impedance. Moreover, it displays an enlarged zone of enhanced permeability. Yet, it reduces the duration of an efficient reservoir exploitation.

The increase of viscosity in the neighborhood of the injection well hinders the hydraulic fracturing process by reducing the pressure inside the reservoir, which leads to a less enhanced permeability.

In summary, the exact zone in which the permeability enhancement is significant depends on the details of the model. In all cases, this zone is widespread so that the flow is able to collect the heat of the rock in its path to the production well. In a broader perspective, the simulations point out that non-Darcian constitutive behaviors of flow and non-Newtonian characteristics of geothermal fluids are worth of investigation. As a further extension to this work, future research should also consider the interactions between the working fluids and other techniques aiming at improving the efficiency of thermal recovery, like the chemical enhancement of HDR reservoirs as well as CO_2-based geothermal systems.

The thermo-hydromechanical framework addresses several approaches to stabilize convection of heat at all treatment stages. The commonly used SUPG method is implemented to heal the oscillations at intermediate stages. The DCM is applied to stabilize convection of heat at late stages near the production well. For instabilities at early stages, the transient advection-diffusion problem is transformed into a steady advection-diffusion-reaction problem, which takes into account the effect of the time step factor on the numerical oscillations (the GSGS method). Ultimately, this method is capable of healing the stubborn oscillations at early stages and when permeability is tremendously increased by hydraulic fracturing.

Generally, while the current developments include a single porosity and a single temperature, a double porosity approach may be worth of consideration to team up with the hydraulic fracturing models, i.e. the fracture porosity.

2.2 A continuum-discontinuum approach to simulate hydraulic fracturing and induced seismicity for oil and gas industry

Unlike the simulations of Sect. 2.1 where the entire volume of the reservoir is the goal of the hydraulic stimulation, the approach presented here focuses on developing fractures close to the borehole for applications related to *shale gas extraction* and scrutinization of *induced seismicity*.

A number of techniques that are rooted in microseismic observations have been developed to aid in the interpretation of fracturing processes. It is often assumed that the time-dependent microseismic cloud is a proxy for the growth of the hydraulic fracture. Based on this assumption, Boroumand and Eaton (2015) developed a geomechanical simulation in which model parameters for an energy-based fracture growth are tuned to fit observed microseismicity in space and time. Shapiro and Dinske (2009b) and coworkers (Shapiro and Dinske, 2009a; Shapiro, Dinske, and Rothert, 2006) have developed a poroelastic approach based on the concept of a seismicity-triggering front. This approach uses a diffusion model that is characterized by either constant diffusivity, where the triggering front has a space-time representation of a parabolic form, or pressure-dependent diffusivity, in which case a cubic-parabolic triggering front emerges under certain assumptions. Some scientists (Cornet, 2000) argued that in the presence of tensile rock failure induced by hydraulic fracturing, the simplified models underlying these approaches do not fully capture the complexity of the spatial distribution of microseismic events, where some events are activated by mechanical rather than diffusional effects.

This research uses a coupled hydro-mechanical Finite Discrete Element Modelling (FDEM) approach to investigate in more detail the link between microseismicity and hydraulic fracture propagation for petroleum applications (AbuAisha et al., 2017). The Discrete Element Method (DEM) has been used to simulate hydraulic fracturing in naturally fractured reservoir. For instance, Duan, Kwok, and Wu (2018) and Damjanac and Cundall (2016) used a DEM approach where rock mass was considered as an assembly of blocks, and contact between these blocks represented discontinuities that exhibited a non-linear mechanical behavior. Damjanac and Cundall, 2016 used lubrication theory to implement fluid flow in the rock mass and consequently hydraulic fracturing. Other authors (Sousani et al., 2015) used a DEM approach to present a solid-fluid coupled framework to investigate the effects of fluid injection on the mechanical behavior of fractured geomaterials on the particle size. Fu, Johnson, and Carrigan (2013) describe a framework that combines the finite element method for geomechanics in the rock matrix, a finite volume approach for resolving hydrodynamics, a DEM approach for joint representation and for interfacial resolution, and an adaptive re-meshing module.

The advantage of the FDEM stems from the fact that while the material is undergoing elastic deformation, only FEM calculations are performed. Calculations become more complex when fractures are initiated. The DEM permits the tracking of fracture initiation and propagation as well as the interaction with preexisting joints. The FDEM approach of this research, implemented using the *Irazu code* (Lisjak et al., 2017), enables history matching of the field-injected pressure profile until shutdown. The model also accounts for the simulated hydraulic fracturing induced microseismicity, mainly due to shear-slip of randomly distributed preexisting joints. Shear-slip takes place due to mechanical stress changes in the medium, primarily due to stress wave spread at the onset of fracturing and during the hydraulic fracture growth, i.e., opening. This chapter aims at giving insights into how the predicted evolution of the hydraulic fracture system correlates to the observed microseismic cloud and compare it to published literature.

2.2.1 An overview of the Finite-Discrete Element Method (FDEM)

The FDEM approach was first suggested by Munjiza, Owen, and Bićanić (1995). It is a hybrid technique that combines the advantages of the FEM and DEM approaches. While the medium

is undergoing elastic deformation, the behavior of intact material is explicitly modelled by the FEM. As the strength of the material is exceeded fractures are initiated, giving rise to discontinuous blocks where the interaction between these blocks is captured by the DEM. The FDEM approach is capable of tracking fracture initiation and propagation by applying the principles of non-linear elastic fracture mechanics[6] (Barenblatt, 1962). The algorithm of the Irazu code, adopted in this study, uses three interconnecting modules (Fig. 2.43) to simulate fluid-driven fractures, as follows:

1. a mechanical solver which calculates the deformation of the intact rock mass as well as the initiation, propagation and interaction of fractures;
2. a cavity volume calculator then captures the changes of the cavity volume due to fracture propagation, the elastic deformation, and fluid compressibility. It also tracks the newly created wet boundaries by checking their connection with the initial source of fluid;
3. a pump model then interacts with the previous two modules to calculate fluid pressure while considering the pumping conditions/injected flow rate.

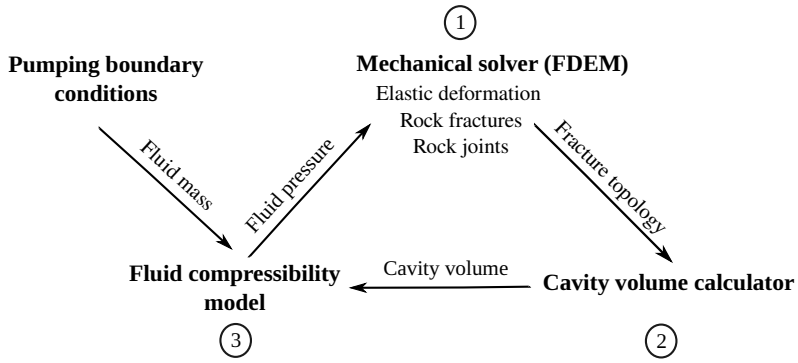

FIGURE 2.43: Interaction between computational modules of the Irazu code.

The Irazu code discretizes the modelling domain with a mesh of elastic triangular Delaunay elements connected to each other at the edges by non-dimensional rectangular cohesive fracture elements (Fig. 2.44). An explicit time integration scheme is employed to solve the equation of motion of the discretized system due to applied stresses.

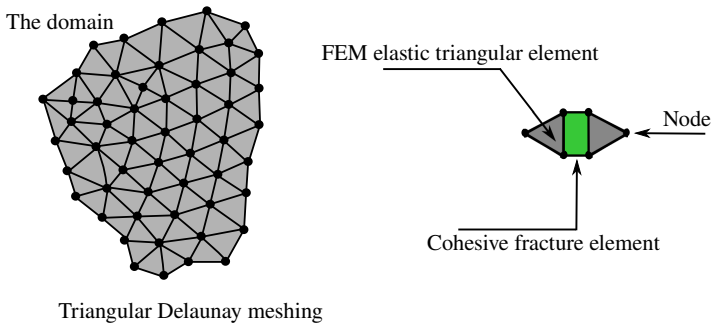

FIGURE 2.44: Triangular Delaunay meshing applied in the Irazu code. The enlarged section shows the contact nature between the elastic and the dimensionless fracture cohesive elements.

While the medium undergoes elastic loading the fracture elements are initially assigned large contact stiffness parameters (penalty parameters) to eliminate them from the elasticity

[6]The global behavior of material undergoing loading is elastic; however, non-linear means that the size of the plastic zone at the fracture tip changes as the fracture grows or as loads change, which is the common case of brittle materials.

matrix, such that all deformations occur in the triangular elements. As soon as the tensile and/or the shear strength of the material is reached, the material starts undergoing inelastic deformation (fracture process zone) that is localized within the fracture elements with the fracturing process expressed in terms of fracture energy dissipation (Lisjak, Grasselli, and Vietor, 2014). Once the fracture energies, G_{Ic} of mode I and G_{IIc} of mode II, are dissipated, the fracture elements are removed and fractures are initiated (Fig. 2.45). At this point, the positions of the separated blocks are tracked by the DEM.

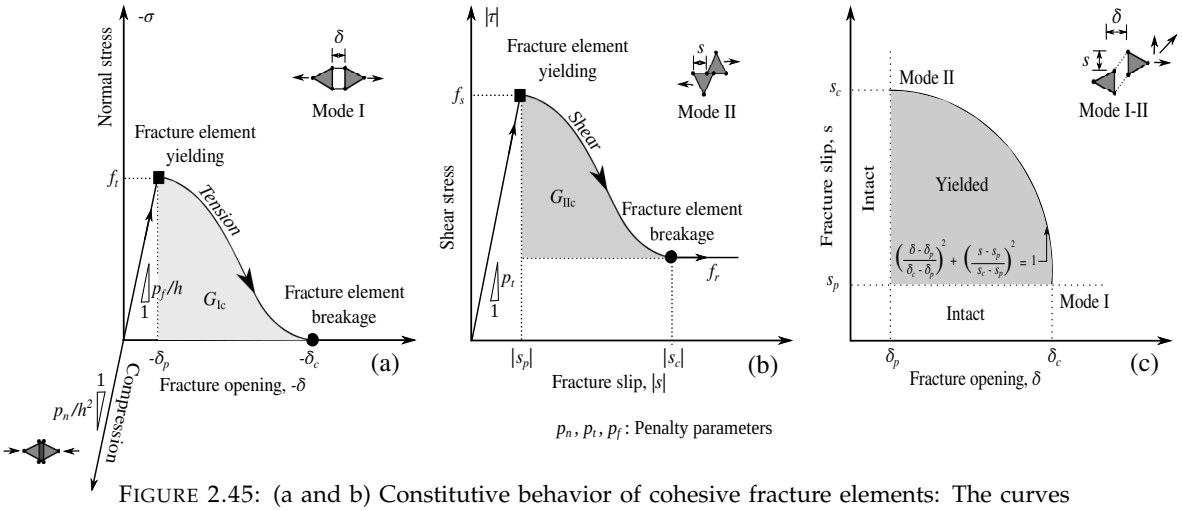

FIGURE 2.45: (a and b) Constitutive behavior of cohesive fracture elements: The curves represent a relationship between normal and tangential bonding stresses, σ and τ, versus fracture relative displacements, δ (opening) and s (sliding). G_{Ic} and G_{IIc} represent the amount of energy dissipated per unit length of fracture for mode I and mode II respectively. (c) Elliptical coupling relationship between fracture opening δ and fracture slip s for mixed-mode fracturing.

2.2.1.1 The FDEM with fluid diffusion

Fluid diffusion and fracture leakoff are implemented in the FDEM approach by considering the existence of flow channels that coincide with the edges of the triangular elements in the initial mesh. The nodes of the triangular elements represent virtual reservoirs where fluid pressure and fluid mass are sequentially calculated. The apertures of the flow channels are assigned initial values a_i that are used to reproduce/calculate the initial permeability of the porous medium using the Poiseuille flow (Fig. 2.46).

As fluid is injected at node N (Fig. 2.46), fluid pressure increases due to a fluid compressibility law (Eq. 2.45), which creates pressure gradients and causes fluid to flow to neighbor nodes (virtual reservoirs) through the flow channels. If the fluid injection rate is greater than the dissipation of fluid pressure through the flow channels, the fluid pressure eventually leads to breaking of the fracture elements and a fracture initiates. The model also accounts for true/physical fluid cavities like boreholes.

$$p^i = \begin{cases} p^{i-1} + K_\lambda \dfrac{\Delta \mathcal{M}}{\rho_\lambda \mathcal{V}^i}, & \text{change in fluid mass;} \\ p^{i-1} + K_\lambda \dfrac{\mathcal{V}^i - \mathcal{V}^{i-1}}{(\mathcal{V}^i - \mathcal{V}^{i-1})/2}, & \text{change in cavity volume;} \\ 0, & \text{for partially saturated media.} \end{cases} \tag{2.45}$$

Based on the initial flow channel aperture a_i, the initial volume of the virtual reservoir $\mathcal{V}$ is determined from the volume of conjunctive channels (Fig. 2.46) for a unity in the third dimension. The initial mass of fluid at each reservoir is calculated by adopting the same concept,

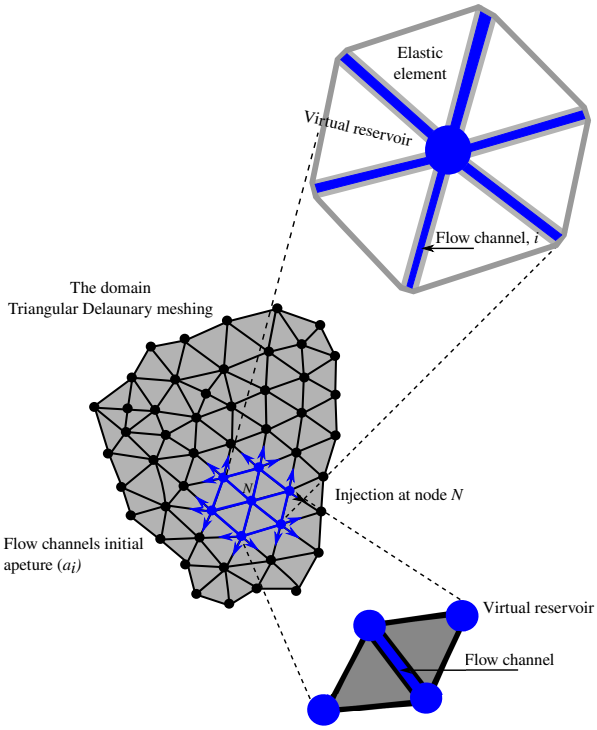

FIGURE 2.46: Conceptual graph illustrating the Delaunay triangulation with embedded fracture elements and the implementation of fluid diffusion in the Irazu code. The flow takes place in channels that are initially assigned a finite aperture (a_i) corresponding to the formation permeability. Each virtual reservoir, where fluid pressure is calculated, receives a mass of fluid from all branching channels (Lisjak et al., 2017).

yet while considering the degree of saturation S. Once the model starts undergoing the external loads and boundary conditions, the pressure and/or fluid masses at the virtual reservoirs change. Within a time step i, the fluid pressure p^i at the virtual reservoirs is calculated while considering any increase/decrease of fluid mass $\Delta\mathcal{M}$, as well as any changes in the cavity volume itself (Lisjak et al., 2017), K_λ and ρ_λ are the fluid bulk modulus and density respectively. Fluid flow in the channels is assumed viscous and laminar; henceforth, it can be described using Darcy's law. The flow q between two reservoirs, 1 and 2, within the time interval i of discretization Δt is described as,

$$q = \frac{\Delta\mathcal{M}}{\Delta t} = f(S)\frac{p_1^i - p_2^i - \rho_\lambda \mathfrak{g}(y_2 - y_1)}{R}, \tag{2.46}$$

with y_1 and y_2 being the elevations of the cavities/reservoirs 1 and 2 respectively. The dimensionless function $f(S)$ relates the permeability of the flow channel to the reservoir degree of saturation. The function $f(S)$ ranges between 0 for perfectly dry reservoirs to 1 for fully saturated reservoirs. R is the flow resistance parameter of the channel that connects the reservoirs 1 and 2, and it is calculated using the cubic law for flow between two parallel plates. While assuming that flow channel aperture varies linearly across its length, R is expressed as,

$$R = 12\frac{\mu}{\rho_\lambda}\int_{l_1}^{l_2}\frac{1}{a(l)^3}\,dl = \frac{6\mu(a_1 + a_2)}{\rho_\lambda a_1^2 a_0^2}\,L, \tag{2.47}$$

where μ is the fluid dynamic viscosity, L is the length of the flow channel, a_1 is the flow channel aperture at reservoir 1 and a_2 is the flow channel aperture at reservoir 2. The channel aperture is bounded between to limits: a_u for maximum opening; and a_l for maximum closure, beyond which further opening or closing have no meaning (Lisjak et al., 2017).

2.2.1.2 Hydromechanical coupling

There are two distinct time discretizations in the Irazu code. The first time scheme is used for the mechanical solver, i.e. deformation and fracturing. The second time scheme is used for the hydraulic solver, i.e. fluid diffusion. Both time schemes are explicit; the hydro-mechanical coupling is achieved by choosing the frequency between the mechanical and hydraulic solvers to attain the prescribed degree of saturation. For instance, the updates from the mechanical solver affect fluid pressure in the medium, and the resulting fluid pressure (from hydraulic solver) affects the mechanical calculations for the next time iteration. The stability of the mechanical solver is achieved by choosing a time step smaller than a critical value, which is proportional to the smallest element size in the model divided by the P-wave velocity of the elastic medium (Munjiza, 2004). The stability of the hydraulic solver, to attain the correct degree of saturation for all cavities and flow channels, is assured by controlling the size of the hydraulic time step (Lisjak et al., 2017),

$$\Delta t \leq \min_{m} \left(\frac{\mathcal{V}_m}{\frac{K_\lambda}{\rho_\lambda} \sum_{n} \frac{1}{R_n}} \right), \tag{2.48}$$

m and n index over all the cavities and flow channels in the boundary problem.

The FDEM method is capable of describing fracture evolution due to modes I and II of failure, as well as a combination of both fracturing modes (Fig. 2.45). Fracture opening due to fluid pressure is seen to be dominated by mode I of failure (Fjaer et al., 2008); however, mechanical deformations/pore pressure changes are expected to trigger shear-slip (mode II of failure) on preexisting joints (Bruel, 2007; Loret, 2018).

2.2.2 Simulating hydraulic fracturing test using the FDEM

The hydraulic fracturing test considered in this research was performed in the Evie member of the Horn River basin located in western Canada (Chou, Gao, and Somerwil, 2011). The Horn River basin is in the strike-slip stress regime (Roche and Baan, 2017). Consequently, the developed hydraulic fracture is vertical normal to the minimum horizontal stress. A 400×400 m horizontal cross section of the formation is simulated. This two-dimensional model represents a simplified domain where the far-field stresses are the maximum horizontal σ_H and the minimum horizontal σ_h stresses. Since the fracture length/radius is greater than its height (Chou, Gao, and Somerwil, 2011), this two-dimensional representation with a classic Perkins–Kern–Nordgren (PKN) fracture model (Adachi et al., 2007) is appropriate. Grid/model dimensions (Fig. 2.47(a)) are determined such that the 400×400 m domain includes the farthest recorded microseismic events in the σ_H-σ_h plane.

Figure 2.47 shows the setup of the two-dimensional computational grid used in this study. Fluid injection is modelled as a point source at an internal node. The mesh is intensively refined with 0.8 m elements in a area of 200×200 m around the injection point. Away from the zone of the intensive refinement, element size is gradually increased to 5.0 m. Medium parameters were assigned following a hydraulic fracturing program in the Horn River basin. Based on overburden density values, the minimum horizontal stress at the injection depth (2980 m) is $\sigma_h = -60$ MPa, while the maximum horizontal stress is $\sigma_H = -75$ MPa (Chou, Gao, and Somerwil, 2011). The initial reservoir pore pressure is 33.9 MPa (Rogers et al., 2010) and the rock permeability is 10^{-19} m^2 (Reynolds and Munn, 2010). This exceptionally low permeability value means that the formation can be treated as impermeable for the timeframe of the simulations (2.7 hr), such that flow is restricted to fractures. The injection rate used in simulations is $Q = 1.4$ l/s. This numerical injection rate is smaller than the value applied in field (0.167 m^3/s). However, considering

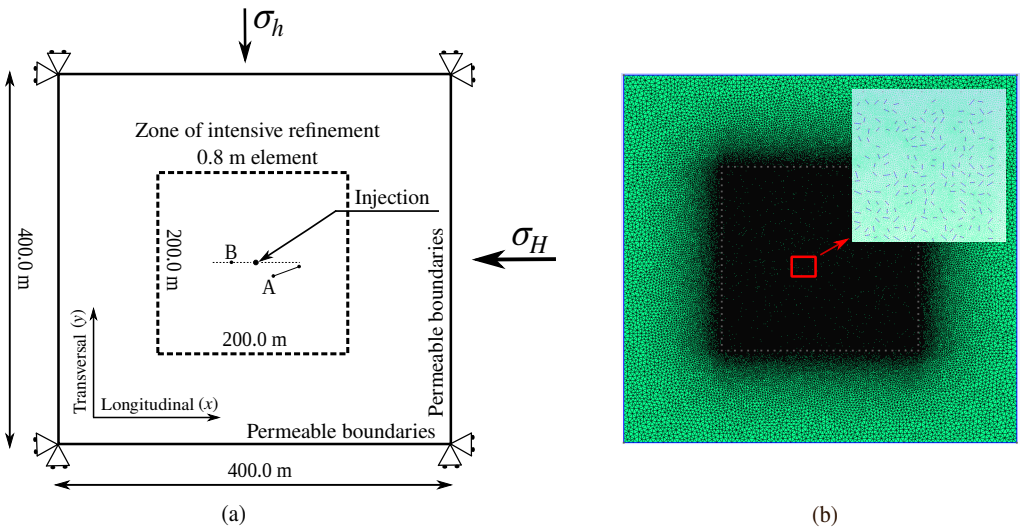

FIGURE 2.47: (a) The geometry and boundary conditions of domain chosen for the hydraulic fracturing simulations and induced seismicity. (b) Triangular Delaunay meshing of the domain showing refinement of element size approaching the wellbore: A zoom-in is displayed to show the random distribution of preexisting joints. Points A and B are displayed to investigate the loading paths during the fracturing process.

that the 3-D geometry is simplified and that no fluid loss/leakof is accounted for, this numerical injection rate is sufficient to insure stable calculations and to reproduce the field injection history (Fig. 2.48(a)).

Chou, Gao, and Somerwil (2011) reported on material and fluid properties pertaining to the rock formation of interest here, namely the Evie member of the Devonian Horn River formation (Table 2.4).

TABLE 2.4: Fluid and material properties pertaining to the porous medium of the Evie formation (Chou, Gao, and Somerwil, 2011). Fracture energy values and computational parameters are calibrated based on the recommendations of Lisjak, Grasselli, and Vietor (2014), Mahabadi et al. (2012), and Tatone and Grasselli (2015)

Nature	Parameter	Value	Unit
Elasticity	Drained Young's modulus E	24.5	GPa
	Drained Poisson's ratio ν	0.2	-
	Rock density ρ_σ	2400	kg/m^3
Fracture	Tensile strength σ_T	5.2	MPa
	Cohesion c	13.5	MPa
	Mode I fracture energy G_{Ic}	10	N/m
	Mode II fracture energy G_{IIc}	100	N/m
	Material internal friction angle ϕ_i	35.0	(°)
	Fracture friction angle ϕ_f	35.0	(°)
Fluid flow	Dynamic viscosity μ	3×10^{-3}	Pa s
	Permeability k	10^{-19}	m^2
	Compressibility K_λ	2.2	GPa
Computational	Damping coefficient η	12.3×10^6	kg/m/s
	Normal contact penalty p_n	245	GPa m
	Shear contact penalty p_t	24.5	GPa m
	Fracture penalty p_f	122.5	GPa m

The smallest element size of 0.8 m is used to avoid mesh sensitivity. Fracture energy values (Tatone and Grasselli, 2015) along with this element size are sufficient to reproduce the breakdown pressure and post-peak behavior of Fig. 2.48(a). The computational parameters (Table 2.4) are calibrated based on the recommendations of Lisjak, Grasselli, and Vietor (2014), Mahabadi et al. (2012), and Tatone and Grasselli (2015). The penalty coefficients, p_n, p_t, p_f are

set equal to $10\times$, $1\times$, and $5 \times E$, respectively. These are the largest possible values that ensured elastic response and did not necessitate a reduction in the time step size. The damping coefficient η should be larger than $0.01\eta_c$ with η_c being the critical viscous damping coefficient $\eta_c = 2h\sqrt{E\rho_\sigma}$ (Munjiza, 2004), and h the element size. For $\eta > 0.01\eta_c$, the high-frequency waves are suppressed and the resulting stress-strain curves mimic those obtained in the quasi-static laboratory tests. In these simulations, η is set equal to η_c.

A set of normally distributed joints with an average length of 1.60 m, random variation of 0.4 m, and fracture density of $0.1/\text{m}^2/\text{m}$ is created in the zone of intensive refinement (Fig. 2.47(b)). These joints are introduced in the model before meshing and they replace the cohesive fracture elements for their length and can be assigned specific hydraulic, elastic, and cohesive/friction properties. The Gmsh code is used to generate the Delaunay triangulation. In this study, joints are assigned the same hydraulic properties as the rock medium; however, they are given zero tensile strength and can only sustain shear stresses due to residual friction only (Eq. 2.49). Consequently, joints are inserted in the model to explore the distribution of microseismic events due to shear-slip induced by mechanical deformation of the medium during the growth of hydraulic fractures (AbuAisha et al., 2017). The size distribution of the joints is based on previous studies in this area (Eaton et al., 2014), whereas joint orientation is random. The maximum shear stress on these joints is determined from the Mohr-Coulomb criterion, expressed in terms of the residual/fracture friction ϕ_f angle and the normal effective stress $\sigma_n^{'}$,

$$f_r = -\sigma_n^{'} \tan(\phi_f), \tag{2.49}$$

where f_r is the maximum shear stress. As joints represent planes of weakness, while hydraulic fracture is growing, medium mechanical deformation affects the stress state on the joint tips. Depending on their random orientations, some joints are more favorable to shear-slip, and their slip gives rise to microseismic events. Fluid flow within the growing hydraulic fracture system is controlled by Darcy's law. Points A and B (Fig. 2.47(a)), at radial distances of 29.5 m and 15 m from the injection point, are recorder nodes to investigate the stress loading paths due to modes I and II of failure. Point A represents a critically stressed joint tip that fails due to mechanical deformation created by fracture growth (mode II failure). Point B is on the fracture trajectory and fails in response to a fluid pressure increase (opening/mode I).

2.2.2.1 Comparison with field data

In this section, simulations are compared with the field example from the Evie formation of the Horn River basin. As expected, simulations generated an approximately bi-wing hydraulic fracture, growing in the direction of the maximum far-field horizontal stress σ_H and perpendicular to the minimum horizontal stress σ_h. Figure 2.48(a) shows that the simulated injection pressure provides a good match to the subsurface injection pressure values. Under a constant rate of injection, the injection pressure increases until the breakdown condition is achieved. Injection pressure then gradually drops to the fracture propagation pressure equal to the minimum far-field horizontal stress (Yew and Weng, 2014).

During the numerical simulation, the calculated fracture length is determined at each time step (fracture envelope). Figure 2.48(b) shows the spatio-temporal migration of observed microseismicity, indicated by black dots, compared with the growth of the hydraulic fracture (red line). Although microseismic activity is characterized by discontinuous rates, possibly due to episodic growth of the hydraulic fracture system in the field (Boroumand and Eaton, 2015), for the most part, the fracture envelope provides an approximation to the triggering front in the sense that the time-distance locations for the majority of microseismic events plot below the curve. This relationship provides validation for the numerical approach, since the smallest element size, fracture energies, and computational parameters are calibrated to history

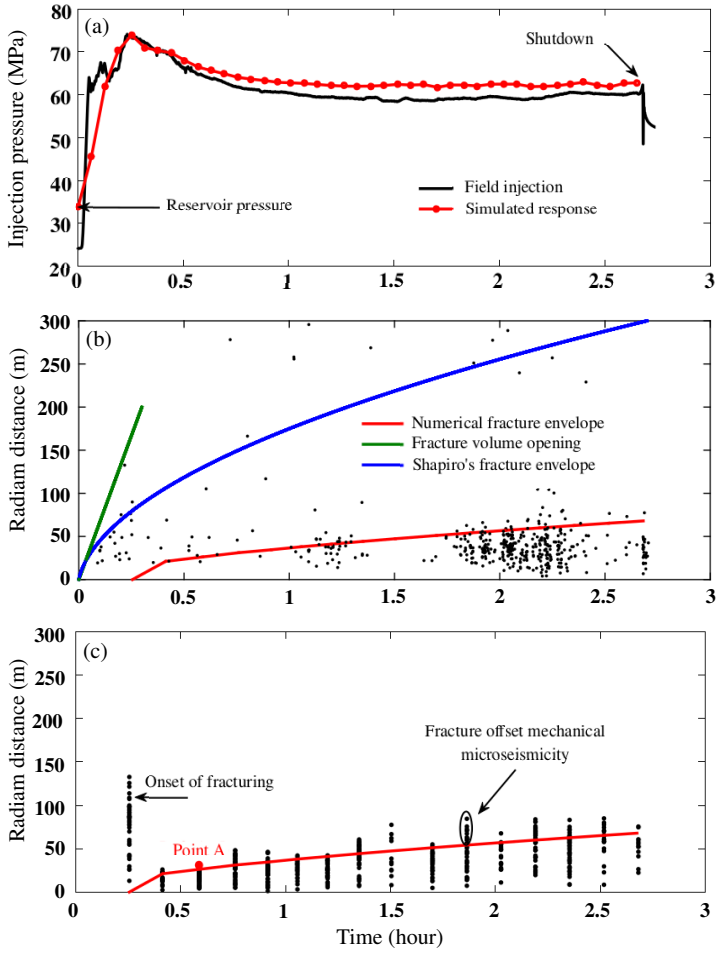

FIGURE 2.48: (a) Irazu numerical injection response correlated to the field injection history until shutdown (2.7 hr). (b) Spatio-temporal migration of the field microseismicity including the fracture envelope derived from simulations (red line), a best-fitting fracture triggering envelope (Shapiro et al. 2006) (blue line) for $\ell_f = 300$ m, and the fracture volume opening curve (Dinske et al. 2010) (green line). (c) Radial distribution of simulated microseismic events with time along with the calculated numerical fracture envelope highlighted in Fig. 2.48(b).

match the injection pressure profile rather than the time-distance behavior of the microseismicity (AbuAisha et al., 2019). Shapiro and Dinske (2009b) and coworkers Shapiro and Dinske (2009a), Shapiro, Dinske, and Rothert (2006), and Shapiro et al. (2002) suggested that the evolution of a hydraulic fracture can be treated as an end-member of a diffusional triggering front. To compare the current fracturing-microseismicity signatures with Shapiro's work, a simplified classic two-dimensional fracture geometry of a PKN fracture model is adopted (Fig. 2.49). The use of this model is appropriate since the fracture length/radius is bigger than its height and that it propagates in the rock section where the extent and concentration of microseismicity is significant (σ_H-σ_h plane) (Reynolds and Munn, 2010).

To investigate the dynamical behavior of induced microseismicity due to fracture growth, Shapiro, Dinske, and Rothert (2006) applied an approximation of the fracture growth based on the principle of volume balance, where the fracture radius ℓ is expressed in terms of injection time t,

$$\ell(t) = \frac{Q_i t}{4h_f C_L \sqrt{2t} + 2h_f w} \tag{2.50}$$

with Q_i being the injection flow rate, h_f the perforated section of the treatment well (Fig. 2.49), w

the fracture aperture, and C_L the fluid loss coefficient. Dinske and T. (2010) suggested that fluid loss overdominates fracture geometry effects over the long-term limit of injection; therefore, Eq. 2.50 reduces to the typical linear pressure diffusional front characterized by the apparent diffusivity $\mathcal{D}$, i.e. $\ell(t) = \sqrt{4\pi\mathcal{D}t}$ (Shapiro et al., 2002).

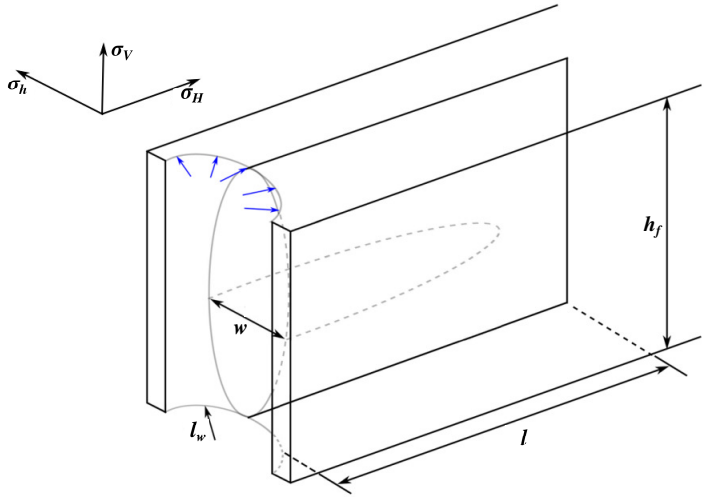

FIGURE 2.49: Schematic diagram demonstrating the PKN fracture geometry adopted in this research. w is the fracture aperture, ℓ the fracture radius, ℓ_w is the borehole radius, and h_f is the perforated section of the treatment well.

Consequently, Dinske and T. (2010) and Shapiro, Dinske, and Rothert (2006) relate the fluid loss coefficient to the apparent diffusivity that best-fits the fracture triggering front (Eq. 2.50) as,

$$C_L = \frac{Q_i}{8h_f\sqrt{2\pi\mathcal{D}}}. \tag{2.51}$$

The fluid loss coefficient can be also calculated using the fracture radius and the fracture cross-sectional area $\mathcal{A}$,

$$C_L = \frac{Q_i t - 2\ell\mathcal{A}}{4\ell h_f\sqrt{2t}}. \tag{2.52}$$

The fracture cross-sectional area is calculated by measuring the slope of the line tangent to the seismic events at time $t = 0$ (Fig. 2.48(b): fracture volume opening curve) (Dinske and T., 2010; Shapiro, Dinske, and Rothert, 2006), in this case $\mathcal{A} = 0.1853\ \mathrm{m}^2$. For a well-perforated section of length $h_f = 30$ m (Reynolds and Munn, 2010), the fracture aperture is $w = \mathcal{A}/h_f = 6.2$ mm. The numerical fracture aperture calculated by simulations is 6.6 mm. The maximum fracture opening is set to $a_u = 10$ mm; hence, the numerical aperture is still smaller than the upper limit. While considering the field injection rate ($Q_i = 0.167\ \mathrm{m}^3/\mathrm{s}$), the best-fitting of Shapiro's fracture triggering front (Eq. 2.50) and Fig. 2.48(b), blue curve), tangent to the fracture volume curve and encompassing almost all of the seismic events, is chosen for a final fracture radius $\ell_f = 300$ m, corresponding to the farthest microseismic event. In this case, an apparent diffusivity $\mathcal{D} = 0.86\ \mathrm{m}^2/\mathrm{s}$ is sufficient to match this fracture triggering front. Based on Eq. 2.51, the corresponding fluid loss coefficient is $1.13 \times 10^{-4}\ \mathrm{m}/\sqrt{\mathrm{s}}$. Dinske and T. (2010) also suggested an approach to calculate the initial reservoir permeability using the fluid loss coefficient and some typical values of the hydrocarbon in the targeted reservoir. If the hydrocarbon in the targeted shale at the Evie formation has the same properties as in the Cotton Valley tight gas reservoir (Dinske and T., 2010) (considering that the initial reservoir pressure in both locations is ~30 MPa and that the operational depth goes to ~2800 m), the following hydrocarbon properties can be assumed: dynamic viscosity $\mu = 0.03$ cP; compressibility $\chi_{T\lambda} = 3.5 \times 10^{-8}\ 1/\mathrm{Pa}$;

porosity $n_\lambda = 0.1$; and pressure difference[7] $\Delta p = 40.1$ MPa. These properties and operational conditions give an initial reservoir permeability of 2.1×10^{-19} m^2 , almost equal to the values attributed to the Evie formation shale (Reynolds and Munn, 2010).

Considering the numerical fracture envelope as a triggering front (Fig. 2.48(b), red curve), some of the observed microseismicity plots well out-side the bounds of the fracture envelope. In particular, at the onset of hydraulic fracturing at ∼0.25 hr, a cluster of microseismic events occurred up to a distance of ∼125 m from the injection location. These events are thought to occur due to the mechanical deformation of the medium/the stress wave spreading in the formation at the breakdown. Fig. 2.48(c) shows the time-distance behavior of simulated microseismicity in relation to the fracture envelope. The apparent discrete occurrence times of these events is an artifact of the numerical procedure, wherein snapshots of the simulation outputs are stored at discrete time intervals to conserve disk space. In a similar fashion to the observed pattern of field microseismicity, it is seen that the computed fracture envelope represents an approximate triggering front with the conspicuous exception of a cluster of events at the onset of fracturing to a radial distance of ∼125 m from the injection point. The events in this cluster are initiated by exceeding the Mohr-Coulomb criterion (Eq. 2.49) on the preexisting fractures/joints, due to stress changes in the medium induced by the hydraulic fracture. The similarity of these events to the early cluster of microseismicity in the observed field dataset suggests that the early cluster has the same cause (i.e. stress changes arising from the breakdown energy spreading in the medium). To see if Shapiro's envelope (Eq. 2.50) can reproduce the numerical fracture envelope, the fluid loss coefficient for the numerical fracture radius at the end of the simulation ($\ell_f = 68$ m), for the field injection rate (0.167 m^3/s), and for $t = 2.7$ hr (treatment time) is calculated, i.e. $C_L = 1.405 \times 10^{-3}$ m$/\sqrt{\text{s}}$. Implementing this value in Eq. 2.50 gives the blue curve in Fig. 2.50 shown below.

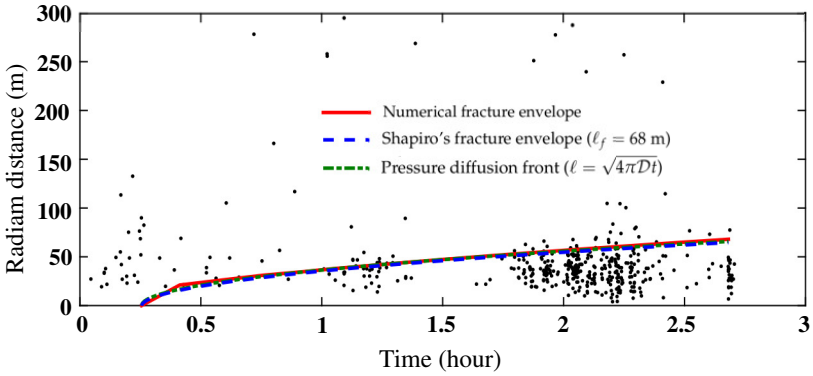

FIGURE 2.50: Spatio-temporal migration of the field microseismicity including the fracture envelope derived from simulations (red solid), Shapiro's fracture triggering envelope (blue dashed line) for $\ell_f = 68$ m, and the linear diffusion front (green dotted line).

Figure 2.50 also shows the linear diffusional front based on the apparent diffusivity calculated by Eq. 2.51, which is identical to Shapiro's fracture envelope. Though identifying triggering fronts from seismic data is far from trivial, these diffusional or non-diffusional envelope techniques compare to each other and can give information on the fluid-driven fracture geometry (ℓ and w), local stress regime, as well as on the fractured reservoir permeability and fracture conductivity (Dinske and T., 2010). The current numerical FDEM approach confirmed the validity of the diffusional envelope technique. However, it is further concluded that in impermeable media, a non-diffusive envelope, i.e., only related to the fracture geometry, can be precisely predicted by Shapiro's fracture envelope, provided that the fracture radius at the end of the treatment is known. It is also concluded that an envelope that encompasses most of the

[7]The pressure difference is calculated considering the initial reservoir pressure 33.9 MPa and the breakdown pressure 74 MPa (Fig. 2.48(a)).

radial distribution of field seismicity, and that excludes the cluster at the onset of fracturing, can give a good approximation of fluid-driven fracture radius in tight gas reservoirs.

2.2.2.2 Loading paths in the FDEM

This section aims at explaining the modes I and II of failure associated with the FDEM approach by investigating the loading paths of the two points, A and B (Fig. 2.47(a)), during the hydraulic fracturing process. Figure 2.51(a) shows the *m-s* loading paths for these two points: the joint-tip point A at a radial distance of 29.5 m and reflex orientation of 218.82° (Figs 2.47(a) and Fig. 2.48(c)) and point B at a radial distance of 15 m on the bi-wing fracture trajectory (Fig. 2.47(a)). The quantities m and s are defined as the mean of the effective principal stress tensor ($m = (\sigma_1^{'} + \sigma_2^{'})/2$) and the magnitude of the deviatoric effective principal stress tensor ($s = |\sigma_1^{'} - \sigma_2^{'}|/2$). The failure envelope (Eq. 2.49) can be expressed in terms of m and s (Fig. 2.51(a)).

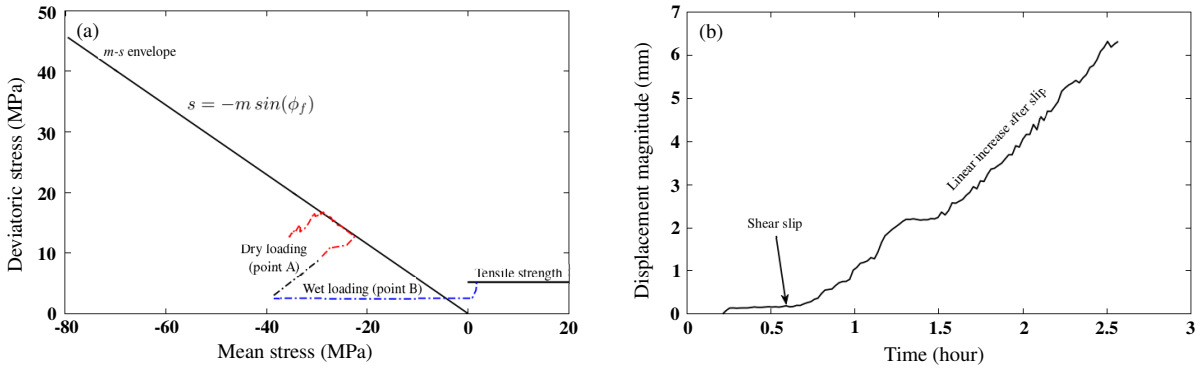

FIGURE 2.51: (a) *m-s* loading paths for two points: point A (Figs 2.47(a) and Fig. 2.48(c)) presented by dotted black and red line (shear-slip, mode II failure); and point B (Fig. 2.47(a)) on the fracture trajectory presented by dotted blue line (tensile mode I failure). (b) Displacement magnitude history at point A: the figure shows sudden increase at the onset of fracturing (∼0.25 hr) followed by slight growth before it starts to increase significantly at shear-slip.

The two loading paths start from the same point/initial effective stress state. As soon as the fluid reaches point B on the fracture trajectory, effective stresses become tensile and the loading path (blue dotted line) moves to touch the tensile failure envelope, which is characterized by mode I failure. However, for point A, and since it is located on a joint tip/weak zone, the dissipation of energy at breakdown reduces (in algebraic sense) the initial effective stress state moving the joint close to failure, which is represented by the first linear change of the dry loading path (black part). The path then continues to grow (red part) until it touches the failure envelope, which is characterized by mode II failure and shear-slip microseismic event. The path then yields to the failure envelope before it starts to show unloading behavior. However, this reduction in initial stresses depends on the orientation of joints, as some orientations, and depending on the anisotropy of the far-field stresses, are more favorable to shear-slip.

The displacement magnitude history at point A exhibits a sudden increase at breakdown (∼0.25 hr), then it continues to grow slightly before it starts to increase considerably at the onset of shear-slip (Fig. 2.51(b)).

2.2.3 Discussion and conclusion

Plotting a radial spatio-temporal distribution of field seismicity during hydraulic fracturing test reveals important dimensional information of the fluid-driven fracture. Such information includes fracture length and aperture, as well as its growth direction which helps understand the stress regime of the rock basin where the test is conducted. Most of the observed field seismicity plot under the bounds of the numerical fracture envelope, except for a cluster of

seismic events at the onset of fracturing. This cluster of seismicity at the onset of fracturing is explained numerically; upon fracture initiation, a stress wave spreads in the medium and causes critically stressed joints (to a certain distance) to slip and give rise to seismic events. These fracturing-onset seismic clusters corresponded to the breakdown peaks of the field injection history.

Chapter 3

Fluid circulation in salt caverns

Renewable energy resources are not dispatchable due to their fluctuating nature. Even-though, some of these resources are controllable, i.e. bioenergy or hydroelectricity, or represent relatively constant sources, i.e. geothermal power, using them on a large scale requires upgrades or even a redesign of the grid infrastructure. Options to absorb large shares of renewable energy into the grid include storage. Gas storage in underground salt caverns is becoming a leading technique (Klumpp, 2016; Caglayan et al., 2020). Such caverns are characterized by their large-scale storage capacities, low investment costs, and low cushion gas requirements (Matos, Carneiro, and Silva, 2019). Nevertheless, the future increasing energy demands necessitate almost daily solicitations of such caverns (AbuAisha and Rouabhi, 2019). Fast charges, mechanical and thermal, are expected to affect the mass exchange rates between the cavern phases. To keep precise tracks/accurate management of the cycled gas quantities, these mass exchanges must be quantified.

Rock salt occurs within sedimentary layers where it has formed from the evaporation of seawater or salty lakes. Rock salt is consequently deposited in cycles which affects its directional properties like the elastic modulus and the permeability. Depending on the location, the rock salt properties, mechanical and hydraulic, differ as well. Solution mining is commonly used to create large caverns in rock salt formations. In this process, a single well, drilled from the ground surface to the targeted depth (Fig. 3.1), is generally used to inject fresh water and withdraw brine through a concentric tubing system, the so called the leaching process (Charnavel, Leca, and Poulain, 1999). Once leaching is completed, the brine in the cavern is reduced to minimal quantities by a debrining phase where it is moved out by a gas injection operation.

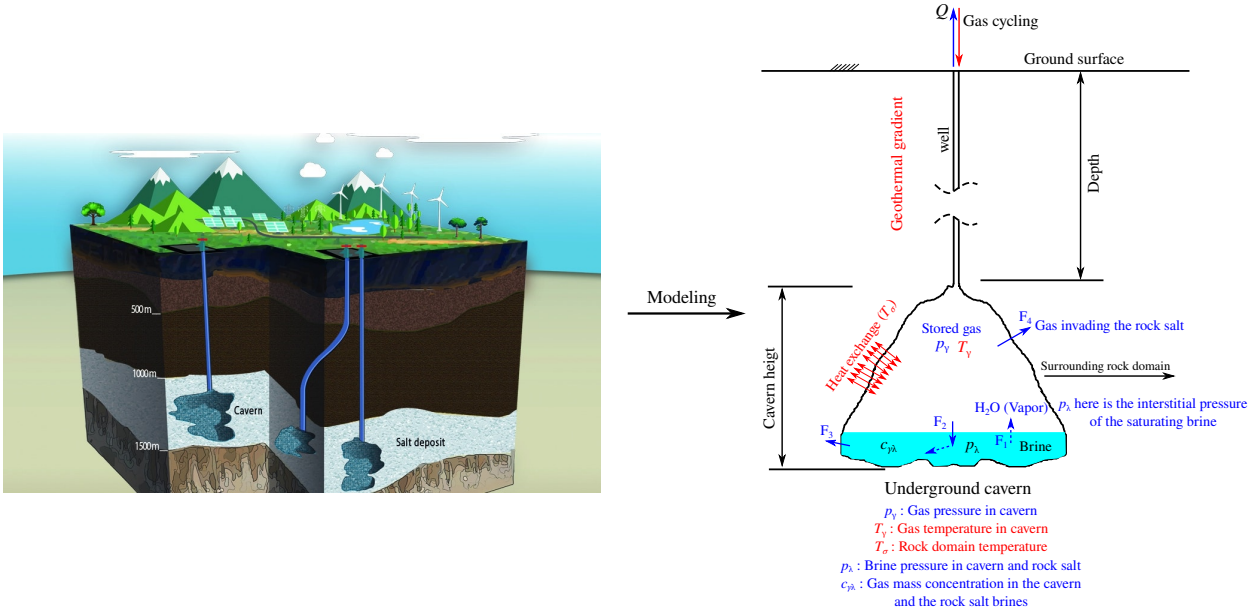

FIGURE 3.1: Schematic representation of gas storage in salt caverns and its mass exchanges between phases.

Figure 3.1 shows an underground cavern filled with gas at a certain pressure and is exchanging heat with the surrounding rock domain. The figure also depicts the amount of brine left in the cavern at the end of the debrining process. Gas within the cavern is expected to experience cycles of pressure and temperature changes according to the intended usage. During its lifetime, the cavern mainly contains, simultaneously or sequentially, two different immiscible phases: the stored humid gas and the brine. The third important phase of this storage outline is the surrounding rock salt domain. This domain is constituted of the salt mass which itself is a mixture of grains or crystals of halite and brine occupying the inter-grain spaces or present in the grains in the form of fluid inclusions. Each of the three phases is characterized by state variables which are for the humid gas: pressure, temperature, and vapor concentration; for the brine: pressure, temperature, concentration of salt and concentration of dissolved gas; and for the rock salt: stress, temperature, and interstitial fluid-phase pressures.

While the cavern is operated, the three phases are interacting as follows (Fig. 3.1): water is evaporating into the stored gas (F_1); stored gas is dissolving in the brine (F_2); brine at the cavern bottom is flowing into the rock salt (F_3); and stored gas is percolating and diffusing into the porous rock salt (F_4).

As stated earlier, in the context of energy transition gas stored within salt caverns is expected to experience fast cycles of injection and withdrawal. This chapter starts by investigating the homogeneity of the stored gas thermodynamic state during fast cycling. This investigation helps building a modelling paradigm that can be used to conduct subsequent studies concerning mass exchanges between the cavern phases.

3.1 Uniformity of the gas thermodynamic state during cycling

The rate of injected or withdrawn mass to/from caverns controls the spatial heterogeneities of the temperature and pressure fields. It also controls the magnitude of gas velocity which represents the driving force for the convective heat transfer with the surrounding rock domain. In order to consider as many industrial concerns during cycling as possible (for instance rock creep and gas percolation into the surrounding rock salt), researchers tend to simplify the cavern thermodynamic problem by neglecting the spatial variations of pressure and temperature which leads to a cavern uniform state. This reduces tremendously the simulation cost, yet it raises up a question about the validity of such assumption during fast cycling, when spatial variations of temperature and pressure are significant. The miscalculation of these variations leads to a miscalculation of the gas density field in the cavern, and consequently, for a given cavern volume, a misestimation of the stored gas mass.

To address this concern, two types of simulations are performed: simplified simulations using an in-house code where a uniform thermodynamic state is assumed within the cavern; and a Computational Fluid Dynamics (CFD) simulations using the COMSOL software. The goal is to compare the simplified simulation results with the complete simulations of COMSOL, where all complexities of the problem are considered, i.e. full mesh refinement, velocity field, convective heat transfer, and the turbulent flow modeling. The simulation results are compared for both slow (seasonal) and fast (daily) cycling where one expects a better match with regard to slow cycling and a more obvious deviation in case of fast solicitations. In both simulations the cavern is assumed full of gas with no brine or insoluble material, and only thermal conduction with the surrounding rock domain is considered.

3.1.1 Thermodynamics of gas stored in salt caverns

This section provides the mathematical problems of the simplified and the complete approaches to solve for the evolution of stored gas thermodynamics.

3.1.1.1 Complete solution of cavern thermodynamics

Injecting or withdrawing gas to/from caverns applies changes to the gas mass density ρ, velocity $\boldsymbol{v}$, and temperature T. The developments of these three fields are calculated using the general balance laws:

$$\begin{array}{lrcl} \text{mass balance:} & \dot{\rho} + \rho \boldsymbol{\nabla} \cdot \boldsymbol{v} & = & 0; \\ \text{momentum balance:} & \rho\, \dot{\boldsymbol{v}} - \boldsymbol{\nabla} \cdot \underline{\underline{\boldsymbol{\sigma}}} & = & \rho \mathfrak{g}; \\ \text{energy balance:} & \rho\, \dot{u} + \boldsymbol{\nabla} \cdot \boldsymbol{\psi} & = & \underline{\underline{\boldsymbol{\sigma}}} : \underline{\underline{\boldsymbol{\nabla}}} \boldsymbol{v}, \end{array} \tag{3.1}$$

where $\underline{\underline{\boldsymbol{\sigma}}}$ is the fluid stress tensor, $\mathfrak{g}$ is the gravitational acceleration vector, u is the specific internal energy, and $\boldsymbol{\psi}$ is the fluid heat flux. The designation of the phase subscript α is removed as the cavern is filled with a mono-component single-phase gas.

Stokes law is used to calculate the stress tensor in a moving fluid undergoing external effects,

$$\underline{\underline{\boldsymbol{\sigma}}} = 2\mu \underline{\underline{\boldsymbol{\mathcal{E}}}}^{d} - p \underline{\underline{\boldsymbol{\delta}}}, \tag{3.2}$$

where μ is the fluid dynamic viscosity, and $\underline{\underline{\boldsymbol{\mathcal{E}}}}^{d}$ is the deviatoric part of the rate of strain tensor $\underline{\underline{\boldsymbol{\mathcal{E}}}} = (1/2)\left(\underline{\underline{\boldsymbol{\nabla}}} \boldsymbol{v} + \underline{\underline{\boldsymbol{\nabla}}} \boldsymbol{v}^{\mathrm{T}}\right)$. Fourier's law is used to describe the relation between heat flux $\boldsymbol{\psi}$ and the temperature gradient $\boldsymbol{\nabla} T$ through the fluid effective thermal conductivity Λ,

$$\boldsymbol{\psi} = -\Lambda \boldsymbol{\nabla} T. \tag{3.3}$$

The fluid state equation can be completely described using two state functions; the mass density $\rho(p,\, T)$, and the heat capacity $C_p(T)$ at a given pressure. The thermodynamic variables are related to each other through the formula $p = \rho T Z$, with Z being the gas compressibility factor. Common examples are when fluid density is assumed constant in case of incompressible fluids, and when $Z = R/M_w$ in case of ideal gases, with M_w being the gas molecular weight and R the universal gas constant. In case of high pressure and low temperature, the assumption of ideal gas is weak and a real gas behavior needs to be considered.

For the relatively short-period simulations (2 months maximum) considered in this work, the mechanical behavior of the rock mass around the cavern is neglected (Labaune et al., 2019); only the thermal interaction between rock and fluid are accounted for. For a time-dependent problem, the temperature field in the surrounding rock mass verifies the following form of the heat equation,

$$\rho_\sigma C_{p\sigma} \partial_t T_\sigma = \Lambda_\sigma \boldsymbol{\nabla} \cdot (\boldsymbol{\nabla} T_\sigma), \tag{3.4}$$

with T_σ being the rock temperature, ρ_σ its density, $C_{p\sigma}$ its heat capacity, and Λ_σ its thermal conductivity.

The non-dimensional numbers of Rayleigh, Reynolds, and Péclet are needed to have an idea about the heat convection regime of cycled gas in the cavern. Most of the underground cavern operations exhibit high Reynolds Re $\sim 10^6$ and Rayleigh Ra $\sim 10^{15}$ numbers (Karimi-Jafari, 2010), which necessitates the integration of a fluid flow turbulent model to solve for velocity disturbances. When the Péclet number is large (Pe > 1), stabilization techniques are required to smooth the spurious instabilities attributed to the convection term in the energy equation (AbuAisha and Loret, 2016b).

Evolution of the thermodynamic state of the gas stored in underground caverns can be solved for by applying the finite element method on the system of Eqs 3.1 along with the proper initial and boundary conditions. However the following points need to be considered:

1. the spatial discretization should be precise and fine enough to describe properly the distribution of the velocity field;

2. adequate mesh refinement must be adopted at the solid-gas interface to account for the convective heat transfer;

3. a turbulent flow model is needed (the k-ϵ for this study) which adds another two variables, namely k and ϵ, to the list of unknowns (AbuAisha and Rouabhi, 2019).

This complete physical model with all related complexities of mesh refinement, spatial variations, convective heat transfer, and turbulent flow is validated in AbuAisha and Rouabhi (2019).

3.1.1.2 Simplified solution of cavern thermodynamics

Underground caverns have large geometries and they are utilized over long periods of time. This renders the complete CFD simulations of gas cycling over their lifetime a tremendous if not a prohibitive task. Since in most cases, underground storage necessitates seasonal/slow cycling, scientists assume that the cavern spatial variations of pressure and temperature are negligible in the main part of the cavern volume (Guo et al., 2017). Henceforth, they apply the concept of a heat transfer coefficient h_c to account for solid-gas heat exchange over the cavern surface,

$$h_c = \frac{\text{Normal thermal conduction at the solid wall}}{\text{Temperature difference between solid and gas}} = \frac{\boldsymbol{\psi} \cdot \boldsymbol{n}}{T_\sigma - T}, \tag{3.5}$$

with $\boldsymbol{n}$ being the cavern inward normal vector and T the gas temperature passing by the wall. Estimation of this coefficient is tedious, however, once *in situ* data is available, it can be precisely predicted (Raju and Khaitan, 2012). In this research, a solid-gas temperature continuity over the cavern surface is assumed. However, the well heat transfer coefficient h_w is calculated using empirical laws, as seen below.

Concerning the cavern well, the velocity and thermodynamic variables are functions of time t and the curvilinear abscissa x along the well axis, i.e. $v(x,t)$, $T(x,t)$, and $p(x,t)$. For this case, the system of Eqs 3.1 becomes:

$$\begin{aligned} \rho\dot{v} - v' &= 0; \\ \rho\dot{v} + p' &= \rho\boldsymbol{g}\cdot\boldsymbol{t} + (L_\zeta/\mathcal{A})\zeta_w; \\ \rho(\dot{u} + p\dot{v}) &= (L_w/\mathcal{A})\psi_w - v(L_\zeta/\mathcal{A})\zeta_w, \end{aligned} \tag{3.6}$$

where the prime denotes the variable derivative along the well axis, $\mathcal{A}$ is the flow cross sectional area, $\boldsymbol{t}$ is the vector tangent to the pipe wall, L_ζ is the well circumference available for fluid flow, and L_w is the well circumference available for heat transfer. These two circumferences are equal in case of simple pipe flow. ψ_w is the heat exchange across the pipe wall, and ζ_w is the friction stress. The quantities ψ_w and ζ_w are usually given by empirical laws (Kaviany, 2002). The stress ζ_w is generally expressed as $\zeta_w = -C_f\rho v|v|/2$. The term ψ_w implies the heat flux across the pipe wall, it can be expressed using the Newton's law as $\psi_w = h_w(T_\sigma - T)$. The following relations are adopted to calculate the empirical coefficients,

$$\begin{aligned} C_f &= 2\Big((8/\mathrm{Re})^{12} + (\mathrm{A}+\mathrm{B})^{-3/2}\Big)^{1/12}, \quad \text{with,} \\ A &= \left(-2.457\,\ln\Big((7/\mathrm{Re})^{0.9} + 0.27(\varepsilon L_\zeta/D_H)\Big)\right), \quad \text{and,} \quad B = (37530/\mathrm{Re})^{16}, \end{aligned} \tag{3.7}$$

and,

$$\begin{aligned} \mathrm{Nu} &= 3.66 \quad \text{for} \quad \mathrm{Re} \leq 2300, \quad \text{and,} \\ \mathrm{Nu} &= (C_f/2)(\mathrm{Re}-1000)\mathrm{Pr}/\Big(1 + 12.7\sqrt{C_f/2}(\mathrm{Pr}^{2/3}-1)\Big) \\ &\quad \text{for} \quad 2300 < \mathrm{Re} < 5\times10^6, \quad \text{and,} \quad 0.5 < \mathrm{Pr} < 2000, \end{aligned} \tag{3.8}$$

where ε is the wall roughness, $D_H = 4\mathcal{A}/L_\zeta$ is the hydraulic diameter, Nu is the Nusselt number, $\mathrm{Pr} = \mu C_p/\Lambda$ is the Prandtl number. The pipe Reynolds number takes the form $\mathrm{Re} = \rho\, v\, D_H/\mu$. The well heat transfer coefficient is expressed in terms of the Nusselt number as $h_w = \Lambda\,\mathrm{Nu}/D_T$, with $D_T = 4\mathcal{A}/L_w$ being the thermal diameter.

The problem is fully coupled in the sense that if the well variables are known, they can be used to determine the unknown parts of the boundary conditions of the cavern and the formation. Using these boundary conditions, the problem in the latest domains can be solved leading to new data that can be put for a next time step solution. With regard to the cavern itself, assuming a uniform thermodynamic state simplifies the system of Eqs 3.1 to:

$$\begin{aligned} Q_e/\mathcal{M} &= -\chi_p \dot{T} + \chi_T \dot{p}; \\ \mathcal{M} C_p \dot{T} - \mathcal{V}\chi_p T \dot{p} &= Q_e^+ (h_t^w - h^c) + \Psi, \end{aligned} \tag{3.9}$$

where $\mathcal{M}$ is the gas mass, $\chi_p = -\nu \partial_T \rho|_p$ is the isobaric volumetric thermal expansion coefficient, $\chi_T = \nu\, \partial_p \rho|_T$ is the isothermal compressibility coefficient, $\mathcal{V}$ is the cavern volume (assumed constant), $h_t^w = h^w + \boldsymbol{v}\cdot\boldsymbol{v}/2$ is the well dynamic/total specific enthalpy, h^c is the cavern specific enthalpy, Q_e is well/external flow rate, Q_e^+ is the positive/injection part of Q_e, and $\Psi = \int_S \boldsymbol{\psi}\cdot\boldsymbol{n}\, d\mathcal{A}$ is the power exchanged between gas and surrounding rock. With the assumption of solid-gas temperature continuity over the cavern surface, this power exchange is calculated using the Fourier conduction equation in the rock formation side.

The assumption of a uniform thermodynamic state leads to considerable simplifications to the mathematical problem. Considering that the time derivatives do not account for convective terms any more, and that the main variables are only functions of time, the system of Eqs 3.9 represents a system of ordinary differential equations of $p(t)$ and $T(t)$. The complexities left stem from the necessity to model a real gas behavior (when necessary and appropriate), and the discretization needed in the rock domain to solve for Eq. 3.4. However, since the cavern thermodynamic behavior is now assumed uniform in its domain (single point behavior), the surrounding rock mass is discretized into finite elements and heat conduction is assumed one-dimensional.

3.1.2 Simulations at the cavern scale

The boundary value problem represents a spherical cavern of volume $\mathcal{V} = 300{,}000\ \mathrm{m}^3$ in a surrounding rock domain. The well extends from the surface at $z = 0$ m to the cavern at $z = z_w = -910$ m. The initial cavern volume averaged temperature and pressure are 40 °C and 22 MPa respectively (Fig. 3.2). Gas is injected at $T = 40$ °C following the program shown in Fig. 3.3. The gas used in the simulations is ideal hydrogen[1] and the cavern is assumed initially full with mass $\mathcal{M}(0) = 4.52 \times 10^6$ kg.

Figure 3.3 shows the injection schemes considered in the simulations in terms of the relative mass change $\tilde{\mathcal{M}} = (\mathcal{M}/\mathcal{M}(0) - 1) \times 100\%$. The first scheme represents fast/daily cycling where the cavern is utilized extensively, and one cycle (4.5 days) leads to a relative mass change in the range [-69% to -29%]. Second scheme represents slow/seasonal cycling utilization where the cavern experiences the same relative mass change, yet over a period of 58.5 days. There are periods of standstill/rest/pause after injection and withdrawal that are marked by constant relative mass change over time. Simulations are run for 60 days to allow for the investigation of thermal exchange between the gas in the cavern and the surrounding rock mass. Points p_1 of withdrawal at ($t = 6.332, \tilde{\mathcal{M}} = -57.6$), p_2 of injection at ($t = 25.87, \tilde{\mathcal{M}} = -51.73$), and p_3 of

[1] The assumption of ideal gas simplifies calculations.

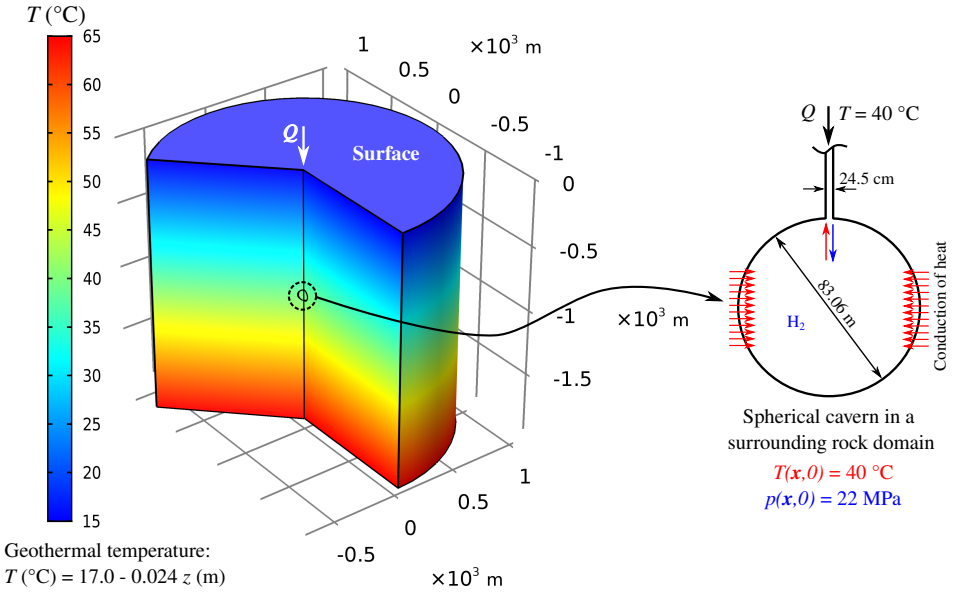

FIGURE 3.2: Schematic diagram of the boundary value problem: it represents a spherical cavern created at depth 910 m in a surrounding rock domain. The geothermal gradient causes a cavern volume averaged temperature of 40 °C. The cavern is assumed initially full of ideal hydrogen with mass $\mathcal{M}(0) = 4.52 \times 10^6$ kg at $p(\boldsymbol{x}, 0) = 22$ MPa.

pause at ($t = 35.66, \tilde{\mathcal{M}} = -29.03$) are displayed on the figure where velocity and temperature profiles analyzed in the upcoming arguments.

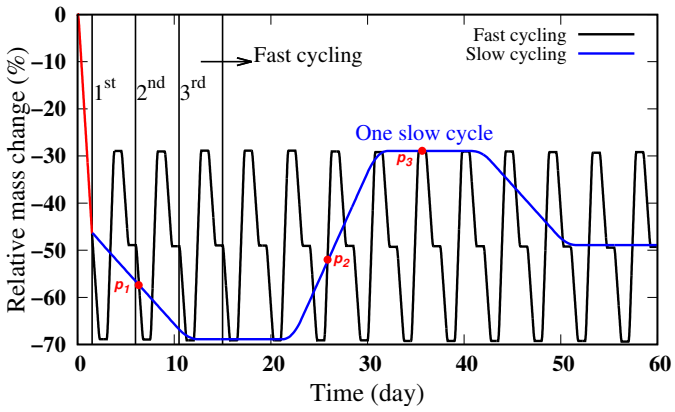

FIGURE 3.3: Two cycling schemes to run the cavern: fast/daily cycling that leads to a relative mass change of [-69% to -29%] in 4.5 days; and slow/seasonal cycling where the cavern experiences the same mass changes yet over a period of 58.5 days. Points p_1 of withdrawal, p_2 of injection, and p_3 of pause, are displayed on the figure to investigate velocity and temperature profiles in the upcoming discussions.

The gas cycling in the spherical cavern is simulated using the simplified approach and the COMSOL/complete approach, and results of the two simulations are correlated for fast and slow cycling. For the complete simulations, the boundary conditions are set as shown in Fig. 3.2. The rock formation far-field temperature boundary conditions are assumed to be of the Dirichlet type, i.e. $T = T_\infty(z)$, with $T_\infty(z)$ being the initial geothermal temperature. In case of the simplified simulations, $T_\infty(z)$ is replaced by its average value over the cavern surface. Gas is injected at $T = 40$ °C following the two schemes of Fig. 3.3. As for the initial conditions, in the complete simulations, the well and cavern are assumed in equilibrium with the surrounding rock $T(\boldsymbol{x}, 0) = T_\infty(z)$. However, in case of the simplified simulations, the cavern temperature is set to $T(0) = 40$ °C. Yet, the same temperature gradient (Fig. 3.2) is applied over the well

length.

Figure 3.4 shows the two-dimensional axisymmetric discretization of the boundary value problem for the complete simulations. The mesh consists of 445304 elements of which 24607 quadrilateral boundary elements to account for solid-gas heat transfer and turbulent flow. Aside from the boundary layer quadrilateral elements, the well is discretized into at least another 5 triangular elements to solve for possible radial variations of its thermodynamic quantities. At this level of discretization, and based on the recommendations of the k-ϵ model, the solution is not mesh dependent (Lacasse, Turgeon, and Pelletier, 2004). For the comparison purpose, a similar one-dimensional discretization with 5000 elements is used in the simplified simulations for the rock domain, and the well is discretized into 1000 elements over its length. Rock thermal diffusivity is set equal to $\mathcal{K}_\sigma = \Lambda_\sigma/(\rho_\sigma C_{p\sigma}) = 0.29 \times 10^{-5}$ m^2/s. Ideal hydrogen is assigned the following thermodynamic and flow properties: $\Lambda = 0.195$ W/m/K; $C_p = 10225$ J/kg/K; and $\mu = 8.75 \times 10^{-6}$ Pa s.

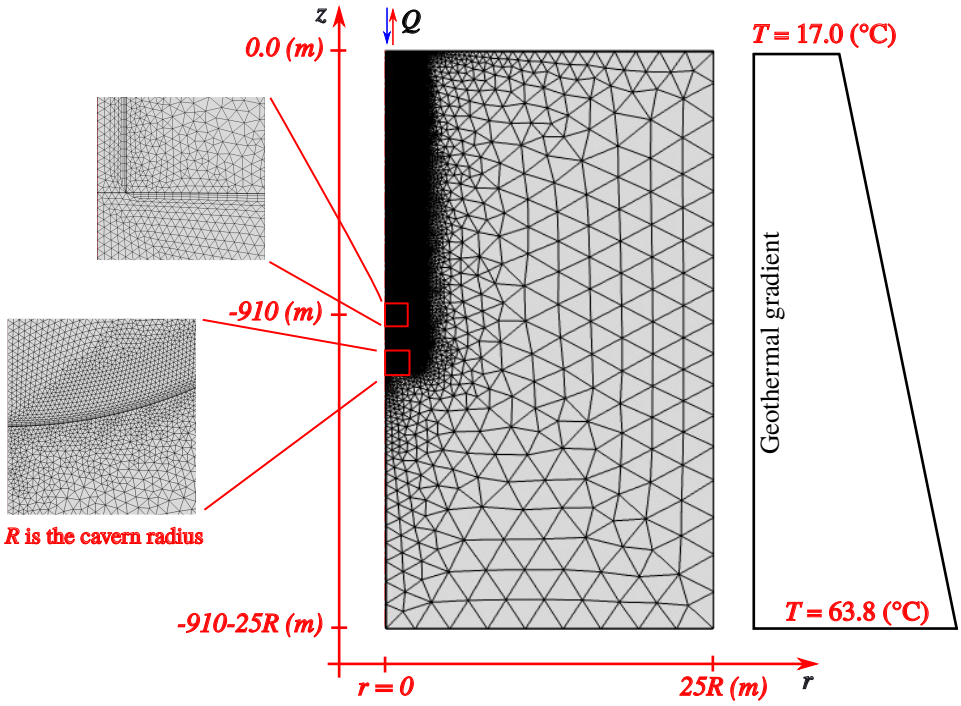

FIGURE 3.4: Two-dimensional axisymmetric discretization of the boundary value problem of Fig. 3.2 for complete simulations. A surrounding rock volume of 25R is chosen around the cavern and well to avoid the effect of far-field boundaries. Mesh is considerably refined on the solid-gas boundary with quadrilateral boundary elements based on the recommendations of the k-ϵ turbulent flow. Mesh is also heavily refined for a certain volume in the rock domain around the cavern and well to better account for the large changes happening close to them in the time-frame of our simulations (60 days). Mesh contains 445304 elements of which 24607 quadrilateral boundary elements.

Figure 3.5 shows a comparison between the simulation results of the complete and the simplified approaches for the volume averaged temperature and pressure during slow and fast cycling. Since pressure histories are mainly affected by mass changes, the simplified and complete pressure histories are quite comparable (Figs 3.5(a, c)). However, the temperature histories show very slight differences in case of slow cycling (Fig. 3.5(b)), yet these differences are noticeable in case of fast cycling and they increase with time before they stabilize eventually (Fig. 3.5(d)).

To further comment on the efficiency of the simplified approach, the temperature and the vertical gas velocity profiles along the treatment well are compared. Figures 3.6(a, b, c) show the well temperature and velocity profiles by the complete (dashed-dotted lines) and the simplified

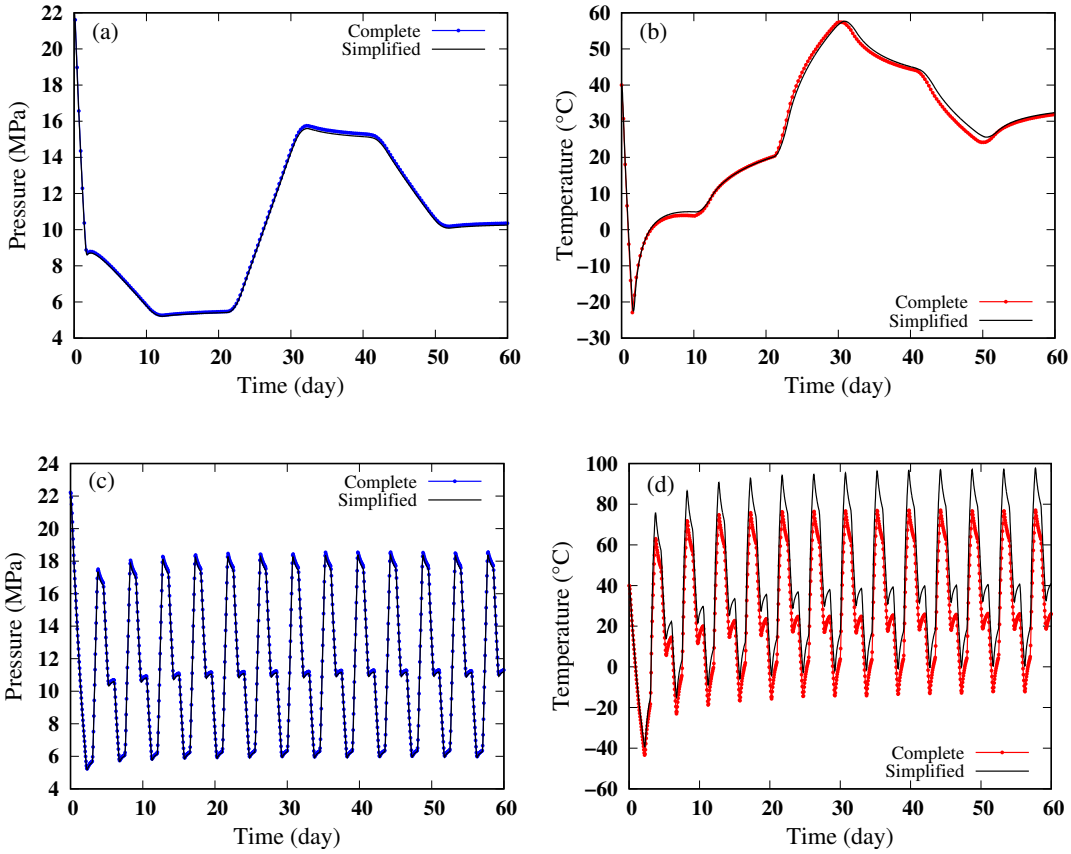

FIGURE 3.5: Development of the cavern pressure and temperature: comparison between slow/seasonal (a, b) and fast/daily (c, d) cycling of the simplified and the complete approaches.

(solid lines) approaches during slow cycling at points p_1 (withdrawal), p_2 (injection), and p_3 (standstill) of Fig. 3.3, and Figs 3.6(d, e, f) show the same profiles yet during fast cycling.

It is clear that these profiles are quite comparable in case of slow cycling, where the velocity profiles are almost vertical, meanwhile the temperature profiles show a curving behavior depending on the state of treatment (withdrawal or injection). In case of pause/standstill, the velocity is equal to zero, and the temperature profiles show linear variations and tend to resemble to the natural geothermal temperature profile. In case of fast cycling (Figs 3.6(d, e, f)), and even-though the velocity profiles are to some point comparable, the temperature profiles are considerably different and they do not show the curving variations anymore due to the fast treatment. In case of the complete approach, these profiles are calculated along the well central line, however in the simplified simulations, there are no radial variations due to the application of 1-D pipe model.

It is interesting to compare the velocity spatial heterogeneities in the cavern volume during these cycling schemes. Figure 3.7 shows the contours of gas velocity magnitude at points p_1, p_2, and p_3 for the same value range of [0 to 0.2] m/s. One can see that, regardless of the treatment stage, gas velocity is significant at the cavern wall. However, in case of injection, velocity becomes also large at the well-cavern connection and it goes all through the cavern volume for fast cycling, yet considerable values never hit the cavern bottom in case of slow cycling. It is also evident that a larger cavern volume is affected by the gas velocity spatial heterogeneities throughout the fast cycling scheme.

The spatial heterogeneities in the velocity field are expected to create corresponding spatial heterogeneities in the temperature and pressure fields. As to quantify the spatial variations of the temperature and pressure over the time course of simulations, the radial and vertical

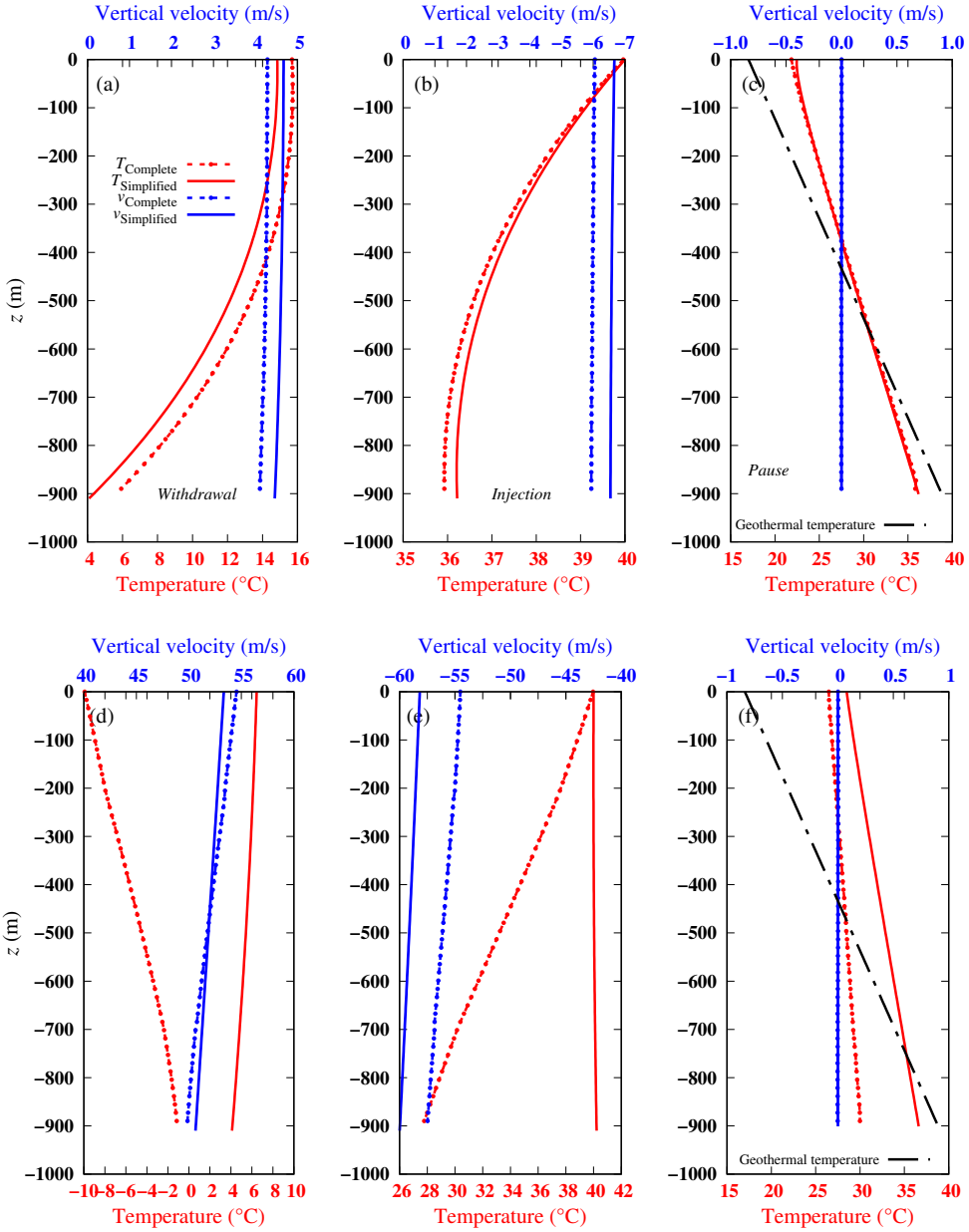

FIGURE 3.6: Development of well temperature and gas velocity profiles during slow cycling (Figs a, b, and c), and during fast cycling (Figs c, d, and e), at points p_1 of withdrawal, p_2 of injection, and p_3 of pause respectively (Fig. 3.3). The figure compares the simulation results of the complete and the simplified approaches.

components of these fields are averaged over the cavern volume (Fig. 3.8) for fast and slow cycling.

The spatial variations of the velocity field affect significantly the radial and vertical variations of the temperature field. Such variations are observed to be at least three-fold higher for fast cycling treatment (Figs 3.8(a, b)). Nonetheless, the radial variations of the pressure field are negligible, and vertical variations are almost comparable between fast and slow cycling (Figs 3.8(c, d)). Vertical pressure variations are mainly related to the gas weight and they are still negligible when compared to the volume averaged values in the range of [5 to 18] MPa. These spatial variations in the thermodynamic variables fields create the solution differences between the simplified and the complete approaches (Fig. 3.5).

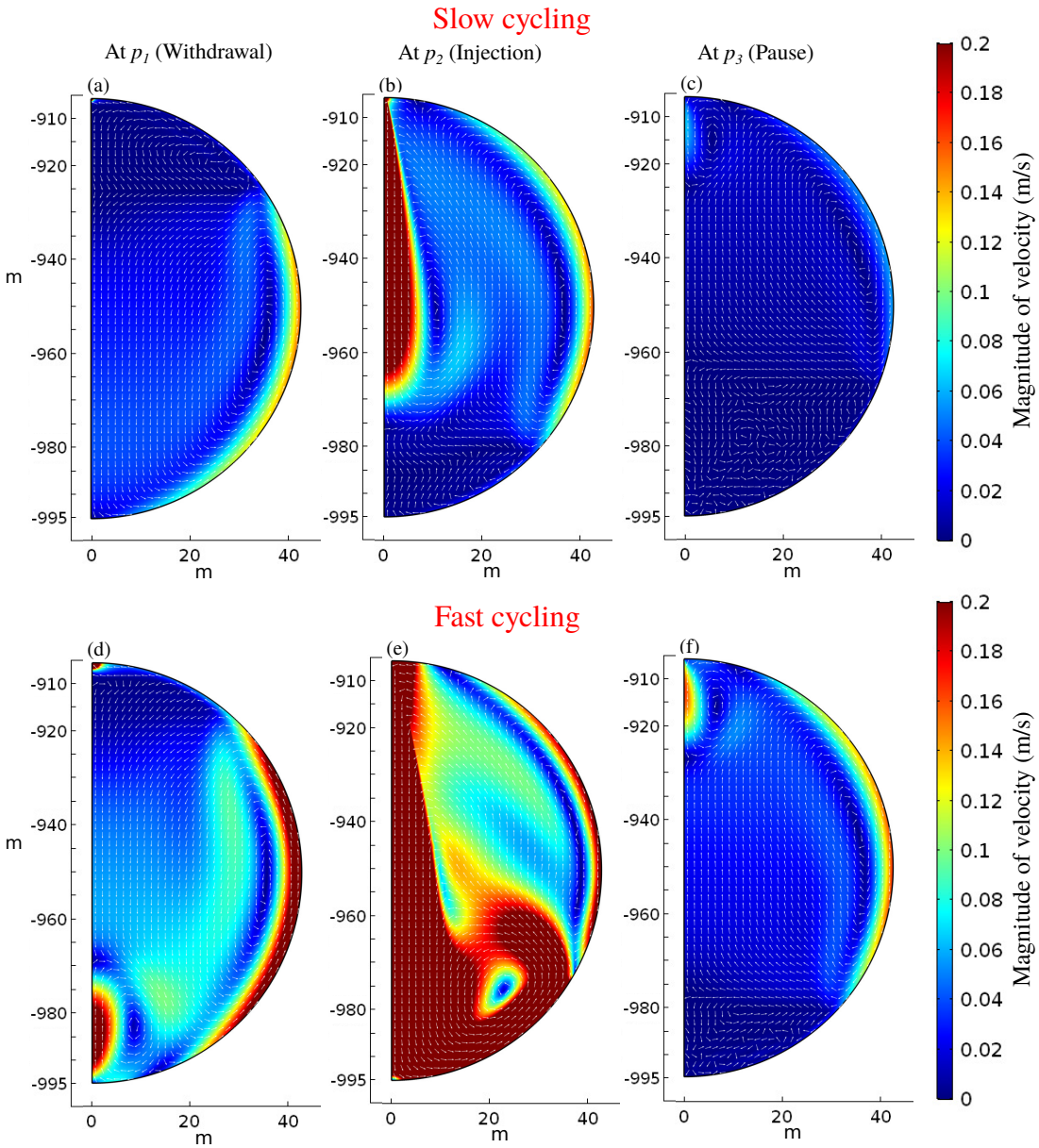

FIGURE 3.7: Contours of the magnitude of gas velocity vector $|\boldsymbol{v}|$. The figure compares the results of slow and fast cycling at points p_1, p_2, and p_3 for the same value range of [0 to 0.2] m/s. White arrows show the gas flow patterns.

3.1.3 Discussion and conclusion

The objective of this research is to know to which level the simplified uniform thermodynamic state simulations of gas storage in underground caverns (used generally) is valid, by comparing it to complete simulations that address all the complexities of the problem, i.e. mesh refinement, gas velocity field, turbulent flow model, and convective heat transfer.

Figure 3.9 shows the absolute value of the relative Kelvin temperature difference ($|1 - T_{\text{Complete}}/T_{\text{Simplified}}| \times 100\%$) between complete and simplified simulations of Figs 3.5(b, d).

Eventually, and despite considering all possible complexities of the problem, the simplified slow cycling simulations for both the well profiles (Figs 3.6(a, b, c)) and the cavern histories (Figs 3.5(a, b)), are quite close to the complete simulations with relative differences that did not exceed 1%. In terms of calculation times, simplified simulations did not last longer than 2 hours, however, complete simulations for fast cycling took approximately 60 days, and for slow cycling 45 days on parallel computation server of 16 cores. There are still more obvious

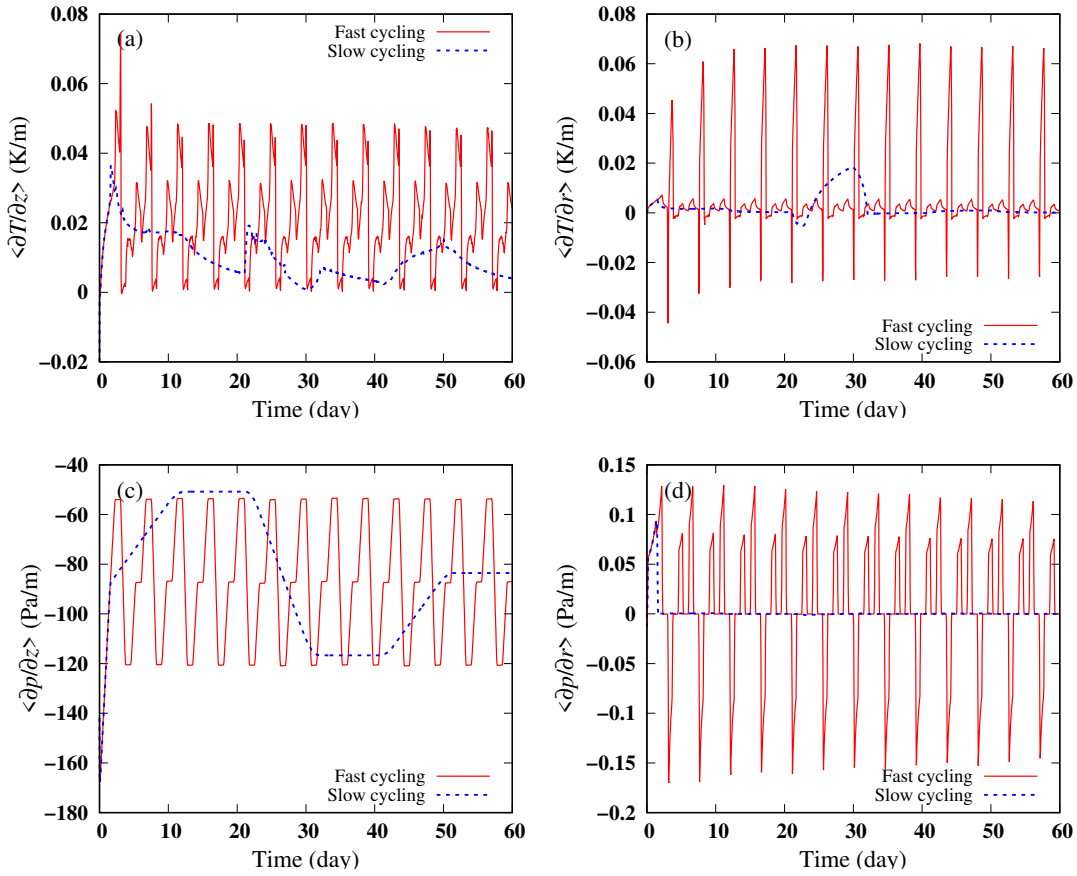

FIGURE 3.8: Volume averaged spatial variations of the gradient of the temperature field (a, b) (K/m), and of the gradient of the pressure field (c, d) (Pa/m).

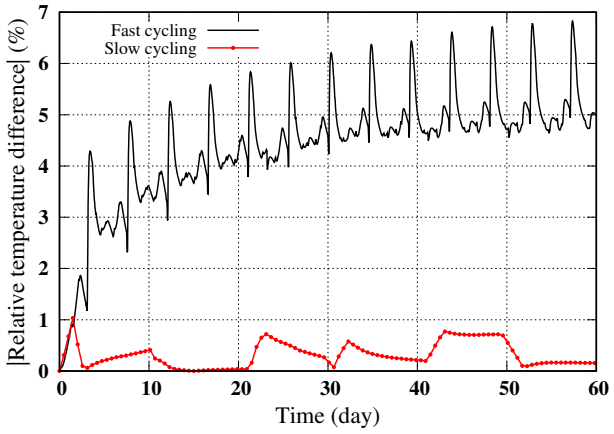

FIGURE 3.9: Relative Kelvin temperature difference $|1 - T_{\text{Complete}}/T_{\text{Simplified}}| \times 100\%$: comparison between complete and simplified simulations for fast and slow cycling of Figs 3.5(b, d).

differences between the complete and simplified simulations results in case of fast cycling that reach relative differences of 7%. Even-though the well velocity profiles are comparable, temperature profiles are considerably different, which renders the use of such simplified approaches questionable in case of fast cycling.

It is understood that a trade-off between accuracy and calculation time needs to be made. It is, until this time, still unfeasible to run complex complete simulations over the entire cavern lifetime, i.e. 30 years and maybe more. Yet, the simplified approaches can give out results in a few days. In case of seasonal utilization of underground caverns, the simplified simulations

are quite efficient in terms of results and calculation cost. In addition to that, such simplified approaches allow researchers to address other problems that are of significant importance to the industry, i..e the thermo-hydromechanical behavior of the rock mass during cycling, real gas behavior, interactions between the cavern species (gas, brine, and insoluble material), multi-phase simulations, and gas percolation into the rock mass. Still, while modern humanity demands on energy increase, the simplified approaches, to a certain level, impose a definite level of inaccuracy that might be unacceptable. The miscalculation of the cavern thermodynamic variables development lead to misestimation of the stored gas mass, as an example.

3.2 Gas migration into the surrounding rock salt

The second part of this chapter concerns the mass exchanges between the cavern phases, they are discussed in the coming three sections. This section focuses on hydrogen permeation into the rock salt during cycling in underground salt caverns (F_4 of Fig. 3.1).

During the cavern operation, hydrogen undergoes changes in its temperature and pressure. Such changes are expected to affect its migration into the surrounding rock domain. Hydrogen invasion into this embracing rock takes place either through the rock salt itself, or through the more permeable and porous interlayers (if they happen to exit). Since underground storage caverns are constructed in networks, the lost hydrogen into the surrounding rock can weaken the neighboring caverns structures. Moreover, the cost of hydrogen production as well as a good management of storage require to keep precise tracks of the injected and withdrawn hydrogen quantities.

Since rock salt contains interstitial brine and is characterized by extremely low permeability and porosity, the application of one-phase generalized Darcian flow to describe hydrogen transport is questionable. Indeed, the cavern thermodynamic state is a function of cycling. Consequently, at the cavern vicinity, both the interstitial rock salt brine pressure and temperature evolutions depend on cycling as well. These changes in the interstitial brine pressure and temperature must influence the migration of hydrogen into the rock domain. The novelty of this research stems from providing a mathematical-numerical model that couples the cavern thermodynamics with the non-isothermal transport mechanisms of hydrogen into the rock salt. Both the Darcian two-phase percolation and the Fickian diffusion are considered as well as the interaction between them. This model addresses as much as possible of the problem complex physics for good estimation of the exchanged hydrogen mass. Besides, it precisely presents the effect of cycling. The adopted van Genuchten model allows to describe the two-phase percolation of hydrogen (characterized by very low viscosity) in rock salt (characterized by very small pore size)[2]. Eventually, an overestimating scenario of model parameters, of diffusion coefficient, and of boundary conditions, is considered to estimate the amount of hydrogen migrated during a 40-year period of hydrogen cycling in a typical spherical cavern.

To quantify hydrogen migration into the rock salt, the interstitial brine pressure must be known. Due to the ambiguity with regard to the inter-grain connectivity of rock salt, the pressure of the interstitial brine is poorly defined. However, its value can be limited to two extremities (Gevantman and Lorenz, 1981):

1. the so-called halmostatic pressure, which considers that the brine occupies a totally connected space in the rock mass. Consequently, this pressure is the equivalent to the hydrostatic pressure calculated using the brine density;

2. a lithostatic pressure, which considers that the brine occupies an isolated space in the rock salt phase. Therefore, the brine pressure is assumed in equilibrium with the geologic

[2]This type of percolation is defined using the capillary and mobility numbers (Yortsos, Xu, and Salin, 1997; Lenormand et al., 1989)

stresses of the rock salt mass. This pressure extremity is calculated using the rock salt density (Bradley, 1975).

3.2.1 Mathematical and numerical model

This section presents the mathematical and numerical models needed to evaluate the quantity of hydrogen transported to the rock salt domain surrounding a typical underground cavern. Simulations are done for a seasonal cycling in a spherical cavern created at 910 m depth and for a 40-year time period (Fig. 3.2).

3.2.1.1 The mathematical model

The mathematical model couples the hydrogen thermodynamics in the cavern with the non-isothermal hydrogen transport in the saturated rock salt domain. To simplify the problem, the following assumptions are made. Some assumptions are adopted for an overestimating study:

- the underground cavern is assumed to be filled with a mono-component single-phase hydrogen;
- hydrogen cycling is seasonal/slow, consequently, a uniform thermodynamic state is assumed within the cavern (Sect. 3.1.1.2) ;
- rock salt domain is assumed saturated with brine;
- for an overestimating study, brine pressure within the rock salt domain is assumed halmostatic;
- rock salt creep due to cavern operation is neglected;
- hydrogen diffusion in the halite structure is neglected;
- hydrogen concentration is initially disregarded in the rock salt domain;
- rock salt, interstitial brine, and the invading hydrogen are assumed in thermal equilibrium;
- hydrogen invasion into the rock salt domain is assumed to follow the van Genuchten percolation model (Yortsos, Xu, and Salin, 1997; Lenormand et al., 1989);
- for an overestimating study, hydrogen entry pressure into the saturated rock salt is neglected.

As an example to model a uniform thermodynamic state within the cavern, the following system of equations is used (Sect. 3.1):

$$\begin{aligned} &\text{mass balance:} && \mathcal{M}\big(-\chi_{p\gamma}\,\dot{T}_\gamma + \chi_{T\gamma}\,\dot{p}_\gamma\big) &&= Q_e - \bar{\pi}_g^\gamma; \\ &\text{energy balance:} && \mathcal{M}\,C_{p\gamma}\,\dot{T}_\gamma - \mathcal{V}\,\chi_{p\gamma}\,T_\gamma\,\dot{p}_\gamma &&= Q_e^+\,C_{p\gamma}(T_\gamma^{\text{inj}} - T_\gamma) - \Psi, \end{aligned} \tag{3.10}$$

with $\bar{\pi}_g^\gamma$ being the exchanged mass rate between the cavern and the rock domain, and T^{inj} is the injection temperature. The well is not modelled here and the specific enthalpy is approximated by $h_\gamma = C_{p\gamma}T_\gamma$. The subscript γ is introduced to designate the gas phase.

Once the cavern thermodynamic state (p_γ and T_γ) is known, it can be used to calculate the hydrogen invasion into the surrounding rock salt domain. Figure 3.10 shows the mechanisms related to hydrogen transport in the saturated rock salt while assuming a van Genuchten two-phase percolation.

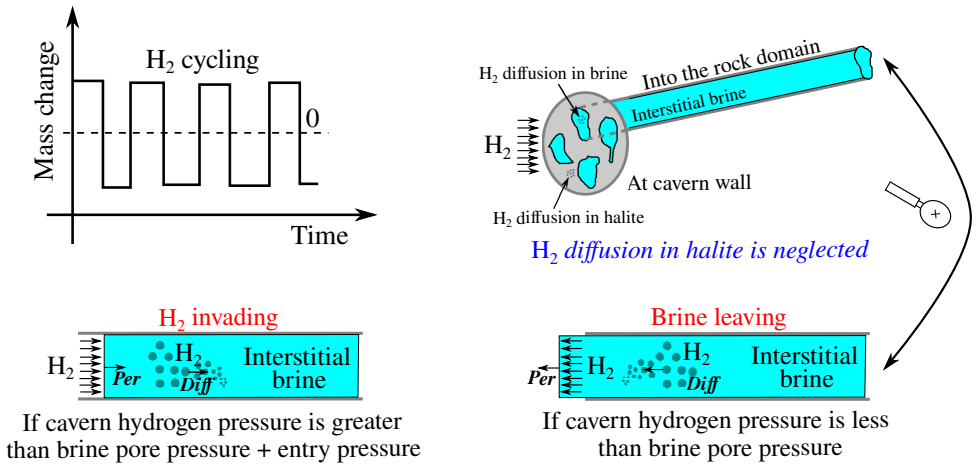

FIGURE 3.10: Schematic representation of hydrogen migration into the rock salt surrounding a slat cavern during cycling.

When hydrogen pressure within the cavern exceeds the rock salt pore pressure plus the entry pressure, hydrogen invades the rock salt in a two-phase percolation type flow. However, when hydrogen pressure becomes less than the interstitial brine pressure, brine moves towards the cavern and tends to pour down the cavern wall. Fickian diffusion of hydrogen in the rock salt interstitial brine is a function of hydrogen cycling. This diffusion is related to the hydrogen mass concentration gradient between the cavern and the rock salt domain. The temperature changes within the cavern lead to temperature changes in the rock salt domain. A temperature continuity is assumed at the cavern wall. The thermo-hydraulic coupling in the rock domain is accounted for through the pressure and temperature effects on the hydrogen and the brine densities.

As the mechanical deformation of the rock salt is neglected, the subsequent percolation-diffusion equations are established in the initial configuration of the solid matrix (Sect. 1.3). The rock salt porosity is denoted by n, and T denotes the temperature for all the phases in the rock salt domain. For each fluid phase $\alpha \in \{\lambda\,(\text{liquid}), \gamma\,(\text{gas})\}$, p_α stands for the pressure, n_α the partial porosity, $S_\alpha = n_\alpha / n$ the saturation degree, and ρ_α the density. In the liquid phase λ, $c_{g\lambda}$ denotes the mass concentration of hydrogen and $\rho_{g\lambda} = c_{g\lambda}\,\rho_\lambda$ denotes its density. For a given quantity X, the apparent value (per unit volume of the entire porous medium) is denoted X^α with $X^\alpha = n_\alpha\, X_\alpha$, where X_α is per unit volume occupied by the α-phase.

The rock salt interstitial brine density is characterized by four state variables which are the brine pressure p_λ, its temperature T, the hydrogen concentration $c_{g\lambda}$, and the salt concentration. In this study, the interstitial brine is assumed saturated with salt at any time. Besides the mass of the dissolved hydrogen is assumed very minor to affect the brine density. Therefore, the mass balance equations of the components b (brine) and g (hydrogen) of the liquid phase can be written in the following form:

$$
\begin{aligned}
\dot{m}_b^\lambda + \boldsymbol{\nabla}\cdot\left[\rho_\lambda\left(1-c_{g\lambda}\right)\boldsymbol{\omega}^\lambda - \rho_\lambda\,\boldsymbol{J}_{g\lambda}\right] &= \pi_b^\lambda;\\
\dot{m}_g^\lambda + \dot{m}^\gamma + \boldsymbol{\nabla}\cdot\left[\rho_\lambda\left(c_{g\lambda}\boldsymbol{\omega}^\lambda + \boldsymbol{J}_{g\lambda}\right) + \rho_\gamma\boldsymbol{\omega}^\gamma\right] &= \pi_g^\gamma;\\
\text{with,}\quad m^\alpha = nS_\alpha\rho_\alpha \quad \text{for} \quad \alpha &\in \{\lambda,\gamma\},\\
m_b^\lambda = (1-c_{g\lambda})\,m^\lambda, \quad \text{and,} \quad m_g^\lambda &= c_{g\lambda}\,m^\lambda,
\end{aligned}
\tag{3.11}
$$

where ρ_α is the density of the α-phase, $\boldsymbol{\omega}^\alpha$ is the filtration velocity of the α-phase, $\boldsymbol{J}_{g\lambda}$ is the Fickian diffusion flux of hydrogen in the liquid λ-phase, π_b and π_g are the total mass creation terms of the two components in the fluid phase. If heat convection in the rock salt domain is neglected, the following energy equation can be used to describe heat transfer within the rock salt domain due to cycling in the cavern,

$$\begin{aligned} m\,C_p\,\dot{T} + \boldsymbol{\nabla}\cdot\boldsymbol{\psi} = 0, \\ \text{with,} \quad m\,C_p = \sum_\alpha m^\alpha C_{p\alpha}, \quad \text{and,} \quad \boldsymbol{\psi} = -\underline{\underline{\boldsymbol{\Lambda}}}\cdot\boldsymbol{\nabla}T, \end{aligned} \tag{3.12}$$

with $\alpha \in \{\lambda,\ \gamma,\ \sigma\ (\text{solid})\}$, and $\underline{\underline{\boldsymbol{\Lambda}}}$ is the saturated rock salt domain thermal conductivity tensor. If the thermal conductivities of the three phases are assumed isotropic, the domain thermal conductivity Λ is expressed by the geometric mean of the phases thermal conductivities (Côté and Konrad, 2005),

$$\Lambda = \Lambda_\sigma^{n_\sigma}\,\Lambda_\lambda^{n_\lambda}\,\Lambda_\gamma^{n_\gamma}. \tag{3.13}$$

In a two-phase percolation flow, the liquid saturation degree S_λ can be calculated using the van Genuchten (1980) expression,

$$\tilde{S}_\lambda = \frac{S_\lambda - S_{\lambda r}}{S_{\lambda s} - S_{\lambda r}} = \left(1 + \left(\frac{p_c}{P_r}\right)^{1/(1-\ell)}\right)^{-\ell}, \tag{3.14}$$

where $p_c = p_\gamma - p_\lambda$ is the capillary pressure, $\tilde{S}_\lambda$ is the effective degree of saturation, the parameters $S_{\lambda r}$ and $S_{\lambda s}$ represent the liquid residual and maximum saturation values respectively ($S_\lambda \in [S_{\lambda r} - S_{\lambda s}]$), ℓ and P_r are model parameters. The equation does not introduce the notion of an entry pressure as it will be neglected in this research.

The hydraulic problem (Eq. 3.11) needs to be completed with constitutive and state laws. The filtration velocity vectors are assumed to follow a Darcian flow nature,

$$\boldsymbol{\omega}^\alpha = -\frac{k_{r\alpha}}{\mu_\alpha}\,\underline{\underline{\boldsymbol{k}}}\cdot\left(\boldsymbol{\nabla}p_\alpha - \rho_\alpha\mathbf{g}\right), \quad \text{for} \quad \alpha \in \{\lambda,\gamma\}, \tag{3.15}$$

where $\underline{\underline{\boldsymbol{k}}}$ is the intrinsic permeability tensor, μ_α is the dynamic viscosity of the α-phase, $\mathbf{g}$ is the gravitational acceleration vector, and $k_{r\alpha}$ is the relative permeability of the α-phase. Relative permeabilities can be calculated using the Mualem-van Genuchten model (Mualem, 1978),

$$k_{r\lambda} = \sqrt{\tilde{S}_\lambda}\left[1 - \left(1 - \tilde{S}_\lambda^{1/\ell}\right)^\ell\right]^2, \quad \text{and} \quad k_{r\gamma} = \sqrt{1-\tilde{S}_\lambda}\left(1 - \tilde{S}_\lambda^{1/\ell}\right)^{2\ell}. \tag{3.16}$$

The diffusion flux of hydrogen in the liquid phase is related to the concentration gradient through the Fick's law,

$$\boldsymbol{J}_{g\lambda} = -\underline{\underline{\boldsymbol{D}}}_{g\lambda}\cdot\boldsymbol{\nabla}c_{g\lambda} = c_{g\lambda}(\boldsymbol{v}_{g\lambda} - \boldsymbol{v}_\lambda), \tag{3.17}$$

where $\underline{\underline{\boldsymbol{D}}}_{g\lambda}$ and $\boldsymbol{v}_{g\lambda}$ are the diffusion coefficient tensor and the diffusive velocity of hydrogen in the λ-phase respectively. This coefficient can be determined experimentally for a given component, a phase, and a porous medium, or empirically from the plain diffusivity in the liquid phase $\bar{D}_{g\lambda}$ modified by the characteristics of the porous network (porosity, turtuosity, and constrictivity) (AbuAisha and Billiotte, 2021). A commonly used expression is $D_{g\lambda} = \bar{D}_{g\lambda}\,n^q$, where q is an empirical parameter that generally lies between 1.8 and 2.4 (Grathwohl, 2012). The exchanged hydrogen mass rate between the cavern and the surrounding rock salt (Eq. 3.10) can, therefore, be calculated as,

$$\bar{\pi}_g^\gamma = \underbrace{\int_{\mathcal{S}} \rho_\gamma\boldsymbol{\omega}^\gamma\cdot\boldsymbol{n}\,d\mathcal{A}}_{\text{Percolated mass rate}} + \underbrace{\int_{\mathcal{S}} \rho_\lambda(\boldsymbol{J}_{g\lambda} + c_{g\lambda}\boldsymbol{\omega}^\lambda)\cdot\boldsymbol{n}\,d\mathcal{A}}_{\text{Diffused mass rate}}, \tag{3.18}$$

with $\boldsymbol{n}$ being the outward unit vector normal to the cavern surface.

The hydrogen phase is assumed to behave as a real gas (AbuAisha et al., 2021). The state equation is described using two state functions; the density $\rho_\gamma(p_\gamma, T_\gamma)$, and the heat capacity $C_{p\gamma}(T_\gamma)$ at a given pressure. The thermodynamic variables are related to each other through the formula $p_\gamma = \rho_\gamma T_\gamma Z$, with Z being the gas compressibility factor. The chemical potential equality between the λ- and γ-phases leads to the definition of the Henry's law $p_\gamma = (K_H/M_w)\rho_{g\lambda} = Hc_{g\lambda}$, with K_H being the Henry's constant, M_w the hydrogen molecular weight, and $H = K_H\rho_\lambda/M_w$. The brine phase is assumed to be slightly compressible, i.e. $\dot{\rho}_\lambda/\rho_\lambda = \chi_{T\lambda}\,\dot{p}_\lambda - \chi_{p\lambda}\,\dot{T}$ with $\chi_{T\lambda}$ and $\chi_{p\lambda}$ being the isothermal compressibility and the isobaric thermal expansion coefficient respectively.

3.2.1.2 Saturated/unsaturated state transition

The set of differential equations and primary variables (Eq. 3.11) needs to be controlled to assure the transition from fully saturated state to unsaturated state, or vice versa. Only the problem of hydrogen appearance in rock salt where the brine phase is always present, is considered in this work. The proposed modeling approach consists of using the dissolution and diffusion phenomena to derive a set of differential equations applicable for both saturated and unsaturated states (Mahjoub et al., 2018).

The choice of the primary variables is crucial. The pressure p_λ can be chosen as the first primary variable because the brine phase is assumed present at any time. With regard to the second unknown, due to dissolution and diffusion phenomena, the mass concentration $c_{g\lambda}$ is a permanent unknown, whether the medium is saturated or unsaturated. Thus, it is chosen as the second primary variable. However, to assure the homogeneity in the primary variables, a pseudo-hydrogen pressure is defined as $\hat{p}_\gamma = Hc_{g\lambda}$. It represents the real hydrogen pressure only when the hydrogen phase is present ($\hat{p}_\gamma = p_\gamma$ if $S_\lambda < 1$), and it is just a definition in the saturated case. To use the same equations in the saturated case, a new pseudo-capillary pressure is introduced $\hat{p}_c = \hat{p}_\gamma - p_\lambda$. The saturation degree is expressed as a function of this pseudo-capillary pressure such that $S_\lambda(\hat{p}_c) = S_\lambda(p_c)$ when $\hat{p}_c \geq 0$ (because $\hat{p}_c = p_c$), and $S_\lambda(\hat{p}_c) = 1$ when $\hat{p}_c < 0$.

Taking these definitions into consideration, the γ-Darcy and Fick laws have to be reformulated and integrated into the conservation equations. The same equation for γ-Darcy law (Eq. 3.15) is used after replacing p_γ by $\hat{p}_\gamma$, with $\rho_\gamma(\hat{p}_\gamma, T_\gamma)$. In Fick's law (Eq. 3.17), $c_{g\lambda}$ is replaced by $\hat{p}_\gamma/H$, and the variation of H is assumed negligible compared to the variation of $\hat{p}_\gamma$. The reformulated mass conservation equations can be cast in the following system of coupled partial differential equations:

$$
\begin{aligned}
\dot{m}_b^\lambda - \boldsymbol{\nabla}\cdot\left(\underline{\underline{\boldsymbol{\mathcal{B}}}}_{b\lambda}\cdot(\boldsymbol{\nabla}p_\lambda - \rho_\lambda\boldsymbol{\mathfrak{g}}) + \underline{\underline{\boldsymbol{\mathcal{B}}}}_{b\gamma}\cdot\boldsymbol{\nabla}\hat{p}_\gamma\right) &= \pi_b^\lambda;\\
\dot{m}_g^\lambda + \dot{m}^\gamma - \boldsymbol{\nabla}\cdot\left(\underline{\underline{\boldsymbol{\mathcal{B}}}}_{g\lambda}\cdot(\boldsymbol{\nabla}p_\lambda - \rho_\lambda\boldsymbol{\mathfrak{g}}) + \underline{\underline{\boldsymbol{\mathcal{B}}^{\boldsymbol{f}}}}_{g\gamma}\cdot\boldsymbol{\nabla}\hat{p}_\gamma + \underline{\underline{\boldsymbol{\mathcal{B}}^{\boldsymbol{p}}}}_{g\gamma}\cdot(\boldsymbol{\nabla}\hat{p}_\gamma - \rho_\gamma\boldsymbol{\mathfrak{g}})\right) &= \pi_g^\gamma;\\
\text{with,}\quad \underline{\underline{\boldsymbol{\mathcal{B}}}}_{b\lambda} = \left[(1-c_{g\lambda})\rho_\lambda k_{r\lambda}/\mu_\lambda\right]\underline{\underline{\boldsymbol{k}}},&\quad \underline{\underline{\boldsymbol{\mathcal{B}}}}_{b\gamma} = (-\rho_\lambda/H)\underline{\underline{\boldsymbol{D}}}_{g\lambda},\\
\underline{\underline{\boldsymbol{\mathcal{B}}}}_{g\lambda} = (c_{g\lambda}\rho_\lambda k_{r\lambda}/\mu_\lambda)\underline{\underline{\boldsymbol{k}}},\quad \underline{\underline{\boldsymbol{\mathcal{B}}^{\boldsymbol{f}}}}_{g\gamma} = (\rho_\lambda/H)\underline{\underline{\boldsymbol{D}}}_{g\lambda},&\quad \text{and,}\quad \underline{\underline{\boldsymbol{\mathcal{B}}^{\boldsymbol{p}}}}_{g\gamma} = (\rho_\gamma k_{r\gamma}/\mu_\gamma)\underline{\underline{\boldsymbol{k}}}.
\end{aligned}
\tag{3.19}
$$

The system of Eqs 3.19 along with the energy conservation (Eq. 3.12) are written in a matrix form as follows,

$$\underbrace{\begin{bmatrix} \mathcal{C}_{b\gamma} & \mathcal{C}_{b\lambda} & \mathcal{C}_{bT} \\ \mathcal{C}_{g\gamma} & \mathcal{C}_{g\lambda} & \mathcal{C}_{gT} \\ 0 & 0 & \mathcal{C}_{T} \end{bmatrix}}_{\text{Storage matrix}} \begin{bmatrix} \dot{\hat{p}}_\gamma \\ \dot{p}_\lambda \\ \dot{T} \end{bmatrix} - \boldsymbol{\nabla} \cdot \underbrace{\begin{bmatrix} \underline{\underline{\boldsymbol{\mathcal{B}}}}_{b\gamma} & \underline{\underline{\boldsymbol{\mathcal{B}}}}_{b\lambda} & \underline{\underline{\mathbf{0}}} \\ \underline{\underline{\boldsymbol{\mathcal{B}}}}^{\boldsymbol{f}}_{g\gamma} + \underline{\underline{\boldsymbol{\mathcal{B}}}}^{\boldsymbol{p}}_{g\gamma} & \underline{\underline{\boldsymbol{\mathcal{B}}}}_{g\lambda} & \underline{\underline{\mathbf{0}}} \\ \underline{\underline{\mathbf{0}}} & \underline{\underline{\mathbf{0}}} & \underline{\underline{\boldsymbol{\Lambda}}} \end{bmatrix}}_{\text{Dispersion matrix}} \cdot \begin{bmatrix} \boldsymbol{\nabla}\hat{p}_\gamma \\ \boldsymbol{\nabla} p_\lambda \\ \boldsymbol{\nabla} T \end{bmatrix} = \underbrace{\begin{bmatrix} -\boldsymbol{\nabla} \cdot \left(\underline{\underline{\boldsymbol{\mathcal{B}}}}_{b\lambda} \cdot \rho_\lambda \mathbf{g}\right) + \pi_b^\lambda \\ -\boldsymbol{\nabla} \cdot \left(\underline{\underline{\boldsymbol{\mathcal{B}}}}^{\boldsymbol{p}}_{g\gamma} \cdot \rho_\gamma \mathbf{g} + \underline{\underline{\boldsymbol{\mathcal{B}}}}_{g\lambda} \cdot \rho_\lambda \mathbf{g}\right) + \pi_g^\gamma \\ 0 \end{bmatrix}}_{\text{Body forces matrix}} \tag{3.20}$$

with,

$$\begin{aligned} \mathcal{C}_{b\gamma} &= n\rho_\lambda \frac{\partial S_\lambda}{\partial \hat{p}_\gamma}\left(1 - \frac{\hat{p}_\gamma}{H}\right) - \frac{n\rho_\lambda S_\lambda}{H}, \\ \mathcal{C}_{b\lambda} &= n\rho_\lambda \frac{\partial S_\lambda}{\partial p_\lambda}\left(1 - \frac{\hat{p}_\gamma}{H}\right) + n\rho_\lambda S_\lambda \chi_{T\lambda}\left(1 - \frac{\hat{p}_\gamma}{H}\right), \\ \mathcal{C}_{bT} &= n\rho_\lambda S_\lambda \chi_{p\lambda}\left(1 - \frac{\hat{p}_\gamma}{H}\right), \end{aligned} \tag{3.21}$$

and,

$$\begin{aligned} \mathcal{C}_{g\gamma} &= -n\rho_\lambda \frac{\partial S_\lambda}{\partial \hat{p}_\gamma}\left(1 - \frac{\hat{p}_\gamma}{H}\right) - \frac{n\rho_\lambda S_\lambda}{H} + n\rho_\gamma(1 - S_\lambda)\chi_{T\gamma}, \\ \mathcal{C}_{g\lambda} &= n\frac{\partial S_\lambda}{\partial p_\lambda}\left(\rho_\lambda \frac{\hat{p}_\gamma}{H} - \rho_\gamma\right), \\ \mathcal{C}_{gT} &= -n\left(\rho_\lambda \frac{\hat{p}_\gamma}{H} S_\lambda \chi_{p\lambda} + \rho_\gamma(1 - S_\lambda)\chi_{p\gamma}\right), \end{aligned} \tag{3.22}$$

and,

$$\mathcal{C}_T = m\, C_p. \tag{3.23}$$

3.2.1.3 The numerical model

The numerical model represents a spherical cavern of volume $\mathcal{V} = 300{,}000$ m^3 in a surrounding rock domain. The well extends from the surface at $z = 0$ m to the cavern top at $z = z_w = -910$ m (Fig. 3.2). The cavern has been leached (full of brine) and is initially in thermal equilibrium with the surrounding rock domain at $T = 40$ °C. The brine pressure within the cavern is also in equilibrium with the rock salt pore pressure at the halmostatic value of $p_\lambda = -\rho_\lambda \mathbf{g} z = 11.2$ MPa. The cavern brine is then replaced by hydrogen during a debrining/filling phase of 90 days where hydrogen pressure of 22 MPa is attained within the cavern. The cavern is later left unsolicited for a similar period of time. Consequently, after 90 days of standstill, the cavern volume averaged temperature and pressure are 46 °C and 22 MPa respectively. The cavern then undergoes seasonal cycling following the program shown in Fig. 3.11 for a 40-year time period, where hydrogen is injected at $T_\gamma^{\text{inj}} = 40$ °C.

Figure 3.11 shows the cycling scheme that will be considered in our simulations in terms of the relative mass change $\tilde{\mathcal{M}} = (\mathcal{M}/\mathcal{M}(0) - 1) \times 100\%$. The program starts with a withdrawal phase of 60 days, cycling then begins where each cycle extends over a 6-month period. Only

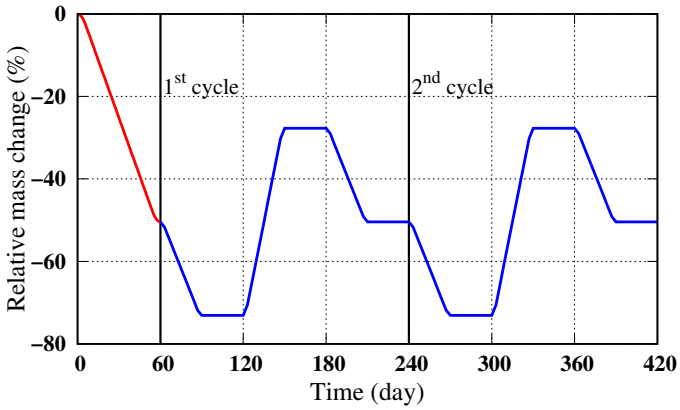

FIGURE 3.11: Imposed cavern relative mass variations. Only the first two cycles are shown, however simulations are run for 40 years.

the first two cycles are shown, however, simulations are conducted for a 40-year time period, i.e. 80 cycles.

The COMSOL available general forms of the coefficient Partial Differential Equations (cPDE), of the domain Ordinary Differential Equations (dODE), and of the boundary Ordinary Differential Equations (bODE) are used to solve the previous systems of equations in a coupled thermo-hydraulic framework. COMSOL gives analytical expressions to track the evolution of the hydrogen viscosity μ_γ, thermal conductivity Λ_γ, and heat capacity $C_{p\gamma}$ as a function of temperature. Hydrogen is modelled as a real gas (AbuAisha et al., 2021). Other van Genuchten, thermal, and hydraulic parameters are detailed in Table (3.1).

TABLE 3.1: Hydraulic, thermal, and van Genuchten parameters to model hydrogen invasion into the rock salt. References: 1. (Grathwohl, 2012); 2. (Gevantman and Lorenz, 1981); 3. (Mahjoub et al., 2018); 4. (Cosenza et al., 1999); 5. (Schulze, Popp, and Kern, 2001b); 6. (Bannach et al., 2005); 7. (Poppei et al., 2006); 8. (Crozier and Yamamoto, 1974); 9. (Lopez-Lazaro et al., 2019); 10. (AbuAisha et al., 2021).

Interpretation	Parameter (unit)	Value	Reference
Rock salt permeability	k (m^2)	1×10^{-20}	[4, 5]
Rock salt porosity	n	0.01	[4, 5]
Brine density	ρ_λ (kg/m^3)	1200	[2]
Brine isothermal compressibility	$\chi_{T\lambda}$ (1/Pa)	46×10^{-11}	[2]
Brine isobaric expansivity	$\chi_{p\lambda}$ (1/K)	45×10^{-5}	[2]
Brine dynamic viscosity	μ_λ (Pa s)	1.32×10^{-3}	[2]
Brine thermal conductivity	Λ_λ (W/m/K)	0.51	[2]
Brine heat capacity	$C_{p\lambda}$ (J/kg/K)	3300	[2]
Rock salt pore pressure	p_λ (Pa)	$-\rho_\lambda \mathfrak{g} z$	Overestimating study
Rock salt density	ρ_σ (kg/m^3)	2200	[6]
Rock salt thermal conductivity	Λ_σ (W/m/K)	6	[6]
Rock salt heat capacity	$C_{p\sigma}$ (J/kg/K)	900	[6]
Maximum brine saturation	$S_{\lambda s}$	1.0	Assumed
Residual brine saturation	$S_{\lambda r}$	0.15	[3]
van Genuchten parameter	P_r (Pa)	8×10^6	[10]
van Genuchten parameter	ℓ	0.5	[7]
Mass creation terms	π_b^λ and π_g^γ ($kg/m^3/s$)	0	Assumed
Hydrogen mass concentration	$c_{g\lambda}$	$\hat{p}_\gamma / H$	Definition
Hydrogen diffusion in brine	$\tilde{D}_{g\lambda}$ (m^2/s)	5×10^{-7}	Overestimated [10]
Diffusion correction parameter	q	2.1	[1]
Henry's constant hydrogen-brine	K_H (l atm/mol)	1300	[8, 9]

3.2.2 Effects of the van Genuchten model parameters

As stated previously, and due to the absence of any literature data with regard to the entry pressure of hydrogen in the saturated rock salt, the entry pressure notion is neglected in this research. This conclusion is pessimistic as it overestimates the total amount of gas lost into the rock domain. The work of AbuAisha et al. (2021) investigated the effect of the Van Genuchten model parameters, particularly P_r and ℓ, and the diffusion coefficient on the migration of hydrogen into the saturated rock salt.

For a P_r range that resembles the hydrogen invasion into the rock salt, the Darcian percolation has a slight dependency on the value of P_r. The parameter ℓ is assigned a value of 0.5 for rock salt in a few research papers. However, possible high values ($\ell \sim 0.9$) can increase considerably the capillary pressure at full brine saturation leading to a naught percolation. A value of $\ell = 0.1$, close to the lowest limit, increases the hydrogen mass percolated into the rock salt domain by 3 folds. The value of the diffusion coefficient $\bar{D}_{g\lambda}$ does not affect directly the Darcian percolation, but rather its diffusive nature. Percolation becomes more of a piston-like for very small values (AbuAisha et al., 2021).

3.2.3 Simulations of hydrogen migration during cycling

A two-dimensional axisymmetric model is adopted to simulate heat and mass exchange with the surrounding rock domain during hydrogen cycling in the real cavern (Fig. 3.2). Figure 3.12 shows the spatial discretization of the rock domain. The cavern is not discretized since a uniform thermodynamic state is assumed within the cavern. Initial and boundary conditions are displayed on the graph.

Figures 3.13(a, b) show the cavern averaged temperature and pressure as a function of cycling. Hydrogen pressure is not showing any changes during cycling as the cavern volume is assumed constant. However, temperature is showing some changes due to the energy exchanged with the surrounding rock salt domain.

Figure 3.13(c) shows the hydrogen pseudo-capillary pressure averaged over the cavern surface during cycling. The behavior of the capillary pressure becomes almost identical after five cycles. The capillary pressure does not exceed 2 MPa for the working and boundary conditions of this typical spherical cavern.

To study the hydrogen mass exchanged with the rock domain, Fig. 3.14(a) shows the brine saturation, and Fig. 3.14(b) shows the radial component of hydrogen filtration velocity averaged over the cavern surface during the first four cycles. Other cycles are not displayed due to similarity and to avoid redundant repetitions.

The debrining and the standstill phases of 180 days have led the brine saturation at the cavern wall to decrease to $\sim$0.981 before any cycling (Fig. 3.14(a)). The subsequent withdrawal has counteracted this reduction in the brine saturation by allowing the percolated hydrogen to leave back to the cavern volume, and again after some cycling, the full brine saturation is reached. Furthermore, hydrogen percolates into and leaves from the rock domain as a function of the cavern hydrogen pressure (Fig. 3.14(b)). This allows for a reduction in the brine saturation at the cavern wall before it sustains the full saturation state (Fig. 3.14(a) and Fig. 3.15(a)).

The Fickian diffusive velocity resembles the brine filtration velocity (Figs 3.14(c, d)). Depending on the direction of hydrogen pressure gradient, hydrogen may diffuse into the rock domain, or pour down the cavern wall along with the leaving brine. The surface averaged radial component of the brine filtration velocity is show in Fig. 3.14(d). It is observed that brine leaves the rock domain into the cavern when the percolated hydrogen leaves the rock domain as well and vice versa. Besides, the thermal effects are noticed on the behavior of the brine filtration and the Fickian diffusive velocities due to the hydro-thermal coupling, especially during the standstill phases.

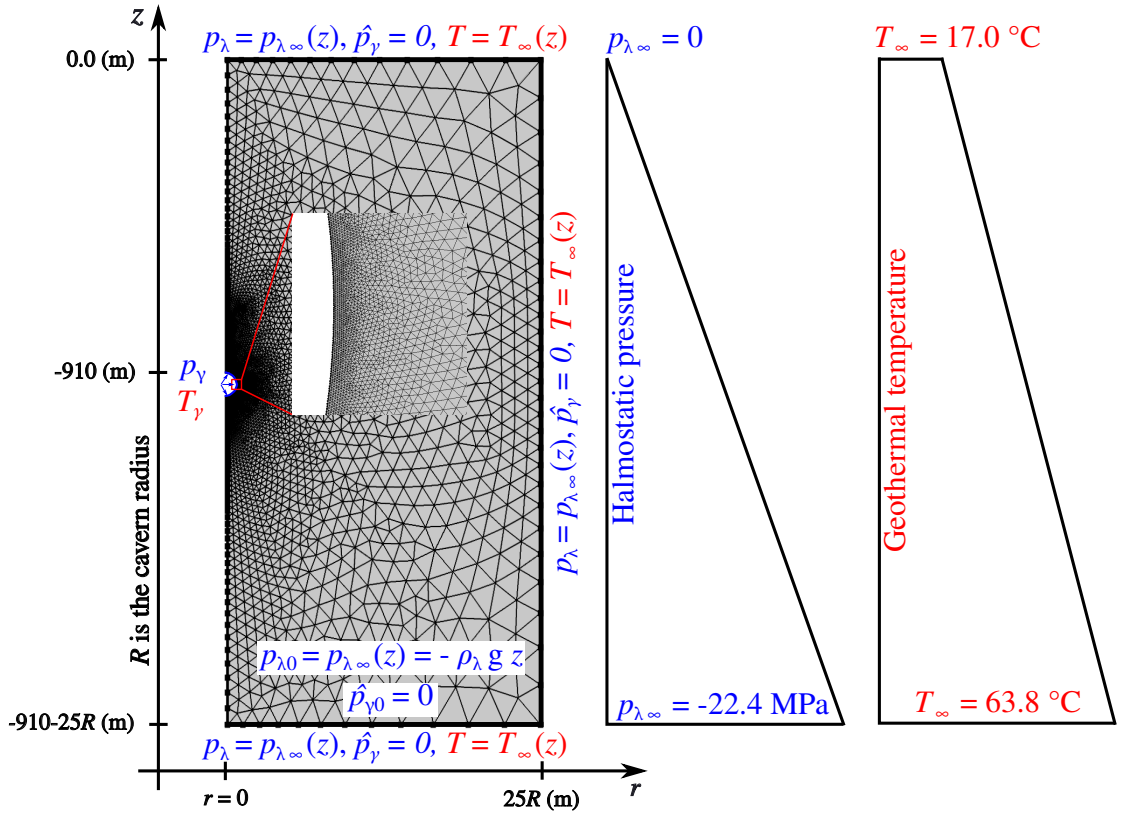

FIGURE 3.12: A two-dimensional axisymmetric discretization of the boundary value problem of Fig. 3.2. A surrounding rock volume of 25R is chosen around the cavern to avoid the effect of far-field boundaries. Mesh is considerably refined close to the cavern wall to account for abrupt changes/large gradients. Mesh contains 160113 triangular elements.

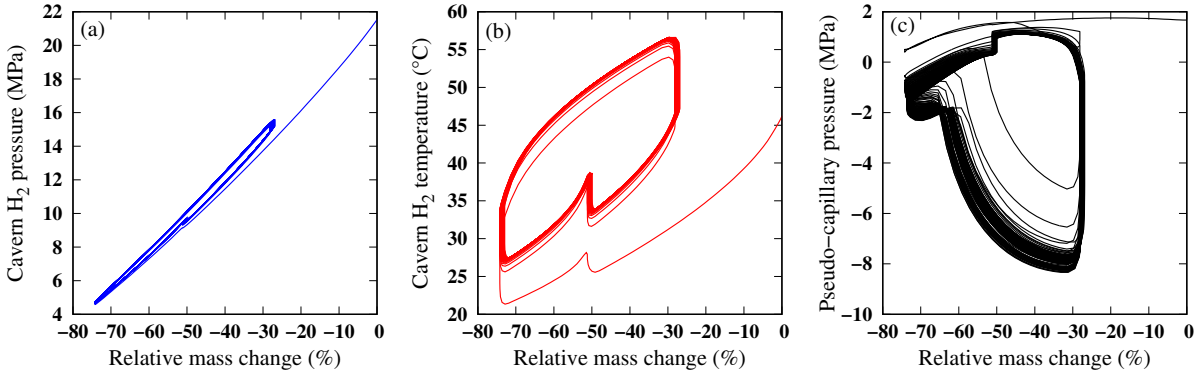

FIGURE 3.13: (a) cavern pressure, (b) cavern average temperature, and (c) hydrogen pseudo-capillary pressure averaged over the cavern surface. The three quantities are presented as a function of cycling/relative mass changes within the cavern.

To understand how the rock domain interstitial brine gets drained by the invading hydrogen, Fig. 3.15(a) shows the time variations of the brine saturation and the pseudo-capillary pressure at the cavern wall for the first four cycles. One can see that hydrogen percolates into the rock domain when the capillary pressure is positive. The brine saturation rate (increasing or decreasing) has an opposite sign to the capillary pressure rate.

To study the zone disturbed by brine pore pressure changes, and hydrogen pseudo-pressure and temperature fluctuations, Fig. 3.15(b) shows the radial profiles of these variables at the end of cycling, i.e. 40 years. The altered zone due to hydrogen invasion into the rock domain has not exceeded ∼15 m after 40 years of seasonal cycling. However, this zone extends to ∼40 m

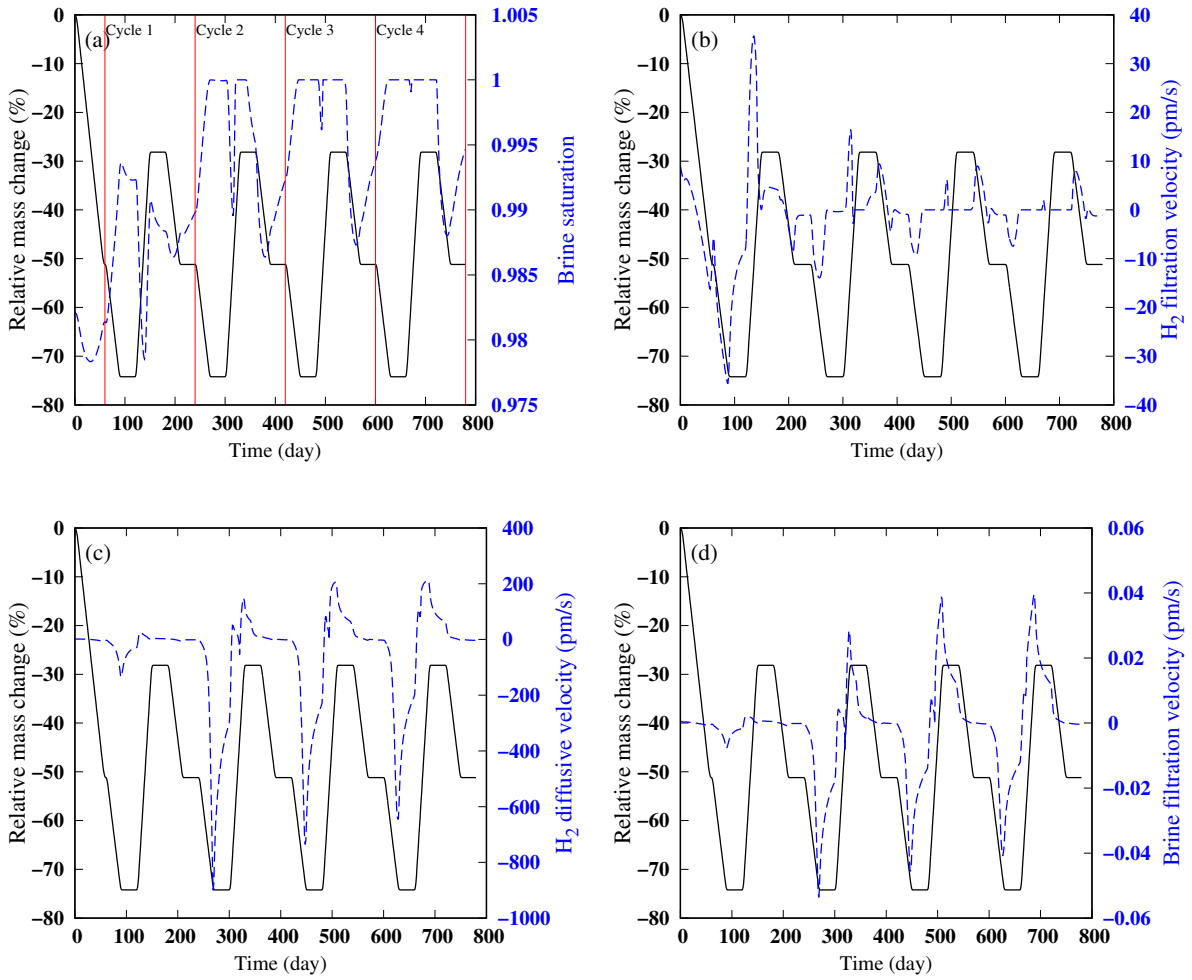

FIGURE 3.14: (a) Brine saturation at the cavern wall, as well as the surface averaged radial components of (b) the hydrogen filtration velocity, (c) the Fickian diffusive velocity, and (d) the brine filtration velocity during the first four cycles.

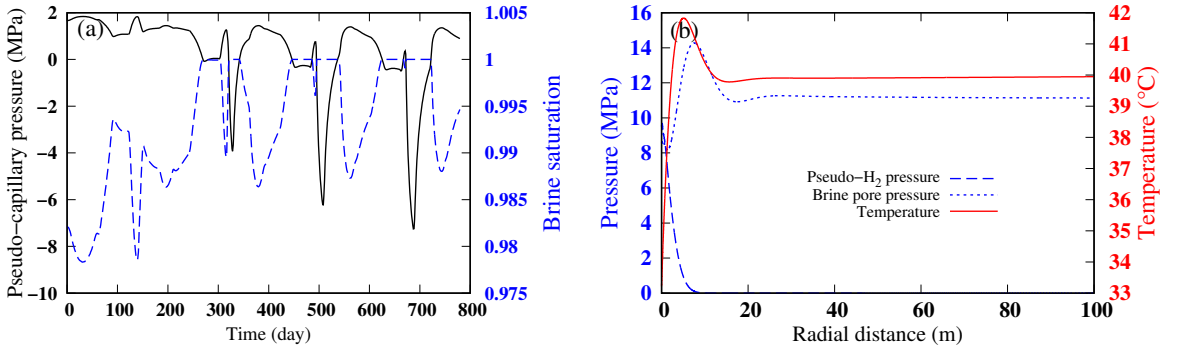

FIGURE 3.15: (a) Time variations of the cavern surface averaged brine saturation and pseudo-capillary pressure for the first four cycles. (b) Radial profiles of interstitial brine pressure, of hydrogen pseudo-pressure, and of temperature within the rock domain at the end of cycling/at 40 years.

due to brine pore pressure and rock domain temperature changes. Knowing the range of these distances helps design a network of underground caverns while avoiding harmful interactions.

Figure 3.16 shows the hydrogen mass exchanged with the surrounding rock domain due to two-phase percolation and the Fickian diffusion. Figure 3.16(a) is a zoom-in of Fig. 3.16(b) for

the first four cycles/800 days.

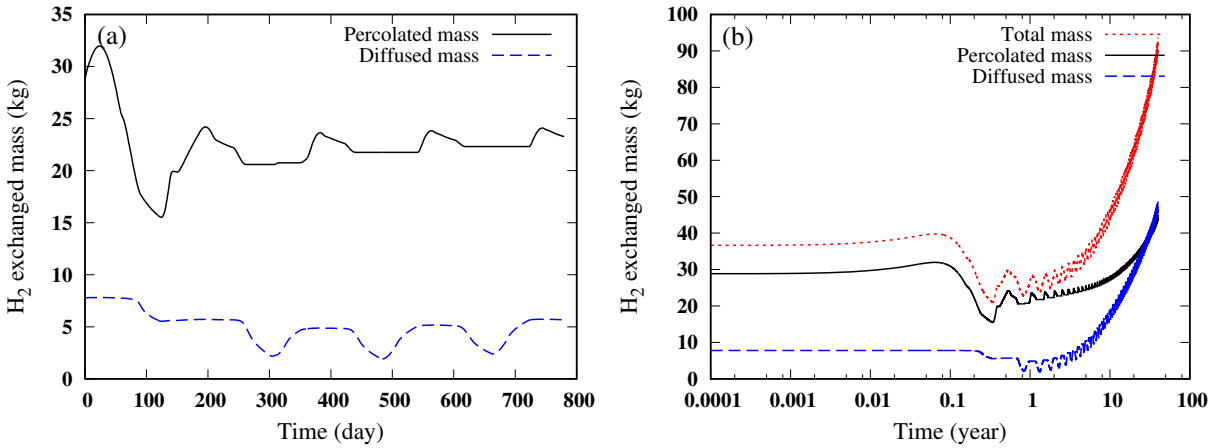

FIGURE 3.16: Darcian percolated and Fickian diffused hydrogen masses during 40 years of cycling. Figure (a) is a zoom-in of figure (b) for the first four years. The debrining and the standstill phases of 180 days have led to the initial percolated and diffused masses observed in figure (a).

Both the percolated and diffused hydrogen masses tend to reduce during withdrawal in accordance with Figs 3.14(b, c). Even-though the Fickian diffused mass is initially smaller than the percolated mass, after ∼25 years of cycling, the diffused mass becomes more significant than the two-phase percolated mass (Fig. 3.16(b)). Eventually, the percolated and the diffused hydrogen masses summed up to ∼93 kg after 40 years of the cavern operation.

3.2.4 Discussion and conclusion

The simulations on the cavern scale are performed such that an overestimating/a pessimistic scenario of lost hydrogen is considered. Therefore, while setting $\ell = 0.5$, the following values of $P_r = 8$ MPa and $\bar{D}_{g\lambda} = 5 \times 10^{-7}$ m^2/s are chosen. Cycling simulations prove that percolation happens mostly when the cavern pressure is close to the maximum cycling value, i.e. $p_\gamma \approx 16$ MPa. Yet, depending on the sign of the pressure gradient, hydrogen percolates into/leaves from the rock domain. The Fickian diffusion resembles the brine filtration, following the pressure gradient direction, hydrogen tends to diffuse into the rock domain or pours down the cavern wall along with the leaving brine. Eventually, the total mass of lost hydrogen sums up to ∼93 kg. This mass is extremely negligible compared to the hydrogen mass manipulated during one cycle ($\mathcal{M} = 2.05$ Mkg), i.e. the percentage of the lost mass to one cycle mass is ∼0.005%.

Increasing energy demands necessitate fast utilization of underground caverns. The severe utilization of salt caverns exposes them to considerable pressure and temperature changes throughout short periods, which may affect the development of the damaged zones . The introduction of a damaged zone, during cycling and at the end of leaching, can affect the total mass of the lost hydrogen. Future studies should include, in a first step, laboratory work to develop mass transport laws that would describe precisely hydrogen migration into the rock salt. In a second step, constitutive laws that quantify the permeability and porosity evolutions of rock salt due to mechanical, hydraulic and thermal charges would be needed. Once these transport and constitutive laws are developed, they can be integrated in the current framework to estimate their effect on hydrogen percolation and diffusion during rock salt damaging/severe exploitation of caverns.

3.3 Gas dissolution in the cavern brine

One promising approach for new clean energy resources is methanation, a technique used to convert carbon dioxide (CO_2) to methane using hydrogen. Methanation is supposed to reply to the energy fluctuating demand, which necessitates large storage of its production elements (H_2 and CO_2) (Mebrahtu et al., 2019). This study focuses on CO_2 dissolution kinetics in brine during storage and cycling in salt caverns in the context of clean energy transition (Zhang et al., 2022). The kinetics is strongly influenced by natural convection, which is caused by density changes related to the concentration of dissolved gas as well as thermal changes driven by gas cycling and the effects of the geothermal gradient. Based on a novel non-dimensional model that couples cavern thermodynamics with the dissolution mechanisms, this study investigates how the natural convection related to mass and thermal changes impacts dissolution kinetics. The numerical model is validated using laboratory measurements, and thereupon upscaled to typical dimensions of a salt cavern.

The effects of gas dissolution in residual brine is neglected in most of existing literature that deals with underground gas storage. It is commonly assumed that the cavern is filled with a mono-component single-phase gas. This assumption is valid if the residual brine volume is insignificant, and if the gas dissolution in the brine is insubstantial; however, residual brine may occupy up to 11% of the cavern volume (Chromik and Korzeniowski, 2021). Furthermore, some gases, especially CO_2, are soluble in brine. Therefore, gas loss due to dissolution needs to be quantified for good management of cycled quantities. This quantification becomes more important when other loss mechanisms are studied, particularly the permeation of gas into the rock domain (Sect. 3.2). Even-though this study focuses on CO_2 dissolution, the developed model is universal; it can be adapted easily to study the kinetics of dissolution of other gases.

3.3.1 The non-dimensional mathematical model

After the filling phase, the cavern brine has initially low concentration of CO_2. As CO_2 is injected into the cavern, a concentration gradient develops at the brine interface. This concentration gradient forms the driving force for the Fickian diffusion. Consequently, convection is created in the brine due to changes in the density field. A thermal convection is further developed due to cycling temperature changes at the brine interface, which interacts with the geothermal gradient of the brine. The velocity field that emerges due to both types of convection is expected to enhance the dissolution of CO_2 in the brine (F_2 of Fig. 3.1).

For each fluid phase $\alpha \in \{\lambda\,(\text{liquid}),\ \gamma\,(\text{gas})\}$, T_α stands for the temperature, p_α the pressure, and ρ_α the density. The subscript σ is used to designate the rock phase. Brine is assumed fully saturated with salt at any time. To simplify the mathematical problem and therefore the numerical simulations, the average gas velocity within the cavern is neglected and a uniform thermodynamic state is proposed (Sect. 3.1). This allows us to avoid the spatial discretization of the cavern domain. Consequently, the cavern thermodynamic state is used as boundary conditions for the dissolution problem in the brine domain, and for the heat transfer problem in both the brine and the rock domains. The velocity field in brine is solved for using the Navier-Stokes equation.

3.3.1.1 Fickian diffusion

At any time, a pressure equality is assumed at the gas-liquid interface $\mathcal{S}_{\gamma\lambda}$, i.e. $p_\lambda(t) = p_\gamma(t)$. The Henry law allows for calculating the mass concentration of the dissolved gas using the Henry constant H and the gas pressure, i.e. $c = c_{g\lambda} = p_\gamma / H$. In the λ-phase the barycentric movement is,

$$\rho_\lambda \boldsymbol{v}_\lambda = \rho_{g\lambda} \boldsymbol{v}_{g\lambda} + \rho_{b\lambda} \boldsymbol{v}_{b\lambda}, \tag{3.24}$$

where $\rho_{g\lambda}$ is the density of the dissolved gas in the λ-phase, $\boldsymbol{v}_{g\lambda}$ is the velocity of the dissolved gas in the λ-phase, and b is the solvent with mass concentration $1-c$. The definition of the diffusion flux $\boldsymbol{J}$ is introduced as:

$$\begin{aligned} \boldsymbol{J} = \boldsymbol{J}_{g\lambda} = c(\boldsymbol{v}_{g\lambda} - \boldsymbol{v}_{\lambda}); \quad \text{or,} \\ -\boldsymbol{J} = \boldsymbol{J}_{b\lambda} = (1-c)(\boldsymbol{v}_{b\lambda} - \boldsymbol{v}_{\lambda}). \end{aligned} \tag{3.25}$$

The gas-liquid interface is assumed still, then at $\mathcal{S}_{\gamma\lambda}$, $\boldsymbol{v}_{b\lambda} = 0$ and $\boldsymbol{v}_{\lambda} = \boldsymbol{J}/(1-c)$. Using Fick's hypothesis, the diffusion flux can be written as $\boldsymbol{J} = -D\,\boldsymbol{\nabla} c$, with D being the intrinsic diffusion coefficient.

3.3.1.2 Fluid state law

The development of the gas and liquid densities due to the thermodynamic changes and dissolution are expressed using the following state laws:

$$\begin{aligned} \text{for gas:} \quad d\rho_{\gamma} &= \partial_p \rho_{\gamma} dp + \partial_T \rho_{\gamma} dT; \\ \text{for liquid:} \quad d\rho_{\lambda} &= \partial_p \rho_{\lambda} dp + \partial_T \rho_{\lambda} dT + \partial_c \rho_{\lambda} dc. \end{aligned} \tag{3.26}$$

The liquid state law assumes that the brine is fully saturated with salt at any time. The effect of the dissolved gas as well as the temperature changes on the density are confined to the body force term of the momentum equation. The λ-phase equation of state becomes,

$$\varepsilon_{\lambda} = \frac{\rho_{\lambda}}{\rho_{\lambda 0}} = 1 + \beta(c - c_0) - \chi_{p\lambda}(T_{\lambda} - T_{\lambda 0}), \tag{3.27}$$

where values of the constant β can be found in literature (Yan, Huang, and Stenby, 2011), and $\rho_{\lambda 0}$ is the initial brine density.

3.3.1.3 Cavern thermodynamics

To simulate a uniform thermodynamic state within the cavern gas space, the system of Eqs 3.10 is used again. The only difference concerns $\bar{\pi}_g^{\gamma}$ that describes the mass rate of gas dissolution in the brine. The system of Eqs 3.10 can be cast in a non-dimensional form by defining the following non-dimensional quantities:

$$\tilde{T}_{\gamma} = \frac{T_{\gamma} - T_{\gamma 0}}{T_{\gamma 0}}; \quad \tilde{p}_{\gamma} = \frac{p_{\gamma}}{p_{\gamma 0}}; \quad \text{and} \quad \tilde{\rho}_{\gamma} = \frac{\rho_{\gamma}}{\rho_{\gamma 0}(T_{\gamma 0},\, p_{\gamma 0})}, \tag{3.28}$$

with $T_{\gamma 0}$ being the initial gas temperature, $p_{\gamma 0}$ the initial gas pressure, and $\rho_{\gamma 0}$ the initial gas density. These definitions imply that:

$$\tilde{\chi}_{T\gamma} = \chi_{T\gamma}\, p_{\gamma 0}; \quad \text{and,} \quad \tilde{\chi}_{p\gamma} = \chi_{p\gamma}\, T_{\gamma 0}, \tag{3.29}$$

where $\tilde{\chi}_{T\gamma}$ is the non-dimensional gas isothermal compressibility and $\tilde{\chi}_{p\gamma}$ is the non-dimensional gas isobaric thermal expansivity. The system of Eqs 3.10 then becomes:

$$\begin{aligned} \text{mass balance:} \quad -\tilde{\chi}_{T\gamma}\,\dot{\tilde{T}}_{\gamma} + \tilde{\chi}_{p\gamma}\dot{\tilde{p}}_{\gamma} &= \frac{Q_e\, L^2}{\mathcal{M}_{\gamma}\, D} - \frac{\bar{\pi}_g^{\gamma}\, L^2}{\mathcal{M}_{\gamma}\, D}; \\ \text{energy balance:} \quad \dot{\tilde{T}}_{\gamma} + A\frac{\tilde{\chi}_{T\gamma}(\tilde{T}+1)}{\tilde{\rho}_{\gamma}}\,\dot{\tilde{p}}_{\gamma} &= \frac{Q_e^{+}\, L^2}{\mathcal{M}_{\gamma}\, D}(\tilde{T}_{\gamma}^{\text{inj}} - \tilde{T}_{\gamma}) - B\tilde{\Psi}, \end{aligned} \tag{3.30}$$

with $A = p_{\gamma 0}/(T_{\gamma 0}\,\rho_{\gamma 0}\,C_{p\gamma})$, $B = 1/(\tilde{\mathcal{V}}_\gamma\,\tilde{\rho}_\gamma)$ with $\tilde{\mathcal{V}}_\gamma$ being the non-dimensional gas volume, and L being the characteristic length (see Eq. 3.32 below). The non-dimensional injection temperature $\tilde{T}_\gamma^{\text{inj}}$ is scaled with respect to $T_{\gamma 0}$ as indicated in Eq. 3.28.

3.3.1.4 Mass balance of the liquid phase

The mass changes of the λ-phase are attributed to the gas dissolution:

$$\rho_\lambda \partial_t c + \rho_\lambda \boldsymbol{v}_\lambda \cdot \boldsymbol{\nabla} c - \boldsymbol{\nabla} \cdot (\rho_\lambda D \boldsymbol{\nabla} c) = 0; \quad \text{with,} \quad \dot{\rho}_\lambda + \rho_\lambda \boldsymbol{\nabla} \cdot \boldsymbol{v}_\lambda = 0. \tag{3.31}$$

Taking L as the dimension of the cavern, L^2/D, D/L, and $\rho_{\lambda 0} D^2/L^2$, as scale factors for length, time, velocity, and pressure, the following non-dimensional quantities and operators are defined:

$$\tilde{t} = t\,\frac{D}{L^2}; \quad \tilde{\boldsymbol{v}}_\lambda = \boldsymbol{v}_\lambda\,\frac{L}{D}; \quad \tilde{P}_\lambda = P_\lambda\,\frac{L^2}{\rho_{\lambda 0} D^2}; \quad \text{and,} \quad \tilde{\nabla}\varphi = \nabla\varphi\, L. \tag{3.32}$$

The mass concentration is normalized with respect to the saturation concentration of the liquid phase c_{sat}, i.e. $\tilde{c} = c/c_{\text{sat}}$. Using the non-dimensional definitions along with Eq. 3.27, the non-dimensional form of Eq. 3.31 can be found:

$$\varepsilon_\lambda \partial_{\tilde{t}} \tilde{c} + \varepsilon_\lambda \tilde{\boldsymbol{v}}_\lambda \cdot \tilde{\boldsymbol{\nabla}} \tilde{c} - \tilde{\boldsymbol{\nabla}} \cdot (\varepsilon_\lambda \tilde{\boldsymbol{\nabla}} \tilde{c}) = 0; \quad \text{with,} \quad \partial_{\tilde{t}} \varepsilon_\lambda + \tilde{\boldsymbol{\nabla}} \cdot (\varepsilon_\lambda \tilde{\boldsymbol{v}}_\lambda) = 0. \tag{3.33}$$

3.3.1.5 Momentum balance of the liquid phase

The momentum balance equation for the liquid phase can be written as,

$$\rho_\lambda \partial_t \boldsymbol{v}_\lambda + \rho_\lambda \boldsymbol{v}_\lambda \cdot \underline{\underline{\boldsymbol{\nabla}}} \boldsymbol{v}_\lambda = -\boldsymbol{\nabla} P_\lambda + \boldsymbol{\nabla} \cdot \underline{\underline{\boldsymbol{\zeta}}} + (\rho_\lambda - \rho_{\lambda 0})\mathfrak{g}, \tag{3.34}$$

with $\underline{\underline{\boldsymbol{\zeta}}}$ being the viscous stress tensor, i.e. $\underline{\underline{\boldsymbol{\zeta}}} = \mu_\lambda \left(\underline{\underline{\boldsymbol{\nabla}}} \boldsymbol{v}_\lambda + \underline{\underline{\boldsymbol{\nabla}}} \boldsymbol{v}_\lambda^{\mathrm{T}}\right) - (2/3)\mu_\lambda \left(\boldsymbol{\nabla} \cdot \boldsymbol{v}_\lambda\right) \underline{\underline{\boldsymbol{\delta}}}$, the brine dynamic viscosity is μ_λ, and $\underline{\underline{\boldsymbol{\delta}}}$ is the second-order Kronecker delta. The λ-phase pressure P_λ is calculated with respect to the gas pressure and to the initial hydrostatic pressure ($p_{\lambda H} = -\rho_{\lambda 0}\mathfrak{g}z$), i.e. $P_\lambda = p_\lambda - p_\gamma - p_{\lambda H}$. At the brine interface, $P_\lambda(t) = 0$ and $p_\lambda(t) = p_\gamma(t)$. Initially in the brine domain, $p_{\lambda 0} = p_{\gamma 0} + p_{\lambda H}$ and $P_{\lambda 0} = 0$.

The non-dimensional form of Eq. 3.34 can be written as,

$$\varepsilon_\lambda \partial_{\tilde{t}} \tilde{\boldsymbol{v}}_\lambda + \varepsilon_\lambda \tilde{\boldsymbol{v}}_\lambda \cdot \underline{\underline{\tilde{\boldsymbol{\nabla}}}} \tilde{\boldsymbol{v}}_\lambda = -\tilde{\boldsymbol{\nabla}} \tilde{P}_\lambda + \mathrm{Pr} \tilde{\boldsymbol{\nabla}} \cdot \underline{\underline{\tilde{\boldsymbol{\zeta}}}} + \mathrm{RaPr}\, \boldsymbol{e}_z, \tag{3.35}$$

with $\underline{\underline{\tilde{\boldsymbol{\zeta}}}} = \underline{\underline{\tilde{\boldsymbol{\nabla}}}} \tilde{\boldsymbol{v}}_\lambda + \underline{\underline{\tilde{\boldsymbol{\nabla}}}} \tilde{\boldsymbol{v}}_\lambda^{\mathrm{T}} - (2/3)\,\tilde{\boldsymbol{\nabla}} \cdot \tilde{\boldsymbol{v}}_\lambda \underline{\underline{\boldsymbol{\delta}}}$ and $\tilde{P}_\lambda$ being the λ-phase non-dimensional pressure. The brine dynamic viscosity is assumed constant. Therefore, the Prandtl number of the natural convection problem is defined as,

$$\mathrm{Pr} = \frac{\mu_\lambda}{\rho_{\lambda 0}\, D}, \quad \text{and the Rayleigh number is } \mathrm{Ra} = \frac{\mathfrak{g}(\varepsilon_\lambda - 1)\rho_{\lambda 0} L^3}{D \mu_\lambda}. \tag{3.36}$$

Since the intrinsic diffusion coefficient of CO_2 in brine is very small, the simulations lead to high values of the Parndtl number ($\mathrm{Pr} \gg 1$). This indicates the dominance of the momentum diffusivity over the chemical/Fickian diffusivity (Busse and Whitehead, 1971). On the other hand, the Rayleigh number characterizes the regime of the gas flow in the brine phase. When the Rayleigh number is small (typically $\mathrm{Ra} < 10^3$), natural convection is negligible. Besides, a turbulent model is necessary to fully describe the velocity field when Buoyancy forces are considerably high, i.e. $\mathrm{Ra} > 10^8$ (Sankar et al., 2011). This research numerical model accounts

only for laminar flow, the Rayleigh number is expected to fall within its range, i.e. $10^3 < \mathrm{Ra} < 10^8$.

3.3.1.6 Energy balance of the liquid phase

The energy equation of the λ-phase can be cast in the following form,

$$\rho_\lambda C_{p\lambda} \partial_t T_\lambda + \rho_\lambda C_{p\lambda} \boldsymbol{v}_\lambda \cdot \boldsymbol{\nabla} T_\lambda - \boldsymbol{\nabla} \cdot (\Lambda_\lambda \boldsymbol{\nabla} T_\lambda) = 0, \tag{3.37}$$

with $C_{p\lambda}$ being the brine heat capacity, and Λ_λ is the brine thermal conductivity. If the non-dimensional brine temperature is defined as $\tilde{T}_\lambda = (T_\lambda - T_{\lambda 0})/T_{\lambda 0}$, and its heat capacity is assumed constant, the non-dimensional form of Eq. 3.37 is written as,

$$\varepsilon_\lambda \partial_{\tilde{t}} \tilde{T}_\lambda + \varepsilon_\lambda \tilde{\boldsymbol{v}}_\lambda \cdot \tilde{\boldsymbol{\nabla}} \tilde{T}_\lambda - \tilde{\boldsymbol{\nabla}} \cdot \left(\frac{\mathcal{K}_\lambda}{D} \tilde{\boldsymbol{\nabla}} \tilde{T}_\lambda \right) = 0, \tag{3.38}$$

the brine thermal diffusivity $\mathcal{K}_\lambda = \Lambda_\lambda / \rho_{\lambda 0} C_{p\lambda}$ is assumed constant.

3.3.1.7 Energy balance of the solid phase

To solve for heat exchange between the fluid phases and the rock domain, the energy equation of the σ-phase is required,

$$\rho_\sigma C_{p\sigma} \partial_t T_\sigma - \boldsymbol{\nabla} \cdot (\Lambda_\sigma \boldsymbol{\nabla} T_\sigma) = 0, \tag{3.39}$$

with $C_{p\sigma}$ being the rock salt heat capacity, and Λ_σ is the rock salt thermal conductivity. Keeping in mind that $\tilde{T}_\sigma = (T_\sigma - T_{\sigma 0})/T_{\sigma 0}$, the non-dimensional form of this equation is,

$$\partial_{\tilde{t}} \tilde{T}_\sigma - \tilde{\boldsymbol{\nabla}} \cdot \left(\frac{\mathcal{K}_\sigma}{D} \tilde{\boldsymbol{\nabla}} \tilde{T}_\sigma \right) = 0, \tag{3.40}$$

where the rock salt thermal diffusivity is $\mathcal{K}_\sigma = \Lambda_\sigma / \rho_\sigma C_{p\sigma}$.

The exchanged power Ψ (Eq. 3.10) has two parts,

$$\Psi = \underbrace{\int_{\mathcal{S}_{\gamma\sigma}} -\Lambda_\sigma \boldsymbol{\nabla} T_\sigma \cdot \boldsymbol{n} \, d\mathcal{A}_{\gamma\sigma}}_{\text{exchanged with rock}} + \underbrace{\int_{\mathcal{S}_{\gamma\lambda}} -\Lambda_\lambda \boldsymbol{\nabla} T_\lambda \cdot \boldsymbol{n} \, d\mathcal{A}_{\gamma\lambda}}_{\text{exchanged with brine}}, \tag{3.41}$$

where the unit normal outward vector is $\boldsymbol{n}$. The surface integrations are calculated over the gas-solid interface $\mathcal{S}_{\gamma\sigma}$ with its area $\mathcal{A}_{\gamma\sigma}$, and the gas-liquid interface $\mathcal{S}_{\gamma\lambda}$ with its area $\mathcal{A}_{\gamma\lambda}$. The non-dimensional exchanged power (Eq. 3.30) is defined as,

$$\tilde{\Psi} = \int_{\tilde{\mathcal{S}}_{\gamma\sigma}} -w_\sigma \tilde{\boldsymbol{\nabla}} \tilde{T}_\sigma \cdot \boldsymbol{n} \, d\tilde{\mathcal{A}}_{\gamma\sigma} + \int_{\tilde{\mathcal{S}}_{\gamma\lambda}} -w_\lambda \tilde{\boldsymbol{\nabla}} \tilde{T}_\lambda \cdot \boldsymbol{n} \, d\tilde{\mathcal{A}}_{\gamma\lambda}, \tag{3.42}$$

with $w_\sigma = (T_{\sigma 0}/T_{\gamma 0}) \left[\Lambda_\sigma / (\rho_{\gamma 0} \, C_{p\gamma} \, D) \right]$ and $w_\lambda = (T_{\lambda 0}/T_{\gamma 0}) \left[\Lambda_\lambda / (\rho_{\gamma 0} \, C_{p\gamma} \, D) \right]$, where $\tilde{S}_{\gamma\sigma}$ and $\tilde{S}_{\gamma\lambda}$ are the non-dimensional interfaces as well as $\tilde{A}_{\gamma\sigma}$ and $\tilde{A}_{\gamma\lambda}$ are their non-dimensional areas.

Since the model is non-dimensional, once validated by the laboratory measurements, it can be applied to other scales. Experimental work is required, some of it considered in this research, in order to establish the key model parameters. Such experiments should be performed under conditions similar to the geological storage, in terms of pressure and temperature.

3.3.2 Initial and boundary conditions

In this section the initial and boundary conditions for the gas dissolution problem, both at the laboratory and at the cavern scales, are defined.

3.3.2.1 Initial conditions

The temperature is controlled at the laboratory scale (Sect. 3.3.3) by placing the dissolution cell in a temperature-controlled basin. Consequently, the temperature of all phases is maintained at T_0. At the cavern scale (Sect. 3.3.5), all phases are initially assumed to be in thermal equilibrium which corresponds to the geothermal gradient. Temperature is non-dimensionalized with respect to an initial T_0.

The gas pressure in the laboratory cell is initially equal to the vapor pressure[3]. However, at the cavern scale, it is determined by the cavern working conditions, i.e. the cavern depth. The initial brine pressure is $P_{\lambda 0} = 0$ because $p_{\lambda 0} = p_{\gamma 0} + p_{\lambda H}$. Subsequent changes in the brine pressure are generated by gas dissolution.

3.3.2.2 Boundary conditions

At the gas-liquid interface, gas can dissolve into or exsolve from the brine phase as a function of the gas pressure. The brine and gas also exchange heat based on the cycling program. There is also heat exchange between these two phases and the surrounding rock domain. At the interface $\mathcal{S}_{\gamma\lambda}$, the following definitions are employed:

- the gas mass concentration is $c = p_\gamma / H$. Its non-dimensional form is $\tilde{c} = c / c_{\text{sat}}$;
- the flow of gas into the λ-phase is expressed as $\boldsymbol{J} \cdot \boldsymbol{n} = K(c - p_\gamma / H)$, with K being an experimental mass transfer coefficient. In a non-dimensional form, this expression becomes $\tilde{\boldsymbol{J}} \cdot \boldsymbol{n} = \tilde{K}(\tilde{c} - p_\gamma / (H\, c_{\text{sat}}))$, with $\tilde{\boldsymbol{J}} = -\boldsymbol{\nabla}\tilde{c}$ and $\tilde{K} = K\,(L/D)$;
- the non-dimensional λ-phase velocity at the interface $\mathcal{S}_{\gamma\lambda}$ takes the following form $\tilde{\boldsymbol{v}}_\lambda = \tilde{\boldsymbol{J}} / (1/c_{\text{sat}} - \tilde{c})$. This is equivalent to $\tilde{\boldsymbol{v}}_\lambda \cdot \boldsymbol{n} = \tilde{K}(\tilde{c} - p_\gamma / (H\, c_{\text{sat}}))/(1/c_{\text{sat}} - \tilde{c})$;
- the mass rate of the dissolved gas is $\bar{\pi}_g^\gamma = -\int_{\mathcal{S}_{\gamma\lambda}} \rho_\lambda \boldsymbol{v}_\lambda \cdot \boldsymbol{n}\, d\mathcal{A}_{\gamma\lambda}$, with $\boldsymbol{n}$ being the normal outward vector. In a non-dimensional form, the following definition is reached,

$$\frac{\bar{\pi}_g^\gamma\, L^2}{\mathcal{M}_\gamma\, D} = \frac{-\int_{\tilde{\mathcal{S}}_{\gamma\lambda}} \varepsilon_\lambda \tilde{\boldsymbol{v}}_\lambda \cdot \boldsymbol{n}\, d\tilde{\mathcal{A}}_{\gamma\lambda}}{\tilde{\mathcal{V}}_\gamma\, \varepsilon_{\gamma\lambda}} = \frac{-\int_{\tilde{\mathcal{S}}_{\gamma\lambda}} \varepsilon_\lambda \left[\dfrac{\tilde{K}(\tilde{c} - p_\gamma / (H\, c_{\text{sat}}))}{1/c_{\text{sat}} - \tilde{c}}\right] d\tilde{\mathcal{A}}_{\gamma\lambda}}{\tilde{\mathcal{V}}_\gamma\, \varepsilon_{\gamma\lambda}}, \tag{3.43}$$

  with $\varepsilon_{\gamma\lambda} = \rho_\gamma / \rho_{\lambda 0}$. During cycling or dissolution, the gas density evolves. Therefore, a gas state law is used to trace the gas density as a function of pressure and temperature (Kunz et al., 2007), i.e. $\rho_\gamma = \rho_\gamma\left(\tilde{p}_\gamma p_{\gamma 0},\, [(\tilde{T}_\gamma T_{\gamma 0}) + T_{\gamma 0}]\right)$;
- the conditions $p_\gamma(t) = p_\lambda(t)$ and $\tilde{P}_\lambda(t) = 0$ are set at time t.

The following other boundary conditions are needed:

- the temperature boundary condition between the brine and the rock phases is defined such that $\tilde{T}_\lambda(t) = \tilde{T}_\sigma(t)$ at any time t;
- between the gas and the rock phases, temperature continuity is assumed, i.e. $\tilde{T}_\gamma(t) = \tilde{T}_\sigma(t)$ at any time t;

[3] The cell is vacuumed and brine is injected into it prior to the gas introduction.

– between the gas and the brine phases, a heat transfer coefficient $h_{\gamma\lambda}$ is introduced, leading to the following non-dimensional heat exchange formula: $-\tilde{\boldsymbol{\nabla}}\tilde{T}_\lambda.\boldsymbol{n} = \tilde{h}_{\gamma\lambda}\left(\tilde{T}_\gamma - \tilde{T}_\lambda\right)$ and $\tilde{h}_{\gamma\lambda} = h_{\gamma\lambda}\left(L/\Lambda_\lambda\right)$;

– an appreciably large rock domain is considered in our modelling to avoid the effect of far-field boundaries. The far-field temperatures are set equal to the geothermal gradient all the time.

The model parameters β and D can be found in literature (Yan, Huang, and Stenby, 2011; Tayeb et al., 2023). The mass transfer coefficient K needs to be adjusted experimentally so that the experimental data and the simulation curves would have the same initiation behavior. The same values of these parameters are used on any scale. However, if such parameters have units, once the equations are worked out in a non-dimensional form, they get scaled by their equivalent scale factors (see Tables 3.2 and 3.3). All the non-dimensionalization details can be found in AbuAisha et al. (2023).

3.3.3 CO_2 dissolution at the laboratory scale scale

Before applying the non-dimensional model at the cavern scale, experimental validation is needed. Laboratory experiments are performed based on a pressure decay test using a PVT (Pressure-Volume-Temperature) cell. In this setup, the CO_2 gas is injected from a tank into the cell that is partially filled with saturated brine. The cell temperature is controlled by placing it into a temperature-controlled basin (Fig. 3.17). Once gas is injected, it starts dissolving in the liquid phase.

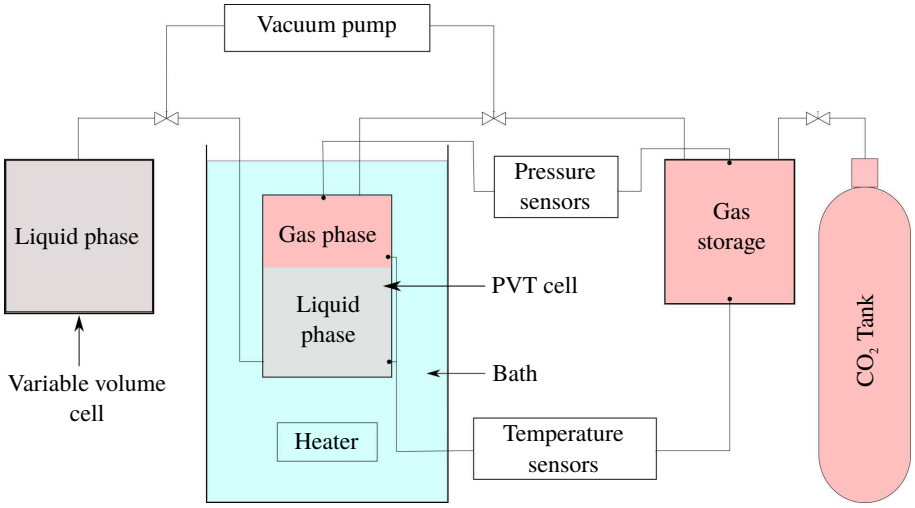

FIGURE 3.17: Schematic representation of the pressure decay PVT cell used to study the CO_2 dissolution in the brine, and to validate the mathematical model.

The PVT cell has a volume of 131.64 cm^3 and a diameter of 4 cm. Two dissolution tests are carried out. In the two tests, the cell is initially filled with saturated brine[4] to a 26.32 cm^3 volume. Gas is subsequently injected at initial pressures that correspond to the geological storage conditions, with the basin temperature set equal to 40 °C.

Table 3.2 shows the test conditions and model parameters of the two PVT cell experiments. The table presents the values as given to a typical dimensional model and as fed to the non-dimensional model of this research. The characteristic length is chosen to be equal to the model radius $L = R = 0.02$ m. It is used along with the intrinsic diffusion coefficient D to calculate the scale factors of Eq. 3.32. The β parameter gives an idea about how the brine density changes

[4]The salt mass represented 22.5% of the solution mass.

TABLE 3.2: Test conditions and model parameters of the two PVT experiments. References: 1. (Tayeb et al., 2023); 2. (Yan, Huang, and Stenby, 2011); 3. (Chabab et al., 2019).

As given to a typical dimensional model							
	$p_{\gamma 0}$ (MPa)	D (m^2/s)	$L = R$ (m)	c_0	β	H (MPa)	K (m/s)
Test 1	12.90	6.5×10^{-9}	0.02	0.01123	0.212	550	2.52×10^{-5}
Test 2	16.87	6.5×10^{-9}	0.02	0.01389	0.212	726	2.52×10^{-5}
Reference	–	[1]	–	Calculated	[2]	[3]	Adjusted
As given to the non-dimensional model							
	$\tilde{p}_{\gamma 0}$		$\tilde{R}$	$\tilde{c}_0$	β	$\tilde{H}$	$\tilde{K}$
Test 1	1.0		1	0.60	0.212	42.64	77.54
Test 2	1.0		1	0.74	0.212	43.03	77.54

[1] The initial brine density is $\rho_{\lambda 0} = 1200$ kg/m^3 and its viscosity is $\mu_\lambda = 3.6 \times 10^{-3}$ Pa s
[2] The scaling of the gas pressure and the Henry coefficient values is done using $p_{\gamma 0} = 12.90$ MPa for test 1 and $p_{\gamma 0} = 16.87$ MPa for test 2
[3] The CO_2 concentrations are scaled with respect to $c_{\text{sat}} = 0.0188$
[4] $\tilde{K} = K\,(L/D)$

as a function of the dissolution. It is already non-dimensional and does not vary between the two approaches. The model parameter K is adjusted experimentally such that the initiation of the numerical response correlates with the experimental data. A real gas behavior is considered in the simulations. A high accuracy state equation is used as described in Kunz et al. (2007). Since the cell is placed in the basin all the time, an isothermal condition is prevailing. Equations 3.33 and 3.35 are only solved for in the brine domain. As an interface boundary condition, the first part of the gas Eq. 3.30 is used without the thermal contribution, and it is completed with Eq. 3.43 to account for the mass exchange. Although the initial CO_2 concentration of the brine should be zero, the fast injection to high pressure has evidently caused some CO_2 to dissolve in the brine during the filling phase. The CO_2 concentration in the brine is normalized with respect to the saturation value ($c_{\text{sat}} = 0.0188$) at $p_\gamma = 14$ MPa and temperature $T_\gamma = 40$ °C. The initial concentrations are calculated by inverse mass calculations between the final and the initial tests statuses (Yang and Gu, 2006). Figure 3.18 shows how our numerical model correlates to the experimental data. The pressure histories are normalized with respect to the initial gas pressure indicated on each figure.

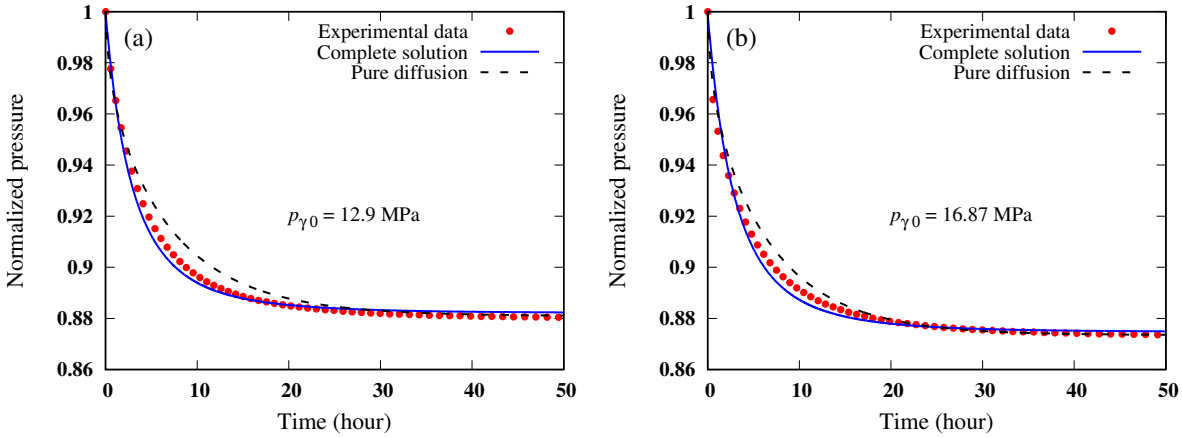

FIGURE 3.18: A comparison between the numerical and the experimental pressure histories for the two laboratory tests: (a) $p_{\gamma 0} = 12.9$ MPa; and (b) $p_{\gamma 0} = 16.87$ MPa. The black curves represent the numerical solutions while considering only pure diffusion ($D_{\text{app}} = 8.6 \times 10^{-8}$ m^2/s).

The black curves (Fig. 3.18) represent the numerical solutions while considering only the diffusion phenomenon, i.e. only Eq. 3.33 in the brine domain. For these solutions to correlate to the experimental data, the diffusion coefficient needs to be enhanced. The method adopted in this research is based on increasing the intrinsic diffusion coefficient gradually until a match is reached between the numerical solution and the experimental data. The match value of the diffusion coefficient is then saved and called an apparent diffusion coefficient D_{app}. Figure 3.18 shows that an apparent diffusion with value $D_{\text{app}} = 8.6 \times 10^{-8}$ m^2/s is sufficient to represent the effect of the convection process.

3.3.4 Thermal effects on the kinetics of dissolution

Although our numerical model reproduces the kinetics of CO_2 dissolution in brine, upscaling it to the cavern scale is arduous. Difficulties stem from the use of the Navier-Stokes equation (3.35). As the model dimension is increased, the body forces represented by the term (Ra Pr) intensify by a power of three. There is a limiting characteristic length after which the numerical convergence becomes exceedingly slow. In this vein, when the two terms ($\tilde{\boldsymbol{\nabla}}\tilde{P}_\lambda$ and Ra Pr $\boldsymbol{e}_z$) are of the same order of magnitude, the simulations run correctly. The use of an apparent diffusion to represent the complex effects of convection (Fig. 3.18) seems to be the solution. However, at the cavern scale, this approach is impractical for two main reasons:

1. in addition to tuning the apparent D parameter, the apparent mass transfer coefficient K also requires tuning, since both of these apparent parameters depend upon the scale of the problem;

2. the cavern brine is characterized by a geothermal gradient, while the gas cycling within the cavern drives significant thermal changes on the brine surface. These thermal effects cannot be neglected at the cavern scale.

The mathematical model developed in Sect. 3.3.1 is general; it accounts for thermal changes effects on the kinetics of dissolution. Equation 3.27 highlights the importance of thermal changes on the natural convection due to density alteration. AbuAisha et al. (2023) have numerically investigated the effect of applying a temperature gradient on the kinetics of dissolution. Different numerical simulations have been conducted while applying different temperature gradients over the laboratory cell (Sect. 3.3.3). It is observed that the dissolution kinetics increases substantially as a function of the temperature gradient. The brine may occupy up to 11% of the cavern volume (Chromik and Korzeniowski, 2021) and will generally be characterized by a linear thermal gradient. Taken together with the cycling effects, it is clear that thermal effects play a significant role for the dissolution process.

3.3.5 CO_2 dissolution at the cavern scale

This section presents the CO_2 dissolution at the cavern scale. To highlight the importance of considering the kinetics of dissolution, two scenarios are considered: namely while accounting for kinetics by coupling the cavern thermodynamics with the dissolution; and while neglecting kinetics and calculating the saturation concentration in a post-treatment strategy. The results of the two scenarios are compared systematically.

3.3.5.1 The numerical model

The numerical model represents a cylindrical cavern of volume $\mathcal{V} = 42412$ m^3 in an infinite rock salt domain (Fig. 3.19). The cavern brine occupies almost 11% of the volume over a height of 1.5 m. The cavern is assumed to be initially full of real CO_2 at a pressure of 16 MPa. The cavern and its brine are in thermal equilibrium with the surrounding rock domain. The geothermal

gradient gives a cavern volume averaged temperature of 44 °C and a temperature difference of 0.045 °C over the brine height.

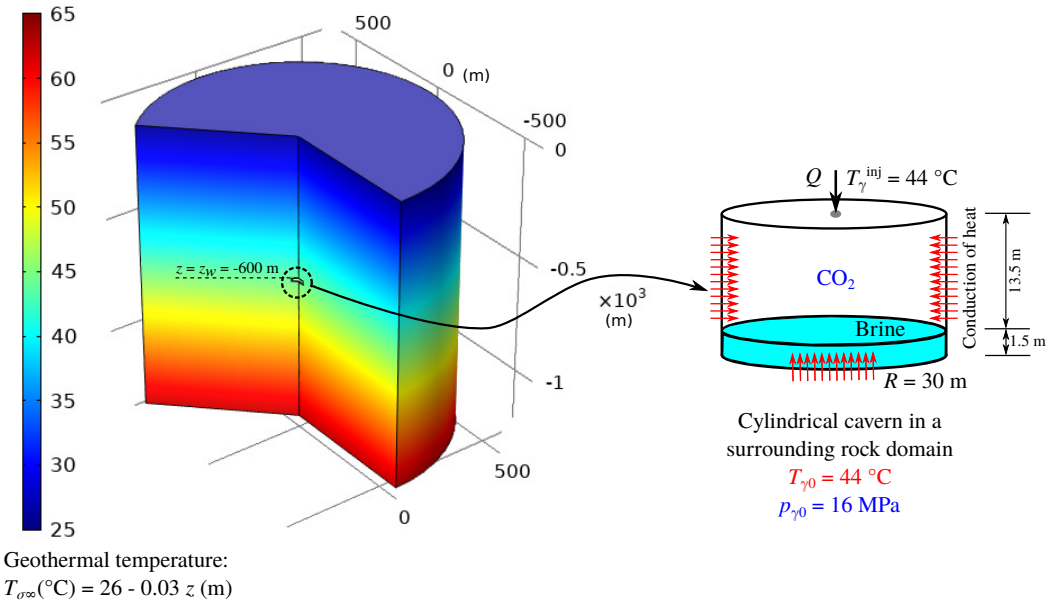

FIGURE 3.19: Schematic diagram of the boundary value problem: it represents a cylindrical cavern created at a depth of 600 m in a surrounding rock salt domain. The geothermal gradient gives a cavern volume averaged temperature of 44 °C. The cavern is assumed initially full of real CO_2 at a pressure of 16 MPa. This figure is presented in the dimensional form.

For simplicity, a homogeneous thermodynamic state is assumed within the cavern. The cavern thermodynamics (Eq. 3.30) is used simply as boundary conditions for heat transfer with the rock domain, and for heat and mass transfer with the brine (Fig. 3.20).

Figure 3.20 shows a two-dimensional axisymmetric discretization of the boundary value problem of Fig. 3.19. The figure represents the model used with the COMSOL software, shown in a non-dimensional form. A typical geothermal gradient of 3 °C/100 m is defined. The far-field boundary conditions are assumed to be of the Dirichlet type. A temperature continuity is assumed between the cavern gas and the rock domain, and between the cavern brine and the rock domain. A heat transfer coefficient $h_{\gamma\lambda} = 12$ (W/m^2/K) is chosen to account for thermal changes between the gas and the brine (Bourne-Webb, Bodas Freitas, and da Costa Gonçalves, 2016). A pressure continuity on the surface $\mathcal{S}_{\gamma\lambda}$ is assured between the two phases all the time. Therefore, initially, $p_\lambda(\boldsymbol{x}, 0) = p_{\gamma 0} + p_{\lambda H}(\boldsymbol{x})$ and $P_{\lambda 0} = \tilde{P}_{\lambda 0} = 0$ every where in the brine domain.

The characteristic length is taken equal to the brine height, i.e. $L = 1.5$ m. The CO_2 concentration is normalized with regard to the saturation value $c_{\text{sat}} = 0.0188$ for an average cycling pressure of $\langle p_\gamma \rangle = 14$ MPa. To account for the effect of the filling phase, the brine is assumed to have an initial CO_2 concentration of $c_0 = 0.0023$ (almost 12% of the saturation value). The Henry coefficient is assumed to be a function of the fluctuating gas pressure during cycling (Chabab et al., 2019). The same values of the model parameters (β, D, and K) of Table 3.2 are used at the cavern scale. Yet, the scale factors of Eq. 3.32 are calculated with respect to the new characteristic length. Table 3.3 presents the non-dimensional model parameters as given to the COMSOL software. The temperatures of the cavern three phases are normalized with respect to $T_0 = 44$ °C. Brine thermo-physical properties are assigned the following values (Gevantman and Lorenz, 1981): $\Lambda_\lambda = 0.51$ (W/m/K); $C_{p\lambda} = 3300$ (J/kg/K); and $\chi_{p\lambda} = 45 \times 10^{-5}$ (1/K).

The operation cycling program for this research is presented in Fig. 3.21. A withdrawal phase is firstly recognized, where the relative mass changes $(\mathcal{M}_\gamma/\mathcal{M}_{\gamma 0} - 1) \times 100\%$ are decreased to -2.5%. Cycling starts subsequently where four cycles are accounted for. This cycling program demonstrates a weekly utilization of the cavern where changes spread out over

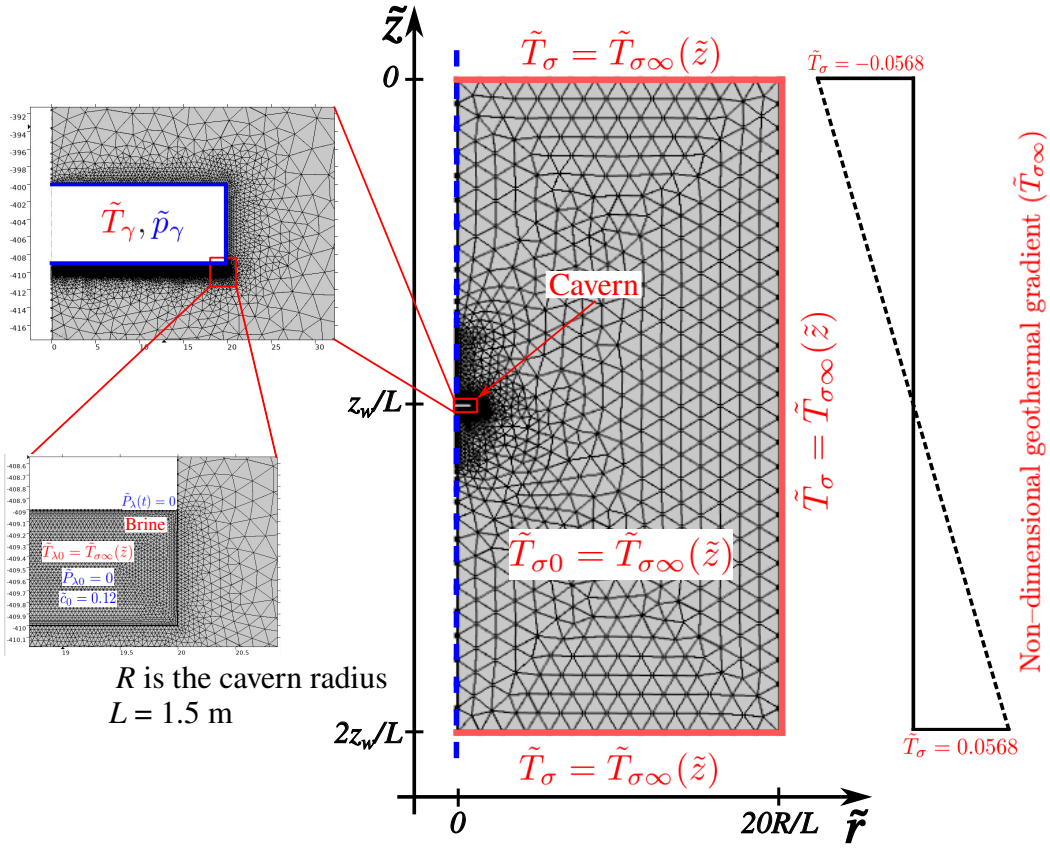

FIGURE 3.20: Two-dimensional axisymmetric discretization of the boundary value problem of Fig. 3.19. A surrounding rock volume of $\tilde{r} = 20R/L$ is chosen around the cavern to avoid the effect of far-field boundaries. The gas domain is not considered in modeling, and only the brine domain is discretized. The cavern thermodynamics ($\tilde{p}_\gamma$, $\tilde{T}_\gamma$) is used as boundary conditions for heat transfer with the rock domain, and heat and mass transfer with the brine. The mesh is heavily refined close to the cavern to account for the abrupt changes taking place close to it. The mesh contains 144665 elements, of which 9183 are quadrilateral boundary elements.

TABLE 3.3: Non-dimansionaml model parameters at the cavern scale. Reference: 1. (Chabab et al., 2019).

$L = H$ (m) (Brine height)	$\tilde{R}$	$\tilde{c}_0$	β	$\tilde{H} = f(\tilde{p}_\gamma)$	$\tilde{K}$	$\tilde{h}_{\gamma\lambda}$
1.5	20	0.12	0.212	Evolving [1]	5815.38	35.29

[1] $D = 6.5 \times 10^{-9}$ m^2/s, $\rho_{\lambda 0} = 1200$ kg/m^3, and $\mu_\lambda = 3.6 \times 10^{-3}$ Pa s
[2] The CO_2 saturation concentration is $c_{\text{sat}} = 0.0188$
[3] $\tilde{K} = K\,(L/D)$, and $\tilde{h}_{\gamma\lambda} = h_{\gamma\lambda}(L/\Lambda_\lambda)$

a period of ∼28 days. Only the first four cycles are presented, however, this program can be repeated over long periods of time.

3.3.5.2 Results and discussion

Two scenarios are adopted to present the results of CO_2 dissolution at the cavern scale. In the first scenario, the kinetics of dissolution is neglected. Hence, the CO_2 saturation concentration c_{sat} is calculated as a function of the cavern thermodynamics (p_γ and T_γ). In this scenario, only the cavern thermodynamics is solved whilst considering heat exchange with the rock and the brine domains. In the second scenario, the cavern thermodynamics is coupled with dissolution in the brine domain, and the entire problem is solved. This enables comparison between simulations of the two scenarios, and consequently insights into the importance of considering the

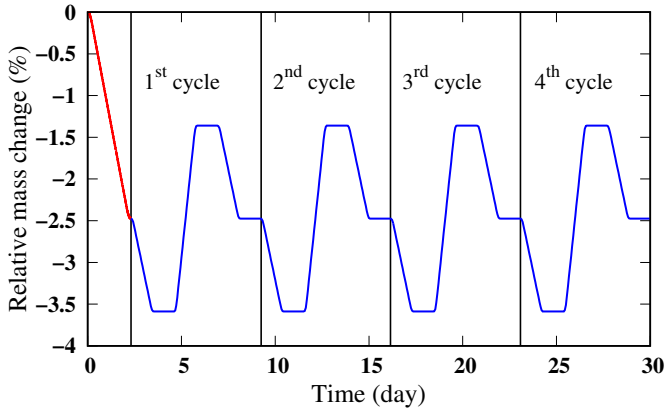

FIGURE 3.21: The cycling program envisaged for this research: a weekly utilization of the cavern with four cycles spreading over ∼28 days. Cycling leads to reasonable mass variations where the cycled CO_2 stays always in its supercritical state.

kinetics of dissolution to periodically calculate the dissolved gas mass.

During the first scenario, the cycling program of Fig. 3.21 is repeated over a period of 2 years. The saturation concentration is subsequently calculated in a post-treatment approach, where such values are found abundantly in the literature. For instance, Fig. 3.22 shows the saturation concentration of CO_2 in brine as a function of temperature and pressure for the range used in this paper (Chabab et al., 2019).

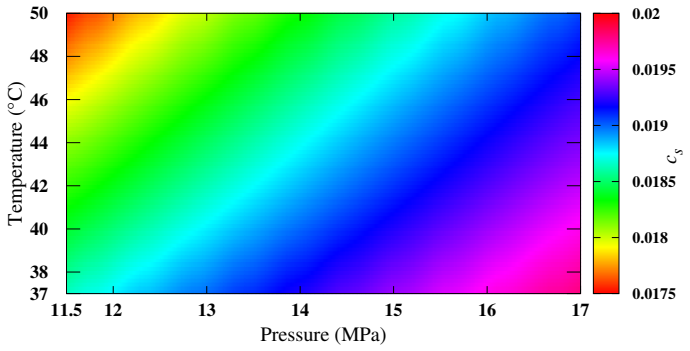

FIGURE 3.22: Saturation concentration of CO_2 in brine as a function of pressure and temperature (Chabab et al., 2019).

Figures 3.23(a, b) show the evolution of the cavern pressure and temperature as a function of cycling over two years. The cavern thermodynamics is used in a post-treatment strategy to calculate the CO_2 saturation concentration in brine as a function of the relative mass variations (Fig. 3.23(c)).

Following Fig. 3.23(b) one can see clearly the effect of heat exchange with the rock and the brine domains on the cavern temperature. This effect is reflected by the cavern pressure, which shows evolving behavior during cycling (Fig. 3.23(a)). The brine CO_2 saturation concentration varies slightly ($c_{\text{sat}} \in [0.0187, 0.0192]$) for the temperature and pressure ranges considered in this research (Fig. 3.23(c)). This saturation concentration can be converted into dissolved CO_2 mass. Knowing the brine volume $\mathcal{V}_\lambda$ and its average density ($\langle\rho_\lambda\rangle = 1158$ kg/m^3), the dissolved CO_2 mass is calculated as $\mathcal{M}_{\gamma\lambda} = c_{\text{sat}}\langle\rho_\lambda\rangle\mathcal{V}_\lambda$. For the CO_2 saturation concentration variations observed in this research, the maximum dissolved mass is expected to be $\mathcal{M}_{\gamma\lambda} \in [91.8, 94.3]$ tons. The initial CO_2 stored mass in the cavern is equal to 29283.8 tons. Therefore, the mass lost due to dissolution is approximately 0.32% of the initial stored mass.

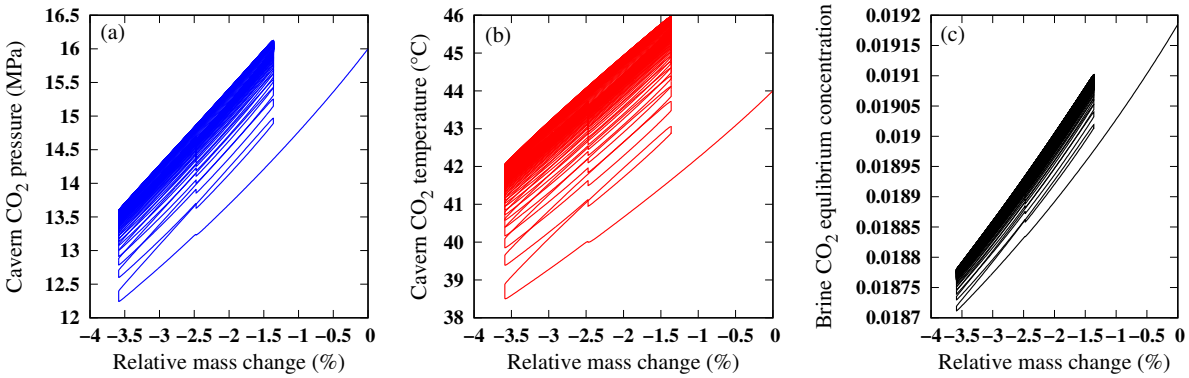

FIGURE 3.23: Cavern CO_2 pressure (a) and temperature (b) as a function of the relative mass variations during 2 years. The cavern thermodynamics is used in a post-treatment approach to calculate the CO_2 saturation concentration in the brine (c).

In the next simulations, the kinetics of dissolution is studied and quantified. To do so, the cavern thermodynamics is coupled with dissolution in the brine domain, and the entire problem is solved numerically. This necessitates solving the Navier-Stockes equation in the brine domain, along with convection due to mass transfer and thermal changes. Such simulations require extended computational time; for 6.5 months of cycling presented in this research the simulations required 3.5 months calculation time. Figure 3.24 shows the cavern thermodynamics as well as the brine CO_2 volume averaged concentration as a function of cycling. Figure 3.24(c) shows how the brine CO_2 concentration increases linearly due to cycling. The figure also demonstrates the kinetics of dissolution where concentration increases from the initial value to almost 37% the saturation value in 6.5 months.

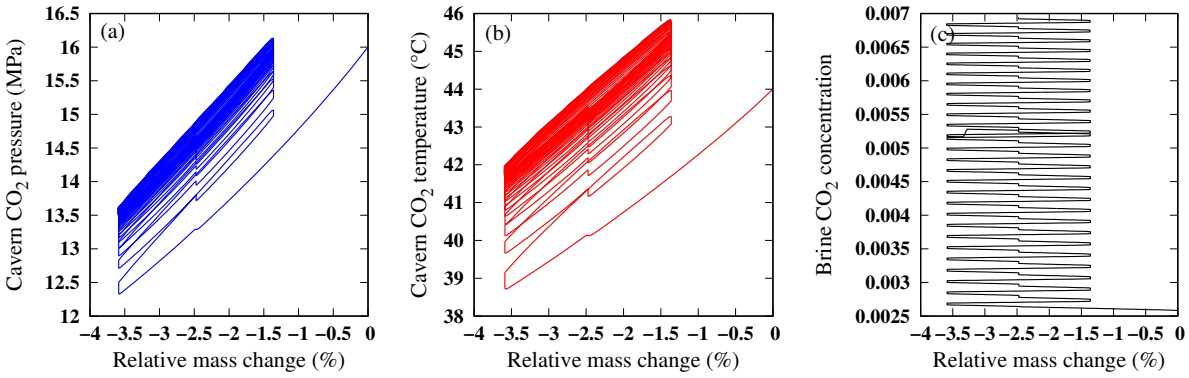

FIGURE 3.24: Cavern CO_2 pressure (a) and temperature (b) as a function of the relative mass variations during 6.5 months. The CO_2 volume averaged concentration in the brine (c) is increasing linearly showing clearly the kinetics of dissolution.

Figure 3.25(b) shows the brine CO_2 concentration averaged over its surface and volume. As for the relatively short time period of simulations (6.5 months), most of the concentration changes take place close to the surface. Therefore, the two responses give almost the same values. However, the surface averaged concentration shows obviously the effect of cycling. The volume averaged concentration is not showing the cycling effect as cycling is taking place very fast compared to the characteristic time of the dissolution problem.

Figure 3.25(a) shows how the brine volume averaged temperature is impacted by cycling. The first withdrawal phase causes a decrease in the brine temperature, before it starts to heat up again following a heating trend similar to that of the cavern (Fig. 3.24(b)). Such temperature changes are expected to alter the brine density and to play a significant role in the dissolution process by natural convection. The small irregularity observed at $t \approx 4$ months is a known

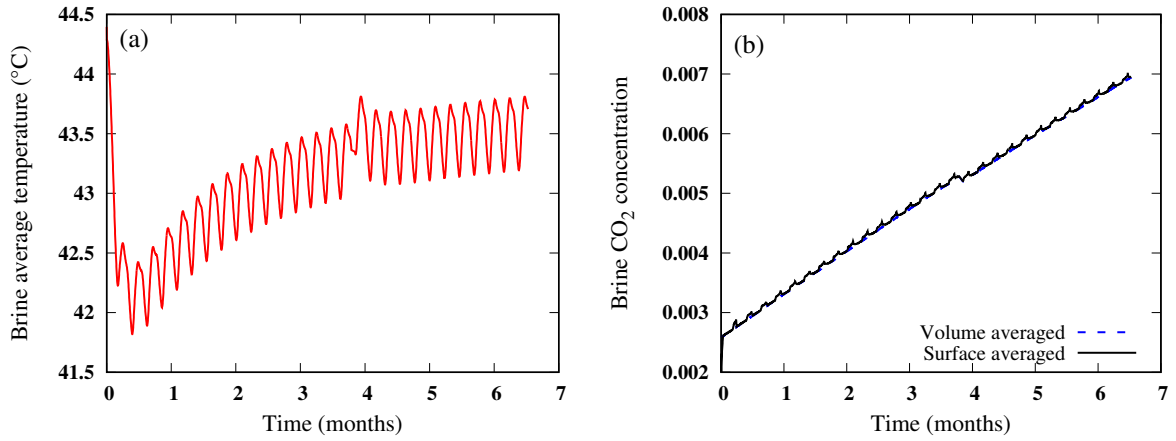

FIGURE 3.25: (a) The evolution of the brine average temperature during the CO_2 cycling. (b) The brine CO_2 concentration averaged over its surface and volume. The surface averaged concentration shows clearly the effects of cycling.

artifact of stopping and restarting the simulation. The software used here could not recover the numerical solution without this perturbation.

The evolution of the CO_2 dissolved mass can be calculated using Eq. 3.43. A total mass of 22.11 tons is dissolved during the 6.5 months of cycling. This mass is 0.076% of the initial stored mass.

Figure 3.26 shows the contours of the velocity, the concentration difference, the temperature, and the pressure fields at 10 days of the cycling. It is observed that even-though the velocity field is generated by convection (mass and thermal), it has values that are not far from $\sim$1 cm/s. The concentration, temperature, and pressure fields follow the trends of the velocity evolution. The values of any pressure perturbations attributed to the dissolution or the thermal effects do not exceed a maximum limit of 1.0 Pascal.

3.3.6 Conclusion

Gas stored in underground salt caverns, and their residual brine, are subjected to geothermal gradients. Such gradients create thermal convection that has important effects on the dissolution process of the stored gases. These effects are enhanced when gas undergoes cycling during storage. As the brine thermal expansivity is relatively high, even small temperature changes lead to significant density variations, highlighting the significance of considering thermal convection when simulating gas dissolution in the context of underground gas storage. In this research, two strategies for the kinetics of dissolution are used in order to predict the ultimate dissolved mass of CO_2. Simulations demonstrate that the ultimate total dissolved mass is approximately 0.32% of the initial stored mass. Although this loss may seem insignificant, the quantification of this loss, during cycling becomes important when other loss mechanisms are studied.

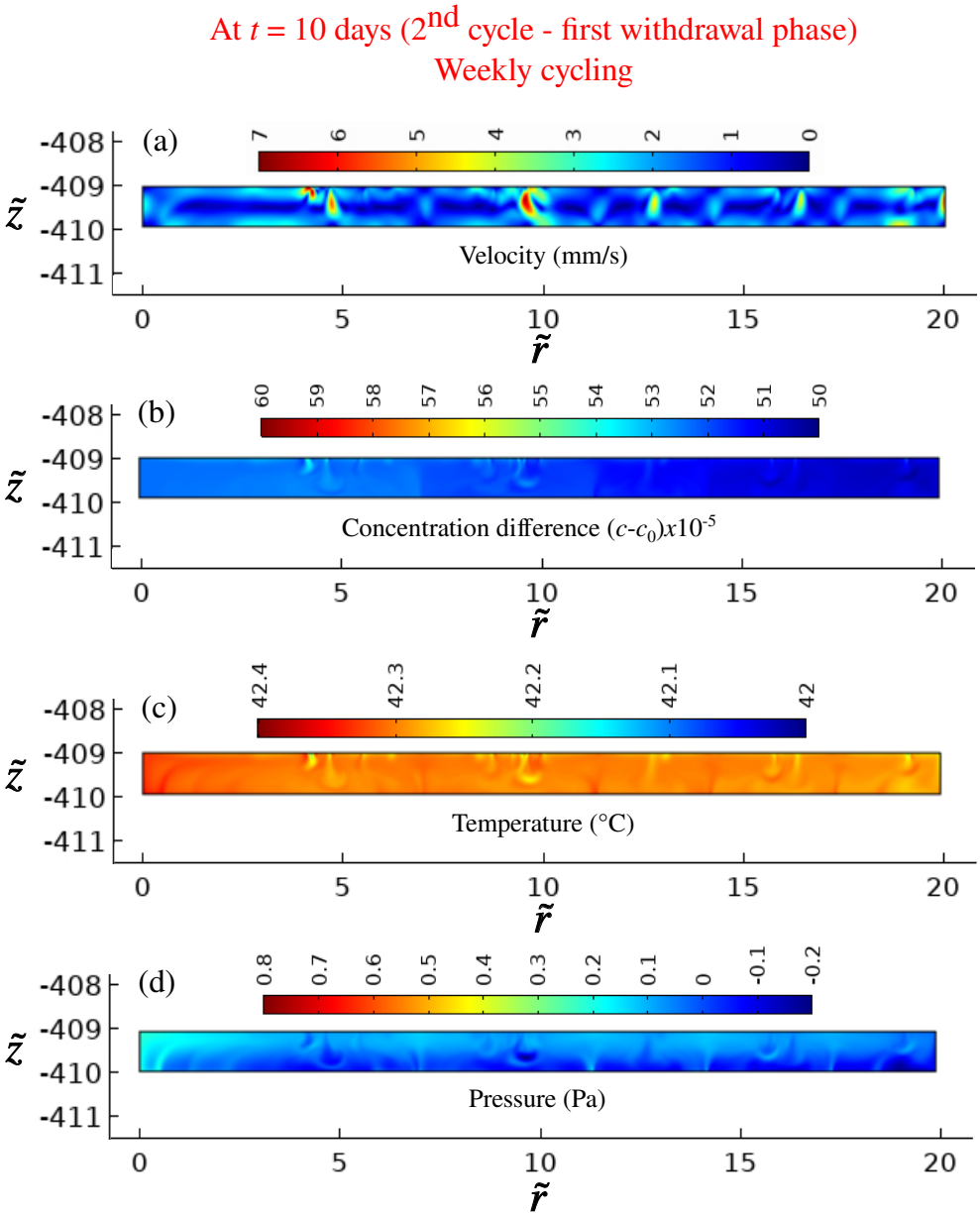

FIGURE 3.26: Contours at 10 days of weekly cycling of: (a) the velocity; (b) the concentration difference ($c - c_0$); (c) the temperature; and (d) the pressure fields. It is clear that the changes in the velocity field are the driving force for any evolution in the other fields.

3.4 Humidification kinetics of the cavern gas

During cycling in salt caverns, gas pressure and temperature evolve. The thermodynamics of the residual brine is also changing. The evaporation of water into the cavern gas (Flux F_1 of Fig. 3.1) is expected to take place due to these changes. The kinetics of evaporation must be studied to estimate the water content in the gas at each moment of cycling. The presence of water vapor may change the thermodynamic behavior of the stored gas, leading to a misestimation of the cavern thermal inventory as well as the cycled gas quantities. Humidity of withdrawn gas creates hydrates that clog pipes and prevents the direct use of gas, leading to additional costs related to dehumidification. This research includes the development of a numerical model that couples the gas thermodynamics with the evaporation mechanisms from the brine. A laboratory gas storage pilot is used to validate the numerical model while considering a fast cycling scenario. Once the numerical model is validated at the laboratory scale, it can be used for *in situ*

applications. This work helps understand why the cavern sump brine remains colder than the surrounding rock, even decades after the cavern is created (Bérest and Louvet, 2020)

3.4.1 Mechanism of evaporation

Evaporation takes place when the molecules of a liquid near its surface absorb enough energy to break the intermolecular bonds and overcome the vapor pressure. This energy removed from the liquid phase reduces its temperature, resulting in evaporative cooling. Evaporation continues until an equilibrium is reached when liquid evaporation is equal to its condensation. Actually, the escaping molecules accumulate as a vapor above the liquid. Many of these molecules return to the liquid, with returning molecules becoming more frequent as the vapor pressure increases. When the process of escape and return reaches an equilibrium, the vapor is said to be *saturated*. For a system consisting of vapor and liquid of a pure substance[5], this equilibrium state is directly related to the vapor pressure of the substance, as given by the Clausius–Clapeyron relation,

$$\ln\left(\frac{p_1}{p_2}\right) = -\frac{\Delta h}{R}\left(\frac{1}{T_2} - \frac{1}{T_1}\right), \tag{3.44}$$

where p_1, p_2 are the vapor pressures at temperatures T_1, T_2 respectively, Δh is the enthalpy of evaporation, and R is the universal gas constant. This relation assumes that water vapor behaves like an ideal gas. If a liquid is heated, when the vapor pressure reaches the ambient pressure the liquid boils.

3.4.2 The mathematical model

There is abundant literature that addresses the problem of gas-water or gas-brine equilibria. Valtz et al. (2004) reported experimental volume liquid equilibria data for the CO_2-water binary systems over a wide temperature ranging from 278.2 to 318.2 K and pressures up to 8 MPa. Salari et al. (2008) have estimated the vapor content of CO_2 in equilibrium with brine. Feistel et al. (2010) developed a sophisticated model for the thermodynamic behavior of humid sea air. Their model is, nevertheless, valid at low pressure values up to 5 MPa maximum, which do not correspond to the underground storage range. Other works focused on studying phase equilibria of energy vectors, for instance Roa Pinto et al. (2021) studied phase equilibrium of hydrogen and natural gas in brine with applications related to storage in salt caverns. Bérest and Louvet (2020) provided a comparative study on the thermodynamic behavior of underground caverns in the presence of vapor.

To present the model of this study, let us assume a mixture of dry gas d and pure water w. The dry gas is assumed to be in the gaseous phase all the time. However, water changes phase, therefore the mixture can contain water vapor v or suspended liquid water l (fog). The dissolution of dry gas in the liquid phase of water is assumed negligible, i.e. the liquid phase of the mixture is only formed of water. The total mass occupying a volume $\mathcal{V}$ of this mixture is $\mathcal{M} = \mathcal{M}_k$, $k = (d, v, l)$. By introducing the mass fractions $d = \mathcal{M}_d/(\mathcal{M}_d + \mathcal{M}_v)$ and $\mathrm{c} = \mathcal{M}_\mathrm{d}/\mathcal{M}$, the composition $\boldsymbol{c} = (c_d, c_v, c_l)$ of the mixture is expressed as:

$$c_d = c; \quad c_v = c/d - c; \quad \text{and}, \quad c_l = 1 - c/d. \tag{3.45}$$

The composition vector of the mixture $\boldsymbol{c}$ becomes a function of a single independent mass fraction which is the dry gas concentration c. The mas fractions c_v and c_l are functions of state (Sect. 1.2), the inequality $c \leq d$ must be satisfied for these fractions to remain positive. Moreover, the equality $d(p, T, c) = c$ describes the saturation of the mixture (dry air, water vapor) where any additional water appears only in the liquid form.

[5] A pure substance is defined as a substance having a constant and uniform chemical composition. A homogeneous mixture of gases which do not react with one another may, therefore, be considered a pure substance.

Based on the approach provided by Rouabhi (2019), in case of phase change of water, the volume $\mathcal{V}$ is the sum of a volume $\mathcal{V}_{dv}$ occupied by the dry gas and water vapor, and a volume $\mathcal{V}_l$ occupied by liquid water, such that $\mathcal{V} = \mathcal{V}_{dv} + \mathcal{V}_l$. Therefore, the specific volumes v_k are defined:

$$v_d = \mathcal{V}_{dv}/\mathcal{M}_d; \quad v_v = \mathcal{V}_{dv}/\mathcal{M}_v; \quad \text{and,} \quad v_l = \mathcal{V}_l/\mathcal{M}_l, \tag{3.46}$$

giving rise to the mixture specific volume which takes the following form,

$$v = c_l v_l + c_d v_d = c_l v_l + c_v v_v. \tag{3.47}$$

A simple model to construct the thermodynamic potential $g(p,T,c)$ is to consider that the partial functions $g_k(p,T,c)$ are those of the pure constituents of mixture $g_k^\circ(p_k,T)$ where p_k is a partial pressure depending on the state (p,T,c),

$$g(p,T,c) = \sum c_k g_k(p,T,c) = \sum c_k g_k^\circ(p_k(p,T,c),T). \tag{3.48}$$

The mechanical and thermodynamic equilibrium equations are needed. Such equilibrium equations ensure the introduction of entropy and the equality of the total pressure to the pressure of the liquid phase. Therefore, in terms of partial pressures (p_d, p_v, p_l), the problem comes down to solving the following system:

$$\begin{array}{lrcl} \text{thermodynamic equilibrium:} & g_v^\circ & = & g_l^\circ; \quad \text{and,} \\ \text{mechanical equilibrium:} & p_d + p_v & = & p_l, \end{array} \tag{3.49}$$

with the following condition on the total pressure and the specific volumes:

$$\begin{array}{lcl} p_l & = & p; \quad \text{and,} \\ c(1 - v_d/v_v)v_d + (1-c)v_l & = & v. \end{array} \tag{3.50}$$

Being among the most precise state laws, the GERG-2004 (Kunz et al., 2007) and GERG-2008 (Kunz and Wagner, 2012) equations are used in this work. The free energy is divided into two parts: an ideal part that describes the behavior of an ideal gas, and a residual part that accounts for deviations from this ideal behavior,

$$f(\rho,T) = f^i(\rho,T) + f^r(\rho,T), \tag{3.51}$$

that when density is low ($\lim_{\rho\to 0} f(\rho,T) = f^i(\rho \to 0, T)$), the behavior of the ideal gas is retrieved. The general form of the GERG model is expressed as:

$$\begin{array}{rcl} f^i(\rho,T) & = & \ln \varrho + a_1 + a_2\mathcal{T} + a_3 \ln(\mathcal{T}) + a_4 \ln\left(1 - e^{-b_4\mathcal{T}}\right); \\ f^r(\rho,T) & = & \displaystyle\sum_{i=1}^{N_1} n_i \mathcal{T}^{t_i} \varrho^{d_i} + \sum_{i=N_1+1}^{N_2} n_i \mathcal{T}^{t_i} \varrho^{d_i} e^{-\varrho^{c_i}}, \end{array} \tag{3.52}$$

with $\varrho = \rho/\rho_c$ and $\mathcal{T} = T_c/T$. The critical point of the fluid is defined by the coordinates (ρ_c, T_c). For each substance, the constants a_i, b_i, c_i, d_i, n_i, and t_i are known. The thermodynamic potential, free enthalpy, becomes,

$$g(p,T,c) = f(p,T,c) + p\partial_p g(p,T,c). \tag{3.53}$$

The behavior of the mixture is described by the mass density ρ, the barycentric velocity $\boldsymbol{v} = \sum c_k \boldsymbol{v}_k$, the temperature T, and the gas concentration c. The balance laws that govern the

evolution of these fields can be expressed by the following field equations:

$$\begin{array}{lrcl} \text{total mass balance:} & \dot{\rho} + \rho\,\boldsymbol{\nabla}\cdot\boldsymbol{v} & = & 0; \\ \text{momentum balance:} & \rho\,\dot{\boldsymbol{v}} - \boldsymbol{\nabla}\cdot\underline{\underline{\boldsymbol{\sigma}}} & = & \rho\,\mathfrak{g}; \\ \text{energy balance:} & \rho\,\dot{u} + \boldsymbol{\nabla}\cdot\boldsymbol{\Psi}_u & = & \underline{\underline{\boldsymbol{\sigma}}} : \underline{\underline{\boldsymbol{\nabla}}}\boldsymbol{v}; \\ \text{gas mass balance:} & \rho\dot{c} + \boldsymbol{\nabla}\cdot(\rho\boldsymbol{J}) & = & \pi^{\gamma}, \end{array} \tag{3.54}$$

with $\bar{\pi}_w^{\gamma}$ being the mass rate of water exchanged through the gas-liquid interface $\mathcal{S}_{\gamma\lambda}$ due to phase change. The internal energy flux $\boldsymbol{\Psi}_u$ is thus written as,

$$\boldsymbol{\Psi}_u = \boldsymbol{\psi} + \rho\partial_c h(p,T,c)\boldsymbol{J}. \tag{3.55}$$

Other quantities are as defined in Sect. 3.1. The derivative of enthalpy with respect to the gas concentration is,

$$\frac{\partial h(p,T,c)}{\partial c} = T\frac{\partial s(p,T,c)}{\partial c}, \tag{3.56}$$

with,

$$\frac{\partial s(p,T,c)}{\partial c} = \left(s_v^{\circ} - s_l^{\circ}\right)\left[1 + \frac{\rho_v}{\rho_d}\right] - s_v^{\circ} + s_d^{\circ}, \tag{3.57}$$

therefore,

$$\frac{\partial h(p,T,c)}{\partial c} = \left(h_v^{\circ} - h_l^{\circ}\right)\left[1 + \frac{\rho_v}{\rho_d}\right] - h_v^{\circ} + h_d^{\circ}. \tag{3.58}$$

The heat capacity of the mixture can be written as (Rouabhi, 2019),

$$C_p(p,T,c) = \partial_T h(p,T,c) = \sum c_k C_{pk} + \left[\left(c_v\partial_{pv}h_v^{\circ} - c_d\partial_{pd}h_d^{\circ}\right)/(\nu_v T) - \partial_T c_l\right](h_v^{\circ} - h_l^{\circ}). \tag{3.59}$$

The dynamic viscosity and the thermal conductivity of the mixture are defined as (Tsilingiris, 2008; Zhang, Gupta, and Baker, 2007),

$$\mu = \sum_{i=d,v,l} \frac{c_i\mu_i}{\sum_{j=d,v,l} c_j\vartheta_{ij}} \tag{3.60}$$

with,

$$\vartheta_{ij} = \frac{\left[1 + \left(\frac{\mu_i}{\mu_j}\right)^{1/2} + \left(\frac{M_{wj}}{M_{wi}}\right)^{1/4}\right]^2}{\left[8\left(1 + \frac{M_{wi}}{M_{wj}}\right)\right]^{1/2}}, \tag{3.61}$$

M_w is the molecular weight and μ_d, μ_v, and μ_l are the dynamic viscosities of the dry gas, the steam, and the liquid water respectively, and,

$$\Lambda = \sum_{i=d,v,l} \frac{c_i\Lambda_i}{\sum_{j=d,v,l} c_j\vartheta_{ij}}, \tag{3.62}$$

with Λ_d, Λ_v, and Λ_l being the thermal conductivities of the dry gas, the steam, and the liquid water respectively.

The mechanical behavior of the rock mass around the cavern is neglected. For a time-dependent problem, the temperature field in the surrounding rock mass verifies the following form of the heat equation,

$$\partial_t T_\sigma = \mathcal{K}_\sigma \boldsymbol{\nabla} \cdot (\boldsymbol{\nabla} T_\sigma). \tag{3.63}$$

3.4.3 Modeling of the brine domain

The residual brine of the cavern is expected to undergo thermal changes due to the geothermal gradient over its height and gas cycling. As in indicated in Sect. 3.3, these thermal changes result in density changes. To describe the velocity field generated by natural convection due to density changes, both the Navier-Stokes equation as well the energy equation in the liquid phase are needed. Considering a computational fluid dynamics framework in the brine domain considerably complicates the numerical calculations. As a simplification, a convectively enhanced conductivity is used in the liquid energy equation to substitute for the effect of the velocity field. This permits us to modelize correctly the heat transfer in the liquid phase while using only the energy equation. Hence, the energy equation in the liquid domain takes the form,

$$\rho_\lambda C_{p\lambda} \partial_t T_\lambda + \boldsymbol{\nabla} \cdot \boldsymbol{\psi}_\lambda = Q_w, \tag{3.64}$$

where Q_w is the heat source attributed to the phase change of the liquid phase, and $\boldsymbol{\psi} = -\Lambda \mathrm{Nu} \boldsymbol{\nabla} T_\lambda$ with Nu being the Nusselt number. Values of the Nusselt number for similar applications can be found in the works of Calcagni, Marsili, and Paroncini (2005) and Hasnaoui, Bilgen, and Vasseur (1992). The heat source related to the phase change of the liquid phase is calculated using the latent heat $\Delta \bar{h}_w$ (Sect. 1.3.2), such that,

$$Q_w = -\bar{\pi}_w^\gamma \Delta \bar{h}_w, \quad \text{with,} \quad \Delta \bar{h}_w = \bar{h}_v - \bar{h}_l. \tag{3.65}$$

At the gas-liquid interface, as a function of cycling, molecules escape the liquid phase. However, many of them return to the liquid until saturation is reached. The material flux between the two phases is expressed as,

$$\boldsymbol{J} \cdot \boldsymbol{n} = K((1 - c) - c_{\mathrm{sat}}), \tag{3.66}$$

therefore it is concluded that,

$$\bar{\pi}_w^\gamma = \frac{1}{\mathcal{V}} \int_{\mathcal{S}_{\gamma\lambda}} \rho \, K(c_{\mathrm{sat}} - (1 - c)) \, d\mathcal{A}_{\gamma\lambda}, \tag{3.67}$$

where K is the mass transfer coefficient (calibrated). The vapor saturation concentration is calculated as $c_{\mathrm{sat}} = 1 - \rho_d / \rho$ (at saturation).

3.4.4 Laboratory gas storage pilot

Gas humidification kinetics at the laboratory scale is presented in this section. The laboratory model consists of a cylindrical high-pressure stainless steel vessel (Fig. 3.27), with dimensions: height ($L = 50$ cm) and radius ($R = 9$ cm) with a volume $\mathcal{V} = 12.3$ l. The model is equipped with a heating system to allow for the generation of natural convection resulting from thermal gradients.

The temperature at the model base is controlled by a circulating fluid, the top temperature can be controlled by a heating collar or left equal to the room temperature. Sides are isolated by an isolating jacket that is wrapped around the system, and the temperature gradient is left to develop naturally by the applied bottom and top temperatures. The objective is to develop a temperature difference over the model height that resembles the geothermal gradients that salt caverns undergo. The pilot is equipped with 15 temperature probes to measure the temperature spatial variations during cycling. Humidity is also measured by 7 sensors that are distributed over the pilot volume.

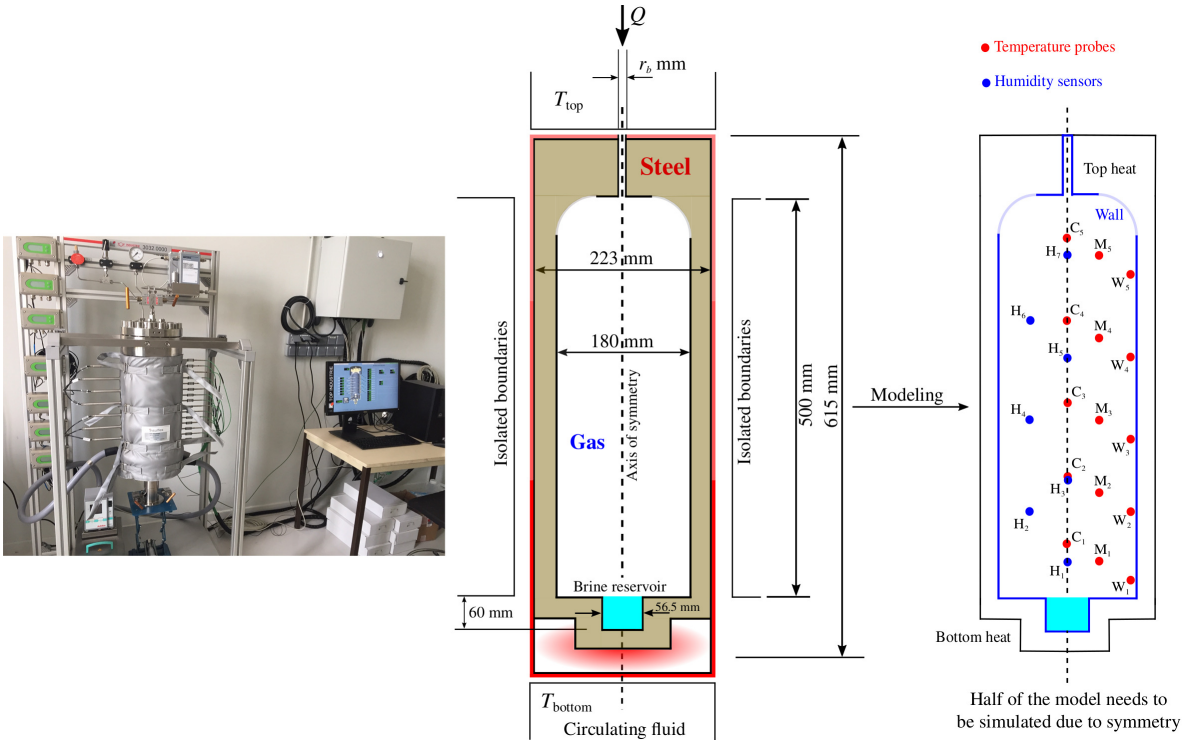

FIGURE 3.27: Schematic diagram of the laboratory model used to reproduce the underground cavern thermodynamic behavior. The figure shows the axes where the vertical temperature profiles are measured, five sensors over each vertical axis: sensors C (86 mm off wall), M (46 mm off wall), and W (6 mm of wall). Sensors are separated by a vertical distance of 28 mm. Humidity is also measured by 7 sensors H_1 to H_7: these sensors are either arranged axially or at 46 mm off the wall and separated vertically by 56 mm distance.

The injection tube has a diameter of 3 mm. A brine reservoir is placed at the model base to study the effect of vapor saturation on the thermodynamic behavior of stored gas during cycling. The reservoir brine height is measured precisely during tests to estimate the quantity of the evaporated water. The pilot steel thermal diffusivity is $\mathcal{K}_\sigma = 3.038 \times 10^{-6}$ m^2/s. This thermal diffusivity allows for a characteristic time along the wall thickness equal to $t = l^2/\mathcal{K}_\sigma = (21.5 \times 10^{-3})^2/3.038 \times 10^{-6} \simeq 152$ s.

3.4.4.1 Laboratory cycling tests

Two laboratory tests, with and without brine in the reservoir, are carried out, with helium used as the storage gas. The objective is to quantify the effect of humidity on the thermodynamic behavior of helium. Tests are performed following this procedure:

- in the humid test the reservoir is filled with saturated brine to a height of 6.15087 cm. In the dry test the reservoir is left empty;
- a helium flush is done to chase out air inside the pilot;
- the top and bottom temperatures of the model are set equal 46 °C and 43 °C respectively, and sides are isolated;
- a filling phase is done where helium pressure within the pilot is increased from atmospheric to 12 MPa;
- the system is left to reach equilibrium during 2.5 days;
- the mass variation program (Fig. 3.28) is fed to the acquisition system to start cycling.

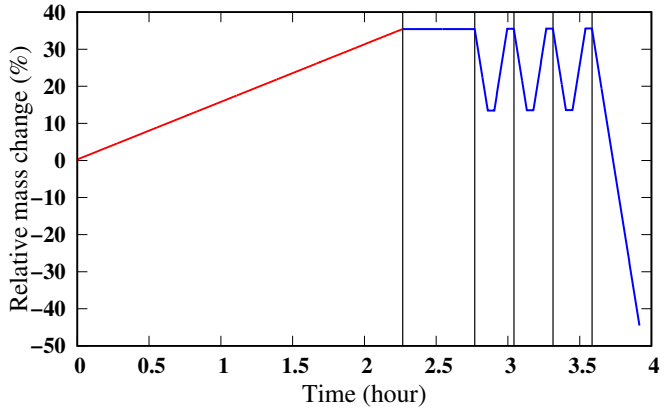

FIGURE 3.28: The program begins with a slow filling phase of ∼2.26 hours followed by a rest phase of ∼0.5 hour. Cycling begins after this rest phase and includes three cycles. Each cycle extends over ∼0.27 hour where withdrawal and injection last for ∼0.09 hour each, and the rest phases last only for ∼0.04 hour each. Cycling is followed by an intense withdrawal phase which extends over ∼0.33 hour. This cycling leads to relative mass changes of ∼[35.43% à -44.51%].

Figure 3.29(a) shows the evolution of the average Relative Humidity (RH) (averaged over the seven sensors) during the stabilization phase. It is observed that saturation (at 85%) is attained after approximately one day. Cycling begins after the stabilization phase (2.5 days). RH is seen to decrease during cycling (Fig. 3.29(b)); a RH of ∼40% is recorded after ∼4 hours. This reduction of humidity is attributed to the injection of dry helium and withdrawal of wet gas.

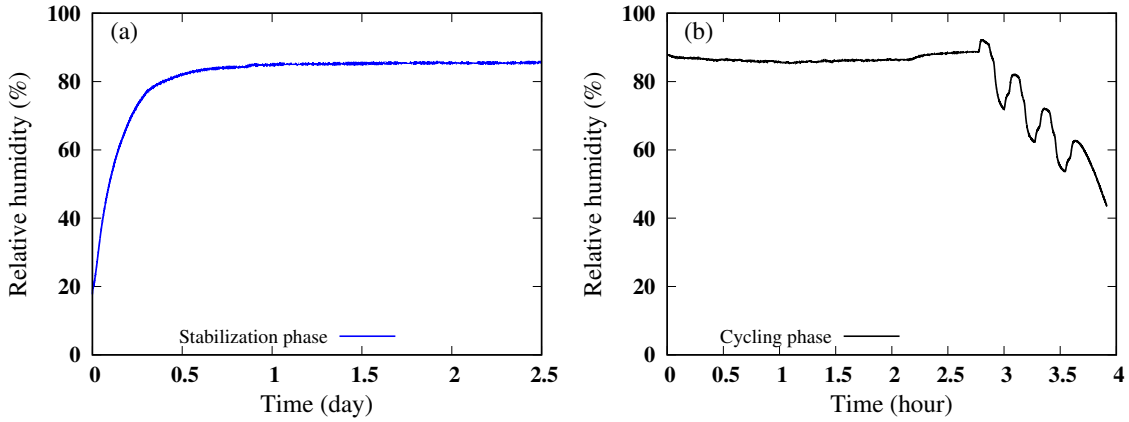

FIGURE 3.29: (a) Evolution of the average RH during the stabilization phase of 2.5 days, and (b) during cycling.

Figure 3.30(a) shows the evolution of the helium pressure during the two cycling tests, wet and dry. The two histories correlate well and any observed differences are minimal. Figure 3.30(b) shows the average temperature histories (averaged over the 15 sensors) during the dry and wet tests, the discrepancies do not exceed ∼0.7 °C.

Figures 3.31, 3.32, and 3.33 show the temperature histories by the wall (W sensors), at middle of the model (M sensors), and axially (C sensors). The experimental results of the wet and dry tests are comparable and differences are minor. The differences are more obvious at the top of the model which is less influenced by the heating source at the bottom (Figs 3.31(b), 3.32(b), and 3.33(b)).

Figure 3.34 shows the RH histories at sensors H_1 (bottom) and H_7 (top) during the dry and wet tests. It is obvious that RH is negligible during the dry test. The H_1 sensor always measures

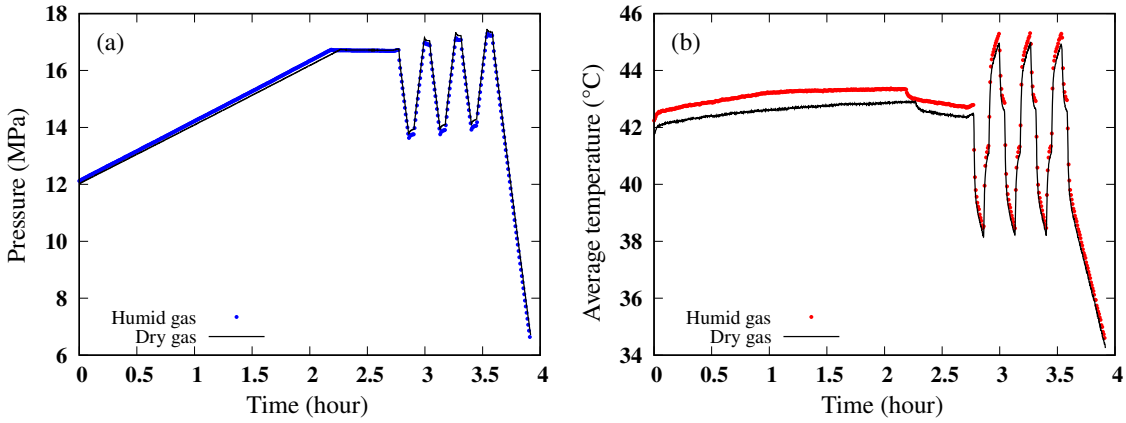

FIGURE 3.30: Pressure (a) and average temperature (b) histories during the two cycling tests of dry and humid helium.

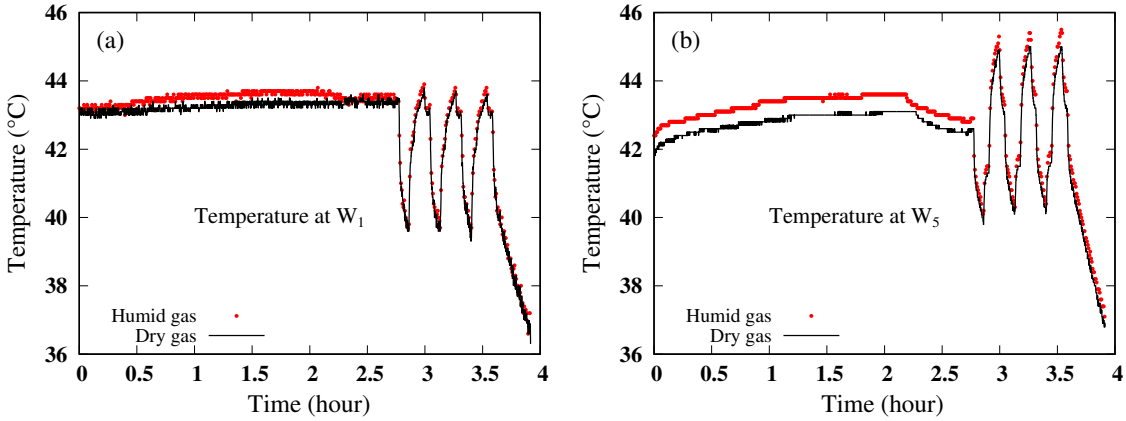

FIGURE 3.31: Wall temperature histories: (a) at the W_1 sensor (bottom) and (b) at the W_5 sensor (top). The figures compare the results of the dry test (continuous lines), and the wet test (dots).

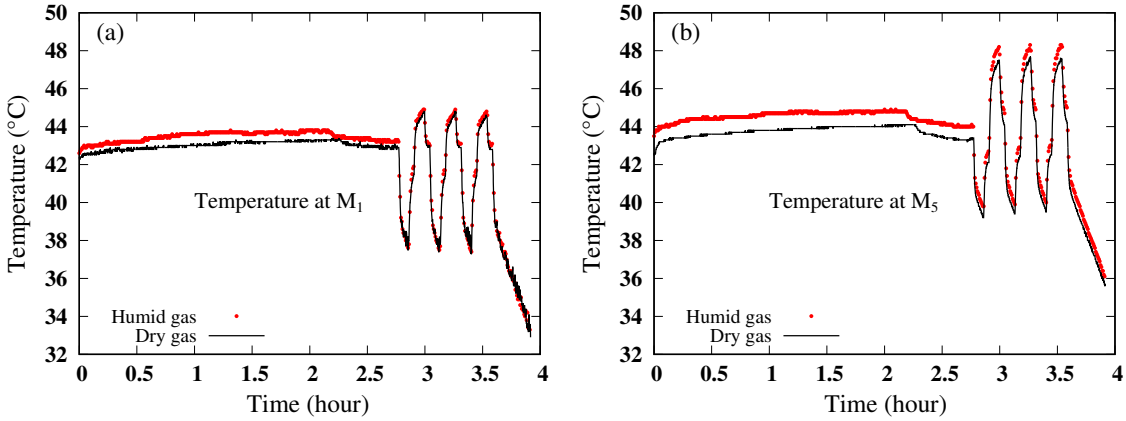

FIGURE 3.32: Temperature histories at middle of the pilot: (a) at the M_1 sensor (bottom) and (b) at the M_5 sensor (top).

a more humid level of gas as it is closer to the reservoir. Nevertheless, RH is more affected by cycling at the sensor H_7.

3.4.4.2 Numerical simulations

The numerical simulation results of the wet test are presented in this section. Simulations of this particular laboratory test are performed by implementing the same boundary and initial

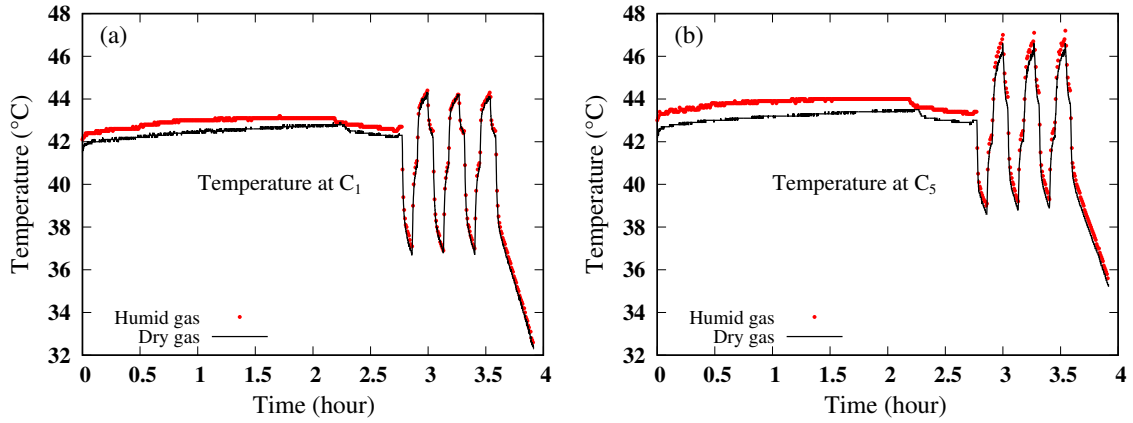

FIGURE 3.33: Axial temperature histories: (a) at the C_1 sensor (bottom) and (b) at the C_5 sensor (top).

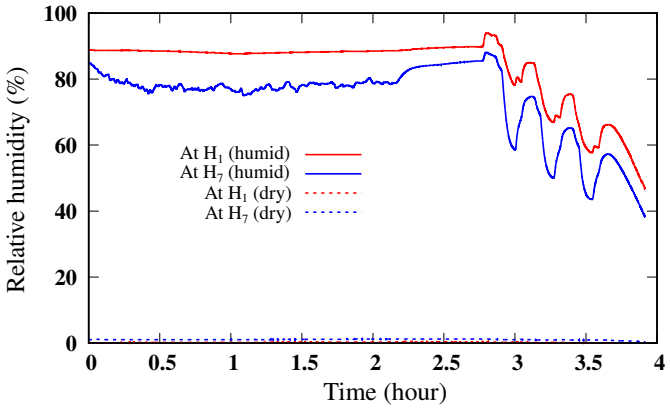

FIGURE 3.34: Evolution of RH at the sensors H_1 (bottom) et H_7 (top) during the dry and wet tests. Humidity is negligible during the dry test.

conditions as in Sect. 3.4.4.1. Only half of the model is simulated due to its two-dimensional axisymmetry. As to abide to COMSOL accuracy requirements for conjugate heat transfer, the k-ϵ turbulent flow, and heat convection (Sect. 3.1), the mesh includes 52554 elements of which 1566 quadrilateral boundary elements (Fig. 3.35).

Vapor diffusion in helium depends on temperature, for this study an average value $D = 1.011 \times 10^{-4}$ m^2/s is used (Schwertz and Brow, 1951). The mass transfer coefficient is parametrized during the stabilization phase to $K = 3.8 \times 10^{-4}$ m/s. Brine thermo-physical properties are presented in Sect. 3.2. COMSOL gives analytical expressions for the evolution of the dynamic viscosity and thermal conductivity of pure water and helium as a function of temperature.

Figure 3.36 shows the evolution of pressure and average temperature during the stabilization phase of 2.5 days. The figure compares the experimental data with the numerical results. Numerical average temperature is averaged over the model volume, however, experimentally, it is averaged over the 15 sensors.

Figure 3.37(a) shows the evolution of average relative humidity during the stabilization phase. It is averaged over the model volume numerically, however, it is averaged over the 7 sensors experimentally. The brine temperature is measured experimentally at the middle of the reservoir (Fig. 3.37(b)), nevertheless, it is averaged over the brine domain numerically. The mass transfer coefficient is the only parameter adjusted numerically, it is value is chosen such that the kinetics of humidification, both experimentally and numerically, best-fit (Fig. 3.37(a)).

Figure 3.38 shows the evolution of the gas pressure and its average temperature in the pilot during cycling. Experimental data and numerical responses are satisfactorily comparable.

(a) Laboratory set-up

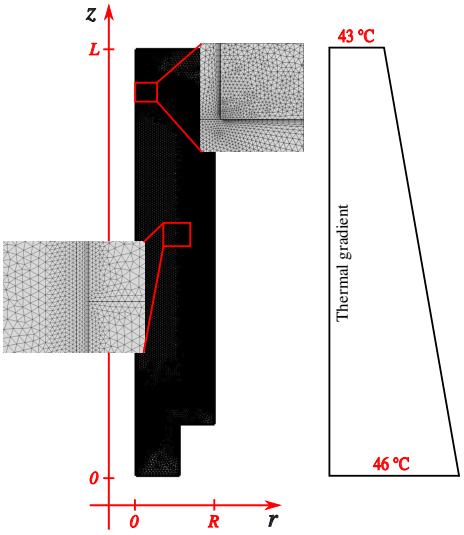

(b) 2-D axisymmetric descritization

FIGURE 3.35: (a) The laboratory set-up: bottom and top temperatures are set equal 46 °C and 43 °C respectively. The model sides are isolated, helium is injected to establish a pressure of 12 MPa, and temperature gradient is left to develop over the model. (b) Two-dimensional axisymmetric discretization of COMSOL.

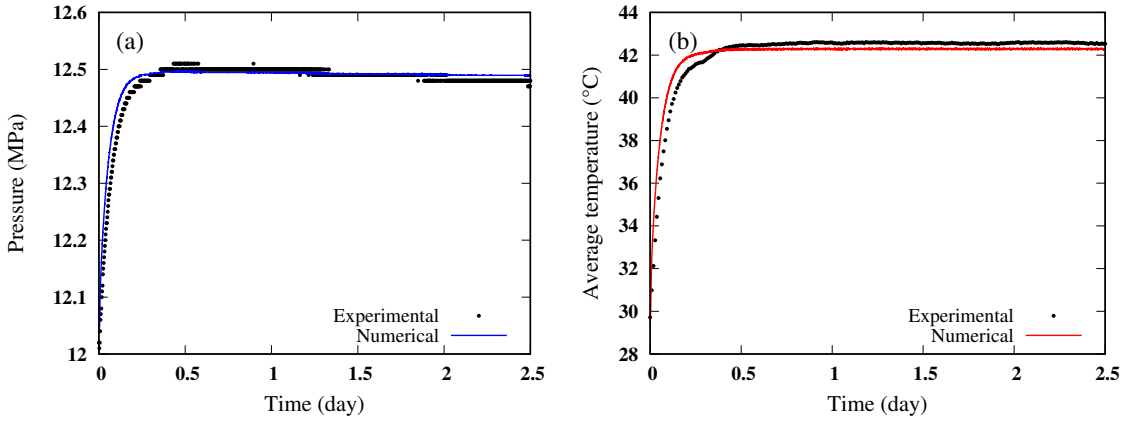

FIGURE 3.36: Evolution of pressure (a) and average temperature (b) in the pilot during the stabilization phase.

However, in case of RH (Fig. 3.39(a)), an important deviation between experimental data and numerical results is observed. This is supposedly attributed to the mass transfer coefficient that is calibrated during the stabilization phase yet never updated during cycling. It is expected that the value of this coefficient to be a function of the gas velocity close to the brine surface. Comparing the numerical results of the brine average temperature to the experimental data (Fig. 3.39(b)), it is noticed that the experimental temperature is changing significantly during the slow filling phase where the pilot RH is relatively not changing, this behavior needs more investigation. Although, the numerical results are stable during the slow filling phase, during cycling they show a slow heating trend that is consistent with the experimental data.

3.4.5 Humidification kinetics at the cavern scale

Studying humidification kinetics while running CFD calculations is numerically expensive. It requires extensive calculation time and memory. In an exploitation context where cycling within

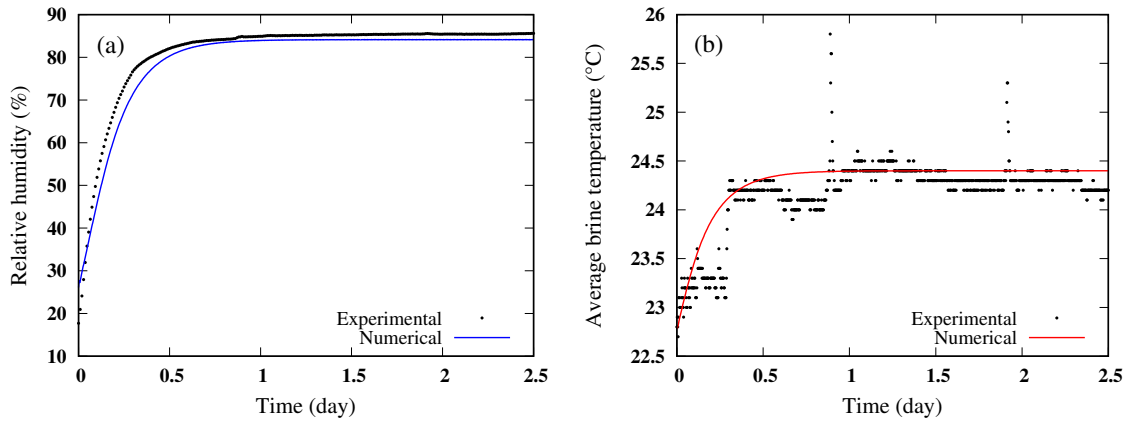

FIGURE 3.37: Evolution of average RH (a) and average brine temperature (b) during the stabilization phase.

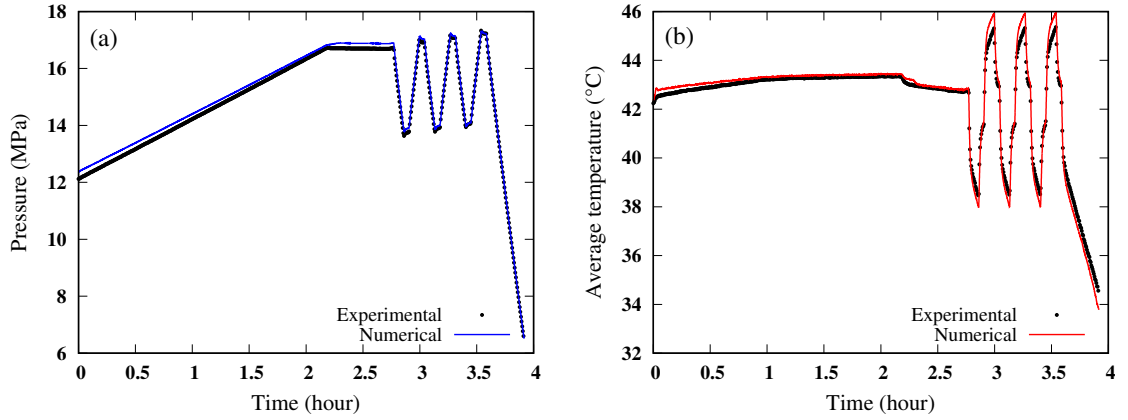

FIGURE 3.38: Evolution of pressure (a) and average temperature (b) in the pilot during cycling.

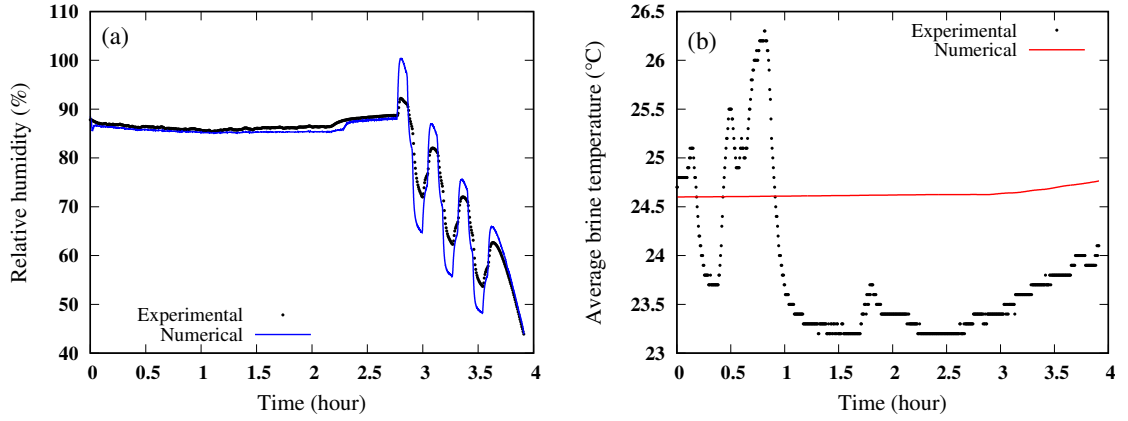

FIGURE 3.39: Evolution of average RH (a) and average brine temperature (b) during cycling.

the cavern expands over its lifetime (30 to 40 years), it is necessary to study the humidification kinetics while assuming a cavern uniform thermodynamic state (Sect. 3.1).

3.4.5.1 Humidification kinetics in a uniform thermodynamic state

In a uniform thermodynamic framework, the system of equations (3.54) becomes:

$$\begin{array}{lccl} \text{total mass balance:} & \mathcal{M}\left(-\chi_p \dot{T} + \chi_T \dot{p} + \beta \dot{c}\right) & = & Q_e; \\ \text{energy balance:} & \mathcal{M} C_p \dot{T} - \mathcal{V}\chi_p T \dot{p} + \mathcal{M} T \partial_c s & = & Q_e^+ (h_t^w - h^c) - \Psi; \\ \text{gas mass balance:} & \tau \dot{c} & = & (1-c) - c_{\text{sat}}, \end{array} \tag{3.68}$$

with $\beta = \nu \partial_c \rho|_{p,T}$, and the humidification characteristic time is τ. Other quantities are as defined previously. The characteristic time is a function of cycling and needs to be calibrated based on field or experimental data. The parameter β can be found using the following expression,

$$\beta = -\rho \left[\frac{1}{\rho_d} \left(1 - \frac{\rho_v}{\rho_l} \right) - \frac{1}{\rho_l} \right]. \tag{3.69}$$

3.4.5.2 A post-treatment approach for humidification kinetics

The objective of this section is to know if the average RH of Fig. 3.29(b) can be reproduced knowing the evolution of gas pressure and its average temperature (Fig. 3.30). To do so, vapor concentration at saturation needs to be calculated for each pressure and temperature value. Therefore, the following equation for humidification kinetics can be used:

$$\dot{c} = \begin{cases} \dfrac{1}{\tau_1} \left[(1-c) - c_{\text{sat}} \right], & (1-c) \geq c_{\text{sat}}; \\ \dfrac{1}{\tau_2} \left[-(1-c) + c_{\text{sat}} \right], & (1-c) < c_{\text{sat}}. \end{cases} \tag{3.70}$$

The two characteristic times are calibrated to $\tau_1 = 85$ s and $\tau_2 = 2500$ s, these two values best-fit the experimental data as shown in Fig. 3.40.

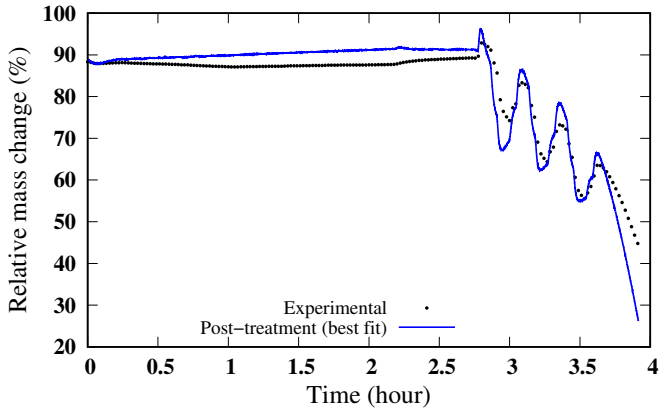

FIGURE 3.40: Evolution of experimental average RH correlated with numerical values calculated using the humid gas state law in a post-treatment approach.

Even-though there are some differences, depending on the application, they can be be accepted, and the kinetics itself is reproduced.

3.4.6 Discussion and conclusion

This work demonstrates that its feasible to reproduce at the laboratory scale thermodynamic evolutions that resemble those of real scale caverns. Such evolutions include the gas pressure,

its temperature, and its vapor content. To focus on the gas humidification kinetics during cycling, this study provides a mathematical model based on the free enthalpy. The laboratory measurements show that the gas pressure and temperature do not change significantly due to the presence of water vapor. However, the presence of the RH itself is important. Depending on the cycling frequency, RH within the cavern changes, with a tendency to decrease in case of fast cycling. The presence of RH in the withdrawn gas is harmful, it clogs conduits and requires additional costs related to dehumidification (wet gas can not be used directly). Still, some simulations need to be performed at the cavern scale while considering several cycling scenarios to have an idea about the effect of cycling on the humidification kinetics, and to estimate the humidification characteristic time at the cavern scale.

Review and perspectives

This document presents the knowledge I acquired over a time-course of 14 years while working on the exploitation of underground energy resources by fluid circulation. I began as a modeler when I developed my skills in the field of the finite element coding of complex physics. During my research at the University of Calgary, I was a part of the microseismic industry consortium, where I got familiarized with the industrial problems and had access to field data. Once I started working at MINES Paris, applied research became essential. At that point, I understood that one can get satisfied by treating each industrial problem using a specific engineering tackle, or delve into the fineness of physics to develop general approaches. In this work, I tried to construct the mathematical and physical models based on thermodynamics. I adopted simplifying approaches in a next step, while quantifying at the same time their effect and range of validity.

This research is characterized by conducting validations at the laboratory scale, and by transferring techniques to communicate it with the real scale applications. The skills I gained through this knowledge are interdependent and multidisciplinary, they fit in the general research axis defined by our team at the Center of Geosciences of MINES Paris for the coming five years. They help me mount or participate in mounting private and industrial projects, and contribute to teaching activities of the University PSL. Recently, we got the funding for a European project (FrHyGe) that concerns large-scale demonstration of underground hydrogen storage.

Specifically, I would further work on the following aspects:

- while gas storage in salt caverns represents a solution to the intermittency problem coherent to renewable energy, cycling is expected to take place rapidly (weekly or daily). An emergency need appears with regard to the FEM codes used to reproduce the stored gas thermodynamics. While the CFD simulations may be precise, conducting them over the cavern lifetime is unfeasible. Future research will focus on exploiting the storage pilot (Sect. 3.4) to enhance the existing FEM codes that assume a uniform thermodynamic state. The pilot experimental results can be reproduced by performing simplified simulations while using a heat transfer coefficient over the pilot wall. This coefficient can be a function of the well velocity or the treatment rate, and it aims at recreating the effect of the velocity field. Once validated, this approach can be generalized to the cavern scale, it can be also enhanced if *in situ* measurements are available from these caverns;

- fast solicitations of salt caverns definitely affects the mechanical integrity of the rock salt surrounding them. The developed mathematical model (Sect. 3.2) does not take into account the mechanical deformation of the rock salt. We are currently conducting research to evaluate the evolution of the rock salt hydraulic properties due to mechanical loading. The results of such a research can be implemented in the current framework to study their effects on the total amount of gas lost into the rock domain;

- basically, this research focuses on CO_2 dissolution in brine. However, future research will include the development of a dissolution cell dedicated to studying hydrogen dissolution kinetics, particularly due to thermal gradients, and for different volume ratios of gas and brine. Hydrogen production is still expensive and available caverns might be large. For a small quantity of hydrogen and to keep a minimum cavern working pressure, caverns

might be half (or more) filled with brine. Geothermal gradients can not be negligible over considerable brine volumes, nor can be the dissolved mass of hydrogen. This illustrates the need to study hydrogen dissolution kinetics in such conditions;

- the storage pilot will be used to study hydrogen humidification kinetics under common storage conditions. The presence of water vapor is observed to have a little effect on helium thermodynamics, however, water vapor diffusion in hydrogen is more important. Thus, this conclusion needs to be verified in the case of hydrogen. The numerical model has to be enhanced with regard to the used mass transfer coefficient on the wet surface. An evolving value as a function of cycling is expected to better reproduce the relative humidity experimental curves;
- as *in situ* data with regard to methane cycling in a real cavern are available, the humid gas model of this study can be used to investigate the cooling effects close to the brine surface. This study demonstrates that, due to evaporation, brine stays colder than the cycled gas. This will help estimate the buffer zone size above the cavern brine during cycling.

These activities will help me acquire new skills and establish new research axis/axes. For instance, I would like to deploy the artificial intelligence technology in the field of induced seismicity due to fluid injection. I proposed an inter-team PhD project concerning the non-diffusive seismicity triggering fronts in a thermo-hydromechanical framework. The results of this project will show how seismic interpretations can improve simulation models and, reciprocally, how fully coupled physics-based modeling can add to earthquake data interpretations in analysis of induced seismic sequences. Outcomes will be valued in terms of publications in peer-reviewed journals.

Appendix A

Detailed Curriculum Vitæ (CV)

Murad AbuAisha Ph.D.

2 Bis Avenue du Général de Gaulle, 77210 Avon, France
murad.abuaisha@minesparis.psl.eu | +33615808952 | 36 years old |

EDUCATION

University of Grenoble, Grenoble, France — March 2011 | May 2014
Ph.D. degree in Geomechanics
Thesis: Enhanced Geothermal Systems (EGS): Hydraulic fracturing in a thermo-poloelastic framework

University of Joseph Fourier, Grenoble, France — September 2009 | July 2010
Master's degree in Mechanics of Solid Materials
Thesis: Digital image correlation: Strain localization and landfill clay barrier reinforcement

University IUG, Gaza, Palestinian Territories — September 2004 | February 2009
Bachelor's degree in Civil Engineering
Graduation project: Design of an artificial island

PROFESSIONAL EXPERIENCE

MINES Paris — Paris, France
Researcher-Teacher (Assistant professor) — May 2017 | Present
Projects: Participating in and mounting several projects with industrial partners: STORENGY, GEOSTOCK, TEREGA, TOTAL, AIRLIQUIDE. Academic partners include other members of the PSL university, and the university of Lorraine

- Uniformity of thermodynamic state of gas stored in underground salt caverns, particularly hydrogen
- Computational Fluid Dynamics (CFD) modeling with turbulent flows
- Conjugate hate transfer and the boundary layer theory
- Mass exchanges between cavern phases: Gas, residual brine, and rock salt
- Non-isothermal two-phase hydrogen permeation in the saturated rock salt
- Geothermal effects on the gas dissolution kinetics in the cavern residual brine during cycling
- Gas humidification kinetics as a function of cycling frequency
- Carbon dioxide sequestration in geological media and induced seismicity
- AI-driven geothermal exploration (new research theme)

University of Calgary — Calgary, Canada
Postdoctoral researcher — November 2014 | May 2017

Project: Modeling and simulating Hydraulic Fracturing (HF) for petroleum industry using continuum/discontinuum approaches and related induced seismicity

- The finite and the discrete element methods to describe linear/nonlinear deformations as well as fracturing of rock formations
- Darcian flow and fluid compressibility law for fluid diffusion in the reservoirs and fracture leakoff
- Tracking and simulating the induced hydraulic fracturing seismicity due to fault activation either by dynamic effects or by fluid pressure changes
- Parallel programming using C++ on a Linux environment and High Performance Computing (HPC) simulations
- Two years of teamwork experience at the department of Geoscience, University of Calgary

CNRS Grenoble, France
Ph.D. researcher March 2011 | March 2014
Project: Enhanced Geothermal Systems (EGS)

- Hot Dry Rock (HDR) reservoir enhancement by Hydraulic Fracturing (HF), in terms of production, impedance, and efficiency of thermal recovery
- Developing a fully coupled HF thermo-poroelastic framework with all the required partial differential equations
- Writing a finite element FORTRAN 90 code to simulate fluid circulation and heat transfer in enhanced large-scale geothermal systems
- Several finite element meshing approaches and implicit time integration schemes for stable solutions of fluid flow and heat transfer
- Navier-Stokes equation for complex flow, fluid Newtonian/non-Newtonian characteristic and Darcian/non-Darcian nature of flow
- Fair knowledge of the physics of fluid flow in dual-porosity media and possible phase changes
- Experience with physically coupled phenomena and numerically challenging stabilization techniques, i.e. heat convection
- ABAQUS and COMSOL expertise, analytical solutions and field data treatment for validation of the numerical approaches
- Three-year experience of teamwork at the Laboratoire 3SR, Grenoble, France

Laboratory 3SR Grenoble, France
Master's internship in material mechanics February 2010 | July 2010
Project: Tensile strength of clays: Applications to landfill clay barriers

- Clay reinforcement by fibers
- Strain localization phenomenon
- Laboratory tests
- Validations using the 3-dimensional digital image correlation

SKILLS

Competencies

- Reservoir geomechanical modeling
- Finite and discrete element methods
- Fluid thermodynamics
- Dissolution kinetics of gas in the aqueous phases
- Kinetics of gas humidification

- Non-isothermal two-phase flows
- Partial differential equations
- Coupled physical phenomena
- Fluid flow mechanics in fractured media and tight reservoirs
- Parallel coding in C++ Linux
- FORTRAN 90, Matlab and Python languages
- **Training in "Supervising Ph.D. students" (PSL)**
- **Training in "Choose teaching methods adapted to the targeted learning" (PSL)**
- **Training in "How do I make sure that the way I teach is appropriate?" (PSL)**
- **Training in "Design an educational slideshow" (PSL)**
- Courses in "Interpersonal communications and relations of work"
- Courses in "Time management and personal organization of work"
- Commercial numerical software: ABAQUS and COMSOL

Language Skills

- Fluent in written and spoken English
- Fluent in written and spoken French
- Fluent in written and spoken Arabic, Hebrew, and Aramaic

SUPERVISING AND COLLABORATION ACTIVITIES

Graduate students
Ph.D. students

- Khashayar Khezri: Dynamic fracturing in a THM framework: Upscaling applications to geo-energy production and induced seismicity
  Co-supervising at 30% November 2023 | November 2026
- Firas Tayeb: Thermodynamics of underground gas storage: From laboratory to salt caverns
  Co-supervising at 60% November 2019 | February 2024

Collaboration with PostDocs

- Angeline Defay: Numerical modeling of hydrogen permeation in the rock salt
  Collaboration at 50% November 2023 | September 2024

Master's internships

- Parth Nigam: Numerical modelling of rock dynamic fracture and study of fluid-driven fracture: FEM and XFEM framework
  Co-supervising at 50% February 2018 | July 2018

Undergraduate students:

- Mini-project UE-14 (five students of MINES Paris). Title: Tightness of underground salt caverns to hydrogen
  Supervising at 100% September 2022 | December 2022
- Option student of ground and underground applications. Title: Energy storage by compressing CO_2 using hydraulic pumps
  Co-supervising at 50% June 2021 | September 2021
- Foreigner option student from the university Mohammed VI polytechnic. Title: Mining through high pressure water jetting: Definition of the pilot testing campaign of SABRE 2020 field tests
  Co-supervising at 50% June 2020 | September 2020

TEACHING ACTIVITIES

At MINES Paris (2017-2023) - Since I started working at the school of mines (MINES Paris), my teaching load was around 35 hours/year:

- November 2023: Courses in the MIG (Métier de l'Ingénieur Généraliste). Title: Prospective study of a strategic resource: Underground gypsum exploitation in Maurienne. Students delivered a report at the end of this option.
- September 2022 - November 2022: Mini-project UE-14. Title: Tightness of underground salt caverns to hydrogen
- September 2021 (one week): Geology field internship for second year students. Title: Geosciences in urban context - Ile de France region
- November 2018 (one week): Courses in the MIG (Métier de l'Ingénieur Généraliste). Title: Hydrogen storage in salt caverns. Students delivered a report at the end of this option.
- September 2017 (one week): Geology field internship for second year students. Geological lecture on rock fracturing - Sisteron region

Invited lecturer at the university of Calgary - Alberta - Canada (2014-2017):

- Introduction to induced seismicity
- Structural engineering

RESEARCH PROJECTS

At MINES Paris (2017-2023) - My history since 2017 of participating in and mounting projects can be listed in the following points:

- February 2024 for 5 years: **Contribution** to the FrHyGe Horizon European project: Full qualification in France of large-scale Hydrogen underground storage and replication from Germany to all European countries.
- October 2023: **Participating in mounting** a Horizon Europe project. Title: G-AIDANCE: Geothermal AI-driven advisory network for comprehensive exploration. *Project was well classified but it was not retained*.
- November 2023 for 10 months: **Contribution** to the project InterCarnot H2toSALTCAV in collaboration with the laboratory GeoRessources of Lorraine university. Title: Hydrogen storage in salt caverns for energy transition. This project helped fund the PostDoc of Angeline Defay listed above.
- September 2023 for 3 years: **Participating in mounting** a Marie-Curie doctoral proposal through the SMILE network (https://smile-msca-dn.eu/). This proposal was accepted and gave rise to the Ph.D. of Khashayar Khezri listed above.
- January 2023 for 2 years in two phases: **Piloting** a CITEPH project concerning tightness of salt caverns to the stored hydrogen. In this project we are working with many industrial partners including: TOTALENERGIES; STORENGY; TEREGA; and GEOSTOCK.
- September 2019 to September 2020: **Contribution** to the HyTREND project (Hydrogen for a carbon-free energy transition). It is a Power to X unifying project from the Carnot M.I.N.E.S institute, funded by the ANR.
- September 2018 to August 2020: **Contribution** to the STOPIL project. Title: Development of an industrial pilot for hydrogen storage in a salt caverns in France. Phase 1: feasibility study. This project included working with many industrial partners especially, STORENGY, GEOSTOCK, AIRLIQUIDE, INERIS, and BRGM.
- May 2017 to April 2020: **Contribution** to the ROSTOCK-H project. Title: Risks and opportunities of geological hydrogen storage in salt caverns in France and Europe. This project was held by AIRLIQUIDE, it had another industrial partners including: INERIS, GEOSTOCK, and University of Lorraine.

At the university of Calgary:
Since I enrolled in my PostDoc, I was a member of the Microseismic Industry Consortium (URL). It is a novel applied-research geophysical initiative dedicated to the advancement of research, education and technological innovations in microseismic methods and their practical applications for resource development. This consortium is a team of industry partners, government agencies, and faculty members.

PUBLICATIONS

Papers in peer reviewed journals:

1. **AbuAisha M.**, & **Tayeb F.** (2024). Gas humidification kinetics during cycling in underground salt caverns: A case study of Helium and Methane. *Paper is under preparation*
2. **Tayeb F.**, Rouabhi A., & **AbuAisha M.** (2024). Effect of cycling frequency on kinetics of hydrogen humidification in salt caverns. *Paper is under preparation*
3. **AbuAisha M.**, Rouabhi A., Hadj-Hassen F., Eaton D., **Tayeb F.**, & Valtz A. (2023). Geothermal effects on CO_2 dissolution kinetics in brine: A non-dimensional model for underground storage in salt caverns. Journal of Natural Gas Science and Engineering **(IF 5.3)**, 117, 205076. https://doi.org/10.1016/j.jgsce.2023.205076
4. **Tayeb F.**, Rouabhi A., **AbuAisha M.**, & Valtz A. (2023). Kinetics of CO_2 dissolution for underground applications. Geoenergy Science and Engineering **(IF 5.4)**, 230, 212061. https://doi.org/10.1016/j.geoen.2023.212061
5. **AbuAisha M.**, Rouabhi A., Billiotte J., & Hadj-Hassen F. (2021). Non-isothermal two-phase hydrogen transport in rock salt during cycling in underground caverns. International Journal of Hydrogen Energy **(IF 7.2)**, 46(9): 6632-6647. https://doi.org/10.1016/j.ijhydene.2020.11.152
6. **AbuAisha M.**, & Billiotte J. (2021). A discussion on hydrogen migration in rock salt for tight underground storage with an insight into a laboratory setup. Journal of Energy Storage **(IF 8.9)**, 38, 102589. https://doi.org/10.1016/j.est.2021.102589
7. **AbuAisha M.**, & Rouabhi A. (2019). On the validity of the uniform thermodynamic state approach for underground caverns during fast and slow cycling. International Journal of Heat and Mass Transfer **(IF 5.4)**, 142, 118424. https://doi.org/10.1016/j.ijheatmasstransfer.2019.07.074
8. **AbuAisha M.**, Eaton D., Priest J., Wong R., Loret B., & Kent A.H. (2018). Fully coupled hydro-mechanical controls on non-diffusive seismicity triggering front driven by hydraulic fracturing. Journal of Seismology **(IF 1.6)**, 23, 109-121. https://doi.org/10.1007/s10950-018-9795-0
9. **AbuAisha M.**, Eaton D., Priest J., & Wong R. (2017). Hydro-mechanically coupled FDEM framework to investigate near-wellbore hydraulic fracturing in homogeneous and fractured rock formations. Journal of Petroleum Science and Engineering **(IF 5.4)**, 154, 100-113. https://doi.org/10.1016/j.petrol.2017.04.018
10. **AbuAisha M.**, Loret B., & Eaton D. (2016). Enhanced Geothermal Systems (EGS): Hydraulic fracturing in a thermo-poroelastic framework. Journal of Petroleum Science and Engineering **(IF 5.4)**, 146, 1179-1191. https://doi.org/10.1016/j.petrol.2016.07.027
11. **AbuAisha M.**, & Loret B. (2016). Influence of hydraulic fracturing on impedance and efficiency of thermal recovery from HDR reservoirs. Geomechanics for Energy and the Environment **(IF 5.1)**, 7, 10-25. https://doi.org/10.1016/j.gete.2016.02.001
12. **AbuAisha M.**, & Loret B. (2016). Stabilization of Forced Heat Convection: Applications to Enhanced Geothermal Systems (EGS). Transport in Porous Media **(IF 2.9)**, 112, 229-252. https://doi.org/10.1007/s11242-016-0642-x
13. Plé O., Tourabi A., & **AbuAisha M.**. (2013). 3-Dimensional digital image correlation for strains determination in clayey soil. Applied Mechanics and Materials, 353-356, 463-466.

https://doi.org/10.4028/www.scientific.net/ AMM.353-356.463
14. Plé O., Ha Le T.N., & **AbuAisha M.**. (2011). Landfill clay barrier: fibre reinforcement technique. Advanced Materials Research, 378-379, 780-784. https://doi.org/10.4028/www.scientific.net/AMR.378-379.780

Conferences:

1. **AbuAisha M.**, Rouabhi A., Hadj-Hassen F., Eaton D., **Tayeb F.**, & Valtz A. (2023). Thermal effects on the kinetics of gas dissolution in brine: A case study of CO_2 storage in salt caverns (a non-dimensional model). DECOVALEX 2023, November 2023, Troyes, France.
2. **AbuAisha M.**, Rouabhi A., Billiotte J., & Hadj-Hassen F. (2022). Hydrogen migration in rock salt during cycling in underground caverns. CouFrac2022, November 2022, Berkeley, United States.
3. **AbuAisha M.**, & Rouabhi A. (2022). Is the hypothesis of a uniform thermodynamic state still valid in hydrogen underground caverns during fast cycling? CouFrac2022, November 2022, Berkeley, United States.
4. Hytrend, un projet power to X de l'Institut Carnot M.I.N.E.S. Christian Beauger, Pascaline Pre, Alain Thorel, Anthony Chesnaud, Charly Lemoine, **AbuAisha M.** et al. Énergie renouvelable et ressources, les enjeux de demain : de l'ingénierie aux territoires, Institut Mines-télécom, Avril 2021, France.
5. **AbuAisha M.**, Eaton D., Priest J., & Wong R. (2016). Simulating HF using FDEM: Effects of pre-existing joints, induced microseismicity and fluid diffusion. Seismological Society of America - Annual meeting, April 2016, Reno, United States.
6. **AbuAisha M.**, Eaton D., Priest J., & Wong R. (2016). Simulating hydraulic fracturing using finite-discrete element method (FDEM): Effects of pre-existing joints and lateral stress gradient, Geoconvention 2016, March 2016, Calgary, Canada.
7. **AbuAisha M.**, Eaton D., Priest J., & Wong R. (2015). Review of hybrid continuum / discontinuum methods for geomechanical modelling of hydraulic fracture growth. Geoconvention 2015, May 2015, Calgary, Canada.
8. **AbuAisha M.**, & Loret B. (2016). Stimulation of Geothermal Reservoirs: Impedance and Efficiency of Thermal Recovery. The 40^{th} Workshop on Geothermal Reservoir Engineering, January 2015, Stanford, CA, United States.
9. **AbuAisha M.**, & Loret B. (2014). Permeability enhancement of HDR reservoirs by hydraulic fracturing. The 14^{th} International Conference of the International Association for Computer Methods and Advances in Geomechanics, September 2014, Kyoto, Japan.

Invited communications:

1. **AbuAisha M.** (2019). Hydraulic fracturing for geothermal and petroleum applications: Continuum/ discontinuum approaches. Seminar at the Karlsruhe Institute of Technology - KIT, May 2019, Karlsruhe, Germany.
2. **AbuAisha M.** (2014). Enhanced Geothermal Systems (EGS): Permeability Stimulation Through Hydraulic Fracturing in a Thermo-Poroelastic Framework. Seminar at the University of Seoul, August 2014, Seoul, South Korea.

Books and book chapters:

1. **AbuAisha M.** (2017). Geothermal reservoir stimulation using the finite element method. Éditions Universitaires Européennes, 978-3330872134.
2. **AbuAisha M.**, Eaton D., Priest J., & Wong R. (2016). Finite discrete element framework for investigating the effect of temperature-dependent dynamic viscosity on hydraulic fracturing. Microseismic Industry Consortium: Annual Research Report, Volume 7.
3. **AbuAisha M.**, Eaton D., Priest J., & Wong R. (2016). Hydraulic fracture growth and migration of induced microseismicity: Application of a fully coupled hydromechanical FDEM approach. Microseismic Industry Consortium: Annual Research Report, Volume 7.

4. **AbuAisha M.**, Eaton D., Priest J., & Wong R. (2016). Simulating hydraulic fracturing using Finite-Discrete Element Method (FDEM): Effects of pre-existing joints and induced seismicity. Microseismic Industry Consortium: Annual Research Report, Volume 6.
5. Eaton D., Mason Mackay, Anton Biryukov, & **AbuAisha M.** (2016). Identifying critically stressed faults without triggering slip: A discussion. Microseismic Industry Consortium: Annual Research Report, Volume 6.
6. **AbuAisha M.**, Eaton D., Priest J., & Wong R. (2015). Finite/Discrete Element Method (FDEM) by Y-Geo: An overview. Microseismic Industry Consortium: Annual Research Report, Volume 5.
7. **AbuAisha M.**, Eaton D., Priest J., & Wong R. (2015). Hydraulic fracture simulation using the GEOS code. Microseismic Industry Consortium: Annual Research Report, Volume 5.

Appendix B

Selected publications

Journal of Petroleum Science and Engineering 146 (2016) 1179–1191

Contents lists available at ScienceDirect

Journal of Petroleum Science and Engineering

journal homepage: www.elsevier.com/locate/petrol

Enhanced Geothermal Systems (EGS): Hydraulic fracturing in a thermo-poroelastic framework

Murad AbuAisha [a,*], Benjamin Loret [b], David Eaton [c]

[a] Departments of Civil Engineering and Geoscience, University of Calgary, Alberta, Canada
[b] Laboratoire 3S–R, Université de Grenoble, Grenoble, France
[c] Department of Geoscience, University of Calgary, Alberta, Canada

ARTICLE INFO

Article history:
Received 20 October 2015
Received in revised form
25 May 2016
Accepted 25 July 2016
Available online 26 July 2016

Keywords:
Hydraulic fracturing
Fracture fabric
Permeability enhancement
Thermo-poroelasticity
Thermal recovery

ABSTRACT

The natural permeability of geothermal reservoirs is typically low and therefore needs to be enhanced to enable efficient use and economic viability. Hydraulic Fracturing (HF) methods, often referred to as hydraulic stimulation, are one of the primary methods used for permeability enhancement. In this research paper, physical processes associated with HF are simulated within a thermo–poroelastic (THM) framework. A fracturing model is introduced as a novel component to the THM framework. This fracturing model is expressed in terms of Terzaghi's effective stress and it governs fracture length and aperture evolution in all directions of space. The distribution and properties of new fractures are used in a parametric analysis to calculate anisotropic fracture-induced permeability tensor at each point in the computational grid. Mechanical, hydraulic, and thermal effects interact in different ways at the vicinity of the inlet and of the outlet. Our results show that thermal cooling primarily contributes to the fracturing process within a zone close to the inlet. In addition, injection pressure and/or flow rate must be increased during the lifetime of the reservoir to compensate for pressure drop caused by increased aperture due to fracture growth.

We tested our fracturing model at the laboratory scale using observations from a homogeneous triaxial test. The model is then integrated into an in–house FORTRAN 90 finite element code that solves the thermo–poroelastic boundary value problem. Numerical simulations for fluid circulation and thermal recovery at the geothermal reservoir of Soultz-sous-Forêts are performed using the fully integrated code.

As expected, at early times heat convection controls the spatial progression of the effective stresses and hydraulic permeability from inlet to outlet. However, the enhancement of permeability due to HF causes a rapid propagation of the heat front in the reservoir. Therefore, the applied injection flow rate effectively controls the evolution of the hydraulic permeability at moderate-to-long times of the HF process. The borehole stability against shear failure is also investigated.

1. Introduction

Geothermal energy is produced by injecting cold fluids into Hot Dry Rock (HDR) reservoirs where temperature gradients are favourable. At the reservoir depth, fluid pressure, effective stresses, rate of fluid loss and thermal recovery are all controlled by the thermo–poroelastic mechanisms (Bruel, 1995a, 1995b). One of the most important factors affecting thermal recovery from HDR reservoirs is the permeability of the fractured medium. Natural HDR reservoirs have low permeability; consequently, the process of injecting geothermal fluids is hindered by large amounts of fluid loss and frustratingly inefficient thermal recovery. Modern geothermal projects are focused on enhancing the permeability of geothermal reservoirs, as emphasized by the term Enhanced Geothermal Systems (EGS). The two main technologies that are currently deployed to extract geothermal energy are hydraulic fracturing and chemical enhancement (Turcotte and Schubert, 2002).

Hydraulic fracturing is implemented by pumping geothermal fluids at considerable flow rates which will eventually lead reservoir fractures to evolve and connect. Representation of thermal recovery from a single fracture embedded in a geothermal reservoir has been developed by Cheng et al. (2001). This approach has been further pursued by Zhou et al. (2009) and Ghassemi et al. (2008) in an investigation of the thermoelastic and poroelastic effects of cold water injection.

Studies that focus on the evolution of HDR reservoir

* Correspondence to: Previously at Université de Grenoble.
E-mail addresses: morad_77_2@hotmail.com (M. AbuAisha), Benjamin.Loret@3sr-grenoble.fr (B. Loret), eatond@ucalgary.ca (D. Eaton).

http://dx.doi.org/10.1016/j.petrol.2016.07.027
0920-4105/

permeability under thermo–poroelastic conditions are scarce. Among the few contributions to this topic, in the context of single fracture reservoirs, Lee and Ghassemi (2011) adopt empirical relationships to relate permeability to effective stresses. Although previous studies are indicative, they do not address the effect of HF on the stability of geothermal boreholes, nor do they study the dependence of HF process on the geostatic conditions prevailing at the reservoir level.

For the purpose of fully describing HF in HDR reservoirs, this study introduces a fracturing model which is integrated into a fully coupled thermo–poroelastic framework (AbuAisha, 2014). At any geometrical point and at any time, this fracturing model is capable of tracking the directional fracture evolution. Indeed, the investigated fracture fabric accounts for both the length and the aperture of fractures over a unit sphere. The updated fracture properties are used to calculate local fluid velocity fields using Navier–Stokes equation for laminar flow. A macroscopic anisotropic permeability tensor, that describes the hydraulic connectivity of the hydraulically fractured medium, is then calculated by applying Darcy's law at each fracture. The thermo-poroelastic model with an evolving hydraulic permeability is implemented in an in–house finite element code (AbuAisha, 2014). The primary variables consist of the solid displacement vector, the fluid pressure, and the temperature.

Circulation tests between two vertical wells separated by a horizontal distance of 450 m are simulated. Thermal recovery from HDR reservoirs can be increased by enhancing geothermal fluid circulation, i.e. increasing the reservoir permeability between injection and production wells. However, the increase of permeability results in shorter periods of economic viability of the geothermal system which will be further discussed in the conclusion of this paper.

Attention is also paid to stability issues associated with the shear failure of the borehole case–shoe. Borehole stability is to be guaranteed in order to achieve a safe HF process of the HDR reservoirs.

2. Thermo-poroelastic framework

The mechanical response of a poroelastic medium undergoing thermal changes while in local thermal equilibrium is governed by two constitutive equations. Two additional equations are needed to define the transport of fluid and the transfer of heat.

2.1. Mechanical constitutive equations

Biot's effective stress of the mixture $\boldsymbol{\sigma} + \kappa p\mathbf{I}$ is expressed in terms of the mechanical strain tensor $\boldsymbol{\varepsilon}$, and of the temperature departure $\theta = T - T_0$ with respect to a reference T_0 as (McTigue, 1986),

$$\boldsymbol{\sigma} + \kappa p\mathbf{I} = 2G\boldsymbol{\varepsilon} + \frac{2G\nu}{1-2\nu}\mathrm{tr}\boldsymbol{\varepsilon}\mathbf{I} - K\alpha_s'\theta\mathbf{I}, \tag{1}$$

where $\boldsymbol{\sigma}$ is the total stress tensor (Pa), p is the pore fluid pressure (Pa), $\mathrm{tr}\boldsymbol{\varepsilon}$ is the volumetric strain, G is the shear modulus (Pa), ν is the drained Poisson's ratio, $\kappa = 1 - K/K_s'$ is the Biot's coefficient, K is the drained bulk modulus (Pa), K_s' is the first bulk modulus of the solid constituent (Pa), α_s' is the first cubical thermal expansion coefficient of the solid ($1/^\circ$C), and $\mathbf{I}$ is the second order identity tensor. The sign convention through this paper attributes negative sign to contractive strains and compressive stresses.

The change of the fluid mass content,

$$\zeta = \kappa\mathrm{tr}\boldsymbol{\varepsilon} + \frac{p}{M} - \bar{\alpha}\theta, \tag{2}$$

involves mechanical, fluid and thermal contributions, with coefficients,

$$\frac{1}{M} = \frac{\kappa}{K_s'} + \phi_0\left(\frac{1}{K_f} - \frac{1}{K_s''}\right),$$
$$\bar{\alpha} = \kappa\alpha_s' + \phi_0\left(\alpha_f - \alpha_s''\right), \tag{3}$$

that feature the second cubical thermal expansion coefficient of the solid α_s'' ($1/^\circ$C), the cubical thermal expansion coefficient of the fluid α_f ($1/^\circ$C), the second bulk modulus of the solid constituent K_s''[1] (Pa), the bulk modulus of the fluid K_f (Pa), and the reference porosity of the mixture ϕ_0. Throughout this paper, the subscripts s and f refer to the solid and fluid constituents respectively.

2.2. Constitutive equations of fluid transport and heat transfer

The constitutive equation of Darcy that describes fluid seepage through the porous medium relates the apparent fluid flux relative to the solid skeleton $\boldsymbol{q}_f$ (m/s) to the fluid pressure gradient,

$$\boldsymbol{q}_f = \phi_0(\boldsymbol{v}_f - \boldsymbol{v}_s) = -\frac{\boldsymbol{k}}{\mu}\cdot(\nabla p - \rho_f\boldsymbol{g}), \tag{4}$$

where $\boldsymbol{k}$ is the permeability tensor of the mixture (m^2), μ is the fluid dynamic viscosity (Pa × s), ρ_f is the intrinsic fluid density ($\mathrm{kg/m}^3$), and $\boldsymbol{g} = g\boldsymbol{e}$ with g being the gravitational acceleration ($\mathrm{m/s}^2$) and $\boldsymbol{e}$ the unit vertical vector directed downwards.

According to Fourier's law of heat conduction, the heat flux $\mathbf{q}_\theta$ (W/m) is related to the negative of temperature gradient $\nabla\theta$ through the effective thermal conductivity k_θ,

$$\mathbf{q}_\theta = -k_\theta\nabla\theta, \tag{5}$$

where we have assumed the porous medium to be in local thermal equilibrium, and consequently the effective thermal conductivity $k_\theta = (1-\phi_0)k_{\theta s} + \phi_0 k_{\theta f}$ (W/m/°C) is obtained by volume averaging over the constituents. Although the analysis focuses on the evolving anisotropy of the permeability tensor, the thermal conductivity of the solid remains isotropic and constant.

2.3. Field equations

The displacement vector, the pore fluid pressure, and the temperature are constrained to satisfy the partial differential equations of the balance of momentum of the whole mixture, of the balance of mass of the fluid, and of the balance of energy of the mixture, according to:

$$\begin{aligned}
&\nabla\cdot\boldsymbol{\sigma} + \boldsymbol{f} = \boldsymbol{0}, \quad \text{balance of momentum,}\\
&\nabla\cdot\boldsymbol{q}_f + \frac{\partial\zeta}{\partial t} = 0, \quad \text{balance of fluid mass,}\\
&\nabla\cdot\mathbf{q}_\theta + \rho c_v\frac{\partial\theta}{\partial t} + \rho_f c_{pf}\boldsymbol{q}_f\cdot\nabla\theta = 0, \quad \text{balance of energy.}
\end{aligned} \tag{6}$$

In these expressions, $\boldsymbol{f} = \rho\boldsymbol{g}$ is the vector of the body forces, with $\rho = (1-\phi_0)\rho_s + \phi_0\rho_f$ being the mass density of the mixture. Exchange of fluids between distinct types of porosities or by phase change is not considered in this paper. The mechanical contribution and the volume heat source have been neglected in the energy equation. The heat storage contribution is expressed in terms of the volumetric isochoric heat capacity of the mixture, $\rho c_v = (1-\phi_0)\rho_s c_{vs} + \phi_0\rho_f c_{vf}$ ($\mathrm{J/m}^3/^\circ$C), which is obtained by volume averaging over the constituents. The energy equation features the convection of heat, due to fluid diffusion in the porous medium, by

[1] In the applications of this research, we shall use the simplifications $K_s' = K_s'' = K_s$ and $\alpha_s'' = \alpha_s' = \alpha_s$.

introducing the isobaric heat capacity of the fluid, i.e. $\rho_f c_{pf} = \rho_f c_{vf} + K_f \alpha_f^2 T$. If the convective term is neglected, the balance of energy equation can be decoupled from the system of equations and solved independently. However, a fully coupled thermo–poroelastic framework is adopted in this work.

2.4. Finite element formulation

An in–house FORTRAN 90 mixed finite element code has been developed to simulate thermo–poroelastic Transient Boundary Value Problems (TBVPs). The primary unknowns are the displacement vector $\boldsymbol{u}$, the pore pressure p, and the change of the mixture temperature θ. Within a generic element e, the primary unknowns are interpolated through the shape functions $\boldsymbol{N}_u$, $\boldsymbol{N}_p$ and $\boldsymbol{N}_\theta$,

$$\boldsymbol{u} = \boldsymbol{N}_u \boldsymbol{u}^e, \quad p = \boldsymbol{N}_p \boldsymbol{p}^e, \quad \theta = \boldsymbol{N}_\theta \boldsymbol{\theta}^e. \tag{7}$$

A generalized Galerkin scheme is adopted and the same interpolation functions are used for the primary unknowns and their variations. A special treatment is required for the convection term AbuAisha, 2014; Ch. 6 and AbuAisha and Loret (2016). Multiplying the field equations by the virtual fields $\delta\boldsymbol{u}$, δp and $\delta\theta$ and integrating by parts over the body V provides the weak form of the problem,

$$\begin{aligned}
&\int_V \nabla(\delta\boldsymbol{u}) : \dot{\boldsymbol{\sigma}}\, dV - \int_V \delta\boldsymbol{u}\cdot\boldsymbol{f}\, dV &&= \int_{\partial V} \delta\boldsymbol{u}\cdot\dot{\boldsymbol{\sigma}}\cdot\boldsymbol{n}\, ds,\\
&\int_V \nabla(\delta p)\cdot\left(-\boldsymbol{q}_f\right) dV + \int_V \delta p\, \dot{\zeta}\, dV &&= \int_{\partial V} \delta p\left(-\boldsymbol{q}_f\right)\cdot\boldsymbol{n}\, ds,\\
&\int_V \nabla(\delta\theta)\cdot\left(-\mathbf{q}_\theta\right) dV + \int_V \delta\theta\left(\rho c_v \dot{\theta} + \rho_f c_{pf} \boldsymbol{q}_f\cdot\nabla\theta\right) dV &&= \int_{\partial V} \delta\theta\left(-\mathbf{q}_\theta\right)\cdot\boldsymbol{n}\, ds,
\end{aligned} \tag{8}$$

where $\boldsymbol{n}$ is the unit outward normal to the boundary ∂V, and the superimposed dot denotes a partial time derivative.

Introducing the discretization (7) in the weak form (8) and assembling the element contributions yields a global non–linear system of equations,

$$\mathbb{D}\dot{\mathbb{X}} + \mathbb{K}\mathbb{X} + \mathbb{C}\mathbb{X} = \mathbb{F}, \tag{9}$$

where $\mathbb{X} = \left[\boldsymbol{u}\ p\ \theta\right]^T$ is the vector of the nodal unknowns, $\mathbb{D}$ is the diffusion matrix, $\mathbb{K}$ is the stiffness matrix, $\mathbb{C}$ is the convection matrix, and the Right-Hand-Side (RHS) vector $\mathbb{F}$ gathers the boundary and volume loadings. Details of the element vectors and matrices are provided in Appendix A.

The semi-discrete equations are integrated over time using a predictor multi-corrector method based on a generalized trapezoidal scheme defined by the scalar $\alpha \in\ ]0, 1]$ AbuAisha, 2014, Ch. 3.

3. Hydraulic fracturing (HF): the model of fracture propagation

In a poroelastic medium, HF can be defined as the process of causing fractures to propagate due to fluid injection. Normally the process of HF is suppressed by the confining stresses stemming from the surroundings. HF is in practice achieved by pumping pressurized fluid to a point the maximum principal effective Terzaghi's stress becomes tensile and exceeds the tensile strength of the rock. HF is henceforth used in a manner that is synonymous with tensile failure of the rock material.

3.1. The thermo-elastic effect on HF

Thermally induced fracturing is a phenomenon observed while injecting cold water into a hot rock layer. The constitutive Eq. (1), which describes the thermo–mechanical response of a saturated porous medium subjected to a thermal strain $\boldsymbol{\varepsilon}^\theta$, can be expressed

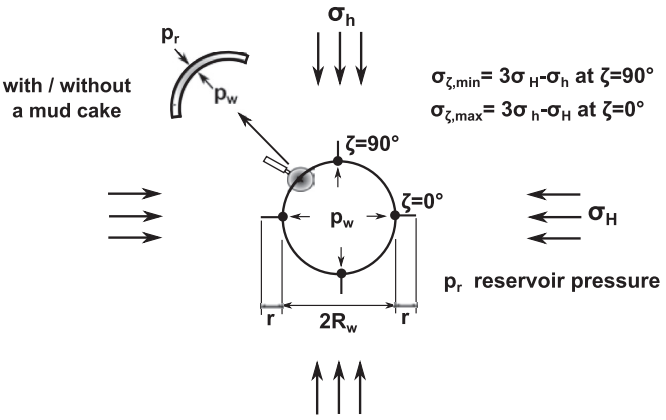

Fig. 1. Vertical wellbore with vertical fractures. Wellbore wall may/may not be lined with a mud cake.

in a compact form,

$$\boldsymbol{\sigma} + \kappa p \mathbf{I} = \boldsymbol{E} : (\boldsymbol{\varepsilon} - \boldsymbol{\varepsilon}^\theta), \tag{10}$$

with $\boldsymbol{E} = (E_{ijkl})$ being the drained elastic tensor. If the porous medium is sufficiently permeable that the diffusion of fluid happens much faster than the diffusion of heat, i.e. the common case when simulating real EGS reservoirs, the term κp can be assumed constant during the cooling period. As a simplification, one may also imagine some restraint on the boundaries freezing the total strain $\boldsymbol{\varepsilon}$. Thus while cooling, the stress associated with the thermal strain tends to become tensile.

3.2. Hydraulic fracturing model (HFM)

This section describes a fracturing model which is capable of ensuring a directionally stable mode I of fracture evolution.

3.2.1. Fracture initiation

To illustrate the concept of fracture initiation, let us consider the following situation presented in Fig. 1. The figure depicts a vertical borehole penetrating a rock formation, which is homogeneous and isotropic in its elastic and transport properties.

Let us assume the far field stresses to be such that the vertical stress is more compressive than the horizontal stresses, i.e. $-\sigma_v > -\sigma_H > -\sigma_h$. As the injection of cold fluid starts, the wellbore pressure p_w increases, and the rock formation cools down leading to a more tensile Terzaghi's effective tangential stress σ'_ζ in the rock formation. With T_c being the material tensile strength, the condition for HF initiation reads (Fjaer et al., 2008),

$$\sigma'_\zeta = T_c. \tag{11}$$

In the presence of a mud cake, the borehole overpressure

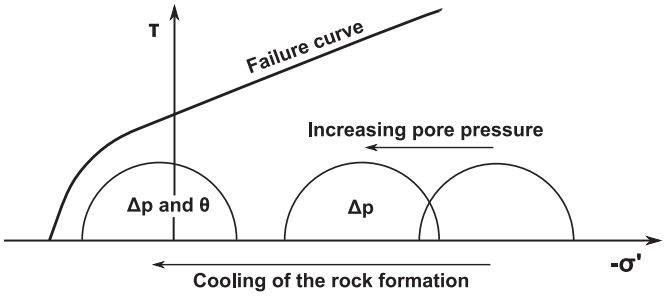

Fig. 2. Mohr circles and failure curve: The effect of increasing pore pressure and decreasing temperature on HF.

required to create the hydraulic fracturing in the direction of the maximum geostatic stress is expressed as in AbuAisha (2014) and Fjaer et al. (2008),

$$p_w^{HF} - p_r^{\infty} = \sigma_H - 3\sigma_h - p_r^{\infty} + \frac{E}{1-\nu}\frac{\alpha_s}{3}\theta + T_c, \tag{12}$$

with θ being the temperature change in the rock near the wellbore and p_r^{∞} the geostatic rock formation pressure.

In the absence of a mud cake and if the pressurization rate is slow enough to ensure steady state conditions during pumping, the overpressure required to create hydraulic fracturing is instead given by Fjaer et al. (2008),

$$p_w^{HF} - p_r^{\infty} = (1-\nu)\left(\sigma_H - 3\sigma_h - p_r^{\infty} + \frac{E}{1-\nu}\frac{\alpha_s}{3}\theta + T_c\right) + \nu p_r^{\infty}. \tag{13}$$

Similar expressions to the fracturing thresholds (Eqs. (12) and (13)) have been documented by Haimson and Fairhurst (1967). Yet, the latter assume the formation to remain elastic everywhere while our expressions use an alternative assumption of fully developed plasticity. As expected, large longitudinal geological stress σ_H, large formation pressure and cooling ease fracturing. Meanwhile, large transversal confinement σ_h and high tensile strength oppose fracturing. Since fracturing is phrased in terms of Terzaghi's effective stress, Eqs. (12) and (13) are derived by formally setting Biot's coefficient to 1 (Fjaer et al., 2008). Note that the pressurization of a medium with permeability smaller than 10^{-18} m^2 is considered equivalent to a HF process in a wellbore lined with a mud cake. Meanwhile porous media with permeability larger than 10^{-18} m^2 are considered permeable and the limit for pressurization without a mud cake shall apply (Fjaer et al., 2008).

In summary, HF technique in EGS is illustrated in Fig. 2. As the injection of cold water begins, the effective geostatic stresses start to decrease. Temperature change (cooling) helps to mitigate the compressive geostatic stresses as well. If pressurization and cooling continue to a point the largest principal Terzaghi's effective stress becomes tensile and exceeds the tensile strength of the rock material, fracturing takes place.

3.2.2. Fracturing criterion

Let us consider again a vertical borehole (Fig. 1) with a group of fractures of average length ℓ and arbitrary normal direction $\boldsymbol{n}$ in the horizontal plane. If the wellbore pressure is gradually increased to a point the normal Terzaghi's effective stress (at the fracture tip) $\sigma_n' = \boldsymbol{n}\cdot\boldsymbol{\sigma}'\cdot\boldsymbol{n}$ becomes tensile and exceeds the limit of material tensile strength, the group of fractures starts propagating and consequently their average aperture increases. An elementary criterion to examine fracture initiation and to track the propagation of the group of fractures in the direction $\boldsymbol{n}$ is adopted,

$$F(\sigma_n', \ell) = f(\ell)\sigma_n'\sqrt{\pi\ell} - K_{Ic} = 0, \tag{14}$$

where K_{Ic} is the material toughness for mode I of fracturing (Pa m$^{0.5}$). The positive scalar valued function $f(\ell)$ controls the kinetics of fracture propagation. This function decreases as the fractures begin to propagate leading to the relaxation of local tensile stresses as the fractures grow away from the zone of stress concentration: this feature ensures the stable growth of fractures. As the fractures start to coalesce, the function $f(\ell)$ reaches an asymptotic value that marks the onset of damage localization and macroscopic failure. The following expression is adopted (Shao et al., 2005),

$$f(\ell) = \eta\begin{cases}\dfrac{\ell_f}{\ell}, & \ell < \ell_f;\\ 1, & \ell \geq \ell_f,\end{cases} \tag{15}$$

where ℓ_f denotes the critical fracture length for accelerated coalescence of microfractures, and η is the fracture growth stabilizing parameter. The rate loading-unloading relationship for a propagating fracture of normal direction $\boldsymbol{n}$ is defined according to the Kuhn-Tucker conditions,

$$\dot{\ell} \geq 0, \quad F(\sigma_n', \ell) \leq 0, \quad \dot{\ell}F(\sigma_n', \ell) = 0. \tag{16}$$

While the constitutive Eq. (14) governs the evolution of the

Table 1
Fracture lengths and apertures for granite gathered from literature.

Average fracture length ℓ (m)	Average fracture aperture w (mm)	Reference
0.006	0.03	Shao et al. (2005)
1.2	0.45	Papanastasiou and Thiercelin (1993)
25	0.50	Bruel (2002)
30	0.18	Rejeb and Bruel (2001)
40	0.32	Kohl and Mégel (2007)

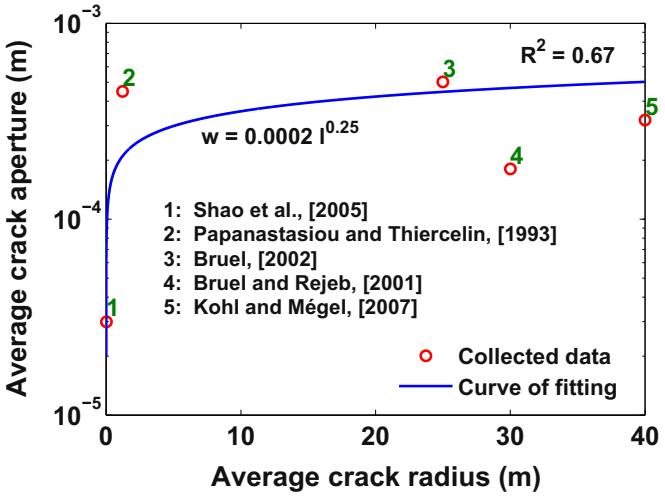

Fig. 3. The relation between the fracture average aperture w and the average length ℓ. Scattered data are collected from five references (Table 1). A power fitting curve (Eq. (17)) with $R^2 = 0.67$ is adopted to represent the data.

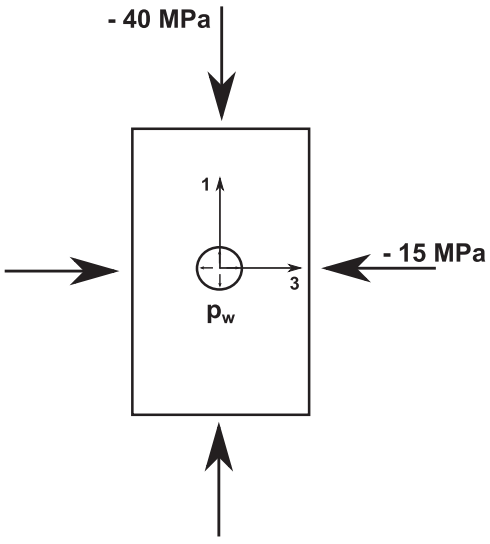

Fig. 4. Parallelepiped sample of the Lac du Bonnet granite subjected to a triaxial stress state with an out of plane stress equal to −10 MPa. The sample is drilled at its center where fluid is injected.

Table 2
Parameters used in testing the HF Model (HFM).

Nature	Parameter	Value	Unit	Reference
Elasticity	Drained Young's modulus E	68	GPa	Shao et al. (2005)
	Drained Poisson's ratio ν	0.21	–	"
Fracture	Initial length of fractures ℓ_0	3.0	mm	Shao et al. (2005)
	Final length of fractures ℓ_f	9.0	mm	"
	Material tensile strength T_c	8.3	MPa	Atkinson (1991)
	Material toughness K_{Ic}	1.87	MPa$\sqrt{m}$	"
	Fracture growth stabilizing parameter η	1.6	–	Parameterized
	Fracture density	2×10^6	$1/m^3$	Shao et al. (2005)
Flow	c_c	0.0001	–	Shao et al. (2005)
	Initial permeability k_0	10^{-21}	m^2	"

fracture length, the change of the fracture width must also be considered. Authors like Klimczak et al. (2010), Shao et al. (2005) and Papanastasiou and Thiercelin (1993) have related the normal increment of fracture aperture w to local grain matrix interaction during fracture growth. Kohl and Mégel (2007) introduce a dilatation angle as well. Following AbuAisha (2014, Ch. 2), the normal fracture aperture is assumed a power function of the fracture length,

$$w(\ell) = 0.0002\ell^{0.25}, \tag{17}$$

where both ℓ and w are measured in meters. This expression (Eq. (17)) fits the data collected from literature in (Table 1) and presented in Fig. 3 for millimetric to metric fractures.

Fracture length and aperture are key ingredients to define Darcy's law. Indeed, at any geometrical point, fractures may develop in any spatial direction $\boldsymbol{n}$. Individual fractures are viewed as channels with plane parallel boundaries. The total permeability provided by the fractures $\boldsymbol{k}_c$ is obtained by averaging the individual Poiseuille flows over the considered spatial directions while assuming a local uniform pressure gradient (Shao et al., 2005),

$$\boldsymbol{k}_c = \frac{1}{48}\frac{N}{V}\int_{\mathbb{S}^2} C(\ell(\boldsymbol{n}))w^3(\boldsymbol{n})\ell^2(\boldsymbol{n})(\mathbf{I} - \boldsymbol{n}\otimes\boldsymbol{n})\, dS, \tag{18}$$

where N/V is the fracture density, i.e. number of fractures per unit volume of rock. A connectivity coefficient,

$$C(\ell(\boldsymbol{n})) = c_c\frac{\ell(\boldsymbol{n}) - \ell_0}{\ell_f - \ell_0}, \tag{19}$$

has been introduced as a crude attempt to indicate that connectivity between fractures increases as the fractures grow in size from the initial value ℓ_0 to the maximum value ℓ_f which signals macroscopic failure. It also involves the dimensionless positive constant c_c which depends on the microstructure of the damaged material and remains to be determined.

The overall permeability tensor of the fractured medium is composed of two parts: the initial permeability tensor denoted as $\boldsymbol{k}_0$ due to the initial porosity, which does not evolve in this analysis, and the fracture–induced permeability tensor denoted by $\boldsymbol{k}_c$. The flows in the two cavities are assumed to take place in parallel and the total permeability tensor is obtained by summation, i.e. $\boldsymbol{k} = \boldsymbol{k}_0 + \boldsymbol{k}_c$.

4. Validation of the HFM against laboratory tests

The mechanism of the previously presented HFM is considered in this section. The simulations of permeability enhancement are validated against the experimental data of Souley et al. (2001) for the Lac du Bonnet granite.

A parallelepiped sample of the Lac du Bonnet granite is drilled at its center where pressurized fluid is injected. While allowing drainage on the boundaries, the sample is subjected to the stress state shown in Fig. 4. Table 2 shows the values of all the parameters used in the simulations.

Drainage at the outer surfaces is allowed, and the initial sample pressure p_r before starting to pump the fluid is zero. The initial permeability of the sample is very low ($k_0 = 10^{-21}$ m^2). Thus, the value of pore pressure required to initiate hydraulic fracturing is calculated based on Eq. (12), i.e. $p_w^{HF} - 0.0 = 13.3$ MPa. Consequently, the fracture growth stabilizing parameter η is determined such that the fractures start propagating at the pumping pressure $p_w^{HF} = 13.3$ MPa. Fig. 5(a) shows that most of the change in the permeability tensor components k_{11} and k_{33} takes place within the interval $p_w \in [15, 24]$ MPa. The ratio k_{11}/k_{33} of the components along the axial and lateral directions depends strongly on the anisotropy of the stress field (Fig. 5(b)). It reaches an early maximum value of about 1.6 but later tends to 1 as the pore pressure

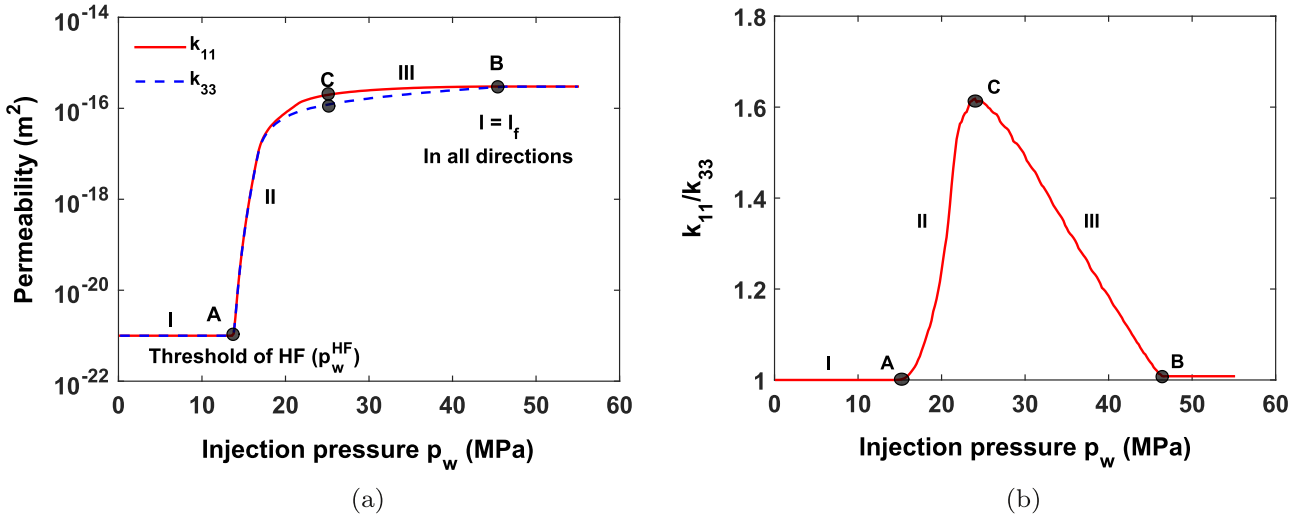

Fig. 5. (a) Permeability evolution in the axial and lateral directions at increasing pumping pressure in a parallelepiped sample of Lac du Bonnet granite (Fig. 4). (b) Variation of the ratio k_{11}/k_{33} with the pumping pressure.

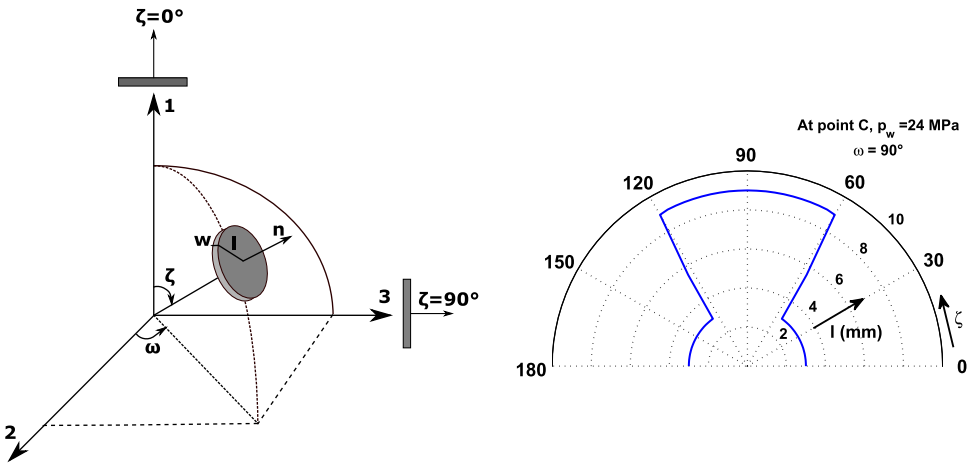

(a) $\zeta - \omega$ position of a fracture of length $\ell(\boldsymbol{n})$ (b) Rose diagram of fracture length

Fig. 6. Directional evolution of fracture length at point C (Fig. 5(a)) with wellbore pressure $p_w = 24$ MPa. (a) $\zeta - \omega$ position of a fracture of length $\ell(\boldsymbol{n})$, (b) Rose diagram of fracture length.

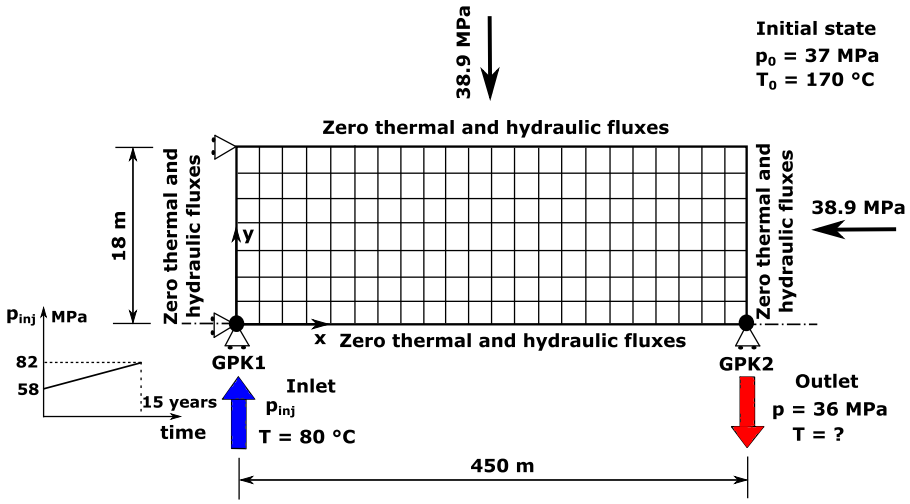

Fig. 7. Mesh, boundary and initial conditions used for the simulations of the HF process at Soultz–sous–Forêts (figure is not to scale).

Table 3
Material properties of Soultz-sous-Forêts reservoir as investigated by Evans et al. (2009). † The initial permeability is typical for granite (Taron and Elsworth, 2009).

Property	Value	Unit
Drained Young's modulus E	54	GPa
Drained Poisson's ratio ν	0.25	–
Bulk modulus of solid grains K_s	50	GPa
Bulk modulus of fluid K_f	2.2	GPa
Dynamic viscosity of fluid μ	3×10^{-4}	Pa × s
Porosity ϕ_0	0.1003	–
Initial permeability† k_0	6.8×10^{-15}	m^2
Solid thermal conductivity $k_{\theta s}$	2.49	W/m/K
Fluid thermal conductivity $k_{\theta f}$	0.6	W/m/K
Solid heat capacity at constant volume c_{vs}	1000	J/kg/K
Fluid heat capacity at constant volume c_{vf}	4200	J/kg/K
Density of solid ρ_s	2910.2	kg/m^3
Unit weight of water γ_f	9800	N/m^3
Cubical thermal expansion of the solid α_s	7.5×10^{-6}	K^{-1}
Cubical thermal expansion of the fluid α_f	1×10^{-3}	K^{-1}

Table 4
Parameters used in the HFM.

Nature	Parameter	Value	Unit	Reference
Fracture	Initial length of fractures ℓ_0	15.0	cm	Evans et al. (2009)
	Final length of fractures ℓ_f	55.0	cm	"
	Material tensile strength T_c	8.3	MPa	Atkinson (1991)
	Material toughness K_{Ic}	1.87	$MPa\sqrt{m}$	"
	Fracture growth stabilizing parameter η	0.04	–	Parameterized
	Fracture density	10^6	$1/m^3$	Bruel, (1995b)

dominates with respect to the applied stress (point B of Fig. 5(b)). This effect is attributed to the fact that the model does not introduce an interaction between fractures.

Fig. 6 shows the directional evolution of the fracture length at the vertical plane $\omega = 90°$ and at a pumping pressure $p_w = 24$ MPa. It is

observable that there is a preferential evolution for fractures oriented in the direction of maximum principal stress −40 MPa with $\zeta = 90°$. Consequently, k_{11} increases significantly in region II as shown in Fig. 5(b): at point C, most of the fractures contributing to the component k_{11} are connected. However, fractures in other orientations continue to grow slowly contributing to the component k_{33}: at point B, fractures in all spatial directions reach the final length ($\ell = \ell_f$), and permeability anisotropy vanishes due to the domination of pore fluid pressure (45 MPa) over the applied stresses. The maximum values of the permeability tensor components shown in Fig. 5(a), k_{11} and k_{33}, are almost equal to the values obtained when this rock is driven to failure under compression (Souley et al., 2001).

5. Simulations of hydraulic fracturing tests at the reservoir scale

The HDR reservoir of Soultz-sous-Forêts is chosen for investigation of our HF model. Here, the HF process is achieved by injecting cold water in a central well, and the hot water is then retrieved via two symmetrically–located production wells.

5.1. Geometry and material properties

Due to symmetry, only a quarter of the reservoir volume is simulated (Fig. 7). The boundary conditions and time course of injection pressure are displayed on the figure as well. Injection is implemented over a period of 15 years as the purpose is to hydraulically enhance the entire volume for the reservoir during the HDR life–time/full production. The nature of the hydraulic and thermal boundary conditions is scrutinized in the work of AbuAisha (2014, Ch. 5). The horizontal finite element mesh is composed of 300 bilinear quadrilateral (Q4) elements, 10 elements in y-direction and 30 elements in x-direction. Cold water is injected from the well GPK1 and left to travel through the geothermal reservoir before it is retrieved at the production well GPK2 450 m away. The size of the reservoir in y-direction is not arbitrary, it is chosen based on the description of Evans et al. (2009).

Poroelastic and thermoelastic properties of the rock formation are gathered in (Table 3). Material properties for the HF model are set in (Table 4).

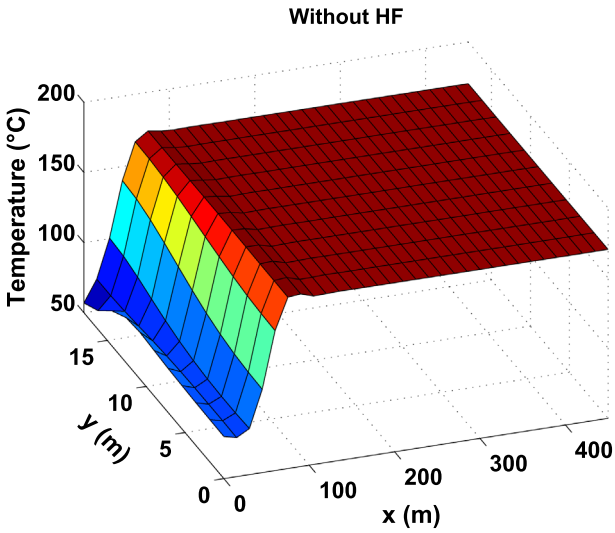

(a) Temperature contours at year 1, no HF

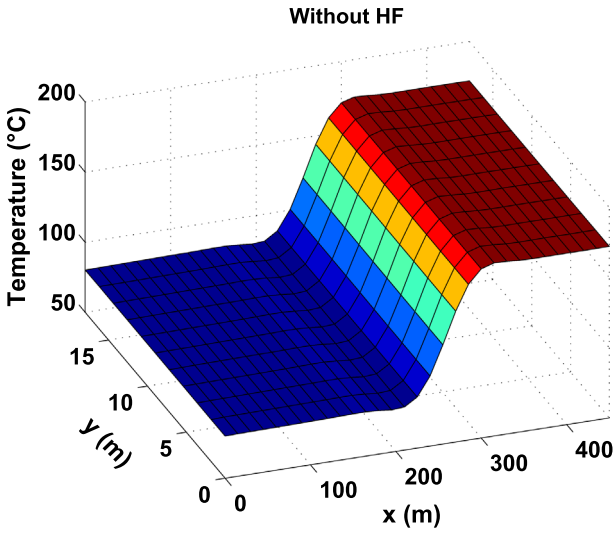

(b) Temperature contours at year 5, no HF

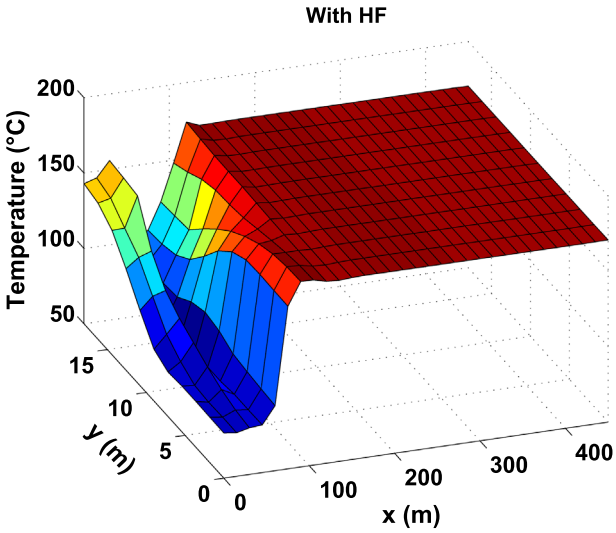

(c) Temperature contours at year 1 with HF

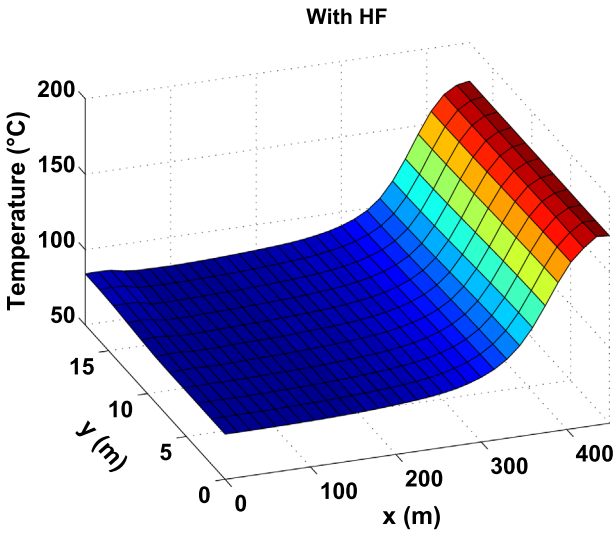

(d) Temperature contours at year 5 with HF

Fig. 8. Contours of the reservoir temperature at two times with/without HF. Hydraulic fracturing clearly speeds up temperature diffusion through convection. (a) Temperature contours at year 1, no HF, (b) Temperature contours at year 5, no HF, (c) Temperature contours at year 1 with HF, (d) Temperature contours at year 5 with HF.

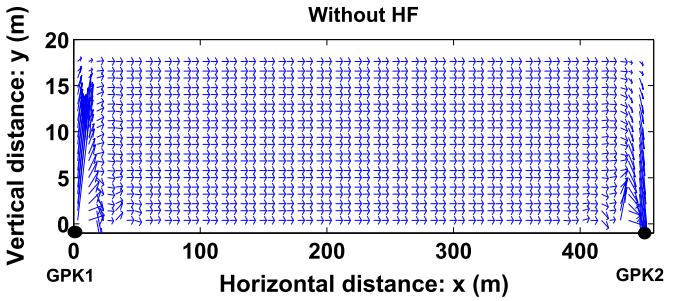

Fig. 9. Scaled fluid velocity vectors at year 1 without HF. The velocity field is not homogeneous in the neighborhood of the wells. However the average velocity of the formation fluid is about $|\boldsymbol{v}| \sim v_x = 9.46 \times 10^{-7}$ m/s.

The initial fracture length ℓ_0 is determined based on the study of Evans et al. (2009) assuming an isotropic directional distribution of fractures. The final fracture length ℓ_f is taken in the range [3 to 4] ℓ_0, and the connectivity coefficient c_c is back-calculated so as to retrieve a permeability with maximum magnitude around 10^{-11} m^2 as shown in Evans et al. (2009, p. 79) for the enhanced reservoir. Initial spatial heterogeneities are likely but they have not been addressed in this work.

5.2. Critical wellbore pressures at GPK1

At the initial state, the reservoir is considered permeable ($k_0 > 10^{-18}$ m^2). Therefore, the wellbore pressure needed to start the HF for a temperature change of $\theta = (80 - 170)$ °C $= -90$ °C is calculated using Eq. (13), i.e. $p_w^{HF} - 37 = 33.93$ MPa. Consequently, the casing–shoe pressure at the injection well GPK1 should be around 71 MPa to initiate hydraulic fracturing. This magnitude is close to the values (around 65 MPa) implemented at Soultz-sous-Forêts to start HF and to measure the minimum geologic stress at a depth of 3.7 km Evans et al., 2009, p. 50. For this numerical simulation, a value of 65 MPa is chosen for the HF pressure as in the field. The fracture growth stabilizing parameter η is determined by Eq. (14), given σ_n' in the direction of the maximum field stress, the HF pressure of 65 MPa, and the material properties of (Table 4). Injection pressure is increasing at GPK1 linearly in time, as pumping starts with 58 MPa and terminates, after 15 years, with 82 MPa (Fig. 7).

Cooling contributes to hydraulic fracturing considerably, i.e. if the thermal contribution is ignored in calculating the fracturing pressure ($p_w^{HF} - 37 = 33.93$ MPa), the overpressure needed to initiate fracturing should increase by 12.15 MPa.

The minimum wellbore pressure needed to avoid shear failure is calculated by Eqs. (B.3) and (B.4). For a friction angle $\vartheta \simeq 42°$ and a compressive strength $C_0 \simeq 130$ MPa typical for granite, and for a vertical burden stress $\sigma_v \simeq -80$ MPa corresponding to 3.7 km depth, the minimum overpressure with respect to the formation pressure is negative. Therefore the borehole (GPK1) is not likely to fail in shear but rather in tension as the wellbore pressure p_w gets close to 65 MPa.

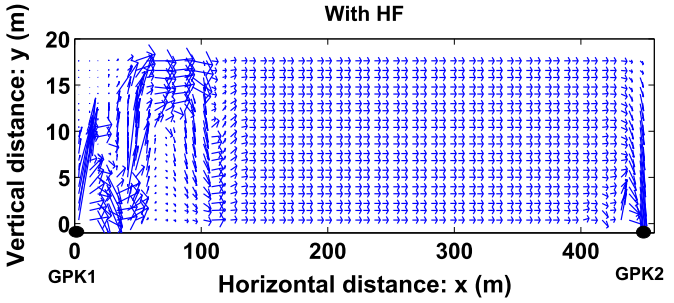

Fig. 10. Scaled fluid velocity vectors at year 1 with HF. The average velocity of the formation fluid in x-direction is $v_x = 10^{-6}$ m/s. Fluid flows following the high permeable paths created by HF (Fig. 13(a)).

5.3. Simulations of hydraulic fracturing and circulation tests

The BVP described in (Section 5.1) is hydraulically enhanced using our fracturing model (HFM). Long term circulation tests at typical periods of 1, 5, 10 and 15 years are simulated for the following cases: with HF by activating the HFM; without HF.

There are three distinct time scales associated with fluid seepage and heat transfer in a poroelastic medium subjected to thermal change:

- the first time scale $t_\theta = L^2/\psi_\theta$ is associated with the diffusive heat transfer. The mixture thermal diffusivity $\psi_\theta = k_\theta/\rho c_v$ (m^2/s) is calculated by volume averaging the heat conductivities and heat capacities over constituents;
- the second time scale $t_p = L^2/C_c$ is associated with the diffusive flow of the pore fluid. The consolidation coefficient $C_c = (\lambda + 2G)(k/\mu)$ (m^2/s) involves a representative value of the permeability k (m^2), the dynamic viscosity μ (Pa × s) and the Lamé's elastic constants λ and G (Pa);
- the third time scale $t_{\text{conv}} = L/|\boldsymbol{v}|$ is associated with the convection of heat, $|\boldsymbol{v}|$ being the magnitude of the fluid velocity in the porous medium. For the next calculations, the magnitude of fluid velocity in the fractured reservoir has a typical magnitude of 10^{-6} m/s (Fig. 10).

For the three time scales, L (m) is a typical length of the BVP considered. For circulation tests over a length of L=450 m, these time scales rank in the following standard order, $t_\theta = 8482.5$ years, $t_{\text{conv}} = 16$ years, and $t_p = 1.6$ days.

It is worthwhile to mention that the Péclet number of this geothermal reservoir based on the operating conditions of Fig. 7 and the mechanical properties of (Table 1) is high, i.e. the continuum Péclet number is Pe=297.3, meanwhile the grid Péclet number is $\text{Pe}_{g,x} = 9.91$. Such a high Péclet number will lead to instabilities in the numerical solution of the temperature field due to heat convection. However, three numerical stabilizing approaches have been introduced to eliminate/mitigate the oscillations, at all injection stages, in the solutions of the temperature field. The commonly used Streamline Upwind/Petrov–Glerkin (SUPG) method is implemented to heal the oscillations at intermediate stages. The Discontinuity Capturing Method (DCM) is also applied to stabilize convection of heat at late stages near the production wells. For instabilities at early stages, the Subgrid Scale/Gradient Subgrid Scale method (SGS/GSGS) is used to transform the transient advection–diffusion problem into a steady advection–diffusion–reaction problem, which takes into account the effect of the time step factor on the numerical oscillations (AbuAisha and Loret, 2016).

The high fluid gradients near the injection well, travelling strongly in y–direction (Fig. 9), cause fast cooling and bring fractures and thus permeability to develop in this direction (Figs. 8(c) and 13(a)).

Since the characteristic time of hydraulic diffusion is of the order of the day, the pressure field has been established in the early times. Therefore the contours of fluid pressure are not showing any significant changes at later times (Figs. 11(a) and 11(b)). However, if HF is activated, the formation pressure tends to become spatially uniform in the region of enhanced permeability while it declines linearly in the regions of low permeability (Figs. 11(c) and 11(d)). The considerable increase of the permeability tensor components in the region of active HF makes the

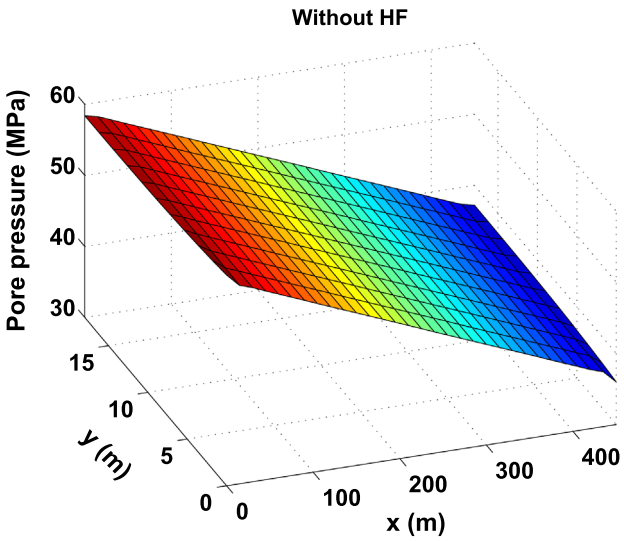

(a) Pressure contours at year 1, no HF

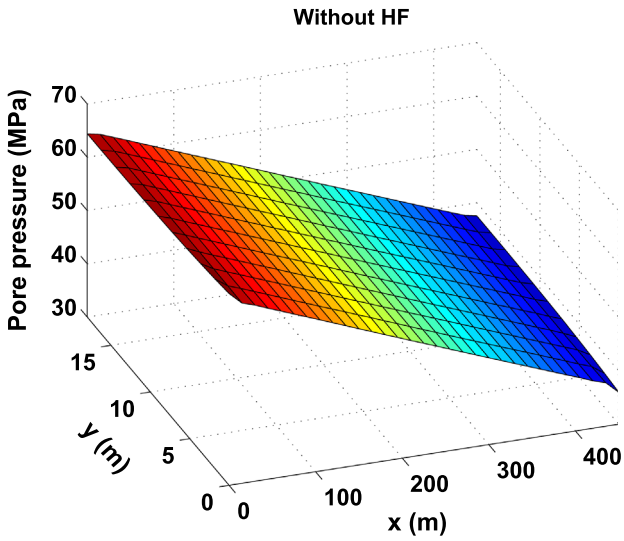

(b) Pressure contours at year 5, no HF

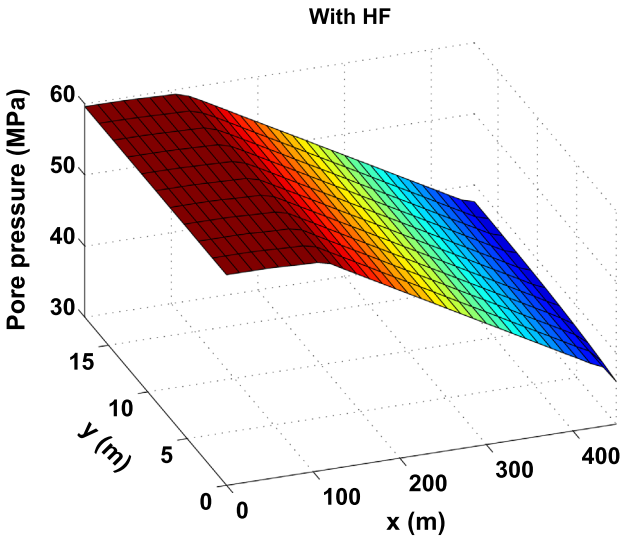

(c) Pressure contours at year 1 with HF

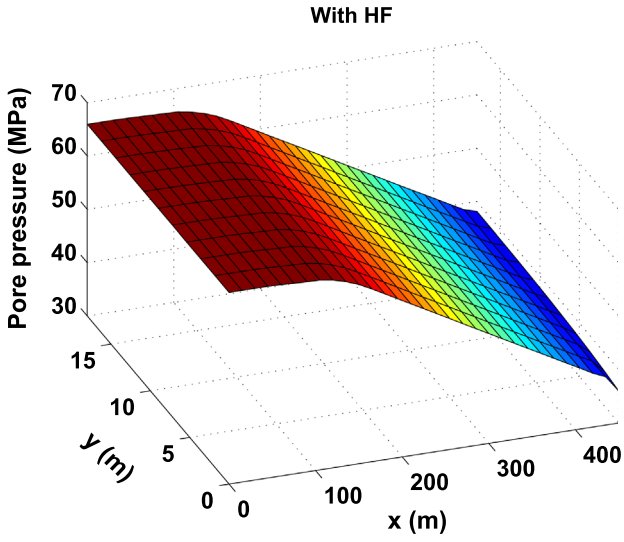

(d) Pressure contours at year 5 with HF

Fig. 11. Contours of the formation pressure at two times with/without HF. The high permeability created by hydraulic fracturing drives fluid pressure contours to become spatially uniform near the injection well. (a) Pressure contours at year 1, no HF, (b) Pressure contours at year 5, no HF, (c) Pressure contours at year 1 with HF, (d) Pressure contours at year 5 with HF.

changes in pore fluid pressure quite small in this region as compared to the situation of unenhanced HDR reservoir. This behavior of pressure distribution was also observed by Lee and Ghassemi (2011) in a three–dimensional context.

Since the reservoir is constrained in x and y directions due to roller displacement, cooling creates near the injection well tensile stresses which mitigate the geologic stresses and contribute to fracture propagation (Figs. 12 and 13). When HF is activated, the distribution of effective stress is irregular following the preferential cooling derived by the new paths created by HF (Figs. 12(c) and 13(a)). The regions of enhanced permeability are characterized by high hydraulic fluxes that carry the heat front by convection (Figs. 10 and Figs. 13(a)). Indeed thermal stresses noticed in the regions of high fluid velocity and/or enhanced permeability are associated with heat convection rather than heat diffusion which is much slower.

Effective stresses are influenced by the heat front in the early stages of the simulation. Behind the heat front, the effective stress contours progressively adopt the pattern of the formation pressure (Figs. 11(d) and 12(d)).

The following observations are derived from the simulations:

1. at the early stage of HF, both the pressurization capacity as well as heat conduction and/or convection are controlling the fracture propagation;
2. after 1 year of pumping, heat effects are still controlling the fracturing process. As expected, permeability components are high in the regions where the effective compressive stresses are lowered by cooling tensile stresses (Figs. 12(c) and 13(a));
3. at year 5 of operation, the enhanced hydraulic system and the high pressurizing capacities lead the heat front to reach the production well (Fig. 8(d)). At this stage, pressure gradients are controlling the process of HF and the patterns of the contours of effective stresses become similar to that of the formation pressure;
4. the previous conclusion wipes off the anisotropy of the permeability tensor and brings k_{xx} to be equal to k_{yy} since the

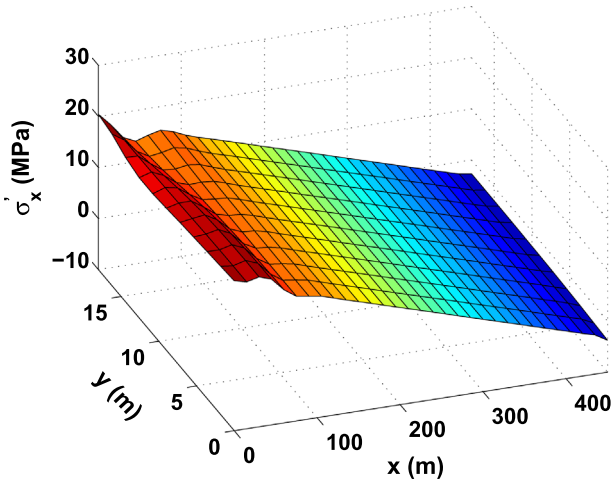

(a) Contours of σ'_{xx} at year 1, no HF

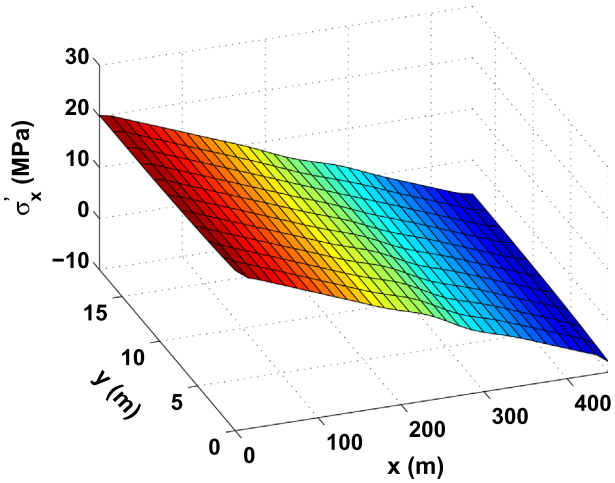

(b) Contours of σ'_{xx} at year 5, no HF

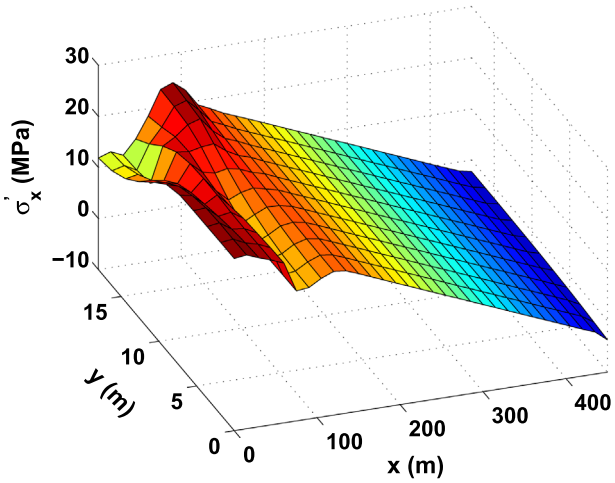

(c) Contours of σ'_{xx} at year 1 with HF

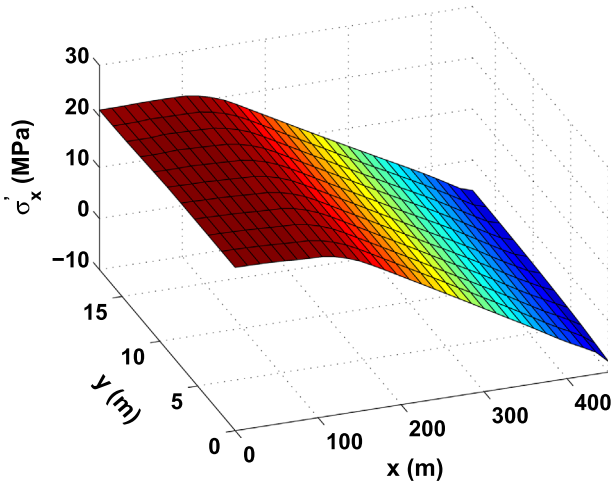

(d) Contours of σ'_{xx} at year 5 with HF

Fig. 12. Contours of longitudinal Terzaghi's effective stress σ'_{xx} at two times with/without HF. Stress contours are influenced by the heat front at early times. However, beyond the heat front, stress contours adopt the pore fluid pressure patterns. (a) Contours of σ'_{xx} at year 1, no HF, (b) Contours of σ'_{xx} at year 5, no HF, (c) Contours of σ'_{xx} at year 1 with HF, (d) Contours of σ'_{xx} at year 5 with HF.

geologic far field stresses are equal (Fig. 14(b)). However, some anisotropy remains close to the injection well due to the initial high permeability enhancement in that region (Fig. 13). This behavior is attributed to the fact that only mode I of fracturing is considered in the aforementioned version of the HF model, and, mostly that no fracture interaction is accounted for;

5. the anisotropy ratio k_{yy}/k_{xx} of the components of the permeability tensor remains in the range $[0.4, 2.5]$ as observed by Schulze et al. (2001) (Fig. 14);
6. the enhanced out-of-diagonal components of the permeability tensor, $k_{xy} = k_{yx}$, keep a magnitude in the range of 10^{-14} m^2, three orders of magnitude smaller than the diagonal components.

6. Conclusions and outlook

Hydraulic fracturing in a thermo–poroelastic framework is addressed in the context of thermal recovery from large scale geothermal systems. To serve as a basic but comprehensive prototype, the thermo–poroelastic framework is first presented with the constitutive and field equations needed to describe heat and fluid transport in single porosity deformable fractured zones. A key element to the approach is the fracturing model which is capable of tracking the directional evolution of the size and aperture of fractures. At any geometrical point, the fracture–induced anisotropic permeability tensor is obtained by directional averaging of Poiseuille flows in the fractures. This fracturing model is integrated into a FORTRAN 90 finite element code to solve for HF in thermo–poroelastic transient BVPs. Thermal recovery from HDR reservoirs is upgraded by enhancing geothermal fluid circulation, namely by increasing the reservoir permeability between injection and production wells by the process of hydraulic fracturing. However, the increase of permeability results in shorter periods of economic viability of the geothermal system. AbuAisha (2014)(Ch. 5, Fig. 5.25) has addressed this phenomenon broadly where simulations have shown that the period during which the recovered water temperature at the production well is higher than 80 °C drops from about 20 years when the permeability is not enhanced to only 10.5 years when hydraulic fracturing is activated. However, these numbers should be taken with caution, as they were obtained while assuming a constant fluid viscosity corresponding to the initial temperature of the reservoir. When the considered working fluid is brine with 0.225 kg of NaCl per kg of solution and when the temperature variation of its viscosity is accounted for in

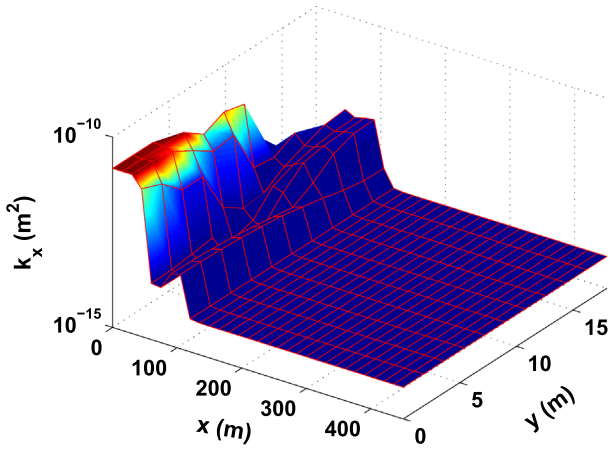

(a) Contours of k_{xx} at year 1

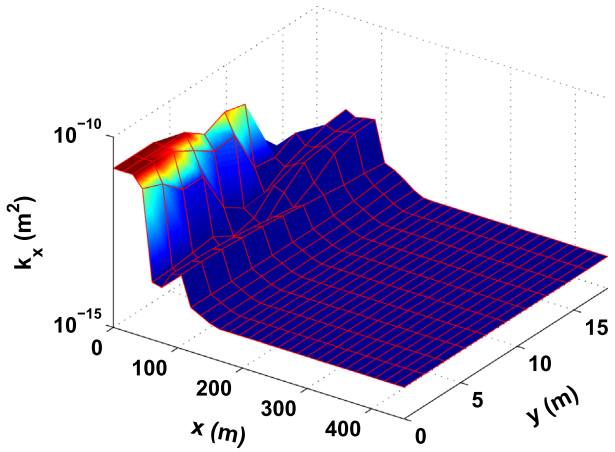

(b) Contours of k_{xx} at year 5

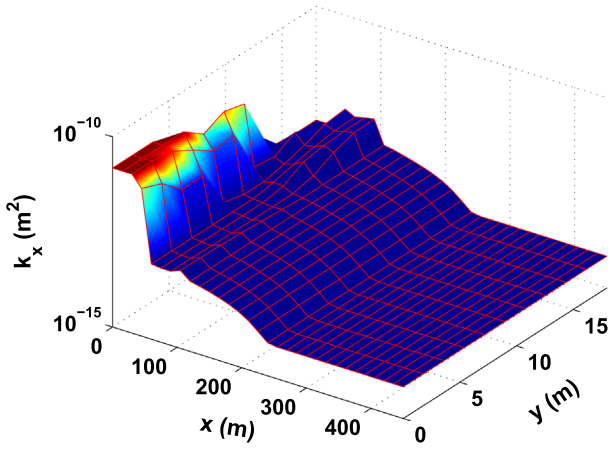

(c) Contours of k_{xx} at year 10

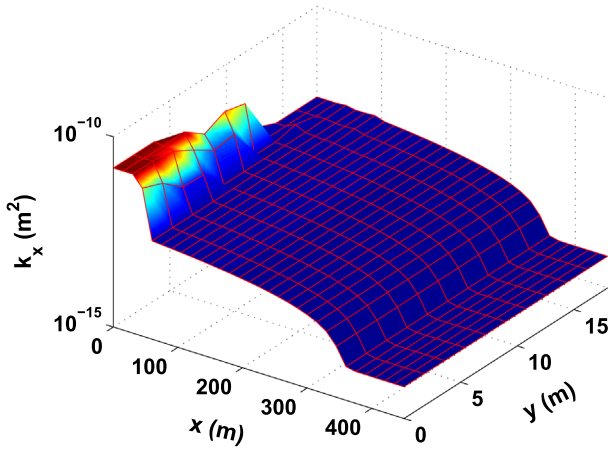

(d) Contours of k_{xx} at year 15

Fig. 13. Contours of the longitudinal permeability component k_{xx} along the inlet-outlet direction at different times during the HF process. Under high pressure gradients, cooling and evolution of heat front affect considerably the contours of effective stresses. Permeability is enhanced in the regions of high tensile effective stresses. (a) Contours of k_{xx} at year 1, (b) Contours of k_{xx} at year 5, (c) Contours of k_{xx} at year 10, (d) Contours of k_{xx} at year 15.

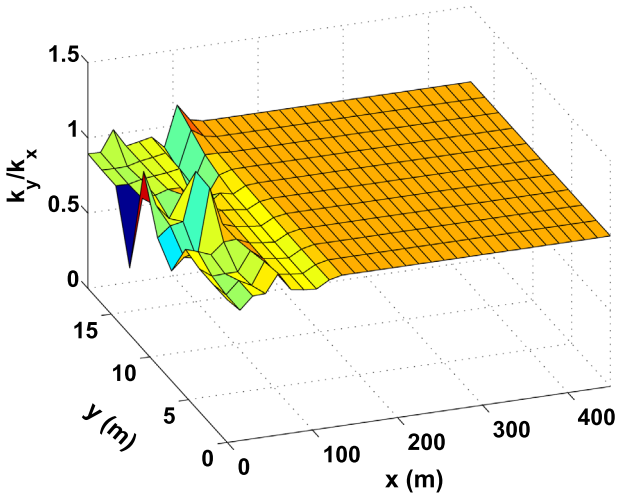

(a) Contours of the ratio k_{yy}/k_{xx} at year 1

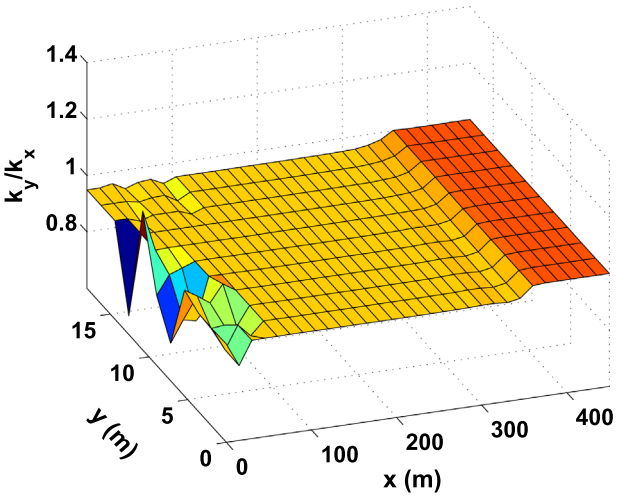

(b) Contours of the ratio k_{yy}/k_{xx} at year 15

Fig. 14. Contours of the ratio k_{yy}/k_{xx} of the components of the permeability tensor at two times during the HF process. Due to equal far field stresses and the assumption of no fracture interaction, the anisotropy of the permeability tensor decreases with time. The anisotropy near the injection well is due to fluid gradients travelling in y-direction (the shorter path). (a) Contours of the ratio k_{yy}/k_{xx} at year 1, (b) Contours of the ratio k_{yy}/k_{xx} at year 15.

the simulations, the economic viability of the geothermal system reaches about 17 years (AbuAisha, 2014)(Ch. 5, Fig. 5.46). In either case the flow impedance of the geothermal system should be observed and should not exceed a value of 1000 MPa s/m^3 for efficient operating conditions (Murphy et al., 1999) and (AbuAisha, 2014)(Ch. 5, Eq. 5.1, Fig. 5.24 and Fig. 5.45).

It has been observed that the use of the same interpolation functions for the displacement vector, the pressure and the temperature fields, does not satisfy the LBB condition in a fully coupled thermo–porelastic framework (Hughes, 2000). As a consequence of this defect, fluid mass loss might be numerically induced. Besides, the activation of HF by using the HFM is noticed to increase the amount of fluid loss. By comparing the fluid fluxes at inlet and outlet, AbuAisha (2014)(Sect. 5.2.2), the fluid mass loss is seen to be less than 2.0% when the HF is not activated compared to 4% when the HF model is used. However, the magnitude of this loss decreases as the fracturing process becomes less intense over time. Using FEM meshes that are considerably refined close to the regions of severe changes may help reducing the amount of fluid loss (AbuAisha, 2014)(Sect. 5.2.1). The smaller mesh element size decreases the grid Péclet number and consequently the numerical instabilities created by heat convection. Another approach to solve the numerical fluid loss problem might be to use a discretization one order higher for the displacement (velocity) than for the pressure/temperature.

This work is to be presented as a prototype in which most, if not all, components may be individually or simultaneously modified. For example, while the present analysis has considered an ideal fluid, future work should pay attention to the nature of geothermal fluids, i.e. their Newtonian or Non-Newtonian character, and to the type of flow, i.e. Non-Darcian flow may also be investigated. Furthermore, the chemical content of actual working fluids and the strong dependence of their dynamic viscosity on temperature are also expected to influence the thermal recovery process. While more sophisticated fracturing models that account for modes I and II of fracture evolution may be envisaged, the influence of the associated parameters has to be established. On a more fundamental side, the interaction between local fractures has to be scrutinized. The current approach considers a single porosity, yet, a more elaborated double porosity model which distinguishes the storage role of pores and the role of hydraulic transport of the fractures is already implemented in the FORTRAN code (Gelet et al., 2012). Consequently, the enhancement of the permeability in double porosity media appears as a natural extension of the present work.

The initial reservoir properties have been assumed spatially uniform which is a considerable simplification. In reality, the pre–existing fractures and faults may lead to a sort of compartmentalization of the reservoir which may modify the flow regimes significantly. Characterizing these discontinuities requires further study.

Acknowledgment

This research was supported by a PhD fellowship of the Centre National de la Recherche Scientifique (CNRS), France (INSEE - National Institute of Statistics and Economic Studies, France, N INSEE: 1 87 04 99 299 002).

Data policy: The numerical simulations were obtained by running in–house FORTRAN 90 code and Matlab m–files. The source codes are available by contacting the corresponding author.

Appendix A. Definition of the finite element matrices

The element diffusion matrix $\mathbb{D}^e$, stiffness matrix $\mathbb{K}^e$ and convection matrix $\mathbb{C}^e$ which are assembled to form the global matrices in (9) and their sub-matrices are listed below:

$$\mathbb{D}^e=\begin{bmatrix}\boldsymbol{D}^e_{\boldsymbol{uu}} & \boldsymbol{D}^e_{\boldsymbol{up}} & \boldsymbol{D}^e_{\boldsymbol{u\theta}}\\ \boldsymbol{D}^e_{\boldsymbol{pu}} & \boldsymbol{D}^e_{\boldsymbol{pp}} & \boldsymbol{D}^e_{\boldsymbol{p\theta}}\\ \boldsymbol{0} & \boldsymbol{0} & \boldsymbol{D}^e_{\boldsymbol{\theta\theta}}\end{bmatrix},\quad \mathbb{K}^e=\begin{bmatrix}\boldsymbol{0} & \boldsymbol{0} & \boldsymbol{0}\\ \boldsymbol{0} & \boldsymbol{K}^e_{\boldsymbol{pp}} & \boldsymbol{0}\\ \boldsymbol{0} & \boldsymbol{0} & \boldsymbol{K}^e_{\boldsymbol{\theta\theta}}\end{bmatrix},\quad \mathbb{C}^e=\begin{bmatrix}\boldsymbol{0} & \boldsymbol{0} & \boldsymbol{0}\\ \boldsymbol{0} & \boldsymbol{0} & \boldsymbol{0}\\ \boldsymbol{0} & \boldsymbol{0} & \boldsymbol{C}^e_{\boldsymbol{\theta\theta}}\end{bmatrix}, \tag{A.1}$$

1. sub–matrices of the diffusion matrix:

$$\boldsymbol{D}^e_{\boldsymbol{uu}}=\int_{V^e}\boldsymbol{B}^T_{\boldsymbol{u}}\boldsymbol{D}\boldsymbol{B}_{\boldsymbol{u}}\,dV^e,\quad \boldsymbol{D}^e_{\boldsymbol{up}}=\int_{V^e}\boldsymbol{B}^T_{\boldsymbol{u}}(-\kappa)\boldsymbol{N}_p\,dV^e,$$
$$\boldsymbol{D}^e_{\boldsymbol{u\theta}}=\int_{V^e}\boldsymbol{B}^T_{\boldsymbol{u}}(-K\alpha'_s)\boldsymbol{N}_\theta\,dV^e,$$
$$\boldsymbol{D}^e_{\boldsymbol{pu}}=\int_{V^e}\boldsymbol{N}^T_p\kappa\mathrm{tr}\boldsymbol{B}_{\boldsymbol{u}}\,dV^e,\quad \boldsymbol{D}^e_{\boldsymbol{pp}}=\int_{V^e}\frac{\boldsymbol{N}^T_p\boldsymbol{N}_p}{M}\,dV^e,$$
$$\boldsymbol{D}^e_{\boldsymbol{p\theta}}=\int_{V^e}\boldsymbol{N}^T_p(-\overline{\alpha})\boldsymbol{N}_\theta\,dV^e,\ \boldsymbol{D}^e_{\boldsymbol{\theta\theta}}=\int_{V^e}\boldsymbol{N}^T_\theta(\rho c_v)\boldsymbol{N}_\theta\,dV^e, \tag{A.2}$$

2. sub–matrices of the stiffness matrix:

$$\boldsymbol{K}^e_{\boldsymbol{pp}}=\int_{V^e}\boldsymbol{B}^T_p\frac{\boldsymbol{k}}{\mu}\boldsymbol{B}_p\,dV^e,\ \boldsymbol{K}^e_{\boldsymbol{\theta\theta}}=\int_{V^e}\boldsymbol{B}^T_\theta k_\theta\boldsymbol{B}_\theta\,dV^e, \tag{A.3}$$

3. sub–matrix of the convection matrix:

$$\boldsymbol{C}^e_{\boldsymbol{\theta\theta}}=\int_{V^e}\boldsymbol{N}^T_\theta\rho_f c_{pf}\boldsymbol{q}_f\boldsymbol{B}_\theta\,dV^e, \tag{A.4}$$

4. the element RHS vector $\mathbb{F}^e=\left[\boldsymbol{R}^e_{\boldsymbol{u}}\ \boldsymbol{R}^e_p\ \boldsymbol{R}^e_\theta\right]^T$:

$$\boldsymbol{R}^e_{\boldsymbol{u}}=\int_{\partial V^e}\boldsymbol{N}^T_{\boldsymbol{u}}\dot{\boldsymbol{\sigma}}\cdot\boldsymbol{n}\,ds^e+\int_{V^e}\boldsymbol{N}^T_{\boldsymbol{u}}\boldsymbol{f}^e\,dV^e,$$
$$\boldsymbol{R}^e_p=\int_{\partial V^e}\boldsymbol{N}^T_p(-\boldsymbol{q}_f)\cdot\boldsymbol{n}\,ds^e+\int_{V^e}\boldsymbol{B}^T_p\frac{\boldsymbol{k}}{\mu}\cdot(\rho_f\boldsymbol{g})dV^e,$$
$$\boldsymbol{R}^e_\theta=\int_{\partial V^e}\boldsymbol{N}^T_\theta(-\mathbf{q}_\theta).\,\boldsymbol{n}\,ds^e. \tag{A.5}$$

All the primary variables are discretized on a four–node bilinear quadrilateral element (Q4) with shape functions N^1, N^2, N^3 and N^4 such that:

$$\boldsymbol{N}_{\boldsymbol{u}}=\begin{bmatrix}N^1 & 0 & N^2 & 0 & N^3 & 0 & N^4 & 0\\ 0 & N^1 & 0 & N^2 & 0 & N^3 & 0 & N^4\end{bmatrix}, \tag{A.6}$$

$$\boldsymbol{N}_p=\boldsymbol{N}_\theta=\begin{bmatrix}N^1 & N^2 & N^3 & N^4\end{bmatrix}. \tag{A.7}$$

The matrix $\boldsymbol{D}$ in the definition of $\boldsymbol{D}^e_{\boldsymbol{uu}}$ is the drained stiffness matrix,

$$\boldsymbol{D}=\begin{bmatrix}K+(4/3)G & K-(2/3)G & 0 & K-(2/3)G\\ K-(2/3)G & K+(4/3)G & 0 & K-(2/3)G\\ 0 & 0 & G & 0\\ K-(2/3)G & K-(2/3)G & 0 & K+(4/3)G\end{bmatrix}, \tag{A.8}$$

with $K=E/(3(1-2\nu))$ being the drained bulk modulus and $G=E/(2(1+\nu))$ the shear modulus. The matrix $\boldsymbol{B}_{\boldsymbol{u}}$ is the strain–displacement matrix,

$$\boldsymbol{B}_{\boldsymbol{u}}=\begin{bmatrix}N^1_{,x} & 0 & N^2_{,x} & 0 & N^3_{,x} & 0 & N^4_{,x} & 0\\ 0 & N^1_{,y} & 0 & N^2_{,y} & 0 & N^3_{,y} & 0 & N^4_{,y}\\ N^1_{,y} & N^1_{,x} & N^2_{,y} & N^2_{,x} & N^3_{,y} & N^3_{,x} & N^4_{,y} & N^4_{,x}\end{bmatrix}, \tag{A.9}$$

$\boldsymbol{B}_p=\nabla\boldsymbol{N}_p$ and $\boldsymbol{B}_\theta=\nabla\boldsymbol{N}_\theta$ are the gradients of the shape functions for the pressure and temperature avriables,

$$\boldsymbol{B}_p = \boldsymbol{B}_\theta = \begin{bmatrix} N^1_{,x} & N^2_{,x} & N^3_{,x} & N^4_{,x} \\ N^1_{,y} & N^2_{,y} & N^3_{,y} & N^4_{,y} \end{bmatrix}. \tag{A.10}$$

Appendix B. Stability of boreholes against shear failure

The theme of HF tests is to cause fractures at the casing–shoe of a wellbore to propagate by pumping geothermal fluids with considerable flow rates, i.e. HF is synonymous to borehole tensile failure.

The conditions for shear failure of wellbores below are highlighted to provide a full perspective for borehole stability during the HF process. The shear failure of a borehole is reached when the deviation of effective stresses around the borehole, due to the change in pore fluid pressure and temperature between the borehole and the formation, exceeds the failure criterion of the rock. Let us start with a vertical borehole with uniform formation pressure and anisotropic far field stresses (Fig. 1). For a linearly elastic material the largest changes in stress states occur at the borehole wall. The expressions of stress distributions on the borehole wall take the form (Fjaer et al., 2008),

$$\sigma_r = -p_w,\ \sigma_\zeta = \sigma_H + \sigma_h - 2(\sigma_H - \sigma_h)\cos 2\zeta + p_w - \frac{E}{1-\nu}\frac{\alpha_s\theta}{3},$$
$$\sigma_z = \sigma_v - 2\nu(\sigma_H - \sigma_h)\cos 2\zeta - \frac{E}{1-\nu}\frac{\alpha_s\theta}{3}. \tag{B.1}$$

σ_H is the maximum far field compressive stress and σ_h is the minimum far field compressive stress. The angle ζ is measured relative to the direction of major horizontal stress σ_H.

There are several stress states under which the borehole is expected to fail. Yet the most common practical stress states are observed for the principal stress magnitudes corresponding to $-\sigma_\zeta > -\sigma_z > -\sigma_r$ and $-\sigma_z > -\sigma_\zeta > -\sigma_r$, with σ_r and σ_z the radial and vertical stress components respectively (Fjaer et al., 2008). Consequently, if the formation pressure p_r^∞ and the temperature change are such that $-\sigma_r$ is lowered to a point it becomes the smallest principal stress in the system (B.1), shear failure of the borehole becomes quite possible.

According to the failure criterion of Mohr–Coulomb, shear failure occurs when,

$$-\sigma'_\zeta = C_0 - \sigma'_r \tan^2\beta, \tag{B.2}$$

where C_0 is the uniaxial compressive strength of the material, $\beta = \pi/4 + \vartheta/2$ is the angle of the failure plane with respect to the maximum principal stress for which failure criterion is fulfilled, and ϑ being the angle of friction for the rock.

The failure criterion for the borehole may be defined in terms of the wellbore pressure. Substituting the system (B.1) in Eq. (B.2) yields the minimum pressure that should be applied to avoid failure, namely when $-\sigma_\zeta > -\sigma_z > -\sigma_r$,

$$p_w > p_w^{\min} = p_r^\infty + \frac{-3\sigma_H + \sigma_h - 2p_r^\infty - C_0}{1 + \tan^2\beta} + \frac{1}{1+\tan^2\beta}\frac{E}{1-\nu}\frac{\alpha_s\theta}{3}, \tag{B.3}$$

while, when $-\sigma_z > -\sigma_\zeta > -\sigma_r$,

$$p_w > p_w^{\min} = p_r^\infty + \frac{-\sigma_v - 2\nu(\sigma_H - \sigma_h) - p_r^\infty - C_0}{\tan^2\beta} + \frac{1}{\tan^2\beta}\frac{E}{1-\nu}\frac{\alpha_s\theta}{3}. \tag{B.4}$$

Obviously, cooling ($\theta < 0$) lowers the required applied pressure, i.e. stabilizes the borehole. The assumption that the formation pressure is uniform gives an approximation about the range of stress deviation at failure. Nevertheless, a position dependent formation pressure is to be considered for more realistic research.

References

AbuAisha, M. 2014, Enhanced geothermal systems: Permeability stimulation through hydraulic fracturing in a thermo–poroelastic framework. PhD thesis, ⟨https://tel.archives-ouvertes.fr/tel-01053612⟩, Université de Grenoble, France.

AbuAisha, M., Loret, B., 2016. Stabilization of forced heat convection: applications to enhanced geothermal systems (EGS). Transp. Porous Media 112 (1), 229–252.

Atkinson, B.K., 1991. Fracture mechanics of rock, second edition. Academic Press Limited, London, Great Britain.

Bruel, D., 1995a. Heat extraction modelling from forced fluid flow through stimulated fractured rock masses: application to the Rosemanowes hot dry rock reservoir. Geothermics 24 (3), 361–374.

Bruel, D., 1995b. Modelling heat extraction from forced fluid flow through stimulated fractured rock masses: evaluation of the Soultz-sous-Forêts site potential. Geothermics 24 (3), 439–450.

Bruel, D., 2002. Impact of induced thermal stresses during circulation tests in an engineered fractured geothermal reservoir. Oil Gas. Sci. Technol. 57 (5), 459–470.

Cheng, A.H.-D., Ghassemi, A., Detournay, E., 2001. Integral equation solution of heat extraction from a fracture in hot dry rock. Int. J. Numer. Anal. Methods Geomech. 25 (13), 1327–1338.

Evans, K., Valley, B., Häring, M., Hopkirk, R., Baujard, C., Kohl, T., Mégel, T., André, L., Portier, S., Vuataz, F., 2009. Studies and support for the EGS reservoirs at Soultz–sous–Forêts. Technical Report, Centre for Geothermal Research, University of Neuchâtel.

Fjaer, E., Holt, R.M., Horsrud, P., Raaen, A.M., Risnes, R., 2008. Petroleum related rock mechanics second edition. Elsevier B.V., Radarweg 29, 1000 AE Amsterdam, Netherlands.

Haimson, B., Fairhurst, C., 1967. Initiation and extension of hydraulic fractures in rocks. Soc. Pet. Eng. 7 (3), 310–318.

Hughes, T.J.R., 2000. The Finite Element Method; Linear Static and Dynamic Finite Element Analysis, second edition. Dover, Mineola.

Gelet, R., Loret, B., Khalili, N., 2012. A thermo-hydro-mechanical coupled model in local thermal non-equilibrium for fractured HDR reservoir with double porosity. J. Geophys. Res.: Solid Earth 117 (B07205), 1–23.

Ghassemi, A., Nygren, A., Cheng, A., 2008. Effects of heat extraction on fracture aperture: a poro-thermoelastic analysis. Geothermics 37 (5), 525–539.

Klimczak, C., Schultz, R.A., Parashar, R., Reeves, D., 2010. Cubic law with aperture-length correlation: implications for network scale fluid flow. Hydrogeol. J. 18 (4), 851–862.

Kohl, T., Mégel, T., 2007. Predictive modeling of reservoir response to hydraulic stimulations at the European EGS site Soultz-sous-Forêts. Int. J. Rock. Mech. Min. Sci. 44 (8), 1118–1131.

Lee, S.H., Ghassemi, A., 2011. Three-dimensional thermo-poro-mechanical modeling of reservoir stimulation and induced microseismicity in geothermal reservoir, in Proceedings of the Thirty-Sixth Workshop on Geothermal Reservoir Engineering, Stanford University, Stanford, California.

McTigue, D.F., 1986. Thermoelastic response of fluid-saturated porous rock. J. Geophys. Res. 91 (B9), 9533–9542.

Murphy, H., Brown, D., Jung, R., Matsunaga, I., Parker, R., 1999. Hydraulics and well testing of engineered geothermal reservoirs. Geothermics 28 (4–5), 491–506.

Papanastasiou, P., Thiercelin, M., 1993. Influence of inelastic rock behaviour in hydraulic fracturing. Int. J. Rock. Mech., Min. Sci. Geomech. Abstr. 30 (17), 1241–1247.

Rejeb, A., Bruel, D., 2001. Hydromechanical effects of shaft sinking at the Sellafield site. Int. J. Rock. Mech. Min. Sci. 38 (1), 17–29.

Schulze, O., Popp, T., Kern, H., 2001. Development of damage and permeability in deforming rock salt. Eng. Geol. 61 (2–3), 163–180.

Shao, J.F., Zhou, H., Chau, K.T., 2005. Coupling between anisotropic damage and permeability variation in brittle rocks. Int. J. Numer. Anal. Methods Geomech. 29 (12), 1231–1247.

Souley, M., Homand, F., Pepa, S., Hoxha, D., 2001. Damage-induced permeability changes in granite: a case example at the URL in Canada. Int. J. Rock. Mech. Min. Sci. 38 (2), 297–310.

Taron, J., Elsworth, D., 2009. Thermal-hydrologic-mechanical-chemical processes in the evolution of engineered geothermal reservoirs. Int. J. Rock. Mech. Min. Sci. 46 (5), 855–864.

Turcotte, D.L., Schubert, G., 2002. Geodynamics, second edition. Cambridge University Press, Cambridge, England, UK.

Zhou, X.X., Ghassemi, A., Cheng, A.H.-D., 2009. A three-dimensional integral equation model for calculating poro- and thermoelastic stresses induced by cold water injection into a geothermal reservoir. Int. J. Numer. Anal. Methods Geomech. 33 (14), 1613–1640.

Journal of Petroleum Science and Engineering 154 (2017) 100–113

Contents lists available at ScienceDirect

Journal of Petroleum Science and Engineering

journal homepage: www.elsevier.com/locate/petrol

Hydro-mechanically coupled FDEM framework to investigate near–wellbore hydraulic fracturing in homogeneous and fractured rock formations

Murad AbuAisha[a,b,*], David Eaton[a], Jeffrey Priest[b], Ron Wong[b]

[a] Department of Geoscience, University of Calgary, Alberta, Canada
[b] Department of Civil Engineering, University of Calgary, Alberta, Canada

ARTICLE INFO

Keywords:
Hydraulic Fracturing (HF)
Pre–existing joints
Isotropic and/or anisotropic stress state
Stress gradient
Finite-Discrete Element Method (FDEM)
Numerical simulations

ABSTRACT

This paper reports on a numerical study that was conducted to investigate near–wellbore behaviour of Hydraulic Fracture (HF) growth using a Finite–Discrete Element Modelling (FDEM) approach. In particular we consider the effect on fracture propagation of pre–existing defects (joints) within the rock medium, as well as physical mechanisms that induce microseismic events. Initial modelling was conducted for an isotropic and homogeneous rock mass subject to isotropic and anisotropic far–field stress states. The introduction of single isolated joints for a rock mass subject to anisotropic far–field stresses that did not intersect the wellbore, such as those created by previous fracturing stages, were seen to impose a lateral stress gradient. The presence of stress gradients leads to asymmetric fracture initiation and growth, generally away from the pre–existing joint, accompanied by an increase in the fluid pressure required to initiate fractures. However, the influence of pre–existing joints diminishes with distance from the wellbore. Due to the high permeability of pre–existing rock joints, fractures prefer to initiate at joint tips after the joint is intersected by a fluid–driven fracture. Based on our simulations, a set of pre–existing, randomly distributed joints around the wellbore leads to microseismic events that are primarily induced by shear slippage on critically stressed joints. For a given injection energy, the presence of multiple joints around a wellbore increases the extent to which fluid–driven fractures can grow. Finally, comparison of our simulation with measured results from low–volume injection test confirms that our approach appears to capture salient aspects of elastic deformation and breakdown pressures in the field.

1. Introduction

Hydraulic fracturing (HF) is a wellbore stimulation method that is used extensively in the development of unconventional oil and gas reservoirs to enhance connectivity of low–permeability (<1 mD) oil and gas–bearing rock formations (Nagel et al., 2011; King, 2010; Hubbert and Willis, 1957; Fjaer et al., 2008). Injection of fluid under high pressure overcomes the rock tensile strength to create and/or extend fractures (AbuAisha, 2014; AbuAisha and Loret, 2016a, 2016b; AbuAisha et al., 2016; Bruel, 1995; Barree et al., 2002). Through the creation of high–permeability pathways, HF serves to increase reservoir drainage by effectively increasing wellbore radius and thus reducing the hydrocarbon flow distance.

Several analytical and numerical approaches have been used to simulate hydraulic fracturing (Adachia et al., 2007). Simple solutions of stress distribution around a borehole provide a starting point for analysis of HF operations (Hubbert and Willis, 1957; Fjaer et al., 2008). In the simplest cases, these solutions are based upon assumptions of elastic, isotropic and homogeneous media (Dusseault, 2013). Other approaches are based on continuum geomechanics models and require mesh–update and expensive computational capacities (Settgast et al., 2016; Shen, 2012), they also face difficulties describing physical interaction between fluid driven fractures and pre–existing joints (Bai et al., 2016). The works of Bai et al. (2016), Bai and Lin (2014) have enhanced the current discrete fracture models (Olson, 2008; Nagel et al., 2011) by introducing the Fluid–Structure Interaction algorithm (FSI). The FSI ensures full coupling between the elastic rock mechanics, fluid flow, and the non–penetration contact conditions, while using a fully implicit time integration scheme. However, the FSI in its current form some limitations that include; the inability of including a wellbore model and hence focusing on near wellbore behavior, and the use of a linear constitutive law for the rock formation. In this context a hybrid technique (FDEM) (Munjiza et al., 1999; Mahabadi et al., 2012; Lisjak et al., 2013) that combines the advantages of the Finite Element

* Corresponding author at: Department of Geoscience, University of Calgary, Alberta, Canada.
E-mail addresses: morad_77_2@hotmail.com (M. AbuAisha), eatond@ucalgary.ca (D. Eaton), japriest@ucalgary.ca (J. Priest), rckwong@ucalgary.ca (R. Wong).

http://dx.doi.org/10.1016/j.petrol.2017.04.018
Received 8 July 2016; Received in revised form 10 April 2017; Accepted 13 April 2017
Available online 17 April 2017

Method (FEM) (Hughes, 2000) and the Discrete Element Method (DEM) (Munjiza, 2004) has been developed that is well suited to this problem. Using a proper non–linear constitutive law, this technique enables investigation of the transition from continuum behaviour of the intact material that is captured by the FEM to discontinuum behavior, where the position of fractured material blocks are tracked using the DEM. The FDEM is also capable of describing rock yielding through the fracture plastic zone using experimental curves that define the fracture energy dissipation. A Hydro–Mechanical mechanical model based on the principle of conservation of mass for a compressible fluid has been added to the FDEM framework (FDEM–HF). The FDEM–HF approach enables phenomena like asymmetric fracture growth (Fischer et al., 2016) and induced microseismicity (Shapiro and Dinske, 2009) to be simulated. These two phenomena are sometimes observed in the field during a HF stimulation test. However, the FDEM–HF in its current form assumes inviscid flow restricted to fractures and it does not account for leakoff into the rock formation.

This paper is organized as follows. First, two HF tests are simulated in an elastic continuous medium, considering both isotropic ($S_{Hmax} = S_{hmin}$) and anisotropic ($S_{Hmax} > S_{hmin}$) far–field stress states. Next, the influence of a lateral stress gradient is investigated by introducing single isolated joints in the medium that are offset from (but close to) the wellbore. Lateral stress gradients have been invoked to explain asymmetric fracture growth. This scenario is investigated indirectly, by considering the effects of proximal fractures that influences the near–wellbore environment. Thirdly, HF simulations are performed while considering a heavily fractured formation in the vicinity of the wellbore, in order to investigate the interaction between a growing hydraulic fracture and natural fractures, and induced microseimicity. Finally, the FDEM–HF approach is used to simulate a low–volume test performed within the Montney Formation in British Columbia, Canada.

2. The FDEM: overview

The FDEM approach was first suggested by Munjiza et al. (1995). It is a hybrid technique that combines the advantages of the FEM and DEM approaches. While the medium is undergoing elastic deformation, the behaviour of intact material is explicitly modelled by FEM. As the strength of the material is exceeded fractures are initiated, giving rise to discontinuous blocks where the interaction between these blocks is captured by DEM. The FDEM approach is capable of tracking fracture initiation and propagation by applying the principles of non–linear elastic fracture mechanics (Barenblatt, 1959, 1962). In this study we use an implementation of the FDEM method known as the Y-Geo code. The Y–Geo code has been broadly discussed and verified against experimental data by Mahabadi et al. (2012), Lisjak et al. (2013), Lisjak et al. (2014a), Lisjak et al. (2014b). This algorithm uses three interconnecting modules (Fig. 1) to simulate fluid–driven fractures, as follows:

1. a mechanical solver which calculates the deformation of the intact rock mass as well as the initiation, propagation and interaction of fractures;
2. a cavity volume calculator then captures the changes of the cavity volume due to fracture propagation, the elastic deformation, and fluid compressibility. It also tracks the newly created wet boundaries by checking their connection with the initial source of fluid;
3. a pump model then interacts with the previous two modules to calculate fluid pressure while considering the pumping conditions/ injected flow rate.

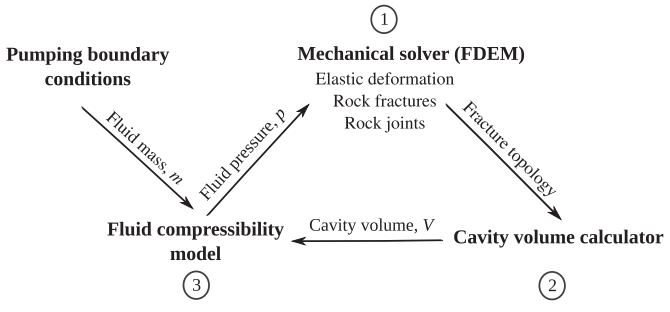

Fig. 1. Interaction between computational modules of the Y-Geo code.

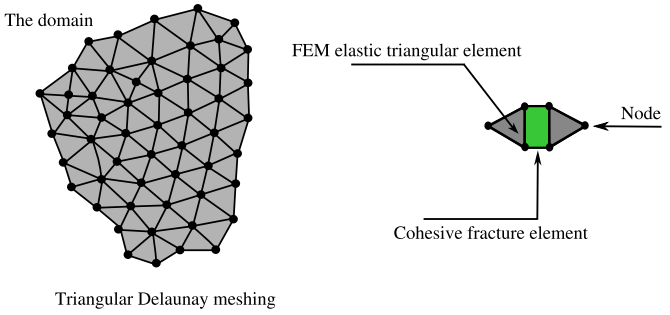

Fig. 2. Triangular Delaunay meshing applied in the Y–Geo code. The enlarged section shows the contact nature between the elastic and the dimensionless fracture cohesive elements.

The Y–Geo code discretizes the modelling domain with a mesh of elastic triangular Delaunay elements connected to each other at the edges by non–dimensional rectangular cohesive fracture elements (Fig. 2). An explicit time integration scheme is employed to solve the equation of motion of the discretized system due to applied stresses.

While the medium undergoes elastic loading the fracture elements are initially assigned large contact stiffness parameters (penalty parameters) to eliminate them from the elasticity matrix, such that all deformations occur in the triangular elements. As soon as the tensile and/or the shear strength of the material is reached, the material starts undergoing inelastic deformation (fracture process zone) that is localized within the fracture elements with the fracturing process expressed in terms of fracture energy dissipation (Munjiza, 2004). Once the fracture energies, G_{Ic} of mode I and G_{IIc} of mode II, are dissipated, the fracture elements are removed and fractures are initiated (Fig. 3). At this point, the positions of the separated blocks are tracked by the DEM.

2.1. Contact detection and interaction of elements

The Y-Geo code is capable of tracking opening (mode I) as well as shearing (mode II) fractures, or combination of both modes. The fracturing mode triggered is based on the relative displacement of the two elastic triangular elements containing the fracture element. Similar to the cohesive model originally proposed for concrete by Hillerborg et al. (1976), a mode I fracture initiates when the fracture tip opening (δ) reaches a critical value (δ_p) which is related to the tensile strength of the rock (f_t) (Fig. 3(a)). As the fracture tip opening increases, the normal bonding stress (σ) is assumed to decrease, based on the fracture dissipation energy G_{Ic}, until a residual opening value (δ_c) is reached and a traction–free surface is created. Mode II of fracturing is simulated by a slip–weakening model (Ida, 1972). The shear bonding stress (τ) is a function of the amount of slip (s) and the normal stress on the fracture (σ_n) (Fig. 3(b)). The critical slip (s_p) corresponds to the shear stress of the rock (f_s), and defined as,

$$f_s = c + \sigma_n \tan(\phi_i), \quad (1)$$

where c is the internal cohesion, ϕ_i is the material internal friction angle. Once the critical slip (s_p) is surpassed, the shear stress is reduced, based on the fracture dissipation energy G_{IIc}, to a residual value (f_r) which is pure frictional resistance,

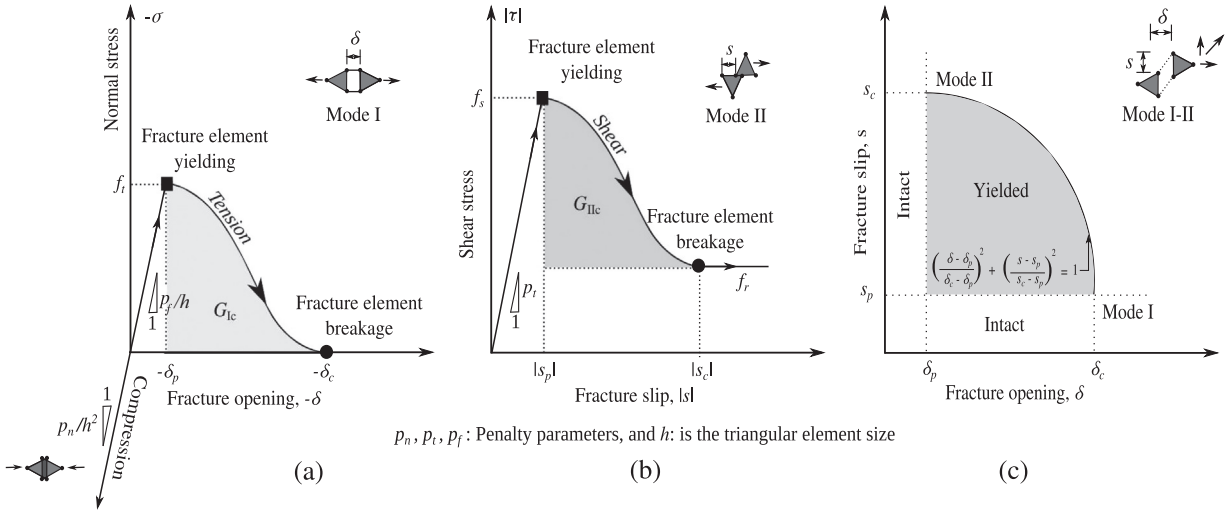

Fig. 3. (a and b) Constitutive behaviour of cohesive fracture elements: The curves represent a relationship between normal and tangential bonding stresses, σ and τ, versus fracture relative displacements, δ (opening) and s (sliding). G_{Ic} and G_{IIc} represent the amount of energy dissipated per unit length of fracture for mode I and mode II respectively. (c) Elliptical coupling relationship between fracture opening (δ) and fracture slip (s) for mixed–mode fracturing (Eq. (3)). Figure is modified from Lisjak et al. (2014).

$$f_r = \sigma_n \tan(\phi_f), \tag{2}$$

where ϕ_f is the fracture friction angle and σ_n is the normal stress acting across the fracture surfaces by the element pair interaction algorithm even after the breakage of the embedded fracture element (Mahabadi et al., 2012).

In the mixed mode I–II of fracturing (Fig. 3(c)), the coupling between fracture opening and slip is defined by an elliptical relationship where failure envelope reads,

$$\left(\frac{\delta - \delta_p}{\delta_c - \delta_p}\right)^2 + \left(\frac{s - s_p}{s_c - s_p}\right)^2 \geq 1. \tag{3}$$

Once the fracture energies are fully dissipated, the fracture elements are removed and fractures are initiated. At this point, the positions of the separated blocks are tracked by the DEM.

2.2. Fluid pressure and hydraulic fracturing

The Y–Geo code utilizes the principle of conservation of mass for a compressible fluid injected in an impermeable medium to calculate fluid pressure and the evolution of hydraulic fractures/fluid–driven fracturing. The HM coupling approach adopted to simulate fluid–driven fracturing by the Y–Geo code is highlighted in Fig. 4.

For each time step within the simulation, the borehole is injected with fluid with the resultant pressure applied as a force to the wet boundary/element nodes that are initially coincident with the borehole. Increasing pressure causes new fractures to be initiated with their topology as well as their connectivity with the previous wet boundaries calculated by the mechanical solver. Considering the new topology and connectivity, the cavity volume is computed and the fluid pressure on the new wet boundaries is recalculated using the fluid compressibility module while considering any incoming fluid mass (Fig. 1). For each time step the fluid pressure inside the cavities/fractures is assumed constant, i.e. no flow due to hydraulic gradients is considered, i.e. similar to an inviscid flow. The assumption of inviscid flow is appropriate as long as we are investigating near wellbore behaviour where convection effects are dominant (Fjaer et al., 2008).

Mathematically, the Green's theorem is used to calculate cavity volume by evaluating a surface integral over all, old and/or new, wet boundaries, given by,

$$V = \frac{1}{2} \oint x\, dy - y\, dx. \tag{4}$$

Once the cavity volume is computed, the fluid compressibility model is implemented to calculate fluid pressure on all the new created wet boundaries,

$$K_f = -V\frac{dp}{dV} = \rho_f \frac{dp}{d\rho_f}, \tag{5}$$

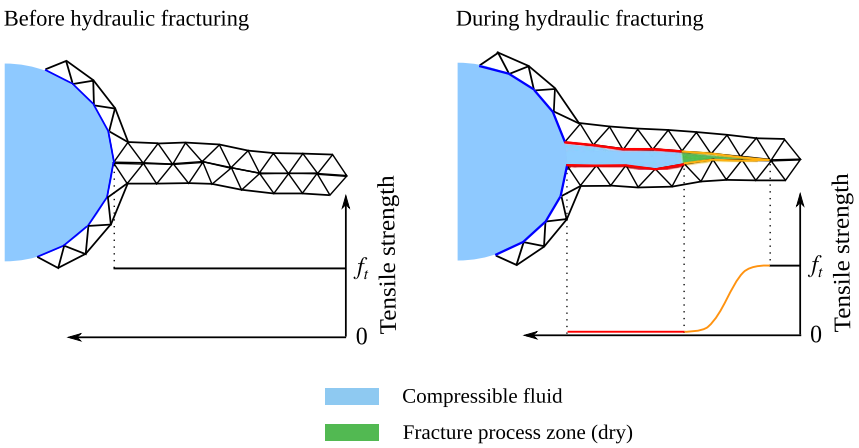

Fig. 4. HF modelling by the Y–Geo code. A mode I fracture, characterized by opening due to tensile stresses, initiates in response to high fluid pressure. Only elements of concern are shown for simplicity. Note the yielding of tensile stresses in the fracture process zone. Figure is modified after (Lisjak et al., 2014b).

Table 1
Rock properties for a HF test of the BVP defined in Fig. 6.

Nature	Parameter	Value	Unit
Elasticity	Young's modulus, E	35	GPa
	Poisson's ratio, ν	0.27	–
	Bulk density, ρ	2500	kg/m^3
Fracture	Tensile strength, f_t	5	MPa
	Cohesion, c	24	MPa
	Mode I fracture energy, G_{Ic}	10	N/m
	Mode II fracture energy, G_{IIc}	80	N/m
	Material internal friction angle, ϕ_i	38	(°)
	Fracture friction angle, ϕ_f	38	(°)
Computational	Damping coefficient, μ	5.6×10^5	kg/m/s
	Normal contact penalty, p_n	350	GPa.m
	Shear contact penalty, p_t	35	GPa.m
	Fracture penalty, p_f	175	GPa.m

with K_f being fluid bulk modulus. While considering the amount of injected fluid at each time step, the fluid mass (m) is integrated from the flow rate to determine fluid pressure (p),

$$p = p_0 + K_f \log\left(\frac{m}{V\rho_{f0}}\right), \tag{6}$$

where p_0 and ρ_{f0} are the reference fluid pressure and density respectively. The length and the orientation of every wet boundary is tracked by the Y–Geo code, and fluid pressure is converted into nodal forces. For instance, the fluid pressure force $\mathbf{F}_{p12}$ acting on a boundary defined by the two nodes 1 and 2 is equal to,

$$\mathbf{F}_{p12} = -\frac{p}{2}\begin{bmatrix} y_2 - y_1 \\ x_2 - x_1 \end{bmatrix}, \tag{7}$$

the equivalent nodal pressure forces are then substituted for in the mechanical solver.

This Hydro–Mechanical (HM) coupling approach will lead to fluid flow in the fractures only and is limited to the time–frame of fracturing.

2.3. Time integration and mesh dependency

The approach used here is based on an explicit second–order finite difference time integration scheme to solve the equation of motion (Eq. (8)) over the discretized domain and consequently calculates the nodal coordinates (Lisjak et al., 2014a, 2014b),

$$\mathbb{M}\ddot{\mathbb{X}} + \mathbb{C}\dot{\mathbb{X}} = \mathbb{R}(\mathbb{X}). \tag{8}$$

$\mathbb{M}$ and $\mathbb{C}$ are the system mass and damping matrices respectively, $\mathbb{X}$ is the vector of the nodal coordinates, and $\mathbb{R}$ is the nodal force vector which includes the contributions from the internal forces $\mathbf{F}_i$, the external loads $\mathbf{F}_e$, and the contact forces $\mathbf{F}_c$. Resisting internal forces ($\mathbf{F}_i$) include effects calculated between interacting elements during the elastic behaviour either in the normal direction (tensile or compressive), or in the tangential direction (Coulomb type friction (Eq. (1))). Contact bonding forces ($\mathbf{F}_c$) include contributions from yielding fracture elements, i.e. during fracture energy dissipation (Fig. 3). Numerical damping is introduced into the system to account for energy dissipation due to non–linear material behaviour or to model quasi–static phenomena by dynamic relaxation (Lisjak et al., 2013). The matrix $\mathbb{C}$ is equal to,

$$\mathbb{C} = \mu\mathbf{I}, \tag{9}$$

where μ and $\mathbf{I}$ are the damping coefficient and the identity matrix respectively. Since an explicit time integration scheme is adopted, the solver is conditionally stable. However, the time step size must be smaller than a critical value, which is proportional to the smallest element size in the model divided by the P–wave velocity of the elastic medium (Munjiza, 2004).

Like any other FEM approaches, the FDEM is mesh–dependent. This mesh–dependency stems from the fact that fractures can only initiate between the triangular elastic elements and therefore their orientation and size can influence both the energy required to initiate fracture and fracture trajectory. In order to mitigate this, the size of the element should be sufficiently smaller than the length of the fracture process zone to accurately represent the bonding stresses (Munjiza, 2004). In our simulations, the nominal element sizes are determined such that the tensile strength of the rock material is reached, and the fracture process zone criteria of Munjiza et al. (1999) is satisfied. In addition, a random discretization of the mesh was adopted to minimize orientation bias of the elements. The Y–Geo code for modeling material fracturing has been extensively verified in the works of Mahabadi et al. (2012), Lisjak et al. (2013), Lisjak et al. (2014a, 2014b). Appendix A provides the results of an analysis to verify the HM coupling presented in this paper against theoretical solutions. In addition, the numerical fracturing thresholds predicted by our FDEM–HF approach are compared to simple fracturing criteria that relate fracturing thresholds to effective stresses and material tensile strength. For instance, and for the material properties of Table 1 and stress values described in Section 3.2, the fracturing threshold for the anisotropic far–field stress state can be calculated by applying the following relation (Fjaer et al., 2008),

$$p^{HF} = \sigma_H^{'} - 3\sigma_h^{'} + ft = -6.\ 8 - 3 \times -4.\ 6 + 5 = 12\ \text{MPa}, \tag{10}$$

with $\sigma_H^{'}$ being the maximum effective horizontal far–field stress, $\sigma_h^{'}$ the minimum effective horizontal far–field stress, and f_t the rock tensile strength. This value of 12 MPa is close to the value obtained numerically by our code ~12.5 MPa (Fig. 11(b)).

2.4. Rock joints

Pre-existing defects/rock joints are modelled using a planar geometry with infinitesimal aperture that can sustain two types of normal and shear forces. Normal forces are calculated through the penalty parameters (p_n and p_f), see Fig. 3(a). The shear forces are calculated through the frictional resistance model (Eq. (2)), see Fig. 3(b). Consequently, the mechanical behaviour of rock joints is tracked through p_n, p_f, and ϕ_f. These two types of forces affect the stress conditions in the area close to the rock joint by generating reaction forces that depend on the shape and size of the perturbed joint area. Due to the HM coupling approach adopted here (inviscid flow), if at any point the rock joint is intersected by a fluid–driven fracture, the fluid pressure percolation is distributed evenly over the entire discontinuity (Fig. 5).

Fig. 5 shows a section of an inclined pre–existing joint in a triangular Delaunay mesh and the representative pressure profiles across the joint while assuming inviscid and viscous flows. Unlike the case of viscous fluid where flow is Darcian, the assumption of inviscid flow will lead to evenly distributed fluid pressure across the joint as soon as the joint is intersected by a fluid–driven fracture. This approach of equally distributed pressure will give rise to stress concentration at the joint tips and fractures will initiate, typically, at the tips due to either mode I (opening) or mode II (sliding/shear slip). In this study, rock joints are applied in the model initially, i.e. stresses are initialized (the geostatic step) while considering the existence of joints.

3. Simulations of HF in elastic homogeneous media

In this section we consider fluid–driven fracturing in a homogeneous elastic medium subject to both isotropic and anisotropic far–field stress states. Although similar results (Zhao et al., 2014) have been discussed by previous authors, this is included here to serve as an introduction for the next sections.

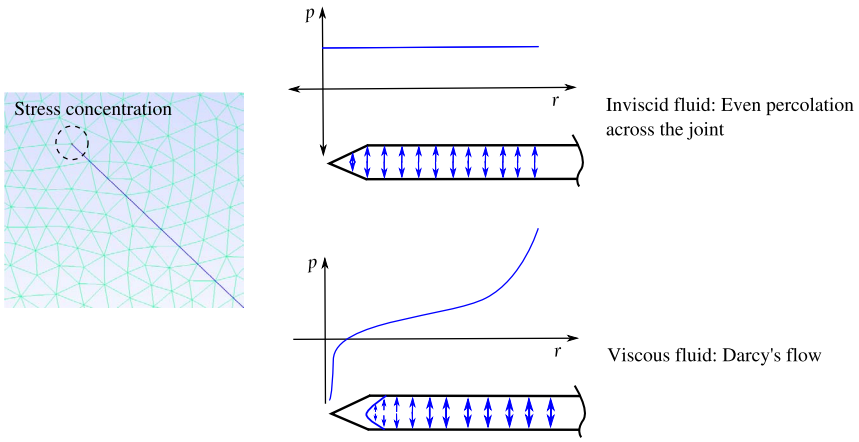

Fig. 5. Fluid pressure profile across an arbitrary joint while assuming inviscid fluid (the approach of this paper) and viscous fluid.

3.1. Geometry, meshing and material properties

The Boundary Value Problem (BVP) considered here is representative of a small–scale low–volume injection test (Hawkes et al., 2013). It uses a vertical wellbore of 0.1 m diameter located in a 8 m × 8 m rock formation. The model represents a barefoot wellbore section without cementing or casing as the rock medium is assumed impermeable. To capture deformation process changes near the wellbore, the mesh is intensively refined with 3.0 mm elements in an area of 0.8×0.8 m^2. Away from the zone of the intensive refinement, element size is gradually increased to 0.3 m (Fig. 6).

Two–dimensional plane strain conditions are modelled. Apparent volumes are calculated assuming unit length in the out–of–plane direction. As the purpose of this section is to study near–wellbore fracturing and the effect of pre–existing joints without imitating any real field situation, we shall assume that the rock layer is bounded and fractures are forced to initiate and evolve in a horizontal plane.

The material properties are listed in Table 1. The input data as well as the *is situ* stress measurements correspond to a granitic formation of 1800 m depth (Evans et al., 2009). Although the geomechanical characteristics of granite differ somewhat from shale formations, the main focus of this work is to investigate fluid–driven fracture topology due to pre–existing joints. Therefore, the specific details of the particular unit are less important. The fracture energy values and the computational parameters of Table 1 are calculated based on the recommendations of Tatone and Grasselli (2015), Lisjak et al. (2014a), Mahabadi (2012). The sign convention adopted in this research attributes negative sign to compressive stresses.

3.2. Boundary and initial conditions

To study the effect of the far–field stress state, HF simulations are performed while assuming: (1) isotropic far–field stresses of $\sigma_h = \sigma_H = -32.6$ MPa and; (2) anisotropic far–field stresses of $\sigma_h = -32.6$ MPa and $\sigma_H = -34.8$ MPa. The formation fluid pressure is set to 28 MPa. As effective stresses are used directly in the calculations, the calculated values of fluid pressure represent the effective fluid pressure (the increment above the formation fluid pressure). A geostatic/elastic step is initially simulated without the wellbore being present by applying the initial far field stresses on the boundary of the model and allowing the forces to come into equilibrium throughout the model (zero velocity). The boundary conditions are then set to zero–displacement to allow for borehole excavation (Fig. 6). The excavation of the borehole is implemented in two steps: the first step involves reduction of the elastic modulus of the borehole material by 10%; in the second step, the elements forming the wellbore are removed. Fluid pressure, applied as nodal forces, is defined by the injection rate and the explicit time step considered. The numerical breakdown pressure (when fracturing is initiated) was found to be reasonably constant at injections rates below (~100 l/s), but started to increase once this threshold value was exceeded. The dependence of breakdown pressure on high injection rates is similar to the laboratory observations that

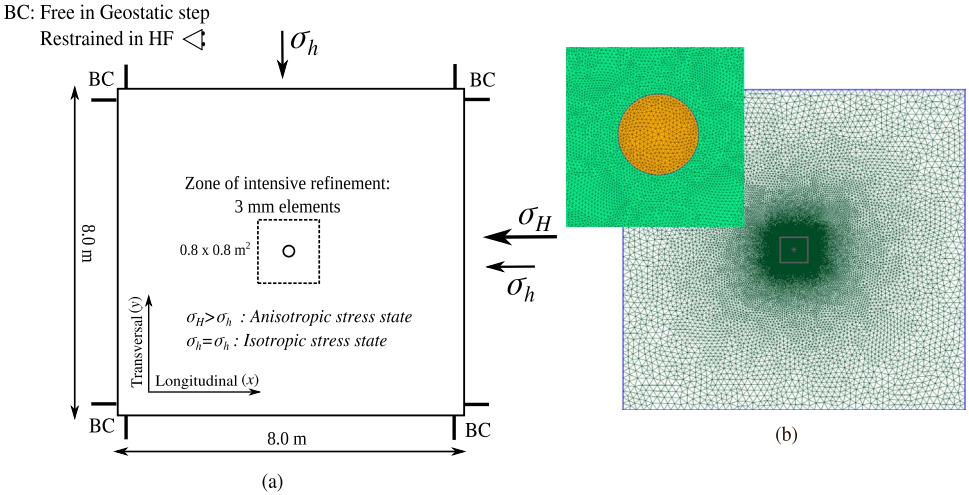

Fig. 6. (a) The geometry and boundary conditions of the BVP chosen for HF simulations. The diameter of the uncased wellbore is 0.1 m. Two cases of far–field stress loading: 1) isotropic when the longitudinal stress is σ_h; 2) anisotropic when the longitudinal stress is σ_H. (b) Triangular Delaunay meshing of the domain showing refinement of element size approaching the wellbore.

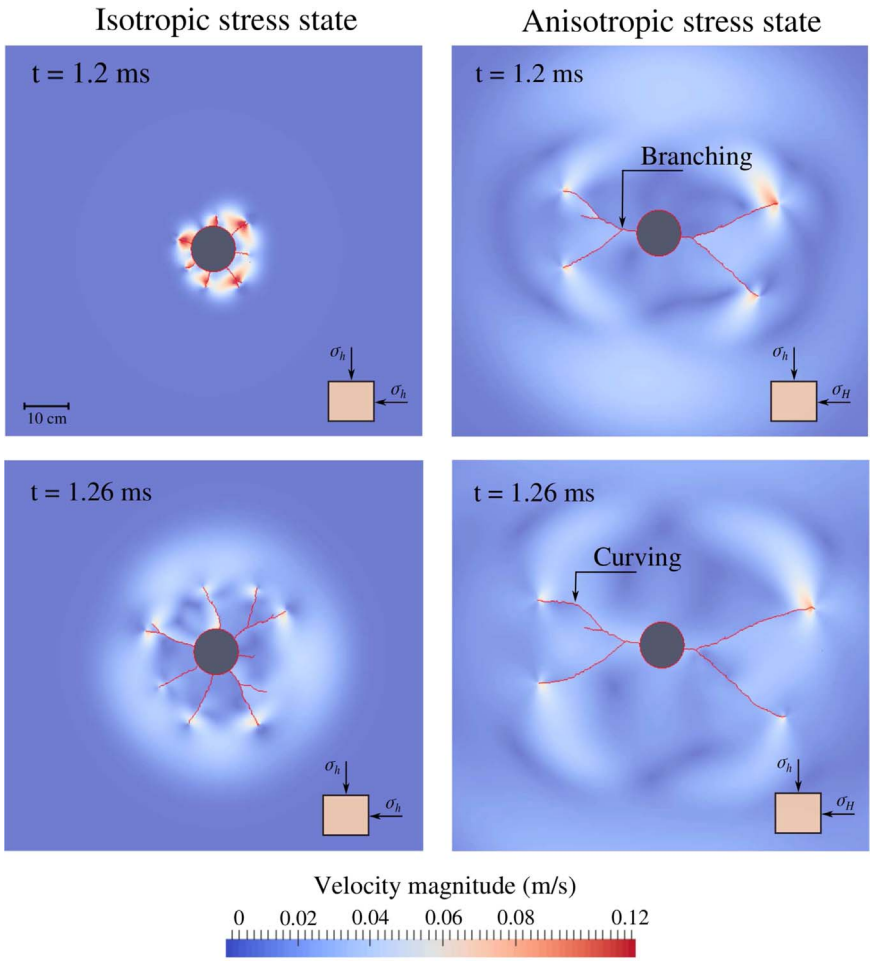

Fig. 7. Fracture topology/trajectory for the cases of isotropic and anisotropic far–field stress states and for two different times. The trajectories are plotted in the field of velocity magnitude. The point at which branching initiates appears to coincide with a transition from near–wellbore stress environment (with a dominant contribution of hoop stress) to a far–field stress.

material strength generally increases for fast loading strain rates Lisjak et al. (2014a), Fig. 8. Therefore, the final stage of the simulation includes injecting fluid into the borehole at constant apparent flow rate of Q=20 l/s that was arbitrarily chosen to be below the threshold limit.

3.3. Simulations and discussion

Fig. 7 shows the fracture trajectories for the two cases of isotropic and anisotropic stress states. These trajectories are plotted in the field of velocity magnitude as an indication of the elastic pulse spreading in the medium due to fracturing. The comparison is shown for the same time for each simulation. The parameter t, shown on this figure and the following ones, represents the time span from the beginning of injection. The Same fracture patterns were obtained for nominal element sizes of 2.0 and 4.0 mm, however, the smallest element size of 3.0 mm is chosen as it reproduces the material tensile strength (Section 2.3). For the simple case of a homogeneous medium subject to isotropic stress state, the initial fracture growth shows complex fracturing similar to that observed in the Barnett shales in north Texas (Vermylen and Zoback, 2011). For the anisotropic stress field, the classical bi–wing tensile fracturing is observed initially, then the bi–wings start to branch and curve yet grow predominantly in the direction of maximum stress.

As expected for hydraulic fracturing (Fjaer et al., 2008), our simulations based on the material properties of Table 1, produce mode I failure for hydraulic fracture patterns presented in this paper except for the cases of joint shear slip (Section 4.2). The initial hoop stress state, due to borehole excavation, has promoted an initial bi–wing fracturing, however, consecutive branching and curving of fractures in the direction of maximum stress is observed. Similar results of branching and curving have been previously reported and verified against experimental data (laboratory specimens) (Tatone and Grasselli, 2015). It has also been observed that the viscosity of the injected fluid affects the generated fracture patterns, wherein less viscous fluids tend to promote branching and curving of fractures (Ishida et al., 2004). In general, the higher the fluid dynamic viscosity, the slower the fluid propagation for the same pressure gradient. This leads to a gradually propagating fluid pressure force that smoothly alters the stress field at the fracture tip and fosters the evolution of a bi–wing fracture pattern.

4. Simulations of HF in jointed rock masses

Rock formations often contain pre-existing joints and fractures that act as zones of weakness and/or stress concentrators (Gale et al., 2007). In some cases such joints may be created due to stresses caused by the drilling processes (Brudya and Zoback, 1999), or exist naturally in certain density in rock layers. In this section we consider the effect of pre–existing joints close to the wellbore on HF and fracture trajectory. It is considered that such joints play an important role in inducing and directing microseismicity (Fischer et al., 2016; Shapiro and Dinske, 2009).

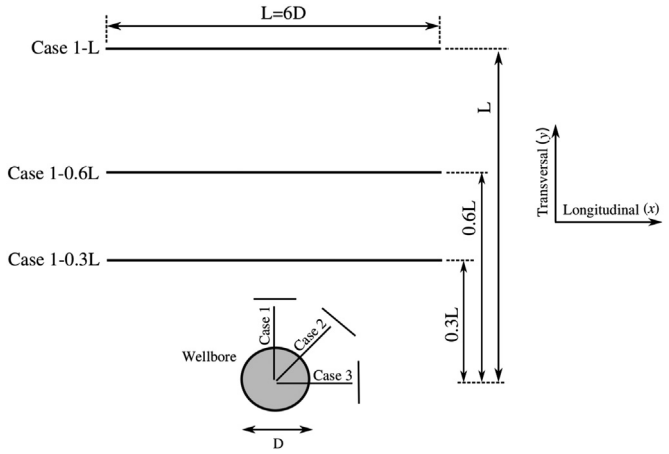

Fig. 8. Longitudinal rock joint of length $L = 6D$ and at distances 0.3 L, 0.6 L and L from wellbore. To study the effect of rock joint orientation, the rock joint is oriented 45° and 90° form the longitudinal, as indicated by case 2 and case 3 respectively.

4.1. Single isolated joints: lateral stress gradient

In this section various scenarios involving a single isolated pre–existing joint close to the wellbore are investigated in relation to fracture growth topology and fracturing pressure. We consider a single rock joint of length L (where $L = 6D$, D is the diameter of the wellbore) located at discrete distances ($0.3L$, $0.6L$ and L) and different orientations (Longitudinal (L) 0°, Oblique (I) 45° and Transversal (T) 90°) to the borehole (Fig. 8). Rock joint length, its distance and orientation to the wellbore are arbitrarily set to explore how the rock joint may influence the initial stress field and the resulting fracture growth. In total, nine simulations were carried out representing the different configurations with all simulations performed under the anisotropic far–field stress state.

The presence of a joint around the wellbore as well as its orientation are expected to affect fracture growth. Indeed, HF induced microseismicity tends to concentrate in the regions where fracture evolution is prevalent (Shapiro and Dinske, 2009). Fluid diffusion is also dominant in the regions of fracture propagation and therefore may influence the long–term shear–slippage microseismic/seismic events (Shapiro and Dinske, 2009).

Fig. 9 shows contours of effective longitudinal stress (σ'_{11}) for the reference case (no rock joints) and for the three cases of different joint orientation at a distance of 0.3 L from the wellbore immediately prior to the onset of fracturing. It can be seen that changes in the stress field (perturbations) occur during the injection of fluid into the borehole, with case 2 giving appreciably greater perturbations in the stress field compared to the reference case where no joint is present. Case 1 is experiencing minor perturbations that are highlighted by the two arrows. However, it can be seen that for a joint normal to the major principal stress (case 3) no appreciable perturbations are observed. These perturbations in the stress field lead to an increase in the onset of fracturing pressure and later time for when fracturing occurs (Fig. 9 and Fig. 11(a)). This is demonstrated by the earlier time span for the reference case and the transversal joint in case 3. The existence of rock joints at this distance from the wellbore lead to stress concentrations around the rock joint, this is especially evident for case 2 where localized zones of shear failure/slip can been seen at the joint tips. This shear slip is due to mode II of failure as indicated by Fig. 3(b) and Eq. (2), and is further highlighted in the following section.

Fig. 10 shows fracture trajectories for the three rock joint orientations described in Fig. 8 at a distance of 0.3 L from the wellbore. It can be inferred that perturbations in the stress field resulting from the presence of the rock joints lead to significantly different fracture evolution/topology; compare for example t=1.26 ms in Fig. 10 with Fig. 7 at the same time. For case 2 with oblique rock joint, it is clear that fractures initiate in a direction that is oriented away from the zone of stress perturbation created by the pre–existing joint. This is also evident for case 1 with a longitudinal joint, albeit to a lesser degree, i.e. if we consider the total fracture length that occurs above and below the borehole centreline, the total fracture length below is longer than that above the borehole centreline. For case 3 with the joint normal to the direction of maximum far–field stress, the joint does not appear to have a significant effect on the initiation or the resultant preferred direction of fracture growth. Once the fracture is initiated however, the stress field resulting from the rock joint seems to suppress any potential branching of the fracture, check case 3 of Fig. 10.

The influence of the rock joint orientation can be also observed in the injection pressure profiles plotted in Fig. 11(a) and the threshold values when fracturing occurs. For case 3, the threshold of fracturing pressure is not significantly altered and closely matches that observed for the reference case with no joints. However, the change in stress field due to the presence of longitudinal or oblique pre–existing joints can be seen to increase the fracturing threshold by ~5.2%. The increase in the fracturing threshold as well as the tendency of fracture growth away from the zone of stress perturbation/pre–existing joints can be attributed to the more work/energy that has to be exerted to overcome these stresses. It is easier for fractures to grow/initiate in the direction of lower stresses (away from perturbations).

Fig. 12 shows fracture topology for the three cases of the fracture joint at a distance 0.6 L from the wellbore. As expected, the effect of pre–existing joints in causing stress perturbations becomes smaller as the joint is located farther away from wellbore. Cases 1 and 2 still exhibit preferential growth of fractures towards left/asymmetric fracture growth, at least for early time frame of stimulation (t < 1.38 ms). However, fractures in case 3 exhibit almost the same fracture growth as if the rock joint did not exist (compare for instance case 3 at 1.26 ms in Fig. 12 with that in Fig. 7).

Fracturing pressure profiles for the three cases of different joint orientations at distance 0.6 L from wellbore are shown in Fig. 11(b). Although fracture growth is somewhat influenced by the stress field the graph shows that the breakdown pressure closely matches that for the case of no joints. In considering Fig. 11, it can be seen that the post–peak behaviour of the pressure is independent of the distance of the joint away from the wellbore. This is usually called the steady fracture growth pressure and it is equal to the far–field stress (Fjaer et al., 2008), in our case 5.5 MPa (as effective/net pressure).

For the rock joint at a distance L from the wellbore, no appreciable differences in fracture trajectories are evident in Fig. 13 when compared with Fig. 7 at 1.26 ms. The relatively high intensity of branching on the right hand side of the wellbore for case 3 can be related to the sort of numerical instabilities due to non–symmetric mesh refinement in the direction of the joint, i.e. direction of maximum far–field stress.

4.2. Multiple joints: induced microseismicity

This section investigates fluid–driven fracture interaction with pre–existing joints in heavily fractured rock formations. It also explores possible Microseismic Events (MEs) due to fracture shear slip incited by rock deformation/fracturing elastic pulses. A set of randomly distributed joints (Fig. 14) with average length of 3.1 cm and fracture density of 320/m^2 was created in the zone of intensive refinement shown in Fig. 6. No joints intersect the borehole to ensure that pure fluid–driven fracture growth occurs before interaction with joints.

Fig. 15 shows the fracture patterns for the two far–field stress scenarios (isotropic and anisotropic) at time 1.36 ms since injection. The joints around the borehole influence the fluid–driven fracture patterns (compare with Fig. 7). Once an existing joint is intersected by a hydraulic fracture, the fluid pressure is spread over the entire new "wet boundary" and leads to fracture initiation at the joint tips (Section

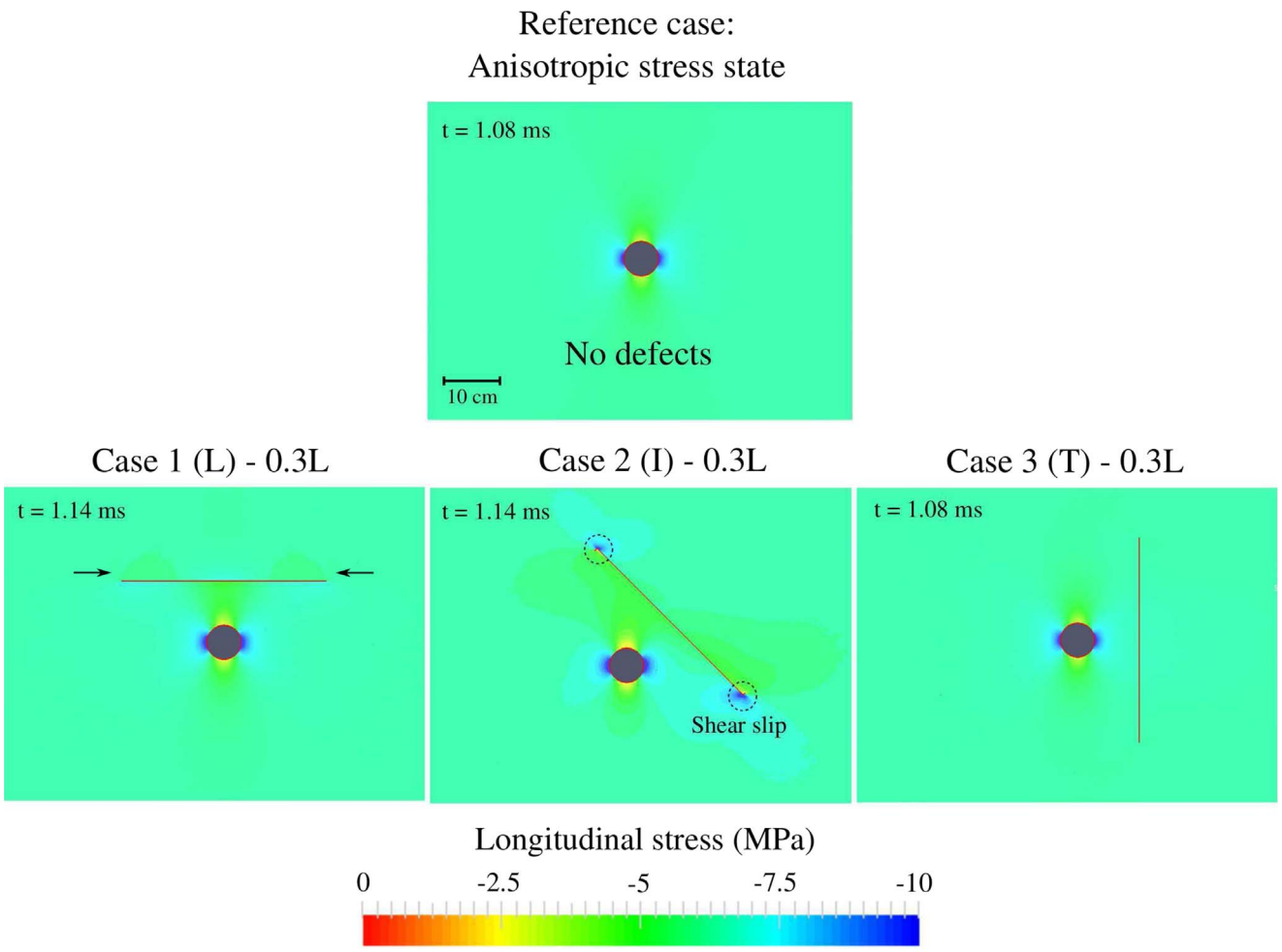

Fig. 9. Effect of pre–existing joint on the field of effective longitudinal stress component (σ'_{11}) just before the initiation of HF. The threshold of fracturing for case 3 is the same as the no joints case, i.e. t=1.08 ms. This can be related to the reduced magnitude of perturbation on stress field created by the transversal joint.

2.4). Possible shear slippage at some joints due to changes in the stress field generated during hydraulic fracturing is observed for both far–field states. These slips will lead to microseismic events (Eq. (2) and mode II of failure) that are not related to the actual fracture propagation; some events are highlighted in the isotropic stress state of Fig. 15.

Fig. 16 shows the ME locations for time spans of 1.28 and 1.4 ms for the isotropic far–field stress state. The breaking of each cohesive fracture element produces a ME. The initial time of the event is the time of element failure and the event position is the center of the element itself. While undergoing deformation, cohesive fracture elements store energy which is released at failure. The Y–Geo code calculates the kinetic energy ($E_{k,y}$) of a yielding fracture element based on the nodal mass (m_i) and nodal velocity ($v_{i,y}$) of each of the four nodes of the element (Lisjak et al., 2013),

$$E_{k,y} = \frac{1}{2}\sum_{i=1}^{n} m_i\, v_{i,y}^2, \quad i = 1,\ 2,\ 3,\ 4. \tag{11}$$

The kinetic energy ($E_k(t)$) of the element nodes is then monitored from the time of yielding (t_y) to time of failure (t_f),

$$\Delta E_k(t) = E_k(t) - E_{k,y}. \tag{12}$$

The microseismic energy (E_e) is calculated as the maximum of $\Delta E_k(t)$ from yielding to failure. E_e is then used to calculate the event magnitude (M_e) by applying the Gutenberg relation (Lisjak et al., 2013),

$$M_e = \frac{2}{3}(\log_{10} E_e - 4.8). \tag{13}$$

It can be seen that the MEs typically follow the evolution of the hydraulic fracture patterns except for some scattered incidents (Fig. 16(a)) that are related to shear slippage at joints due to changes in stresses induced by elastic deformation of the medium. Fig. 17 shows the magnitudes of the MEs, which corresponds to the range of values associated with induced HF microseismicity (Schoenball et al., 2010). As highlighted previously, the HM approach adopted gives rise to joints being subject to uniform fluid pressure as soon as the joint is intersected by fluid–driven fracture, i.e. the rock joints are assumed to have infinite permeability. In reality, joints and the rock matrix will have finite permeability and therefore stress changes away from the hydraulic fractures will be somewhat different due to diffusion driven pressure changes. Consequently, occurrence and location of MEs maybe more widespread than suggested by our simulations. In addition, the space distribution of the pre–existing joints (Fig. 14) will also change fracture topology and location of MEs. The following points are observed:

1. pre–existing joints create a pre–fracturing stress state that affects the patterns of the initiated fractures and increases the threshold of fracturing;
2. stress gradients, simulated here by pre–existing joints, lead to asymmetric fracture growth with a tendency for fractures to develop in the direction of lower stress;
3. rock joints increase the extent to which fluid–driven fractures can reach;
4. the HM coupling approach adopted in our simulations ensures that once a joint is intersected by a fluid–driven fracture, the fluid

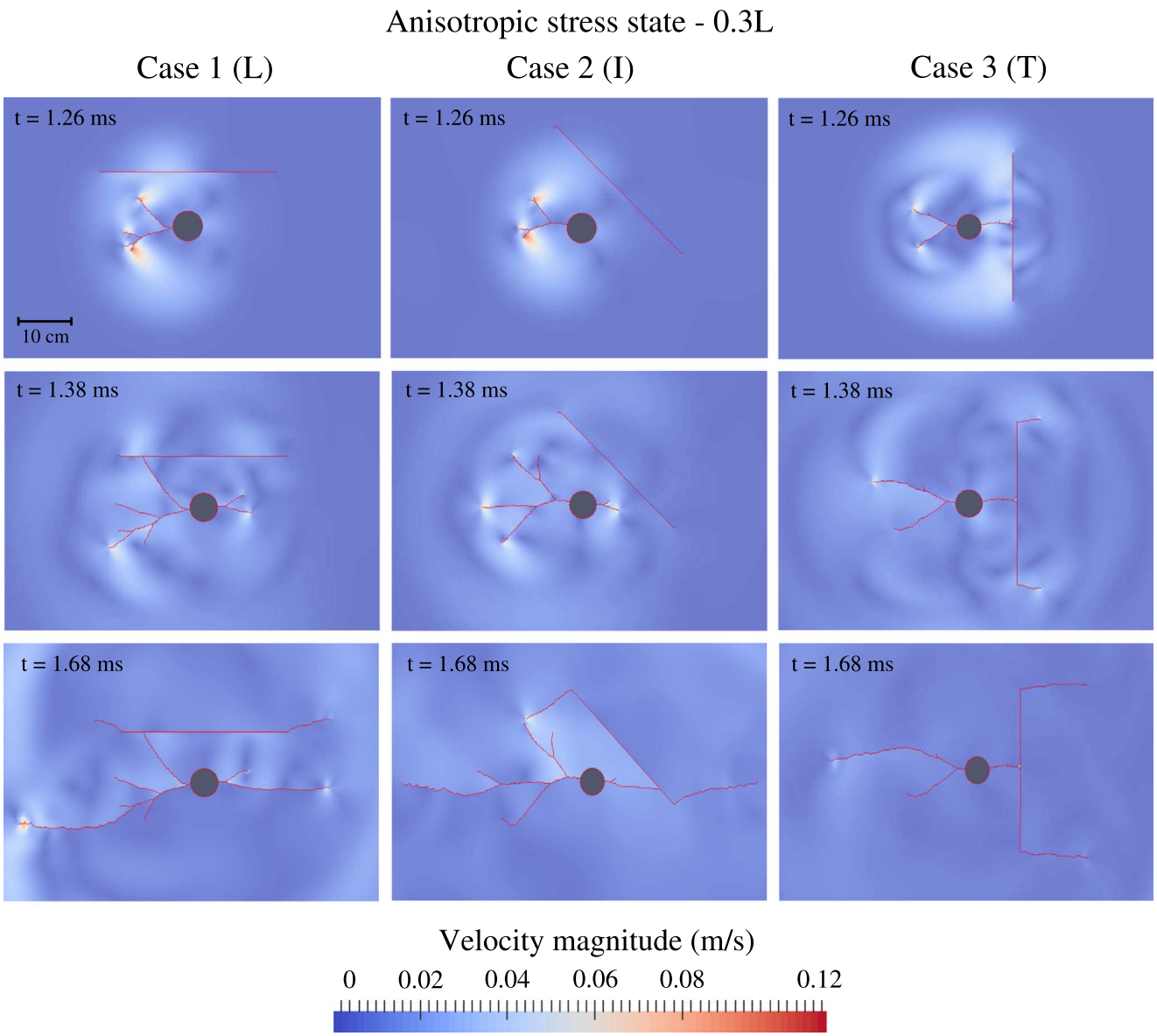

Fig. 10. Fracture trajectories for the three cases of joint configurations described in Fig. 8 at times of 1.26, 1.38 and 1.68 ms and at distance 0.3 L from wellbore. The trajectories are plotted in the field of velocity magnitude.

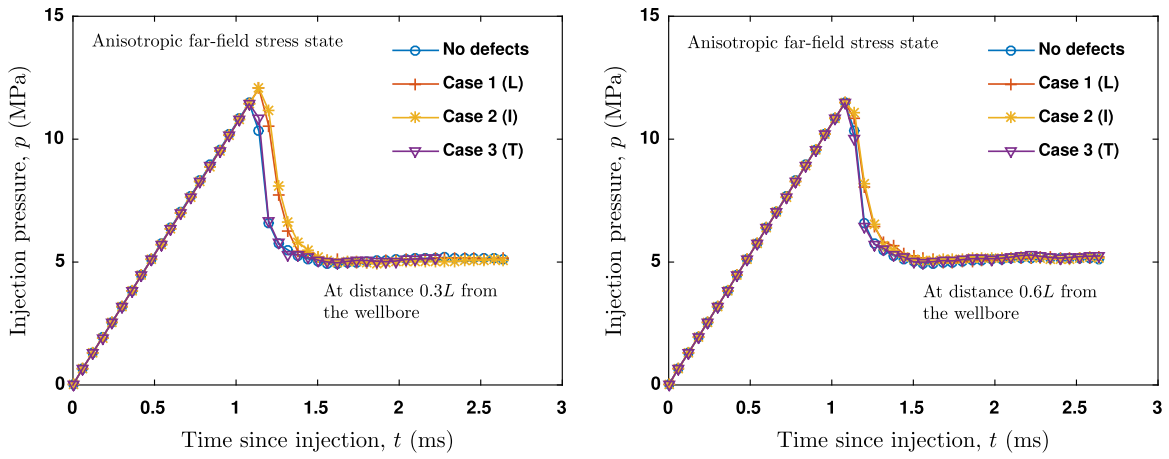

(a) Joint at distance $0.3L$ from wellbore (b) Joint at distance $0.6L$ from wellbore

Fig. 11. Numerical fracturing pressure profiles for the three cases of joint configurations described in Fig. 8 at distances: (a) 0.3 L; (b) 0.6 L from the wellbore.

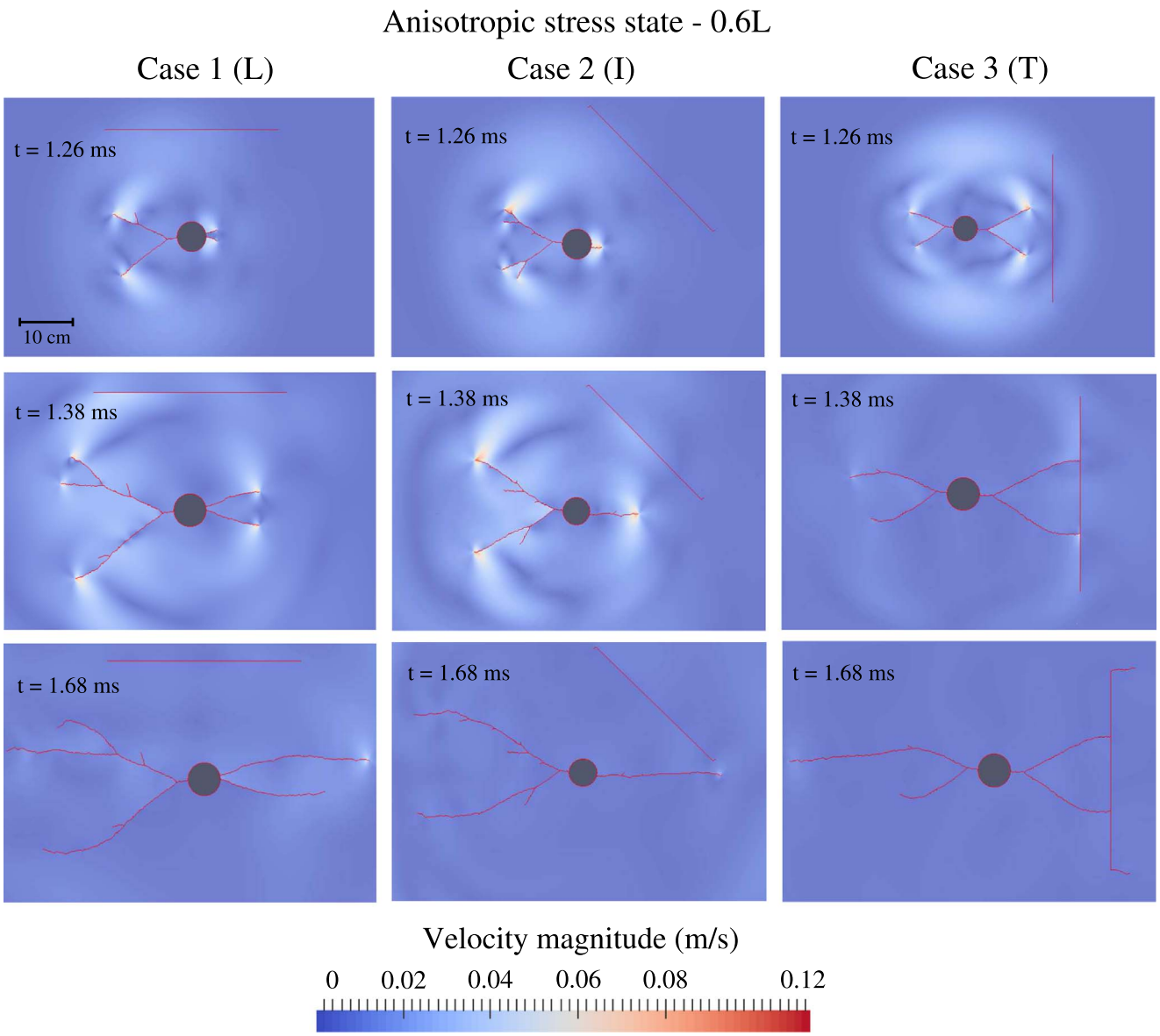

Fig. 12. Fracture trajectories for the three cases of joint configurations described in Fig. 8 at times of 1.26, 1.38 and 1.68 ms and at distance 0.6 L from wellbore. The trajectories are plotted in the field of velocity magnitude.

pressure is applied over the whole joint, and therefore new fractures initiate at the joint tips. The influence of rock matrix and joint permeability may give rise to different stress conditions;

5. in our simulations, MEs due to joint shear slippage result from elastic rock deformation only. Such events can go as far as the fluid–driven fractures as long as there are critically stressed joints that might be activated, see the propagation of MEs between Fig. 16(a) and (b). This behaviour may also occur if stress changes are induced by enhanced pore pressure diffusion within the rock matrix.

5. Simulating a low–volume field injection test

The purpose of this section is to compare the breakdown pressure derived from the Y-Geo code against a field test. The field data represents the fluid pressure response during a low–volume injection test in the Farrell Creek Montney reservoir, north–east British Columbia, Canada (McLellan et al., 2014; Fan, 2015). A horizontal wellbore was drilled in the direction of the minimum horizontal stress σ_h perpendicular to σ_H (Fig. 18) and to a Total Vertical Depth (TVD) of 2099 m. At this location the ambient stress state is anisotropic with $\sigma_H^{'} = -15.5$ MPa and $\sigma_V^{'} = -18.3$ MPa, and the reservoir pressure $p = 34.84$ MPa. The mechanical properties pertaining to the rock formation at this depth are ($E = 42.5$ MPa, $\nu = 0.17$, $f_t = 10.75$ MPa, $c = 21.1$ MPa, $G_{\mathrm{Ic}} = 100$ N/m, $G_{\mathrm{IIc}} = 150$ N/m, and $\phi_i = \phi_f = 46.5°$). The maximum *in situ* stress σ_H orientation was determined from borehole breakouts and found to be around 42° from north.

A 15 m × 15 m vertical cross section of the formation is simulated, and it is assumed that the rock volume is homogeneous and isotropic for the volume considered. The model represents a two–dimensional domain where the far–field stresses are the maximum horizontal σ_H and vertical/overburden σ_V stresses. As the reservoir is seen to expand considerably in the horizontal plane, and as the directions of the major principal stresses (σ_V and σ_H) represent the favourable directions for fracture growth, fracture evolution in the third direction can be assumed negligible and the two–dimensional (σ_V–σ_H) approach becomes reasonable. Grid dimensions are obtained by determining the model size beyond which further increases yielded no change in simulation results (Fig. 18). Gravitational effect is considered and the

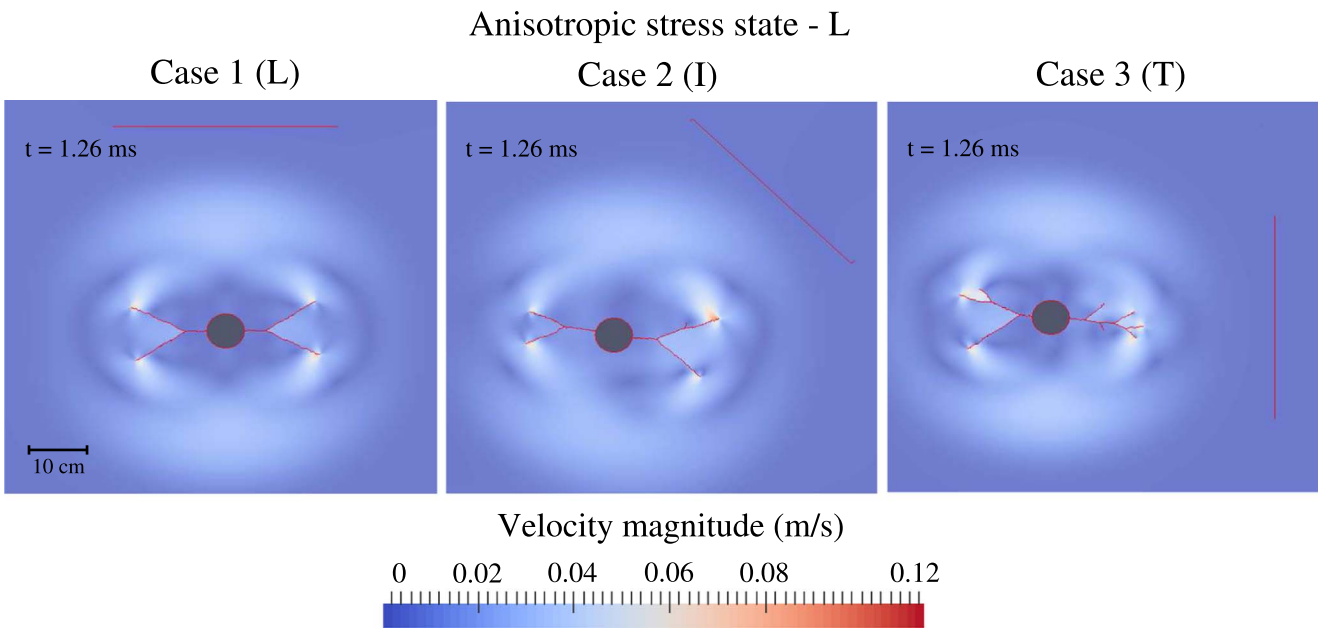

Fig. 13. Fracture trajectories for the three cases of joint configurations described in Fig. 8 at time of 1.26 ms and at distance L from wellbore. The trajectories are plotted in the field of velocity magnitude.

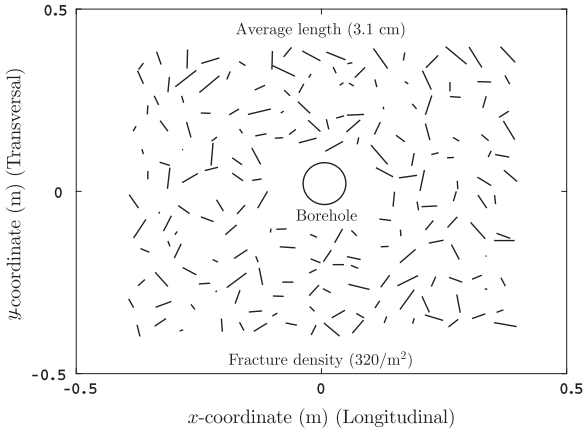

Fig. 14. A set of randomly distributed joints generated around the borehole to study fracture interaction and shear–slip microseismicity. Joint length is normally distributed around 3.1 cm and fracture density is 320/m^2.

injection rate is used as in the field test, i.e. Q = 1.0 m^3/min, i.e. 16.67 l/s, which is lower than the threshold injection rate highlighted previously.

Fig. 19 shows a comparison between the injection pressure derived from the numerical simulation and the field data during the elastic and the pre–shutdown period. The numerical response captures the linear increase in fluid pressure during the field trial as well as the breakdown pressure of ~76 MPa. The good correlation between simulation and field test up to the breakdown pressure might indicate the pre–assumed isotropic nature of the rock formation at this location. The simulated post–peak behaviour differs from the field, due to a variety of effects such as leakoff that are not accounted for in our current analysis.

6. Conclusions and future work

A hybrid FEM/DEM approach with inviscid flow is utilized in this study to track fluid–driven fractures topology in both homogeneous and pre–fractured media. Consistent with HF field observations, our study shows that an isotropic stress state favours complex fracture growth compared with anisotropic stress state. Fluid–driven fracture patterns are significantly influenced by pre–existing joints/fractures that can increase the extent of fracture growth. Rock joints that are offset from the wellbore give rise to stress gradients that lead to asymmetric fracture growth with a tendency for fractures to initiate and grow in a direction away from the rock joint. Due to the hydro–mechanical approach adopted in Y-Geo (inviscid fluid and infinite joint permeability), once a hydraulic fracture intersects a pre–existing joint, the fluid induced fracture system exploits and extends natural fractures at the joint tips. However, a finite joint permeability may give rise to different phenomena once intersected by a fluid–driven fracture. Changes in the stress field resulting from elastic deformation of the rock through hydraulic fracturing initiate localized shear slip of pre–existing joint tips, which gives rise to mode II microseismic events that are remote from evolving hydraulic fractures. This would suggest that changes in local stresses due to fluid diffusion and leakoff from pressurized hydraulic fractures may lead to critically stressed joints exhibiting shear slip that might be more widespread and of greater magnitude than those observed in our simulation.

The Y-Geo code utilized in this study has reproduced certain features predicted by empirical observations and has been used to explore more complex fracturing scenarios. Understanding such behaviour is important for predicting the direction and extent of hydraulic fractures, the potential induced microseismicity, and the relationship to field tests.

Acknowledgment

The authors would like to thank the sponsors of the Microseismic Industry Consortium and NSERC for their financial support.

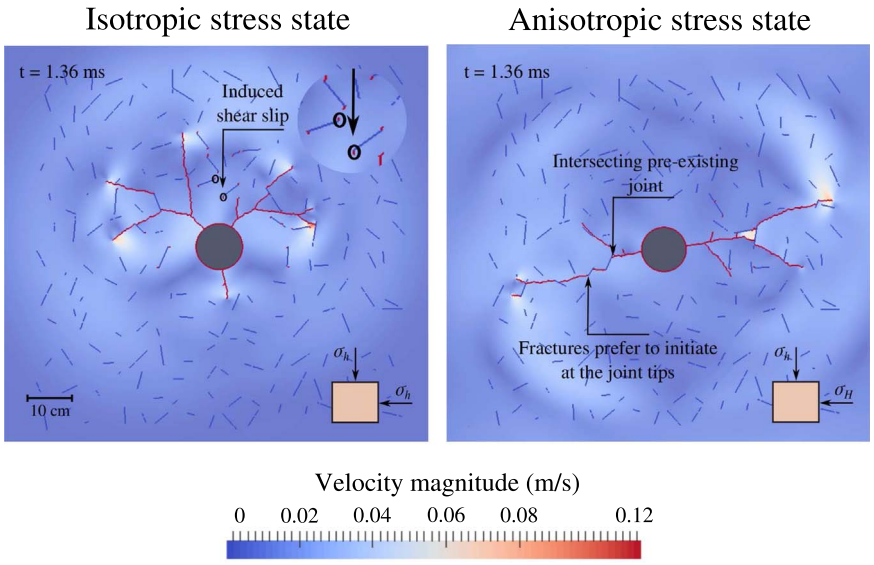

Fig. 15. Fracture patterns for the cases of isotropic and anisotropic stress states in a heavily fractured rock formation (Fig. 14) at time of 1.36 ms since injection. The trajectories are plotted in the field of velocity magnitude.

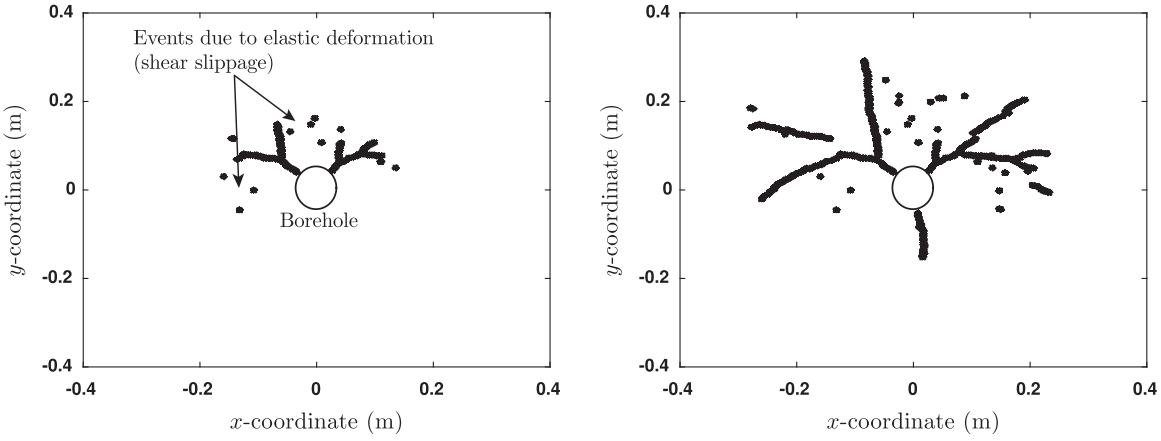

Fig. 16. ME locations due to fracturing with the isotropic far–field stress state. The MEs follow the fracture topology except for some scattered locations incited by fracturing elastic pulses/formation deformation.

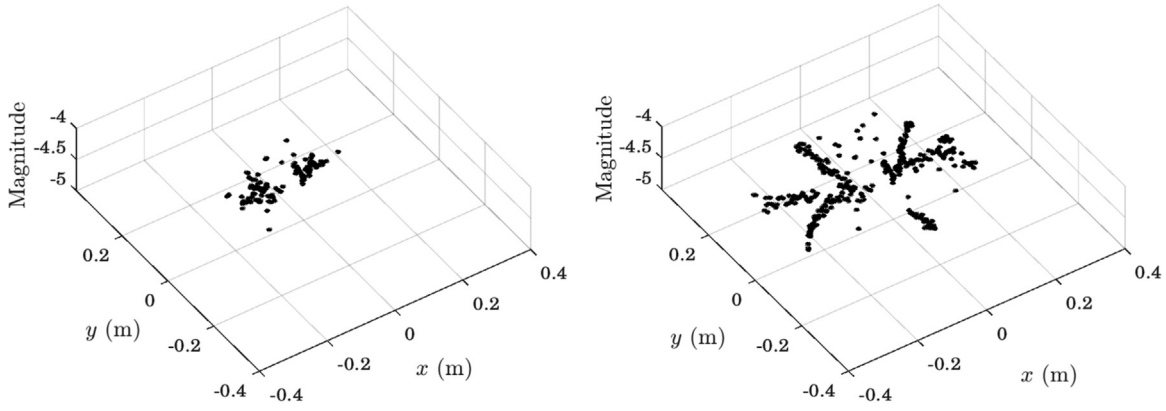

Fig. 17. Magnitudes of the microseismic events presented in Fig. 16. The values are in the range of monitored HF induced microseismicity.

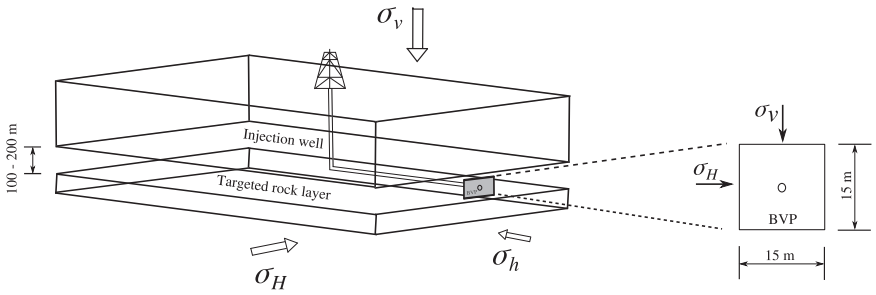

Fig. 18. Schematic diagram of the targeted hydraulic fracturing site at the Farrell Creek Montney reservoir. The targeted shale layer is bounded to a vertical height that ranges between 100 and 200 m and it is seen to expand to considerable lengths in the horizontal plane. The extent of the model was determined such that further dimension increases yielded no change in simulation results. The BVP domain is refined such that the smallest triangular element size (6 mm) corresponds to the rock tensile strength of f_t = 10.75 MPa.

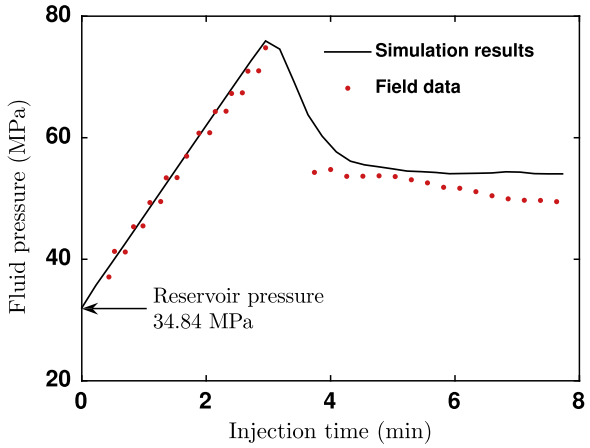

Fig. 19. Low–volume injection test pressure profile within the Montney Formation. The red dots represent the field data and the solid line shows the numerical response by FDEM–HF/the Y–Geo code.

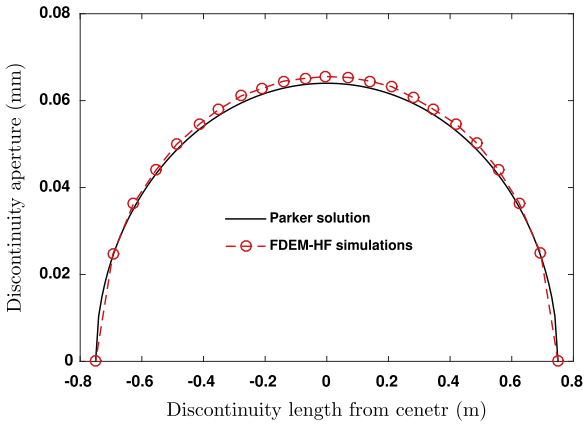

Fig.A.21. Evolution of the discontinuity aperture (Fig. A.20(a)) due to uniform fluid injection: Comparison between the analytical solution of Parker (1981) (solid line) and the simulations by the FDEM-HF/the Y-Geo code with inviscid flow (dashed line with circles).

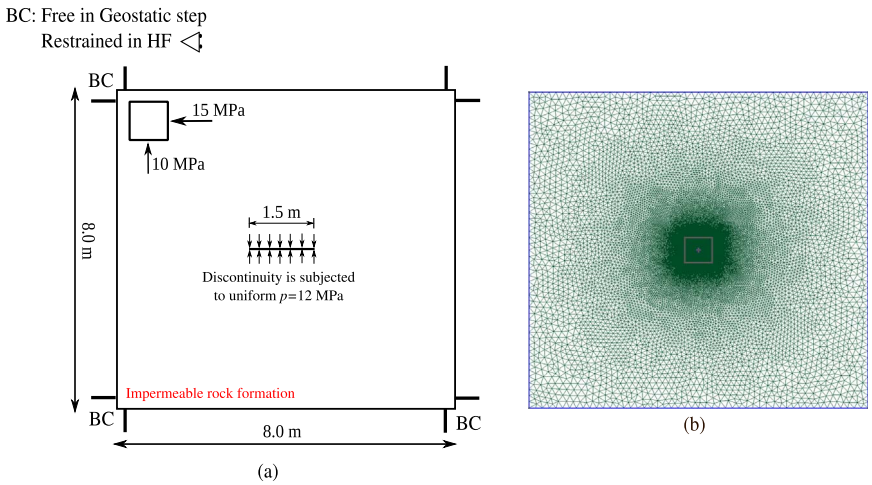

Fig.A.20. (a) A discontinuity subjected to uniform fluid pressure of 12 MPa and embedded in high strength linear elastic medium. (b) Triangular Delaunay meshing of the domain where element size range goes from 0.003 to 0.3 m.

Appendix A. Verification of the Hydro–Mechanical (HM) coupling

This section aims at verifying the Hydro–Mechanical (HM) approach adopted in this paper while assuming inviscid flow. However, the mechanical behaviour of fracturing by the FDEM alone has been intensively verified in the works of Mahabadi et al. (2012), Lisjak et al. (2013), Lisjak et al. (2014a). The BVP represents a discontinuity subjected to a uniform injection pressure and embedded in high strength linear elastic impermeable rock formation (Fig. A.20).

High elastic parameters are used to ensure linear elasticity, i.e. E=45 MPa and ν = 0.2. Tensile strength, cohesion and fracture energies are given irreal high values as well to prevent fracture length growth. Far–field stresses are displayed on the graph. Parker (1981), p.33 found an analytical solution to describe the development of the fracture aperture (Fig. A.20(a)) in plane–strain condition,

$$w(x) = \frac{2\sigma'(1-\nu^2)}{E}\sqrt{\ell^2 - x^2}, \tag{A.1}$$

where σ' is the opening effective stress $(-10 + p)$ MPa, ℓis the discontinuity half length, and p is the pressure inside the discontinuity. The change in the discontinuity aperture due to fluid injection is displayed in Fig. A.21. This figure shows that there is a good correlation between the analytical solution of Parker and the results of simulations obtained by the FDEM–HF/the Y–Geo code.

References

AbuAisha, M., Loret, B., 2016a. Influence of hydraulic fracturing on impedance and efficiency of thermal recovery from HDR reservoirs. Geomechanics for Energy and the Environment, http://dx.doi.org/10.1016/j.gete.2016.02.001.

AbuAisha, M., Loret, B., 2016. Stabilization of forced heat convection: applications to Enhanced Geothermal Systems (EGS). Transp. Porous Media 111 (1), 1–24.

AbuAisha, M., Loret, B., Eaton, D., 2016. Enhanced Geothermal Systems (EGS): hydraulic fracturing in a thermo-poroelastic framework. J. Pet. Sci. Eng. 146, 1179–1191.

AbuAisha, M., 2014. Enhanced geothermal systems: Permeability stimulation through hydraulic fracturing in a thermo-poroelastic framework. (Ph.D. thesis), Université de Grenoble, France, April.

Adachia, J., Siebritsb, E., Peirce, A., Desrochesd, J., 2007. Computer simulation of hydraulic fractures. Int. J. Rock. Mech. Min. Sci. 44 (55), 739–757.

Bai, J., Lin, A., 2014. Interaction between multiple injections using tightly coupled fluid-structure interaction computational algorith. In: the Abu Dhabi International Petroleum Exhibition and Conference, Paper SPE 171735, Abu Dhabi, UAE, November; 10–13.

Bai, J., Dusterhoft, R., Walters, H.G., Sperrazza, N., McNealy, T., 2016. Coupled geomechanics and fluid flow computational algorithm for hydraulic fracturing simulations: case studies. In: the 50th US Rock Mechanics/Geomechanics Symposium, Houston, Texas, USA, June;26–29.

Barenblatt, G.I., 1959. The formation of equilibrium cracks during brittle fracture. General ideas and hypotheses. axially-symmetric cracks. J. Appl. Math. Mech. 23 (3), 622–636.

Barenblatt, G.I., 1962. The mathematical theory of equilibrium cracks in brittle fracture. Adv. Appl. Mech. 7, 55–129.

Barree, R.D., Fisher, M.K., Woodrrof, R.A., 2002. A practical guide to hydraulic fracture diagnostic technologies. In: the SPE Annual Technical Conference and Exhibition, Paper SPE 77442, San Antonio, Texas, USA, 29 September - 2 October.

Brudya, M., Zoback, D.M., 1999. Drilling-induced tensile wall-fractures: implications for determination of in-situ stress orientation and magnitude. Int. J. Rock. Mech. Min. Sci. 36 (2), 191–215.

Bruel, D., 1995. Modelling heat extraction from forced fluid flow through simulated fractured rock masses: evaluation of the soultz-sous-forêts site potential. Geothermics 24 (3), 439–450.

Dusseault, M.B., 2013. Geomechanical aspects of shale gas development. In: Marek, K., Dariusz, L. Rock mechanics for resources, energy and environment. Leiden: CRC Press, P. 39–56.

Evans, K., Valley, B., Häring, M., Hopkirk, R., Baujard, C., Kohl, T., Mégel, T., André, L., Portier, S., Vuataz, F., 2009. Studies and support for the EGS reservoirs at Soultz–sous–Forêts. Technical report,Centre for Geothermal Research – CREGE, c/o CHYN, University of Neuchâtel.

Fan, S., 2015. Diagnostic fracture injection test analysis. Technical report, Encana Corporation, 27 May-10 June 2015.

Fischer, T., Hainzl, S., Dahm, T., 2016. The creation of an asymmetric hydraulic fracture as a result of driving stress gradients. Geophys. J. Int. 179 (1), 634–639.

Fjaer, E., Holt, R.M., Horsrud, P., Raaen, A.M., Risnes, R. 2008. Petroleum related rock mechanics. Elsevier B.V., Radarweg 29, 1000 AE Amsterdam, The Netherlands, second edition.

Gale, W.F.J., Reed, M.R., Holder, J., 2007. Natural fractures in the Barnett shale and their importance for hydraulic fracture treatments. AAPG Bull. 91 (4), 603–622.

Hawkes, V.R., Anderson, I., Bachman, R.C., Settari, A., 2013. Interpretation of closure pressure in the unconventional montney using PTA techniques. In: the SPE Hydraulic Fracturing Technology Conference, Paper SPE 163825, The Woodlands, Texas, USA, February; 4–6.

Hillerborg, A., Modéer, M., Petersson, P.E., 1976. Analysis of crack formation and crack growth in concrete by means of fracture mechanics and finite elements. Cem. Concr. Res. 6 (6), 773–781.

Hubbert, M.K., Willis, D.G., 1957. Mechanics of hydraulic fracturing. Trans. Am. Inst. Min. Metall. Eng. 210, 153–169.

Hughes, T.J.R., 2000. The finite element method; linear static and dynamic finite element analysis second edition. Dover Publications Inc, Mineola, New York.

Ida, Y., 1972. Cohesive force across the tip of a longitudinal-shear crack and griffith's specific surface energy. J. Geophys. Res. 77 (20), 3796–3805.

Ishida, T., Chen, Q., Mizuta, Y., Roegiers, C., 2004. J. Influence of fluid viscosity on the hydraulic fracturing mechanism. Trans. ASME 126 (3), 190–200.

King, G., 2010. Thirty years of gas shale fracturing: What have we learnt? In: the SPE Annual Technical Conference and Exhibition, Paper SPE 133456, Florence, Italy, September 19–22.

Lisjak, A., Liu, Q., Zhao, Q., Mahabadi, K.O., Grasselli, G., 2013. Numerical simulation of acoustic emission in brittle rocks by two-dimensional finite-discrete element analysis. Geophys. J. Int. 195 (1), 423–443.

Lisjak, A., Grasselli, G., Vietor, T., 2014a. Continuum-discontinuum analysis of failure mechanisms around unsupported circular excavations in anisotropic clay shales. Int. J. Rock. Mech. Min. Sci. 65, 96–115.

Lisjak, A., Mahabadi, O.K., Kaifosh, P., Vietor, T., Grasselli, G., 2014b. A preliminary evaluation of an enhanced FDEM code as a tool to simulate hydraulic fracturing in jointed rock masses. Rock. Eng. Rock. Mech.: Struct. Rock. Mass., 1427–1432.

Mahabadi, O.K., Lisjak, A., Munjiza, A., Grasselli, G., 2012. Y-geo: a new combined finite-discrete element numerical code for geomechanical applications. Int. J. Geomech. 12 (6), 676–688.

Mahabadi, K.O., 2012. Investigating the influence of micro-scale heterogeneity and microstructure on the failure and mechanical behaviour of geomaterials. (Ph.D. thesis), University of Toronto, Toronto, Canada.

McLellan, P., Anderson, I., Wong, J., Mostafavi, V., 2014. Geomechanical characterization of the Farrell Creek Montney reservoir, northeast British Columbia. Technical report, Talisman Energy, Calgary, Alberta, Canada, May.

Munjiza, A., Owen, D.R.J., Bicanic, N., 1995. A combined finite-discrete element method in transient dynamics of fracturing solids. Eng. Comput. 12 (2), 145–174.

Munjiza, A., Andrews, K., White, J., 1999. Combined single and smeared crack model in combined finite-discrete element analysis. Int. J. Numer. Methods Eng. 44 (1), 41–57.

Munjiza, A., 2004. The Combined Finite-Discrete Element Method. John Wiley & Sons ltd, Chichester, West Sussex, England.

Nagel, N., Houston, I., Damjanac, B., Gracia, X., 2011. Discrete element hydraulic fracture modeling-evaluationg changes in natural fracture aperture and transmissivity. In: the Canadian Unconventional Resources Conference, Paper SPE 148957, Calgary, Canada, November 15–17.

Nagel, N., Gil, I., 2011. Sanchez-Nagel, M., Branko, D., 2011. Simulating hydraulic fracturing in real fractured rock - overcoming the limits of Pseudo3D models. In: the SPE Hydraulic Fracturing Technology Conference and Exhibition, Paper SPE 140480, Woodlands, Texas, USA, January; 24–26.

Olson, J., 2008. Multi-fracture propagation modeling: Applications to hydraulic fracturing in shales and tight gas sands. In: The 42nd U.S. Rock Mechanics Symposium (USRMS), San Francisco, California, 29 June-2 July.

Parker, P.A., 1981. The mechanics of fracture and fatigue: An introduction. E. & F N. Spon in association with Methuen, Inc., New York NY 10017, 1981.

Schoenball, M., Müller, T.M., Müller, B.I.R., Heidbach, O., 2010. Fluid-induced microseismicity in pre-stressed rock masses. Geophys. J. Int. 180, 813–819.

Settgast, R., Fu, P., Walsh, S., White, J., Annavarapu, C., Ryerson, F., 2016. A fully coupled method for massively parallel simulation of hydraulically driven fractures in 3–dimensions. Int. J. Numer. Anal. Methods Geomech.. http://dx.doi.org/10.1002/nag.2557.2016.

Shapiro, S.A., Dinske, C., 2009. Fluid-induced seismicity: pressure diffusion and hydraulic fracturing. Geophys. Prospect. 57 (2), 301–310.

Shen, X., 2012. Modeling fracture with continuum damage and its numerical application to stimulation estimates. In: the 46th US Rock Mechanics/Geomechanics Symposium, Chicago, Illinois, USA, June; 24–27.

Tatone, B.S.A., Grasselli, G., 2015. A calibration procedure for two-dimensional laboratory-scale hybrid finite-discrete element simulations. Int. J. Rock. Mech. Min. Sci. 75, 56–72.

Vermylen, P.J., Zoback, D.M., 2011. Hydraulic fracturing, microseismic magnitudes, and stress evolution in the Barnett shale, Texas, USA. In: the SPE Hydraulic Fracturing Technology Conference and Exhibition, Paper SPE 140507, The Woodlands, Texas, USA, January; 24–26.

Zhao, Q., Lisjak, A., Mahabadi, O., Grasselli, G., 2014. Numerical simulation of hydraulic fracturing and associated microseismicity using finite-discrete element method. J. Rock. Mech. Geotech. Eng. 6 (6), 574–581.

Journal of Energy Storage 38 (2021) 102589

Contents lists available at ScienceDirect

Journal of Energy Storage

journal homepage: www.elsevier.com/locate/est

A discussion on hydrogen migration in rock salt for tight underground storage with an insight into a laboratory setup

Murad AbuAisha[1,*], Joël Billiotte[1]

MINES ParisTech, PSL Research University, Centre de Géosciences, 35 rue Saint Honoré, 77300, Fontainebleau, France

ARTICLE INFO

Keywords:
Underground salt caverns
Hydrogen storage
Saturated rock salt
Hydrogen percolation and diffusion
Cavern thermodynamics

ABSTRACT

Hydrogen is being regarded as a primary vector in the energy transition process towards a less polluted planet. The tremendous and increasing energy demands necessitate finding large-scale storage techniques. Underground salt caverns seem to be promising. Nevertheless, the fast solicitations (thermal and mechanical) of these caverns, to reply to the fast demands, imply damage to the ambient rock salt. There is a general scientific ambiguity about the transport mechanisms taking place in the rock salt intact/damaged, particularly for hydrogen. In this paper we provide a detailed review about these transport mechanisms while the cavern undergoes cycling. This review helped us define a mathematical approach to simulate hydrogen migration in the rock salt around underground caverns. We ended up by presenting a patent laboratory setup that we are currently using to define any required model parameters experimentally.

1. Introduction

In the context of energy transition, hydrogen storage in underground salt caverns is becoming a leading technique [1–5]. This is related to the tremendous research on hydrogen production which promotes future cheap and facile product [6,7]. Moreover, the underground salt caverns offer large-scale storing techniques able reply to the intermittency problems [8–10] and the increasing demands [11–13]. Not to forget that such caverns have also low investment costs and low cushion gas requirements [13]. Nevertheless, the future increasing energy demands will necessitate almost daily solicitations of the caverns [14]. Such fast charges, mechanical and thermal, are expected to affect the transport integrity/tightness of the rock salt embracing these caverns [15,16]. To keep precise tracks/accurate management of the cycled hydrogen quantities, the hydrogen mass exchanged with the rock salt or other phases within the underground caverns must be minimized [17].

Rock salt occurs within sedimentary rocks where it has formed from the evaporation of seawater or salty lakes. Rock salt is consequently deposited in cycles which affects its directional properties like the elastic modulus and the permeability. Depending on the location, the rock salt properties, mechanical and hydraulic, differ as well. Most of the available literature treats rock salt as impermeable non-porous halite. The tightness of the underground salt caverns needs to be further investigated. There is a general ambiguity about gas, a priori hydrogen, migration in the rock salt. As hydrogen storage is becoming a hot interesting research topic, its transport mechanisms in the rock salt is also getting considerable attention. Even if the intact rock salt may be hydrogen tight, the severe required utilization of caverns will imply damage to this rock [18]. This damage incites modification to the transport properties of the rock salt and the entire tightness of the storage system [19]. There have been a few scientific articles that discussed seepage around underground caverns. For instance, Liu et al. [20,21] have presented cavern scale studies to investigate the underground tightness for hydrogen, natural gas, and oil. Their approach assumed that these fluids filtrate through the rock salt following a Darcian one-phase flow type. They concentrated their research, mainly, on seepage in the interlayers rather than the intact or the cycling-damaged rock salt. Besides, rock salt contains interstitial fluids and is characterized by very low permeabilities and porosities. These factors render the assumption of one-phase Darcian flow questionable. Nuclear waste storage in rock salt has been also a research subject for quite few scientists [22–24]. Their works proved that disposal of heat-generating nuclear waste in salt formations is attractive because the material is essentially impermeable, self-sealing, and thermally conductive. However, in particular, Ghanbarzadeh et al. [25] extended their research to seek a broader understanding of fluid percolation in the deformable rock salt formations used for nuclear waste storage. They concluded that the low permeability of static rock salt is due to a percolation threshold. However, deformation may be able to overcome this threshold and allow fluid flow. Interestingly, they observed that percolation

* Corresponding author.
E-mail addresses: murad.abuaisha@mines-paristech.fr (M. AbuAisha), joel.billiotte@mines-paristech.fr (J. Billiotte).
[1] Both authors contributed equally to the scientific content of this paper.

https://doi.org/10.1016/j.est.2021.102589
Received 21 January 2021; Received in revised form 9 April 2021; Accepted 10 April 2021

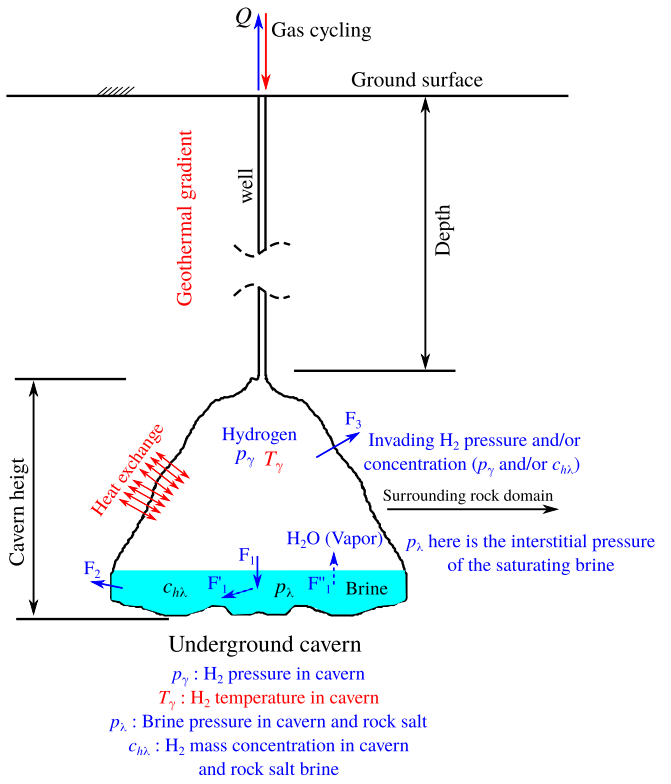

Fig. 1. Schematic representation of hydrogen storage in salt caverns and its flow or exchanges between phases.

occurred at porosities considerably below the static threshold due to deformation-assisted percolation. There is, however, considerable literature that treats hydrogen percolation in clay sedimentary basins in the context of radioactive waste storage [26,27].

The main contribution of this scientific paper is to provide a resume about hydrogen transport in rock salt. This resume is gathered from the available scientific literature and our expertise of understanding the problem. By firstly addressing the interactions of phases within an underground cavern, we end up by discussing all possible transport mechanisms in the embracing rock salt. Eventually, we conclude by providing a modeling approach that would help scientific researchers develop a comprehensive mathematical model for hydrogen migration in the saturated rock salt. The paper seals up by providing a patent laboratory setup [28] that could be used to calibrate correctly the parameters of the suggested mass transport models.

2. Hydrogen storage in salt caverns

Solution mining is commonly used to create large caverns in rock salt formations. In this process, a single well, drilled from the ground surface to the targeted depth (Fig. 1), is generally used to inject fresh water and withdraw brine through a concentric tubing system, the so called the leaching process [29,30]. Once leaching is completed, the brine in the cavern is reduced to minimal quantities by a debrining phase where it is moved out by a gas injection operation.

Fig. 1 shows an underground cavern filled with hydrogen at a certain pressure and is exchanging heat with the surrounding rock domain. The figure also depicts the amount of brine left in the cavern at the end of the debrining process. Hydrogen within the cavern is expected to experience cycles of pressure and temperature changes according to the intended usage. During its life time, the cavern will mainly contain, simultaneously or sequentially, two different immiscible phases: the stored gas and the brine. The third important phase of this storage outline is the surrounding rock salt domain. This domain is constituted of the salt mass which itself is a mixture of grains or crystals of halite and brine occupying the inter-grain spaces or present in the grains in the form of fluid inclusions. Each of the three phases is characterized by state variables which are for hydrogen: the pressure and the temperature, for brine: the pressure, the temperature, and the concentration of salt, and for the rock salt: the stress and the temperature. Since hydrogen may be present in the non-gaseous phase in the other phases (brine and solid), its presence will be characterized by a concentration. For the rock salt which is a mixture of solid and brine, the presence of hydrogen can be characterized by an overall concentration or a pressure. It is worthwhile to mention that the definition of gas concentration is very delicate. In this research, we would choose the mass concentration ($c_{h\lambda}$), where the density of hydrogen in the liquid phase $\rho_{h\lambda}$ is defined as $\rho_{h\lambda} = c_{h\lambda} \times \rho_\lambda$, with ρ_λ being the density of the liquid phase.

While the cavern is operated, the three phases are interacting as follows (Fig. 1): water is evaporating into the stored hydrogen (F_1''); hydrogen is dissolving in the brine (F_1 and F_1') and is percolating and diffusing into the porous rock salt (F_3); brine at the cavern bottom is flowing into the rock salt (F_2).

3. Hydrogen–brine interaction

Interactions between hydrogen and brine take place at the hydrogen–brine interface in the cavern (flow F_1 in Fig. 1) and they are defined by the solubility of hydrogen in brine according to Henry's law [31]. The definitions of the Henry's law parameters must account for the temperature and pressure ranges of the storage [32–34]. The solubility induces a flow of the dissolved hydrogen in the brine (flow F_1' in Fig. 1) which globally and gradually enriches the brine according to two mechanisms:

1. diffusion, which is characterized by a diffusion coefficient of the dissolved hydrogen in the brine, of which the value is dependent on the brine state variables (pressure, temperature) as well as the NaCl concentration [35]. The works of Chabab et al. [36,37] have proven that the saturated nature of the brine may require the use of sophisticated models[2] which take into account the interactions between the solution components, i.e. pressure, temperature, and concentration [36]. One can think of this as an apparent diffusion coefficient where the value is no longer a constant but a function of the brine saturation and the cavern working conditions.
2. convection, due to the circulation induced in the brine by the heat exchanges at the brine–rock salt interface and the non-equilibrium of the temperature between these two phases. The non-equilibrium of temperature is further enhanced during the cycling of the storage process and by the differences in thermal properties of the two phases, i.e. rock salt and brine. The driving force behind this convection is mainly the variations in the brine density with temperature [38,39].

Accounting for all these phenomena of convection, the cavern working conditions, as well as the brine saturation, leads to the definition of an apparent diffusion coefficient that can be two orders of magnitude higher than the binary diffusion coefficient [40]. It is also important to study the kinetics of diffusion as will be discussed in Section 8. The brine itself being an NaCl solution, the solvent (H_2O) can be exchanged through the hydrogen–brine interface (flow F_1'' in Fig. 1). This results in an existence of a partial pressure of water-vapor in the gas phase of hydrogen [41].

[2] Comparison between models is presented in Chabab et al. [36].

4. Brine–rock salt interaction

Depending on the degree of salinity of brine at the bottom of the cavern, the brine–rock salt interface can move due to dissolution or precipitation. Salt can precipitate from brine onto the interface or the interface can be worn away by the brine to achieve saturation continuity at the cavern working temperature and pressure conditions [42–44]. Even if its natural porosity is quite low (~0.01%) [45,46], due to its geologic formation, the rock salt can be considered as a porous medium saturated with brine [47, p. 32] with a zero concentration of hydrogen. However, traces of liquid or gaseous hydrocarbons are common in rock salt [48]. Therefore, the state variables for the rock salt interstitial brine are the temperature and pressure.

Due to the ambiguity with regard to knowing the inter-grain connectivity of rock salt, the pressure of the interstitial brine is poorly defined. However, its value can be limited to two extreme values [47]:

1. the so-called halmostatic pressure, which considers that the brine occupies a totally connected space in the rock mass. Consequently, this pressure is the equivalent to the hydrostatic pressure calculated using the brine density (~1200 kg/m^3);
2. a lithostatic pressure, which considers that the brine occupies an isolated space in the rock salt phase. Therefore, the brine pressure is assumed in equilibrium with the isotropic stresses of the rock salt mass. This pressure extremity is calculated using the rock salt density (~2160 kg/m^3) [49].

During cycling, the cavern brine pressure will be equal to that of hydrogen and its value will vary as a function of time between two extreme values:

1. a minimum pressure, equal to the halmostatic pressure during the cavern leaching, but which may be lower than this during its operation;
2. a maximum pressure, which will always be lower than the lithostatic pressure to preserve the integrity of the rock salt mass. Usually, the maximum operation pressure of the cavern is limited to 80% of the surrounding minimum horizontal stresses [50].

Consequently, we can consider the existence of a brine flow (flow F_2 in Fig. 1) linked to a pressure difference between the cavern brine and the brine saturating the rock salt. Since the pressure in the rock salt mass is not known for certain, the concept of permeation [51], flow proportional to the pressure imposed at the interface,[3] is often preferred to that of convection, flow proportional to the local pressure gradient. Likewise, the mechanism of movement of brine in the rock salt mass is uncertain and discussed between two hypotheses: a movement in a network of connected pores characterized by a very low permeability quantifiable by Darcy's law (Fig. 2(a)); and a movement of isolated brine masses by a process of dissolution and precipitation at the brine–rock salt interface under the effect of slight changes in stresses and/or temperature created by changes in the cavern working conditions, including the induced creep at the cavern boundary (Fig. 2(b)) [52,53].

Depending on the value of the pressure of rock salt brine (halmostatic or lithostatic), flow F_2 can be incoming or outgoing with respect to the brine–rock salt interface. However it seems that the hypothesis of a halmostatic pressure is favored for some reasons. The first is that it leads to the most critical conditions with regard to the security of storage with maximum flow towards the surrounding rock salt. The second is that it underpins a large-scale connected porosity and therefore critical conditions for safety analysis. The assumption of halmostatic pressure allows, as well, for an assessment of fluxes by considering Darcy's law and using permeability values determined in the laboratory on test specimens [55]. For instance, authors like Bérest et al. [56] have conducted *in situ* pressure monitoring tests in an idle salt cavern filled with brine at a pressure almost 4 MPa above the halmostatic pressure. They then analyzed the pressure at the head of the filled cavern. Once the effects linked to the deformation of the rock salt mass (atmospheric pressure, creep, leaks and terrestrial tides), and to the temperature were corrected [57], the pressure difference between the brine in the cavern and a halmostatic pressure in the rock salt was used to correlate to the measured flux during the test period. The measured flow was low to very low, from a few tens to a few m^3 per year, compared to the volume of the cavern (7500 to 8000 m^3). Note that the evolution of this flow was approximated using Darcy's law with a permeability value of the rock mass of the same order of magnitude as values determined in the laboratory (order of 10^{-20} m^2) for this layered rock salt (Bresse basin – France) [58]. There have been also some other *in situ* tests to investigate nitrogen and oil leaks around the cavern well and correlate them to Darcian flow [59]. Durup et al. [60] presented a deep cavern abandonment study. The objective was to study the pressure build-up effect on the integrity of a closed salt cavern.

In the case of hydrogen storage, hydrogen dissolved in the cavern brine can, by advection, propagate into the rock salt mass due to this permeation flow (flow F_2). Since the rock salt has very low porosity, mainly constituted by grain boundaries [61], the phenomenon of transverse dispersion can be neglected. Consequently, the penetration distance of hydrogen is calculated by considering the flow speed of the brine in the rock salt mass deduced from Darcy's law with a pressure field characterized by spherical divergence. Henceforth, where the rock salt domain is invaded by the cavern brine, dissolved hydrogen concentration in the rock salt is equal to that in the cavern brine divided by the porosity of the rock salt, i.e. a factor of 10^{-2} to 10^{-3}, assuming that the rock salt is neither damaged nor disturbed by the creation of the cavern and/or by the operation of the repository. This evaluation of the penetration distance, which neglects the Fickian diffusion of hydrogen, can be corrected and maximized by taking into account a longitudinal diffusion with a diffusion coefficient deduced from that of hydrogen in brine. This diffusion coefficient should only consider the effects of the porous medium (porosity, tortuosity, and constrictivity) [62]. All of this leads to the fact that hydrogen concentration in the rock salt domain at the cavern bottom be much lower than that in the cavern brine. Since hydrogen concentration in the cavern brine cannot be but minimal[4], the entire flow F_2 seems to be negligible.

Taking into account the effects of damage and/or disturbance on the hydraulic properties of the rock salt mass also implies taking into account the distribution of fluids (brine, water vapor and possibly hydrogen) in the porosity increased by this damage and/or disturbance. These mechanisms will be analyzed in more detail in the section discussing the interaction between hydrogen and the rock salt mass.

5. Hydrogen–rock salt interaction

At the hydrogen–rock salt interface, the penetration of hydrogen into the saturated rock can take place either [63]:

1. in the solid phase itself, i.e. the halite crystals;
2. in the fluid phases occupying the rock pores (brine, water vapor, or gas).

These are two different mechanisms, the first is similar to gas diffusion in solids or what is defined as permeation. The second is similar to gas diffusion in brine saturating the pores or to a two-phase flow in porous media, if the pores are not saturated, or if they are desaturated by the percolation of hydrogen.

[3] In the permeation concept pressure is replaced by a concentration and flow is calculated using experimental permeation coefficients.

[4] Available literature, for instance Chabab et al. [37], proves that hydrogen dissolves in very small quantities in saturated brine compared to other gases, i.e. CO_2.

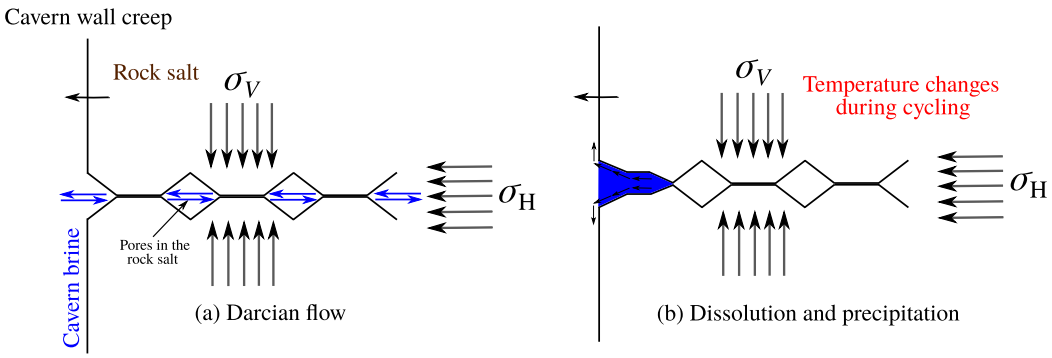

Fig. 2. Schematic diagram representing the movement of brine in the rock salt domain: (a) by Darcian flow characterized by a very small permeability; (b) by dissolution and precipitation.

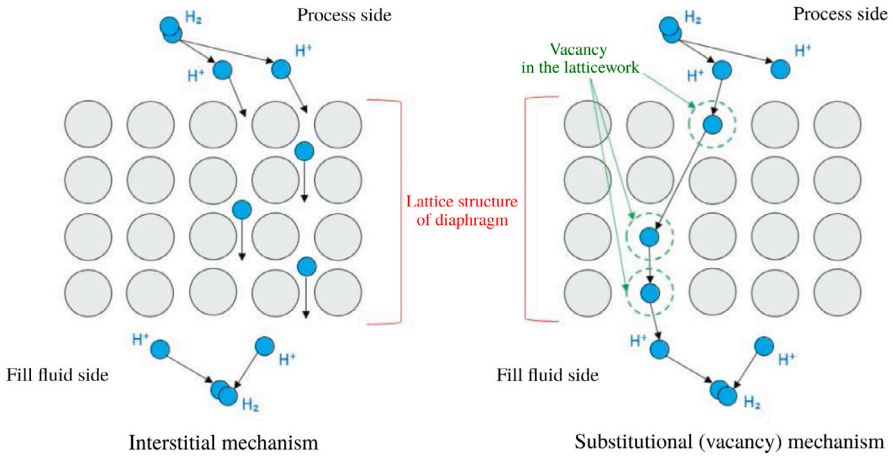

Fig. 3. Mechanism of hydrogen permeation in the metallic diaphragms.
Source: Figure reproduced from Yokogawa [54].

5.1. Permeation in the halite crystals

Diffusion of gas into solids is called permeation. This phenomenon is responsible for gas permeability of polymer pipes and is particularly important in the case of hydrogen with metals [64,65]. This permeability deficiency of metals with respect to hydrogen results from the high availability of electrons in a metal. On the metal surface, the dihydrogen molecule can dissociate and each hydrogen atom ionizes in the H^+ form, i.e. a proton. As the size of the proton is much smaller than the distance between the atoms of the crystal lattice, it moves easily through the crystallized structure of the metal, and even over significant thicknesses. The mobility of protons is greatly enhanced by the presence of vacancies in the crystal structure. This permeation mechanism is illustrated in Fig. 3 from a technical report about the problems caused by hydrogen permeation in pressure transmitters [54].

On the other face of the diaphragm, and even if it is in contact with a liquid, the protons will recombine into dihydrogen molecules. This flow of protons will lead to the formation of hydrogen bubbles in the liquid, and this is reinforced by the significantly low solubility of hydrogen. In the case of pressure transmitters, this permeation is equivalent to a leakage in the pressure measurement of the gas phase. The formation of bubbles in the liquid phase modifies its compressibility. Therefore it causes the respiration of the pressure sensors and the deformation of the diaphragm, particularly during temperature variations. Finally the exchange of electrons in the crystal lattice weakens the metal [54].

Permeation is characterized by a coefficient whose ratio is the permeability with units as mol/(s m^2 Pa) in the SI system and more practically in m^3 (STP)/(s m^2 Pa), or with more exotic units (Barrer or GPU) [66]. The value of the permeability coefficient can be determined

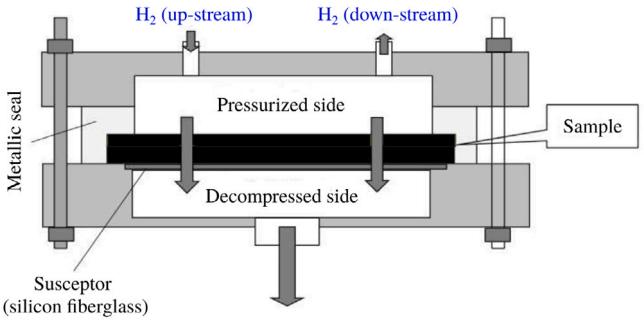

Fig. 4. Schematic representation of a laboratory model to measure the hydrogen permeability coefficient [67].

experimentally by measuring the flow of hydrogen through a sample of known thickness (Fig. 4) [67]. The evaluation of the flow is carried out in the downstream chamber either by measuring the evolution of the hydrogen concentration by gas chromatography, or by measuring the pressure. It can be also calculated by the measuring the pressure difference between the upstream and the downstream chambers.

The interpretation of this model measurements is made by considering that the transfer of gas into the solid is governed by diffusion according to Fick's law. Therefore, the only state variable of the gas in the solid is its concentration. At the gas–solid interface, it is generally assumed that the gas penetration is governed by Henry's law (form of solubility). The use of this law allows to relate the gas pressure applied to the sample surface to concentrations at the limits of the sample [68].

With regard to hydrogen permeation in halite lattice structure, the comparison between the size of a hydrogen atom (106 pm) and the atomic space in the crystal lattice of halite (34 pm) [69], shows that the diffusion of hydrogen in the atomic form is not possible. However, as hydrogen protons have a radius of 0.84 fm, it would be possible that hydrogen diffuses in the ionic form. Yet, since halite is already an ionic solid, ionization of hydrogen atoms is usually not possible. It follows that the phenomenon of hydrogen permeation in metals and its importance cannot be as significant in rock salt. The value of a permeability coefficient or a diffusion coefficient of hydrogen in halite crystal, which generally constitutes the solid phase of rock salt, can only be very small. It is the same with all minerals, except for ores, graphite and clay minerals, which have electrically non-neutral surfaces, and which can create preferential and rapid migration paths of protons by moving to electronegative sites on the surface of minerals [70]. This proton conduction phenomenon is usually taken into consideration in the safety analysis of radiolysis hydrogen produced by nuclear waste often stored in clayey rocks. For this particular case, this conduction mechanism is associated to water molecules saturating the space between the clay particles and the hydrogen dissolved in this interstitial fluid [71].

5.2. Diffusion in the interstitial brine

The porosity of rock salt is saturated with brine. Since brine is in equilibrium with halite (the solid phase), it is necessarily saturated with sodium chloride NaCl [47]. This porosity is formed by the joints between crystals or halite grains and the fluid inclusions. This defines a connected porosity, a priori (the grain boundaries), and an unconnected porosity (the fluid inclusions) [61]. If the fluid inclusions are very numerous (milky salt), and representing a significant relative volume (a few %), then porosity associated with the grain boundaries is low to very low (less than 1% to zero). Measuring this kind of porosity is tremendously tough, with particular difficulty with respect to eliminating the artifacts related to the sample preparation and the deconfinement of the rock salt logs [61].

Considering that hydrogen diffusion in halite crystals is very low, a preliminary approach is to consider that it will diffuse in the brine saturating the rock salt. It is then possible to carry out an evaluation of the penetration of hydrogen using Fick's law with [63]:

1. a concentration of dissolved hydrogen on the cavern surface deduced from the storage pressure and Henry's law;
2. an effective diffusion coefficient of hydrogen in the rock salt brine via its connected porosity.

The value of the effective diffusion coefficient D (m^2/s) is deduced from that of hydrogen in brine $\bar{D}$ (m^2/s) by adjusting it using three coefficients [72]:

$$D = \bar{D} \times n \times \frac{\delta}{\tau^2}, \quad \text{with:} \tag{1}$$

- the first is equal to the porosity (n), which represents a reduction in the volume of the brine due to the presence of the solid phase;
- the second is the inverse of the square of the tortuosity (τ), which represents the relative elongation of the diffusion paths relative to a fluid due to the texture of the porosity;
- the last coefficient (δ) represents the constrictivity factor which depends on the flow regime imposed by the shape of the pores and their size. When the pore size decreases and becomes smaller than the mean free path of the solute molecules of the solvent, the diffusion regime changes from molecular to transitional, and then to slip for which the Knudsen number[5] is less than unity. This will be discussed in details in the next section.

[5] The Knudsen number (K_n) is a dimensionless number defined as the ratio of the molecular mean free path length to a representative physical length scale.

There is almost no available literature on hydrogen diffusion in the saturated brine. However, since hydrogen diffusion in water is well known ($\bar{D} = 6.1 \times 10^{-9}$ m^2/s at 25 °C) [73,74], the viscosity models for electrolyte solutions [75–77] can be used to approximately calculate its diffusion coefficient in brine. Using the Stokes–Einstein law [78], the viscosity models give $\bar{D} \approx 4.6 \times 10^{-9}$ m^2/s at 25 °C for hydrogen in the saturated brine. Another handy way to calculate the effective diffusion coefficient is to use the relation of Grathwohl [79], i.e. $D = \bar{D} \times n^q$. The empirical parameter q usually lies between 1.8 and 2.4.

Regardless of the method used to determine the effective diffusion coefficient, by molecular simulations or experiments, its implementation in Fick's law allows for possible simple analytical solutions [80]. The use of Fick's law also permits to define a characteristic time linked to the diffusion. Such time can be compared to that calculated by convection and to have, particularly for long periods, an evaluation of a penetration distance. This distance into the rock salt mass is mathematically proportional to the square root of the product of the effective diffusion coefficient and time [80].

As stated in Section 4, if hydrogen concentration in the rock salt is to be considered as a state variable, we can, rigorously, assume its initial value to be zero. However, certain underground mines of evaporite rocks (potash, carnalite) and rock salt are known to have some concentrations of hydrogen in the void of their galleries. The origin of this hydrogen is linked to the radiolysis of water under the effect of radioactive minerals present in the rock salt mass [26,42]. Consequently, hydrogen can be observable in the rock salt fluid inclusions and its release is subsequent to the creation of damaged and/or disturbed zones [81]. The creation of these zones increase the connected porosity which will be unsaturated and which will allow for a flow of hydrogen towards the farther galleries. This kind of flow drains hydrogen from the grain boundaries and the fluid inclusions [82]. The damage or disturbance of the host rock can be induced by thermal gradients and stresses [83]. Some studies have looked at the diffusion of gas, including hydrogen, contained in fluid inclusions mainly due to temperature variations. For instance, Clark et al. [81] found that the migration distances were of the order of a few tens of micrometers for inclusions in quartz.

In case of rock salt, the experimental determination of the effective diffusion coefficient is challenging. This hardness is attributed to several reasons of which: (1) the difficulty to keep interstitial brine in equilibrium with the solid phase, and so that no convective movement of the brine may be induced by the field of constraints imposed; (2) preventing any water vapor exchanges with the injected gas (water vapor comes usually from the external atmosphere of the sample) [84].

5.3. Convective flow in the rock salt

Convective flow of hydrogen in the rock salt takes place due to bulk motion of the gas. This bulk motion can happen in one-phase or two-phase natures.

5.3.1. One-phase flow

In this simplistic approach, we assume that we have only one fluid filling the pores of the rock salt mass. The flow of this fluid is governed by Darcy's law. The use of Darcy's law requires using the fluid pressure as a state variable, and to characterize the permeability of the rock salt with regard to the fluid used [85]. This gives rise to difficulties, namely, the value of the fluid pressure in the rock salt domain, i.e. halmostatic, lithostatic, or an intermediate value. The permeability of the rock salt, with regard to one-phase flow, needs to be experimentally calculated. The calculation of the permeability of rock salt is an experimental challenge. This is due to the very low values, less than 10^{-20} m^2 in case of the intact rock. The difficulty is also experimental, where it is almost impossible to define a representative state of the actual rock mass, not disturbed, by the sample preparation and the test conditions.

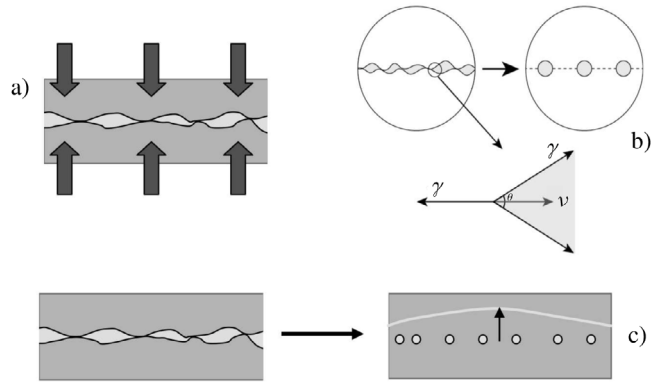

Fig. 5. Crack healing/sealing and permeability reduction in rock salt. (a) Mechanical closure of cracks due to compaction of the rock by elastic deformation or plastic flow. (b) Necking down of cracks and pores to form arrays of disconnected tubular and spherical inclusions. Here γ denotes the surface energy vectors, θ the dihedral angle of the crack, and v the crack migration velocity. (c) Crack and pore occlusion through fluid-assisted grain boundary migration (recrystallization).
Source: Figure is modified from Koelemeijer et al. [86].

Test conditions should be perfect where no parasite flows or leaks on the sample boundaries are allowed [45].

Due to the very low permeability of the rock salt, almost all of the measurements are carried out using gas as the measuring fluid. They are also done in transient conditions with pressures, or pressure gradients that are quite different from the *in situ* rock salt conditions. Using gas as a measuring fluid involves removing the sample brine, generally by drying, whether thermal or vacuum . Drying extracts water from brine, but the salt remains in the porosity. Therefore, the pore space that would be traveled by the measuring gas is necessarily different from that initially exited. To mimic the *in situ* rock salt stress conditions, laboratory measurements are usually performed under loads. However, rock salt is sensitive to the state of stress, particularly the deviatoric stresses, which generate creep (Fig. 5). The use of an isotropic confinement state can cancel rock salt creep globally, but not locally. Local changes include development of the grain contacts and healing of the damage defects with water vapor bubbles [86].

Due to the very low porosity of rock salt, it is difficult to define the hydromechanical coupling using Biot's effective stresses [87]. However, reality shows that there is a very strong hydromechanical coupling [88,89]. This coupling is related to the tremendous increase of the permeability with damage [19]. It is also observed during laboratory tests, where measurements made with the same difference between confining stress and upstream gas pressure were not equivalent [19]. This suggested that the upstream gas pressure was an addition to the stress in the direction of flow, where different deviatoric stress states induced different changes in porosity [45].

The very low value of permeability is attributed to the very low porosity and to the presence of inter-grains constrictions at their contacts (Fig. 6). Measurements showed that pore size of rock salt varies from 0.01 to 300 μm with major concentration of pore size being smaller than 1.0 μm [61,90].

With very small pore dimensions, fluid flow is affected by the interactions between the fluid molecules and the solid surface. The importance of these interactions is assessed by comparing the mean free path of a molecule ζ (m) to that of a characteristic pore dimension (d_p) via the Knudsen number ($K_n = \zeta / d_p$). In the case of gas flow, the average free path is evaluated with the following expression [91],

$$\zeta = \frac{R\,T_\gamma}{\sqrt{2}\,\pi\,d_m^2\,p_\gamma\,N}, \tag{2}$$

with R (J/mol/K) being the universal gas constant, T_γ (K) the gas absolute temperature, d_m (m) the kinetic diameter of the gas (289 pm for hydrogen), p_γ (Pa) the gas pressure, and N (1/mol) the Avogadro constant. For hydrogen storage in a typical cavern at 1000 m depth, during seasonal operations, hydrogen pressure changes between 16 and 5 MPa, and the corresponding temperature ranges between 65 and 28 °C [50]. However for extreme daily utilization of the cavern, and for the same pressure changes, the cavern average temperature ranges between 95 and −40 °C [14]. Table 1 shows that the mean free path of hydrogen traveling in rock salt varies between 0.86 and 1.70 nm for extreme daily utilization of a typical cavern.

Depending on the value of the Knudsen number (Table 1), the equation used to describe the gas flow in the rock salt is different (Fig. 7). In case of an intact salt, most of the domain (red box) is located in the "slip flow". However, if the rock salt pore dimensions are less than the smallest average (5×10^{-7} m of Fig. 6), transition flow may take place.

It is, therefore, quite probable that hydrogen will flow in a slip regime in the rock salt. The interaction gas–solid in this regime is characterized by the Klinkenberg effect [93]. Consequently, the apparent permeability of gas k_a (m^2) flowing in a porous medium is related to the intrinsic permeability k (m^2) via the following relation,

$$k_a = k\left(1 + \frac{b}{\langle p_\gamma \rangle}\right), \tag{3}$$

with b (Pa) being an empirical parameter (usually called the slip factor), $\langle p_\gamma \rangle$ (Pa) the mean pressure at which the apparent permeability is calculated. The influence of gas on the calculated permeability is related to the size of the molecules. Thus, for the same tested sample, the slip factor b depends on the measurement gas. Besides, the influence of the sample, i.e. the porous medium, is not explicit, as it depends on the testing conditions as well. Empirical relations, such as proportionality with an inverse power of the permeability, are usually proposed to calculate the slip factor [45,94].

5.3.2. Two-phase flow

In this approach we assume the effective penetration of hydrogen into the rock salt porosity to imply a displacement of the brine. It is a two-phase immiscible flow in a porous medium. In this flow the hydrogen constitutes the non-wetting displacing phase and the brine the wetting displaced phase.

In a porous medium, these two immiscible phases are separated by an interface characterized by surface energy or surface tension. In case of air and saturated brine, this energy is 1.13 times greater than in the case of water, i.e. 82 mN/m at 25 °C and at the atmospheric pressure [95]. Studies have shown that increasing temperature from 27 to 100 °C increased the surface energy by 17%. However, increasing pressure from 5 to 25 MPa reduced it by 28% [96,97]. Since in underground caverns, increasing pressure is associated with increasing temperature, changes in surface tension could be crucially neglected. Fukuzawa et al. [98] have shown that the hydrogen-water surface tension is equal to 74.81 mN/m at temperature 4.7 °C and atmospheric pressure. At this particular temperature, the surface tension barely showed any pressure dependency. We could not find in literature any studies on hydrogen-brine surface tension. However, if we assume the same increase as in water-brine surface energy, we will find an approximate value of 84.5 mN/m at 25 °C and at the atmospheric pressure. We still could assume a further increase at normal temperature conditions of 25 °C. Based on the curvature of the gas-liquid interface, the surface energy results in a positive pressure difference between the two phases. This pressure difference can be quantified using Jurin's law, or directly using the Young-Laplace equation [99]. Both equations indicate that the interfacial pressure difference is proportional to the surface tension and inversely proportional to the characteristic size of the pores. To give an order of magnitude for hydrogen-brine interface, a pore radius of 1 μm corresponds to a pressure difference of ~0.1 MPa, meanwhile a pore radius of 1 nm corresponds to a pressure difference of ~85 MPa. The interfacial pressure difference defines a condition called the entry

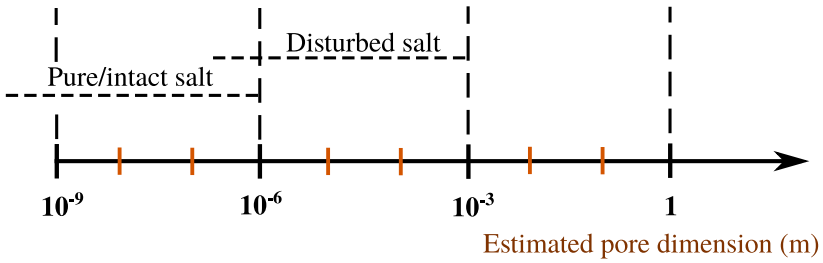

Fig. 6. Estimation of the pore dimension in rock salt [19,61,90].

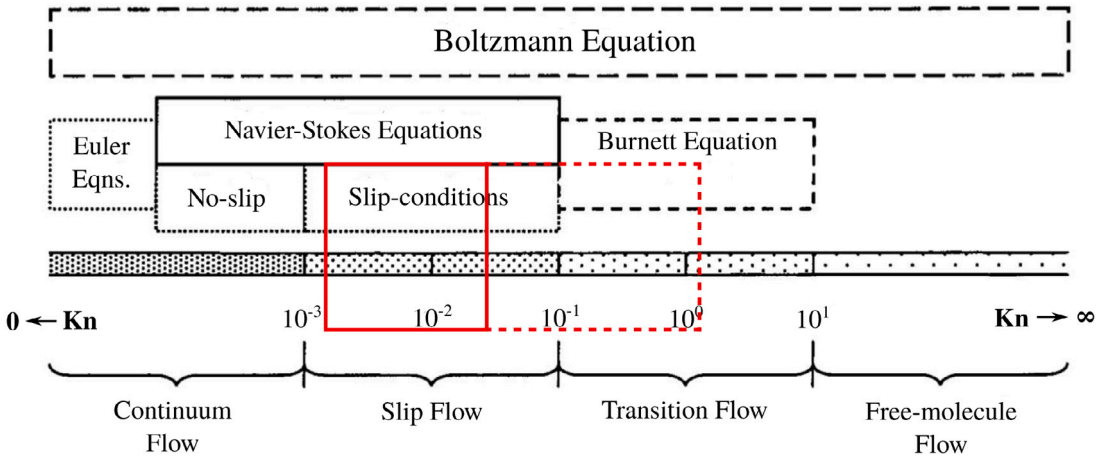

Fig. 7. Flow type and associated equation based on the Knudsen number. (For interpretation of the references to color in this figure legend, the reader is referred to the web version of this article.)
Source: Modified from Roy et al. [92].

Table 1
Mean free path of hydrogen traveling in rock salt under daily cavern utilization.

Pressure (MPa)	Temperature (°C)	ζ (nm)	K_n for $d_p = 10^{-6}$ m	K_n for $d_p = 5 \times 10^{-7}$ m	K_n for $d_p = 10^{-9}$ m
16	95	0.86	0.86×10^{-3}	0.17×10^{-2}	0.86
5	−40	1.70	1.70×10^{-3}	0.35×10^{-2}	1.70

pressure. The gas pressure in contact with the porous medium must exceed the pressure of the interstitial fluid and the entry pressure so that gas may invade the medium and replace the pore liquid. Penetration is conditioned by the size of the largest pores on the surface of the porous medium, meanwhile invasion is linked to the average radius. If we assume the rock salt to be intact at the end of the cavern leaching, for a pore size of 1×10^{-8} m, the required entry pressure is around 34 MPa. This value is very approximative, as for intact rock salt the pore size varies widely (Fig. 6). For applications with regard to hydrogen storage in porous media, and hydrogen production in underground repositories of radioactive waste, researchers have assigned values of 2 to 5 MPa to the pressure entry in the case of argillite repositories [27,100] (with relatively large porosities), and up to 15 MPa in the case of shale [101].

Hydrogen distribution in the partially desaturated pore space depends on two dimensionless numbers. The first is called the capillary number Ca, which represents the relative effect of viscous drag forces versus surface tension forces acting across the gas-liquid interface. The second number defines the mobility M, which represents the viscosity ratio of the displaced fluid to the displacing gas [102,103]. Depending on the values of these two dimensionless numbers, the flow will have different morphologies and will require different simulation methods to quantify the penetration distance (Fig. 8). In case of hydrogen-brine flow, the mobility number is important. Besides, the high capillary pressure, linked to the small pore size, makes the application of Darcian approaches quite inaccurate. Therefore, only percolation type approaches, with or without gradient, should be used. These approaches are characterized by the absence of a finite size of a representative elementary volume. Henceforth, at the percolation threshold, even-though the over all saturation of hydrogen is quite small, its penetration distance could still be considerable [17].

Under the conditions of hydrogen storage in underground salt caverns, the log(M) is always positive, and the capillary number is quite insignificant due to the small viscous forces of hydrogen. This necessitates that hydrogen flow in rock salt to be located in the lower right quarter of Fig. 8. Consequently, a flow pattern of either viscous fingering (percolation with gradient), capillary fingering (percolation), or intermediate of the two is expected. It is the same domain usually used to model the migration of radiolysis hydrogen in the clay rock hosting a repository of radioactive waste [26,27]. Lefort [104] defined this flow pattern or domain as a hyper-slow drainage, and he found that a flow of viscous fingering (percolation with gradient) would stabilize after a distance of a few thousand pores. The gas invasion then continued over a stable front which made it possible to describe it either by a generalized Darcian flow or a Buckley-Leverett model. However, these models require establishing, experimentally or conceptually (by using van Genuchten and/or Brooks-Corey models [105,106]), hydraulic parameters that take into account the local hydrogen saturation. Yet, if we consider a steep desaturation front, the flow can be reduced to a piston type flow [107]. With all the cited references, the relevance of these models and their applicability to the salt rock cannot be solidly established, including Lefort [104] analysis. This is attributed to the

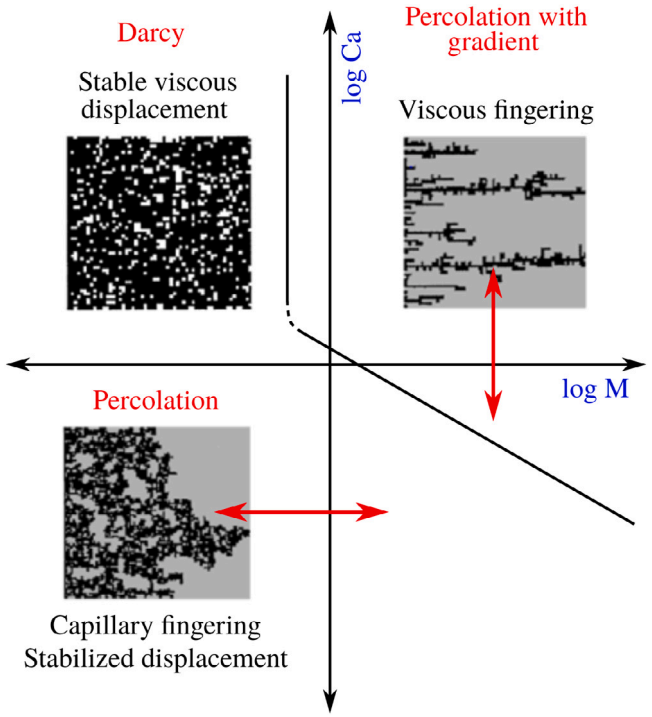

Fig. 8. Lenormand diagram [103] describing the reasons of drainage in a porous medium. The non-wetting phase (hydrogen μ_1) is replacing the wetting phase (brine μ_2) as a function of the capillary number Ca and the mobility number $M = \mu_2/\mu_1$.

very low porosity and morphology of the rock salt pores, which are grain boundaries, therefore of crack type with contact points [61].

Whatever approach is chosen to model hydrogen-salt rock exchanges (diffusion, single-phase, or two-phase flow), the transient modeling as a function of the cavern pressure cycles requires the determination of additional parameters. These parameters include the effective porosity for the diffusion, the storage coefficient for the single-phase flow and the capillary pressure-saturation and relative permeability-saturation relationships for the two-phase flow. The experimental determination of such parameters is very delicate, especially under the *in situ* conditions. A transient approach would be necessary to estimate the hydrogen quantity exchanged with the rock salt mass and to obtain a transient spatial distribution. However, one would anticipate that due to the very low permeability of the rock salt, hydrogen pressure cycles might have very small influence distances. Therefore, it might be possible to consider a constant value of the pressure or of the concentration at the solid rock salt-hydrogen interface. This value could be the average or even the maximum storage pressure to maximize the determined penetration, and which allows to determine a characteristic speed for each of the modes of movement. In case of Fickian diffusive movement, the penetration distance is directly quantifiable as function of the effective diffusion coefficient. In case of a single-phase or a two-phase flow, we can consider the flow to be governed by the displacement of the brine, which depends only on the permeability of the rock salt mass and the pressure difference.

All of these approaches consider a displacement of the fluid molecules with regard to a fixed solid surface. The calculated penetration distance must be corrected by the displacement of the rock salt towards the cavern. Such displacement is induced by the creep of the rock salt under the effect of mechanical stresses. The creep stresses are, themselves, induced by the leaching and the operation of the cavern. If the cavern wall displacement is considered, the effective penetration distance will be less than those determined by previous approaches.

6. Influence of the damaged zone

Under the effect of stresses induced by leaching and operation of underground caverns, the damage criteria can be met which may modify the rock salt hydraulic properties [50]. This phenomenon leads to the creation of a damaged zone which extends from the cavern surface to a certain distance beyond which the rock retains its initial properties, particularly the hydraulic ones. The rock salt damage results in the development of microcracks or cracks which can develop on different scales. This causes an increase in the rock porosity which can range from very large, say five-fold the initial value, to a few millipercents [18]. Likewise, the permeability of rock salt samples taken from damaged areas in the vicinity of underground galleries showed considerable increase in their permeability, i.e. more than three orders of magnitude [19,55].

The intrinsic permeability of the intact or *in situ* rock salt is extremely low, less than 10^{-20} m^2, and its porosity is saturated with brine. As a result, any damage induced porosity cannot be saturated by an overall displacement of the brine. It will, therefore, be occupied by a gas phase composed of water vapor from brine at a partial pressure in accordance with the brine-gas interface determinable by the Kelvin equation. This mass transfer of water vapor can create a local oversaturation of the brine and a localized precipitation of halite. Likewise, damage can connect fluid inclusions to the defects created and bring the content of these inclusions, i.e. liquid or gaseous hydrocarbons and gases (nitrogen, CO_2, and hydrogen) into the connected porous network. On the other side, some oxide inclusions maybe reduced to metal or even form metal hydrides. The formation of methane is most likely due to the reaction between Na_2CO_3 and hydrides or metal as reported in Zhu et al. [7]. Meanwhile, CO_2 methanation *in situ* formed from LaNi5H5 catalyzed via Metallic as reported in Zhong et al. [108].

Even if the permeability of the damaged zone is much higher than that of the intact rock salt, any displacement of brine out of the damaged zone necessarily implies a flow of brine into the farther intact rock salt. This means that the occupation of the damage-created unsaturated porosity happens as result of increasing the partial or total pressure of hydrogen, and by the flow of the initial brine towards the intact rock salt mass. To estimate the hydrogen penetration into the rock salt as part of a safety analysis, it is possible to decouple these modes. Therefore, it will be acceptable to consider the whole damaged area to be invaded and pressurized by hydrogen with a uniform representative pressure. However, at the edge of the damaged zone, hydrogen applies a pressure to the brine of the intact rock salt. The analysis of hydrogen penetration and displacement of brine could be described using the methods mentioned in Section 5.

The estimation of the size of the damaged zone necessitates the development of sophisticated models to describe creep in rock salt due to pressure and temperature cyclings [109–111]. The model/material parameters are usually determined experimentally [15,112]. However, this zone is sometimes considered as disturbed and not damaged. The stress induced microcracks and cracks might have developed, but the density, and especially the connectivity, of these defects do not lead to an increase in permeability (Fig. 5). As a result, this zone would have a hydraulic behavior similar to the intact rock salt, since the changes in porosity do not intervene. This needs to be investigated by laboratory tests which will be highlighted in Section 8.

7. Influence of temperature

Pressure variations induced during gas cycling generate temperature variations at the cavern surface. In the context of hydrogen transport in rock salt, these temperature variations may have transport effects that must be taken into account. These effects can be divided into two main groups: the first is related to the modification of hydrogen and brine viscosities; the second is attributed to the modification of the rock salt hydraulic properties. Thermal changes usually cause an increase in

the permeability due to the presence of insolubles that have different expansion coefficients than that of halite. We can cite the case of anhydrite and calcite nodules which represent dilation anisotropies unlike those of halite. With a temperature increase, the dilation anisotropies cause local deformation incompatibilities generating thermal damage. Le Guen et al. [113] have experimentally measured a permeability increase of approximately 1.7 times due to a temperature increase of 34 °C.

Temperature changes also induce migration of fluid inclusions, therefore of elements of non-connected porosity. The inclusions migrate towards the hot zones under a dissolution effect on their hot side and a precipitation effect on the cold side. The speed of migration depends on the importance of the temperature gradient, the size of the inclusion, and of its content. In the case of strong gradients, close to a heating element of 150 °C, this migration can generate significant disturbances with the creation of tubes resulting from the coalescence of the migrating inclusions, and with a supply of brine from the grain boundaries (Fig. 9) [114]. Fig. 9 is deduced from a study that concerned a thermal test performed in the Amélie mine (Haut–Rhin France).

More generally, the migration of fluid inclusions goes through the redistribution of the inter-crystalline brine in the connected porosity inducing a set of mechanisms and reactions which can modify the hydraulic properties of the rock salt. For instance, Fig. 10 shows that conduits in rock salt can be created by several driving forces. Such driving forces can include temperature changes or mineral vapor pressure. The result is a displaced pore fluid or vapor that goes into the creation of a new connected porosity (inter-crystalline redistribution) that is also altered by the external stresses or the induced pore pressure gradient itself.

In the case of hydrogen storage, the temperature variations of the stored hydrogen can be significant, i.e. −40 to 95 °C (considering fast and excessive utilization). We recommend that these effects be accounted for in the models describing rock salt creep [109], as well as in the fluid phases hydraulic properties and densities. However, temperature related mechanisms are expected to be located in the vicinity of the cavern wall, therefore in the damaged area. Consequently, the temperature related modifications of hydraulic properties of the rock salt of the damaged zone would probably have no influence compared to the mechanical or pressure effects

8. Modeling approach with perspectives

The previous literature review helps understand all possible transport mechanisms of hydrogen gas in the rock salt surrounding an underground cavern during cycling. Deploying this study, we can come out with the following modeling scenario:

1. the assumption that the surrounding rock salt domain is saturated with brine at the halmostatic pressure is favored. It leads to the most critical conditions with regard to the security of storage with maximum flow towards the rock salt (Section 4);
2. Hydrogen Fickian diffusion in the rock salt lattice is tremendously small and can be neglected (Section 5.1);
3. One-phase convective flow hypothesis of hydrogen in the saturated rock salt is dubious. This is attributed to the presence of the liquid phase in the *in situ* rock salt, as well as the difficulties to define the flow nature and the hydraulic parameters (Section 5.3.1);
4. assuming two-phase transport of hydrogen into the ambient rock salt mass seems to be the comprehensive or the most convincing theory (Fig. 11). However, this transport should address: the Fickian diffusion of hydrogen into the saturating brine (Section 5.2); and the percolation of the drying phase (hydrogen) by displacing the wetting phase (brine) (Section 5.3.2);
5. accounting for rock salt creep or damage during cycling is very important. The created disturbed zone might be the only place where hydrogen can migrate (Section 6);
6. As rock salt has relatively high thermal transport properties (compared to other rocks), non-isothermal models need to be considered for hydrogen migration into it (Section 7).

Consequently, to thoroughly describe hydrogen transport in the saturated rock salt, the developed mathematical model must strongly couple: the cavern thermodynamics (p_γ and T_γ); the development of the disturbed or damaged zone; the transfer of heat into the rock salt domain, and the two-phase percolation with the Fickian diffusion. This mathematical model is already developed and published in the work of AbuAisha et al. [17]. Fig. 12 shows all the transport mechanics of hydrogen that take place within an underground cavern. The figure also presents our research methodology to consider the most convincing and influential mechanisms.

It is worthwhile to mention that our previous research focuses on the flux F_3 of Fig. 1. To ensure the hydrogen-tightness of the entire storage system, the other fluxes, particularly F_1 should be quantified[6]. Hydrogen dissolution in the saturated brine has been a very interesting research subject recently [37,116,117]. Even-though these articles present hydrogen dissolution at different pressures and temperatures, none of them treats the kinetics of the dissolution as function of time. Another challenging task to this framework, is the determination of the two-phase percolation-diffusion model parameters. A van-Genuchten type model seems interesting (Section 5.3.2), however, an experimental approach must be conceived to calibrate its parameters. We provide the following patent laboratory setup (Fig. 13) [28] to evaluate the van Genuchten model parameters, as well as to study the Kinetics of hydrogen dissolution. This laboratory setup consists of a hydrogen-tight steel cell of 110 mm height and 55 mm diameter.

8.1. The permeation laboratory test

In the first approach, a saturated rock salt sample (dimensions are displayed on Fig. 13(a)) is placed within the cell in away it occupies most of the void. The entire cell is placed in a water basin of a certain temperature. Non-damaged as well as damaged (by creep laboratory tests) samples can be studied. The goal is to reduce as much as possible the hydrogen volume around the sample so that any tiny pressure changes can be measured. The pressure of hydrogen is then increased by injection. Injection in this case is translated by a valve opening, where a flow between this cell and a pressurized reserve takes place almost instantly. The entire cell is then left for stabilization. The void hydrogen pressure will drop from its initial value $p_{\gamma 0}$ to its final value $p_{\gamma f}$ over a time period Δt.

Fast injection of hydrogen will increase its temperature T_γ. Consequently, there will be heat exchange between hydrogen and the rock salt sample, as well as between hydrogen and the steel. Hydrogen will also invade the sample in a two-phase type flow and in Fickian diffusion. The quantity p_λ represents the initial brine pore pressure within the sample, and $\tilde{p}_\gamma$ the pressure of hydrogen invading the sample. The two pressures are distinguished as two-phase percolation is accounted for. Solution starts by integrating all this physics in our mathematical model and numerically solve it. This will help determine the van-Genuchten parameters and the diffusion coefficient that mostly fit the experimental curve of pressure drop. However, injected pressure values need to be so high (around 20 MPa) to allow for hydrogen entry into the saturated rock salt. This laboratory test can be conducted on intact and damaged rock salt samples. Damaged samples would have undergone creep conditions, due to thermo-mechanical charges, similar to rock salt around real caverns. The objective is to compare the transport properties of intact and damaged rock salt samples.

[6] Flux F_2 is deemed negligible compared to other fluxes (see the argument of Section 4).

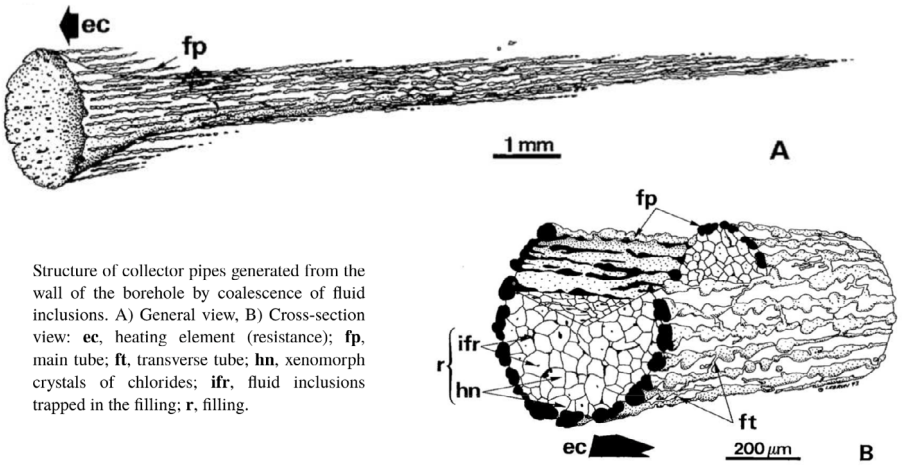

Structure of collector pipes generated from the wall of the borehole by coalescence of fluid inclusions. A) General view, B) Cross-section view: **ec**, heating element (resistance); **fp**, main tube; **ft**, transverse tube; **hn**, xenomorph crystals of chlorides; **ifr**, fluid inclusions trapped in the filling; **r**, filling.

Fig. 9. Schematic diagram of a tube created by fluid inclusions migration in the vicinity of a heating element. *Source:* Figure is reproduced from Lebrun et al. [114].

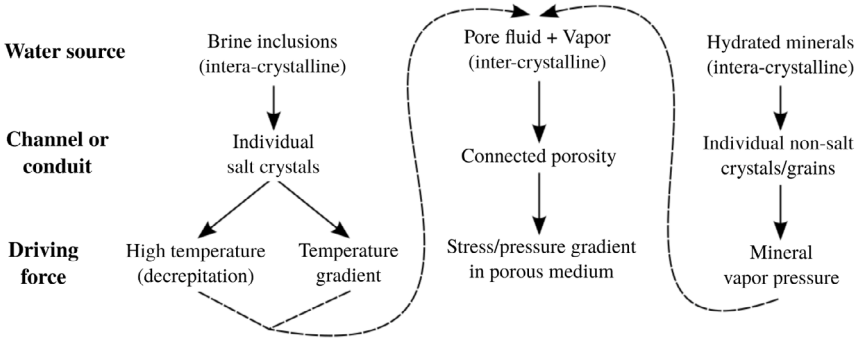

Fig. 10. Relations between mechanisms and brine movements induced by temperature gradients. *Source:* Figure is reproduced from Kuhlman and Malama [115].

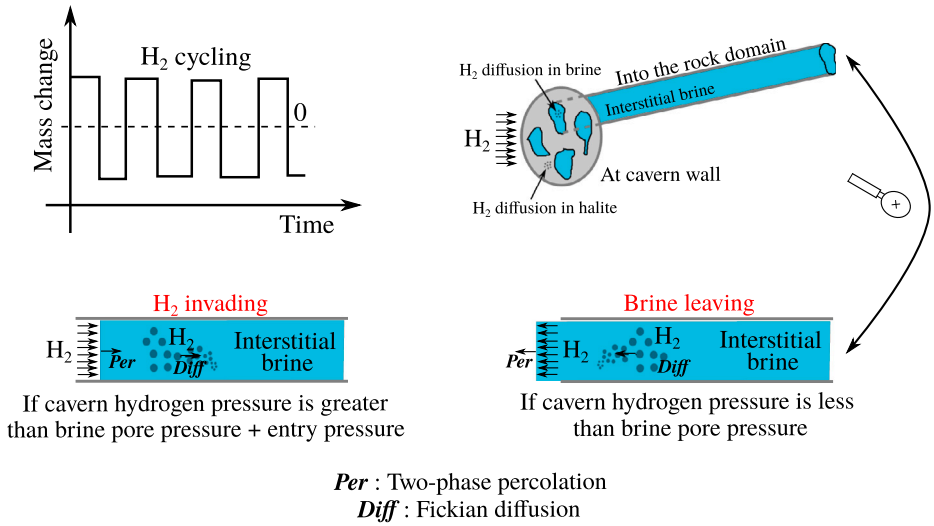

Fig. 11. Schematic diagram illustrating the migration of hydrogen into the saturated rock salt during cycling in underground caverns.

8.2. The dissolution laboratory test

In the second approach, the same cell is filled with NaCl saturated brine to a certain volume and is submerged in bathtub to insure a fixed temperature. Hydrogen is injected in the left void to a certain initial pressure value $p_{\gamma 0}$. The system is then left to stabilize over time until a final hydrogen pressure value is reached $p_{\gamma f}$. This test can be run at different pressure and temperature values to study the effect of cavern working conditions on the dissolution kinetics. As in the first test, injection is expected to increase the void hydrogen temperature. Therefore, it is conceivable that there will be heat exchange between the void hydrogen and the steel, as well as between the void hydrogen and the brine.

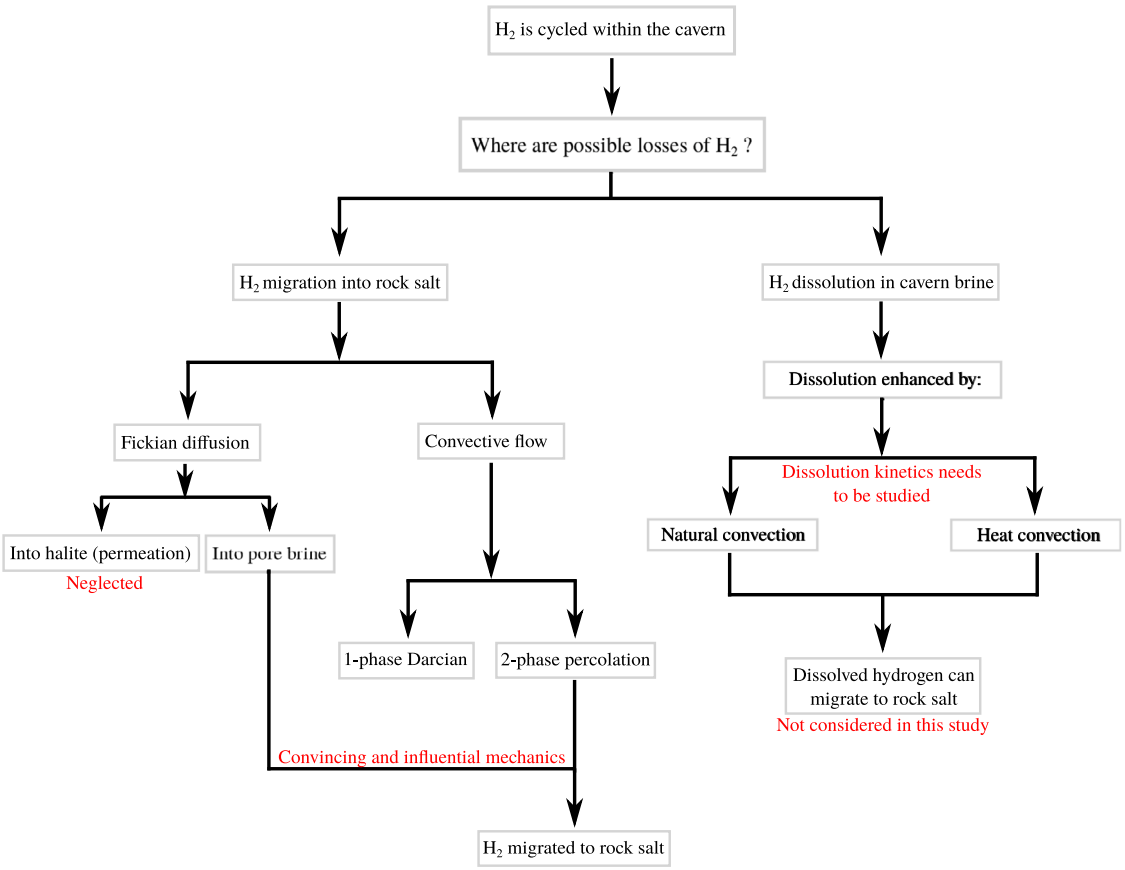

Fig. 12. Our research methodology presenting the transport mechanisms of hydrogen that happen within an underground cavern.

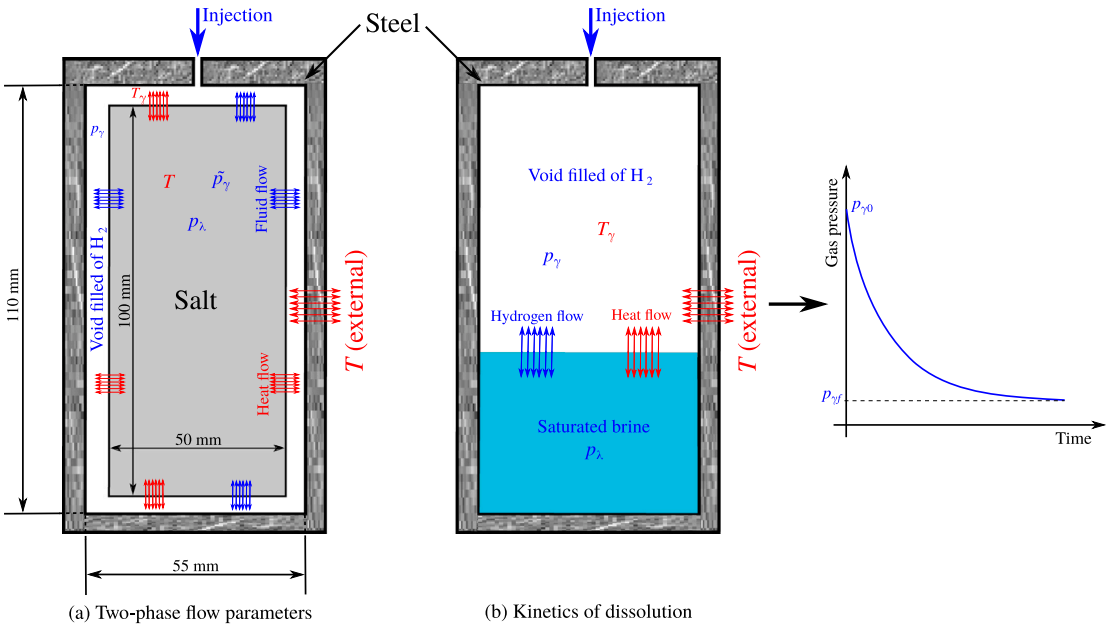

Fig. 13. A schematic diagram of our proposed laboratory setup to study hydrogen permeation in the saturated rock salt as well as the kinetics of its dissolution in the saturated brine. In figure (a), the quantities p_λ and $\tilde{p}_\gamma$ represent the initial brine pore pressure within the saturated sample (atmospheric), and the initial hydrogen pseudo-pressure (zero initially), see AbuAisha et al. [17] for details. In figure (b), p_λ is the saturated brine pressure (atmospheric).

In a real caver, usually there is a thermal gradient over the cavern brine volume. Due to the limited size of our laboratory cell, the effect of a temperature gradient may be difficult to tackle. We are currently conducting such laboratory tests to evaluate the van-Genuchten model parameters along with Fickian diffusion, as well as the kinetics of hydrogen dissolution.

9. Conclusion

Due to the present-day ambiguity with regard to gas transport in rock salt, this article provides a detailed literature review about hydrogen migration in the saturated rock salt. This review is outlined in the context of underground energy storage, where precise tracks and management of the stocked hydrogen quantities are of significant importance. The objective is to draw a general scheme that can be used in developing a mathematical model for this type of gas migration.

It was indispensable to firstly understand how all phases of an underground cavern interact. Then to address the migration of hydrogen into the embracing rock salt, we needed to conceive the hydraulic nature and properties of this rock salt, i.e. porosity, permeability, and the *in situ* pore pressure or stresses. Rock salt is mostly seen as an impermeable medium. However, this is not necessarily the case, especially, when it undergoes creep due to thermo-mechanical charges from the cavern it surrounds. We sought to understand all possible transport mechanisms when hydrogen is pushed into damageable saturated rock salt. These mechanisms included the Fickian diffusion into the halite structure, into the pore brine as well. They also included the convective flow of the gas itself, where the one-phase approach was compared to the two-phase drainage. We emphasized on the necessity to consider the effect of temperature in the damaged zone of the rock salt, as well as the hydraulic properties of the fluid phases. This article aims at helping researchers find direct and concise answers to their questions with regard to hydrogen, and generally gas, transport in rock salt. We will use it to enhance our mathematical-numerical model already published in AbuAisha et al. [17]. It serves as well for our future publications about hydrogen permeation in the saturated rock salt, and the kinetics of its dissolution in the saturated brine.

Though the available literature concerning gas migration in rock salt is very scarce, it promotes the research outline of this article. For instance Jockwer and Wieczorek [118] have stated that the presence of a damaged zone (DRZ) is the main factor for gas transport in rock salt. They conducted experiments and simulations concerning helium, neon, and butane. They found that the diffusion coefficient of these gases increased by two orders of magnitude in the DRZ. Out of the DRZ, the measured permeabilities were in the order of 10^{-19} and 10^{-20} m^2, and the pseudo gas pressure slightly penetrated the rock salt in a two-phase piston-like flow. Senger et al. [119] studied gas (particularly air) migration in concrete. They have found that the gas penetrated distances were limited to 1.5 m after 4 years of injection. The two-phase gas saturation depended on the permeabilities, yet it was less than 0.1 for permeabilities in the order of 10^{-19} m^2. Generally, the existed literature already confirms that permeable interlayers are the main transport conduits around salter caverns [20,21].

The current developments include the utilization of the suggested laboratory setup to calibrate the two-phase percolation-diffusion model parameters for intact and damaged rock salt. Once these model parameters are known, they can be transferred to real scale prototype caverns where hydrogen percolation in rock salt is investigated. There is currently a European project of a prototype salt cavern (EZ53) where the percolation and diffusion of hydrogen in the rock salt is studied on the real scale. The objective is to quantify the amount of hydrogen lost into the rock domain during cycling, and see if it affects the management of the cycled masses.

CRediT authorship contribution statement

Murad AbuAisha: Wrote down the ideas of this paper in the final form..

Acknowledgments

Authors would like to thank Géodénergies, France and the French Association Nationale de Recherche (ANR) for their financial support via the three projects: ROSTOCK–H, STOPIL–H, and HyTrend. We are, as well, expressing a deep feeling of gratitude to Prof. Christophe Coquelet for his efforts in bringing out this work.

References

[1] D.G. Caglayan, N. Weber, H.U. Heinrichs, J. en, M. Robinius, P.A. Kukla, D. Stolten, Technical potential of salt caverns for hydrogen storage in europe, Int. J. Hydrogen Energy 45 (2020) 6793–6805.
[2] M. Deveci, Site selection for hydrogen underground storage using interval type–2 hesitant fuzzy sets, Int. J. Hydrogen Energy 43 (19) (2018) 9353–9368.
[3] M. McPherson, N. Johnson, M. Strubegger, The role of electricity storage and hydrogen technologies in enabling global low-carbon energy transitions, Appl. Energy 216 (2018) 649–661.
[4] F. Klumpp, Comparison of pumped hydro, hydrogen storage and compressed air energy storage for integrating high shares of renewable energies–potential, cost-comparison and ranking, J. Energy Storage 8 (2016) 119–128.
[5] M. Iordache, D. Schitea, M. Deveci, I.Z. Akyurt, I. Iordache, An integrated ARAS and interval type-2 hesitant fuzzy sets method for underground site selection: Seasonal hydrogen storage in salt caverns, J. Pet. Sci. Eng. 175 (2019) 1088–1098.
[6] J.D. Holladay, J. Hu, D.L. King, Y. Wang, An overview of hydrogen production technologies, Cat. Today 139 (4) (2009) 244–260.
[7] Y. Zhu, L. Ouyang, H. Zhong, J. Liu, H. Wang, H. Shao, Z. Huang, M. Zhu, Closing the loop for hydrogen storage: Facile regeneration of $NaBH_4$ from its hydrolytic product, Angewandte Chemie Int. Ed. 59 (22) (2020) 8623–8629.
[8] S. Koohi-Fayegh, M.A. Rosen, A review of energy storage types, applications and recent developments, J. Energy Storage 27 (2020) 101047.
[9] T. Demirel, M. Deveci, G. Vardar, Location selection for underground natural gas storage using choquet integral, J. Nat. Gas Sci. Eng. 45 (2017) 368–379.
[10] M. Deveci, Ç.N. Demirel, R. John, E. Özcan, Fuzzy multi-criteria decision making for carbon dioxide geological storage in Turkey, J. Nat. Gas Sci. Eng. 27 (2) (2015) 692–705.
[11] C.R. Matos, J.F. Carneiro, P.P. Silva, Overview of large–scale underground energy storage technologies for integration of renewable energies and criteria for reservoir identification, J. Energy Storage 21 (2019) 241–258.
[12] A. Ozarslan, Large–scale hydrogen energy storage in salt caverns, Int. J. Hydrogen Energy 37 (19) (2012) 14265–14277.
[13] D. Pamucar, M. Deveci, D. Schitea, L. Erişkin, M. Iordache, I. Iordache, Developing a novel fuzzy neutrosophic numbers based decision making analysis for prioritizing the energy storage technologies, Int. J. Hydrogen Energy 45 (43) (2020) 23027–23047.
[14] M. AbuAisha, A. Rouabhi, On the validity of the uniform thermodynamic state approach for underground caverns during fast and slow cycling, Int. J. Heat Mass Transfer 142 (2019) 118424.
[15] K. Khaledi, E. Mahmoudi, M. Datcheva, T. Schanz, Stability and serviceability of underground energy storage caverns in rock salt subjected to mechanical cyclic loading, Int. J. Rock Mech. Min. Sci. 86 (2016) 115–131.
[16] P. Labaune, A. Rouabhi, Dilatancy and tensile criteria for salt cavern design in the context of cyclic loading for energy storage, J. Nat. Gas Sci. Eng. 62 (2019) 314–329.
[17] M. AbuAisha, A. Rouabhi, J. Billiotte, F. Hadj-Hassen, Non–isothermal two–phase hydrogen transport in rock salt during cycling in underground caverns, Int. J. Hydrogen Energy 46 (3) (2021) 6632–6647.
[18] T. Popp, H. Kern, O. Schulze, Evolution of dilatancy and permeability in rock salt during hydrostatic compaction and triaxial deformation, J. Geophys. Res. – Solid Earth 106 (B3) (2001) 4061–4078.
[19] J.C. Stormont, $In-situ$ Gas permeability measurements to delineate damage in rock salt, Int. J. Rock Mech. Min. Sci. 34 (7) (1997) 1055–1064.
[20] W. Liu, Z. Zhang, J. Chen, D. Jiang, F. Wu, J. Fan, Y. Li, Feasibility evaluation of large–scale underground hydrogen storage in bedded salt rocks of China: A case study in Jiangsu province, Energy 198 (2020) 117348.
[21] W. Liu, J. Chen, D. Jiang, X. Shi, Y. Li, J.J.K. Daemen, C. Yang, Tightness and suitability evaluation of abandoned salt caverns served as hydrocarbon energies storage under adverse geological conditions (AGC), Appl. Energy 178 (2016) 703–720.
[22] F.D. Hansen, C.D. Leigh, Salt disposal of heat–generating nuclear waste, in: SandIa Report: SAND2011–0161, Sandia National Laboratories, Albuquerque, New Mexico 87185 and Livermore, California 94550, 2011.
[23] J. Ślizowski, L. Lankof, Salt–mudstones and rock–salt suitabilities for radioactive–waste storage systems: rheological properties, Appl. Energy 75 (1–2) (2003) 137–144.
[24] K.S. Johnson, S. Gonzales, Salt Deposits in the United States and Regional Geologic Characteristics Important for Storage of Radioactive Waste, Earth Resource Associates, INC., Athens, Georgia, the USA, 1978.
[25] S. Ghanbarzadeh, M.A. Hesse, M. Prodanović, J.E. Gardner, Deformation–assisted fluid percolation in rock salt, Science (Geology) 3506264 (2015) 1069–1072.
[26] A. Bechtel, S.M. Savin, S. Hoernes, Oxygen and hydrogen isotopic composition of clay minerals of the bahloul formation in the region of the bou grine zinc–lead ore deposit (Tunisia) evidence for fluid–rock interaction in the vicinity of salt dome cap rock, Chem. Geol. 156 (1999) 191–207.
[27] B. Amaziane, A.Ž. Keko, M. Jurak, Modeling compositional compressible two–phase flow in porous media by the concept of the global pressure, Comput. Geosci. 18 (3–4) (2014) 297–309.

[28] Hannon M. J., Full immersion pressure–pulse decay. United States Patent PCT/US2016/031502. International Publication Number: WO 2016/179593A1, 2016 10 2016.

[29] Y. Charnavel, D. Leca, F. Poulain, Advanced geometrical modelling of salt dissolution during cavern leaching – illustration with a case study, in: The SMRI Meeting, Las Vegas, Nevada, USA, 1999.

[30] E. Pernette, M. Dussaud, Underground storages at Tersanne and Etrez: prediction and simulation of cavity leaching in a salt layer charged with insoluble materials, in: The sixth International Symposium on Salt, Toronto, Canada, May, 1983, pp. 26–27.

[31] J. Jaffré, A. Sboui, Henry's law and gas phase disappearance, Transp. Porous Media 82 (2010) 521–526.

[32] M. Geng, Z. Duan, Prediction of oxygen solubility in pure water and brines up to high temperatures and pressures, Geochim. Cosmochim. Acta 74 (2010) 5631–5640.

[33] T.J. Barrett, G.M. Anderson, J. Lugowski, The solubility of hydrogen sulphide in 0-5 m nacl solutions at 25°–95°C and one atmosphere, Geochim. Cosmochim. Acta 52 (1988) 807–811.

[34] T.E. Crozier, S. Yamamoto, Solubility of hydrogen in water, seawater, and nacl solutions, J. Chem. Eng. Data 19 (3) (1974) 242–244.

[35] J.M. Gossett, Measurement of Henry's law constants for C_1 and C_2 chlorinated hydrocarbons, Environ. Sci. Technol. 21 (1987) 202–208.

[36] S. Chabab, P. Théveneau, J. Corvisier, C. Coquelet, P. Paricaud, C. Houriez, E. E. Ahmar, Thermodynamic study of the CO_2 – H_2O – NaCl system: Measurements of CO_2 solubility and modeling of phase equilibria using soreide and whitson, electrolyte CPA and SIT models, Int. J. Greenhouse Gas Control 91 (2019) 102825.

[37] S. Chabab, P. Théveneaua, C. Coquelet, J. Corvisier, P. Paricaud, Measurements and predictive models of high–pressure H_2 solubility in brine (H_2o+NaCl) for underground hydrogen storage application, Int. J. Hydrogen Energy 45 (56) (2020) 32206–32220.

[38] C. Beckermann, S. Ramadhyani, R. Viskanta, Natural convection flow and heat transfer between a fluid layer and a porous layer inside a rectangular enclosure, J. Heat Transfer 109 (1986) 363–370.

[39] R.F. Bergholz, Instability of steady natural convection in a vertical fluid layer, J. Fluid Mech. 2 (84) (1978) 743–768.

[40] A. Soubeyran, A. Rouabhi, C. Coquelet, Thermodynamic analysis of carbon dioxide storage in salt caverns to improve the power–to–gas process, Appl. Energy 242 (2019) 1090–1107.

[41] D. Singh, K.K. Sirkar, Desalination of brine and produced water by direct contact membrane distillation at high temperatures and pressures, J. Membr. Sci. 389 (2012) 380–388.

[42] W. Kloppmann, P.H. Négrel, J. Casanova, H. Klinge, K. Schelkes, C. Guerrot, Halite dissolution derived brines in the vicinity of a permian salt dome (N German Basin), evidence from boron, strontium, oxygen, and hydrogen isotopes, Geochim. Cosmochim. Acta 65 (22) (2001) 4087–4101.

[43] S.M. Hassanizadeh, T. Leijnse, On the modeling of brine transport in porous media, Water Resour. Res. 24 (3) (1988) 321–330.

[44] K.S. Johnson, Dissolution of salt on the east flank of the permian basin in the southwestern U.S.A, J. Hydrol. 54 (1981) 75–93.

[45] M. Schlichtenmayer, Bannach A., Renewable Energy Storage in Salt Caverns – a Comparison of the Thermodynamics and Permeability Between Natural Gas, Air, and Hydrogen, RR2015-1 Research Project Report, prepared for Solution Mining Research Institute, D–095596 Freiberg, Germany, 2015.

[46] T. Popp, H. Kern, Ultrasonic wave velocities, gas permeability and porosity in natural and granular rock salt, Phys. Chem. Earth 23 (3) (1998) 373–378.

[47] L.H. Gevantman, Physical Properties Data for Rock Salt. U.S. Department of Commerce/National Bureau of StandArds, U.S. Government Printing Office, Washington, D.C, 1981, p. 20402.

[48] J. Hammer, M. Pusch, C. Häher, C. Ostertag-Henning, N. Thiemeyer, G. Zulauf, Hydrocarbons in rock salt of the gorleben salt dome–amount, origin and influence on geomechanical properties, in: L. Roberts, K. Mellegard, F. Hansen (Eds.), The Mechanical Behavior of Salt VIII, Taylor & Francis Group, London, 2015, pp. 69–75.

[49] J.S. Bradley, Abnormal formation pressure, AAPG Bull. 59 (6) (1975) 957–973.

[50] A. Rouabhi, G. Hévin, A. Soubeyran, P. Labaune, F. Louvet, A multiphase multi–component modeling approach of underground salt cavern storage, Geomechan. Energy Environ. 12 (2017) 21–35.

[51] S.W. Rutherford, D.D. Do, Review of time lag permeation technique as a method for characterisation of porous media and membranes, Adsorption 3 (4) (1997) 283–312.

[52] B. Martin, K. Röller, B. Stöckhert, Low–stress pressure solution experiments on halite single–crystals, Tectonophysics 308 (1999) 299–310.

[53] C.J. Spiers, P.M.T.M. Schutjens, Intergranular pressure solution in nacl: Grain–to–grain contact experiments under the optical microscope, Oil & Gas Sci. Technol. 54 (6) (1999) 729–750.

[54] Yokogawa, Hydrogen Permeation. Application Note, Yokogawa Corporation of America, 2018.

[55] P.H. Cosenza, M. Ghoreychi, Effects of very low permeability on the long–term evolution of a storage cavern in rock salt, Int. J. Rock Mech. Min. Sci. 36 (1999) 527–533.

[56] P. Bérest, B. Brouard, G. Hévin, Twelve–year monitoring of the idle Etrez salt cavern, Int. J. Rock Mech. Min. Sci. 48 (2011) 168–173.

[57] P. Bérest, J. Bergues, B. Brouard, Review of static and dynamic compressibility issues relating to deep underground salt caverns, Int. J. Rock Mech. Min. Sci. 36 (1999) 1031–1049.

[58] P. Bérest, J. Bergues, B. Brouard, J.G. Durup, B. Guerber, A salt cavern abandonment test, Int. J. Rock Mech. Min. Sci. 38 (2001) 357–368.

[59] P. Bérest, B. Brouard, J.G. Durup, Tightness tests in salt–cavern wells, Oil & Gas Sci. Technol. – Rev. IFP 56 (5) (2001) 451–469.

[60] J.G. Durup, F. Vidal, C. Rolin, Pilot abandonment test of a very deep gas storage salt cavern, Oil & Gas Sci. Technol. – Rev. IFP 62 (3) (2007) 287–296.

[61] C. Jianwen, L. Erbing, L. Jin, Characterization of microscopic pore structures of rock salt through mercury injection and nitrogen absorption tests, Geofluids (2018) http://dx.doi.org/10.1155/2018/9427361.

[62] J. Van Brakel, P.M. Heertjes, Analysis of diffusion in macroporous media in terms of a porosity, a tortuosity and a constrictivity factor, Int. J. Heat Mass Transf. 17 (9) (1974) 1093–1103.

[63] C.K. Ho, S.W. Webb, Gas Transport in Porous Media, Springer, 3300 AA Dordrecht, The Netherlands, 2006.

[64] H. Wipf, Solubility and diffusion of hydrogen in pure metals and alloys, Physica Scripta, T 94 (2001) 43–51.

[65] R. Hempelmann, Diffusion of hydrogen in metals, J. Less-Common Metals 101 (1984) 69–96.

[66] O.V. Malykh, A. Golub Yu, V.V. Teplyakov, Polymeric membrane materials: New aspects of empirical approaches to prediction of gas permeability parameters in relation to permanent gases, linear lower hydrocarbons and some toxic gases, Adv. Colloid Interface Sci. 164 (2011) 89–99.

[67] H.L. Eschbach, F. Gross, S. Schulien, Permeability measurements with gaseous hydrogen for various steals, Vacuum 13 (1963) 543–547.

[68] H. Yukawa, G.X. Zhang, N. Watanabe, M. Morinaga, T. Nambu, Y. Matsumoto, Analysis of hydrogen diffusion coefficient during hydrogen permeation through niobium and its alloys, J. Alloys Compd. 476 (2009) 102–106.

[69] D. Aquilano, F. Otálora, L. Pastero, J.M. Garcí a Ruiz, Three study cases of growth morphology in minerals: Halite, calcite and gypsum, Prog. Cryst. Growth Charact. Mater. 62 (2) (2016) 227–251.

[70] L. Ortiz, G. Volckaert, D. Mallants, Gas generation and migration in boom clay, a potential host rock formation for nuclear waste storage, Eng. Geol. 64 (2002) 287–296.

[71] E. Jacops, K. Wouters, G. Volckaert, H. Moors, N. Maes, C. Bruggeman, R. Swennen, R. Littke, Measuring the effective diffusion coefficient of dissolved hydrogen in saturated boom clay, Appl. Geochem. 61 (2015) 175–184.

[72] S.W. Webb, K. Pruess, The use of fick's law for modeling trace gas diffusion in porous media, Transp. Porous Media 51 (2003) 327–341.

[73] T.R. Ferrell, M.D. Himmelblau, Diffusion coefficients of hydrogen and helium in water, AlChE J. 13 (4) (1967) 702–708.

[74] A. Pray, E.C. Schweickert, H.B. Minnichi, Solubility of hydrogen, oxygen, nitrogen, and helium in water at elevated temperatures, Ind. Eng. Chem. 44 (5) (1952) 1146–1151.

[75] S.P. Cadogan, J.P. Hallett, G.C. Maitland, J.P.M. Trusler, Diffusion coefficients of carbon dioxide in brines measured using^{13}C pulsed–field gradient nuclear magnetic resonance, J. Chem. Eng. Data 60 (1) (2015) 181–184.

[76] B.R. Breslau, F. Miller, On the viscosity of concentrated aqueous electrolyte solutions, J. Phys. Chem. 74 (5) (1972) 1056–1061.

[77] Aspentech, Physical property methods and models, Aspen Ref. Manual 11 (2001) 12–18.

[78] P.S. Cadogan, P.J. Hallett, C.G. Maitland, P.J. Martin Trusler, Diffusion coefficients of carbon dioxide in brines measured using^{13}C pulsed–field gradient nuclear magnetic resonance, J. Chem. Eng. Data 60 (2015) 181–184.

[79] P. Grathwohl, Diffusion in Natural Porous Media: Contaminant Transport, Sorption/Desorption and Dissolution Kinetics, Springer, US, New York, 1998.

[80] J. Crank, The mathematics of diffusion, second ed., Oxford University Press, Walton street, Oxford OX2 6DP, UK, 1973.

[81] G.J. Clark, C.W. White, D.D. Allred, B.R. Appleton, I.S.T. Tsong, Hydrogen concentration profiles in quartz determined by a nuclear reaction technique, Phys. Chem. Mineral. 3 (2) (1978) 199–211.

[82] U.T. Mello, G.D. Karner, R.N. Anderson, Role of salt in restraining the maturation of subsalt source rocks, Mar. Pet. Geol. 12 (7) (1995) 697–716.

[83] R.O. Foumier, The transition from hydrostatic to greater than hydrostatic fluid pressure in presently active continental hydrothermal systems in crystalline rock, Geophys. Res. Lett. 18 (5) (1991) 955–958.

[84] H.J. Sutherland, S.P. Cave, Argon gas permeability of new mexico rock salt under hydrostatic compression, Int. J. Rock Mech. Min. Sci. Geomech. Abstr. 17 (5) (1980) 281–288.

[85] Y.S. Wu, K. Pruess, P. Persoff, Gas flow in porous media with klinkenberg effects, Transp. Porous Media 32 (1998) 117–137.

[86] P.J. Koelemeijer, C.J. Peach, C.J. Spiers, Surface diffusivity of cleaved nacl crystals as a function of humidity: Impedance spectroscopy measurements and implications for crack healing in rock salt, J. Geophys. Res. 117 (B01205) (2012).

[87] M. Mahjoub, A. Rouabhi, M. Tijani, S. Granet, S. M'Jahad, J. Talandier, Numerical study of callovo-oxfordian argillite expansion due to gas injection, Int. J. Geomech. 18 (1) (2018) 04017134.
[88] K. Kim, R.Y. Makhnenko, Coupling between poromechanical behavior and fluid flow in tight rock, Transp. Porous Media 135 (2020) 487–512.
[89] D. Zhang, L. Jeannin, G. Hevin, P. Egermann, L. Potier, F. Skoczylas, Is Salt a Poro-Mechanical Material? in: the 52nd U.S. Rock Mechanics/Geomechanics Symposium, Seattle, the USA, 2018.
[90] C. De Las Cuevas, Pore structure characterization in rock salt, Eng. Geol. 47 (1–2) (1997) 17–30.
[91] A.S. Ziarani, R. Aguilera, Knudsen's permeability correction for tight porous media, Transp. Porous Media 91 (1) (2012) 239–260.
[92] S. Roy, R. Raju, H.F. Chuang, B.A. Cruden, M. Meyyappan, Modeling gas flow through microchannels and nanopores, J. Appl. Phys. 93 (8) (2003) 4870.
[93] L. Klinkenberg, The permeability of porous media to liquids and gases. Paper API41200 Presented at the Drilling and Production Practice, New York, 1 January, 1941.
[94] N. Zisser, G. Nover, Anisotropy of permeability and complex resistivity of tight sandstones subjected to hydrostatic pressure, J. Appl. Geophys. 68 (3) (2009) 356–370.
[95] O. Ozdemira, S.I. Karakashev, A.V. Nguyen, J.D. Miller, Adsorption and surface tension analysis of concentrated alkali halide brine solutions, Mineral. Eng. 22 (3) (2009) 263–271.
[96] Y. Liu, H.A. Li, R. Okuno, Measurements and modeling of interfacial tension for CO_2/CH_4/Brine systems under reservoir conditions, Ind. Eng. Chem. Res. 55 (48) (2016) 12358–12375.
[97] C.A. Aggelopoulos, M. Robin, O. Vizika, Interfacial tension between CO_2 and brine (NaCl + $CaCl_2$) at elevated pressures and temperatures: The additive effect of different salts, Adv. Water Resour. 34 (4) (2011) 505–511.
[98] K. Fukuzawa, K. Watanabe, K. Yasuda, R. Ohmura, Interfacial tension measurements in the (CO_2 + H_2) gas mixture and water system at temperatures from 271.2 K to 280.2 K and pressures up to 7.0 MPa, J. Chem. Thermodyn. 119 (2018) 20–25.
[99] M.A. Rodrí guez Valverde, M.T. Miranda, Derivation of jurin's law revisited, Eur. J. Phys. 32 (2011) 49–54.
[100] A. Ern, I. Mozolevski, Discontinuous Galerkin method for two–component liquid–gas porous media flows, Comput. Geosci. 16 (3) (2012) 677–690.
[101] W.T. Pfeiffer, S.A. al Hagrey, D. Köhn, W. Rabbel, S. Bauer, Porous media hydrogen storage at a synthetic, heterogeneous field site: numerical simulation of storage operation and geophysical monitoring, Environ. Earth Sci. 75 (1177) (2016).
[102] Y.C. Yortsos, B. Xu, D. Salin, Phase diagram of fully developed drainage in porous media, Phys. Rev. Lett. 79 (23) (1997) 4581–4584.
[103] R. Lenormand, Flow through porous media: limits of fractal patterns, Proc. R. Soc. Lond. Ser. A Math. Phys. Eng. Sci. 4231864 (1989) 159–168.
[104] P. Lefort, étude Des Déplacements Gaz–Eau Dans Les Argilites Du Callovo–Oxfordien à L'Aide de la Théorie de la Percolation En Gradient (Ph.D. thesis), INP Toulouse, 2014.
[105] A.V. Akhmetzyanova, A.G. Kushner, V.V. Lychagin, Mass and heat transport in the two–phase buckley–leverett model, J. Geom. Phys. 113 (2017) 2–9.
[106] H.J. Morel-Seytoux, P.D. Meyer, M. Nachabe, J. Tourna, M.T. van Genuchten, R.J. Lenhard, Parameter equivalence for the brooks–corey and van genuchten soil characteristics: preserving the effective capillary drive, Water Res. Res. Banner 32 (5) (1996) 1251–1258.
[107] B.S. Sukhija, D.V. Reddy, P. Nagabhushanam, S. Hussain, Recharge processes: piston flow vs preferential flow in semi-arid aquifers of India, Hydrog. J. 11 (3) (2003) 387–395.
[108] D. Zhong, L. Ouyang, J. Liu, H. Wang, Y. Jia, M. Zhu, Metallic Ni nanocatalyst *in situ* formed from lani5h5 toward efficient CO2 methanation, Int. J. Hydrogen Energy 44 (55) (2019) 29068–29074.
[109] K. Khaledi, E. Mahmoudi, M. Datcheva, T. Schanz, Analysis of compressed air storage caverns in rock salt considering thermo-mechanical cyclic loading, Environ. Earth Sci. 75 (1149) (2016).
[110] J.Q. Deng, Q. Yang, Y.R. Liu, Time–dependent behaviour and stability evaluation of gas storage caverns in salt rock based on deformation reinforcement theory, Tunn. Undergr. Space Technol. 42 (2014) 277–292.
[111] S.N. Moghadam, H. Mirzabozorg, A. Noorzad, Modeling time–dependent behavior of gas caverns in rock salt considering creep, dilatancy and failure, Tunn. Undergr. Space Technol. 33 (2013) 171–185.
[112] G. Wang, K. Guo, M. Christianson, H. Konietzky, Deformation characteristics of rock salt with mudstone interbeds surrounding gas and oil storage cavern, Int. J. Rock Mech. Min. Sci. 48 (6) (2011) 870–877.
[113] C. Le Guen, M. Deveughèle, J. Billiotte, J. Brulhet, Gas permeability changes of rocksalt subjected to thermo–mechanical stresses, Quart. J. Eng. Geol. 26 (1993) 327–334.
[114] P. Lebrun, J. Billiotte, M. Deveughèle, J.M. Le Cléac'h, Local increase of rock salt porosity by coalescence of fluid inclusions under the effect of a thermal gradient, C. R. Acad. Sci. 320 (7) (1995) 555–561.
[115] K.L. Kuhlman, B. Malama, Brine flow in heated geologic salt, in: Sandia report SAND2013-1944, 2013, p. 128.
[116] J.S.R. Pinto, P. Bachaud, T. Fargetton, N. ferrando, L. Jeannin, F. Louvet, Modeling phase equilibrium of hydrogen and natural gas in brines: application to storage in salt caverns, Int. J. Hydrogen Energy 46 (5) (2021) 4229–4240.
[117] D. Li, C. Beyer, S. Bauer, A unified phase equilibrium model for hydrogen solubility and solution density, Int. J. Hydrogen Energy 43 (1) (2018) 512–529.
[118] N. Jockwer, K. Wieczorek, ADDIGAS. Advective and Diffusive Gas Transport in Rock Salt Formations. GRS–234, Contact Number: 02 E 9824 Project Final Report, Gesellschaft fuer Anlagen– und Reaktorsicherheit mbH (GRS, Berlin, Germany, 2008.
[119] R. Senger, B. Lanyon, P. Marschall, S. Vomvoris, Numerical modeling of the gas migration test at the grimsel test site (switzerland), Nucl. Technol. 164 (2) (2008) 155–168.

INTERNATIONAL JOURNAL OF HYDROGEN ENERGY 46 (2021) 6632–6647

Available online at www.sciencedirect.com

ScienceDirect

journal homepage: www.elsevier.com/locate/he

Non–isothermal two–phase hydrogen transport in rock salt during cycling in underground caverns

Murad AbuAisha[*], *Ahmed Rouabhi*, *Joël Billiotte*, *Faouzi Hadj–Hassen*

MINES ParisTech, PSL Research University, Centre de Géosciences, 35 Rue Saint Honoré, Fontainebleau, 77300, France

HIGHLIGHTS

- Hydrogen migration in the context of underground storage is presented.
- Transport mechanisms between the cavern phases are discussed.
- Cavern thermodynamics is coupled with the transport mechanisms.
- Model parameters effects are investigated in a parametric study.
- Cycling simulations proved that the amount of lost hydrogen rests negligible.

GRAPHICAL ABSTRACT

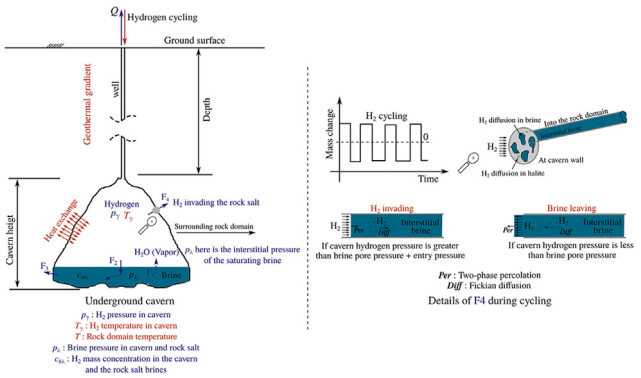

ARTICLE INFO

Article history:
Received 14 September 2020
Received in revised form
5 November 2020
Accepted 16 November 2020
Available online 18 December 2020

Keywords:
Underground salt caverns
Cavern thermodynamic state
Saturated rock salt
Two–phase hydrogen percolation and diffusion
Thermo–hydraulic coupling

ABSTRACT

For a good management and precise tracks of hydrogen quantities stored in salt caverns, this paper presents a study on hydrogen transport in rock salt during cycling. It provides a novel mathematical–numerical model that couples the cavern thermodynamics with the transport mechanisms of hydrogen in the saturated rock salt in a fully coupled thermo–hydraulic framework. Both the two–phase Darcian percolation and the Fickian diffusion are used to account for hydrogen migration in the interstitial brine of the rock salt. Due to the absence of experimental data, a parametric study is furnished. The effect of cycling within the cavern on the migration mechanisms is discussed in detail. Simulations have confirmed the dependency of the Darcian percolation on the model parameters. However, for similar applications, this dependency might be limited. The value of the Fickian diffusion coefficient affects indirectly the Darcian percolation. The two–phase percolation becomes more of a piston–like for very small values of the diffusion coefficient. On a real–scale typical cavern, and over a period of 40 years, simulations have proven that the quantity of hydrogen lost into the surrounding rock salt is unimportant. Besides, cycling renders this quantity more insignificant.

* *Corresponding author.*
E-mail addresses: murad.abuaisha@mines-paristech.fr (M. AbuAisha), ahmed.rouabhi@mines-paristech.fr (A. Rouabhi), joel.billiotte@mines-paristech.fr (J. Billiotte), faouzi.hadj_hassen@mines-paristech.fr (F. Hadj–Hassen).
https://doi.org/10.1016/j.ijhydene.2020.11.152

Introduction

Driven by concerns related to climate change, energy transition has led to the use of new clean energy resources [1]. Hydrogen has been regarded as an important energy vector in this transition [2–4]. However, the increasing energy demands and the intermittency problems [5–7] require large–scale storage techniques [8,9]. Underground salt caverns offer the most promising option owing to their low investment cost and low cushion gas requirement [9]. Rock salt/halite occurs within sedimentary rocks where it has formed from the evaporation of seawater or salty lakes. Rock salt is consequently deposited in cycles which affects its directional properties like the elastic modulus and the permeability. Depending on the location, the rock salt properties, mechanical and hydraulic, differ as well.

During cavern operation, hydrogen undergoes changes in its temperature and pressure. Such changes are expected to affect its migration into the surrounding rock domain. Hydrogen invasion into this embracing rock takes place either through the rock salt itself, or through the more permeable and porous interlayers (if they happen to exit). Since underground storage caverns are constructed in networks, the lost hydrogen into the surrounding rock can weaken the neighboring caverns structure. Moreover, the cost of hydrogen production as well as a good management of storage require to keep precise tracks of the injected and withdrawn hydrogen quantities. Studies addressing hydrogen or gas transport through rock salt are scarce. For instance, *Liu* et al. [10] provided a cavern scale study to estimate the hydrogen tightness. Their approach assumed that hydrogen filtrates through the rock salt following a Darcian flow type. Besides, they assigned a relatively small permeability value to the rock salt while assuming a zone of dilatancy. They eventually concluded that the salt caverns are hydrogen–tight except for the regions of interlayers which can also be considered as hydrogen–tight for permeabilities less than 10^{-18} m^2. *Liu* et al. [11] presented a general study about gas tightness of abandoned salt caverns. Though their study did not include hydrogen, they have concluded that the permeability of the interlayers was a key factor in influencing gas seepage in the vicinity of the caverns and that interlayers formed primary channels for gas migration. They used as well a generalized Darcian flow type model to evaluate the fluid seepage around the cavern. They found that the upper threshold permeability of the interlayers must be no more than 10^{-16} to 10^{-17} m^2 to guarantee tightness when storing natural gas, and no more than 10^{-16} m^2 when storing oil. There are, however, considerable research papers that treat hydrogen percolation and diffusion in the clay sedimentary basins in the context of radioactive waste storage [12,13].

Since rock salt contains interstitial brine and characterized by extremely low permeabilities and porosities, the application of one–phase generalized Darcian flow to describe hydrogen transport is questioned. Moreover, none of the available literature is addressing the effect of cavern cycling on the migration mechanisms. Indeed, the cavern thermodynamic state is a function of cycling. Consequently, in the cavern vicinity, both the interstitial rock salt brine pressure and temperature evolutions are functions of cycling as well. These changes in the interstitial brine pressure and temperature must influence the migration of hydrogen into the rock domain. The novelty of this research stems from providing a mathematical–numerical model that couples the cavern thermodynamics with the non–isothermal transport mechanisms of hydrogen into the rock salt. Both the Darcian two–phase percolation and the Fickian diffusion are considered as well as the interaction between them. This model addresses as much as possible of the problem complex physics for good estimation of the exchanged hydrogen mass. Besides, it precisely presents the effect of cycling. Due to the absence of any literature or experimental data treating hydrogen migration in saturated rock salt, we offered a parametric study that investigated the effect of the two–phase van Genuchten model parameters as well as the Fickian diffusion coefficient on the total mass of exchanged hydrogen. The van Genuchten model allows to describe the two–phase percolation of hydrogen (characterized by very low viscosity) in rock salt (characterized by very small pore size).[1] Eventually, an overestimating scenario of model parameters, of diffusion coefficient, and of boundary conditions, was considered to estimate the amount of hydrogen migrated during a 40–year period of hydrogen cycling in a typical spherical cavern.

This paper proceeds as follows: the problem of hydrogen migration in the context of underground storage is first presented; the expected transport mechanisms between the cavern phases are discussed; the mathematical and numerical models are then shown for cycling in a typical spherical cavern; after the parametric study is implemented, an overestimating scenario is simulated for a 40–year time period of cycling. The simulations have shown that even for a pessimistic scenario of overestimating model parameters and boundary conditions, the amount of lost hydrogen into the rock domain rests very negligible compared to the cycled mass of hydrogen.

Hydrogen migration in rock salt

This section aims at addressing the problem of hydrogen exchange/transport mechanisms in the context of underground storage. Each mechanism is described briefly and an overall conclusion is eventually drawn about the mechanism that will be considered in the simulations.

Hydrogen storage in salt caverns

Solution mining is commonly used to create large caverns in rock salt formations. In this process, a single well, drilled from the ground surface to the targeted depth (Fig. 1(a)), is generally used to inject fresh water and withdraw brine through a

[1] This type of percolation is defined using the capillary and mobility numbers, for details see *Yortsos* et al. [14], *Lenormand* [15].

concentric tubing system (the leaching process) [16,17]. Once leaching is completed, brine within the cavern is reduced to minimal quantities by a debrining/filling phase where it is moved out by hydrogen injection [18,19].

Fig. 1(a) shows an underground cavern filled with hydrogen at a certain pressure and temperature. The figure also depicts the amount of brine left in the cavern at the end of the debrining process. Hydrogen within the cavern is expected to experience cycles of pressure and temperature changes according to the intended usage. During its life time, the cavern mainly contains, simultaneously or sequentially, two different immiscible phases: the stored hydrogen and the brine. The third important phase of this storage outline is the surrounding rock salt domain. This domain is constituted of the salt mass which itself is a mixture of grains or crystals of halite and the brine occupying the inter–grain spaces. Each of the three phases is characterized by state variables which are for hydrogen: the pressure and the temperature, for brine: the pressure, the temperature, the salt concentration, and the hydrogen concentration, for the rock salt: the stress and the temperature. Since hydrogen may be present in the non–gaseous phase in the other phases (brine and solid), its presence will be characterized by a mass concentration.

While the cavern is operated, the three phases are interacting as follows (Fig. 1(a)): brine is evaporating into the stored hydrogen (F_1); hydrogen is dissolving in the brine (F_2) and is percolating and diffusing into the porous rock salt (F_4); brine at the cavern bottom is flowing into the rock salt with its dissolved hydrogen (F_3).

Transport mechanisms

Transport mechanisms between phases include three components: the cavern hydrogen–brine interaction; the brine–rock salt interaction; and the hydrogen–rock salt interaction. The first component happens at the hydrogen–brine interface within the cavern where hydrogen dissolves in brine (flow F_2 in Fig. 1(a)) according to Henry's law [20]. The dissolution induces a flow of hydrogen in the brine which enriches the hydrogen concentration by diffusion [21,22] and convection [23,24].

In the second component the brine–rock salt interface moves depending on the degree of salinity of the cavern brine. Salt can precipitate from brine onto the interface or the interface can be worn away by the brine to achieve saturation continuity at the cavern working temperature and pressure [25–27]. As the cavern brine pressure is equal to the cavern hydrogen pressure, cavern brine can flow into the saturated rock salt, or the interstitial rock salt brine can move out into the cavern (flow F_3 in Fig. 1(a)). Due to the ambiguity with regard to knowing the inter–grain connectivity of rock salt, the pressure of the interstitial brine is poorly defined. However, its value can be limited to two extreme values [28]:

1. The so–called halmostatic pressure, which considers that the brine occupies a totally connected space in the rock mass. Consequently, this pressure is the equivalent to the hydrostatic pressure calculated using the brine density;
2. A lithostatic pressure, which considers that the brine occupies an isolated space in the rock salt phase. Therefore, the brine pressure is assumed in equilibrium with the geologic stresses of the rock salt mass. This pressure extremity is calculated using the rock salt density [29].

At the hydrogen–rock salt interface (see also Fig. 1(b)), the penetration of hydrogen into the saturated rock salt (flow F_4 in Fig. 1(a)) can take place either [30]:

1. In the solid phase itself, i.e. the halite crystals;
2. In the interstitial brine.

These are two different mechanisms, the first is equivalent to hydrogen diffusion in the solids [31,32]. The second includes hydrogen Fickian diffusion in the interstitial brine and the two–phase Darcian percolation [13,33,34].

During cycling, the fluxes F_2, F_3, and F_4 need to be considered in order to calculate the total mass of exchanged hydrogen. Only flow F_4 will be considered in this research paper. Flows F_2 and F_3 will be addressed in a future research.

Mathematical and numerical models

This section presents the mathematical and numerical models needed to evaluate the quantity of hydrogen transported to the rock salt domain surrounding a typical underground cavern. Simulations are done for a seasonal cycling in a spherical cavern created at 910 m depth and for a 40–year time period.

The mathematical model

The mathematical model couples the hydrogen thermodynamics in the cavern with the non–isothermal hydrogen transport in the saturated rock salt domain. To simplify the problem, the following assumptions are made. Some assumptions are adopted for an overestimating study:

1. The underground cavern is assumed to be filled with a mono–component single–phase hydrogen;
2. Hydrogen cycling is seasonal/slow, consequently, a uniform thermodynamic state is assumed within the cavern [35];
3. Rock salt domain is assumed saturated with brine;
4. For an overestimating study, brine pressure within the rock salt domain is assumed halmostatic;
5. For an overestimating study, rock salt creep due to cavern operation is neglected;
6. Hydrogen diffusion in the halite structure is neglected;
7. Hydrogen concentration is initially disregarded in the rock salt domain;
8. Rock salt, interstitial brine, and the invading hydrogen are assumed in thermal equilibrium;
9. Hydrogen invasion into the rock salt domain is assumed to follow the van Genuchten percolation model [14,15];
10. For an overestimating study, hydrogen entry pressure into the saturated rock salt is neglected.

Hydrogen thermodynamics in underground caverns is presented in the work of *Rouabhi* et al. [36] and *AbuAisha and*

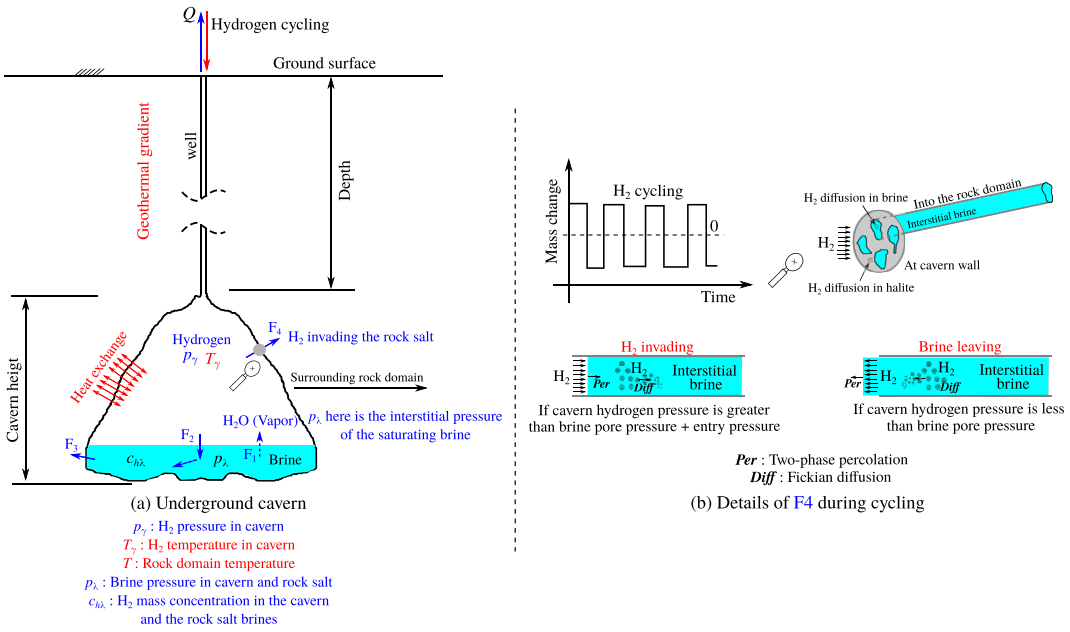

Fig. 1 – (a) Schematic representation of hydrogen storage in salt caverns and its transport mechanisms between phases. (b) Transport of hydrogen into the rock salt domain (flux F_4).

Rouabhi [35]. As an example to modeling a uniform thermodynamic state within the cavern, the following system of equations is used:

$$\begin{aligned} \text{mass balance:}\quad & \mathcal{M}\left(-\chi_{p\gamma}\dot{T}_\gamma+\chi_{T\gamma}\dot{p}_\gamma\right) = Q_e-\Im; \\ \text{energy balance:}\quad & \mathcal{M}C_{p\gamma}\dot{T}_\gamma-\mathcal{V}\chi_{p\gamma}T_\gamma\dot{p}_\gamma = Q_e^+C_{p\gamma}\left(T_\gamma^{\text{inj}}-T_\gamma\right)-\Psi, \end{aligned} \tag{1}$$

where $\mathcal{M}$ (kg) is the cavern hydrogen mass, T_γ (K) is the cavern uniform hydrogen temperature, $\chi_{p\gamma}$ (1/K) is the hydrogen isobaric thermal expansivity, p_γ (Pa) is the cavern uniform hydrogen pressure, $\chi_{T\gamma}$ (1/Pa) is the hydrogen isochoric compressibility, Q_e (kg/s) is the well/external flow rate, Q_e^+ is the positive/injection part of Q_e, $\Im$ (kg/s) is the internal/exchanged mass rate between the cavern and the rock domain, $C_{p\gamma}$ (J/kg/K) is the hydrogen heat capacity at a given pressure, $\mathcal{V}$ (m^3) is the cavern volume, T_γ^{inj} (K) is the injection temperature, and Ψ (W) is the power exchanged between the cavern hydrogen and the surrounding rock. Both the exchanged power Ψ and mass rate $\Im$ are positive when given to the rock domain.

Once the cavern thermodynamic state (p_γ and T_γ) is known, it can be used to calculate the hydrogen invasion into the surrounding rock salt domain. Fig. 1(b) shows the mechanisms related to hydrogen transport in the saturated rock salt while assuming a van Genuchten two–phase percolation. When hydrogen pressure within the cavern exceeds the rock salt pore pressure plus the entry pressure, hydrogen invades the rock salt in a two phase percolation type flow. However, when hydrogen pressure becomes less than the interstitial brine pressure, brine moves towards the cavern and tends to pour down the cavern wall. Fickian diffusion of hydrogen in the rock salt interstitial brine is function of hydrogen cycling. This diffusion is related to the hydrogen mass concentration gradient between the cavern and the rock salt domain. The temperature changes within the cavern lead to temperature changes in the rock salt domain. In this study, rock salt, interstitial brine, and the invading hydrogen are assumed to be in local thermal equilibrium. Besides, a temperature continuity is assumed at the cavern wall. The thermo-hydraulic coupling in the rock domain is accounted for through the pressure and temperature effects on the hydrogen and the brine densities.

As the mechanical deformation of the rock salt is neglected, the subsequent percolation–diffusion equations are established in the initial configuration of the solid matrix. The rock salt porosity is denoted by n, and T denotes the temperature for all the phases in the rock salt domain. For each fluid phase $\alpha\in\{\lambda\ (\text{liquid}),\ \gamma\ (\text{gas})\}$, p_α stands for the pressure, n_α the partial porosity, $S_\alpha = n_\alpha/n$ the saturation degree, and ρ_α (kg/m^3) the density. In the liquid phase λ, $c_{h\lambda}$ denotes the mass concentration of hydrogen and $\rho_{h\lambda} = c_{h\lambda}\,\rho_\lambda$ denotes its density. For a given quantity X, the apparent value (per unit volume of the entire porous medium) is denoted X^α with $X^\alpha = n_\alpha\,X_\alpha$, where X_α is per unit volume occupied by the α–phase.

The rock salt interstitial brine density is characterized by four state variables which are the brine pressure p_λ, its temperature T, the hydrogen concentration $c_{h\lambda}$, and the salt concentration. In this study, the interstitial brine is assumed saturated with salt at any time. Besides the mass of the dissolved hydrogen is assumed very minor to affect the brine density. Therefore, the mass balance equations of the

components b (brine) and h (hydrogen) of the liquid phase can be written in the following form [37–39],

$$\begin{aligned} &\dot{m}_b^\lambda + \nabla[\rho_\lambda(1-c_{h\lambda})\boldsymbol{v}_\lambda - \rho_\lambda \boldsymbol{\mathcal{J}}_{h\lambda}] = \pi_b,\\ &\dot{m}_h^\lambda + \dot{m}^\gamma + \nabla[\rho_\lambda(c_{h\lambda}\boldsymbol{v}_\lambda + \boldsymbol{\mathcal{J}}_{h\lambda}) + \rho_\gamma \boldsymbol{v}_\gamma] = \pi_h,\\ &\text{with} \quad m^\alpha = nS_\alpha\rho_\alpha \quad \text{for} \quad \alpha\in\{\lambda,\gamma\},\\ &m_b^\lambda = (1-c_{h\lambda})\,m^\lambda, \quad \text{and} \quad m_h^\lambda = c_{h\lambda}\,m^\lambda, \end{aligned} \tag{2}$$

where ρ_α is the density of the α–phase, $\boldsymbol{v}_\alpha$ (m/s) is the filtration velocity of the α–phase, $\boldsymbol{\mathcal{J}}_{h\lambda}$ (m/s) is the Fickian diffusion of hydrogen in the liquid phase λ, π_b and π_h (kg/m^3/s) are the total mass creation terms of the two components in the fluid phase. If heat convection in the rock salt domain is neglected, the following energy equation can be used to describe heat transfer within the rock salt domain due to cycling in the cavern,

$$\begin{aligned} &m\,C_p\,\dot{T} + \nabla\boldsymbol{\psi} = 0,\\ &\text{with,} \quad m\,C_p = \sum_\alpha m^\alpha C_{p\alpha}, \quad \text{and,} \quad \boldsymbol{\psi} = -\underline{\underline{\boldsymbol{\Lambda}}}.\nabla T, \end{aligned} \tag{3}$$

with $\alpha \in\{\lambda,\ \gamma,\ \sigma$ (solid)$\}$, and $\underline{\underline{\boldsymbol{\Lambda}}}$ (W/m/K) is the saturated rock salt domain thermal conductivity tensor. If the thermal conductivities of the three phases are assumed isotropic, the domain thermal conductivity Λ is expressed by the geometric mean of the phases thermal conductivities [40],

$$\Lambda = \Lambda_\sigma^{n_\sigma}\,\Lambda_\lambda^{n_\lambda}\,\Lambda_\gamma^{n_\gamma}. \tag{4}$$

In a two–phase percolation flow, the liquid saturation degree S_λ can be calculated using the *van Genuchten* [41] expression,

$$\widetilde{S}_\lambda = \frac{S_\lambda - S_{\lambda r}}{S_{\lambda s} - S_{\lambda r}} = \left(1 + \left(\frac{p_c}{P_r}\right)^{1/(1-\ell)}\right)^{-\ell}, \tag{5}$$

where $p_c = p_\gamma - p_\lambda$ is the capillary pressure, $\widetilde{S}_\lambda$ is the effective degree of saturation, the parameters $S_{\lambda r}$ and $S_{\lambda s}$ represent the liquid residual and maximum saturation values respectively ($S_\lambda\in[S_{\lambda r} - S_{\lambda s}]$), ℓ and P_r (Pa) are model parameters. The equation does not introduce the notion of an entry pressure as it will be neglected in this research.

The hydraulic problem (Eq. (2)) needs to be completed with constitutive and state laws. The filtration velocity vectors are assumed to follow a Darcian flow nature,

$$\boldsymbol{v}_\alpha = -\frac{k_{r\alpha}}{\mu_\alpha}\,\underline{\underline{\boldsymbol{k}}}.(\nabla p_\alpha - \rho_\alpha \boldsymbol{g}), \quad \text{for} \quad \alpha\in\{\lambda,\gamma\}, \tag{6}$$

where $\underline{\underline{\boldsymbol{k}}}$ (m^2) is the intrinsic permeability tensor, μ_α (Pa s) is the dynamic viscosity of the α–phase, $\boldsymbol{g}$ (m/s^2) is the gravitational acceleration vector, and $k_{r\alpha}$ is the relative permeability of the α–phase. Relative permeabilities can be calculated using the Mualem–van Genuchten model [42],

$$k_{r\lambda} = \sqrt{\widetilde{S}_\lambda}\left[1 - \left(1 - \widetilde{S}_\lambda^{1/\ell}\right)^\ell\right]^2, \quad \text{and} \quad k_{r\gamma} = \sqrt{1-\widetilde{S}_\lambda}\left(1 - \widetilde{S}_\lambda^{1/\ell}\right)^{2\ell}. \tag{7}$$

The diffusion vector of hydrogen in the liquid phase is related to the concentration gradient through the Fick's law,

$$\boldsymbol{\mathcal{J}}_{h\lambda} = -\underline{\underline{\boldsymbol{D}}}_{h\lambda}.\nabla c_{h\lambda} = c_{h\lambda}(\boldsymbol{v}_{h\lambda} - \boldsymbol{v}_\lambda), \tag{8}$$

where $\underline{\underline{\boldsymbol{D}}}_{h\lambda}$ (m^2/s) and $\boldsymbol{v}_{h\lambda}$ (m/s) are the diffusivity coefficient tensor and the diffusive velocity of hydrogen in the λ–phase respectively. This coefficient can be determined experimentally for a given component, a phase, and a porous medium [43], or empirically from the plain diffusivity in the liquid phase ($\overline{D}_{h\lambda}$) modified by the characteristics of the porous network (porosity, tortuosity, and constrictivity). A commonly used expression is $D_{h\lambda} = \overline{D}_{h\lambda}\,n^q$, where q is an empirical parameter that generally lies between 1.8 and 2.4 [21]. The exchanged hydrogen mass rate between the cavern and the surrounding rock salt can, therefore, be calculated as,

$$\Im = \underbrace{\int_S \rho_\gamma\,\boldsymbol{v}_\gamma.\boldsymbol{n}\,d\mathcal{A}}_{\text{Percolated mass rate}} + \underbrace{\int_S \rho_\lambda(\boldsymbol{\mathcal{J}}_{h\lambda} + c_{h\lambda}\,\boldsymbol{v}_\lambda).\boldsymbol{n}\,d\mathcal{A}}_{\text{Diffused mass rate}}, \tag{9}$$

with $\boldsymbol{n}$ being the outward unit vector normal to the cavern surface.

The hydrogen phase is assumed to behave as a real gas (see Appendix A). The state equation is described using the two state functions; the density $\rho_\gamma(p_\gamma,\ T_\gamma)$, and the heat capacity $C_{p\gamma}(T_\gamma)$ at a given pressure. The thermodynamic variables are related to each other through the formula $p_\gamma = \rho_\gamma\,T_\gamma\,Z$, with Z (J/kg/K) being the gas compressibility factor. The chemical potential equality between the λ– and γ–phases leads to the definition of the Henry's law $p_\gamma = (K_H/M_h)\rho_{h\lambda} = Hc_{h\lambda}$, with K_H (L Pa/mol) being the Henry's constant, M_h (kg/mol) the hydrogen molecular weight, and $H = K_H\,\rho_\lambda/M_h$ (Pa). The brine phase is assumed to be slightly compressible, i.e. $\dot{\rho}_\lambda/\rho_\lambda = \chi_{T\lambda}\,\dot{p}_\lambda - \chi_{p\lambda}\,\dot{T}$ with $\chi_{T\lambda}$ (1/Pa) and $\chi_{p\lambda}$ (1/K) being the isochoric compressibility and the isobaric thermal expansion coefficient respectively.

Saturated/unsaturated state transition

The set of differential equations and primary variables (Eq. (2)) needs to be controlled to assure the transition from fully saturated state to unsaturated state, or vice versa. In this paper, we only consider the problem of hydrogen appearance in rock salt where the brine phase is always present. The modeling approach of *Mahjoub* et al. [38] is proposed. It consists of using the dissolution and diffusion phenomena to derive a set of differential equations applicable for both saturated and unsaturated states.

The choice of the primary variables is crucial. The pressure p_λ can be chosen as the first primary variable because the brine phase is assumed present at any time. With regard to the second unknown, due to dissolution and diffusion phenomena, the mass concentration $c_{h\lambda}$ is a permanent unknown, whether the medium is saturated or unsaturated. Thus, it is chosen as the second primary variable. However, to assure the homogeneity in the primary variables, a pseudo–hydrogen pressure is defined as $\widetilde{p}_\gamma = Hc_{h\lambda}$. It represents the real hydrogen pressure only when the hydrogen phase is present ($\widetilde{p}_\gamma = p_\gamma$ if $S_\lambda < 1$), and it is just a definition in the saturated case. To use the same equations in the saturated case, a new

pseudo–capillary pressure is introduced $\tilde{p}_c = \tilde{p}_\gamma - p_\lambda$. The saturation degree is expressed as a function of this pseudo–capillary pressure such that $S_\lambda(\tilde{p}_c) = S_\lambda(p_c)$ when $\tilde{p}_c \geq 0$ (because $\tilde{p}_c = p_c$), and $S_\lambda(\tilde{p}_c) = 1$ when $\tilde{p}_c < 0$.

Taking these definitions into consideration, the γ–Darcy and Fick laws have to be reformulated and integrated into the conservation equations. The same equation for γ–Darcy law (Eq. (6)) can be used after replacing p_γ by $\tilde{p}_\gamma$, with $\rho_\gamma(\tilde{p}_\gamma, T_\gamma)$. In Fick's law (Eq. (8)), $c_{h\lambda}$ is replaced by $\tilde{p}_\gamma/H$, and the variation of H is assumed negligible compared to the variation of $\tilde{p}_\gamma$. The reformulated mass conservation equations can be cast into the following system of coupled partial differential equations,

$$\dot{m}_b^\lambda - \nabla\left(\underline{\underline{\mathfrak{B}}}_{b\lambda}.(\nabla p_\lambda - \rho_\lambda \boldsymbol{g}) + \underline{\underline{\mathfrak{B}}}_{b\gamma}.\nabla\tilde{p}_\gamma\right) = \pi_b,$$

$$\dot{m}_h^\lambda + \dot{m}^\gamma - \nabla\left(\underline{\underline{\mathfrak{B}}}_{h\lambda}.(\nabla p_\lambda - \rho_\lambda \boldsymbol{g}) + \underline{\underline{\mathfrak{B}}}^f_{h\gamma}.\nabla\tilde{p}_\gamma + \underline{\underline{\mathfrak{B}}}^p_{h\gamma}.\left(\nabla\tilde{p}_\gamma - \rho_\gamma \boldsymbol{g}\right)\right) = \pi_h,$$

$$\text{with } \underline{\underline{\mathfrak{B}}}_{b\lambda} = [(1-c_{h\lambda})\rho_\lambda k_{r\lambda}/\mu_\lambda]\underline{\underline{k}},\ \underline{\underline{\mathfrak{B}}}_{b\gamma} = (-\rho_\lambda/H)\underline{\underline{D}}_{h\lambda},$$
$$\underline{\underline{\mathfrak{B}}}_{h\lambda} = (c_{h\lambda}\rho_\lambda k_{r\lambda}/\mu_\lambda)\underline{\underline{k}},\ \underline{\underline{\mathfrak{B}}}^f_{h\gamma} = (\rho_\lambda/H)\underline{\underline{D}}_{h\lambda},\ \text{and},\ \underline{\underline{\mathfrak{B}}}^p_{h\gamma} = (\rho_\gamma k_{r\gamma}/\mu_\gamma)\underline{\underline{k}}. \quad (10)$$

The numerical model

The numerical model represents a spherical cavern of volume $\mathcal{V} = 300,000\ m^3$ in a surrounding rock domain. The well extends from the surface at z = 0 m to the cavern top at $z = z_w = -910$ m (Fig. 2(a)). The cavern has been leached (full of brine) and is initially in thermal equilibrium with the surrounding rock domain at $T = 40\ ^\circ C$. The brine pressure within the cavern is also in equilibrium with the rock salt pore pressure at the halmostatic value of $p_\lambda = -\rho_\lambda\ g\ z = 11.2$ MPa. The cavern brine is then replaced by hydrogen during a debrining/filling phase of 90 days where hydrogen pressure of 22 MPa is attained within the cavern. The cavern is later left unsolicited for a similar period of time. Consequently, after 90 days of standstill, the cavern volume averaged temperature and pressure are 46 °C and 22 MPa respectively. Cavern then undergoes seasonal cycling following the program shown in Fig. 2(b) for a 40–year time period, where hydrogen is injected at $T_\gamma^{inj} = 40\ ^\circ C$.

Fig. 2(b) shows the cycling scheme that will be considered in our simulations in terms of relative mass change $\tilde{\mathcal{M}} = (\mathcal{M}/\mathcal{M}(0) - 1) \times 100\%$. The program starts with a withdrawal phase of 60 days, cycling then begins where each cycle extends over a 6–month period. Only the first two cycles are shown, however, simulations are conducted for a 40–year time period, i.e. 80 cycles.

Since there are no available COMSOL modules that couples computational fluid dynamics with the two–phase percolation and diffusion in porous media, the available general forms of the coefficient Partial Differential Equations (cPDE), of the domain Ordinary Differential Equations (dODE), and of the boundary Ordinary Differential Equations (bODE), are used to solve our systems of equations in a coupled thermo–hydraulic framework. COMSOL gives analytical expressions to track the evolution of the hydrogen viscosity μ_γ, thermal conductivity Λ_γ, and heat capacity $C_{p\gamma}$ as functions of temperature (see Appendix B). Other van Genuchten, thermal, and hydraulic parameters are detailed in Table 1.

Parametric study

Due to the lack of any experimental data treating hydrogen invasion into the rock salt, this parametric study is presented before performing simulations on the cavern scale. The objective of this section is to investigate the effect of the van Genuchten parameter (P_r) and the hydrogen–brine diffusion coefficient ($\overline{D}_{h\lambda}$) on the percolation–diffusion phenomenon. The chosen van Genuchten parameter and diffusion coefficient values will then be used in a real–scale cavern simulations, and while assuming a pessimistic or an overestimating scenario with regard to the total mass of lost hydrogen. To simplify the calculations, this study is performed for a one–dimensional axisymmetric transient boundary value problem (Fig. 3(a)).

Initial and boundary conditions are set similar to the working conditions of the spherical cavern (Fig. 2(a)). Hydrogen concentration is initially neglected in the rock domain ($c_{h\lambda} = 0$). Consequently, the initial rock salt pseudo–hydrogen pressure is assumed equal to zero ($\tilde{p}_{\gamma 0} = 0$). The initial rock salt interstitial brine pressure is set equal to the halmostatic value $p_{\lambda 0} = 11.2$ MPa. The cavern (injection point) is initially assumed in thermal equilibrium with the surrounding rock domain at $T = 40\ ^\circ C$. The cavern is filled gradually with hydrogen during a 90–day time period, where the cavern pressure is increased from halmostatic to ~16 MPa (around the maximum cycling value of the real cavern (Fig. 9(a)). Injection then stops and hydrogen is left to diffuse and/or percolate into the rock domain. Fig. 3(b, c) show the hydrogen pressure and temperature within the cavern during a 5–year time period.

During filling, the cavern averaged temperature increases from 40 °C to ~46.2 °C. Heat exchange with the colder surrounding rock salt is observed in Fig. 3(c) during 5 years. To simulate the two–phase hydrogen percolation into the rock salt, the van Genuchten parameter $\ell = 0.5$ is used as cited in a few articles for rock salt [47]. Similar works have used a van Genuchten parameter $P_r \in [10–15]$ MPa for air and nitrogen percolations in concrete, granite, or crushed rock salt [38,47,50]. For this study, simulations are performed for $P_r = 8$ and 15 MPa. The residual saturation $S_{\lambda r} = 0.15$ is used as in *Mahjoub* et al. [38] and *Poppei* et al. [47]. The possibility to have a fully brine saturated state is taken into consideration by setting $S_{\lambda s} = 1$. To investigate the effect of Fickian diffusion on the total hydrogen mass lost into the rock salt, a wide range (3 orders of magnitude) of diffusion coefficient is considered, i.e. $\overline{D}_{h\lambda} = 5 \times 10^{-7}$ or $5 \times 10^{-10}\ m^2/s$. Consequently, four simulations are performed: for $P_r = 8$ MPa and $\overline{D}_{h\lambda} = 5 \times 10^{-7}$ or $5 \times 10^{-10}\ m^2/s$; and for $P_r = 15$ MPa and $\overline{D}_{h\lambda} = 5 \times 10^{-7}$ or $5 \times 10^{-10}\ m^2/s$. Results are simultaneously correlated and analyzed.

Fig. 4(a) shows the brine saturation evolution as function of the capillary pressure for the two values of the van Genuchten

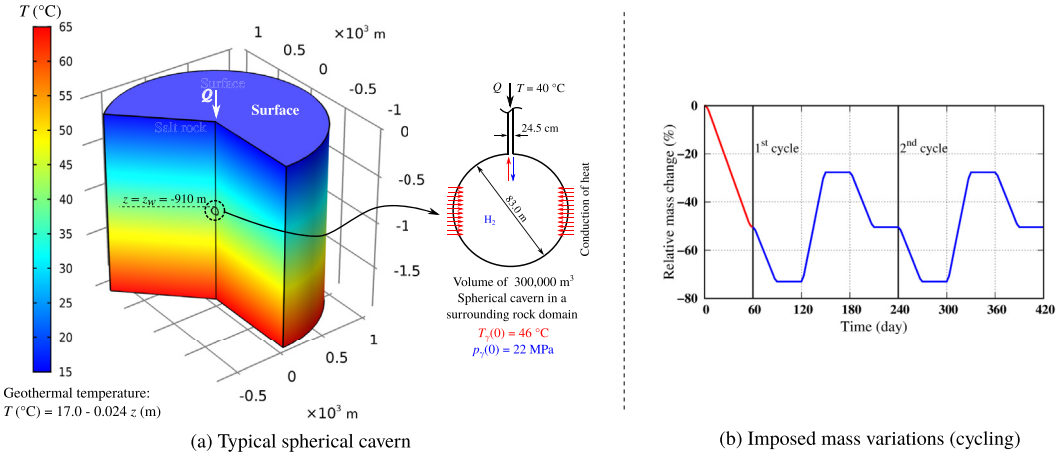

(a) Typical spherical cavern (b) Imposed mass variations (cycling)

Fig. 2 – (a) Schematic diagram of the boundary value problem: it represents a spherical cavern created at 910 m depth in a surrounding rock salt domain. The cavern has been filled with hydrogen during a 90–day time period, and then left unsolicited for an equivalent period of time. This has led to a cavern volume averaged temperature and pressure of 46 °C and 22 MPa respectively. (b) Imposed cavern relative mass variations; only the first two cycles are shown.

parameter P_r. It is obvious that a tremendous cavern pressure is needed for hydrogen to invade the rock salt in a pure or even a semi–pure nature ($S_\lambda < 0.15$). For typical working conditions of our typical spherical cavern, capillary pressure ranges between 0 and ~4 MPa. Consequently, hydrogen saturation in the pore brine is expected to be very low (<0.05), i.e. $S_\lambda > 0.95$. It is also observed that a lower value of the parameter P_r allows for a more significant percolation of hydrogen for the same capillary pressure.

Fig. 5 shows the rock salt radial profiles of pseudo–hydrogen pressure, of brine pore pressure, and of temperature for the transient boundary value problem of Fig. 3(a). Hydrogen exists only in the domain where the pseudo–pressure is grater than zero ($S_\lambda < 1$). It is observed that the rock domain temperature is minimally affected by the choice of the diffusion coefficient and the van Genuchten parameter P_r (Fig. 5(c, f)). Fig. 5(b, e) show that the rock salt brine pressure is also independent of the value of the diffusion coefficient. However, the van Genuchten definition (Eq. (5)) necessitates that the brine pore pressure be dependent of the parameter P_r. Comparing Fig. 5(a, d) demonstrates that the percolation is slightly affected by the value of the diffusion coefficient. For instance, for both values of $\overline{D}_{h\lambda}$, hydrogen percolates to a distance of almost ~1.3 m after 5 years. However, when the diffusion coefficient value is significant, percolation continues to show a diffusive nature where the affected domain could reach a distance of ~3 m after 5 years. Before percolation takes place (t < 89 days (Fig. 6(a)), the

Table 1 – Hydraulic, thermal, and van Genuchten parameters to model hydrogen invasion into the rock salt.

Interpretation	Parameter (unit)	Value	Reference
Rock salt permeability	k (m^2)	1×10^{-20}	[44,45]
Rock salt porosity	n	0.01	[44,45]
Brine density	ρ_λ (kg/m^3)	1200	[28]
Brine isochoric compressibility	$\chi_{T\lambda}$ (1/Pa)	46×10^{-11}	[28]
Brine isobaric expansivity	$\chi_{p\lambda}$ (1/K)	45×10^{-5}	[28]
Brine dynamic viscosity	μ_λ (Pa s)	1.32×10^{-3}	[28]
Brine thermal conductivity	Λ_λ (W/m/K)	0.51	[28]
Brine heat capacity	$C_{p\lambda}$ (J/kg/K)	3300	[28]
Rock salt pore pressure	p_λ (Pa)	$-\rho_\lambda\, g\, z$	Overestimating Study
Rock salt density	ρ_σ (kg/m^3)	2200	[46]
Rock salt thermal conductivity	Λ_σ (W/m/K)	6	[46]
Rock salt heat capacity	$C_{p\sigma}$ (J/kg/K)	900	[46]
Maximum brine saturation	$S_{\lambda s}$	1.0	Assumed
Residual brine saturation	$S_{\lambda r}$	0.15	[38]
van Genuchten parameter	P_r (Pa)	8×10^6 or 15×10^6	Parametric study
van Genuchten parameter	ℓ	0.5	[47]
Mass creation terms	π_b and π_h (kg/m^3/s)	0	Assumed
Hydrogen mass concentration	$c_{h\lambda}$	$\widetilde{p}_\gamma/H$	Definition
Hydrogen diffusion in brine	$\overline{D}_{h\lambda}$ (m^2/s)	5×10^{-7} or 5×10^{-10}	Parametric study
Diffusion correction parameter	q	2.1	[21]
Henry's constant hydrogen–brine	K_H (L atm/mol)	1300	[48,49]

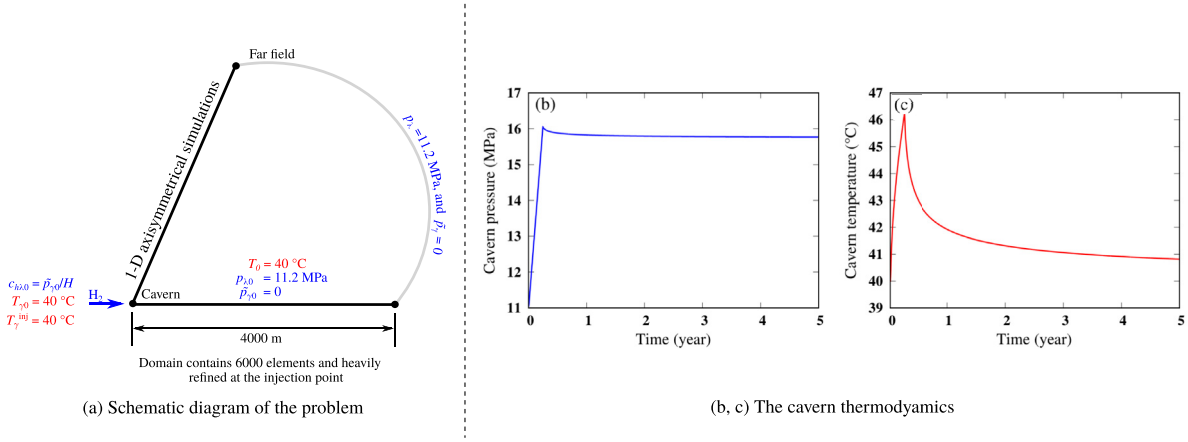

Fig. 3 – (a) Schematic diagram representing the transient boundary value problem to perform the parametric study of hydrogen invasion into saturated rock salt. The cavern volume averaged (b) pressure, and (c) temperature. Injection continues through 90 days, it then stops allowing for heat transfer and hydrogen mass exchange with the rock salt.

chosen value of P_r has no effect on the hydrogen pressure profiles in the rock domain (see the black curves in Fig. 5(a, d)). As expected, it is seen that smaller values of the parameter P_r allow for more percolation of hydrogen (compare red and blue curves of Fig. 5(a, d)).

Fig. 6 shows the histories of the brine saturation at the cavern wall, of the percolated and of the Fickian diffused hydrogen masses into the rock salt domain. The exchanged masses are calculated by integrating Eq. (9) over time and over a surface equivalent to that of the cavern in Fig. 2(a).

Fig. 6(a) shows that the two–phase percolation starts after almost ~89 days. Due to the low capillary pressure, i.e. $p_c \in$ [2-3] MPa, the brine saturation is very slightly altered (minimum of ~0.985). Fig. 6(b) shows the hydrogen mass percolated into the rock salt domain. Obviously, a more significant diffusion coefficient and a smaller P_r value allow for a more percolated mass into the rock salt, which translates into a lesser brine saturation. Unlike percolation, hydrogen starts to diffuse into the rock salt domain as soon as a hydrogen pressure gradient is established between the cavern and the rock domain (Fig. 6(c)). It is also noticed that the Fickian diffusion is significant before percolation. However, as soon as percolation starts, hydrogen replaces brine by a certain saturation which creates two phases, and the Fickian diffusion rate becomes very slow. One can also see that hydrogen diffuses more for a greater value of the parameter P_r. Actually, a larger P_r indicates a less percolation which promotes the Fickian diffusion. This remark is strengthened by noticing that the deviation of the black curves of Fig. 6(c) takes place instantly with percolation, i.e. $t \approx 89$ days. This conclusion is less obvious when the diffusion coefficient is very low (blue curves of Fig. 6(c)).

Though a value of $\ell = 0.5$ has been used in literature for two–phase flow in rock salt, it is intriguing to investigate the effect of this parameter on the percolation and diffusion of hydrogen. Henceforth, for $P_r = 8$ MPa, Fig. 4(b) shows the brine saturation as function of the parameter ℓ. It is conceivable and expected that the percolation depends on the value of ℓ, however, this dependency becomes less significant for a quite low hydrogen saturation, i.e. $S_\lambda \approx 0.98$ (see the zoom–in of Fig. 4(b)). When ℓ approaches 0.9, the capillary pressure exceeds 4 MPa, which is translated into no percolation at all for the working and boundary conditions of this one–dimensional problem (Fig. 7(a)).

Fig. 7 shows the percolated and diffused hydrogen masses for $P_r = 8$ MPa, $\overline{D}_{h\lambda} = 5 \times 10^{-7}$ m^2/s, and $\ell = \{0.1, 0.5, 0.9\}$.

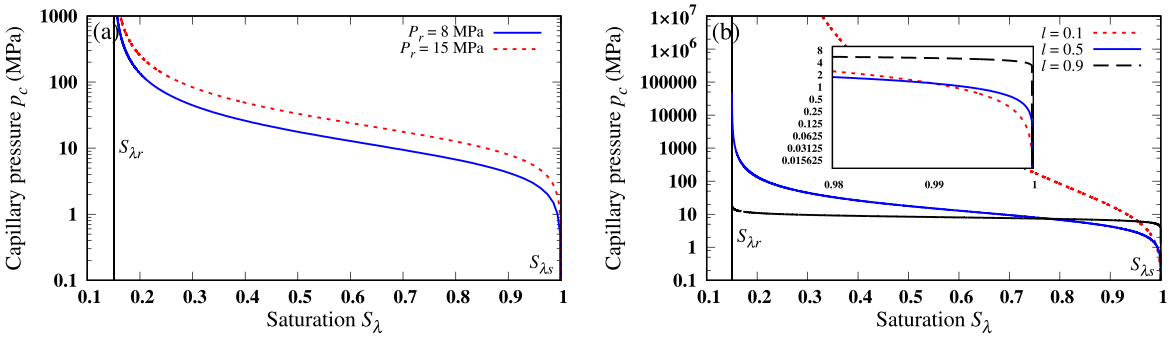

Fig. 4 – Capillary pressure as calculated by the van Genuchten equation (Eq. (5)), (a) for $\ell = 0.5$ and $P_r = \{8, 15\}$ MPa, and (b) for $P_r = 8$ MPa and $\ell = \{0.1, 0.5, 0.9\}$.

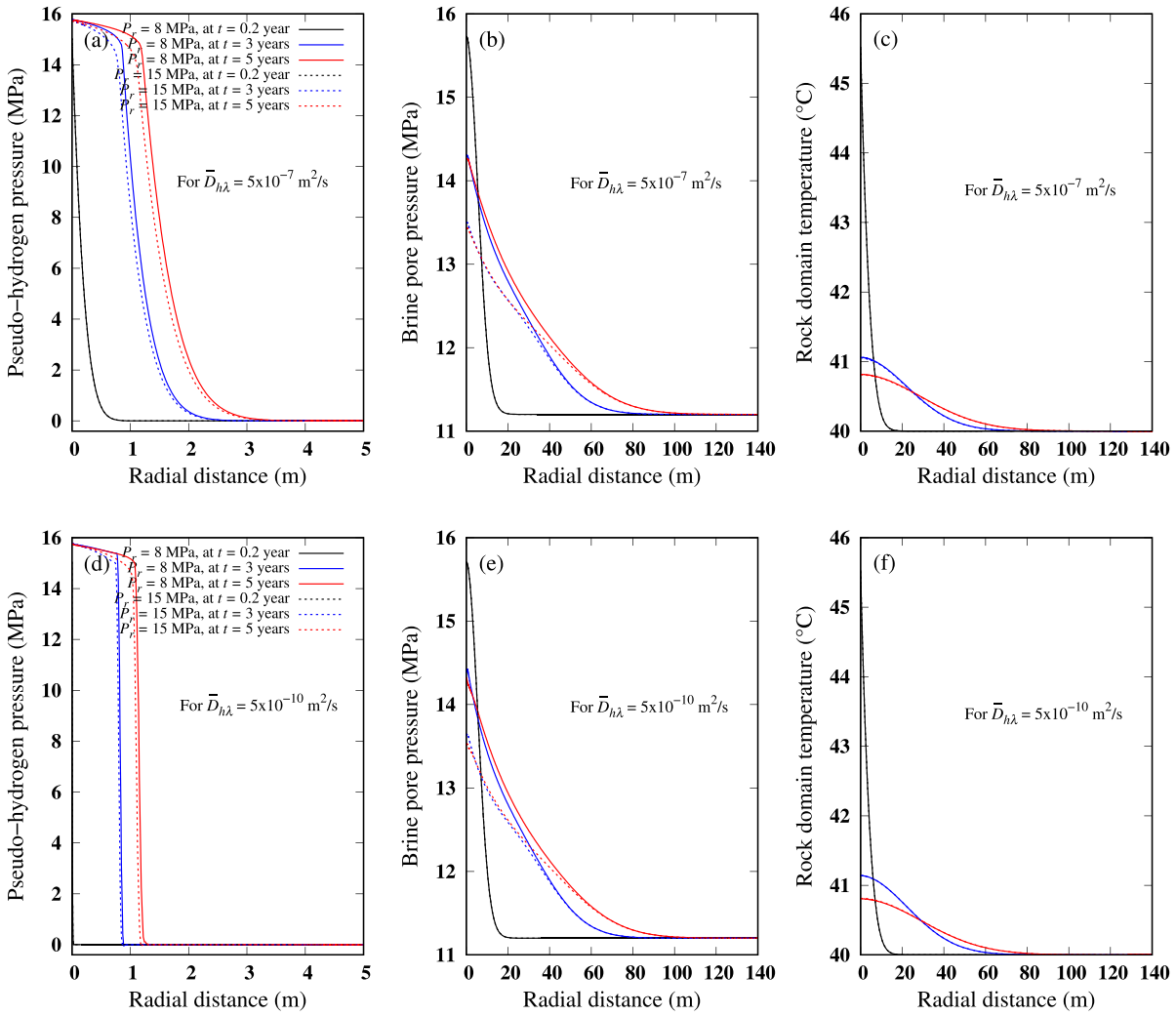

Fig. 5 – (a, d) Pseudo-hydrogen pressure, (b, e) brine pore pressure, and (c, f) rock salt temperature radial profiles at three distinct times of 0.2, 3, and 5 years. These profiles are traced within the rock domain and shown for the four permutations of P_r and $\bar{D}_{h\lambda}$ values.

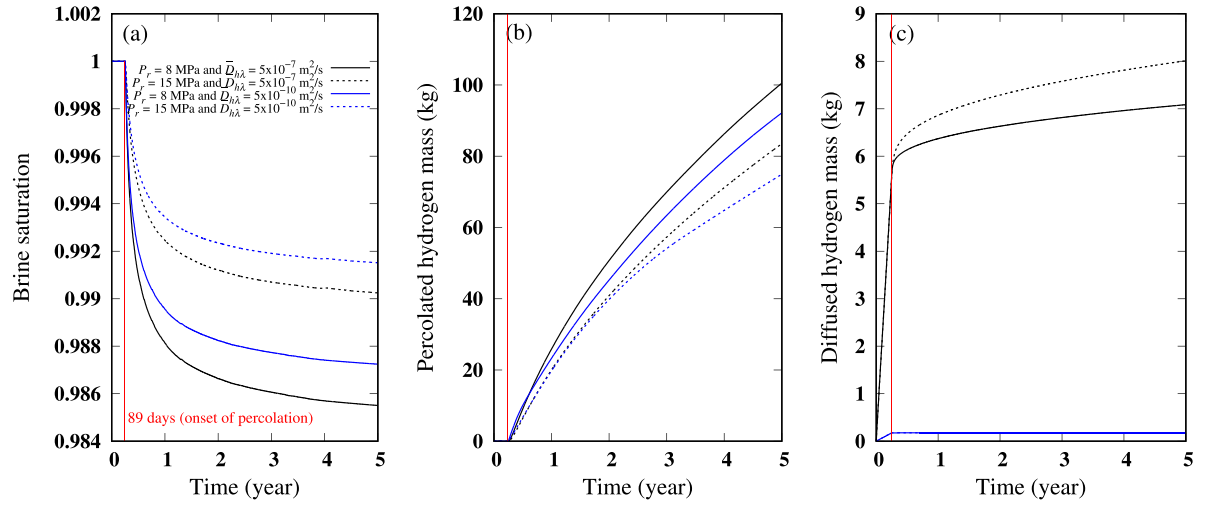

Fig. 6 – (a) Brine saturation history at the cavern wall, (b) two–phase percolated hydrogen mass history, and (c) Fickian diffused hydrogen mass history. Histories are shown for the four permutations of P_r and $\bar{D}_{h\lambda}$ values.

Reducing ℓ to 0.1 increases the percolated mass by 2.65 folds. However, no percolation is observed for $\ell \approx 0.9$.

As expected, when there is no percolation, hydrogen diffuses the most (black curve of Fig. 7(b)). For $\ell = \{0.1, 0.5\}$, Fickian diffusion gets affected by the percolation and its parabolic behavior changes as soon as percolation starts (blue and red curves of Fig. 7(b)). Percolation happens a bit earlier for $\ell = 0.1$, which is attributed to a lower capillary pressure for the same saturation (see the zoom–in of Fig. 4(b) for $S_\lambda \in [0.99–1]$). For the coming stimulations on the cavern scale, we will assume van Genuchten parameters of $P_r = 8$ MPa, of $\ell = 0.5$, and a hydrogen–brine diffusion coefficient of $\overline{D}_{h\lambda} = 5 \times 10^{-7}$ m^2/s.

Cavern–scale cycling simulations

A two–dimensional axisymmetric model was adopted to simulate heat and mass exchange with the surrounding rock domain during hydrogen cycling in the real cavern (Fig. 2(a)). Fig. 8 shows the spatial discretization of the rock domain. The cavern is not discretized since a uniform thermodynamic state is assumed within the cavern. Initial and boundary conditions are displayed on the graph.

Fig. 9(a, b) show the cavern averaged temperature and pressure as function of cycling. Hydrogen pressure is not showing any changes during cycling as the cavern volume is assumed constant. However, temperature is showing some changes due to the energy exchanged with the surrounding rock salt domain.

Fig. 9(c) shows the hydrogen pseudo–capillary pressure averaged over the cavern surface during cycling. The behavior of the capillary pressure becomes almost identical after five cycles. The capillary pressure does not exceed 2 MPa for the working and boundary conditions of this typical spherical cavern.

To study the hydrogen mass exchanged with the rock domain, Fig. 10(a) shows the brine saturation, and Fig. 10(b) shows the radial component of hydrogen filtration velocity averaged over the cavern surface during the first four cycles. Other cycles are not displayed due to similarity and to avoid redundant repetitions.

The debrining and the standstill phases of 180 days (Section The numerical model) have led the brine saturation at the cavern wall to decrease to ~0.981 before any cycling (Fig. 10(a)). The subsequent withdrawal has counteracted this reduction in the brine saturation by allowing the percolated hydrogen to leave back to the cavern volume, and again a full brine saturation is reached. Furthermore, hydrogen would percolate into and leave from the rock domain as a function of the cavern hydrogen pressure (Fig. 10(b)). This allows for a reduction in the brine saturation at the cavern wall before it sustains the full saturation state (Figs. 10(a) and 11(a)).

The Fickian diffusive velocity resembles the brine filtration velocity (Fig. 10(c, d)). Depending on the direction of hydrogen pressure gradient, hydrogen may diffuse into the rock domain, or pour down the cavern wall along with the leaving brine. The surface averaged radial component of the brine filtration velocity is show in Fig. 10(d). It is observed that brine moves into the cavern volume when the percolated hydrogen leaves the rock domain and vice versa. Besides, the thermal effects are noticed on the behavior of the brine filtration and the Fickian diffusive velocities due to the hydro–thermal coupling, especially during the standstill phases.

To understand how the rock domain interstitial brine gets drained by the invading hydrogen, Fig. 11(a) shows the time variations of the brine saturation and the pseudo–capillary pressure at the cavern wall for the first four cycles. One can see that hydrogen percolates into the rock domain when the capillary pressure is positive. Besides, the hydrogen saturation rate (increasing or decreasing) has the same sign as the capillary pressure rate.

To study the zone disturbed by brine pore pressure changes, hydrogen pseudo–pressure and temperature fluctuations, Fig. 11(b) shows the radial profiles of these variables at the end of cycling, i.e. 40 years. The altered zone due to hydrogen invasion into the rock domain has not exceeded ~15 m after 40 years of seasonal cycling. However, this zone extends to ~40 m due to brine pore pressure and rock domain

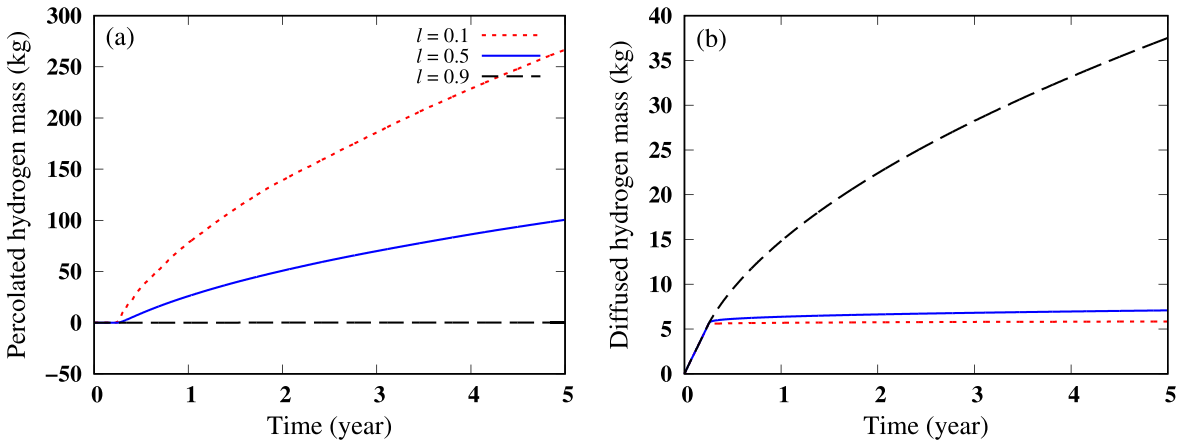

Fig. 7 – (a) Percolated and (b) diffused hydrogen masses through 5 years for $P_r = 8$ MPa, $\overline{D}_{h\lambda} = 5 \times 10^{-7}$ m^2/s, and $\ell = \{0.1, 0.5, 0.9\}$.

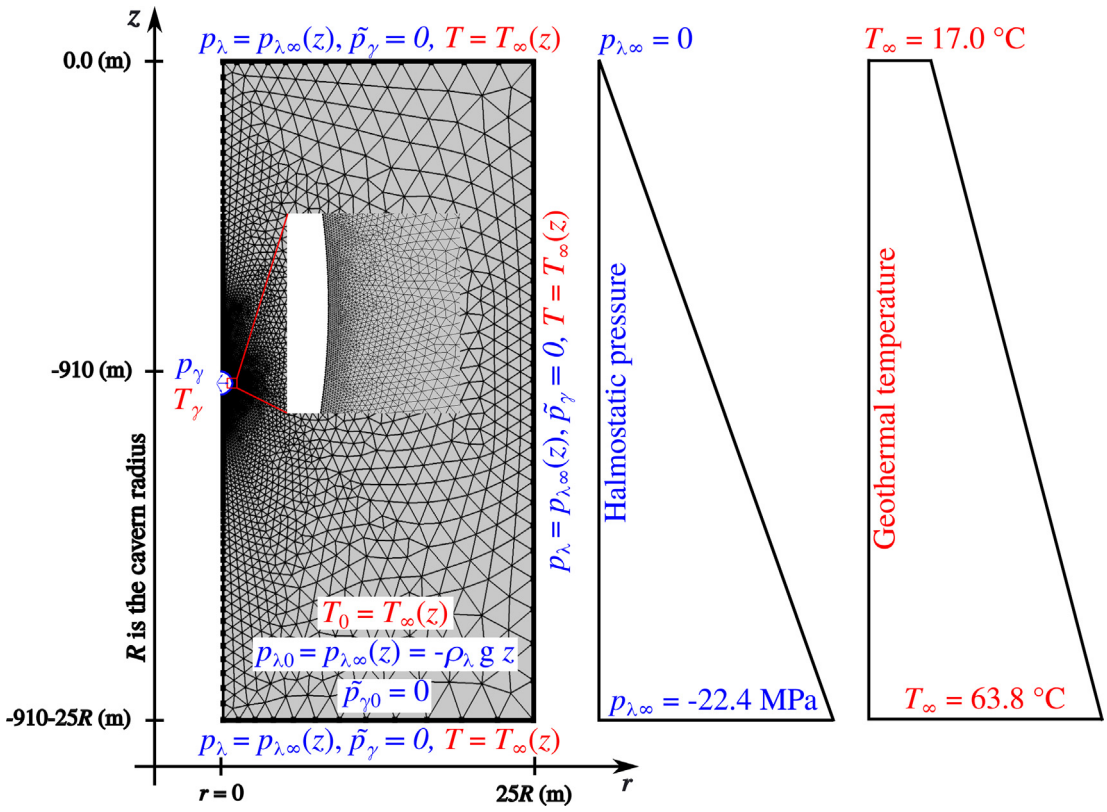

Fig. 8 – A two–dimensional axisymmetric discretization of the boundary value problem of Fig. 2(a). A surrounding rock volume of 25R is chosen around the cavern to avoid the effect of far–field boundaries. Mesh is considerably refined close to the cavern wall to account for abrupt changes/large gradients. Mesh contains 160,113 triangular elements.

temperature changes. Knowing the range of these distances helps design a network of underground caverns while avoiding harmful interactions.

Fig. 12 shows the hydrogen mass exchanged with the surrounding rock domain due to two–phase percolation and the Fickian diffusion. Fig. 12(a) is a zoom–in of Fig. 12(b) for the first four cycles/800 days.

Both the percolated and diffused hydrogen masses tend to reduce during withdrawal in accordance with Fig. 10(b, c). Even–though the Fickian diffused mass is initially smaller than the percolated mass, after ~25 years of cycling, the diffused mass becomes more significant than the two–phase percolated mass (Fig. 12(b)). Eventually, the percolated and the diffused hydrogen masses summed up to ~93 kg after 40 years of the cavern operation.

Discussion

For a P_r range that resembles the hydrogen invasion into the rock salt, Section Parametric study has shown that the Darcian percolation has a slight dependency on the value of P_r.

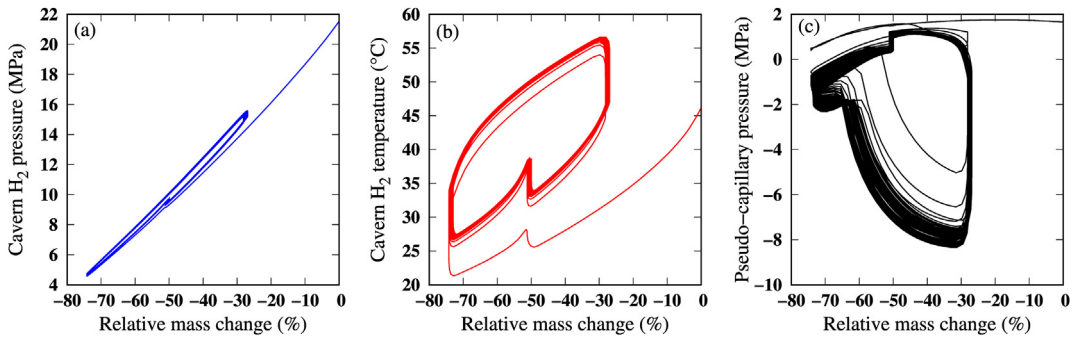

Fig. 9 – (a) cavern average pressure, (b) cavern average temperature, and (c) hydrogen pseudo–capillary pressure averaged over the cavern surface. The three quantities are presented as function of cycling/relative mass changes within the cavern.

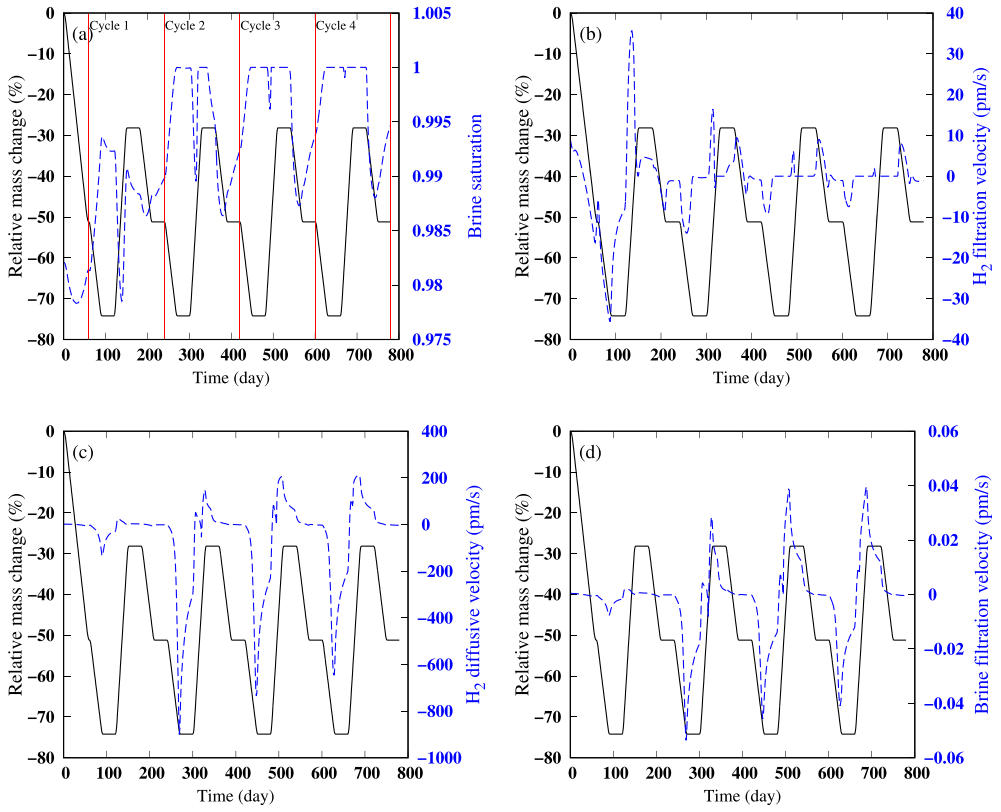

Fig. 10 – (a) Brine saturation at the cavern wall, as well as the surface averaged radial components of (b) the hydrogen filtration velocity, (c) the Fickian diffusive velocity, and (d) the brine filtration velocity during the first four cycles.

The parameter ℓ has been assigned a value of 0.5 for rock salt in a few research papers. However, possible high values ($\ell \sim 0.9$) can increase considerably the capillary pressure at full brine saturation leading to a naught percolation. A value of $\ell = 0.1$, close to the lowest limit, has increased the hydrogen mass percolated into the rock salt domain by 3 folds (Fig. 7(b)).

The value of the diffusion coefficient $\overline{D}_{h\lambda}$ does not affect directly the Darcian percolation, but rather its diffusive nature. Percolation becomes more of a piston–like for very small values. Consequently, hydrogen mass lost due to percolation differed a little bit depending on the diffusion coefficient value (Fig. 6(b)). However, it is natural that the hydrogen mass lost due to Fickian diffusion is almost 50 times larger for a 3–order of magnitude higher diffusion coefficient (Fig. 6(c)).

The simulations on the cavern scale have been performed such that an overestimating/a pessimistic scenario of lost hydrogen is considered. Therefore, while setting $\ell = 0.5$, values of $P_r = 8$ MPa and $\overline{D}_{h\lambda} = 5 \times 10^{-7}$ m^2/s have been chosen. Cycling simulations prove that percolation happens mostly when the cavern pressure is close to the maximum cycling value, i.e. $p_\gamma \approx 16$ MPa. Yet, depending on the sign of the pressure gradient, hydrogen may percolate into/leave from the rock domain. The Fickian diffusion resembles the brine filtration, following the pressure gradient direction,

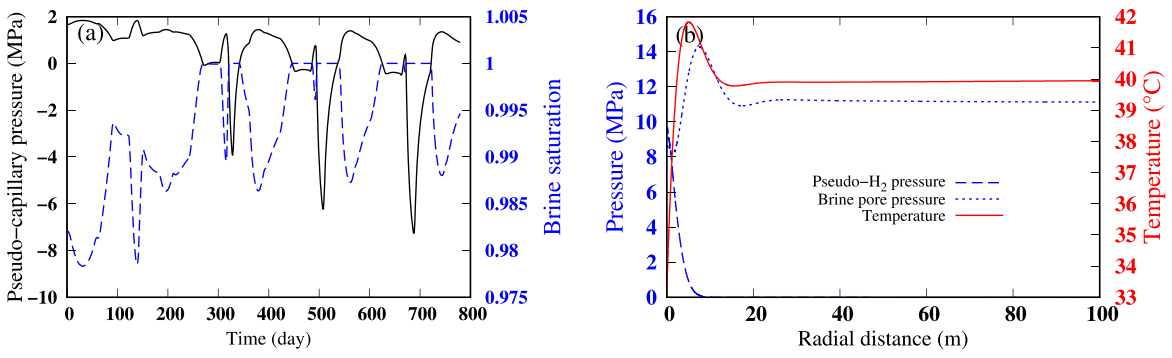

Fig. 11 – (a) Time variations of the cavern surface averaged brine saturation and pseudo–capillary pressure for the first four cycles. (b) Radial profiles of interstitial brine pressure, of hydrogen pseudo–pressure, and of temperature within the rock domain at the end of cycling/at 40 years.

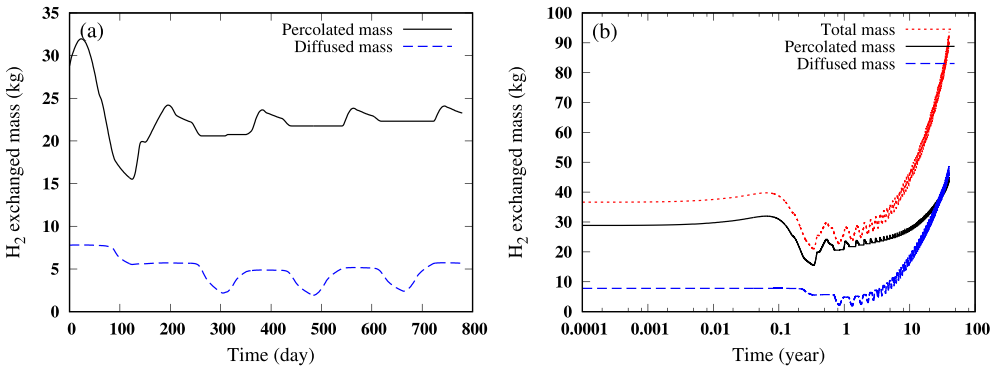

Fig. 12 – Darcian percolated and Fickian diffused hydrogen masses during 40 years of cycling. Figure (a) is a zoom–in of figure (b) for the first four years. The debrining and the standstill phases of 180 days (Section The numerical model) have led to the initial percolated and diffused masses observed in figure (a).

hydrogen tends to diffuse into the rock domain or pours down the cavern wall along with the leaving brine. Eventually, the total mass of lost hydrogen sums up to ~93 kg. This mass is extremely negligible compared to the hydrogen mass manipulated during one cycle ($\mathcal{M} = 2.05$ Mkg), i.e. the percentage of the lost mass to one cycle mass is ~ 0.005%.

Though a wide range of model parameters is studied, our research rests limited to its numerical nature. A laboratory validation is needed. We assume a homogeneous rock salt all around the spherical cavern. However, rock salt can be widely heterogeneous. Besides, this research does not introduce any permeable interlayers, nor does it account for damaged zones. The implementation of heterogeneities in rock salt, whether in the mechanical or the hydraulic properties, affects the transported/exchanged quantity of hydrogen. This effect can be direct as in the case of increased permeability, or indirect as in the case of weaker or more damageable rock salt.

The available research concerning gas migration in rock salt promotes the results found in our research. For instance *Jockwer and Wieczorek* [52] have stated that the presence of a damaged zone (DRZ) is the main factor for gas transport in rock salt. They conducted experiments and simulations concerning helium, neon, and butane. They found that the diffusion coefficient of these gases increased by two orders of magnitude in the DRZ. Out of the DRZ, the measured permeabilities were in the order of 10^{-19} and 10^{-20} m^2, and the pseudo gas pressure slightly penetrated the rock salt in a two–phase piston–like flow (compare to Fig. 5(d)). *Senger* et al. [50] studied gas (particularly air) migration in concrete. They have found that the gas penetrated distances were limited to 1.5 m after 4 years of injection (compare to Fig. 5(a, d)). The two–phase gas saturation depended on the permeabilities, yet it was less than 0.1 for permeabilities in the order of 10^{-19} m^2. Generally, the existed literature already confirms that permeable interlayers are the main transport conduits around salt caverns [10,11].

Conclusion and perspectives

In general, for an overly assumed diffusion of hydrogen in brine ($\overline{D}_{h\lambda} = 5 \times 10^{-7}$ m^2/s) [51], a null pressure entry, and overestimating van Genuchten parameters, the hydrogen mass lost to the rock domain remains very negligible. Yet, increasing energy demands necessitate fast utilization of underground caverns. The severe utilization of salt caverns exposes them to considerable pressure and temperature changes throughout short periods, which may affect the development of the damaged zones. The introduction of a damaged zone, during cycling and at the end of leaching, can affect the total mass of the lost hydrogen. Future studies will include, in a first step, laboratory work to develop mass transport laws that would describe precisely hydrogen migration into the rock salt. In a second step, constitutive laws that quantify the permeability and porosity evolutions of rock salt due to mechanical, hydraulic and thermal charges would be needed. Once these transport and constitutive laws are developed, they can be integrated in our current frame work to estimate their effect on hydrogen percolation and diffusion during rock salt damaging/severe exploitation of caverns.

Though our simulations have demonstrated that cycling reduces the total amount of transported hydrogen (Fig. 12(b)), the role of heterogeneities, whether mechanical or hydraulic, needs also to be investigated in a future research. Moreover, in a laboratory hydrogen storage model, we are currently investigating the importance of other fluxes, F_2, F_3, and F_1 of Fig. 1; F_1 is expected to have an impact on the hydrogen thermodynamic behavior. Once these fluxes are quantified, their payoffs should be compared and/or added to the flux F_4, presented in this research, to draw a general conclusion about the hydrogen–tightness of salt caverns.

Declaration of competing interest

The authors declare that they have no known competing financial interests or personal relationships that could have appeared to influence the work reported in this paper.

Acknowledgment

Authors would like to thank Géodénergies and the French Association Nationale de Recherche (ANR) for their financial support via the two projects: ROSTOCK–H; and STOPIL–H.

Appendix A. Real hydrogen state law

A real gas behavior is assumed in our simulations of hydrogen storage and migration into the rock salt. The hydrogen state equation can be completely described using two state functions; the mass density $\rho_\gamma(p_\gamma, T_\gamma)$, and the heat capacity $C_{p_\gamma}(T_\gamma)$ at a given pressure [36]. The thermodynamic variables are related to each other through the formula,

$$\rho_\gamma = \frac{p_\gamma}{T_\gamma Z}, \tag{A.1}$$

with Z being the hydrogen compressibility factor. Eq. A.1 can be written in a derivative form as,

$$\frac{d\rho_\gamma}{\rho_\gamma} = \chi_{T_\gamma}\, dp_\gamma - \chi_{p_\gamma}\, dT_\gamma, \tag{A.2}$$

with χ_{T_γ} being the hydrogen isochoric compressibility and χ_{p_γ} the hydrogen isobaric thermal expansivity. Integrating Eq. A.2 gives,

$$\ln\left(\frac{\rho_\gamma}{\rho_{\gamma 0}}\right) = \int_{p_{\gamma 0}}^{p_\gamma} \chi_{T_\gamma}\, dp_\gamma - \int_{T_{\gamma 0}}^{T_\gamma} \chi_{p_\gamma}\, dT_\gamma, \tag{A.3}$$

which can be written as,

$$\rho_\gamma = \rho_{\gamma 0} \exp\left(\int_{p_{\gamma 0}}^{p_\gamma} \chi_{T_\gamma}\, dp - \int_{T_{\gamma 0}}^{T_\gamma} \chi_{p_\gamma}\, dT_\gamma \right), \tag{A.4}$$

with $\rho_{\gamma 0}$, $p_{\gamma 0}$, and $T_{\gamma 0}$ being the hydrogen density, pressure, and temperature at the reference state. Both χ_{T_γ} and χ_{p_γ} are functions of the thermodynamic variables, i.e. $\chi_{T_\gamma} = \chi_{T\gamma 0}\,(p_\gamma/p_{\gamma 0})^{b_T}$, and $\chi_{p_\gamma} = \chi_{p\gamma 0}\,(T_\gamma/T_{\gamma 0})^{a_p}$, with $\chi_{T\gamma 0}$ and $\chi_{p\gamma 0}$ being the values of $\chi_{T\gamma}$ and $\chi_{p\gamma}$ at the reference state respectively, and b_T and a_p are dimensionless constants. Once the reference state is fixed, Eq. A.4 can be extended to,

$$\begin{aligned}\rho_\gamma =& \rho_{\gamma 0} \exp\left(p_{\gamma 0} \frac{\chi_{T\gamma 0}}{1+b_T} \left[\left(\frac{p_\gamma}{p_{\gamma 0}}\right)^{1+b_T} - 1 \right] \right. \\ & \left. - T_{\gamma 0} \frac{\chi_{p\gamma 0}}{1+a_p} \left[\left(\frac{T_\gamma}{T_{\gamma 0}}\right)^{1+a_p} - 1 \right] \right).\end{aligned} \tag{A.5}$$

A high accuracy equation of state was used in our simulations [53]. Once the model parameters are known, Eq. A.5 can be fed to COMSOL where a real thermodynamic behavior of hydrogen is solved for.

The reference state is set to ($p_{\gamma 0}$, $T_{\gamma 0}$, $\rho_{\gamma 0}$) = (1.0 MPa, −100 °C, 1.391 kg/m^3), then for a temperature range of $T_\gamma \in$ [−100 to 100]°C, and a pressure range of $p_\gamma \in$ [1 to 25] MPa, the following values of model parameters fitted best the data of *Kunz and Wagner* [53]: $\chi_{T\gamma 0}$ = 1.04562 (1/MPa); $\chi_{p\gamma 0}$ = 5.4738 × 10^{-3} (1/K); b_T = −1.05526; and a_p = −1.002851. Fig. A.1 shows the relative error (ϵ_ρ) in the hydrogen density as calculated by *Kunz and Wagner* [53] and by Eq. A.5.

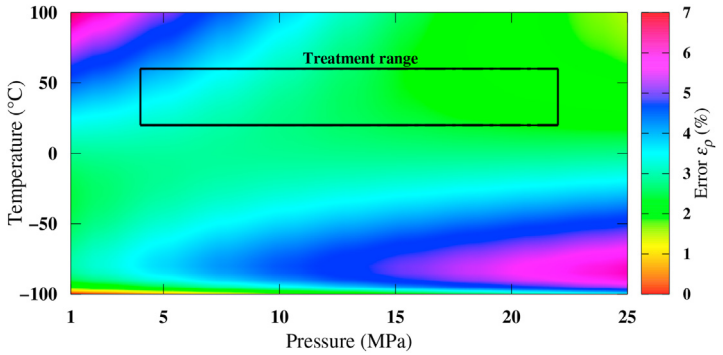

Fig. A.1 – Relative error (ϵ_ρ) in the hydrogen density as calculated by *Kunz and Wagner* [53] and by Eq. A.5.

The range of pressure and temperature changes during the cavern cycling (Fig. 9(a, b)) is displayed on Fig. 1, where the

error percentage in the calculated hydrogen density does not exceed 5.0%.

Appendix B. COMSOL equations

COMSOL gives analytical expressions to track the evolution of hydrogen dynamic viscosity μ_γ, thermal conductivity Λ_γ, and heat capacity $C_{p\gamma}$ as functions of temperature. During hydrogen cycling, for $T_\gamma \in [290 - 235]$ K, the dynamic viscosity changes as,

$$\mu_\gamma = 2.14524642\times10^{-6} + 2.54245\times10^{-8}T_\gamma - 1.0235587\times10^{-11}T_\gamma^2 + 2.80895021\times10^{-15}T_\gamma^3, \tag{B.1}$$

the thermal conductivity changes as,

$$\Lambda_\gamma = 0.00517975922 + 6.72778\times10^{-4}T_\gamma - 3.0388973\times10^{-7}T_\gamma^2 + 6.58874687\times10^{-11}T_\gamma^3, \tag{B.2}$$

and the heat capacity changes as,

$$C_{p\gamma} = 10808.501 + 21.5799904T_\gamma - 0.04447203 18T_\gamma^2 + 3.85401176\times10^{-5}T_\gamma^3 - 1.14979447\times10^{-8}T_\gamma^4. \tag{B.3}$$

REFERENCES

[1] Lattin CW, Utgikar PV. Transition to hydrogen economy in the United States: a 2006 status report. Int J Hydrogen Energy 2007;32:3230–7.

[2] McPherson M, Johnson N, Strubegger M. The role of electricity storage and hydrogen technologies in enabling global low-carbon energy transitions. Appl Energy 2018;216:649–61.

[3] Caglayan DG, Weber N, Heinrichs HU, Linßen J, Robinius M, Kukla PA, Stolten D. Technical potential of salt caverns for hydrogen storage in Europe. Int J Hydrogen Energy 2020;45:6793–805.

[4] Deveci M. Site selection for hydrogen underground storage using interval type–2 hesitant fuzzy sets. Int J Hydrogen Energy 2018;43(19):9353–68.

[5] Lehner M, Tichler R, Steinmüller H, Koppe M. Power–to–gas: technology and business models. Springer; 2014.

[6] Götz M, Lefebvre J, Mörs F, Koch AM, Graf F, Bajohr S, Reimert R, Kolb T. Renewable Power-to-Gas: a technological and economic review. Renew Energy 2016;85:1371–90.

[7] Iordache M, Schitea D, Deveci M, Akyurt IZ, Iordache I. An integrated ARAS and interval type-2 hesitant fuzzy sets method for underground site selection: seasonal hydrogen storage in salt caverns. J Petrol Sci Eng 2019;175:1088–98.

[8] Ozarslan A. Large–scale hydrogen energy storage in salt caverns. Int J Hydrogen Energy 2012;37(19):14265–77.

[9] Pamucar D, Deveci M, Schitea D, Erişkin L, Iordache M, Iordache I. Developing a novel fuzzy neutrosophic numbers based decision making analysis for prioritizing the energy storage technologies. Int J Hydrogen Energy 2020;45(43):23027–47.

[10] Liu W, Zhang Z, Chen J, Jiang D, Wu F, Fan J, Li Y. Feasibility evaluation of large–scale underground hydrogen storage in bedded salt rocks of China: a case study in Jiangsu province. Energy 2020;198:117348.

[11] Liu W, Chen J, Jiang D, Shi X, Li Y, Daemen JJK, Yang C. Tightness and suitability evaluation of abandoned salt caverns served as hydrocarbon energies storage under adverse geological conditions (AGC). Appl Energy 2016;178:703–20.

[12] Bechtel A, Savin SM, Hoernes S. Oxygen and hydrogen isotopic composition of clay minerals of the Bahloul Formation in the region of the Bou Grine zinc–lead ore deposit (Tunisia): evidence for fluid–rock interaction in the vicinity of salt dome cap rock. Chem Geol 1999;156:191–207.

[13] Amaziane B, Keko AŽ, Jurak M. Modeling compositional compressible two–phase flow in porous media by the concept of the global pressure. Comput Geosci 2014;18(3–4):297–309.

[14] Yortsos YC, Xu B, Salin D. Phase diagram of fully developed drainage in porous media. Phys Rev Lett 1997;79(23):4581–4.

[15] Lenormand R. Flow through porous media: limits of fractal patterns. Proc Royal Soc A 1989;423(1864):159–68.

[16] Charnavel Y, Leca D, Poulain F. Advanced geometrical modelling of salt dissolution during cavern leaching – illustration with a case study. In: The SMRI meeting, Las Vegas. USA: Nevada; 1983.

[17] Pernette E, Dussaud M. Underground storages at Tersanne and Etrez: prediction and simulation of cavity leaching in a salt layer charged with insoluble materials. In: The sixth international symposium on salt. Toronto: Canada; 1983.

[18] Caglayan DG, Weber N, Heinrichs HU, Linßen J, Robinius M, Kukla PA, Stolten D. Technical potential of salt caverns for hydrogen storage in Europe. Int J Hydrogen Energy 2020;45(11):6793–805.

[19] Wang T, Yang C, Wang H, Ding S, Daemen JJK. Debrining prediction of a salt cavern used for compressed air energy storage. Energy 2018;147:464–76.

[20] Jaffré J, Sboui A. Henry's law and gas phase disappearance. Transport Porous Media 2010;82:521–6.

[21] Grathwohl P. Diffusion in natural porous media: contaminant transport, sorption/desorption and dissolution kinetics. US, New York: Springer; 1998.

[22] Pray A, Schweickert EC, Minnichi HB. Solubility of hydrogen, oxygen, nitrogen, and helium in water at elevated temperatures. Ind Eng Chem 1952;44(5):1146–51.

[23] Beckermann C, Ramadhyani S, Viskanta R. Natural convection flow and heat transfer between a fluid layer and a porous layer inside a rectangular enclosure. J Heat Tran 1986;109:363–70.

[24] Bergholz RF. Instability of steady natural convection in a vertical fluid layer. J Fluid Mech 1978;2(84):743–68.

[25] Kloppmann W, Négrel PH, Casanova J, Klinge H, Schelkes K, Guerrot C. Halite dissolution derived brines in the vicinity of a Permian salt dome (N German Basin). Evidence from boron, strontium, oxygen, and hydrogen isotopes. Geochem Cosmochim Acta 2001;65(22):4087–101.

[26] Hassanizadeh SM, Leijnse T. On the modeling of brine transport in porous media. Water Resour Res 1988;24(3):321–30.

[27] Johnson KS. Dissolution of salt on the east flank of the permian basin in the southwestern U.S.A. J Hydrol 1981;54:75–93.

[28] Gevantman LH. Physical properties data for rock salt. Washington, D.C.: U.S. Department of Commerce/National Bureau of Standards. U.S. Government Printing Office; 1981. p. 20402.

[29] Bradley JS. Abnormal Formation Pressure. AAPG (Am Assoc Pet Geol) Bull 1975;59(6):957–73.

[30] Ho CK, Webb SW. Gas transport in porous media. 3300 AA Dordrecht, The Netherlands: Springer; 2006.

[31] Wipf H. Solubility and Diffusion of Hydrogen in Pure Metals and Alloys. Phys Scripta 2001;T94:43–51.

[32] Hempelmann R. Diffusion of hydrogen in metals. J Less Common Met 1984;101:69–96.
[33] Pfeiffer WT, al Hagrey SA, Köhn D, Rabbel W, Bauer S. Porous media hydrogen storage at a synthetic, heterogeneous field site: numerical simulation of storage operation and geophysical monitoring. Environ Earth Sci 2016;75:1177.
[34] Morel–Seytoux HJ, Meyer PD, Nachabe M, Tourna J, van Genuchten MT, Lenhard RJ. Parameter equivalence for the Brooks–Corey and van Genuchten soil characteristics: preserving the effective capillary drive. Water Resour. Res Banner 1996;32(5):1251–8.
[35] AbuAisha M, Rouabhi A. On the validity of the uniform thermodynamic state approach for underground caverns during fast and slow cycling. Int J Heat Mass Tran 2019;142:118424.
[36] Rouabhi A, Hévin G, Soubeyran A, Labaune P, Louvet F. A multiphase multi–component modeling approach of underground salt cavern storage. Geomech Energy Environ 2017;12:21–35.
[37] Angelini O, Chavant C, Chénier E, Eymard R, Granet S. Finite volume approximation of a diffusion–dissolution model and application to nuclear waste storage. Math Comput Simulat 2011;81(10):2001–17.
[38] Mahjoub M, Rouabhi A, Tijani M, Granet S, M'Jahad S, Talandier J. Numerical study of Callovo-Oxfordian argillite expansion due to gas injection. Int J GeoMech 2018;18(1):04017134.
[39] Xu WJ, Shao H, Hesser J, Wang W, Schuster K, Kolditz O. Coupled multiphase flow and elasto–plastic modelling of in–situ gas injection experiments in saturated claystone (Mont Terri Rock Laboratory). Eng Geol 2013;157:55–68.
[40] Côté J, Konrad JM. A generalized thermal conductivity model for soils and construction materials. Rev Canad Géotech 2005;42(2):443–58.
[41] van Genuchten MT. A closed–form equation for predicting the hydraulic conductivity of unsaturated soils. Soil Sci Soc Am J 1980;44(5):892–8.
[42] Mualem Y. Hydraulic conductivity of unsaturated porous media: generalized macroscopic approach. Water Resour Res 1978;14(2):325–34.
[43] Rebour V, Billiotte J, Deveughèle M, Jambon A, Le Guen C. Molecular diffusion in water–saturated rocks: A new experimental method. J Contam Hydrol 1997;28(1):71–93.
[44] Cosenza Ph, Ghoreychi M, Bazargan–Sabet B, de Marsily G. In situ rock salt permeability measurement for long term safety assessment of storage. Int J Rock Mech Min Sci 1999;36:509–26.
[45] Schulze O, Popp T, Kern H. Development of damage and permeability in deforming rock salt. Eng Geol 2001;61:163–80.
[46] Bannach A, Wagler T, Walden S, Klafki M. Technology enhancement for 1) inventory assessment and mechanical integrity testing of gas–filled solution mined caverns and 2) mechanical integrity tests of solution mines and liquid storage caverns. 2005. GRI–05/0175 project final report, prepared for Gas Research Institute (contract number 8750), D–095596 Freiberg, Germany.
[47] Poppei J, Mayer G, Hubschwerlen N, Resele G. Flooding of an abandoned salt mine modeling two–phase flow in complex mine structures. In: The proceedings of the TOUGH symposium. Berkeley, California: Lawrence Berkeley National Laboratory; 2006. May 15–17.
[48] Crozier TE, Yamamoto S. Solubility of hydrogen in water, seawater, and NaCl solutions. J Chem Eng Data 1974;19(3):242–4.
[49] Lopez–Lazaro C, Bachaud P, Moretti I, Ferrando N. Predicting the phase behavior of hydrogen in NaCl brines by molecular simulation for geological applications. BSGF – Earth Sci Bull 2019;190:7.
[50] Senger R, Lanyon B, Marschall P, Vomvoris S. Numerical modeling of the gas migration test at the Grimsel test site (Switzerland). Nucl Technol 2008;164(2):155–68.
[51] Ferrell TR, Himmelblau MD. Diffusion Coefficients of Hydrogen and Helium in Water. AlChE J 1967;13(4):702–8.
[52] Jockwer N, Wieczorek K. ADDIGAS. Advective and diffusive gas transport in rock salt formations. 2008. GRS–234, contact number: 02 E 9824 project final report, Gesellschaft fuer Anlagen– und Reaktorsicherheit mbH (GRS), Berlin, Germany.
[53] Kunz O, Wagner W. The GERG–2008 Wide–Range Equation of State for Natural Gases and Other Mixtures: An Expansion of GERG-2004. J Phys Chem Ref Data 2012;57(11):3032–91.

230 (2023) 212061

Contents lists available at ScienceDirect

Geoenergy Science and Engineering

journal homepage: www.sciencedirect.com/journal/geoenergy-science-and-engineering

Kinetics of CO_2 dissolution for underground applications

Firas Tayeb [a,*], Ahmed Rouabhi [a], Murad AbuAisha [a], Alain Valtz [b]

[a] MINES Paris, PSL University, Centre de Géosciences, 35 rue St Honoré, 77300 Fontainebleau, France
[b] MINES Paris, PSL University, Centre Thermodynamique des Procédés, 35 rue St Honoré, 77300 Fontainebleau, France

ARTICLE INFO

Keywords:
Gas storage
Kinetics of CO_2 dissolution
Saturated brine
Pure diffusion model
Natural convection

ABSTRACT

In the current energy transition context, underground storage of carbon dioxide (CO_2) in salt caverns and aquifers has emerged as a promising solution for the Power-to-Gas process complications. However, mass exchange between the CO_2 and the aqueous phase present in the storage site remains a major problem. This paper addresses the question of the kinetics of this mass exchange by performing both experimental and numerical investigations. A series of experiments under storage conditions were carried out in a PVT (Pressure–Volume–Temperature) cell, exposing a volume of CO_2 to pure water or brine at low and high pressure values ranging between 10 and 16.8 MPa and at constant temperatures of 30 and 40 °C. In order to interpret the obtained experimental results and to characterize the transient mass exchange, two modeling approaches were developed: a simplified one based on pure diffusion, and a second combining pure diffusion with density-driven natural convection. Both modeling approaches have proven accurate in predicting the kinetics of CO_2 dissolution. The scope of this study is limited to the laboratory scale but it can be used to quantify the CO_2 dissolution on the storage site scale.

1. Introduction

Indeed, more renewable energy sources must be included in the energy mix in order to make the transition from fossil to low-carbon energy. Energy storage is required to reply to the needs of energy transition since renewable energy sources are intermittent. In fact, long-term and large-capacity power storage, as well as reserve production capability, are necessary. Due to its long-term, high-capacity power storage and reserve generation potential, Power-to-Gas has become a viable technology for dealing with rising renewable energy percentages (Götz et al., 2016; Blanco-Martín et al., 2021). As a result, storage facilities must be integrated into the power system. Thanks to their low investment, operating expenses, and low cushion requirements, the most promising storage options are underground salt caverns and aquifers (Caglayan et al., 2020). The majority of published research addressing underground storage often neglects the role of gas dissolution in the aqueous solution and assumes an instantaneous thermodynamic equilibrium. The validity of this assumption might be questionable when the volume of the liquid phase is comparable to, or exceeds, the volume of the stored gas, or when the gas in question, such as carbon dioxide (CO_2), exhibits high solubility in the aqueous solution. Therefore, in order to gain a better understanding of the behavior of CO_2 in underground storage sites, we will investigate its kinetics of dissolution on a laboratory scale.

Usually, the study of the thermodynamic equilibrium of CO_2 dissolved in the aqueous solution is more frequent than the kinetics of dissolution. Large numbers of solubility data have been published in the literature, however diffusivity data remain scarce (Chabab et al., 2020; Akinfiev and Diamond, 2003). This work focuses on the quantification of the rate of mass transfer over time of CO_2 into pure water/ brine. There have been some studies to investigate the diffusion of CO_2 in water (Tan and Thorpe, 1992; Tamimi et al., 1994; Frank et al., 1996; Mutoru et al., 2011). These studies have almost exclusively focused on low pressures of CO_2. Another element influencing CO_2 diffusion in aqueous solution is the salinity of the water. So far, only a few works in literature have measured the diffusion coefficient of CO_2 in brine. For example, Azin et al. (2013) investigated the diffusion of CO_2 in brine over a pressure range of [5.90 – 6.90] MPa. Shi et al. (2018) compared the evolution over time of the mass transfer of CO_2 in brine-saturated porous media at a pressure of 6 MPa. Due to these very limited experimental data, many aspects of the effect of salt on kinetics of dissolution of CO_2 are not well understood. Further clarification, especially for saturated brine and high pressures, is needed to better understand the role of salt on the kinetics of CO_2 dissolution in aqueous solution at the underground storage conditions. In this work, two numerical approaches were proposed to solve the problem of CO_2 dissolution

* Corresponding author.
E-mail addresses: firas.tayeb@minesparis.psl.eu (F. Tayeb), ahmed.rouabhi@minesparis.psl.eu (A. Rouabhi), murad.abuaisha@minesparis.psl.eu (M. AbuAisha), alain.valtz@minesparis.psl.eu (A. Valtz).

https://doi.org/10.1016/j.geoen.2023.212061
Received 18 August 2022; Received in revised form 12 April 2023; Accepted 2 May 2023
Available online 4 July 2023
2949-8910/

in the brine. The first approach considers only pure diffusion. It is quite interesting because it only accounts for the Fickian diffusion without the complexities of natural convection (Farajzadeh et al., 2007; Upreti and Mehrotra, 2000; Zhang et al., 2015). Another more complex modeling approach has been proposed in this study which aims to include the different physical processes accompanying the dissolution of CO_2. Its purpose is to study the influence of natural convection on the kinetics of mass transfer. In fact, the stored CO_2 in the underground storage site is in contact with the brine. This contact between the liquid and gaseous phases initiates the dissolution of CO_2 into the brine by a molecular diffusion process. At the CO_2-brine interface, a concentration gradient is created which causes a density variation in the brine. This density gradient generates rapid homogenization of the liquid phase by natural convection. The role of natural convection is expected to be crucial in the transport of dissolved CO_2 due to the acceleration of its transfer rate in the brine. There are a few works that raise the question of the integration of the natural convection into the model of dissolution (Hassanzadeh et al., 2007; Farajzadeh et al., 2009; Soubeyran et al., 2019).

The main purpose of this paper is to study the kinetics of dissolution of CO_2 in pure water and brine during pressure decay experiments using a PVT cell under storage conditions. The study investigates CO_2 dissolution at the laboratory scale, aiming to build a strong foundation for understanding and applying these processes in underground caverns and aquifers. The experimental tests performed evaluate all the variable components, including the ratio of gas and liquid volumes, salinity, gas pressure, and temperature. Two numerical models are then developed that can fully describe the obtained experimental results: a diffusion model based on Fick's law of diffusion and Henry's law; and a model that takes into account the density-driven natural convection phenomenon. The dissolved gas is described by the real gas model and a general boundary condition that takes into consideration all mass transfer indispensable parameters is used at the interface. The diffusion coefficient is used as a key parameter to show the effect of natural convection on the mass transfer of CO_2 into pure water and brine. Additionally, a calibration of this coefficient for different brine salinities was determined. Even though this study is performed on the laboratory scale, it can be used to investigate the kinetics of CO_2 dissolution on the storage site scale. This article is organized as follows: the laboratory investigations of the pressure decay experiments are described first; the model assumptions are then presented; and the numerical results are discussed. We end the article with conclusions.

2. Laboratory investigations

The technique used in this work is the pressure decay method to determine diffusion coefficient using a PVT cell because it is more simple and does not require sampling and phase analysis. This method is based on considering the measured pressure decay as CO_2 diffuses into the water and brine (Riazi, 1996). This section will focus on the presentation of the experimental set-up, procedure, and results.

2.1. Experimental set-up

Materials used to carry out the experiments were CO_2 with a purity of 99.99%, deionized pure water, and sodium chloride (99.6% pure). The sodium chloride was dissolved in distilled water to obtain the sodium chloride solution. The main goals of the conducted experiments are to study the kinetics of the mass transfer of CO_2 in brine at a constant temperature and to determine the time needed to reach the saturation concentration of the gas in the water or the brine. An experimental setup is installed as part of this study as shown in Fig. 1. The method used in this work is the pressure decay method which consists in measuring the evolution of the pressure after bringing gaseous and liquid phases into contact inside a constant-volume PVT cell and letting the system reach the thermodynamic equilibrium naturally. The experiments were performed using two cylindrical PVT cells which have total volumes of 96.48 cm^3 and 131.64 cm^3. Each cell is immersed in a bath to maintain a constant temperature. These tests were carried out with three salinities and different volumes of brine as shown in Table 1 in order to study the impact of the salt concentration, the temperature, and the variation of liquid volume on the mass transfer of CO_2.

During the tests, two platinum temperature probes were located above and below the cell to verify the low thermal gradient throughout the cell (calibrated for the temperature range of 5-70 °C with an accuracy of ±0.03 °C) and a pressure sensor placed at the top was used to measure the gas pressure (calibrated for the pressure range of 1-200 bar with an accuracy of ±6 mbar). The top port of the PVT cell is connected to a gas storage cylinder with a volume of 100 cm^3 where the pressure and temperature can be measured. Thus, the density and the mass of the CO_2 introduced into the cell can be evaluated. The bottom port is connected to a variable volume cell containing the liquid phase in order to introduce a precisely known volume into the PVT cell (Fig. 1).

The PVT cell was evacuated using a vacuum pump before the beginning of the experiment. The liquid is the first phase introduced into the cell. After that, the gas phase is introduced as fast as possible until reaching the desired pressure. Once this pressure is reached, the cell is hermetically closed and the system evolves freely while the pressure and temperature are recorded every 5 s. The equilibrium is reached only when the pressure of the system no longer changes.

2.2. Experimental procedure

We have examined the different variable components of the experiments by varying the ratio between the volumes of gas and liquid, the salinity, the gas pressure, and the temperature. The variations in temperature are limited to underground storage conditions. Table 1 summarizes all the performed tests at two different temperatures (T_0 = {30, 40} °C). Since the system's temperature remains constant during the tests, the variations in CO_2 pressure were attributed only to CO_2 transfer into the liquid phase. Tests 1, 2 and 3 were performed at 30 °C using the same volume of CO_2 in the cell and three different pressures in order to study the impact of changing the pressure on the rate of CO_2 mass transfer in the pure water. All the tests from 4 to 10 were carried out at T_0 =40 °C using different salinities (c_{salt} = {11, 22.5}%) and different volumes of liquid to study the influence of these parameters on the kinetics of dissolution. Moreover, we did two tests 11 and 12 using a saturated brine with a salinity of c_{salt}= 22.5% and high initial pressures of CO_2 ($p_{\gamma 0}$ = {129, 168.7} bar).

2.3. Experimental results

The rate of CO_2 mass transfer in the aqueous solution is determined by measuring the pressure of CO_2 over time during the pressure decay tests. Fig. 2 shows the 12 experimental results of the measured pressures of the different performed tests presented in Table 1. The gas pressure drops dramatically in the beginning of all the experiments until it stabilizes at the end of the tests when the thermodynamic equilibrium is reached. It means that the mass transfer rate of CO_2 in aqueous solution is much higher in the early stages of the experiments and progressively declines over time. However, changing the salinity, initial pressure of CO_2 and the liquid volume have some effects on the kinetics of dissolution. These effects will be discussed in the following paragraphs.

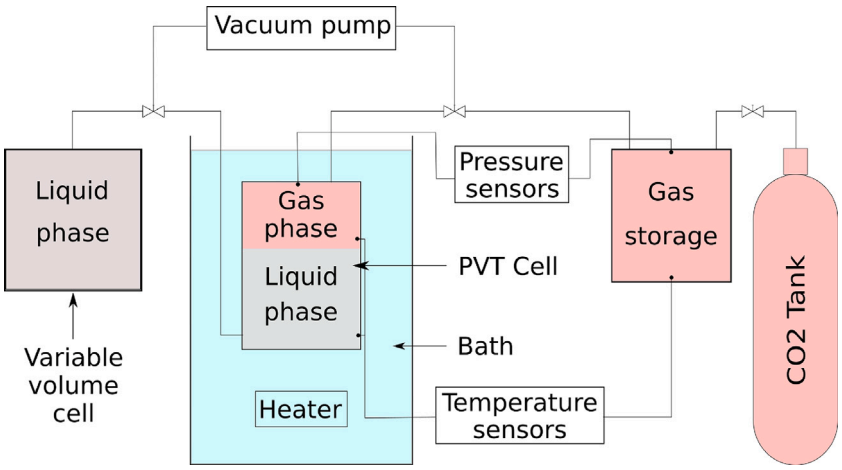

Fig. 1. Schematic diagram illustrating the CO_2 diffusion experiment.

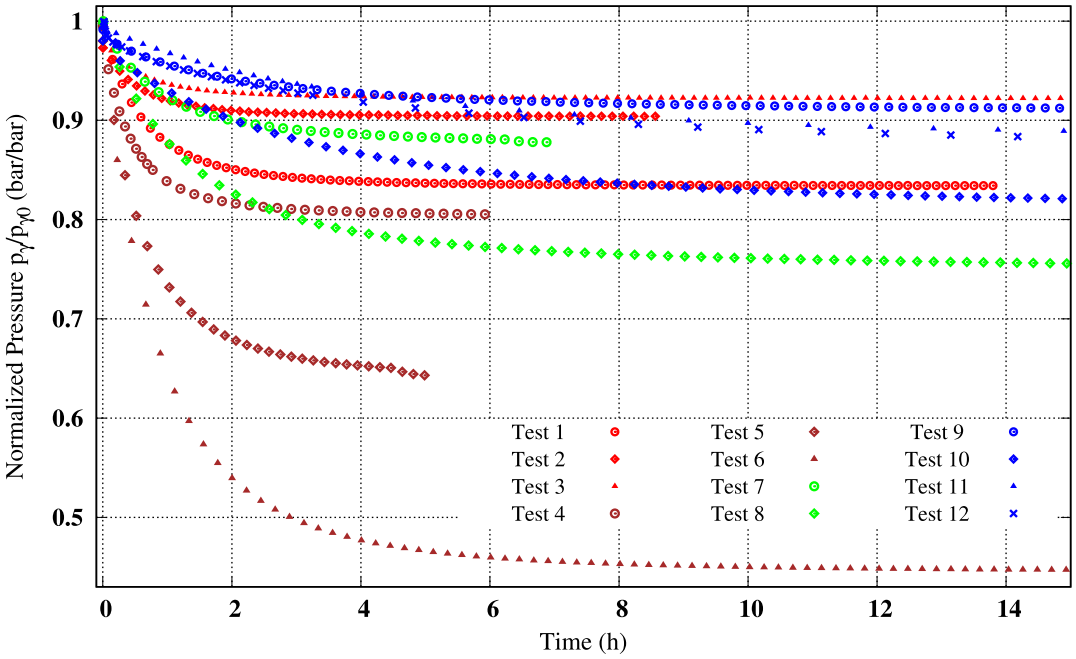

Fig. 2. Measured CO_2 pressure decay curves of all the performed tests.

Table 1
Details of the experiments performed under different laboratory conditions.

Test numbers	Temperature T_0 (°C)	Initial pressure $p_{\gamma 0}$ (bar)	Liquid volume V_λ (cm^3)	Gas volume V_γ (cm^3)	Salinity c_{salt} (%)
1	30	10	30.39	101.25	0
2	30	41.5	30.39	101.25	0
3	30	48.8	30.39	101.25	0
4	40	10.5	28.45	68.03	0
5	40	10.5	48.24	48.24	0
6	40	10	90.5	41.14	0
7	40	10.5	28.45	68.03	11
8	40	10.5	48.24	48.24	11
9	40	10.5	28.45	68.03	22.5
10	40	10.5	48.24	48.24	22.5
11	40	129	105.31	26.32	22.5
12	40	168.7	105.31	26.32	22.5

2.3.1. Effect of salinity

In order to study the effect of the salinity on the rate of CO_2 mass transfer over time, tests 4, 7 and 9 (Table 1) were performed with a liquid volume $V_\lambda = 28.45$ cm^3 using pure water and two mass concentrations c_{salt} of NaCl (11%,22.5%) at 40 °C. Fig. 2 shows that the presence of salt in the solution reduces the solubility of CO_2 in brine. The CO_2 dissolves in pure water faster than in the brine. In fact, the thermodynamic equilibrium is reached within 4 h in pure water, within 7 h in the brine with $c_{salt} = 11\%$, and within 15 h in the brine with $c_{salt} = 22.5\%$. This same effect is observed for tests 5, 8 and 10 which were performed with another liquid volume $V_\lambda = 48.24$ cm^3 at a constant temperature of 40 °C using pure water and two salinities (11%,22.5%). The introduction of salt into the water reduces the rate of CO_2 mass transfer at the end of the experiment when the diffusion process dominates the convection. This behavior is related to the fact that the presence of NaCl in the solution increases the viscosity of the water, which causes the slow movement of CO_2 in the water. This decreases the motion of CO_2 molecules in the water and affects the rate of CO_2 diffusion (Zarghami et al., 2017).

2.3.2. Effect of initial gas pressure and volume of liquid phase

The first three tests performed (Table 1) emphasize the influence of changing the initial pressure of CO_2 at a constant temperature ($T_0 = 30$ ° C) on the gas pressure decline at infinite time. In fact, the gas pressure drop (Fig. 2) is less important in tests 2 and 3 using a high initial pressure ($p_{\gamma 0} = 41.5$ and 48.8 bar respectively) than the test 1 using a low initial pressure ($p_{\gamma 0} = 10$ bar). Thus, the solubility of CO_2 depends clearly on the initial gas pressure. Furthermore, Tests 4, 5 and 6 (Table 1) were performed with pure water to study the impact of changing the volume on the kinetics of CO_2 mass transfer. Fig. 2 shows that the equilibrium pressure decreases as the volume of the liquid phase introduced increases. This gas pressure drop is due to the change in the mass of the gas phase: a low volume of the liquid phase induces a low mass of dissolved CO_2. Moreover, the duration of dissolution rises as the volume of the liquid phase in the tests increases. Since the section of the cell is constant, the volume of the liquid phase is proportional to the height of the cell. A higher volume results in a larger distance between the interface and the bottom of the cell, therefore increasing the diffusion time of the dissolved gas in the aqueous solution.

3. Model set-up

This section describes the complete model including pure diffusion and density-driven natural convection. It assigns an ordinary differential equation at the liquid–gas interface to calculate the loss of gas pressure over time and determines the dissolution velocity in the liquid phase.

In what follows, subscripts will be used to designate quantities of interest. The Greek letters (α, γ, λ) subscripts are used to name the phases: α for a generic phase, γ for the gas phase, and λ for the liquid phase.

The cell of a height h contains two phases: the gas γ (CO_2 in our case) of a height L_γ and the liquid λ (pure water or brine) of a height L_λ separated by an interface $\Sigma_{\gamma\lambda}$ at abscissa $z = 0$ (Fig. 3). Each occupies a domain Ω_α of volume V_α and exchanges material across $\Sigma_{\gamma\lambda}$.

In order to model the experiment (Fig. 1), the problem can be divided into three periods. For $t \leq 0$, the cell contains only the λ phase. Thus, the λ phase of mass M_λ is considered in hydrostatic equilibrium under very low pressure. The duration of the injection of the gas t_0 is considered very short that no measurements are available during this period. For $0 \leq t \leq t_0$, the mass M_γ of the γ phase is injected into the cell with a constant injection rate. The evolution of the total mass of fluid contained in the system at any time t can be expressed as: $M(t) = M_\lambda + M_\gamma \times (t/t_0)$. For $t \geq t_0$, the mass transfer between the two phases takes place and the system evolves towards its state of equilibrium. The conservation of mass imposes: $M(t) = M(t_0) = M_\lambda + M_\gamma$ and $\dot{M} = 0$.

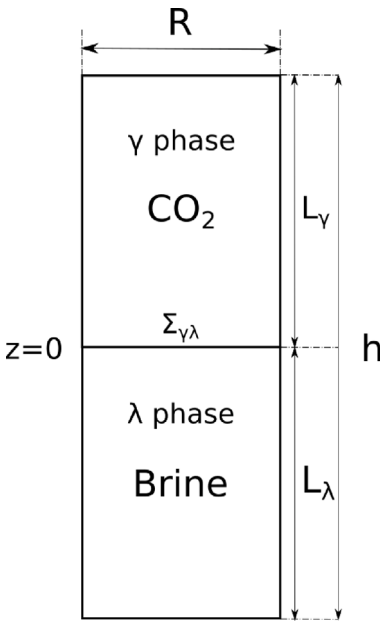

Fig. 3. Schematic representation of the CO_2 - brine model inside a closed PVT cell.

In order to model the pressure–decay tests, the following simplifying assumptions are used: the volume of the two phases V_α does not vary and the interface $\Sigma_{\gamma\lambda}$ is fixed with abscissa $z = 0$ and with a constant section. The cell is considered to be perfectly sealed and the mass transfer from the λ phase to the γ phase is neglected. Therefore, any loss of pressure measured experimentally is only due to the mass transfer of the γ phase into the λ phase across the interface $\Sigma_{\gamma\lambda}$. The temperature is uniform throughout the cell and remains constant during the test. For the λ phase, its density ρ_λ depends only on the mass concentration of the dissolved gas c and the mass concentration of the brine salt c_{salt}. We consider also that the γ phase is governed by real gas law and its density ρ_γ can be expressed:

$$\rho_\gamma = \frac{p_\gamma}{T Z_\gamma}, \tag{1}$$

where p_γ is the pressure of the γ phase, T is the temperature which is considered constant and Z_γ is the gas compressibility factor which is assumed to be a function of p_γ (Kunz et al., 2007). Programming and simulation were carried out using the finite element package of Comsol multiphysics. The field equations were solved with the transport of diluted species and laminar flow modules. At the interface, an ordinary boundary differential equation was used.

3.1. Governing equations

The conservation of mass in the λ phase can be written as:

$$\begin{aligned} &\text{the density field:} && \dot{\rho_\lambda} + \rho_\lambda \vec{\nabla}.\vec{v_\lambda} &&= 0; \\ &\text{the concentration field:} && \rho_\lambda \dot{c} + \vec{\nabla}.\left(\rho_\lambda \vec{J}\right) &&= 0, \end{aligned} \tag{2}$$

where $\vec{J}$ denotes the diffusion flux vector, $\vec{v}_\lambda$ the velocity vector in the λ phase, and $\vec{\nabla}$ the nabla operator. For any function φ, the material derivative is expressed as $\dot{\varphi} = \partial_t \varphi + \vec{v}_\lambda.\vec{\nabla}\varphi$.

The Navier–Stokes momentum equation is given by:

$$\rho_\lambda \dot{\vec{v}}_\lambda = -\vec{\nabla} p_\lambda + \vec{\nabla}.\underline{\underline{\xi_\lambda}} + \rho_\lambda \vec{g}, \tag{3}$$

where $\vec{g}$ is the gravitational acceleration vector, $\underline{\underline{\xi_\lambda}}$ is the fluid stress tensor $\underline{\underline{\xi_\lambda}} = \mu(\vec{\nabla}\vec{v_\lambda} + \vec{\nabla}\vec{v_\lambda}^{\,T}) - (2/3)(\vec{\nabla}.\vec{v_\lambda})\underline{\underline{\delta}}$, with μ is the λ phase dynamic viscosity and $\underline{\underline{\delta}}$ is the second-order Kronecker delta.

Assuming that λ is initially at rest ($\vec{v}_\lambda = \vec{0}$ and $\underline{\underline{\xi_\lambda}} = \underline{\underline{0}}$), the gradient of the pressure ($p_\lambda(\vec{x}, t=0) = p_{\lambda 0}(\vec{x})$) can be expressed by the following equation: $\vec{\nabla} p_{\lambda 0} = \rho_{\lambda 0}\vec{g}$. So, the Navier–Stokes momentum Eq. (3) can be expressed as follows where $p = p_\lambda - p_{\lambda 0}$:

$$\rho_\lambda \dot{\vec{v}}_\lambda = -\vec{\nabla} p + \vec{\nabla}.\underline{\underline{\xi_\lambda}} + (\rho_\lambda - \rho_{\lambda 0})\vec{g}. \tag{4}$$

The density ρ_λ is considered to be dependent on the concentration of the dissolved gas c:

$$\rho_\lambda = \rho_{\lambda 0}(1 + \beta c), \tag{5}$$

where β is the volumetric expansion coefficient. The mass rates of the two phases λ and γ can be written as:

$$\begin{aligned} \dot{M}_\gamma &= M_\gamma \dot{p}_\gamma \left(\frac{1}{p_\gamma} - \frac{\partial_{p_\gamma} Z_\gamma}{Z_\gamma} \right); \\ \dot{M}_\lambda &= -\int_{\Sigma_{\gamma\lambda}} \rho_\lambda \vec{v}_\lambda . \vec{n}\, dA = -\dot{M}_\gamma, \end{aligned} \tag{6}$$

with $\vec{n}$ being the normal vector outwardly directed unit vector to Ω_λ. The barycentric momentum $\rho_\lambda \vec{v}_\lambda$ can be decomposed as $\rho_\lambda \vec{v}_\lambda = \rho_n \vec{v}_n + \rho_b \vec{v}_b$ where the subscripts n and b are respectively referring to the dissolved gas and the solvent (pure water or brine solution). In order to model the gas diffusion in the λ phase, a physical model based on Fick's law is used to interpret the experimental data where D is the diffusion coefficient:

$$\vec{J} = -D\vec{\nabla} c. \tag{7}$$

3.2. Initial and boundary conditions

The initial conditions of the system are:

$$\begin{cases} p(\vec{x}, t=0) = 0; \\ \vec{v}_\lambda(\vec{x}, t=0) = \vec{0}; \\ c(\vec{x}, t=0) = 0. \end{cases} \tag{8}$$

The liquid phase λ is not initially expected to contain any γ phase concentration. However, for only high pressure of the gas, it is clear that some γ phase has dissolved in the λ phase during the filling phase as a result of the rapid injection. Inverse mass calculations between the final and initial mass of the gas in the liquid phase were used to determine the initial concentrations of the gas (Yang and Gu, 2006).

Assuming that there is no mass transfer from the λ phase to the γ phase across the interface $\Sigma_{\gamma\lambda}$, we can write $\vec{v}_b = \vec{0}$. So, $\vec{v}_\lambda$ can be expressed as:

$$\vec{v}_\lambda = \frac{\vec{J}}{1-c}, \quad \text{at } \Sigma_{\gamma\lambda}. \tag{9}$$

Different types of boundary conditions have been proposed at the interface $\Sigma_{\gamma\lambda}$ in the literature. A number of studies have used the Dirichlet type boundary condition which specifies the species concentration at the gas–liquid interface (Zhang et al., 2015; Upreti and Mehrotra, 2000)]. Other studies have examined the Neumann type boundary condition for which the derivative of concentration across the boundary is given (Farajzadeh et al., 2009; Moghaddam et al., 2012).

In this work, we will use the Robin type boundary condition for the concentration of the dissolved gas because it is the most general form of the boundary condition at the interface which take into consideration all mass transfer indispensable parameters: gas solubility; the diffusion coefficient; and the interface resistance ($1/K$), where $D\partial_z c(z=0,t) = K(c(z=0,t) - c^s)$, and with c^s being the saturation concentration of the dissolved gas.

To sum up, the boundary conditions used in this work at $\Sigma_{\gamma\lambda}$ can be summarized as:

$$\text{Boundary Conditions} \begin{cases} p_\lambda(z=0,t) = p_\gamma(t) \Rightarrow p(z=0,t) = 0; \\ \vec{v}_\lambda = \dfrac{-D\vec{\nabla} c}{1-c}; \\ \vec{J}.\vec{n} = K\left(c - \dfrac{p_\gamma(t)}{H} \right). \end{cases} \tag{10}$$

The solubility of the γ phase in brine is expressed by Henry's law as $c^s = p_\gamma / H$ where H is Henry's coefficient, which depends on the temperature, the gas pressure, and the salinity.

4. Numerical results and discussion

This section focuses on the obtained numerical results of the two developed models: the first model, which is the pure diffusion model, takes into account only Fick's law of diffusion; the second model, in addition to the Fickian diffusion, considers a density-driven natural convection phenomenon in order to estimate more accurately the diffusion coefficient. Table 2 presents all the common parameters used in the two models. In fact, the data of Henry's coefficient in pure water was provided by Akinfiev and Diamond (2003) thermodynamic model, which is based on 362 published experimental measurements of the solubility of CO_2 in water and the data of Henry's coefficient in brine was interpreted from the article of Chabab et al. (2019), which provides the solubilities of CO_2 at different pressures and temperatures. Moreover, the initial density of the aqueous solution $\rho_{\lambda 0}$ was provided by Archer and Carter (2000) which depends on the salinity and temperature. Our two models are used to calibrate the parameters D (the diffusion coefficient) and K (the mass transfer coefficient) (Eq. (11)). These parameters influence the evolution of pressure and concentration of the dissolved gas over time. In our work, the mass transfer coefficient is assumed constant as shown in Table 2 and the diffusion coefficient is considered dependent on salinity c_{salt}:

$$D = \frac{D_0}{\eta(c_{\text{salt}})}, \tag{11}$$

where D_0 is either equal to the calibrated diffusion coefficient D_{diff} in the model of pure diffusion presented in Section 4.1 or the real diffusion coefficient (the molecular diffusion coefficient of CO_2 in pure water) D_{real} in the diffusion and convection model described in Section 4.2. Frank et al. (1996) indicated that the molecular diffusion coefficient of CO_2 in pure water is between 1.97×10^{-9} and 3.07×10^{-9} m^2/s for temperatures below 45 °C.

In order to reach equilibrium at the interface, the CO_2 dissolves into the brine when the two phases come into contact. However, the flow is limited by the interface resistance ($1/K$). When the resistance is high, the flow is less significant, which reduces the initial increase in dissolved gas concentration at the interface. As a result, the pressure curve's slope gradually becomes less steep. After then, the dissolved gas at the interface starts to diffuse into the brine, causing a temporary drop in concentration at the interface, which is then compensated by the mass transfer to the liquid phase. Physically, the dissolved gas rapidly diffuses into the liquid phase when the diffusion is more significant, limiting the evolution of the concentration at the interface (Reza Etminan et al., 2013). However, the concentration at the interface increases rapidly to reach saturation as the resistance is larger at the interface. It causes a large variation in concentration between the surface and the bottom of the cell. Then, the concentration at the interface decreases gradually until it reaches equilibrium concentration at the end.

In this section, the two numerical models will be presented and discussed in detail by comparing the results with the literature. In order to avoid redundancy, Figs. 4–7 represent the comparison between the normalized pressure $p_\gamma(t)/p_{\gamma 0}$ obtained by the two models and the experimental data.

4.1. Pure diffusion model

The pure diffusion model was used as a first approach to interpret the observed pressure decay results presented in Section 2.3. As mentioned above, this approach is based only on Fick's law of diffusion to fit the experimental data by choosing a calibrated diffusion coefficient for the different salinity of the aqueous solution as shown in expression (11). After calibrating the parameters using experimental data, this

Table 2
Calibrated parameters of the two models.

T_0 (°C)	c_{salt} (%)	$p_{\gamma 0}$ (bar)	H (MPa/mass fraction)	$\rho_{\lambda 0}$ (kg/m^3)	K (m/s)
30	0	10	79.28	995.5	0.252
		41.5	97.29		
		48.8	102.93		
40	0	10.5	99.07	992	
	11	10.5	184.27	1070	
	22.5	10.5	287.81	1158	
		129	550.08		
		168.7	726.64		

Table 3
Calibrated parameters of the diffusion coefficient expression (11) for the pure diffusion model.

c_{salt} (%)	D_{diff} (m^2/s)	η
0	1.1×10^{-7}	0
11		1.96
22.5		4

model can reasonably describe the duration of CO_2 dissolution regardless of the volume of water or brine introduced into the cell. In what follows, the numerical normalized pressure determined using this first model is presented with dashed lines. Fig. 4 compares the normalized experimental pressure profiles (tests 1,2,3 in Fig. 2) with the predicted pressure profiles for CO_2 in pure water at different pressures and at a constant temperature T= 30 °C. Furthermore, Fig. 5 shows that the numerically calculated pressures for CO_2 in pure water predict the experimental pressure profiles (tests 4, 5, 6 in Fig. 2) at varying liquid volumes and at constant temperature T= 40 °C. The diffusion coefficient is the most significant parameter controlling the kinetics of the dissolution process. This coefficient influences the rate of mass transfer of the gas within the liquid phase, which is determined by measuring the pressure drop of CO_2 over time. In this study, the calibrated value of the diffusion coefficient in pure water is $D_{diff} = 1.1 \times 10^{-7}$ m^2/s which is independent of the gas initial pressure, the temperature and the ratio between the liquid and gas volumes. The calibrated value of the diffusion coefficient using the pure diffusion model is two orders of magnitude larger than the molecular diffusivity of CO_2 in pure water. The difference between the molecular and the calibrated diffusion coefficients is explained by the fact that the phenomena associated with dissolved gas diffusion in the liquid phase are neglected, despite their importance in the overall mass transfer process.

On the other hand, the adjusted diffusion coefficient decreases when the concentration of salt in the water increases. This coefficient is divided by almost 2 for brine concentration of c_{salt}=11% (tests 7, 8 in Fig. 2) and by 4 for brine concentration of c_{salt} = 22.5% (tests 9, 10, 11, 12 in Fig. 2). Table 3 provides a summary of the values that were retained for the diffusion coefficient which is function of the salinity as shown in expression (11). These values represent the average of the adjustments made for the various volumes of tested brine and the initial gas pressure. Figs. 6 and 7 represent the obtained numerical pressure profiles which are in good agreement with the experimental results at low and high initial gas pressures.

To sum up, the pure diffusion model, which is based on many simplifying assumptions, is quite interesting for modeling the kinetics of CO_2 dissolution in pure water and brine. It estimates the diffusion coefficient values (Table 3), which are approximately one hundred times higher than the molecular diffusion coefficient, by fitting the Pressure-Decay tests and numerical results.

To describe the mass transfer process with more precision, a more complex modeling approach will be proposed in this work, which aims to include the different physical processes, including natural convection, that accompany the dissolution of CO_2.

4.2. Diffusion and convection model

This approach takes into consideration the Navier–Stokes momentum Eq. (4) to incorporate density-driven natural convection into the simulation. It is more complex than the pure diffusion model of the previous section, but uses the same initial and boundary conditions presented in Section 3.

Natural convection plays a significant role in the dissolution of CO_2 in water and brine due to the rapid homogenization of the liquid phase. It is created by the density gradient in the brine, which is caused by the concentration gradient of the dissolved gas.

In this work, the density of the brine is proportional to the concentration of the dissolved gas c as shown in Eq. (5). The values of β used in the various tests are reported in the Table 4, which are based on the measurement of CO_2-saturated brine density in the work of Yan et al. (2011). The dynamic viscosity μ depends on the temperature and the salinity of the brine and its values were taken from the study of Kestin et al. (1981) which contains viscosity data of various brine temperatures and salinities. Only the laminar regime was considered in this study for the reason that the Reynolds number Re is very small and the Rayleigh number Ra is less than 10^5 (Bird et al., 2007):

$$\begin{cases} \mathrm{Re} = \dfrac{\rho_\lambda \|\vec{v}\| R}{\mu} < 2300; \\ \mathrm{Ra} = \dfrac{\beta c g \rho_{\lambda 0} R^3}{\mu D} < 10^5, \end{cases}$$

where $\|\vec{v}\|$ is the magnitude of the fluid velocity and R is the radius of the cell. Besides, the molecular diffusion coefficient of CO_2 in pure water $D_{real} = 2 \times 10^{-9}$ m^2/s was used in the diffusion and convection model to reproduce the Pressure-decay tests (Table 1) at various temperature, water volumes, and initial gas pressures. The results obtained from the CO_2 pressure profiles in pure water (solid lines) are presented in Figs. 4 and 5. Moreover, As shown in Table 4, the diffusion coefficient decreases when the concentration of NaCl increases which is the same influence observed using the pure diffusion model. Figs. 6 and 7 represent the measured results of the pressure drop and the obtained numerical results of the complete model of diffusion and convection. This model well-estimates the evolution of the pressure of the dissolved gas over time at low and high initial pressures of CO_2 and at different brine salinities. Throughout all simulated experiments, the slope of the normalized gas pressure curve is strong at the beginning and becomes less steep as the experiment progresses, which means that the mass transfer rate is considerably reduced during the early phases of the experiments and continues to decrease with time. This model predicts the kinetics and duration of dissolution of CO_2 in aqueous solution with more precision.

Fig. 8 shows the dissolved gas concentration field, the magnitude of the fluid velocity field and its vector at various times. The results of Test 4 are explicitly shown. The dissolution of CO_2 begins as soon as the liquid and gas phases come into contact. Initially, the acceleration of the mass transfer process is related to the convection process. In fact, the CO_2 concentration is high near the top of the cell, causing a density difference in the liquid phase. Therefore, convection tends

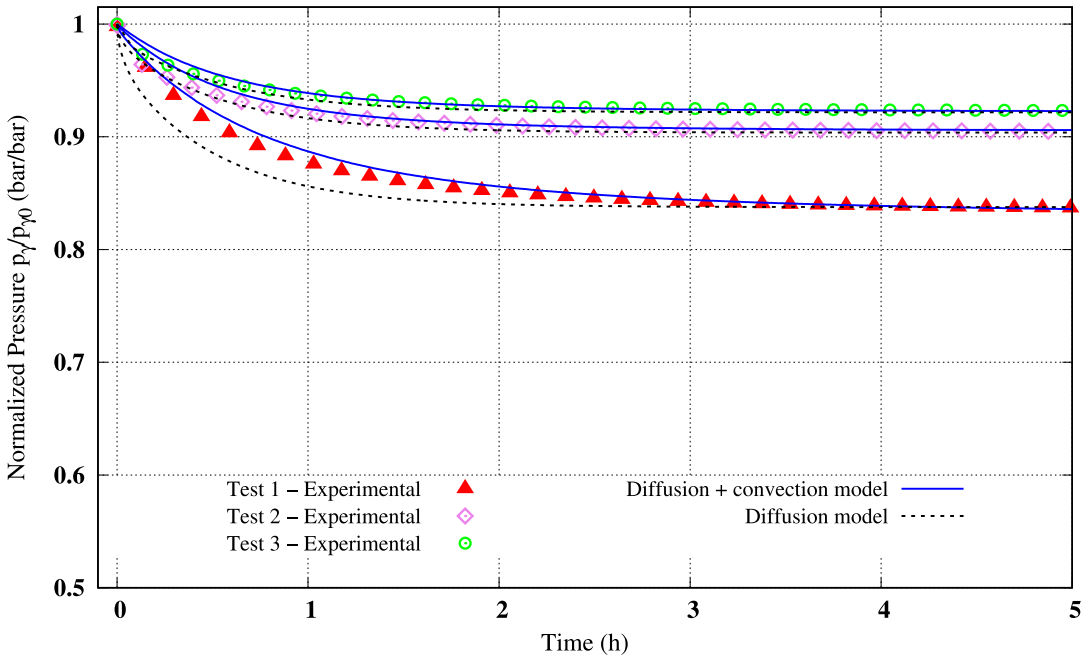

Fig. 4. Comparison between the measured pressure data of CO_2 in pure water and the numerical models using different initial pressures ($p_{\gamma 0}$= 10, 41.5, 48.8 bar) at T_0= 30 °C.

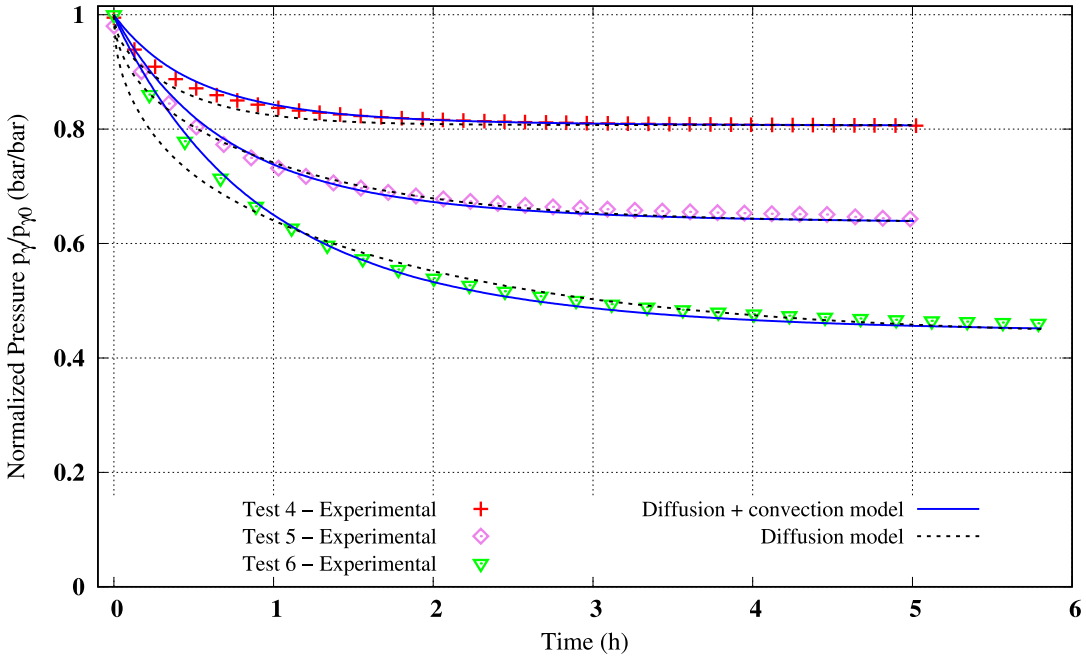

Fig. 5. Comparison between the measured pressure data of CO_2 in different volumes of pure water (V_λ= 28.45, 48.24, 90.5 cm^3) and the numerical models at T_0= 40 °C.

to quickly homogenize the liquid phase. The Rayleigh number is high enough to justify the appearance of convective vortices in the liquid phase, regardless of volume. Fig. 8 clearly shows the formation of these vortices by observing the direction of the velocity vector of the liquid phase. After 5 h, the homogenization of the brine reduces the gap between the maximum and minimum concentrations and reduces the norm of velocity. Therefore, the concentration gradient between the interface $\Sigma_{\gamma\lambda}$ and the bottom of the cell and the brine density gradient are very small, reducing the instability between the top and bottom of the liquid phase. These observations are explained by the fact that the diffusion process tends to occur above convection. In fact, regardless of the salinity, initial pressure, and volume of the liquid, the effect of convection is reduced over time in all experiments.

Table 4
The density coefficients β, the dynamic viscosities, and the calibrated parameters of the diffusion coefficient expression (11) used in the diffusion and convection model.

T_0(° C)	c_{salt}(%)	β	μ(Pa.s)	D_{real}(m^2/s)	η
30	0	0.18	796.5	2×10^{-9}	0
40		0.26	653.8		
	11	0.24	848		1.21
	22.5	0.22	1139.4		2.5

Overall, the estimation of the values of the diffusion coefficient from the results of Pressure-Decay tests using the complete diffusion and

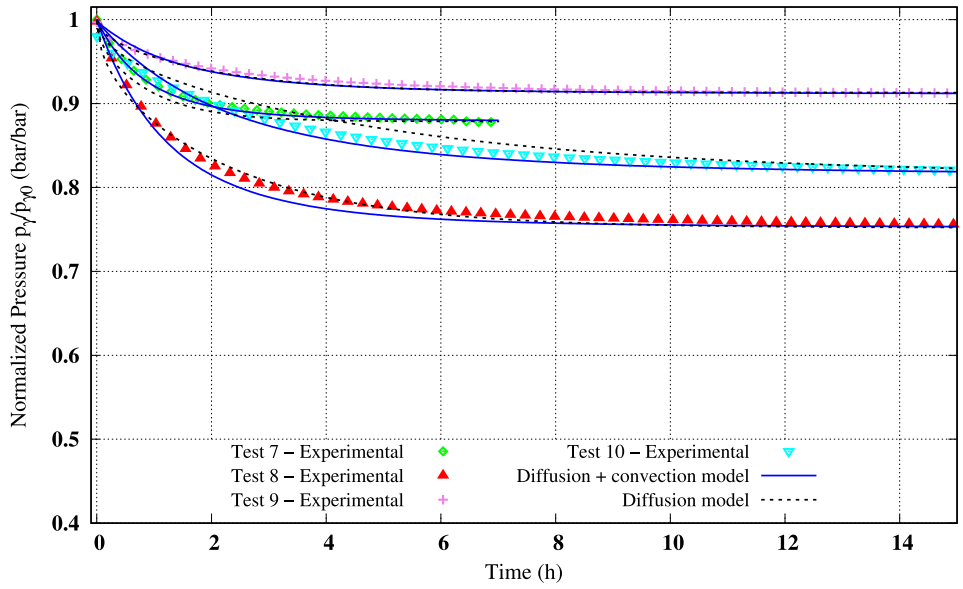

Fig. 6. Comparison between the measured pressure data of CO_2 in different salinities (c_{salt}=11, 22.5%) of the brine and the numerical models at T_0= 40 °C.

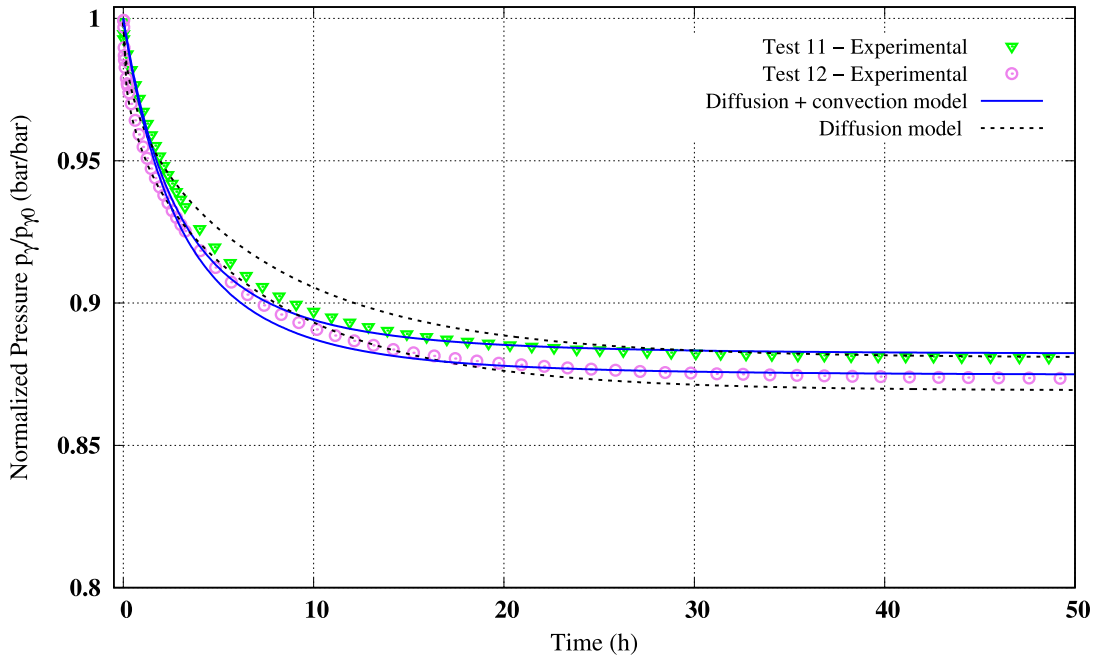

Fig. 7. Comparison between the measured pressure data of CO_2 in saturated brine (c_{salt} = 22.5%) with P_0 = 129, 168.7 bar and the numerical models at T_0= 40 °C.

convection model (Table 4) is more accurate than the pure diffusion model and its values are equal to the value of the molecular diffusivity of CO_2 in water and brine. This model is general and can be used to predict the kinetics of dissolution of CO_2 in water and brine under geological storage conditions.

4.3. Comparison between the two developed models with the literature

This section provides a comparison of our obtained results and previous studies on the CO_2 diffusion coefficient in water/brine. The calibrated values of the diffusion coefficient in the literature using the model of pure diffusion are two orders of magnitude larger than the molecular diffusivity of CO_2 into pure water. Farajzadeh et al. (2009) evaluated this parameter between 1.4×10^{-7} m^2/s and 2.8×10^{-7} m^2/s for pressures ranging from 1 to 5 MPa and at 30 °C. Shi et al. (2018) adjusted it at 2.9×10^{-7} m^2/s under pressure of 5.9 MPa and temperature of 30 °C. Only a few works in literature introduced natural convection in the study of the mass transfer of CO_2 into water. For instance, Gholami et al. (2015) explained the importance of the phenomenon of natural convection in the acceleration of the equilibrium in the Pressure-Decay test models, compared to those limited to simple diffusion. Furthermore, Farajzadeh et al. (2009) demonstrated that the adjustment of the diffusion coefficient, based on a convection–diffusion model, is close to the molecular diffusion coefficient of CO_2 into water. Other studies focus on the critical time after which instabilities caused by the density gradient take precedence over CO_2 diffusion (Hassanzadeh et al., 2007; Riaz and Cinar, 2014).

To further validate the results of this work, we compared our two models with the experimental results of the dissolution of CO_2 in pure water published by Farajzadeh et al. (2009). The initial gas pressures are $p_{\gamma 0}$ = {10.1,19.4,32.1} bar at T_0= 30 °C. Fig. 9 represents the

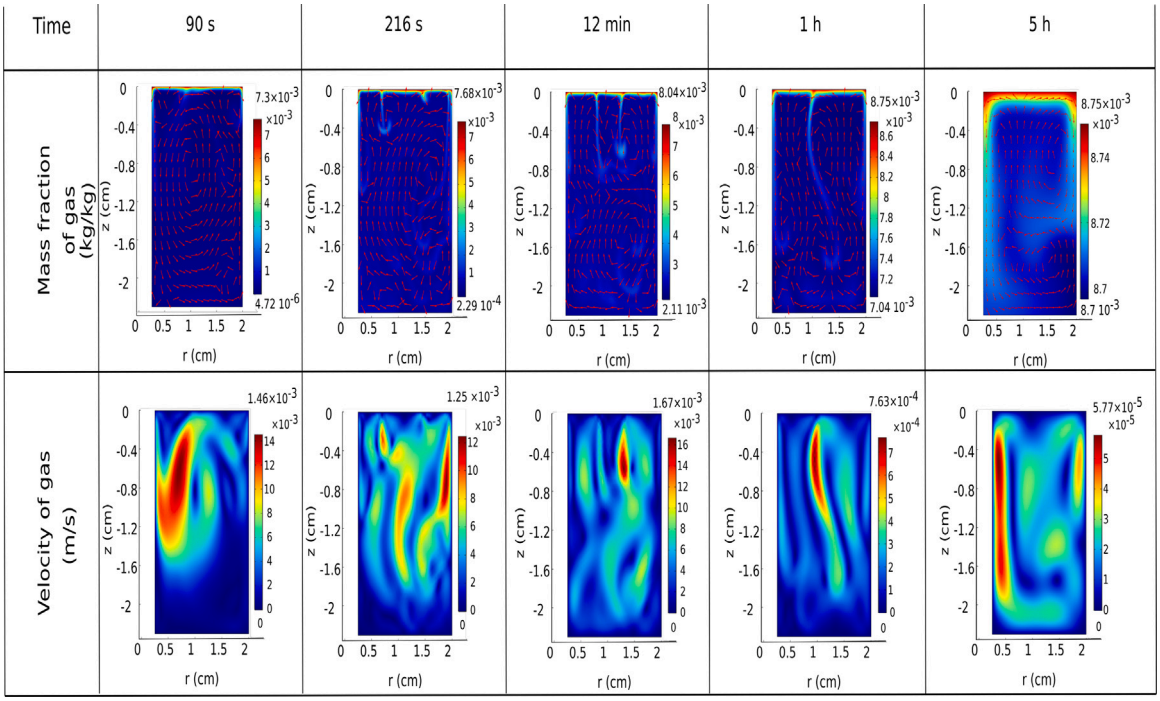

Fig. 8. Evolution of CO_2 concentration and velocity profiles of test 4 with time.

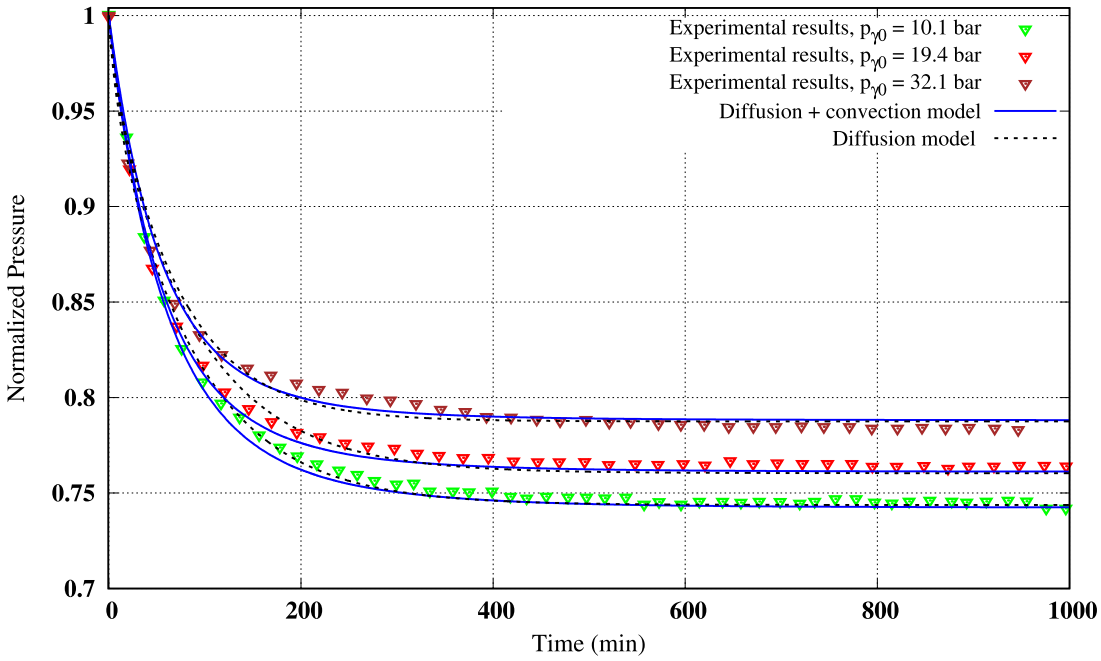

Fig. 9. Comparison between the measured pressures data of CO_2 in pure water published by Farajzadeh et al. (2009) and the numerical models with $p_{\gamma 0}$ = {10.1,19.4,32.1} bar at T_0= 30 °C.

normalized pressure drop of CO_2 obtained from the pure diffusion model (dashed lines) using the calibrated diffusion coefficient 1.1×10^{-7} m^2/s and (Table 3) and the diffusion and convection model (solid lines) using the molecular diffusion coefficient 2×10^{-9} m^2/s (Table 4). The results of pressure using the two developed models adjust very well with the published experimental data for different initial gas pressures and there is a good agreement between the values of the diffusion coefficient of CO_2 in pure water used in this work and the values found in the literature.

In addition, there are a few works in the literature that mentioned the influence of adding salt in the liquid phase on the value of the diffusion coefficient. For example, Perera et al. (2018) indicated a drop in the CO_2 diffusion coefficient to around 50% using a brine with a salinity of c_{salt}=18% compared to pure water. The value of this coefficient reported by Sell et al. (2013) is divided by 3 for a brine with a salinity of c_{salt}=21.7%. Furthermore, Shi et al. (2018) estimated that the diffusion coefficient is around 1.1×10^{-7} m^2/s which is divided by a factor of 2.6 compared to the value in pure water.

The same influence on the diffusion coefficient was observed using the two models in this work by adding salt to the aqueous solution. In fact, the obtained values of this coefficient presented in Tables 3 and 4 compared to D_0 are divided, respectively, by factors of 2 and 1.21 for concentration of brine $c_{salt} = 11\%$ and factors of 4 and 2.5 for concentration of brine $c_{salt} = 22.5\%$.

5. Conclusions

In this paper, we studied the kinetics of CO_2 dissolution in aqueous solution under underground storage conditions. This was firstly accomplished through an experimental investigation based on the measurement of the CO_2 gas pressure inside a PVT Cell, exposing a volume of CO_2 to pure water or brine at a given temperature. The pressure drop during testing reflected the loss of gas mass resulting from the dissolution process. This drop depends on the salinity of the liquid phase and on the volume ratio between the liquid and gas phases. In order to interpret the experimental results and quantitatively characterize the mass exchange process, two physical models based on a suitable interface boundary condition were developed. The first model, which considers only pure diffusion, can correctly model the pressure drop, but it requires an apparent diffusion coefficient that is too higher compared to the molecular diffusivity of CO_2 in water or brine. To overcome this problem, a second model, more complex than the first, was proposed. It includes, besides pure diffusion, a natural convection process that accelerates the CO_2 dissolution and gives more accurate results. The two models and the associated calibrated parameters resulting from this work on the laboratory scale can be used on the scale of the underground storage. It is worth noting that the second model, being based on more physical phenomena, will certainly give more relevant predictions. However, performing simulations on the underground storage scale may be time-consuming due to its numerical complexity.

CRediT authorship contribution statement

Firas Tayeb: Conceptualization, Software, Writing – original draft. **Ahmed Rouabhi:** Conceptualization, methodology, Software. **Murad AbuAisha:** Software, Validation. **Alain Valtz:** Validation.

Declaration of competing interest

The authors declare that they have no known competing financial interests or personal relationships that could have appeared to influence the work reported in this paper.

Data availability

The authors are unable or have chosen not to specify which data has been used.

References

Akinfiev, N.N., Diamond, L.W., 2003. Thermodynamic description of aqueous nonelectrolytes at infinite dilution over a wide range of state parameters. Geochim. Cosmochim. Acta 67 (4), 613–629. http://dx.doi.org/10.1016/S0016-7037(02)01141-9.

Archer, D.G., Carter, R.W., 2000. Thermodynamic properties of the nacl + H2O system. 4. heat capacities of H2O and NaCl(aq) in Cold-Stable and supercooled states. J. Phys. Chem. B 104 (35), 8563–8584. http://dx.doi.org/10.1021/jp0003914, Publisher: American Chemical Society.

Azin, R., Mahmoudy, M., Raad, S.M.J., Osfouri, S., 2013. Measurement and modeling of CO2 diffusion coefficient in Saline Aquifer at reservoir conditions. Cent. Eur. J. Eng. 3 (4), 585–594. http://dx.doi.org/10.2478/s13531-012-0069-2.

Bird, R.B., Stewart, W.E., Lightfoot, E.N., 2007. Transport Phenomena, second rev. ed Wiley, New York.

Blanco-Martín, L., Rouabhi, A., Hadj-Hassen, F., 2021. Use of salt caverns in the energy transition: Application to power-to-gas–oxyfuel. J. Energy Storage 44, 103333. http://dx.doi.org/10.1016/j.est.2021.103333.

Caglayan, D.G., Weber, N., Heinrichs, H.U., Linßen, J., Robinius, M., Kukla, P.A., Stolten, D., 2020. Technical potential of salt caverns for hydrogen storage in Europe. Int. J. Hydrogen Energy 45 (11), 6793–6805. http://dx.doi.org/10.1016/j.ijhydene.2019.12.161.

Chabab, S., Théveneau, P., Coquelet, C., Corvisier, J., Paricaud, P., 2020. Measurements and predictive models of high-pressure H2 solubility in brine (H2O+NaCl) for underground hydrogen storage application. Int. J. Hydrogen Energy 45 (56), 32206–32220. http://dx.doi.org/10.1016/j.ijhydene.2020.08.192.

Chabab, S., Théveneau, P., Corvisier, J., Coquelet, C., Paricaud, P., Houriez, C., Ahmar, E.E., 2019. Thermodynamic study of the CO2 – H2O – NaCl system: Measurements of CO2 solubility and modeling of phase equilibria using Soreide and Whitson, electrolyte CPA and SIT models. Int. J. Greenhouse Gas Control 91, 102825. http://dx.doi.org/10.1016/j.ijggc.2019.102825.

Farajzadeh, R., Barati, A., Delil, H.A., Bruining, J., Zitha, P.L.J., 2007. Mass transfer of CO2 into water and surfactant solutions. Petrol. Sci. Technol. 25 (12), 1493–1511. http://dx.doi.org/10.1080/10916460701429498.

Farajzadeh, R., Zitha, P.L.J., Bruining, J., 2009. Enhanced mass transfer of CO2 into water: Experiment and modeling. Ind. Eng. Chem. Res. 48 (13), 6423–6431. http://dx.doi.org/10.1021/ie801521u.

Frank, M.J.W., Kuipers, J.A.M., van Swaaij, W.P.M., 1996. Diffusion coefficients and viscosities of CO2 + H2O, CO2 + CH3OH, NH3 + H2O, and NH3 + CH3OH liquid mixtures. J. Chem. Eng. Data 41 (2), 297–302. http://dx.doi.org/10.1021/je950157k, Publisher: American Chemical Society.

Gholami, Y., Azin, R., Fatehi, R., Osfouri, S., Bahadori, A., 2015. Prediction of carbon dioxide dissolution in bulk water under isothermal pressure decay at different boundary conditions. J. Mol. Liq. 202, 23–33. http://dx.doi.org/10.1016/j.molliq.2014.11.031.

Götz, M., Lefebvre, J., Mörs, F., McDaniel Koch, A., Graf, F., Bajohr, S., Reimert, R., Kolb, T., 2016. Renewable power-to-gas: A technological and economic review. Renew. Energy 85 (C), 1371–1390.

Hassanzadeh, H., Pooladi-Darvish, M., Keith, D.W., 2007. Scaling behavior of convective mixing, with application to geological storage of CO2. AIChE J. 53 (5), 1121–1131. http://dx.doi.org/10.1002/aic.11157.

Kestin, J., Khalifa, H.E., Correia, R.J., 1981. Tables of the dynamic and kinematic viscosity of aqueous KCl solutions in the temperature range 25–150 °C and the pressure range 0.1–35 MPa. J. Phys. Chem. Ref. Data 10 (1), 57–70. http://dx.doi.org/10.1063/1.555640, Publisher: American Institute of Physics.

Kunz, O., Klimeck, R., Wagner, W., Jaeschke, M., 2007. The GERG-2004 Wide-Range Equation of State for Natural Gases and Other Mixtures.

Moghaddam, R.N., Rostami, B., Pourafshary, P., Fallahzadeh, Y., 2012. Quantification of density-driven natural convection for dissolution mechanism in CO 2 sequestration. Transp. Porous Media 92 (2), http://dx.doi.org/10.1007/s11242-011-9911-x.

Mutoru, J.W., Leahy-Dios, A., Firoozabadi, A., 2011. Modeling infinite dilution and Fickian diffusion coefficients of carbon dioxide in water. AIChE J. 57 (6), 1617–1627. http://dx.doi.org/10.1002/aic.12361.

Perera, P.N., Deng, H., Schuck, P.J., Gilbert, B., 2018. Diffusivity of carbon dioxide in aqueous solutions under geologic carbon sequestration conditions. J. Phys. Chem. B 122 (16), 4566–4572. http://dx.doi.org/10.1021/acs.jpcb.8b00802.

Reza Etminan, S., Pooladi-Darvish, M., Maini, B.B., Chen, Z., 2013. Modeling the interface resistance in low soluble gaseous solvents-heavy oil systems. Fuel 105, 672–687. http://dx.doi.org/10.1016/j.fuel.2012.08.048.

Riaz, A., Cinar, Y., 2014. Carbon dioxide sequestration in saline formations: Part I—Review of the modeling of solubility trapping. J. Pet. Sci. Eng. 124, 367–380. http://dx.doi.org/10.1016/j.petrol.2014.07.024.

Riazi, M.R., 1996. A new method for experimental measurement of diffusion coefficients in reservoir fluids. J. Pet. Sci. Eng. 14 (3), 235–250. http://dx.doi.org/10.1016/0920-4105(95)00035-6.

Sell, A., Fadaei, H., Kim, M., Sinton, D., 2013. Measurement of CO2 diffusivity for carbon sequestration: A microfluidic approach for reservoir-specific analysis. Environ. Sci. Technol. 47 (1), 71–78. http://dx.doi.org/10.1021/es303319q.

Shi, Z., Wen, B., Hesse, M.A., Tsotsis, T.T., Jessen, K., 2018. Measurement and modeling of CO2 mass transfer in brine at reservoir conditions. Adv. Water Resour. 113, 100–111. http://dx.doi.org/10.1016/j.advwatres.2017.11.002.

Soubeyran, A., Rouabhi, A., Coquelet, C., 2019. Thermodynamic analysis of carbon dioxide storage in salt caverns to improve the power-to-gas process. Appl. Energy 242, 1090–1107. http://dx.doi.org/10.1016/j.apenergy.2019.03.102.

Tamimi, A., Rinker, E.B., Sandall, O.C., 1994. Diffusion coefficients for hydrogen sulfide, carbon dioxide, and nitrous oxide in water over the temperature range 293-368 K. J. Chem. Eng. Data 39 (2), 330–332. http://dx.doi.org/10.1021/je00014a031.

Tan, K.K., Thorpe, R.B., 1992. Gas diffusion into viscous and non-Newtonian liquids. Chem. Eng. Sci. 47 (13), 3565–3572. http://dx.doi.org/10.1016/0009-2509(92)85071-I.

Upreti, S.R., Mehrotra, A.K., 2000. Experimental measurement of gas diffusivity in bitumen: results for carbon dioxide. Ind. Eng. Chem. Res. 39 (4), 1080–1087. http://dx.doi.org/10.1021/ie990635a.

Yan, W., Huang, S., Stenby, E.H., 2011. Measurement and modeling of CO2 solubility in NaCl brine and CO2–saturated NaCl brine density. Int. J. Greenhouse Gas Control 5 (6), http://dx.doi.org/10.1016/j.ijggc.2011.08.004.

Yang, C., Gu, Y., 2006. Accelerated mass transfer of CO2 in reservoir brine due to density-driven natural convection at high pressures and elevated temperatures. Ind. Eng. Chem. Res. 45 (8), 2430–2436. http://dx.doi.org/10.1021/ie050497r.

Zarghami, S., Boukadi, F., Al-Wahaibi, Y., 2017. Diffusion of carbon dioxide in formation water as a result of CO2 enhanced oil recovery and CO2 sequestration. J. Petrol. Explor. Prod. Technol. 7 (1), 161–168. http://dx.doi.org/10.1007/s13202-016-0261-7.

Zhang, W., Wu, S., Ren, S., Zhang, L., Li, J., 2015. The modeling and experimental studies on the diffusion coefficient of CO2 in saline water. The assessment of CO2 utilization technology in China, J. CO2 Utiliz. The assessment of CO2 utilization technology in China, 11, 49–53.http://dx.doi.org/10.1016/j.jcou.2014.12.009,

Bibliography

AbuAisha, M. (2014). "Enhanced Geothermal Systems: Permeability stimulation through hydraulic fracturing in a thermo-poroelastic framework". PhD dissertation. Grenoble, France: Université de Grenoble.

AbuAisha, M. and J. Billiotte (2021). "A discussion on hydrogen migration in rock salt for tight underground storage with an insight into a laboratory setup". In: *Journal of Energy Storage* 38, p. 102589. ISSN: 2352-152X. DOI: https://doi.org/10.1016/j.est.2021.102589.

AbuAisha, M. and B. Loret (2016a). "Influence of hydraulic fracturing on impedance and efficiency of thermal recovery from HDR reservoirs". In: *Geomechanics for Energy and the Environment* 7, pp. 10–25. ISSN: 2352-3808. DOI: https://doi.org/10.1016/j.gete.2016.02.001.

— (2016b). "Stabilization of Forced Heat Convection: Applications to Enhanced Geothermal Systems (EGS)". In: *Transport in Porous Media* 112.1, 229–252. DOI: https://doi.org/10.1007/s11242-016-0642-x.

AbuAisha, M., B. Loret, and D. Eaton (2016). "Enhanced Geothermal Systems (EGS): Hydraulic fracturing in a thermo-poroelastic framework". In: *Journal of Petroleum Science and Engineering* 146, pp. 1179–1191. ISSN: 0920-4105. DOI: https://doi.org/10.1016/j.petrol.2016.07.027.

AbuAisha, M. and A. Rouabhi (2019). "On the validity of the uniform thermodynamic state approach for underground caverns during fast and slow cycling". In: *International Journal of Heat and Mass Transfer* 142, p. 118424. ISSN: 0017-9310. DOI: https://doi.org/10.1016/j.ijheatmasstransfer.2019.07.074.

AbuAisha, M. et al. (2017). "Hydro-mechanically coupled FDEM framework to investigate near–wellbore hydraulic fracturing in homogeneous and fractured rock formations". In: *Journal of Petroleum Science and Engineering* 154, pp. 100–113. ISSN: 0920-4105. DOI: https://doi.org/10.1016/j.petrol.2017.04.018.

AbuAisha, M. et al. (2019). "Fully coupled hydro-mechanical controls on non-diffusive seismicity triggering front driven by hydraulic fracturing". In: *Journal of Seismology* 23.1, pp. 109–121. ISSN: 1573-157X. DOI: https://doi.org/10.1007/s10950-018-9795-0.

AbuAisha, M. et al. (2021). "Non-isothermal two-phase hydrogen transport in rock salt during cycling in underground caverns". In: *International Journal of Hydrogen Energy* 46.9, pp. 6632–6647. ISSN: 0360-3199. DOI: https://doi.org/10.1016/j.ijhydene.2020.11.152.

AbuAisha, M. et al. (2023). "Geothermal effects on CO2 dissolution kinetics in brine: A non-dimensional model for underground storage in salt caverns". In: *Gas Science and Engineering* 117, p. 205076. ISSN: 2949-9089. DOI: https://doi.org/10.1016/j.jgsce.2023.205076.

Adachi, J. et al. (2007). "Computer simulation of hydraulic fractures". In: *International Journal of Rock Mechanics and Mining Sciences* 44.5, pp. 739–757. ISSN: 1365-1609. DOI: https://doi.org/10.1016/j.ijrmms.2006.11.006.

Atkinson, B. K. (1991). *Fracture Mechanics of Rock*. Second edition. London, Great Britain: Academic Press Limited.

Bannach, A. et al. (2005). *Technology enhancement for (1) inventory assessment and mechanical integrity testing of gas-filled solution mined caverns and (2) mechanical integrity tests of solution mines and liquid storage caverns*. Tech. rep. GRI–05/0175 project final report, prepared for Gas Research Institute.

Barenblatt, G. I. (1962). "The Mathematical Theory of Equilibrium Cracks in Brittle Fracture". In: ed. by H.L. Dryden et al. Vol. 7. Advances in Applied Mechanics. Elsevier, pp. 55–129. DOI: https://doi.org/10.1016/S0065-2156(08)70121-2.

Baria, R. et al. (2000). "Progress at the European HDR project at Soultz-sous-Forêts: Preliminary results from the deepening of the well GPK2 to 5000 m". In: *Proceedings World Geothermal Congress 2000*. Kyushu, Tohoku, Japan.

Battistelli, A., C. Calore, and K. Pruess (1997). "The simulator TOUGH2/EWASG for modelling geothermal reservoirs with brines and non-condensible gas". In: *Geothermics* 26.4, 437 – 464. DOI: https://doi.org/10.1016/S0375-6505(97)00007-2.

Baumgärtner, J. et al. (1996). "The European HDR project at Soultz-sous-Forêts: Stimulation of the second deep well and first circulation experiment". In: *Proceedings of the 21th Workshop on Geothermal Reservoir Engineering*. Stanford, California: Stanford University.

Bear, J. (1972). *Dynamics of fluids in porous media*. American Elsevier Publishing Company, Inc.

Boroumand, N. and D. W. Eaton (2015). "Energy-based hydraulic fracture numerical simulation: Parameter selection and model validation using microseismicity". In: *Geophysics* 80.5, W33–W44. DOI: https://doi.org/10.1190/geo2014-0091.1.

Bourne-Webb, P. J., T. M. Bodas Freitas, and R. A. da Costa Gonçalves (2016). "Thermal and mechanical aspects of the response of embedded retaining walls used as shallow geothermal heat exchangers". In: *Energy and Buildings* 125, pp. 130–141. ISSN: 0378-7788. DOI: https://doi.org/10.1016/j.enbuild.2016.04.075.

Bradley, J. S. (1975). "ABNORMAL FORMATION PRESSURE". In: *AAPG Bulletin (American Association of Petroleum Geologists)* 59.6, pp. 957–973.

Brooks, Alexander N. and Thomas J.R. Hughes (1982). "Streamline upwind/Petrov-Galerkin formulations for convection dominated flows with particular emphasis on the incompressible Navier-Stokes equations". In: *Computer Methods in Applied Mechanics and Engineering* 32.1, pp. 199–259. ISSN: 0045-7825. DOI: https://doi.org/10.1016/0045-7825(82)90071-8.

Bruel, D. (1995a). "Heat extraction modelling from forced fluid flow through stimulated fractured rock masses: application to the Rosemanowes hot dry rock reservoir". In: *Geothermics* 24.3. Hot Dry Rock (HDR) Reservoir Modelling Activities within Europe, pp. 361–374. ISSN: 0375-6505. DOI: https://doi.org/10.1016/0375-6505(95)00014-H.

— (1995b). "Modelling heat extraction from forced fluid flow through stimulated fractured rock masses: evaluation of the soultz-sous-forets site potential". In: *Geothermics* 24.3. Hot Dry Rock (HDR) Reservoir Modelling Activities within Europe, pp. 439–450. ISSN: 0375-6505. DOI: https://doi.org/10.1016/0375-6505(95)00019-M.

— (2007). "Using the migration of the induced seismicity as a constraint for fractured Hot Dry Rock reservoir modelling". In: *International Journal of Rock Mechanics and Mining Sciences* 44.8, pp. 1106–1117. ISSN: 1365-1609. DOI: https://doi.org/10.1016/j.ijrmms.2007.07.001.

Burger, J., P. Sourieau, and M. Combarnous (1985). *Thermal methods of oil recovery*. Paris: Editions Technip.

Busse, F. H. and J. A. Whitehead (1971). "Instabilities of convection rolls in a high Prandtl number fluid". In: *Journal of Fluid Mechanics* 47.2, pp. 305–320. DOI: https://doi.org/10.1017/S0022112071001071.

Bérest, P. and F. Louvet (2020). "Aspects of the thermodynamic behavior of salt caverns used for gas storage". In: *Oil & Gas Science and Technology–Revue d'IFP Energies nouvelles* 75, p. 57.

Caglayan, D. G. et al. (2020). "Technical potential of salt caverns for hydrogen storage in Europe". In: *International Journal of Hydrogen Energy* 45.11, pp. 6793–6805. ISSN: 0360-3199. DOI: https://doi.org/10.1016/j.ijhydene.2019.12.161.

Calcagni, B., F. Marsili, and M. Paroncini (2005). "Natural convective heat transfer in square enclosures heated from below". In: *Applied thermal engineering* 25.16, pp. 2522–2531. DOI: https://doi.org/10.1016/j.applthermaleng.2004.11.032.

Chabab, S. et al. (2019). "Thermodynamic study of the CO2-H2O-NaCl system: Measurements of CO2 solubility and modeling of phase equilibria using Soreide and Whitson, electrolyte CPA and SIT models". In: *International Journal of Greenhouse Gas Control* 91, p. 102825. ISSN: 1750-5836. DOI: https://doi.org/10.1016/j.ijggc.2019.102825.

Charnavel, Y., D. Leca, and F. Poulain (1999). "Advanced geometrical modelling of salt dissolution during cavern leaching – illustration with a case study". In: The SMRI Meeting. Las Vegas, Nevada, USA.

Chen, Y., C. Zhou, and Y. Sheng (2007). "Formulation of strain-dependent hydraulic conductivity for a fractured rock mass". In: *International Journal of Rock Mechanics and Mining Sciences* 44.7, pp. 981–996. ISSN: 1365-1609. DOI: https://doi.org/10.1016/j.ijrmms.2006.12.004.

Chen, Z., G. Huan, and Y. Ma (2006). *Computational Methods for Multiphase Flows in Porous Media*. SIAM.

Chou, Q., J. Gao, and M. Somerwil (Jan. 2011). "Analysis of Geomechanical Data for Horn River Basin Gas Shales, NE British Columbia, Canada". In: vol. All Days. SPE Middle East Unconventional Resources Conference and Exhibition, SPE–142498–MS.

Chromik, M. and W. Korzeniowski (2021). "A Method to Increase the Leaching Progress of Salt Caverns with the Use of the Hydro-Jet Technique". In: *Energies* 14.18. ISSN: 1996-1073. DOI: https://doi.org/10.3390/en14185833.

Class, H., R. Helmig, and P. Bastian (2002). "Numerical simulation of non-isothermal multiphase multicomponent processes in porous media.: 1. An efficient solution technique". In: *Advances in Water Resources* 25.5, pp. 533–550. ISSN: 0309-1708. DOI: https://doi.org/10.1016/S0309-1708(02)00014-3.

Cornet, F. H. (Feb. 2000). "Comment on 'Large-scale in situ permeability tensor of rocks from induced microseismicity' by S. A. Shapiro, P. Audigane and J.-J. Royer". In: *Geophysical Journal International* 140.2, pp. 465–469. ISSN: 0956-540X. DOI: https://doi.org/10.1046/j.1365-246x.2000.00018.x.

Cornet, F.H., Th. Bérard, and S. Bourouis (2007). "How close to failure is a granite rock mass at a 5km depth?" In: *International Journal of Rock Mechanics and Mining Sciences* 44.1, pp. 47–66. ISSN: 1365-1609. DOI: https://doi.org/10.1016/j.ijrmms.2006.04.008.

Cosenza, Ph. et al. (1999). "In situ rock salt permeability measurement for long term safety assessment of storage". In: *International Journal of Rock Mechanics and Mining Sciences* 36.4, pp. 509–526. ISSN: 1365-1609. DOI: https://doi.org/10.1016/S0148-9062(99)00017-0.

Crozier, T. E. and S. Yamamoto (1974). "Solubility of hydrogen in water, sea water, and sodium chloride solutions". In: *Journal of Chemical and Engineering Data* 19.3, pp. 242–244.

Côté, J. and J. M. Konrad (2005). "A generalized thermal conductivity model for soils and construction materials". In: *Canadian Geotechnical Journal* 42.2, pp. 443–458. DOI: https://doi.org/10.1139/t04-106.

Damjanac, B. and P. Cundall (2016). "Application of distinct element methods to simulation of hydraulic fracturing in naturally fractured reservoirs". In: *Computers and Geotechnics* 71, pp. 283–294. ISSN: 0266-352X. DOI: https://doi.org/10.1016/j.compgeo.2015.06.007.

Dinske, C. and Shapiro S. A. Rutledge J. T. (2010). "Interpretation of Microseismicity Resulting from Gel and Water Fracturing of Tight Gas Reservoirs". In: *Pure and Applied Geophysic* 167.1, pp. 169–182. DOI: https://doi.org/10.1007/s00024-009-0003-6.

Duan, K., C. Kwok, and W. Wu (2018). "DEM modeling of hydraulic fracturing in permeable rock: influence of viscosity, injection rate and in situ states". In: *Acta Geotechnica* 13, pp. 1187–1202. ISSN: 1861-1133. DOI: https://doi.org/10.1007/s11440-018-0627-8.

Eaton, D. W. et al. (2014). "Breakdown of the Gutenberg-Richter relation for microearthquakes induced by hydraulic fracturing: influence of stratabound fractures". In: *Geophysical Prospecting* 62.4, pp. 806–818. DOI: https://doi.org/10.1111/1365-2478.12128.

Evans, K. et al. (2009). *Studies and Support for the EGS Reservoirs at Soultz-sous-Forêts*. Tech. rep. University of Neuchâtel: Centre for Geothermal Research - CREGE.

Everett, D. H. (1975). "Thermodynamics of multiphase fluids in porous media". In: *Journal of Colloid and Interface Science* 52.1, pp. 189–198. ISSN: 0021-9797. DOI: https://doi.org/10.1016/0021-9797(75)90316-1.

Feistel, R. et al. (2010). "Thermodynamic properties of sea air". In: *Ocean Science* 6.1, pp. 91–141. DOI: https://doi.org/10.5194/os-6-91-2010.

Fer, F. (1970). *Thermodynamique macroscopique, Tome I: systèmes fermés*. Gordon and Breach, Science Publishers Ltd.

— (1971). *Thermodynamique macroscopique, Tome II: systèmes ouverts*. Gordon and Breach, Science Publishers Ltd.

Fjaer, E. et al. (2008). *Petroleum related rock mechanics*. Second edition. Radarweg 29, 1000 AE Amsterdam, The Netherlands: Elsevier B.V.

Forsyth, P. A. and R. B. Simpson (2012). "A two-phase, two-component model for natural convection in a porous medium". In: *International Journal for Numerical Methods in Fluids* 12.7, pp. 655–682. DOI: https://doi.org/10.1002/fld.1650120705.

Francke, H. and M. Thorade (2010). "Density and viscosity of brine: An overview from a process engineers perspective". In: *Geochemistry* 70. Geoenergy: From Visions to Solutions, pp. 23–32. ISSN: 0009-2819. DOI: https://doi.org/10.1016/j.chemer.2010.05.015.

Fries, T. P. and H. G. Matthies (2004). "A Review of Petrov-Galerkin Stabilization Approaches and an Extension to Meshfree Methods". In: *Informatikbericht Nr. 2004-01. Technische Universitaet Braunschweig*. Braunschweig, Germany.

Fu, P., S. M. Johnson, and C. R. Carrigan (2013). "An explicitly coupled hydro-geomechanical model for simulating hydraulic fracturing in arbitrary discrete fracture networks". In: *International Journal for Numerical and Analytical Methods in Geomechanics* 37.14, pp. 2278–2300. DOI: https://doi.org/10.1002/nag.2135.

Gelet, R., B. Loret, and N. Khalili (2012a). "A thermo-hydro-mechanical coupled model in local thermal non-equilibrium for fractured HDR reservoir with double porosity". In: *Journal of Geophysical Research: Solid Earth* 117.B7, B07205. DOI: https://doi.org/10.1029/2012JB009161.

— (2012b). "Borehole stability analysis in a thermoporoelastic dual-porosity medium". In: *International Journal of Rock Mechanics and Mining Sciences* 50, pp. 65–76. ISSN: 1365-1609. DOI: https://doi.org/10.1016/j.ijrmms.2011.12.003.

— (2013). "Thermal recovery from a fractured medium in local thermal non-equilibrium". In: *International Journal for Numerical and Analytical Methods in Geomechanics* 37.15, pp. 2471–2501. DOI: https://doi.org/10.1002/nag.2145.

Gevantman, L. H. and J. Lorenz (1981). *Physical properties data for rock salt*. Vol. 167. US Department of Commerce, National Bureau of Standards.

Grathwohl, P. (2012). *Diffusion in Natural Porous Media: Contaminant Transport, Sorption/Desorption and Dissolution Kinetics*. Topics in Environmental Fluid Mechanics. Springer US. ISBN: 9781461556831.

Gray, W. G. and C. T. Miller (2014). *Introduction to the Thermodynamically Constrained Averaging Theory for Porous Medium Systems*. Springer.

Grecksch, G. et al. (2003). "Hydraulic fracturing at the European HDR/HFR test site Soultz-sous-Forêts (France) a conceptual model". In: *Proceedings of the European Geothermal Conference*. Leibniz Institute for Applied Geosciences, Germany.

Guo, C. et al. (2017). "Numerical investigation of a joint approach to thermal energy storage and compressed air energy storage in aquifers". In: *Applied Energy* 203, pp. 948–958. ISSN: 0306-2619. DOI: https://doi.org/10.1016/j.apenergy.2017.06.030.

Harari, I. (2004). "Stability of semidiscrete formulations for parabolic problems at small time steps". In: *Computer Methods in Applied Mechanics and Engineering* 193.15. Recent Advances in Stabilized and Multiscale Finite Element Methods, pp. 1491–1516. ISSN: 0045-7825. DOI: https://doi.org/10.1016/j.cma.2003.12.035.

Hasnaoui, M., E. Bilgen, and P. Vasseur (1992). "Natural convection heat transfer in rectangular cavities partially heated from below". In: *Journal of Thermophysics and Heat transfer* 6.2, pp. 255–264. DOI: https://doi.org/10.2514/3.353.

Hassanizadeh, M. S. and W. G. Gray (1990). "Mechanics and thermodynamics of multiphase flow in porous media including interphase boundaries". In: *Advances in Water Resources* 13.4, pp. 169–186. ISSN: 0309-1708. DOI: https://doi.org/10.1016/0309-1708(90)90040-B.

Hauke, G., G. Sangalli, and M. H. Doweidar (2007). "COMBINING ADJOINT STABILIZED METHODS FOR THE ADVECTION-DIFFUSION-REACTION PROBLEM". In: *Mathematical Models and Methods in Applied Sciences* 17.02, pp. 305–326. DOI: https://doi.org/10.1142/S0218202507001929.

Hughes, T. J. R. (2000). *The Finite Element Method; Linear Static and Dynamic Finite Element Analysis*. Second edition. Dover, Mineola: Paris: Editions Technip.

Hughes, T. J. R., L. P. Franca, and G. M. Hulbert (1989). "A new finite element formulation for computational fluid dynamics: VIII. The galerkin/least-squares method for advective-diffusive equations". In: *Computer Methods in Applied Mechanics and Engineering* 73.2, pp. 173–189. ISSN: 0045-7825. DOI: https://doi.org/10.1016/0045-7825(89)90111-4.

Jiang, F., L. Luo, and J. Chen (2013). "A novel three-dimensional transient model for subsurface heat exchange in enhanced geothermal systems". In: *International Communications in Heat and Mass Transfer* 41, pp. 57–62. ISSN: 0735-1933. DOI: https://doi.org/10.1016/j.icheatmasstransfer.2012.11.003.

John, V. and P. Knobloch (2007). "On spurious oscillations at layers diminishing (SOLD) methods for convection–diffusion equations: Part I – A review". In: *Computer Methods in Applied Mechanics and Engineering* 196.17, pp. 2197–2215. ISSN: 0045-7825. DOI: https://doi.org/10.1016/j.cma.2006.11.013.

Jupe, A.J. et al. (1995). "Modelling of a european prototype hdr reservoir". In: *Geothermics* 24.3. Hot Dry Rock (HDR) Reservoir Modelling Activities within Europe, pp. 403–419. ISSN: 0375-6505. DOI: https://doi.org/10.1016/0375-6505(95)00017-K.

Karimi-Jafari, M. (2010). "Comportement transitoire des cavités salines profondes". PhD dissertation. Paris, France: Ecole Polytechnique X.

Kaviany, M. (2002). *Principles of Heat Transfer in Porous Media*. Second edition. New York, USA: John Wiley & sons.

Klimczak, C. et al. (2010). "Cubic law with aperture-length correlation: implications for network scale fluid flow". In: *Hydrogeology Journal* 18, pp. 851–862. DOI: https://doi.org/10.1007/s10040-009-0572-6.

Klumpp, F. (2016). "Comparison of pumped hydro, hydrogen storage and compressed air energy storage for integrating high shares of renewable energies-Potential, cost-comparison and ranking". In: *Journal of Energy Storage* 8, pp. 119–128. ISSN: 2352-152X. DOI: https://doi.org/10.1016/j.est.2016.09.012.

Kolditz, O. (1995). "Modelling flow and heat transfer in fractured rocks: dimensional effect of matrix heat diffusion". In: *Geothermics* 24.3. Hot Dry Rock (HDR) Reservoir Modelling Activities within Europe, pp. 421–437. ISSN: 0375-6505. DOI: https://doi.org/10.1016/0375-6505(95)00018-L.

Kolditz, O. et al. (2012). *Thermo-Hydro-Mechanical-Chemical Processes in Porous Media*. Volume 86. Springer.

Kondepudi, D. and I. Prigogine (2014). *Modern Thermodynamics: From Heat Engines to Dissipative Structures*. John Wiley and Sons, Ltd.

Kunz, O. and W. Wagner (2012). "The GERG-2008 wide-range equation of state for natural gases and other mixtures: an expansion of GERG-2004". In: *Journal of chemical & engineering data* 57.11, pp. 3032–3091. DOI: https://doi.org/10.1021/je300655b.

Kunz, O. et al. (2007). *The GERG-2004 wide-range equation of state for natural gases and other mixtures*.

Labaune, P. et al. (2019). "Dilatancy Criteria for Salt Cavern Design: A Comparison Between Stress- and Strain-Based Approaches". In: *Rock Mechanics and Rock Engineering* 51.2, pp. 599–611. ISSN: 1434-453X. DOI: https://doi.org/10.1007/s00603-017-1338-4.

Lacasse, D., E. Turgeon, and D. Pelletier (2004). "On the judicious use of the $k - \epsilon$ model, wall functions and adaptivity". In: *International Journal of Thermal Sciences* 43.10, pp. 925–938. ISSN: 1290-0729. DOI: https://doi.org/10.1016/j.ijthermalsci.2004.03.004.

Lee, S. H. and A. Ghassemi (2010). "Thermo-poroelastic analysis of injection-induced rock deformation and damage evolution". In: *Proceedings of the Thirty-Fifth Workshop on Geothermal Reservoir Engineering*. Stanford, California: Stanford University.

— (2011). "Three-dimensional thermo-poro-mechanical modeling of reservoir stimulation and induced microseismicity in geothermal reservoir". In: *Proceedings of the Thirty-Sixth Workshop on Geothermal Reservoir Engineering*. Stanford, California: Stanford University.

Lenormand, R. et al. (1989). "Flow through porous media: limits of fractal patterns". In: *Proceedings of the Royal Society of London. A. Mathematical and Physical Sciences* 423.1864, pp. 159–168. DOI: https://doi.org/10.1098/rspa.1989.0048.

Likhachev, E.R. (2003). "Dependence of water viscosity on temperature and pressure". In: *Technical Physics* 48.4, 514 – 515. DOI: https://doi.org/10.1134/1.1568496.

Lisjak, A., G. Grasselli, and T. Vietor (2014). "Continuum–discontinuum analysis of failure mechanisms around unsupported circular excavations in anisotropic clay shales". In: *International Journal of Rock Mechanics and Mining Sciences* 65, pp. 96–115. ISSN: 1365-1609. DOI: https://doi.org/10.1016/j.ijrmms.2013.10.006.

Lisjak, A. et al. (2017). "A 2D, fully-coupled, hydro-mechanical, FDEM formulation for modelling fracturing processes in discontinuous, porous rock masses". In: *Computers and Geotechnics* 81, pp. 1–18. ISSN: 0266-352X. DOI: https://doi.org/10.1016/j.compgeo.2016.07.009.

Lopez-Lazaro, C. et al. (2019). "Predicting the phase behavior of hydrogen in NaCl brines by molecular simulation for geological applications". In: *Bulletin de la Société Géologique de France* 190.1.

Loret, B. (2018). *Fluid injection in deformable geological formations: Energy related issues*. Springer.

Loret, B. and F. M. F. Simões (2017). *Biomechanical aspects of soft tissues*. Crc Press.

Lund, J. (2009). "Development and Utilization of Geothermal Resources". In: *Proceedings of ISES World Congress 2007*, Vol. I –Vol. V.

Mahabadi, O. K. et al. (2012). "Y-Geo: New Combined Finite-Discrete Element Numerical Code for Geomechanical Applications". In: *International Journal of Geomechanics* 12.6, pp. 676–688. ISSN: 1365-1609. DOI: https://doi.org/10.1061/(ASCE)GM.1943-5622.0000216.

Mahjoub, M. et al. (2018). "Numerical Study of Callovo-Oxfordian Argillite Expansion due to Gas Injection". In: *International Journal of Geomechanics* 18.1, p. 04017134. DOI: https://doi.org/10.1061/(ASCE)GM.1943-5622.0001050.

Marle, C. M. (1982). "On macroscopic equations governing multiphase flow with diffusion and chemical reactions in porous media". In: *International Journal of Engineering Science* 20.5, pp. 643–662. ISSN: 0020-7225. DOI: https://doi.org/10.1016/0020-7225(82)90118-5.

Matos, C. R., J. F. Carneiro, and P. P. Silva (2019). "Overview of Large-Scale Underground Energy Storage Technologies for Integration of Renewable Energies and Criteria for Reservoir Identification". In: *Journal of Energy Storage* 21, pp. 241–258. ISSN: 2352-152X. DOI: https://doi.org/10.1016/j.est.2018.11.023.

McTigue, D. F. (1986). "Thermoelastic response of fluid-saturated porous rock". In: *Journal of Geophysical Research: Solid Earth* 91.B9, pp. 9533–9542. DOI: https://doi.org/10.1029/JB091iB09p09533.

Mebrahtu, C. et al. (2019). "Chapter 5 - CO2 Methanation: Principles and Challenges". In: *Horizons in Sustainable Industrial Chemistry and Catalysis*. Ed. by Stefania Albonetti, Siglinda

Perathoner, and Elsje Alessandra Quadrelli. Vol. 178. Studies in Surface Science and Catalysis. Elsevier, pp. 85–103. DOI: https://doi.org/10.1016/B978-0-444-64127-4.00005-7.

Mualem, Y. (1978). "Hydraulic conductivity of unsaturated porous media: Generalized macroscopic approach". In: *Water Resources Research* 14.2, pp. 325–334. DOI: https://doi.org/10.1029/WR014i002p00325.

Munjiza, A. (2004). *The Combined Finite-Discrete Element Method*. USA: John Wiley & Sons, Ltd.

Munjiza, A., D. R. Owen, and N. Bićanić (1995). "A combined finite-discrete element method in transient dynamics of fracturing solids". In: *Engineering Computations* 12, pp. 145–174. URL: https://api.semanticscholar.org/CorpusID:120965932.

Murphy, H. et al. (1999). "Hydraulics and well testing of engineered geothermal reservoirs". In: *Geothermics* 28.4, pp. 491–506. ISSN: 0375-6505. DOI: https://doi.org/10.1016/S0375-6505(99)00025-5.

Papanastasiou, P. (1999). "The effective fracture toughness in hydraulic fracturing". In: *International Journal of Fracture* 96.2, 127 – 147. DOI: https://doi.org/10.1023/A:1018676212444.

Papanastasiou, P. and M. Thiercelin (1993). "Influence of inelastic rock behaviour in hydraulic fracturing". In: *International Journal of Rock Mechanics and Mining Sciences & Geomechanics Abstracts* 30.7, pp. 1241–1247. ISSN: 0148-9062. DOI: https://doi.org/10.1016/0148-9062(93)90102-J.

Poppei, J. et al. (2006). "Flooding of an abandoned salt mine modeling two-phase flow in complex mine structures". In: *The proceedings of the TOUGH symposium*. Berkeley, California: Lawrence Berkeley National Laboratory.

Raju, M. and S. K. Khaitan (2012). "Modeling and simulation of compressed air storage in caverns: A case study of the Huntorf plant". In: *Applied Energy* 89.1. Special issue on Thermal Energy Management in the Process Industries, pp. 474–481. ISSN: 0306-2619. DOI: https://doi.org/10.1016/j.apenergy.2011.08.019.

Reynolds, M. M. and D. L. Munn (Feb. 2010). "Development Update for an Emerging Shale Gas Giant Field—Horn River Basin, British Columbia, Canada". In: vol. All Days. SPE Unconventional Resources Conference / Gas Technology Symposium, SPE–130103–MS.

Roa Pinto, J. S. et al. (2021). "Modeling phase equilibrium of hydrogen and natural gas in brines: Application to storage in salt caverns". In: *International Journal of Hydrogen Energy* 46.5, pp. 4229–4240. ISSN: 0360-3199. DOI: https://doi.org/10.1016/j.ijhydene.2020.10.242.

Roche, V. and M. van der Baan (2017). "Modeling of the in situ state of stress in elastic layered rock subject to stress and strain-driven tectonic forces". In: *Solid Earth* 8.2, pp. 479–498. DOI: https://doi.org/10.5194/se-8-479-2017.

Rogers, S. et al. (Oct. 2010). "Understanding Hydraulic Fracture Geometry and Interactions in the Horn River Basin through DFN and Numerical Modeling". In: vol. All Days. SPE Canada Unconventional Resources Conference, SPE–137488–MS.

Rouabhi, A. (2019). "Problèmes de thermodynamique et de thermo-hydro-mécanique associés à l'exploitation du sous-sol". In: *Matériaux et structures en mécanique [physics.class-ph]. Sorbonne Université*.

Rouabhi, A. et al. (2017). "A multiphase multicomponent modeling approach of underground salt cavern storage". In: *Geomechanics for Energy and the Environment* 12, pp. 21–35. ISSN: 2352-3808. DOI: https://doi.org/10.1016/j.gete.2017.08.002.

On Estimating the Water Content of CO2 in Equilibrium with Formation Brine (June 2008). Vol. All Days. PETSOC Canadian International Petroleum Conference, PETSOC–2008–084. DOI: https://doi.org/10.2118/2008-084.

Sankar, M. et al. (2011). "Numerical study of natural convection in a vertical porous annulus with discrete heating". In: *International Journal of Heat and Mass Transfer* 54.7, pp. 1493–1505. ISSN: 0017-9310. DOI: https://doi.org/10.1016/j.ijheatmasstransfer.2010.11.043.

Santoyo, E. et al. (2001). "Rheological property measurement of drilling fluids used in geothermal wells". In: *Applied Thermal Engineering* 21.3, pp. 283–302. ISSN: 1359-4311. DOI: https://doi.org/10.1016/S1359-4311(00)00003-X.

Santoyo-Gutiérrez, S., G. Espinosa, and G. Amaro-Espejo (2005). "Effect of variable rheological properties of drilling muds and cements on the temperature distribution in geothermal wells." In: *Proceedings of World Geothermal Congress 2005*. Turkey, Antalya.

Schulze, O., T. Popp, and H. Kern (2001a). "Development of damage and permeability in deforming rock salt". In: *Engineering Geology* 61.2. Geosciences and Nuclear Waste Disposal, pp. 163–180. ISSN: 0013-7952. DOI: https://doi.org/10.1016/S0013-7952(01)00051-5.

— (2001b). "Development of damage and permeability in deforming rock salt". In: *Engineering Geology* 61.2, pp. 163–180. ISSN: 0013-7952. DOI: https://doi.org/10.1016/S0013-7952(01)00051-5.

Schwertz, F. A. and J. E. Brow (May 1951). "Diffusivity of Water Vapor in Some Common Gases". In: *The Journal of Chemical Physics* 19.5, pp. 640–646. ISSN: 0021-9606. DOI: https://doi.org/10.1063/1.1748306.

Shao, J. F., H. Zhou, and K. T. Chau (2005). "Coupling between anisotropic damage and permeability variation in brittle rocks". In: *International Journal for Numerical and Analytical Methods in Geomechanics* 29.12, pp. 1231–1247. DOI: https://doi.org/10.1002/nag.457.

Shapiro, S. A. and C. Dinske (2009a). "Fluid-induced seismicity: Pressure diffusion and hydraulic fracturing". In: *Geophysical Prospecting* 57.2, pp. 301–310. DOI: https://doi.org/10.1111/j.1365-2478.2008.00770.x.

— (2009b). "Scaling of seismicity induced by nonlinear fluid-rock interaction". In: *Journal of Geophysical Research: Solid Earth* 114.B9. DOI: https://doi.org/10.1029/2008JB006145.

Shapiro, S. A., C. Dinske, and E. Rothert (2006). "Hydraulic-fracturing controlled dynamics of microseismic clouds". In: *Geophysical Research Letters* 33.14. DOI: https://doi.org/10.1029/2006GL026365.

Shapiro, S. A. et al. (Jan. 2002). "Characterization of fluid transport properties of reservoirs using induced microseismicity". In: *Geophysics* 67.1, pp. 212–220. ISSN: 0016-8033. DOI: https://doi.org/10.1190/1.1451597.

Sousani, M. et al. (2015). "Simulation of the hydraulic fracturing process of fractured rocks by the discrete element method". In: *Environmental Earth Sciences* 73, pp. 8451–8469. ISSN: 1866-6299. DOI: https://doi.org/10.1007/s12665-014-4005-z.

Svendsen, B. and K. Hutter (1995). "On the thermodynamics of a mixture of isotropic materials with constraints". In: *International Journal of Engineering Science* 33.14, pp. 2021–2054. ISSN: 0020-7225. DOI: https://doi.org/10.1016/0020-7225(95)00044-X.

Tatone, B. S. A. and G. Grasselli (2015). "A calibration procedure for two-dimensional laboratory-scale hybrid finite–discrete element simulations". In: *International Journal of Rock Mechanics and Mining Sciences* 75, pp. 56–72. ISSN: 1365-1609. DOI: https://doi.org/10.1016/j.ijrmms.2015.01.011.

Tayeb, F. et al. (2023). "Kinetics of CO2 dissolution for underground applications". In: *Geoenergy Science and Engineering* 230, p. 212061. ISSN: 2949-8910. DOI: https://doi.org/10.1016/j.geoen.2023.212061.

Tezduyar, T. E. and Y. J. Park (1986). "Discontinuity-capturing finite element formulations for nonlinear convection-diffusion-reaction equations". In: *Computer Methods in Applied Mechanics and Engineering* 59.3, pp. 307–325. ISSN: 0045-7825. DOI: https://doi.org/10.1016/0045-7825(86)90003-4.

Tsilingiris, P.T. (2008). "Thermophysical and transport properties of humid air at temperature range between 0 and 100°C". In: *Energy Conversion and Management* 49.5, pp. 1098–1110. ISSN: 0196-8904. DOI: https://doi.org/10.1016/j.enconman.2007.09.015.

Turcotte, D. L. and G. Schubert (2002). *Geodynamics*. Second edition. Cambridge, England, UK: Cambridge University Press.

Valtz, A. et al. (2004). "Vapour-liquid equilibria in the carbon dioxide-water system, measurement and modelling from 278.2 to 318.2K". In: *Fluid Phase Equilibria* 226, pp. 333–344. ISSN: 0378-3812. DOI: https://doi.org/10.1016/j.fluid.2004.10.013.

van Genuchten, M. Th. (1980). "A Closed-form Equation for Predicting the Hydraulic Conductivity of Unsaturated Soils". In: *Soil Science Society of America Journal* 44.5, pp. 892–898. DOI: https://doi.org/10.2136/sssaj1980.03615995004400050002x.

Yan, W., S. Huang, and E. H. Stenby (2011). "Measurement and modeling of CO2 solubility in NaCl brine and CO2-saturated NaCl brine density". In: *International Journal of Greenhouse Gas Control* 5.6, pp. 1460–1477. ISSN: 1750-5836. DOI: https://doi.org/10.1016/j.ijggc.2011.08.004.

Yang, C. and Y. Gu (2006). "Accelerated Mass Transfer of CO2 in Reservoir Brine Due to Density-Driven Natural Convection at High Pressures and Elevated Temperatures". In: *Industrial & Engineering Chemistry Research* 45.8, pp. 2430–2436. ISSN: 0888-5885. DOI: https://doi.org/10.1021/ie050497r.

Yew, C. H. and X. Weng (2014). *Mechanics of Hydraulic Fracturing*. Second edition. USA: Gulf Professional Publishing.

Yin, S., M. B. Dusseault, and L. Rothenburg (2009). "Thermal reservoir modeling in petroleum geomechanics". In: *International Journal for Numerical and Analytical Methods in Geomechanics* 33.4, pp. 449–485. DOI: https://doi.org/10.1002/nag.723.

Yortsos, Y. C., B. Xu, and D. Salin (1997). "Phase diagram of fully developed drainage in porous media". In: *Physical Review Letters* 79.23, pp. 4581–4584. DOI: https://doi.org/10.1103/PhysRevLett.79.4581.

Zhang, J., A. Gupta, and J. Baker (2007). "Effect of relative humidity on the prediction of natural convection heat transfer coefficients". In: *Heat transfer engineering* 28.4, pp. 335–342. DOI: https://doi.org/10.1080/01457630601122823.

Zhang, X. et al. (2022). "Large-scale CO2 disposal/storage in bedded rock salt caverns of China: An evaluation of safety and suitability". In: *Energy* 249, p. 123727. ISSN: 0360-5442. DOI: https://doi.org/10.1016/j.energy.2022.123727.